Modélisation des réponses calciques de réseaux d'astrocytes : Relations entre topologie et dynamiques

Jules Lallouette

N° d'ordre 2014ISAL0122
Année 2014

Thèse

Modélisation des réponses calciques de réseaux d'astrocytes : Relations entre topologie et dynamiques

Présentée devant
L'institut national des sciences appliquées de Lyon

Pour obtenir
Le grade de docteur

École doctorale
École doctorale Informatique et Mathématiques (ED512)

Par
Jules Lallouette
Ingénieur INSA Lyon Informatique

Soutenance prévue le 4 Décembre 2014 devant la Commission d'examen :

Jury MM.

Hugues Berry	Directeur de recherche, INRIA, Directeur de thèse
Bruno Cessac	Directeur de recherche, INRIA, Rapporteur
Alain Destexhe	Directeur de recherche, CNRS, Examinateur
Marja-Leena Linne	Directrice de recherche, Tampere University, Rapporteuse
Aude Panatier	Chargée de recherche, CNRS, Examinatrice
Hédi Soula	Maître de conférence, INSA, Examinateur
Laurent Venance	Directeur de recherche, INSERM, Examinateur

Laboratoire de recherche :
Laboratoire d'InfoRmatique en Image et Systèmes d'information
LIRIS CNRS UMR5205

INSA Direction de la Recherche - Ecoles Doctorales – Quinquennal 2011-2015

SIGLE	ECOLE DOCTORALE	NOM ET COORDONNEES DU RESPONSABLE
CHIMIE	**CHIMIE DE LYON** **http://www.edchimie-lyon.fr** Sec : Renée EL MELHEM Bat Blaise Pascal 3e etage 04 72 43 80 46 Insa : R. GOURDON	M. Jean Marc LANCELIN Université de Lyon – Collège Doctoral Bât ESCPE 43 bd du 11 novembre 1918 69622 VILLEURBANNE Cedex Tél : 04.72.43 13 95 directeur@edchimie-lyon.fr
E.E.A.	**ELECTRONIQUE, ELECTROTECHNIQUE, AUTOMATIQUE** **http://edeea.ec-lyon.fr** Sec : M.C. HAVGOUDOUKIAN eea@ec-lyon.fr	M. Gérard SCORLETTI Ecole Centrale de Lyon 36 avenue Guy de Collongue 69134 ECULLY Tél : 04.72.18 60.97 Fax : 04 78 43 37 17 Gerard.scorletti@ec-lyon.fr
E2M2	**EVOLUTION, ECOSYSTEME, MICROBIOLOGIE, MODELISATION** **http://e2m2.universite-lyon.fr** Sec : Safia AIT CHALAL Bat Darwin - UCB Lyon 1 04.72.43.28.91 Insa : H. CHARLES Safia.ait-chalal@univ-lyon1.fr	Mme Gudrun BORNETTE CNRS UMR 5023 LEHNA Université Claude Bernard Lyon 1 Bât Forel 43 bd du 11 novembre 1918 69622 VILLEURBANNE Cédex Tél : 06.07.53.89.13 e2m2@ univ-lyon1.fr
EDISS	**INTERDISCIPLINAIRE SCIENCES-SANTE** **http://www.ediss-lyon.fr** Sec : Safia AIT CHALAL Hôpital Louis Pradel - Bron 04 72 68 49 09 Insa : M. LAGARDE Safia.ait-chalal@univ-lyon1.fr	Mme Emmanuelle CANET-SOULAS INSERM U1060, CarMeN lab, Univ. Lyon 1 Bâtiment IMBL 11 avenue Jean Capelle INSA de Lyon 696621 Villeurbanne Tél : 04.72.68.49.09 Fax :04 72 68 49 16 Emmanuelle.canet@univ-lyon1.fr
INFOMATHS	**INFORMATIQUE ET MATHEMATIQUES** **http://infomaths.univ-lyon1.fr** Sec :Renée EL MELHEM Bat Blaise Pascal 3e etage infomaths@univ-lyon1.fr	Mme Sylvie CALABRETTO LIRIS – INSA de Lyon Bat Blaise Pascal 7 avenue Jean Capelle 69622 VILLEURBANNE Cedex Tél : 04.72. 43. 80. 46 Fax 04 72 43 16 87 Sylvie.calabretto@insa-lyon.fr
Matériaux	**MATERIAUX DE LYON** **http://ed34.universite-lyon.fr** Sec : M. LABOUNE PM : 71.70 –Fax : 87.12 Bat. Saint Exupéry Ed.materiaux@insa-lyon.fr	M. Jean-Yves BUFFIERE INSA de Lyon MATEIS Bâtiment Saint Exupéry 7 avenue Jean Capelle 69621 VILLEURBANNE Cedex Tél : 04.72.43 71.70 Fax 04 72 43 85 28 Ed.materiaux@insa-lyon.fr
MEGA	**MECANIQUE, ENERGETIQUE, GENIE CIVIL, ACOUSTIQUE** **http://mega.universite-lyon.fr** Sec : M. LABOUNE PM : 71.70 –Fax : 87.12 Bat. Saint Exupéry mega@insa-lyon.fr	M. Philippe BOISSE INSA de Lyon Laboratoire LAMCOS Bâtiment Jacquard 25 bis avenue Jean Capelle 69621 VILLEURBANNE Cedex Tél : 04.72 .43.71.70 Fax : 04 72 43 72 37 Philippe.boisse@insa-lyon.fr
ScSo	**ScSo*** **http://recherche.univ-lyon2.fr/scso/** Sec : Viviane POLSINELLI Brigitte DUBOIS Insa : J.Y. TOUSSAINT viviane.polsinelli@univ-lyon2.fr	Mme Isabelle VON BUELTZINGLOEWEN Université Lyon 2 86 rue Pasteur 69365 LYON Cedex 07 Tél : 04.78.77.23.86 Fax : 04.37.28.04.48

*ScSo : Histoire, Géographie, Aménagement, Urbanisme, Archéologie, Science politique, Sociologie, Anthropologie

Remerciements

Résumé

Pendant les 20 dernières années, les astrocytes, un type de cellules cérébrales ayant été jusque là relativement ignoré des neuroscientifiques, ont peu à peu gagné en notoriété grâce à de multiples découvertes. Jusque dans les années 80, les rôles attribués aux astrocytes étaient principalement des rôles de 'soutien' aux neurones: maintenir l'homéostasie cérébrale (i.e. l'équilibre des concentrations ioniques extracellulaires, et des niveaux de neurotransmetteurs) ; fournir de l'énergie (sous la forme d'adénosine triphosphate (ATP) ou de lactate) aux neurones ; protéger les neurones en cas de situations pathologiques (en cas d'ischémie consécutive à un accident vasculaire cérébral par exemple). Contrairement aux neurones, les astrocytes ne transmettent pas de signaux électriques. C'est ce 'silence' qui a conduit les premiers neuroscientifiques à leurs attribuer des taches 'subalternes', réservant le beau rôle (pensée, sentiments, et toute manifestation complexe du cerveau) aux neurones. Seulement ce n'est pas que les astrocytes ne 'parlaient' pas, c'est qu'on ne savait pas les écouter. En effet, les astrocytes sont actifs mais communiquent par des changements intracellulaires de leurs concentrations en calcium. Ces changements n'ont cependant pu être observés qu'après l'invention de fluorochromes spécifiques permettant de rendre visible des variations de calcium intracellulaires. Depuis, les astrocytes sont de plus en plus reconnus comme des cellules actives du système nerveux central. Des découvertes récentes semblent même indiquer que, loins d'agir en autarcie, les astrocytes répondent à l'activité neuronale et sembleraient, bien que cela soit plus débattu, moduler la transmission synaptique par le relargage de molécules spécifiques appellées 'gliotransmetteurs' (en référence aux neurotransmetteurs). Les neurones communiquent en effet principalement par l'intermédiaire de points de contact, appellés synapses, par lesquels un neurone présynaptique communique par le relargage de neurotransmetteurs avec un neurone postsynaptique. Ces synapses sont très petites (moins d'un micromètre) et extrêmement nombreuses dans le cerveau, on estime le nombre de neurones dans le cerveau humain à plus de 90 milliards et chaque neurone forme en moyenne 10 000 synapses. Les astrocytes, grâce à à leur morphologie complexe formée de branches principales (visibles en vert sur la figure 1A) qui se ramifient à plusieurs reprises en branches de plus en plus fines (visible en rouge sur la figure 1A), entourent les synapses et peuvent donc 'écouter' et 'répondre' à l'activité synaptique par des élevations de concentration de leur calcium intracellulaire. On estime que chaque astrocyte peut ainsi envelopper jusqu'à 2 millions de synapses dans le cerveau humain (140 000 chez les rongeurs).

Comme les neurones, les astrocytes forment des réseaux grâce à l'expression de protéines transmembranaires spécifiques appellées connexines (visibles en rouge sur la partie gauche

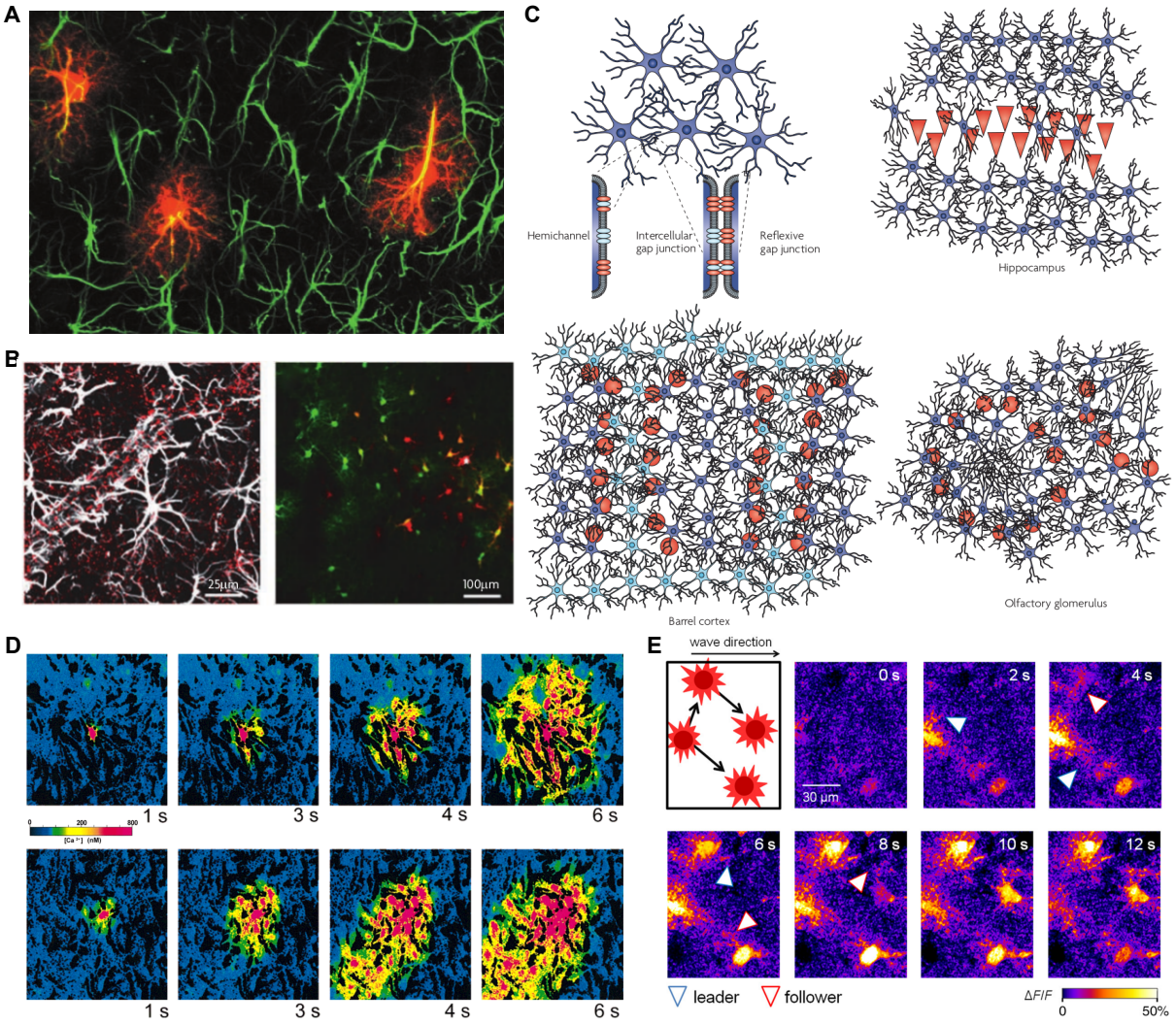

Figure 1: Diversité morphologique des astrocytes. **A** Immunomarquage des protéines GFAP dans la région CA1 du stratum radiatum. Les trois astrocytes remplis de fluorochrome (*rouge*) ont une morphologie bien plus complexe que celle que l'on voit avec l'immunomarquage (*vert*). Image extraite de Bushong et al. (2002). **B** Partie gauche : immunomarquage des protéines GFAP en *blanc* et des Connexines en *rouge*. Les connexines sont exprimées en bordure de territoires. Partie droite: immunomarquege GFAP en *vert* associé à une injection de fluorochrome (*rouge*) dans l'astrocyte pointé par la flèche blanche. La diffusion du fluorochrome par les jonctions gap permet de visualiser le réseau auquel l'astrocyte est rattaché. Certains astrocytes proches de l'injections ne font pas partie du réseau. Image prise de Giaume et al. (2010). **C** Représentation schématique de différentes topologies de réseaux d'astrocytes. Image prise de Giaume et al. (2010). **D** Propagation de vagues de calcium initiées par stimulation méchanique d'une culture cellulaire. Haut: en condition normale, la vague se propage de manière concentrique. Bas: en perfusant le milieu extracellulaire, la vague est emportée dans la direction de perfusion, indiquant la présence de communication paracrine. Image prise de Charles (1998). **E** Visualisation in vivo de vagues de calcium dans l'hippocampe d'une souris. Image prise de Kuga et al. (2011).

de la figure 1B). Ces connexines s'apparient et peuvent ainsi créer une jonction gap, connectant les cytosols de deux astrocytes et permettant la diffusion de petites molécules entre astrocytes. La façon dont ces réseaux sont connectés n'est cependant pas triviale ; la partie droite de la figure 1B montre, par injection dans l'astrocyte pointé par la flèche blanche d'un fluorochrome pouvant diffuser à travers les jonctions gap, que certains astrocytes (en vert) proches de l'astrocyte injecté ne font pas partie du même réseau. Ainsi, il n'a été découvert que très récement que la topologie de ces réseaux pourrait s'averer plus complexe que la vision qui dominait jusqu'alors : celle d'un syncitium astrocytaire dépourvu de spécificités topologiques. La figure 1C représente schématiquement differentes topologies de réseaux d'astrocytes dans différentes zones de cerveaux de rongeurs. Dans le stratum pyramidale de l'hippocampe, la forte présence de neurones (triangles rouges dans le quart supérieur droit) empêche les astrocytes d'être fortement connectés. Dans le cortex somatosensoriel (quart inférieur gauche) et dans le bulbe olfactif (quart inférieur droit), les astrocytes sont plus connectés à l'intérieur de certaines structures qu'à l'extérieur.

Ces réseaux d'astrocytes, en plus de contribuer au rôle de maintien de l'homéostasie, permettent la propagation de vagues de calcium. La Figure 1D par exemple (ligne supérieure), présente la propagation d'une vague de calcium déclenchée par stimulation mécanique dans une culture cellulaire. Contrairement aux neurones, dont les influx nerveux se propagent à une vitesse proche de 100m.s^{-1}, les vagues de calcium dans les réseaux d'astrocytes se propagent beaucoup plus lentement, à $15\mu\text{m.s}^{-1}$. Deux voies de signalisation sont connues pour la propagation de vagues calciques astrocytaires:

– l'une implique la diffusion par les jonctions gap d'un second messager l'inositol 1,4,5-triphosphate (IP_3) qui provoque l'ouverture de canaux perméables au calcium sur le reticulum endoplasmique (qui agit içi comme un réservoir de calcium);
– l'autre implique la diffusion extracellulaire d'ATP qui active des récepteurs couplés aux protéines G (récepteurs purinergique de la famille P2Y dans ce cas) qui, en conséquence, stimulent la production intracellulaire d'IP_3.

La seconde voie de signalisation est mise en évidence par la figure 1D (ligne inférieure): le milieu de culture est mis en mouvement par perfusion du coin supérieur droit vers le coin inférieur gauche, la vague de calcium est provoquée de la même manière que précédemment mais cette fois la vague de calcium se propage dans la même direction que la perfusion, indiquant qu'un messager extra-cellulaire est à l'oeuvre. Les premières expériences réalisées sur des animaux vivants (in vivo) ont révélés des réponses calciques d'astrocytes à l'activité neuronale mais ces réponses restaient généralement restreintes à un ou quelques astrocytes. L'existence de vague de calcium dans des conditions physiologiques a donc été mise en doute et leurs présence dans les cultures cellulaires ou les preparations en tranches a été perçue comme un artefact de ces systèmes. Des expériences in vivo encore plus récentes viennent cependant contredire cette hypothèse, des vagues de calcium de grande ampleur ayant été observées dans l'hippocampe de souris (figure 1E, zoom sur 4 astrocytes). Il semble en effet que certains facteurs expérimentaux communs aux premières études in vivo (la puissance du laser du microscope deux-photons ou encore l'utilisation d'animaux anesthésiés) influencent l'activité calcique des astrocytes et empêchent donc l'observation de vagues calciques conséquentes. Pour résumer, deux réseaux, de neurones et d'astrocytes, cohabitent ainsi dans le cerveau ; mais, alors que les réseaux de neu-

rones ont fait l'objet de beaucoup de recherches expérimentales et théoriques, les réseaux d'astrocytes restent encore mal connus. De plus, la découverte récente de leurs différentes topologies conduit à s'interroger sur le rôle que celles çi pourraient jouer sur la propagation de vagues calciques. Les travaux présentés dans cette thèse portent ainsi principalement sur ce thème. En effet, autant au niveau subcellulaire qu'inter-cellulaire, les mécanismes gouvernant l'activité calcique des astrocytes restent mals connus. Même dans le cas le plus documenté de la réponse somatique des astrocytes à une stimulation neuronale, les caractéristiques précises que la stimulation doit avoir pour évoquer une réponse des astrocytes sont inconnues. Il en est de même pour la transmission de vagues de calcium dans des réseaux d'astrocytes: on ignore encore les possibles effets de la complexité récemment documentée des réseaux d'astrocytes sur la propagation de ces vagues. Les travaux présentés dans cette thèse utilisent des outils de modélisation et de simulation afin d'étudier ces différentes questions.

Le chapitre IV porte sur l'étude de la communication de neurones vers astrocytes et fait état de travaux menés en collaboration avec le groupe de Yael Hanein à l'université de Tel-Aviv. Nos collaborateurs ont travaillé sur la partie experimentale du problème et nous nous sommes occuppés de la partie théorique. Nous avons utilisé un modèle mathématique de signalisation calcique astrocytaire (représenté sur la figure 2A) dont on pourrait résumer le fonctionnement de la façon suivante :

- la concentration en IP_3 intracellulaire de l'astrocyte i augmente suite à une stimulation neuronale glutamatergique ou à l'activation d'un de ses voisins;
- l'IP_3 se lie aux recepteurs IP_3R du reticulum endoplasmique, ce qui provoque un relargage de calcium dans le cytosol (et donc un 'pic' de calcium intracellulaire), qui augmente encore le relargage de calcium ;
- une trop grande concentration de calcium inhibe les IP_3Rs qui ferment leur canaux et mettent fin au relargage de calcium ;
- le calcium est réintegré dans le reticulum endoplasmique par des pompes SERCA ;
- durant ce cycle, une quantité additionelle d'IP_3 a été créée et peut donc diffuser de l'astrocyte i à ses voisins, ce qui peut, s'il y atteint une concentration suffisante, perpetuer la vague calcique.

Ce chapitre nous permet tout d'abord de valider experimentalement le comportement de notre modèle de signalisation calcique astrocytaire en vérifiant bien que les résultats experimentaux et les simulations du modèle sont en accord. Ensuite, dans ce chapitre, nous cherchons à déterminer quelles sont les charactéristiques qui déterminent la réponse ou l'absence de réponse d'astrocytes à des stimulations neuronales. Pour ce faire, nous utilisons un dispositif experimental représenté sur la figure 2B et visible sur la figure 2C (Multi Electrode Array) permettant de contrôler la fréquence d'activation des neurones tout en bloquant la transmission synaptique. Nous pouvons ainsi étudier spécifiquement la communication de neurones vers astrocytes. Pour chaque expérience, nous construisons son équivalent simulé en estimant le réseau d'astrocytes de cette expérience (figure 2D). Les résultats expérimentaux démontrent que la réponse des astrocytes dépend principalement de la fréquence de stimulation, autrement dit, les astrocytes jouent en quelque sorte le rôle d'un filtre passe-haut. Les simulations montrent la même chose mais permettent en revanche de mieux comprendre l'hétérogénéité des réponses astrocytaires. En effet, certains astrocytes répondent à des fréquences de stimulation neuronales plus faible que d'autres.

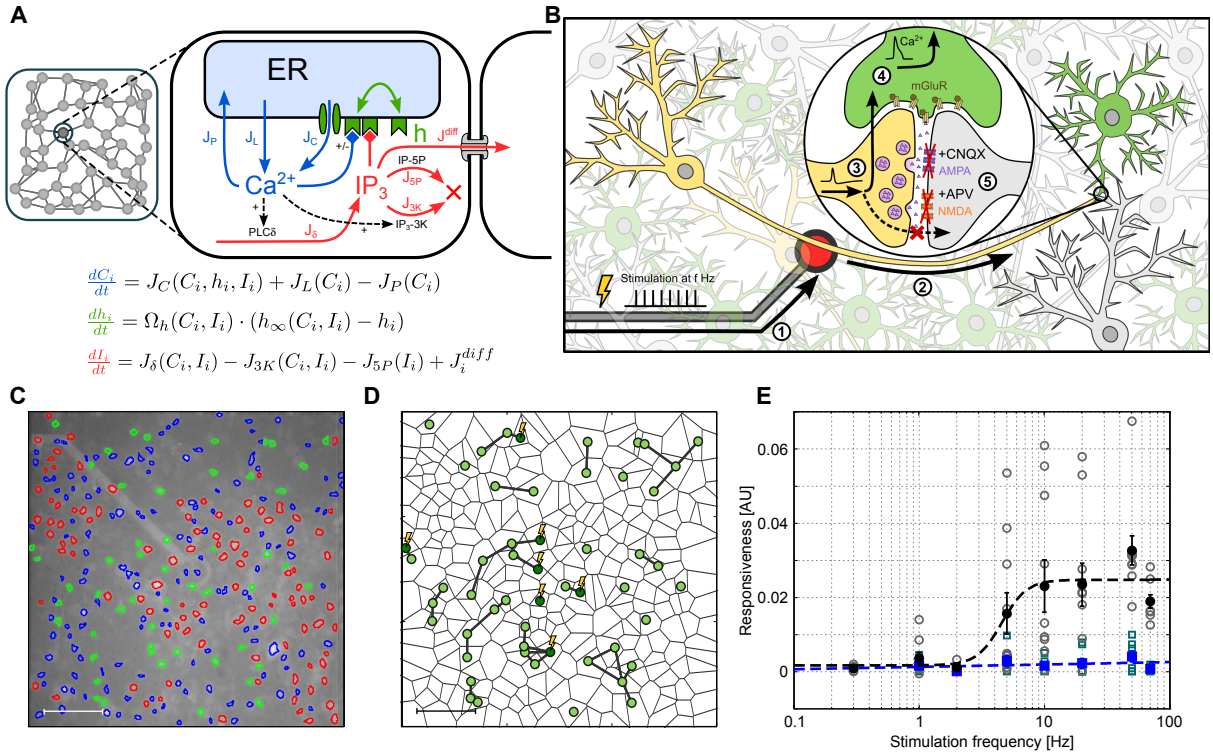

Figure 2: Modèle de dynamiques calciques et signalisation neurones-astrocytes. **A** Representation schématique du modèle utilisé. Chaque astrocyte est constitué du modèle de signalisation calcique représenté à droite de la figure. Le second messager responsable de la propagation des vagues de calcium, l'IP_3, diffuse par les jonctions gap et conduit à l'activation des astrocytes lorsqu'il est suffisament accumulé. Les équations associées à chaque astrocyte sont écrites en bas. Le réseau sur la gauche représente la façon dont les astrocytes sont interconnectés. **B** Représentation schématique du protocol experimental utilisé lors de l'étude de la communication neurones-astrocytes (chapitre IV). Les communications neurones-neurones sont bloqués par l'adjonction de CNQX et d'APV, des bloqueurs de récepteurs ionotropiques postsynaptiques. Seule la communication neurone-astrocyte reste active et les neurones sont stimulés par des électrodes extracellulaires à une certaine fréquence. **C** Image représentative des culture mixtes neurones-astrocytes utilisées pour étudier la communication de neurones vers astrocytes. Les cellules sont identifiées automatiquement: en vert les astrocytes, en rouge les neurones, et en bleu les cellules dont le signal calcique n'a pas permis d'identifier si ces cellules étaient des neurones ou des astrocytes. **D** Reconstruction du réseau d'astrocytes qui sera ensuite utilisé pour simuler le modèle. Les éclairs indiquent les astrocytes (cercles verts) qui seront stimulés par des neurones. **E** Les astrocytes ne répondent aux stimulations neuronales qu'au delà d'une certaine fréquence de stimulation, et pas simplement au delà d'une intensité de stimulation.

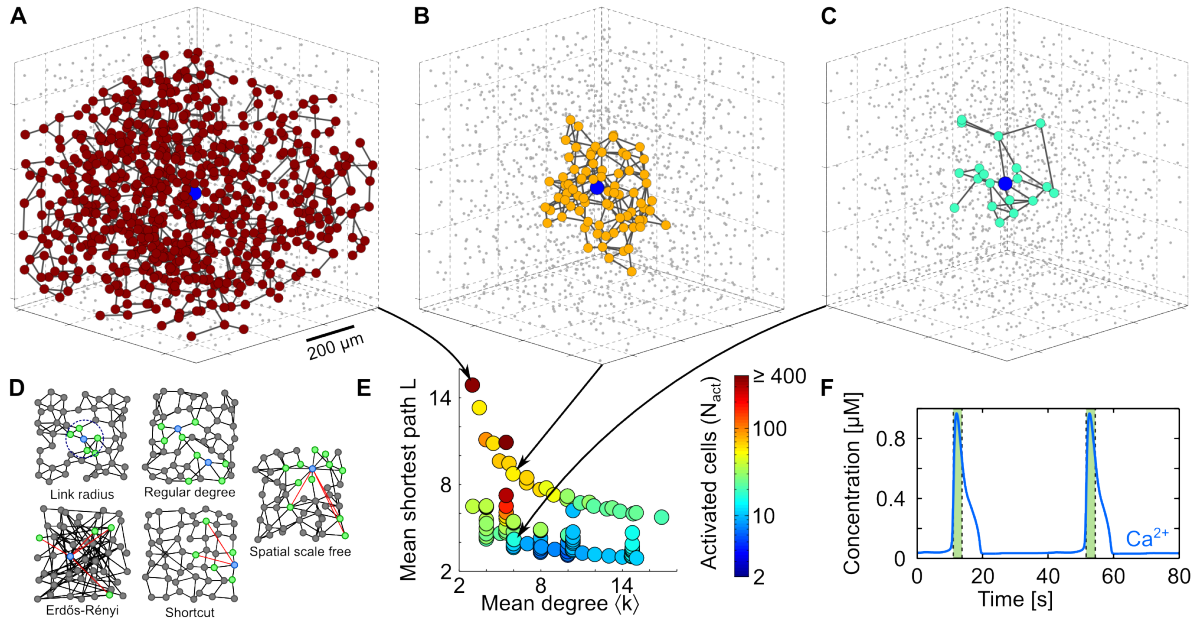

Figure 3: Influence de la topologie de réseaux d'astrocytes sur la propagation de vagues calciques. **A**, **B** et **C** Visualisation en 3D de tous les astrocytes activés par une vague de calcium venant du centre du réseau (de l'astrocyte *bleu*). Le code couleur correspond au nombre d'astrocytes activés (c.f. E). **D** Représentation en 2D des différentes topologies de réseaux d'astrocytes utilisées lors des simulations (les vrais réseaux sont en 3D). **E** Toutes les topologies sont représentées en fonction de leur degré moyen $\langle k \rangle$ et de leur plus petit chemin moyen L. Le code couleur correspond au nombre d'astrocytes N_{act} activés par la vague de calcium. Plus les réseaux sont peu couplés et ont de hautes valeurs de L, plus les vagues de calcium activent d'astrocytes. **F** Exemple de signal calcique simulé par le modèle ; un astrocyte est considéré comme étant activé (zone vertes) lorsque sa concentration en Ca^{2+} dépasse 0.7μM.

De plus, les fréquences maximales d'ocillation calcique dans les astrocytes semblent être distribuées de façon bimodale. Dans le modèle, les même hétérogénéités de fréquence de réponse et de fréquences d'oscillation calciques sont présentes et sont directement liées au nombre de voisins auxquels un astrocyte est connecté. Si un astrocyte est couplé par jonctions gap à beaucoup de ses voisins, il ne répond qu'à des fréquences de stimulation neuronales très élevées avec des oscillations calciques de faible fréquence (inversement pour les astrocytes peu/non couplés). Cette hypothèse est indirectement vérifiée dans les données expérimentales en montrant que la fréquence à laquelle un astrocyte commence à répondre est correllée à sa fréquence maximale d'oscillation calciques.

Ayant montré que la façon dont les astrocytes sont connectés peut avoir un effet important sur leur signalisation calcique au niveau de chaque astrocyte, nous étudions, dans le chapitre V, l'effet que différentes topologies de réseaux d'astrocytes peuvent avoir sur la propagation de vagues calciques. Pour ce faire, nous simulons la même stimulation et sans changer les paramètres biophysiques du modèle mais en ne changeant que les topologies de réseaux. Bien que la figure 3D présente une version 2D de ces différentes topologies, toutes les simulations sont réalisés en 3D. Les réseaux testés vont ainsi de réseaux dont les astrocytes ne sont connectés qu'avec leurs proches voisins, jusqu'à des réseaux com-

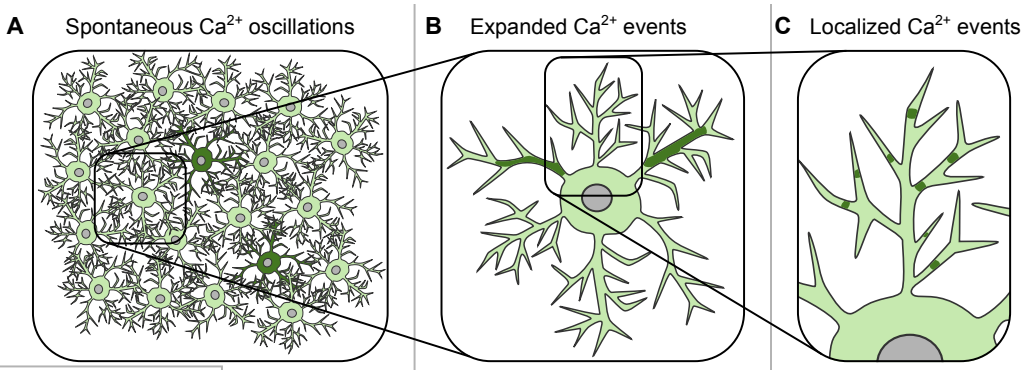

Frequency [Hz]			
per subregion (1 µm)	-	-	~ 0.03 Hz
per process (20 µm)	-	~ 0.016 Hz	~ 1.2 Hz
per astrocyte (50 µm)	~ 0.015 Hz	~ 0.12 Hz	~ 9 Hz

Figure 4: Les astrocytes oscillent aléatoirement à plusieurs échelles spatiales. **A** Les astrocytes peuvent s'activer aléatoirement même en l'absence de stimulation neuronale. La fréquence à laquelle ils s'activent est relativement faible mais l'on ignore encore si ces activations jouent un rôle. **B** À l'intérieur de chaque astrocytes, des sous parties de prolongements cytoplasmiques peuvent s'activer aléatoirement. **C** À une échelle spatialle encore plus faible, des petites parties de prolongements cytoplasmiques distants s'activent aussi aléatoirement. Ces processus sont actifs à des échelles spatiales qui vont de 1 à 50μm et à des fréquences (rapportées à un astrocytes) qui peuvent varier de 0.01 à 10 Hz.

plètement aléatoires (Erdős-Rényi) ou dont les degrés sont fortement hétérogènes. Toutes les simulations se comportent de la même façon contre-intuitive: plus les réseaux sont connectés, moins les vagues de calcium se propagent; de même, plus les liens sont restreints à un voisinage spatial, plus les vagues calciques se propagent loin. Ces résultats sont synthétiquement représentés par les figures 3A, B, C et E (c.f. légende de la figure). L'on montre ensuite que le même comportement peut être qualitativement reproduit par un modèle très simplifié de la façon dont les vagues calciques se propagent. Ce type d'effet, du à des charactéristiques statistiques des réseaux simulés permet par exemple de mieux comprendre certains phénomènes expérimentaux qui n'avaient pas été traités sous cet angle. Ainsi, il est compréhensible que les cultures cellulaires soient plus propices aux vagues calcique que les réseaux d'astrocytes in vivo, étant donné que le milieu de culture réduit fortement leur degré moyen $\langle k \rangle$.

Enfin, le chapitre VI traite des oscillations calciques aléatoires et spontanées observées dans les astrocytes à plusieurs échelles spatialles (c.f. figure 4A, B, C), de la sous partie de leurs prolongements cytoplasmiques ($\approx 1\mu$m) à l'astrocyte entier ($\approx 50\mu$m). On ignore encore le rôle, si elles en ont un, de ces oscillations spontanées qui sont indépendantes de l'activité neuronale. Nous avons donc étudié, en simulant ce même type d'oscillations à des fréquences variées dans notre modèle de signalisation calcique, l'effet sur la propagation de vagues de calcium. Pour certaines gammes de fréquences (qui dépendent des charactéristiques topologiques des réseaux d'astrocytes), la propagation de vagues de calcium est favorisée alors qu'elle est perturbée par toute autre fréquence. Ce phénomène de résonnance stochastique permet d'interpréter ces oscillations spontanées autrement que

comme un bruit inévitable mais nuisible à la communication inter-astrocytaire.

En résumé, nous proposons que la topologie des réseaux d'astrocytes a (1) des répercussion au niveau cellulaire, modulant la réponse des astrocytes à des stimulations neuronales; (2) contrôle la propagation de vagues de calcium inter-astrocytaire en la favorisant lorsque les réseau sont peu couplés; (3) joue un rôle important dans l'apparation de phénomènes de résonance stochastique; (4) peut être dynamiquement modulée par l'activité neuronale.

Mots-clés : Astrocyte, signalisation calcique, réseaux complexes, topologie de réseau, neurosciences computationnelles.

English title, abstract and keywords

Modeling calcium responses in astrocyte networks: Relationships between topology and dynamics

Over the last 20 years, astrocytes, a hitherto under-investigated type of brain cells, have gradually rose to prominence owing to multiple experimental discoveries. In contrast with neurons, these cells do not propagate electrical signals but communicate instead through changes in their intracellular calcium concentration. Recent discoveries indicate that, far from being isolated cells, astrocytes respond to neuronal activity and, although this is still controversial, seem to modulate synaptic transmission through the release of 'gliotransmitter' molecules (in reference to neurotransmitters). Like neurons, astrocyte are organized in networks and communicate their calcium activity by intercellular diffusion of second messengers, forming intercellular calcium waves. Two networks, one of neurons and the other of astrocytes, thus coexist in the brain; while neuronal networks have been the subject of intense experimental and theoretical investigations, astrocyte networks have been much less investigated. Notably, it was only discovered recently that astrocyte network topology could be more complex than what the hitherto dominant view held (astrocytes organized in a syncytium deprived of any topological specificities). The work presented in this thesis is mainly related to the effect that different network topologies could have on astrocyte calcium signaling. The mechanisms that drive calcium signaling in astrocytes are, at both subcellular and intercellular levels, still not completely understood. Even in the best documented case of astrocyte somatic response to neuronal stimulation, the precise characteristic required from the stimulation to elicit an astrocytic response are still unknown. Similarly, the mechanisms governing intercellular calcium wave propagation in astrocyte networks are not fully known; notably, the effects of the recently documented network heterogeneity on calcium wave propagation have not been investigated. Finally, at the subcellular level, astrocytes display an extremely ramified and complex morphology that also hosts calcium activity. The work presented in this thesis make use of modeling and simulation in order to determine the possible effects of astrocyte network organization on their calcium signaling. We propose that astrocyte network topology: (1) controls single-cell responses to neuronal stimulation; (2) drives the propagation of intercellular calcium waves by favoring it when networks are weakly coupled; (3) can determine the appearance of stochastic resonance phenomena; (4) can be modulated by neuronal activity.

Keywords : Astrocyte, calcium signalisation, complex network, network topology, computational neurosciences.

List of publications

Publications

Gilad Wallach*, Lallouette*, J., Herzog, N., De Pittà, M., Ben Jacob, E., Berry, H., and Hanein, Y. Glutamate Mediated Astrocytic Filtering of Neuronal Activity. *PLoS Computational Biology*. **In Press**.
* : These authors contributed equally to this work

Lallouette, J., De Pittà, M., Ben-Jacob, E., and Berry, H. Sparse short-distance connections enhance calcium wave propagation in a 3d model of astrocyte networks. *Frontiers in computational neuroscience*, 8, 2014.

Lallouette, J. and Berry, H.. Topology drives calcium wave propagation in 3d astrocyte networks. In *Proceedings of the European Conference on Complex Systems 2012*, pages 453–463. Springer, 2013.

Communications

Lallouette, J., De Pittà, M., Ben-Jacob, E. and Berry, H. The topology of astrocyte networks controls the propagation of intercellular calcium waves. *CNS Quebec 2014* (poster).

Lallouette, J., Goldberg, M., De Pittà, M., Ben-Jacob, E. and Berry, H. The remarkable effect of network topology on calcium wave propagation in astrocyte networks. *FENS Barcelona 2012* (poster).

Lallouette, J., and Berry, H. Topology drives calcium wave propagation in 3D astrocyte networks. *ECCS 2012* (Oral presentation).

Contents

List of Figures

List of Tables

Part A

Astrocyte physiology and network modeling

Chapter I

Astrocyte physiology

I.1 Historical perspective

Similarly to numerous experimental sciences, the development of neurosciences was strongly driven by the discovery of new experimental procedures that opened up worlds of previously unknown complexity. Before 1873 and the invention, by Camillo Golgi, of its now famous staining technique, the study of brain was dominated by disciplines with phenomenological approaches like phrenology; the brain was mainly considered as an homogeneous tissue with specialized areas corresponding to different psychological traits. Although the cellular theory was developing during the 18th and the early 19th century, the observation of nerve cells was very preliminary because of the technical limitations imposed by light microscopy without staining. The invention of Golgi staining, that allowed the observation of whole cells with their detailed processes, paved the way to the neural doctrine promoted by Santiago Ramón y Cajal. This latter described in great details neuronal structures and posited that neurons constituted independent territories, in opposition to the reticularist school of thought which defended the idea that neurons were all connected into a diffuse network. Galvani's work on frog nerve-muscle preparations already demonstrated at the end of the 18th century that nerve signaling was electrical and, at the end of the 19th century, the first measurements of action potentials hinted that exchanges of Na^+ and K^+ were at play. By the end of the 19th century, most neuroscientists were thus convinced that neurons were the cellular substrate to thoughts and emotions.

During the 20th century, the development of several experimental techniques allowed fast progresses. Intracellular electrodes together with the voltage-clamp technique allowed Alan Hodgkin and Andrew Huxley to record action potentials from the giant squid axon and develop an ionic theory of membrane excitability in 1952. The later development and subsequent improvements of the patch-clamp technique then allowed, around 1980, the investigation of neurons in slices, in vivo, and the detailed characterization of the properties of ion channels that supported the aforementioned excitability. In parallel to these

electrophysiological progresses, the first neurotransmitter, acetylcholine, was discovered in 1914, followed by noradrenalin in 1946. At the end of the 20th century, neurotransmitters were thought to be exclusively used by neurons; but the eventual recognition that non-neuronal cells also expressed neurotransmitter receptors and could themselves release neurotransmitters fundamentally changed the way these cells were perceived.

I.1.1 From Nervenkitt to astroglia

For a detailed account of the history of astroglia, the interested reader can report himself to Kettenmann and Ransom (2004) and Verkhratsky and Butt (2013). The preceding neurocentric summary reflected the prevailing opinions among the neuroscientific community until the very end of the 20th century. In parallel however, non-neuronal cells were not completely ignored but, even if they were discovered during the same period, they were not seen as having the same functional significance as neurons. From the middle of the 19th century, neuroscientists believed that a distinction could be made in the brain between active elements giving rise to higher brain functions and passive elements playing various menial roles. This view was partly fueled by the characterization, by Rudolf Ludwig Karl Vichow in 1856, of non-neuronal cells as 'Nervenkitt' (or neuroglia in english) which he viewed as a connective tissue, even devoid of cellular organization, which offered structural support for neurons. The term itself, 'glia', was derived from greek to express the concept of an informal sticky mass. Ironically, some cells that would later be known as glial cells were identified but without linking them to neuroglia: among others, retinal radial glial cells (Müller cells) were identified in 1851 by Heinrich Müller and radial glial cells in the cerebellum (Bergman glial cells) were identified by Karl Bergman in 1857. Camillo Golgi, making use of his newly invented staining technique, was the first to show that the sticky mass was not so informal but was rather composed of cells that were different from neurons. Although being a promoter of the neural doctrine, Santiago Ramón y Cajal was also interested in glia and showed that astrocytes, that were named that way because of their star-like shape, originated from radial glia and still divided in the adult brain. During the next century, the glial family tree increased with the development of staining techniques that were specific to some glial cells: in 1893, specific staining of astrocytes allowed to characterize their protoplasmic and fibrous versions (occuring respectively in grey and white matter); oligodendrocytes, were characterized as myelinating glial cells in 1921; microglial cells were characterized as cells reacting to brain damage in 1932; and finally, in 1980, NG2-glia were characterized as oligodendrocyte progenitor cells.

While new glial cells were being discovered, their perceived role in brain functioning gradually changed. In contrast with Virchow's views, Golgi posited that glial cells, because of their specific position contacting both blood vessels and neurons, may be responsible for 'feeding' neurons. Carl Weigert, even after the discovery of the cellular nature of glia, defended that these cells were only structural elements, filling the space that was not occupied by neurons. Ramón y Cajal had a different view and thought that glial cells were mainly isolating neurons at their contact points and could control the information flow between neurons by morphological changes. This view was one of the firsts to posit

an active role for glial cells; in 1907 Ernesto Lugaro was already suggesting that astroglial processes were closely associated to synaptic structures and that neuroglia was taking up or degrading chemicals used for neuronal communication (that would later be characterized as neurotransmitters). The involvement of astrocytes in scar formation following brain damage and in several pathologies were documented during the 1920s. In 1951, Fernando de Castro suggested that glial cells could participate in neural transmission by releasing neuroactive substances. These new active roles for neuroglial cells were not however widely accepted by the neuroscientists community and, up until the 1980's, glial cells were still viewed as relatively passive elements of the brain.

The advent of new experimental techniques helped change this view. First, in the late 1950's, although being electrically passive, glial cells were shown to be electrically coupled. This single fact however did not change the perception of glial cells as passive supporting cells. The concomitant introduction of specific cell-culture techniques to isolate astrocytes (McCarthy and De Vellis, 1980) and of fluorescent calcium dyes were instrumental in revealing that astrocytes, although electrically passive, were chemically active with changes in their intracellular Ca^{2+} concentration. Early experiments first demonstrated that astrocytes expressed receptors to neurotransmitters like Glutamate and GABA (Kettenmann and Schachner, 1985) and were thus capable of sensing neuronal activity. This astrocytic response to neuro-transmitters was then shown, in cell cultures, to be able to propagate over long distances to other astrocytes (Cornell-Bell et al., 1990). Recognized astrocyte abilities thus switched in approximately 10 years from passive elements to cells that responded to neuronal activity and could communicate between themselves. The last 'missing piece', the astrocyte-to-neuron communication pathways, was revealed in the 1990s (Nedergaard, 1994; Parpura et al., 1994; Pasti et al., 1997) by showing astrocyte-caused glutamate-dependent calcium increases in neurons. Finally, with the recent improvement of imaging techniques, we are now starting to discover the intricate subcellular signaling phenomena that happen in astrocyte processes relatively independently of the hitherto observed somatic Ca^{2+} activity.

I.1.2 Astroglial diversity

Since this thesis is primarily concerned with astrocytes, we will focus on the morphological characteristics that astrocytes display and quickly review the morphologies of some other astroglial cells. We must first stress that precise characterization of astrocytes among glial cells is not straightforward; while some characteristics like their stellate morphology or the expression of specific markers are sometimes used, they do not allow the characterization of all astrocytes. As an example, the expression of intermediate filament proteins that form astrocyte cytoskeleton such as Glial Fibrillary Acidic Proteins (GFAP, Figure I.1B shows immunolabeling of astrocytic GFAP in *green*) and vimentin, which are both classical marker for astrocytes, can change between brain regions and even be absent in some astrocytes (Verkhratsky and Butt, 2013). Astroglial cells can be classified in several subcategories; here, we will only present a subset of these categories and the interested reader might refer himself to Zhang and Barres (2010) or Verkhratsky and Butt (2013)

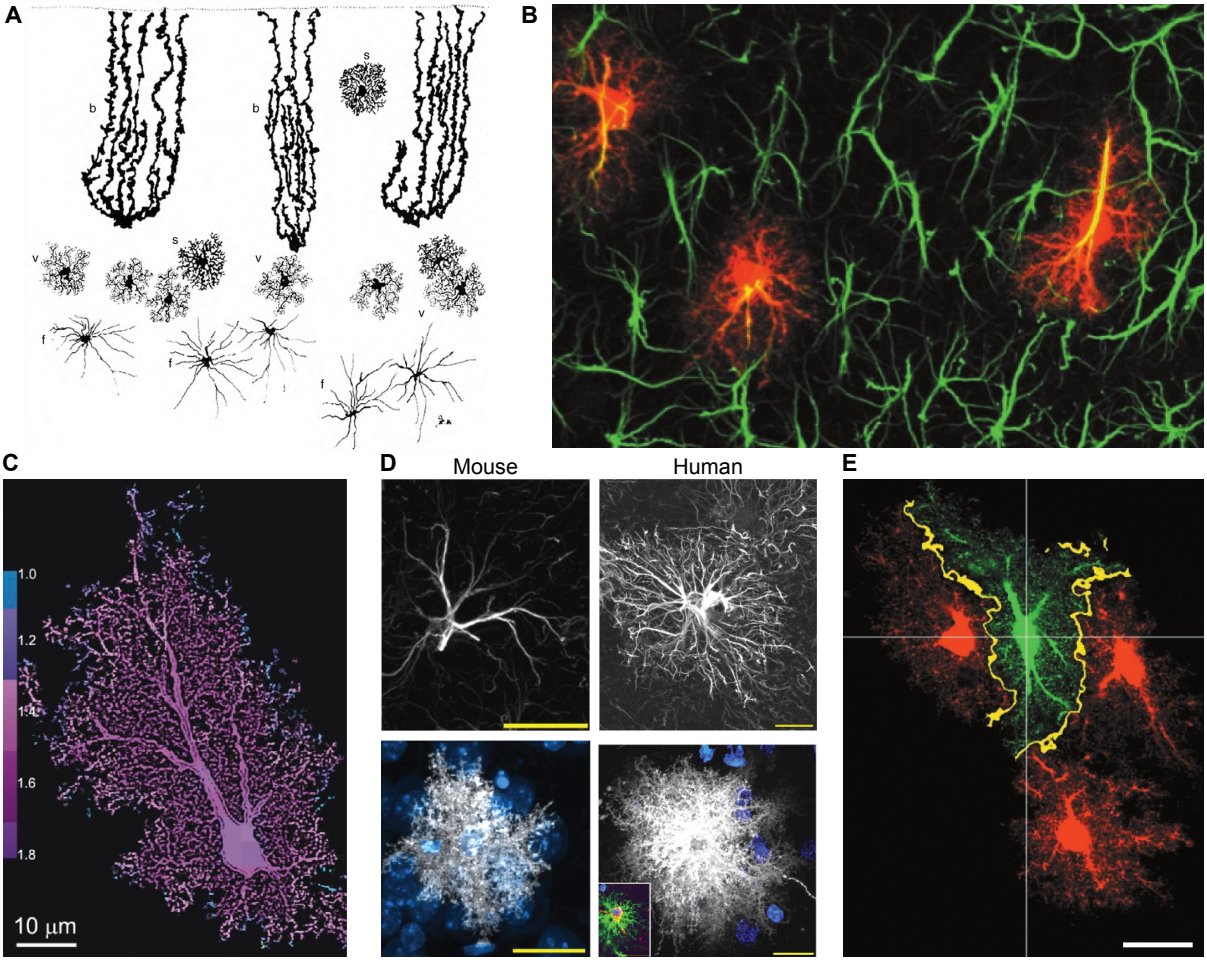

Figure I.1: Astroglia morphological diversity. **A** Golgi staining by Ramón y Cajal of various astroglia subtypes in humans. Letters indicate the different types: b, Bergmann glia. s, smooth protoplasmic astrocytes. v, velate astrocytes. f, fibrous astrocytes. Taken from Zhang and Barres (2010). **B** GFAP immunolabeling of LY-filled astrocytes in CA1 stratum radiatum. Dye-filled astrocytes (*red*) show much more complex processes than what can be seen from GFAP immunolabeling (*green*). Taken from Bushong et al. (2002). **C** Orthogonal slice through a confocal volume of a dye-filled astrocyte. Smaller subprocesses are well visible. Taken from Shigetomi et al. (2013). **D** Comparison between typical mouse (left column) and human (right column) protoplasmic astrocytes. Top row show GFAP labeling in *white* and bottom row show astrocytes labeled with DiI (*white*) showing all their fine processes. Human astrocytes are bigger and more complex than mice astrocytes. Scale bars are all 20μm. Taken from Oberheim et al. (2009). **E** Optical slices through neighboring protoplasmic astrocytes filled with distinct fluorescent dyes. The *green* astrocyte shares its borders (*yellow* regions) with other *red* astrocytes. Processes of protoplasmic astrocytes rarely interdigitate and each astrocyte describes a separate anatomical domain. Scale bar 20 μm. Taken from Bushong et al. (2002).

for a more detailed account.

Astrocytes and radial glia are two prominent types of astroglial cells which we evoked previously. Radial glia are astroglial cells that are prominently present during brain development and from its early stages. These cells are progenitor cells that can produce neurons, astrocytes or oligodendrocytes. They display elongated processes across the

height of the cortex which assist neuronal migration during embryonic stages of development. After development, most radial glia disappear and only radial glia-like cells are conserved in the mature brain: Müller cells in the retina that mainly support neurons; and Bergmann glia in the cerebellum which are represented in Figure I.1A (letter b).

The other prominent type of astroglial cells is constituted of astrocytes and all their subtypes. Although astrocytes can be divided in many different categories (Kimelberg, 2009), some of which only exist in specific species, we will only mention here their two main categories: fibrous and protoplasmic astrocytes which are respectively found in white and grey matter. We will focus on their morphological characteristics and on the factors that might shape the way they connect with each other. Figure I.1A shows both fibrous (letter f) and protoplasmic (letters v and s) astrocytes. Fibrous astrocytes display relatively long processes (up to 300μm) which are usually unbranched and contact both capillaries and myelinated axons (at node of Ranvier). Interestingly, processes of fibrous astrocytes are often interdigitated allowing the possibility of relatively distant contact between fibrous astrocytes. Protoplasmic astrocytes have smaller processes which are however much more complex. In mice, 5 to 10 main processes extend from the soma and these processes are further ramified in extremely fine sub-processes, forming a very complex arborisation. This complex view of protoplasmic astrocyte is however relatively recent and was made possible by the introduction of new staining techniques like filling the cells with fluorescent dyes via patch electrodes. The improvement brought forth by these techniques can be seen in Figure I.1B on which we can see immunolabeling of GFAP protein (in *green*) together with three distinct dye-filled astrocytes (in *red*); while the main processes are clearly visible with the immunolabeling technique, the detailed processes visible by dye-filling are completely invisible to GFAP immunolabeling. This specific morphology of protoplasmic astrocytes is thus less star-like than previously thought and more sponge-like. This characteristic is especially visible in Figure I.1C where very fine subprocesses are visible and densely packed in a relatively large region. This detailed arborisation allow protoplasmic astrocytes in rodent to contact approximately 140000 synapses with a single astrocyte (Bushong et al., 2002). Interestingly, the morphology, both in terms of number of processes and complexity of arbor, can vary between brain regions and especially between species. As an example, Figure I.1D compares the morphologies of typical protoplasmic astrocytes in both mousse (left column) and humans (right columns). While mice astrocytes have relatively few main processes (≈ 5, top row shows GFAP labeling), human astrocytes can have up to 40 main processes (Oberheim et al., 2009). Additionally, since human astrocytes are also bigger than mice astrocytes, they could contact up to 2 million synapses (Oberheim et al., 2009). Finally, this dense arborisation displayed by protoplasmic astrocytes goes together with the absence of interdigitations between astrocytic processes. Protoplasmic astrocytes thus tend to define separate territories and only contact other astrocytes at their boundaries. Figure I.1E shows this phenomenon: astrocytes are filled with two different fluorescent dyes (represented in *green* and *red*) and points that lie at the boundary between astrocytes are represented in *yellow*. The fact that these astrocytes do not send long processes and do not penetrate the processes of other astrocytes is a strong indication that connections between these astrocytes must be restricted to very short distances. Protoplasmic astrocytes can also be separated in subtypes, among which the vellate astrocytes represented in Figure I.1A (letter v) that

are smaller and usually present in densely packed regions. Interestingly, other astrocyte types in some species can have very long (up to 1mm) and sometimes unbranched processes that could thus form long distance connections with each other; among these, one can cite polarized astrocytes that are found in primates, interlaminar astrocytes found in the cerebral cortex of higher primates, or varisoce projection astrocytes that are only found in humans (Oberheim et al., 2009; Verkhratsky and Butt, 2013).

I.1.3 Astrocyte roles in healthy brain function

To give an idea of the current understanding of astrocyte functions in the healthy brain, we will quickly review some of their main roles, some of which were already evoked in the historical introduction. Since we will talk about gliotransmission in Section I.3, we will not cover this subject in this section.

I.1.3.1 Homeostatic and protective function

As described in the historical introduction, homeostasis, together with structural support, was one of the early roles attributed to glia. We now know that glia, and specifically astrocytes are involved in several important homeostatic regulations. First, astrocytes contribute to ion homeostasis in the extracellular space which is very important for correct functioning of neurons. Relatively small changes in extracellular concentrations of Na^+ or K^+ can indeed depolarize neurons, lead to longer action potential and eventually to the end of neuronal excitability. Potassium homeostasis constitutes the most documented ion homeostasis role for astrocytes (D'Ambrosio et al., 1998; Walz, 2000); astrocytes uptake K^+ and thus maintain its extracellular concentration around 2-3 mM, and release it in distant areas where the extracellular concentration of K^+ is lower or in the blood stream (Verkhratsky and Butt, 2013). This K^+ buffering mechanisms is especially important during epilepsy when extracellular K^+ accumulates (Steinhäuser et al., 2012). Interestingly, part of this K^+ uptake could be dependent on astrocytic Ca^{2+} activity (Wang et al., 2012). Astrocytes have also been shown to be involved in pH regulation (Deitmer and Rose, 2010) as well as water homeostasis through Aquaporin channels (Verkhratsky and Butt, 2013).

Additionally, astrocytes play neuroprotective roles during brain trauma by responding to injuries with a graded process called reactive astrogliosis. Effects of this process can range from slight morphological changes and enhanced GFAP expression in astrocytes to complete modifications of astrocytes and the formation of glial scars that isolate the lesion from the healthy parts of the brain. Detailed account of this mechanisms can be found in Verkhratsky and Butt (2013).

I.1.3.2 Structural support

Structural support was the other role attributed to glia at a very early time. With the advent of new experimental techniques like immuno-labeling and dye-filling of specific cells, this structural support role is now more elaborated than the connective tissue role evoked in the historical introduction. As presented in the previous sections, astrocytes organize in separate anatomical domains or territories (Bushong et al., 2002; Nedergaard et al., 2003). Figure I.2A shows a schematic representation of these territories together with blood vessels. Astrocytes send specialized processes to blood vessels, also called endfeet which enwrap them and allow nutrients and ion exchange between blood and astrocytes. Since the blood stream is separated from the brain parenchyma by the blood-brain barrier (BBB), astrocytes express specific transporters and channels in their endfeet (represented in Figure I.2C) to regulate exchanges through this glial-vascular interface. Most astrocytes are connected to blood vessels by at least one endfoot and are contacting up to 100,000 synapses inside their territories. They are thus ideally positioned, between blood vessels and neurons to offer support to neuronal functioning and a single astrocyte can be viewed as a metabolically independent glia-neurone-vascular unit (Verkhratsky and Butt, 2013).

I.1.3.3 Metabolic support

Although astrocytes only represent 5 tp 10% of the cumulated glucose consumption (i.e. metabolization) of neurons and astrocytes, they take up (i.e. they transport inside the cell) as much glucose as neurons do (Verkhratsky and Butt, 2013). This discrepancy is explained by the fact that astrocytes actually take-up glucose to then deliver it to neurons under another form. This process, called the Astrocyte-Neuron Lactate Shuttle (Pellerin and Magistretti, 2011) is schematically represented in Figure I.2B. Astrocytes actually transform glucose into lactate through glycolysis and then release this lactate in the extracellular space through lactate transporter MCT1 where it will be taken-up by neurons through lactate transporter MCT2. This process is dependent on synaptic activity: when synapses are strongly active, astrocyte processes enwrapping these synapses are taking up the main part of the glutamate that accumulated in the synaptic cleft (the rest being taken up by neurons) through glutamate transporters EAAT and this glutamate intake indirectly stimulates glycolysis. Detailed mechanisms are described in Pellerin and Magistretti (2011); Stobart and Anderson (2013). Interestingly, lactate has recently been reported to mediate synaptic plasticity by stimulating the expression of synaptic plasticity-related genes (Yang et al., 2014). This finding is the first to indicate a direct link between the metabolic support role of astrocytes and their role in modulation of synaptic plasticity.

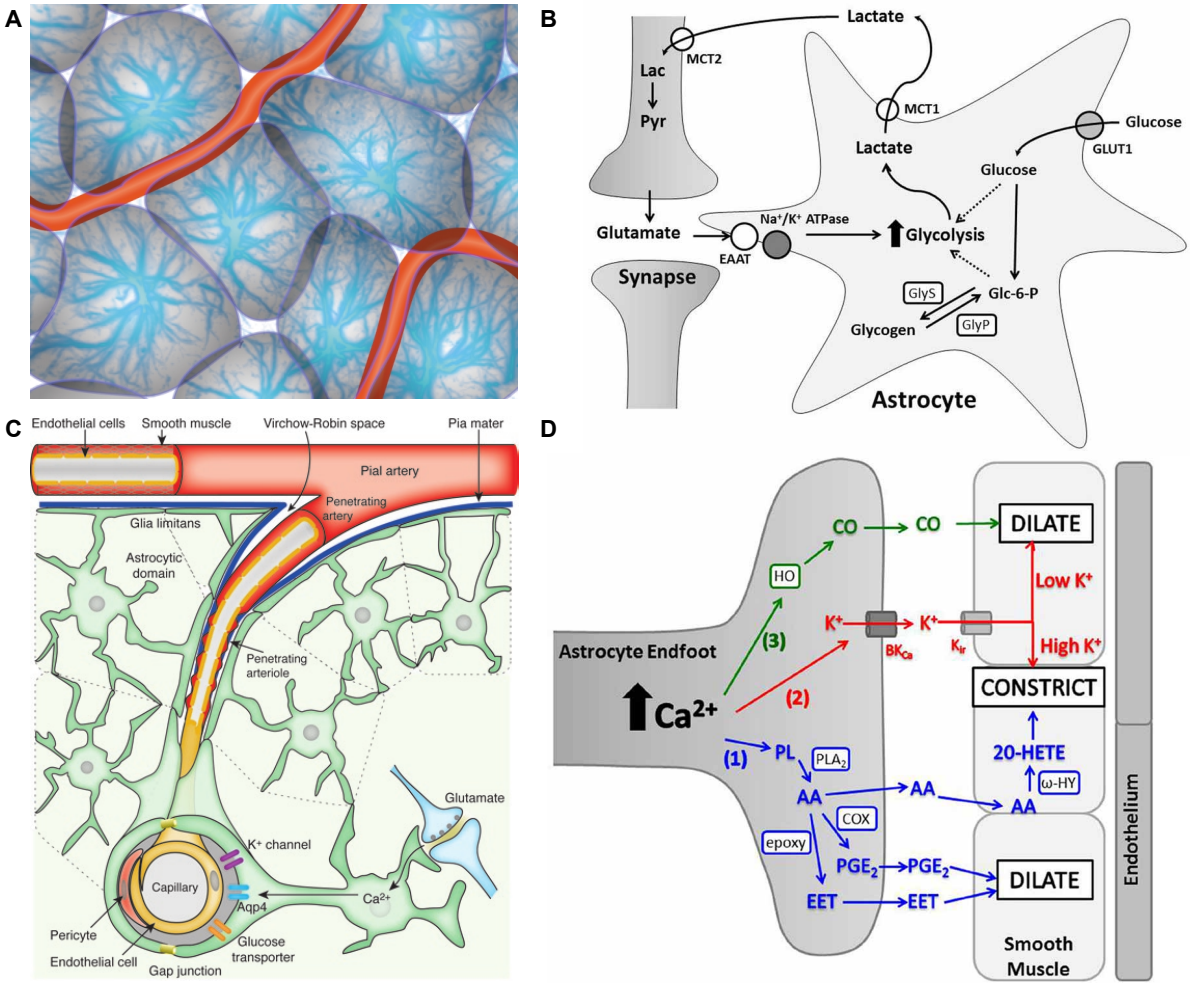

Figure I.2: Main astrocyte support roles in healthy brain functions. **A** Astrocyte territories are always connected to at least one blood vessel. Astrocytes stained for GFAP (*blue*) and vessels are schematically represented in *red*. Taken from Nedergaard et al. (2003). **B** Astrocytes transform Glucose into Lactate and deliver it to neurons. This process is stimulated by synaptic activity through astrocyte glutamate uptake. Taken from Stobart and Anderson (2013). **C** Astrocytes are in close apposition to both blood vessels and synapses. Arterioles are surrounded by astrocyte endfeet that express, among other proteins, the glucose transporters also represented on B. Taken from (Iadecola and Nedergaard, 2007). **D** Intracellular Ca^{2+} in astrocyte endfeet trigger the release of vasoactive molecules that can have either vasoconstrictive or vasodilatative effects. Different colors denote different pathways. Taken from Stobart and Anderson (2013).

I.1.3.4 Blood flow regulation

As represented in Figure I.2C, the brain is irrigated through relatively large pial arteries that are located on the its surface; in some places, branching smaller arteries penetrate in the brain and branches in even smaller capillaries. When neuronal activity occurs, excitatory glutamate releases trigger Ca^{2+} increase in postsynaptic neurons which can either (1) activate Nitric Oxyde (NO) synthase that produces NO which diffuses to capillaries and produces vasodilatation; or (2) stimulate the production of arachidonic acid which also indirectly produces vasodilatation. These processes thus link increased neuronal activity and modification of blood flow in capillaries. As represented in Figure I.2C and D however, astrocytes also regulate the blood flow. Glutamatergic activity at synapses elicit Ca^{2+} increases in astrocytes that propagate through their endfeet; in the endfeet, the Ca^{2+} increase can have different effects (differently colored pathways in Figure I.2D) that can either provoke vasodilatation (Metea and Newman, 2006) or vasoconstriction (Mulligan and MacVicar, 2004; Metea and Newman, 2006). The detailed pathways leading to these effects are described in details in Iadecola and Nedergaard (2007) and Stobart and Anderson (2013) and possible consequences for functional neuroimaging in Figley and Stroman (2011). Interestingly, evidence indicate that the occurrence of vasoconstricting or vasodilatiting effects can depend on the brain metabolic state (Gordon et al., 2008): under low oxygen conditions, astrocyte-mediated vasoconstriction is blocked and astrocyte-mediated vasodilatation is enhanced. Since astrocyte are GJC coupled, these mechanisms of blood flow control might operate at a network level (Giaume et al., 2010): increased synaptic activity might trigger Ca^{2+} waves that, by spanning different astrocytes, might produce coordinated vasodilatation; since glucose also diffuses across GJC, increased glucose take up in astrocytes near blood vessels can then be redistributed through astrocytic networks (Rouach et al., 2008). This scenario is strengthened by the recent observation of large scale Ca^{2+} waves in vivo that modulate blood flow in brain capillaries (Kuga et al., 2011). Although astrocyte-mediated vasoactive effects start to be well documented, recent studies reported that astrocytic Ca^{2+} increase in endfeet might be independent from vasoactive effects and could even precede these effects (Nizar et al., 2013; Bonder and McCarthy, 2014). We must thus remember that neurons are at least as important as astrocytes for blood flow regulation.

I.1.3.5 Regulation of synaptogenesis

Although the hitherto evoked functions are of chief importance in basic brain functioning, astrocytes have also been evidenced to be involved in much more 'high level' functions related to learning. In particular, astrocytes have been linked to the creation, support and deletion of synapses in the healthy brain (Eroglu and Barres, 2010; Clarke and Barres, 2013). More than 15 years ago, in vitro experiments showed that co-culturing neurons and glial cells led to the formation of 7 times more synapses than culturing neurons alone (Pfrieger and Barres, 1997). Synapse formation for example, has been linked to the secretion of cholesterol by astrocytes (Goritz et al., 2005). While recent studies also point towards roles of astrocytes in the deletion of synapses (Eroglu and Barres, 2010),

a substantial number of studies have focused on astrocyte modulation of synapses with sometimes contradicting results. This specific synaptic modulation role of astrocytes will be reviewed in more details in Section I.3. Finally, as mentioned earlier, protoplasmic astrocytes exert their actions on non-overlapping territories and the control of synaptogenesis thus seems to be regional (Tsai et al., 2012).

I.1.3.6 Higher brain functions

Additionally to all these supporting and homeostatic effects, astrocytes have also recently been linked to 'higher' brain functions. Among the few recent articles tackling this possibility, one can cite Halassa et al. (2009) in which the authors genetically prevented gliotransmission and concluded that astrocytes modulate the accumulation of sleep pressure through gliotransmission and A1 adenosine receptors, and Han et al. (2012) in which astrocyte CB1 cannabinoid receptors were found to be involved in the working memory impairments caused by cannabinoids. Blocking vesicular release in astrocytes in vivo was found to disrupt gamma oscillatory activity in neurons together with specific alterations of recognition memory (Lee et al., 2014). Interestingly, even supporting roles like the Astrocyte-Neuron Lactate Shuttle could be linked to long-term memory formation (Suzuki et al., 2011). Finally, one of the most convincing work has been done by Maiken Nedergaard's group (Han et al., 2013): they successively engrafted human astrocytes (which are bigger and more complex than rodent astrocytes) on neonatal immunodeficient mice and showed that engrafted animals performed better on several learning tasks. This striking behavioral effect thus constitutes a strong indication towards involvement of astrocytes in high level brain functioning. The interested reader can report himself to Fields et al. (2013) for a recent account of these type of effects.

I.1.4 Astrocytes and pathologies

Since, as presented above, astrocytes are involved in brain homeostasis, they often play important roles in neurological pathologies even when they are not the primary target of the pathology. We will only focus here on the pathologies involving astrocytes but numerous other pathologies are involving non-astrocyte glial cells. For a comprehensive reviews of these pathologies, the interested readers can report himself to Verkhratsky and Butt (2013). Although some pathologies are caused by astroglial dysfunctions, like Alexander disease in which a mutation on the GFAP gene provokes strong deficits in white matter, most of the pathologies that we will review here involve astroglia without specifically targeting astrocytes. As a generic mechanism following brain trauma, cellular oedemas are provoked by the disruption of water homeostasis by astrocytes: changes in osmotic pressure (e.g. higher extracellular K^+) triggers strong ion influx in astrocytes and subsequent swelling as water enters astrocytes through aquaporin channels. This astrocyte swelling can have secondary effects and exacerbate brain damage by, for example, compressing blood vessels and limiting blood circulation (Verkhratsky and Butt, 2013).

Neurodegenerative diseases The involvement of astrocytes in neurodegenerative disease is a relatively recent topic of study since these pathologies were usually viewed as neuronal pathologies. A detailed account of the recognition of astrocytes as players in these pathologies can be found in Verkhratsky et al. (2012b) and Rodríguez and Verkhratsky (2011). Neuroglia (i.e. not only astrocytes) is affected at early stages of most neurodegenerative diseases and control their progression in many cases (Verkhratsky and Butt, 2013). When neurodegenerative diseases reach later stages that involve the formation of specific lesions (like senile plaques in Alzheimer's disease), astrocytes undergo reactive astrogliosis (as mentioned in Section I.1.3.1) and isolate the lesioned area by the formation of glial scars. Even without the formation of specific lesions, neuronal degeneration, as in Parkinson's disease, is sufficient to trigger astrogliosis and the activation of microglia. Several different neurodegenerative diseases involve deficient glutamate clearance by astrocytes generally due to decreases or loss of expression of EAAT glutamate transporters: this process is at play in Amyotrophic Lateral Sclerosis (Rossi and Volterra, 2009); in Wernicke encephalopathy (Hazell et al., 2010); and in Huntington's disease in which it is linked with neuronal deaths in the cortex and striatum (Estrada-Sánchez and Rebec, 2012). Alzheimer's disease (AD) is one of the neurodegenerative diseases in which, although our knowledge of the underlying processes is still fragmentary, astrocytes seem to be involved in several different ways (Rodríguez and Verkhratsky, 2011). The profound neuronal losses that lead to strong cognitive impairments that result from Alzheimer's disease are linked to deposits of a specific protein Amyloid-β (Aβ) both in the walls of blood vessels and in the extracellular space of the grey matter where it forms senile plaques, and to intracellular accumulation of abnormal tau-proteins (Kandel et al., 2000a). As in other pathologies, astrocytes in late stages of AD undergo reactive astrogliosis, displaying increased GFAP expression and cellular hypertrophy. Interestingly, Aβ alone can trigger reactive astrogliosis in vitro and induces spontaneous Ca^{2+} transients and oscillations which in turn contribute to neurotoxicity (Chow et al., 2009). These abnormal Ca^{2+} oscillations have also been observed in vivo alongside with intercellular Ca^{2+} waves which mainly originated from astrocytes near Aβ deposits (Kuchibhotla et al., 2009). Additionally, Aβ has been found to decrease the expression of glutamate transporters, further promoting neuron death by excitotoxicity. Finally, although astrocytes in healthy brains do not synthesize Aβ, the occurence of brain insults that trigger astrogliosis could activate a gene that enables Aβ production by astrocytes (Roßner et al., 2005).

Stroke and ischaemia Since, as we evoked previously, astrocytes are involved in homeostatic roles, it is not surprising that they play prominent roles during strokes and ischaemia, i.e. when the blood flow is interrupted in a given brain area, leading to oxygen and nutrient depletion. In the ischemic core, where oxygen and nutrient depletion are the strongest, neurons die first and are followed later by astrocytes; at some distance from the ischemic core, in the so-called 'penumbra', ion homeostasis as well as nutrient availability are disrupted but cells are not dead yet. In this region, since astrocytes can survive ischaemia much longer than neurons, they play a protective role to neurons. Astrocytes can, through anaerobic glycolysis, maintain ATP production and thus ensure that their intracellular ion concentration stays regulated while at the same time producing lactate that they feed to glucose-deprived neurons. The death of cells in the ischemic core pro-

vokes strong increases in extracellular glutamate concentrations which, if not decreased, leads to excitotoxicity (by Ca^{2+} entry through AMPA and NMDA channels) and further neuronal deaths. In this context, astrocytes protect neurons by acting as the main glutamate sink by taking up glutamate through their EAAT glutamate transporters and also help buffer extracellular K^+ increases that also resulted from cell deaths. Additionally, astrocytes protect neurons by scavenging Radical Oxygen Species (ROS, which are harmful to neurons when they accumulate) and by releasing neuroprotective factors that either help reduce ischemic damages or improve recovery post-ischaemia. Finally, the already mentioned process of reactive astrogliosis leads to the formation of glial scars that isolate the lesion. Although all these effects are beneficial to neurons and ensure the containment of the ischemic core, astrocytes can also, in some conditions, worsen the situation. The role of astrocytes as glutamate sinks is thus a double-edged sword as they can switch from being glutamate sinks to glutamate sources by several processes (Malarkey and Parpura, 2008) among which : (1) reversal of glutamate transporters due to increased Na^+ concentration (Na^+ is co-transported inside astrocytes alongside with glutamate); (2) ATP released from dead neurons open P2X7 purinoceptors that allow glutamate release ; (3) Ca^{2+} elevations that trigger glutamate exocytosis. Astrocytes can also mediate the progression of the infarct core; Ca^{2+} intercellular waves that originate from the infarct core can trigger glutamate release by astrocytes in the penumbra and promote neuronal death by excitotoxicity. The same processes that are involved in the protection of neurons can thus also extend the damage; since the propagation of intercellular Ca^{2+} waves and the spatial buffering of K^+ by astrocytes are linked to GJC coupling between astrocytes, these GJC have been proposed as controlling the switch of astrocytes from a protective to a destructive role (Farahani et al., 2005).

Epilepsy Epileptic seizures are provoked by a slow depolarization of neurons at an epileptic focus (termed Paroxysmal Depolarization Shift, or PDS) that then propagates to larger groups of neurons and generates abnormal synchrony with high spiking frequencies. Epilepsy has been linked to several modifications of astrocytes such as their loss of domain organization (Oberheim et al., 2008), decreased expression of inward rectifying K^+ channels that thus impaired K^+ buffering (Steinhäuser et al., 2012; Bedner and Steinhäuser, 2013), and increased amplitude of Ca^{2+} signals in response to glutamate stimulation (Carmignoto and Haydon, 2012). Interestingly, in Tian et al. (2005) the authors show that astroglial Ca^{2+} waves precede PDS in vivo, pointing towards glutamate release from astrocytes that could trigger the PDS. In accordance with this hypothesis, antiepileptic drugs have been found to inhibit astroglial Ca^{2+} signaling.

Gliomas Gliomas are brain tumours that account for the majority of malignant brain tumours and that develop from glial cells. Astrocytomas are brain tumours arising from astrocytes and are the most common gliomas. Since the brain is enclosed in the skull and the cells are densely packed, gliomas cannot disseminate malignant cells easily. Instead, they kill neurons by excitotoxicity by secrecting large ammount of glutamate (among other mechanisms) and thus make room for their expansion (de Groot and Sontheimer, 2011). Interestingly, malignant cell migration is driven by Ca^{2+} oscillations (Verkhratsky

and Butt, 2013).

I.2 Astrocytes as excitable cells

As stated previously, astrocytes were thought of as passive cells until the 1980s because they lack electrical excitability due to their very low density of voltage-operated channels. After the introduction of Ca^{2+}-sensitive dyes that allowed to monitor Ca^{2+} concentrations in cells, astrocytes were shown to display relatively quick variations (several seconds) in cytoplasmic Ca^{2+} concentration (Cornell-Bell et al., 1990). Astrocytes were thus chemically excitable instead of being electrically excitable. Ca^{2+} concentration in astrocytes is affected by numerous different pathways (some of which are represented in Figure I.3A); to avoid Ca^{2+}-mediated toxicity, the resting free Ca^{2+} (i.e. unbound by Ca^{2+}-binding proteins) concentration in the cytoplasm must remain relatively low (around 0.1μM). To achieve this, free Ca^{2+} is either sequestered in Ca^{2+} stores and buffered (i.e. bound by Ca^{2+}-binding proteins) in the cell cytoplasm or pumped-out of the cell by different proteins embedded in the plasma membrane that allow exchanges with the extra-cellular space. Ca^{2+} concentration in the extracellular space and in these Ca^{2+} stores are thus relatively high (around 2mM and 0.5mM respectively) and transient increases in cytoplasmic Ca^{2+} are mediated by Ca^{2+} fluxes from these highly concentrated compartments to the cytoplasm. Dynamic opening and closing of Ca^{2+} permeable channels on Ca^{2+} stores membranes or cell membrane thus regulate the properties of Ca^{2+} signaling in astocytes. Interestingly, these mechanisms are not restricted to astrocytes but are also at play in hepatocytes, cardiomyocytes, smooth muscle cells, and many other cell types (Falcke, 2004; Dupont et al., 2007; Leybaert and Sanderson, 2012). Although astrocytes have been recently demonstrated to display transient increases in Na^+ and to propagate Na^+ waves (Bernardinelli et al., 2004), we will only focus here on Ca^{2+} excitability.

I.2.1 Ca^{2+} sources and sinks

We will not review here all the possible Ca^{2+} sources that have been documented in astrocytes, we will rather focus on the most documented sources and on those that will play a role in the following chapters. The interested reader might want to report himself to Dupont et al. (2007); Nedergaard et al. (2010); Verkhratsky et al. (2012a) for comprehensive reviews on this subject.

I.2.1.1 Intracellular Ca^{2+} stores

In astrocytes, Ca^{2+} stores are mainly represented by two types of compartments: mitochondria and endoplasmic reticulum (ER). Although very recent finding link specific mitochondrial Ca^{2+} exchanges with astrocyte intracellular Ca^{2+} signaling (Reyes and Parpura, 2008; Parnis et al., 2013), we will focus here on the most documented pathway involving Ca^{2+} release and sequestration in the ER. Further details on mitochondrial contributions to Ca^{2+} signaling in astrocytes are provided in (Verkhratsky et al., 2012a).

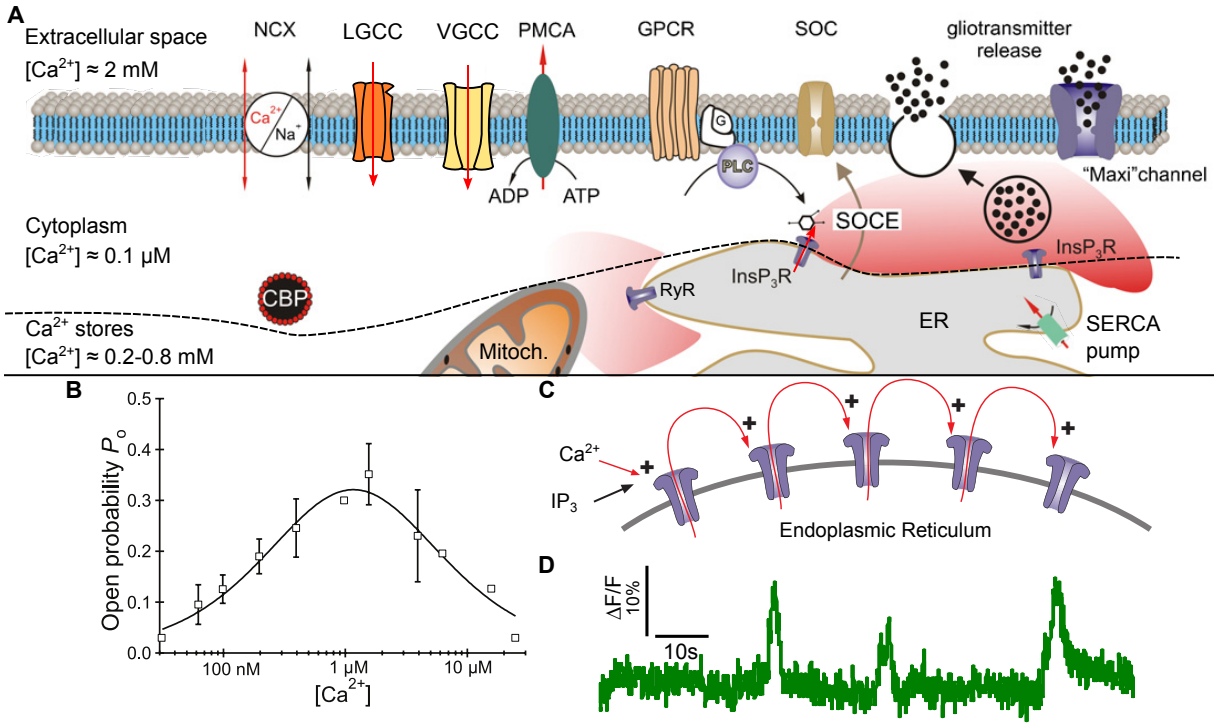

Figure I.3: Ca^{2+} signaling in astrocytes. **A** Schematic representation of Ca^{2+} dynamics in astrocytes. Ca^{2+} increases or decreases in the cytoplasm are mediated by channels on the cell membrane and by channels on the Endoplasmic Reticulum (ER) and Mitochondria. Ca^{2+} entry in the cytoplasm can be mediated by the reversal of the sodium-calcium exchanger (NCX), by ligand gated Ca^{2+} channels (LGCC), by voltage gated calcium channels (VGCC), by store-operated calcium channels (SOC), and by inositol triphosphate receptors (IP_3R) and Ryanodin receptors (RyR) on the ER membrane. Ca^{2+} clearance from the cytoplasm is ensured by the normal functioning of NCX, by the Plasmalemmal Ca^{2+} ATP-ase (PMCA) calcium pump, and by Sarco/Endoplasmic Reticulum Ca^{2+} ATP-ase (SERCA) pump on the ER membrane. In the cytoplasm, free Ca^{2+} gets bound to Ca^{2+}-binding proteins (CBP). When an agonist activate a G protein-coupled receptor (GPCR), Phospholipase C (PLC) enzymes produce IP_3 that open IP_3R, releasing Ca^{2+} from the ER (*red* shaded area). This Ca^{2+} increase can trigger exocytotic or channel-dependent (Maxi channel) release of gliotransmitter. Taken and modified from Nedergaard et al. (2010). **B** Example of relationship between the open probability of IP_3R and Ca^{2+} concentration in the cytoplasm. Empty squares correspond to experimetnal data and the *black* curve is fitted. Taken and modified from Foskett et al. (2007). **C** Binding of IP_3 to IP_3R initiates Ca^{2+} release from the ER (*red* arrows) that can then bind to nearby IP_3R or RyR and elicit Ca^{2+} release therein by Ca^{2+}-dependent Ca^{2+}-release (CICR), thus propagating an intracellular Ca^{2+} wave that involves the whole astrocyte. Taken and modified from Verkhratsky and Butt (2013). **D** Typical fluorescent signal obtained with the Ca^{2+}-sensitive fluorescent dye Oregon-Green Bapta-I. Ca^{2+} increases in the whole soma are captured in response to glutamate-mediated stimulation. Taken from Figure IV.3A.

The basic mechanisms of ER-dependent Ca^{2+} excitability are mediated by inositol 1,4,5-triphosphate receptors (IP_3R) present on the ER membrane (*purple* channels represented in Figure I.3A and B). IP_3R channels are formed by four subunits and their opening is mediated by a wide range of ligands. IP_3 and Ca^{2+} are the two main ligands and we will thus focus on these; for a detailed account of IP_3R channels ligands and properties, the interested reader can report himself to Foskett et al. (2007). IP_3 bindings to IP_3R increase its opening probability and the channel can open at four different conductance levels (Watras et al., 1991). This increase in opening probability is due to the fact that, at low IP_3 concentration, Ca^{2+} inhibits channel opening but when IP_3 concentrations increase, the effect of Ca^{2+} is reversed and then favors channel opening (Leybaert and Sanderson, 2012). Actually, the relationship between IP_3 concentration and opening probability is bell-shaped, as represented in Figure I.3B: for low Ca^{2+} concentrations, increasing Ca^{2+} concentrations leads to an increase in opening probability; for high Ca^{2+} concentration, further increases in Ca^{2+} lead to decreases in opening probability. The first increase, for low Ca^{2+} concentrations, mediates a positive feedback mechanism, called calcium induced calcium release (CICR) whereby opening of few IP_3R locally increases the Ca^{2+} concentration and thus further accentuates the opening of IP_3Rs, provoking a fast opening of lots of IP_3R channels.

Figure I.3B represents this CICR mechanism as a spatial mechanism: locally released Ca^{2+} (*red* arrow on the left) diffuses in the cytoplasm and provokes the opening of IP_3Rs located further away. This process can span the whole cell, giving rise to an intracellular regenerative Ca^{2+} wave (Berridge et al., 2003; Leybaert and Sanderson, 2012). Once the Ca^{2+} concentration in the cytoplasm gets higher, Ca^{2+} actually inhibits the opening of IP_3R and inactivates IP_3R. The Ca^{2+} outflux from the ER thus stops and Ca^{2+} gets reintegrated in the ER through Sarco/Endoplasmic Reticulum Ca^{2+}-ATPase (SERCA) pump (inward *red* arrow in Figure I.3A). Additionally, when free Ca^{2+} is released in the cytoplasm, it gets buffered by various calcium-binding proteins (CBP in Figure I.3A). As explained earlier, these Ca^{2+} dynamics can be monitored by using Ca^{2+}-sensitive fluorescent dyes. Figure I.3D shows a typical recording of the changes in fluorescent activity of such a dye in the soma of a cultured astrocyte subjected to neuronal stimulation. Other Ca^{2+}-permeable channels are present on the ER membrane (Dupont et al., 2007); notably, ryanodine receptors (RyR) also display CICR mechanisms and might be at play during astrocytic Ca^{2+} responses (Verkhratsky et al., 2012a).

IP_3 concentration thus controls store-mediated Ca^{2+} activity and the link between extracellular signaling events (by neurons or other astrocytes) is mediated by G-protein coupled receptors (GPCR in Figure I.3A) of the Gq subtype (mGluR1, mGluR5, P2Y1, ...): when agonists bind to GPCRs, it triggers an intracellular cascade that eventually leads to the production of IP_3 by the PLCβ enzyme. If the IP_3 increase provoked by these GPCRs is sufficient it can trigger a Ca^{2+} surge in the cytoplasm. If IP_3 levels stayed constant from this moment on, Ca^{2+} oscillations would persist for a much longer time than what is visible in Figure I.3D. IP_3 is however degraded by two main pathways (Shears, 1992): one that is Ca^{2+}-independent and mediated by a 5-phosphatase (IP-5P); the other is Ca^{2+}-dependent, mediated by IP_3 3-kinase (IP_3-3K), and degrades IP_3 at high Ca^{2+} concentrations.

I.2.1.2 Ca^{2+} entry from extracellular space

The high Ca^{2+} concentration in the extracellular space enables Ca^{2+} store-independent signaling mechanisms: opening Ca^{2+} permeable channels on the cell membrane allows Ca^{2+} to flow along the concentration gradient and enter the cytoplasm. This signaling pathway is mediated by several different types of proteins. First, Ca^{2+} entry can be mediated by ligand-gated Ca^{2+} channels (LGCC in Figure I.3) like AMPA or NMDA glutamate receptors (Verkhratsky et al., 2012a) (although the resulting Ca^{2+} currents are relatively small (Nedergaard et al., 2010)) or by P2X purinoceptors that are sensitive to ATP. Changes in membrane potential can also trigger Ca^{2+} entry through voltage gated Ca^{2+} channels (VGCC in Figure I.3A) like L-type channels (Pina-Benabou et al., 2001; Latour et al., 2003). Finally, Ca^{2+} entry can happen through store-operated channels (SOC in Figure I.3A) which open upon ER depletion and may involve transient receptor potential (TRP) channels (Golovina, 2005; Nedergaard et al., 2010). Additionally, under certain conditions (like Na^{+} accumulation in the cytoplasm), the sodium-calcium exchanger (NCX) can reverse and actually bring Ca^{2+} in the cytoplasm (Rusakov et al., 2014).

In Ca^{2+} store-mediated signaling, the Ca^{2+} concentration gets back to the resting state by reintegration of Ca^{2+} in the ER through SERCA pumps. The same type of mechanism is at play on the cell membrane, Ca^{2+} gets extruded from the cytoplasm under normal conditions by the NCX and by plasma membrane Ca^{2+}-ATPase (PMCA in Figure I.3A). Other Ca^{2+}-permeable channels are expressed on the cell membrane and a more complete account of these can be found in Verkhratsky et al. (2012a).

I.2.2 Multiscale Ca^{2+} activity in astrocytes

Since the discovery of Ca^{2+} activity in astrocytes, calcium imaging has made much progresses. Initial Ca^{2+} indicators were not sensitive enough to detect Ca^{2+} changes in astrocyte processes and even less in their very small sub-processes. The introduction of new Ca^{2+} indicators and the development of two-photon microscopy, imaging astrocyte main processes became possible and was even more facilitated with cell-permeant Ca^{2+} indicators. Recently, a new range of experimental techniques has allowed the expression of genetically encoded Ca^{2+} indicators (GECI) directly into the astrocytes either in a cytosolic form or in a membrane-bound form. This latter allows the observation of very fine processes that were invisible with classical Ca^{2+} indicators. The differences between these indicators are visible in Figure I.4A: on the left, a cell permeant dye (Fluo-4AM) with which only cell soma and a main process are clearly visible; on the right, a cytosolic GECI (cyto-GCaMP3) already provides better visualization for soma and main processes; in the middle, a membrane-bound GECI (Lck-GCaMP3) allows the investigation of Ca^{2+} dynamics in very fine subprocesses. The higher spatio-temporal allowed by these new Ca^{2+} indicators is beginning to reveal a much more complex picture of Ca^{2+} signaling in astrocytes with some Ca^{2+} signals that stay confined in distant processes without affecting the soma.

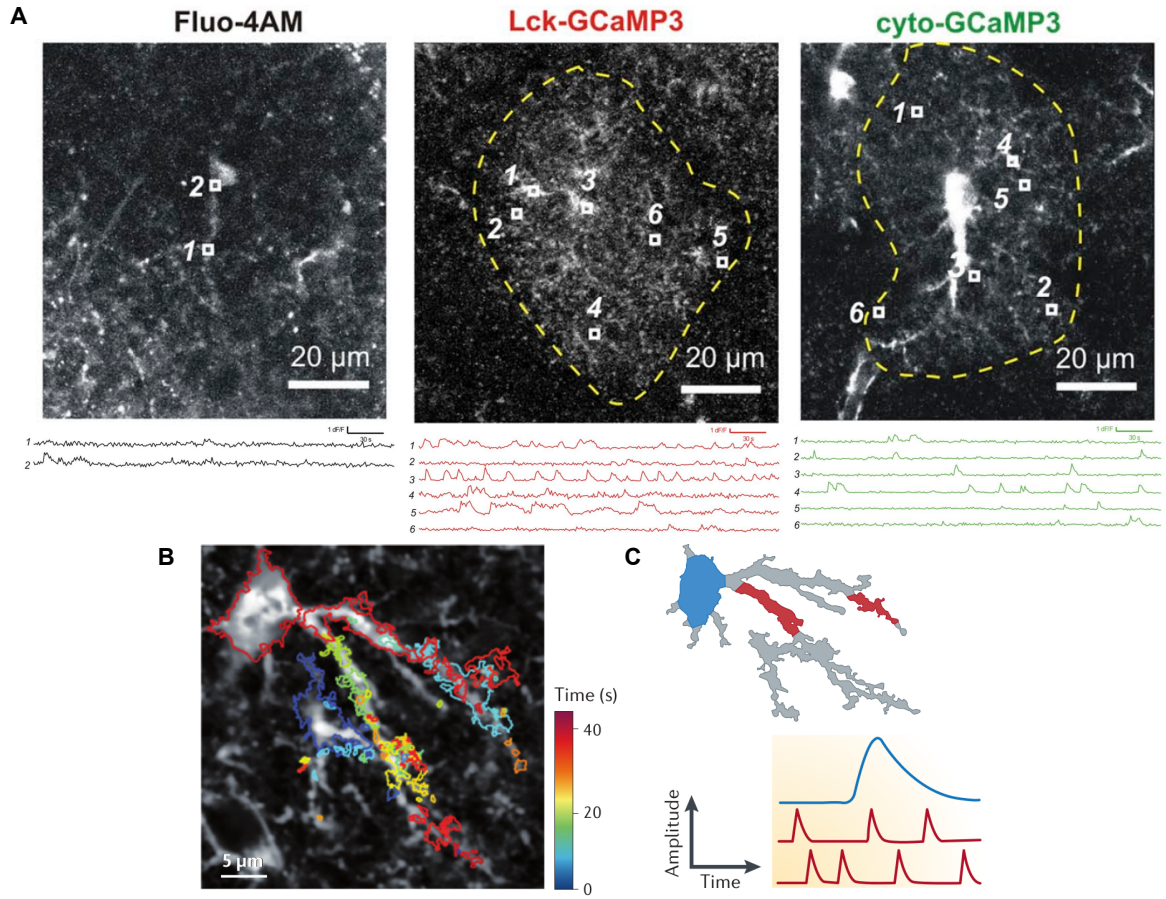

Figure I.4: Astrocytes display Ca^{2+} activity at several spatial scales. **A** The top row shows representative images of astrocytes loaded with Fluo-4AM (left), expressing membrane bound Ca^{2+} indicator Lck-GCaMP3 (middle), and expressing cytosolic Ca^{2+} indicator cyto-GCaMP3 (right). Small numbered squares indicate ROI whose corresponding signals are plotted on the bottom row. Taken and modified from Shigetomi et al. (2013). **B** Representation of Ca^{2+} events that happened in astrocytic processes and soma during 40 seconds of recording. Contours represent the maximal extent of Ca^{2+} events and are color-coded according to the time of initiation. Events in processes can be independent from each other and from event in the soma. Taken from (Volterra et al., 2014). **C** Schematic representation of signaling events in processes and in the soma: somatic Ca^{2+} events are stronger and longer than those that take place in the processes. Taken from (Volterra et al., 2014).

We will present Ca^{2+} signals in astrocytes in spatial ascending order, which is roughly the reverse of their discovery.

I.2.2.1 Ca^{2+} activity in processes

With the use of membrane-bound GECI, most recent experiments are investigating Ca^{2+} signals in very small bushy processes (see Figure I.4A, middle). Shigetomi et al. (2013) for example, revealed a wide variety of highly localized frequent short events ($\approx$ 5s) within entire hippocampal astrocyte teritories in acute hippocampal slices (as it can be seen on *red*

signals in the middle part of Figure I.4A). Ca^{2+} signals were visible up to 50μm away from the soma and they categorized the parts of subprocesses which display highly frequent Ca^{2+} activity as being 'Ca^{2+} microdomains'. Signal strength was mostly independent of location but most of the Ca^{2+} signals happened further than 20μm from the soma. This finding was further corroborated by a very recent article in which the authors managed to image Ca^{2+} activity in small subprocesses in vivo (Kanemaru et al., 2014). In agreement with Shigetomi et al. (2013), they found that most of the activity was concentrated in the processes and subprocesses. They also witnessed a new type of Ca^{2+} event, that they called 'Ca^{2+} twinkles', which were more lengthy (60s), localized ($\approx$ 10μm), sometimes wave-like and involving IP_3R. Interestingly, they showed that, although it does not happen frequently, Ca^{2+} signals in processes can sometimes propagate to the cell soma at $\approx 15\mu m.s^{-1}$. In addition to the spatially restricted Ca^{2+} events that take place in the subprocesses, the main processes also display larger 'expanded' events (Di-Castro et al., 2011). Some of the spatially restricted Ca^{2+} events in subprocesses were shown to be dependent on extracellular Ca^{2+} concentration while other Ca^{2+} signals in main processes were linked to GPCR activation (Shigetomi et al., 2010; Di-Castro et al., 2011). Interestingly, thin subprocesses seem to be devoid of Ca^{2+} stores (Patrushev et al., 2013) so it might explain why extracellular Ca^{2+} is involved. Finally, other spatially restricted events in main processes were shown to be dependent on mGluR type 5 receptors (Panatier et al., 2011). Additional quantification of these Ca^{2+} signals was provided by Wu et al. (2014), in which the authors quantify both the spatial extent and duration of Ca^{2+} signals in cell culture and hippocampal slices. The authors show that both of these measures seem to be power-law distributed; they only have data that span less than 2 decades so the power-law claim might be unjustified but it indicates at least that the distribution has a heavy-tail: small spatially and temporally restricted events are very frequent and large Ca^{2+} events that can engulf the whole astrocyte do happen with significant frequency.

Figure I.4B shows an astrocyte soma and its main processes with contours of Ca^{2+} events color-coded with their time of occurrence. A lot of small and intermediate events happen in the processes and one of them eventually propagate to the soma. The Ca^{2+} signal in the soma is higher in amplitude and longer than the signals in the processes (schematic representation in Figure I.4C). The rules linking the occurrence of Ca^{2+} signals in small subprocesses to Ca^{2+} signals in main processes to, eventually, Ca^{2+} signals in the astrocyte soma are still unknown and this constitute a major question for future investigations.

I.2.2.2 Ca^{2+} activity in soma

Going up a spatial scale, Ca^{2+} signals in cell soma were identified much before the observation of Ca^{2+} signals in processes and subprocesses and they were thus considered independently of what happened in the complex process structure. We will thus review the main types of Ca^{2+} activity in astrocyte soma and the underlying pathways.

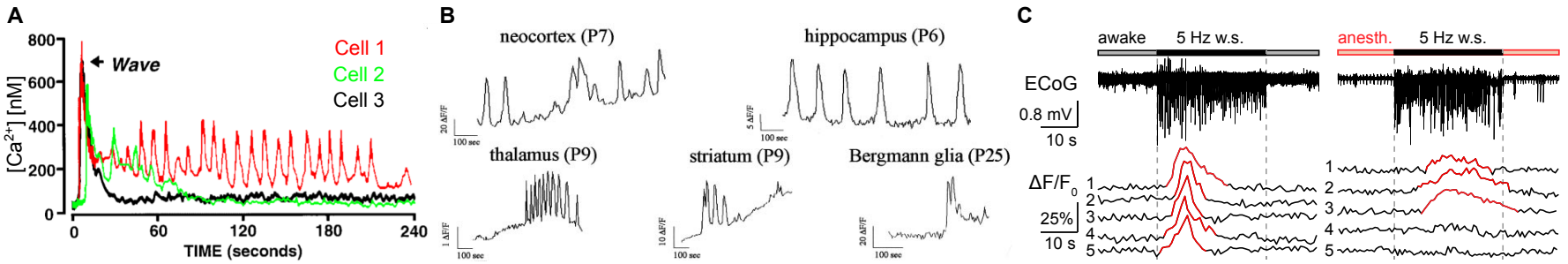

Figure I.5: Astrocytes display a wide variety of somatic Ca^{2+} signal shapes. **A** Examples of somatic Ca^{2+} signals in cultured astrocytes responding to mechanical stimulation for 3 different astrocytes (*red*, *green*, and *black* traces). Taken and modified from Charles (1998). **B** Examples of spontaneous somatic Ca^{2+} signals in distinct CNS regions of animals with different ages (P6-P25, slices). Taken from Aguado et al. (2002). **C** In vivo recording of somatic Ca^{2+} activity during whisker stimulation (w.s., middle part in both plots) in awake (left plot) and anesthetized (right plot) animals. Neuronal activity is recorded through extracellular electrocorticogram (ECoG). Taken from Thrane et al. (2012).

Table I.1: Examples of single astrocyte oscillations.

Area	Prep.	Conditions	Type	Pathway	Anim.	Age	Freq. (Hz)	Source
Hipp.	in situ	Normal	Spont. Osc.	IP_3	Mice	10-17d	0.00347 – 0.0333	Nett et al. (2002)
NeoCx	in situ	Epileptiform	Spont. Osc.	IP_3	Mice	3-14d	0.01 (P3 to P11) – 0.03 (P14)	Tashiro et al. (2002)
Cx	In vivo	Alzheimer	Spont. Osc.	?	Mice	180-240d	Higher than in WT	Kuchibhotla et al. (2009)
Cx	In vivo	Anesthetized	Oscillations	Neur. Act.	Rats	12-16d	0.00202 ± 0.00163 [1]	Hirase et al. (2004)
-	-	-	Plateau	-	-	-	0.00196 ± 0.00096 [2]	Hirase et al. (2004)
Cx	In Vivo	Visual stim.	Oscillations	?	Ferret	39-45d	?	Schummers et al. (2008)
Cx	In Vivo	Whisker stim.	Oscillations	mGluR	Mice	42-56d	?	Wang et al. (2006)
Hipp.	in situ	IP3 uncaging	Oscillations	IP3	mice	10-15d		Fiacco and McCarthy (2004)
VBT	in situ	PN [a] < 10	Spont. Osc.	VGCC[3]	Rats	5-17d	0.01 (62% of cells) [4]	Parri et al. (2001)
-	-	PN > 10	Spont. Osc.	-	-	-	- (18% of cells)	Parri et al. (2001)
Cx	in situ	Normal	Spont. Osc.	A1R (in part)	Mice	13-15d	0.0075	Poskanzer and Yuste (2011)
-	-	Electr. stim.	Oscillations	-	-	-	0.00875	Poskanzer and Yuste (2011)

a. PostNatal days

[1] 11 to 24% of cells
[2] 52% of cells, duration: 160.4 ± 114.9 s
[3] Ca^{2+} stores also contributed
[4] 0.003Hz overall

Transient somatic Ca^{2+} elevations can either occur spontaneously, as intrinsic oscillations in the absence of neuronal activity (Parri et al., 2001; Nett et al., 2002; Hirase et al., 2004), or be triggered by neurotransmitters released during synaptic activity (Pasti et al., 1997; Araque et al., 1999; Wang et al., 2006; Schummers et al., 2008; Bernardinelli et al., 2011; Thrane et al., 2012). Although other sources of Ca^{2+} are sometimes involved, both of these Ca^{2+} elevations are usually dependent on Ca^{2+} release from stores, and specifically ER, that produces CICR as presented above. Table I.1 presents examples of astrocyte oscillations reported by different articles in various brain regions and under different experimental conditions. Some of these oscillations are spontaneous ('Type' column) while other are elicited through some kind of stimulation ('Conditions' column). The presence of a dash symbol indicates that the information is identical to the one provided one row above. In the case of spontaneous oscillations, Ca^{2+} elevations can also be mediated in part by VGCC (Parri et al., 2001).

Figure I.5 displays the shapes of somatic Ca^{2+} signals from different astrocytes in culture in response to stimulation (Figure I.5A), or occurring spontaneously in slices of different brain regions (Figure I.5B). The responses can range from isolated increases (cell 3 in *black* in Figure I.5A or hippocampal astrocyte in Figure I.5B) to relatively high frequency oscillations (cell 1 in *red* in Figure I.5A or thalamic astrocyte in Figure I.5B) and even plateaus (Bergmann glia in Figure I.5B). Interestingly, the responsiveness and shape of Ca^{2+} oscillations in astrocytes during in vivo studies can be directly linked to sensory stimulations (Wang et al., 2006; Schummers et al., 2008; Nimmerjahn et al., 2009). Figure I.5C presents one of the conclusion from a recent study (Thrane et al., 2012) that reported that sensory stimulus (whisker stimulation) elicited less astrocytic responses and modified response shapes in anesthetized animals (left plot) than in awake animals (left plot) while the neuronal activity was unchanged. We must thus keep in mind that older in vivo studies in anesthetized animals might have underestimated astrocytic responses.

Signaling between neurons and astrocytes has been observed at glutamatergic, noradrenergic, cholinergic, and GABAergic synapses in the hippocampus, the thalamus, and the cortex (Volterra and Meldolesi, 2005; Haydon and Carmignoto, 2006; Santello and Volterra, 2009; Halassa and Haydon, 2010; Navarrete et al., 2012, 2013). In several brain areas, astrocytes have been shown to display isolated responses involving only one astrocyte or a few spatially close astrocytes (Sasaki et al., 2011); this suggests that, on top of their anatomical domains, astrocytes might organize into functional domains and selectively respond to neuronal stimulations (Bernardinelli et al., 2011). This type of organization has been observed in the ferret visual cortex, where astrocyte responses were shown to be selective to the orientation of visual stimuli, in close association with neuronal spatial receptive fields (Schummers et al., 2008). Similar signaling has also been observed in the somatosensory cortex (Winship et al., 2007; Schipke et al., 2008), in the motor cortex (Haas et al., 2006), in the olfactory bulb (De Saint Jan and Westbrook, 2005), in Bergmann glia (Nimmerjahn et al., 2009), and in mice visual cortex (Paukert et al., 2014).

The shape and properties of somatic Ca^{2+} oscillations in astrocytes are governed not only by the type of stimulation received but also by intrinsic cell properties. Astrocytes

can discriminate between different neuronal inputs by responding with different Ca^{2+} oscillations to different synaptic pathways. Astrocytic Ca^{2+} elevations were measured in response to the stimulation of specific glutamatergic synapses in the hippocampus (Perea and Araque, 2005b) and in the barrel cortex (Schipke et al., 2008). Astrocytes could also use their Ca^{2+} dynamics as integrators of activity, responding with somatic Ca^{2+} elevations to concomitant synaptic inputs (Perea et al., 2009). As an example, hippocampal astrocytes have been shown to respond with Ca^{2+} elevations to the stimulation of Schaffer collaterals (Porter and McCarthy, 1996) and of nerve fibers of the alveus (Araque et al., 2002). Interestingly, when both Schaffer collaterals and nerve fibers of the alveus are stimulated with low stimulation frequency ($\approx$ 1Hz), the Ca^{2+} response of hippocampal astrocytes is higher than what would be expected from the sum of the responses to separate stimulations with the same frequency (supralinear summation); in contrast, when higher stimulation frequencies are used, the reverse happens and the summation becomes sublinear (Perea and Araque, 2005b).

Astrocyte networks constitute the next spatial scale and will be treated in Section I.4.

I.2.3 Activators: from neurons to astrocytes...

Astrocytes express a wide variety of receptors to neurotransmitters and neuromodulators; a detailed account of these can be found in Verkhratsky and Butt (2013). Like neurons, astrocyte can express both ionotropic and metabotropic receptors; we already mentioned some of the Ca^{2+} permeable ionotropic receptors previously and will thus only focus here on metabotropic receptors that are involved in neuron-astrocyte communications.

Astrocytes express type I metabotropic glutamate receptors (mGluR1 and mGlur5) that are coupled to phospholipase C and transform PIP_2 in IP_3, thus being able to provoke the opening of IP_3Rs on the ER (Dani et al., 1992; Porter and McCarthy, 1996; Aguado et al., 2002; Wang et al., 2006). Remarkably, a very recent study (Sun et al., 2013) reported that mGluR type I are expressed in young animals but are no longer expressed after the third postnatal week. In contrast, mGluR type II receptors (and specifically mGluR3), which are expressed in both young and adult rodents, regulate intracellular levels of cyclic adenosine monophosphate (cAMP) which are not directly linked to Ca^{2+} signaling (Sun et al., 2013).

Astrocytes also express purinoceptors which are generally divided into adenosine (P1) and ATP (P2Y) receptors. Adenosine receptors A_1 and A_3 regulate PLC and thus IP_3 synthesis in astrocytes (Burnstock et al., 2011); there are other types of adenosine receptors expressed by astrocytes that regulate other functions that are not directly linked to Ca^{2+} signaling (Boison et al., 2009). P2Y metabotropic ATP receptors are widely expressed in astrocytes (Verkhratsky et al., 2009) and they are also linked to PLC and IP_3 synthesis. Synaptically released ATP (Larsson et al., 2011) has notably been found to trigger astrocytic Ca^{2+} signaling in situ (Di-Castro et al., 2011). ATP and P2Y receptors have also been proposed as underlying intercellular Ca^{2+} wave propagation by extracellu-

lar diffusion of ATP (Guthrie et al., 1999; Cotrina et al., 2000); this point will be treated in Section I.4.

In addition to responding to excitatory neurotransmitters like glutamate, astrocytes also express γ-aminobutyric acid (GABA, an inhibitory neurotransmitter) receptors in both ionotropic ($GABA_A$) and metabotropic ($GABA_B$) forms (Veléz-Fort and Angulo, 2012; Verkhratsky and Butt, 2013). At Schaffer collateral as well as cortical synapses, astrocyte Ca^{2+} responses were linked to retrograde endocannabinoid signaling from postsynaptic terminals via the activation of cannabinoid receptor type 1 (CB_1R) (Min and Nevian, 2012; Navarrete et al., 2013). Finally, recent in vivo experiments demonstrated the involvement of adrenergic receptors (αAR and βAR) in Ca^{2+} signaling (Ding et al., 2013; Paukert et al., 2014).

I.3 Astrocyte-Neurons interaction: ... and back to neurons

While neuron to astrocyte communication pathways were the first to be identified, they did not necessarily imply that astrocytes were actively involved in neuronal signaling. The role of astrocytes as regulators of synaptic transmission in the so-called tripartite synapse (pre and post-synaptic elements together with an astrocyte process) was asserted by the characterization of an astrocyte-to-neuron communication through the release of various substances (or gliotransmitters) by astrocytes.

I.3.1 Gliotransmission

When astrocytes display Ca^{2+} activity, either spontaneous or in response to neuronal stimulation, one of the consequences, in specific conditions, can be the release of gliotransmitters. These gliotransmitters can act on neighboring neurons, other astrocytes, and also blood vessels (as we already mentioned before) (Haydon and Carmignoto, 2006). We will quickly review here the main gliotransmitters that affect neurons, their effects, and the recent controversies that surrounded the concept of gliotransmission.

I.3.1.1 Pathways

Well characterized gliotransmitters include glutamate, D-serine, GABA and ATP (Bezzi et al., 2004; Pascual et al., 2005; Montana et al., 2006; Henneberger et al., 2010; Parpura and Zorec, 2010). The release of gliotransmitters is thought as being primarily achieved through Ca^{2+}-dependent exocytosis. In particular, glutamate and ATP have both been shown to be released by this mechanism (Zorec et al., 2012) and, although definitive evidence is still lacking, D-serine release also seems to be dependent on this mechanism (Mothet et al., 2005; Bergersen et al., 2012). D-serine, after being released from astrocytes, act as a co-agonist with glutamate at postsynaptic NMDA receptors (Papouin et al., 2012). Other release mechanisms are however at play; diffusion of transmitters from astrocyte intracellular space, where concentrations of glutamate, GABA and ATP are much higher than in the extracellular space, can be mediated by various transmembrane channels. ATP and glutamate have thus been reported to permeate through 'maxi' Cl^- channels (Sabirov and Okada, 2009), volume-regulated anion channels (Volterra and Meldolesi, 2005), and unpaired connexins (called hemichannels) (Spray et al., 2006) whose opening can be mediated by Ca^{2+} dependent mechanisms (Decrock et al., 2011). Pannexin1 has also been shown to form transmembrane anion channels (Ma et al., 2012) and has been suggested to support ATP release from astrocytes (Verkhratsky and Butt, 2013). Bestrophin1 which are also anion channels have been shown to mediate GABA release from astrocytes (Lee et al., 2010). Finally, the reversal of GABA transporters GAT-3 have been shown, in response to increases in intracellular Na^+ or depolarizations, to release

GABA in the extracellular space in the neocortex (Kirischuk et al., 2012).

Although different mechanisms of gliotransmitter release are Ca^{2+}-dependent, the different pathways by which Ca^{2+} signaling can be achieved correspond to the release of different gliotransmitters (Santello and Volterra, 2009). For example, purinergic GPCRs (P2Y family) are more associated with glutamate release (Jourdain et al., 2007; Perea and Araque, 2007) while mGluRs are associated with ATP release (which gets quickly degraded in adenosine in the extracellular space) (Pascual et al., 2005; Gordon et al., 2009; Panatier et al., 2011). Additionally, it seems that different gliotransmitters are contained in different intracellular structures: ATP is contained in dense-core granules (Coco et al., 2003) or in lysosomes (Jaiswal et al., 2007; Zhang et al., 2007; Li et al., 2008); glutamate and D-serine are contained in microvesicles (Bezzi et al., 2004; Jourdain et al., 2007; Bergersen et al., 2012). Some experiments in culture thus indicate that Ca^{2+} signals that trigger glutamate exocytosis do not trigger ATP release (Marchaland et al., 2008) and vice versa (Coco et al., 2003; Li et al., 2008).

When gliotransmitters are released in the extracellular space, they can diffuse to both pre and post-synaptic terminals and exert modulating effects on synaptic transmission (Volterra and Meldolesi, 2005). For example, glutamate released by astrocytes can increase the synaptic release probability (and thus mediate short-term potentiation effects) by activating NR_2B-containing NMDARs at excitatory synapses in the hippocampal dentate gyrus (Jourdain et al., 2007), or by activating presynaptic mGluRs at Schaffer collateral synapses in the CA1 area of hippocampus (Fiacco and McCarthy, 2004; Perea and Araque, 2007). Astrocytic glutamate release on inhibitory synapses in the hippocampus was found to mediate either increased synaptic release when binding to ionotropic glutamate receptors (Kang et al., 1998), or inhibition of synaptic release through kainate receptors and mGluRs (Liu et al., 2004a,b). The astrocytic release of ATP, which is extracellularly degraded to adenosine, has been reported to bind to presynaptic P_2Y_1 receptors while adenosine binds to A_1 and A_{2A} receptors. While P_2Y_1 and A_1 receptors have been linked to decreases in synaptic release probability (Zhang et al., 2003; Pascual et al., 2005), A_{2A} receptors have been linked to increases in synaptic release probability (Panatier et al., 2011).

In addition to their presynaptic effects, gliotransmitters could also influence synaptic transmission by binding to postsynaptic receptors. The release of D-serine, which acts as a co-agonist with glutamate to NMDARs, can thus affect postsynaptic NMDARs, modulating neuronal firing and possibly participating in the induction of long-term potentiation (LTP) (Fellin et al., 2004; Bains and Oliet, 2007; Henneberger et al., 2010). Astrocytic ATP release could also affect postsynaptic terminals by binding to postsynaptic ionotropic P2X receptors and promoting LTP by the insertion of postsynaptic AMPARs (Gordon et al., 2005). Gliotransmitters can thus affect synaptic transmission at both presynaptic and postsynaptic terminals in response to spontaneous or neuron-evoked intracellular Ca^{2+} increases. This bidirectional communication between neurons and astrocytes led to reconsider synapses from bipartite (pre and post synaptic terminals) to tripartite (with the astrocyte) structures. However, the exact effects of astrocytes on synaptic transmission and whether these effects occur under physiological conditions have been the object

of a still ongoing debate.

I.3.1.2 Controversies

In contrast to the studies we just cited, several experiments conducted in recent years failed to witness changes in synaptic transmission after selectively stimulating astrocytes through GPCR-dependent pathways (Fiacco et al., 2007; Petravicz et al., 2008; Agulhon et al., 2010). Interestingly, hypotheses were proposed to explain these discrepancies: in pathological conditions and under reactive gliosis, both microglial cells and reactive astrocytes secrete substances like pro-inflammatory cytokines that may control gliotransmitter release (Agulhon et al., 2012; Santello and Volterra, 2012). For example, astrocytic glutamate release at hippocampal excitatory synapses could be regulated by extracellular levels of tumor necrosis factor-α (TNFα) (Domercq et al., 2006; Santello et al., 2011) or by microglial release of ATP (Pascual et al., 2011).

In addition to the astrocyte to neuron communication pathways, the communication from neurons to astrocytes might also be different in physiological conditions in adult animals (Zhang and Barres, 2010). For example, as we pointed out above, the expression of mGluRs may switch during the development from mGlur5 to mGluR3 (Sun et al., 2013) and thus prevent mGluR-dependent astrocytic Ca^{2+} signaling in astrocytes. Other experiments at similar developmental stages however reported the expression of mGluR5 in astrocytic microdomains close to hippocampal glutamatergic synapses (Grosche and Reichenbach, 2013). Additionally, the putative effect of astrocytic ATP, through its degradation to adenosine, on A_1Rs might not be linked to astrocytic ATP release but to neuronal adenosine release (Lovatt et al., 2012). The effect of astrocytes could rather be linked to their confining of adenosine to individual synapses with their adenosine transporters (Fredholm, 2012; Lovatt et al., 2012).

In both directions, from neurons to astrocytes and from astrocytes to neurons, the effect of neurotransmitters and gliotransmitters are not always systematic and which processes happen under pathological or physiological conditions is still unknown. The interested reader might report himself to Agulhon et al. (2012); Nedergaard and Verkhratsky (2012); Verkhratsky and Butt (2013) for more details about the controversies surrounding gliotransmission.

I.3.2 Indirect effects

In addition to direct signaling effects, the homeostatic roles of astrocytes may also be involved in controlling synaptic plasticity. Notably, ionic and transmitter homeostasis were shown to be involved in modulation of synaptic strength. For example, regulation of synaptic strength was reported at excitatory hippocampal synapses when astrocytic processes underwent morphological changes that controled their insertion in the synaptic

cleft (Pannasch et al., 2014). Interestingly, these changes were linked to Connexin 30, a protein that can also be involved in GJC formation, but that was in this case controlling the insertion of astrocytic process in the synaptic cleft. The farther astrocyte processes were inserted in the cleft, the lower the concentration of glutamate because of increased glutamate uptake by the astrocyte. Similarly, hypothalamic astrocyte shrinkage during lactation has been linked to higher levels of glutamate in the synaptic cleft and to strengthened synaptic transmission (Panatier and Oliet, 2006; Verkhratsky and Butt, 2013). In addition to these local effects, coupling of astrocytes by GJC has been reported to control synaptic strength by facilitating the clearance of glutamate and K^+ (Pannasch et al., 2011). Finally, as mentioned before, even lactate release by astrocytes has recently been reported as promoting plasticity by potentiating NMDA signaling in neurons (Yang et al., 2014).

We only gave here a very brief account of all the phenomenons, direct and indirect, that might play a role in shaping synaptic transmission and plasticity; more detailed descriptions can be found in Agulhon et al. (2012); Verkhratsky and Butt (2013); Pannasch and Rouach (2013).

I.4 Astrocytes are interconnected cells

In addition to having bidirectional communication pathways with neurons, astrocytes also communicate with each other through the propagation of intercellular calcium waves (ICW). Astrocytes are indeed interconnected by the expression of transmembrane Connexin (Cx) proteins which, when aligned with other Cx on other astrocytes, form gap junction channels (GJC) that allows the diffusion of small molecules directly from cytosol to cytosol. Additionally, the release of gliotransmitters by astrocyte, such as ATP, does not only mediate astrocyte-to-neuron communication but can also mediate astrocyte-to-astrocyte communications by supporting the propagation of ICW. The interaction between neurons and astrocytes should thus not only be considered at the level of the tripartite synapse but also at the network level. These network-level interactions are still mostly unknown and are likely to be highly complex: the timescales involved range from several milliseconds (synaptic transmission) to tens of seconds (astrocyte activation) while the spatial scales range from under 1μm (tripartite synapse) to several tens of μm (one astrocyte) to even few millimeters (astrocyte networks). In this section, we will review some of the ICW observed in vitro, in situ and in vivo, and present the different mechanisms that can support these ICW. We will then discuss the increasingly recognized organization of astrocytes as proper networks, with coupling heterogeneities, in opposition to the traditional syncytial view.

I.4.1 Inter-astrocyte signaling

I.4.1.1 Intercellular Ca^{2+} waves in vitro and in vivo

The first observations of ICW date back to the 90s when Cornell-Bell et al. (1990) reported the propagation of glutamate-induced ICW in cultured astrocytes. ICWs in these preparations could be elicited either by focal transmitter (e.g. glutamate) stimulation (Cornell-Bell et al., 1990) or by mechanical stimulation (Charles et al., 1991) and propagated at $\approx 15\mu m.s^{-1}$; an example of mechanically-induced ICW is presented in Figure I.6A (top row). These early findings were confirmed by other experiments and the ICWs were found to depend on the release of Ca^{2+} from Ca^{2+} stores: rather than consisting in a large Ca^{2+} release in the stimulated cell that would have propagated along astrocytes, these ICWs actually consisted in sequential Ca^{2+} release from the ER, as described in Section I.2 (this is more visible in Figure I.6B). ICWs were then observed in acute slices from various brain regions (Parri et al., 2001; Schipke et al., 2002; Sul et al., 2004; Weissman et al., 2004) as well as in the retina (Newman and Zahs, 1997; Kurth-Nelson et al., 2009). In these experiments, ICW propagated at roughly the same speed as in cell cultures. Table I.2 presents examples of ICW in culture, in situ, and in vivo; one can see from this table that the extent of ICW is highly variable. In cultures, ICW extent can be multiplied by a factor 4 by changing the origin of the astrocyte from diencephalic (hypothalamus and other areas) to telencephalic (cortex and other areas) (Peters et al., 2005b) or by a factor 2 when comparing astrocytes from hypothalamus to astrocytes from hippocampus

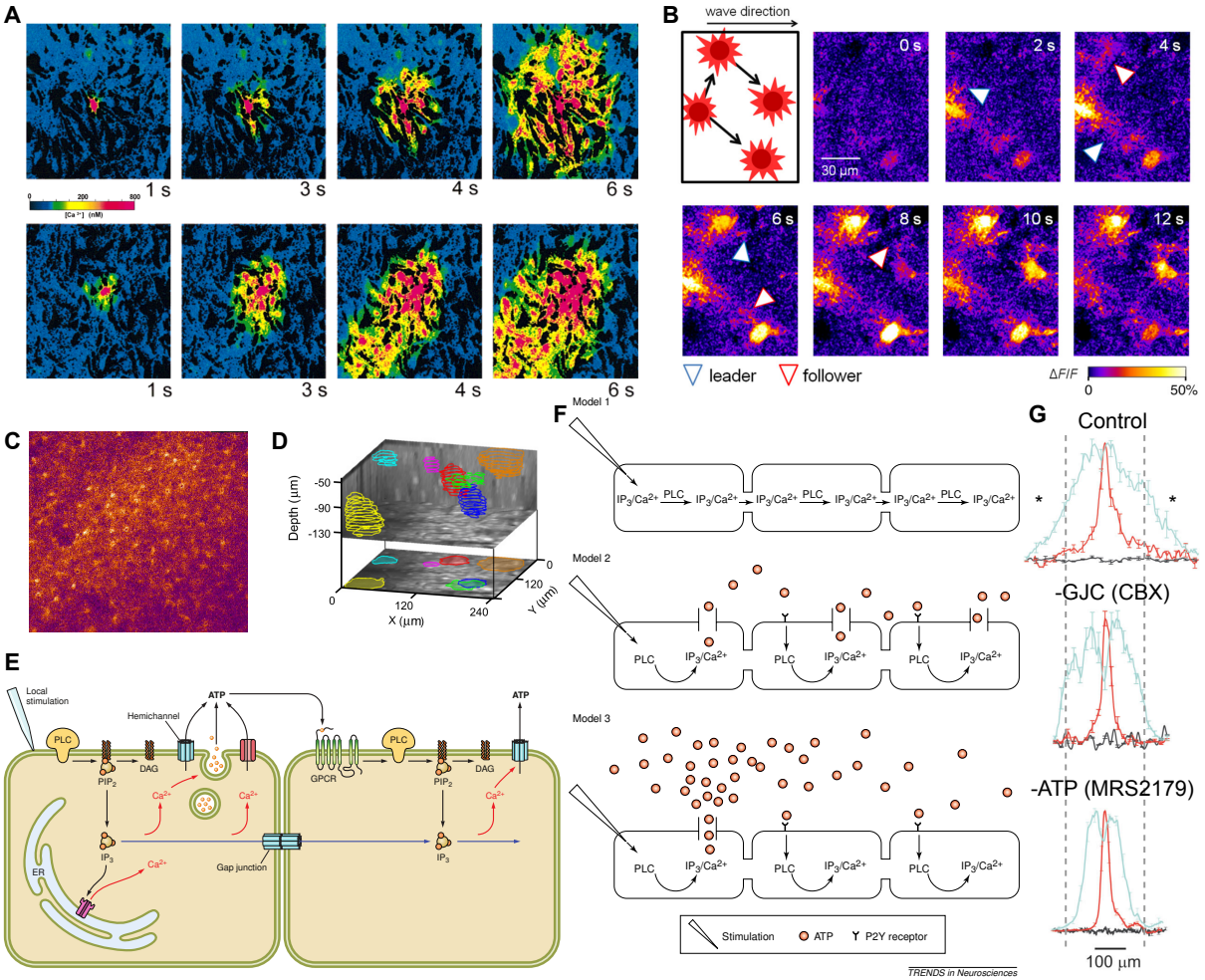

Figure I.6: Intercellular Ca^{2+} waves in astrocyte networks. **A** Mechanically-induced Ca^{2+} wave in a mixed glia culture. Top row presents control condition in which the wave is elicited by mechanical stimulation of the cell in the center. The wave propagates concentrically. Bottom row corresponds to the same setup as the top row but with rapid perfusion of the extracellular medium from the top right to the bottom left. After being mechanically elicited, the wave propagates preferentially to the bottom left quadrant, indicating the presence of an extracellular messenger. Taken from Charles (1998). **B** Close-up of 4 astrocytes during the propagation of large calcium waves in the hippocampus of anesthetized animals. Taken from Kuga et al. (2011). **C** Large scale calcium wave in hippocampal astrocytes can engulf hundreds of astrocytes. Taken from Kuga et al. (2011). **D** Smaller Ca^{2+} waves whose propagation was resolved in 3D were found to propagate in Bergman glia (colored contours indicate the waves maximum extent). Taken from Nimmerjahn et al. (2009). **E** Schematic representation of mechanisms of ICW propagation. Two main routes have been proposed, one involves the diffusion of IP_3 directly from cytosol to cytosol throug GJC and the other involved ATP release and diffusion in the extracellular space. Taken from Leybaert and Sanderson (2012). **F** Different combinations of these mechanisms can be imagined. Notably, the release of ATP could be regenerative or not. Taken from Nedergaard et al. (2003). **G** ICW propagation profiles before (*black* line), after 1s (*red* traces) and after 15s (*blue* line) of propagation. Top subplot: mechanically-elicited ICW propagation in control condition; middle subplot: the GJC-blocker carbenoxolone (CBX) is added; bottom subplot: the P2Y1 receptor antagonist MRS2179 is added. Vertical gray lines were added and represent the full width at half maximal height (FWHM) for the control condition. Taken and modified from Bowser and Khakh (2007).

(Blomstrand et al., 1999a). In situ experiments also display this ICW extent variability: only 1 to 5 astrocytes were activated in the ventrobasal thalamus of P5-P17 rats (Parri et al., 2001) while up to 35 astrocytes were activated in the neocortex of developing rats (Weissman et al., 2004).

The advent of more efficient Ca^{2+} imaging techniques eventually allowed the investigation of in vivo ICW. First reports of Ca^{2+} imaging in vivo seemed to indicate that ICW might be an artifact of culture or slices and may not occur in physiological condition. For example, experiments conducted in rat (Hirase et al., 2004) or mice (Wang et al., 2006) cortices, or in Ferret visual cortex (Schummers et al., 2008) reported Ca^{2+} elevations that remained restricted to individual astrocytes and did not propagate as ICW even upon sensory stimulation of the animals (Wang et al., 2006; Schummers et al., 2008). Later reports displayed small ICWs encompassing ≈ 10 astrocytes (Hoogland et al., 2009; Sasaki et al., 2011). More recent in vivo experiments however challenged this view and emitted several hypothesis explaining why ICW were not common in previous in vivo experiments. Notably, Kuga et al. (2011) showed that large scale ICW that engulfed over a hundred astrocytes and propagated at $\approx 60 \mu m.s^{-1}$ occurred in vivo in mice hippocampus in unstimulated animals. Figure I.6B and C respectively show close up of propagation of these waves and a larger view showing a high number of astrocytes being engulfed by the ICW. Interestingly, they reported that the intensity of the two-photon laser used for Ca^{2+} imaging was critically involved: only low ($< 10mW$) laser intensities allowed the observation of these large ICWs; higher laser intensities completely blocked these ICWs and increased sporadic astrocyte activity. A second hypothesis was emitted by Thrane et al. (2012) who, as mentioned previously, showed that anesthesia disrupted Ca^{2+} signaling in mice cortex. In agreement with this hypothesis, Nimmerjahn et al. (2009) showed relatively large (up to ≈ 36 cells) ICW in Bergmann glial networks of awake animals (represented in Figure I.6D). Additionally, ICW were shown to propagate in mice cortex in vivo in pathological conditions such as Alzheimer's disease (Kuchibhotla et al., 2009). The physiological relevance of ICW is thus still a point of debate and further in vivo experiments in awake animals might shed more light on their involvement in neuron-astrocyte interplay.

Two different pathways are usually evoked as supporting ICW propagation in astrocytes (schematic representation in Figure I.6E):
- diffusion of IP_3 from cytosol to cytosol by GJC that readily provokes Ca^{2+} activity by binding to IP_3R on the ER;
- extracellular diffusion of a messenger (usually ATP) that activates other astrocytes by binding to GPCRs (P2Y family) and provoking the synthesis of IP_3 therein.

We will present both pathways and the extent to which one might dominate the other in certain conditions.

Table I.2: Examples of astrocyte ICW.

Area	Prep.	Conditions	Pathway	GJC	Animal	Age	Extent (μm)	Nb. Astro.	Speed (μm/s)	Source
CC[5]	in situ	Normal	ATP	?	Mice	5-8d	150	N.A.	13.9 ± 1.8	Schipke et al. (2002)
Hipp.	in situ	Evoked [6]	ATP	?	Mice	7-12d	120	5	10.7 ± 0.82	Sul et al. (2004)
-	-	Evoked[7]	-	-	-	-	N.A.	17	N.A.	Sul et al. (2004)
Cx	Culture	Evoked[8]	GJC	?	Rats	1-3d	150	N.A.	4.12	Iwabuchi et al. (2002)
Ret.	In Vivo	Spontaneous	ATP	?	Rats	20-100d	67.7 ± 9.3 [9]	N.A.	22.1 ± 5.0	Kurth-Nelson et al. (2009)
Cx	In vivo	AD[10]	?	?	Mice	180-240d	196 ± 41	N.A.	22.7 ± 6.4	Kuchibhotla et al. (2009)
NeoCx[11]	in situ	Development	ATP[12]	?	Rats	E16-E17	75[13]	35	6.0 ± 0.07	Weissman et al. (2004)
Ret.	in vitro	Mech. stim.	?	?	Rats	adult	400	N.A.	13.8 ± 0.4	Newman and Zahs (1998)
VBT	in situ	Normal	?	?	Rats	5-17d	N.A.	1 to 5	3.67 ± 0.92	Parri et al. (2001)
SC[14]	Culture	Mech. stim.	GJC	WT	Mice	neonatal	80	N.A.	21.23 ± 0.6	Scemes et al. (2000)
-	-	-	ATP	Cx43KO	-	-	78	N.A.	23.09 ± 0.99	Scemes et al. (2000)
Tel.[15]	Culture	Mech. stim.	GJC	?	Chick	E17	$58\text{x}10^3$ μm^2	40	2 cells/s	Peters et al. (2005b)
-	-	+ 10 nM mel.[16]	GJC	?	-	-	$58\text{x}10^3$ μm^2	40	-	Peters et al. (2005b)
Dien.[17]	-	Mech. stim.	GJC	?	-	-	$59\text{x}10^3$ μm^2	45	2 cells/s	Peters et al. (2005b,a)
-	-	+ 10 nM mel.	GJC	?	-	-	$75\text{x}10^3$ μm^2	54	2.5 cells/s	Peters et al. (2005b,a)
Tel.	-	Mech. stim.	?	?	Mouse	1	$466\text{x}10^3$ μm^2	460	8.5 cells/s	Peters et al. (2005b)
-	-	+ 10 nM mel.	?	?	-	-	$466\text{x}10^3$ μm^2	460	-	Peters et al. (2005b)
Dien.	-	Mech. stim.	GJC	?	-	-	$136\text{x}10^3$ μm^2	125	5 cells/s	Peters et al. (2005b)
-	-	+ 10 nM mel.	?	?	-	-	$225\text{x}10^3$ μm^2	214	7 cells/s	Peters et al. (2005b)
Cx	Culture	Mech. stim.	GJC[18]	48.1%	Rats	7-11d	76.6%	N.A.	N.A.	Blomstrand et al. (1999a)
Hipp.	-	-	-	100%	-	-	100%	N.A.	-	Blomstrand et al. (1999a)
BS[19]	-	-	-	48.8%	-	-	41.9%	N.A.	-	Blomstrand et al. (1999a)
Hypoth.	-	-	-	101.4%	-	-	51.5%	N.A.	-	Blomstrand et al. (1999a)
Hipp.	In Vivo	Anesthetized	ATP/GJC[20]	yes	Mice	9-25d	N.A.[21]	116 ± 43	61 ± 22	Kuga et al. (2011)

[5]Corpus Callosum
[6]Glu uncaging
[7]ATP
[8]caged calcium ionophore
[9]0.2 (20d) - 1(120d) wave/min/mm^2
[10]Near Aβ plaques
[11]Radial glia
[12]P2Y1 / Cx hemichannels
[13]1-1 wave/min/mm^2
[14]Spinal Cord
[15]Telencephalic (Cx.)
[16]melatonin, decreases GJC
[17]Diencephalic (Hypoth.)
[18]abolished by 18α-GA
[19]Brain Stem
[20]Inhibited by suramin, CBX and TTX / Provoked by ATP
[21]0.3 wave/min that propagate out of the field

I.4.1.2 Gap junction channels

GJC are formed by the apposition of two Connexin (Cx) proteins that are either located on the same astrocyte (reflexive gap junction) or on different astrocytes (intercellular gap junction) (Giaume et al., 2010). When apposed, Cx proteins allow the diffusion of small molecules and ions through their central pore and can thus mediate cytosol-to-cytosol diffusion. Astrocytes mainly express Cx43 and Cx30 (Giaume et al., 1991; Rouach et al., 2002; Koulakoff et al., 2008) and we will thus only mention these Cxs.

The idea that GJC mediated ICWs in astrocytes was suggested by the fact that ICW propagation was prevented by GJC-blockers (Venance et al., 1997; Verkhratsky and Butt, 2013) and by experiments in which glioma cells devoid of GJC did not support ICW propagation while ICW were rescued by forced Cx43 expression (Charles et al., 1992). This idea was further reinforced by experiments showing that flash photolysis of caged IP_3 injected in a single astrocyte was sufficient to induce ICW in the injected astrocytes but also in distant astrocytes because of diffusion through GJC (Leybaert et al., 1998). Involvement of GJC in ICW is also attested in more recent studies by the reduction or prevention of ICW when GJC-blocker are applied (Iwabuchi et al., 2002; Haas et al., 2006; Lacar et al., 2011; Kuga et al., 2011). Additionally, ICWs supported by GJC usually display specific properties: the transmission is delayed at cell borders and the ICW does not necessarily propagate in a concentric way (because of heterogeneities in GJC coupling) (Peters et al., 2005b; Leybaert and Sanderson, 2012).

From Figure I.6E, one can see that the stimulated cell first produces IP_3 through the GPCR-dependent activation of PLCβ and this IP_3 then propagates to neighboring astrocytes through GJC. An important step is however omitted from this schematic representation, Venance et al. (1997) indeed showed that when Ca^{2+} rises in astrocyte, it activates the production of additional IP_3 by PLCδ. This fact provides a mechanism for regenerative ICW: when an astrocyte receives IP_3 from its neighbors, if it is sufficient to trigger a Ca^{2+} rise, IP_3 will again be produced and diffused to the next astrocytes, thus propagating the ICW front further. One could argue that, given their small size, Ca^{2+} ions could also diffuse through GJC and thus support ICW propagation instead of IP_3; this mechanism is however prevented by the strong buffering of Ca^{2+} in the cytoplasm (the effective diffusion coefficients of Ca^{2+} and IP_3 are respectively ≈ 13 and $\approx 280 \mu m^2.s^{-1}$) (Leybaert and Sanderson, 2012).

Finally, GJC-dependent ICW are of special interest in the context of neuron-astrocyte interplay because neurons have been shown to regulate Cx expression in astrocytes (Rouach et al., 2000, 2002; Koulakoff et al., 2008) and GJC permeability can be regulated by a high number of compounds, including some being released by neurons (Rouach et al., 2002; Orellana et al., 2013). Interestingly, unapposed Cx proteins form hemichannels (Giaume et al., 2010) which could open under certain conditions (including Ca^{2+} increases) and mediate the release of ATP in the extracellular space (Leybaert and Sanderson, 2012). Cxs could thus be involved in both GJC and extracellular route for ICW propagation.

I.4.1.3 Purinergic signaling

Early experiments indicated that GJCs were not the only pathway involved in ICW propagation: some ICWs in cultured astrocytes were found to propagate across cell-free zones (Charles, 1998) and their propagation direction could be controlled by rapid perfusion of the extracellular medium in a given direction (Hassinger et al., 1996). The latter phenomenon is represented in Figure I.6A on the bottom row, the extracellular medium is flowing from the top right corner to the bottom left corner and the mechanically-triggered ICW follows this direction. Analysis of the extracellular medium in cultures after ICW triggering suggested that ATP was the extracellular messenger involved in ICW propagation (Guthrie et al., 1999). Since ATP diffuses in the extracellular space, it is not constrained by heterogeneities in GJC coupling and the resulting ICW propagate in a more concentric manner compared with GJC-dependent ICWs (Peters et al., 2005b; Leybaert and Sanderson, 2012).

Figure I.6E represents different mechanism for ATP release; as explained previously, ATP could be released through unapposed Cx proteins (hemichannels) (Leybaert and Sanderson, 2012), but it could also be released by exocytosis of ATP-containing vesicles (Bowser and Khakh, 2007), or even by the opening of 'maxi' channels as evoked previously (Sabirov and Okada, 2009). Some of these mechanisms might be Ca^{2+} dependent (De Vuyst et al., 2009), which would provide a regenerative mechanism for ATP-mediated ICWs, or even ATP-dependent (Anderson et al., 2004). When ATP is released in the extracellular space, it binds to purinergic GPCRs of the P2Y family (P2Y1, P2Y2 and P2Y4 in astrocytes) and induces IP_3 formation by PLCβ (Verkhratsky and Butt, 2013). ATP can also activate ionotropic ATP receptors of the P2X family and thus induce Ca^{2+} entry in the cytoplasm (Leybaert and Sanderson, 2012).

Similarly to the GJC-mediated pathway, several experiments addressed whether ATP-mediated ICWs were based on regenerative ATP release (Figure I.6F, middle plot). Evidence towards regenerative ATP release was given by the fact that the width of cell-free zone in cultures seemed to have little effect on the ICW propagation in cells after the cell-free zone (Hassinger et al., 1996). Additionally, since blockers of P2 receptors decreased the size of the ATP wave, it was assumed that regenerative ATP release was at play (Newman, 2001; Kurth-Nelson et al., 2009). Other experiments however seem to indicate that ATP release is not regenerative and happens only at one cell; Arcuino et al. (2002) show for example that spontaneous ICW initiated by lowering extracellular Ca^{2+} were mediated by ATP release from a single cell that then diffused and activated nearby astrocytes without triggering further ATP release (Figure I.6F bottom plot).

In addition to the presence of Cx hemichannels, that links both pathways to the expression of Cx proteins, further links have been investigated between Cx expression and ATP-dependent signaling. As an example, increased Cx43 expression was linked to increased ATP release from hemichannels (Cotrina et al., 1998) and down-regulation of Cx43 in cultured spinal cord astrocytes was shown to decrease P2Y1 expression and increase P2Y4 expression (Scemes et al., 2000; Suadicani et al., 2003).

I.4.1.4 Interactions between the two pathways

GJC-dependent and ATP-dependent mechanisms are not necessarily exclusive and it seems that in some cases, both pathways can be involved in propagating ICWs. Forced expression of Cx43 in human astrocytoma cells was shown to mediate different ICWs depending on the specific P2Y receptors that were expressed (among P2Y1, P2Y2 and P2Y4) (Suadicani et al., 2004). In some other cases, both pathways can be independent: ICWs in the corpus callosum and the cerebellum are mediated only by ATP (Schipke et al., 2002; Nimmerjahn et al., 2009) and ICWs in the neocortex are primarily mediated by GJC and are independent from ATP waves (Haas et al., 2006). In the hippocampus, both pathways seem to be involved (Kuga et al., 2011; Torres et al., 2012) since both GJC-blockers and P2 receptor antagonist reduce ICW extent.

Figure I.6G is an interesting example of interaction between the two pathways, it presents the profiles of mechanically-induced ICWs in cultured hippocampal astrocytes; the *light blue* curve represents the ICW profile 15s after the initiation of the ICWs. In Bowser and Khakh (2007), the article from which these figures were taken, the authors claim that these ICWs are purely dependent on the ATP pathway by quantifying the full width at half maximum (FWHM) value of these ICW profiles. *Vertical gray dashed* lines were added and represent the FWHM in the control case (top subplot). When GJC blockers are added (middle subplot), the FWHM is nearly the same as in the control case but the astrocytes that were activated further away (marked by stars on the top subplot) are no longer activated; when a P2 receptor antagonist is added (bottom subplot), the FWHM is decreased and the wave propagated to much lower extents. In this example, ATP-only and GJC-only pathways both supported ICWs that propagated to a lower extent than the combination of both pathways.

Comprehensive reviews of ICWs can be found in Scemes and Giaume (2006); Fiacco and McCarthy (2006); Leybaert and Sanderson (2012).

I.4.2 Astrocyte networks

During the 80s, the discovery of widely expressed GJC coupling between astrocytes and some cases of coupling between astrocytes and other glial cells in cultures led to the concept of a panglial syncytium (Verkhratsky and Butt, 2013). GJC between astrocytes and other glial cells were however found to be much rarer in situ and in vivo and restricted to certain developmental and regional situations (Theis and Giaume, 2012). Additionally, GJC between astrocytes were found to be more complex than initially thought and to actually form networks whose topologies could change depending on the brain region investigated (Giaume et al., 2010). The pioneering studies revealing the complexity of astrocyte networks were mostly done by the group of Christian Giaume from College de France.

First, astrocytes as suggested by the fact that their protoplasmic subtype form non-

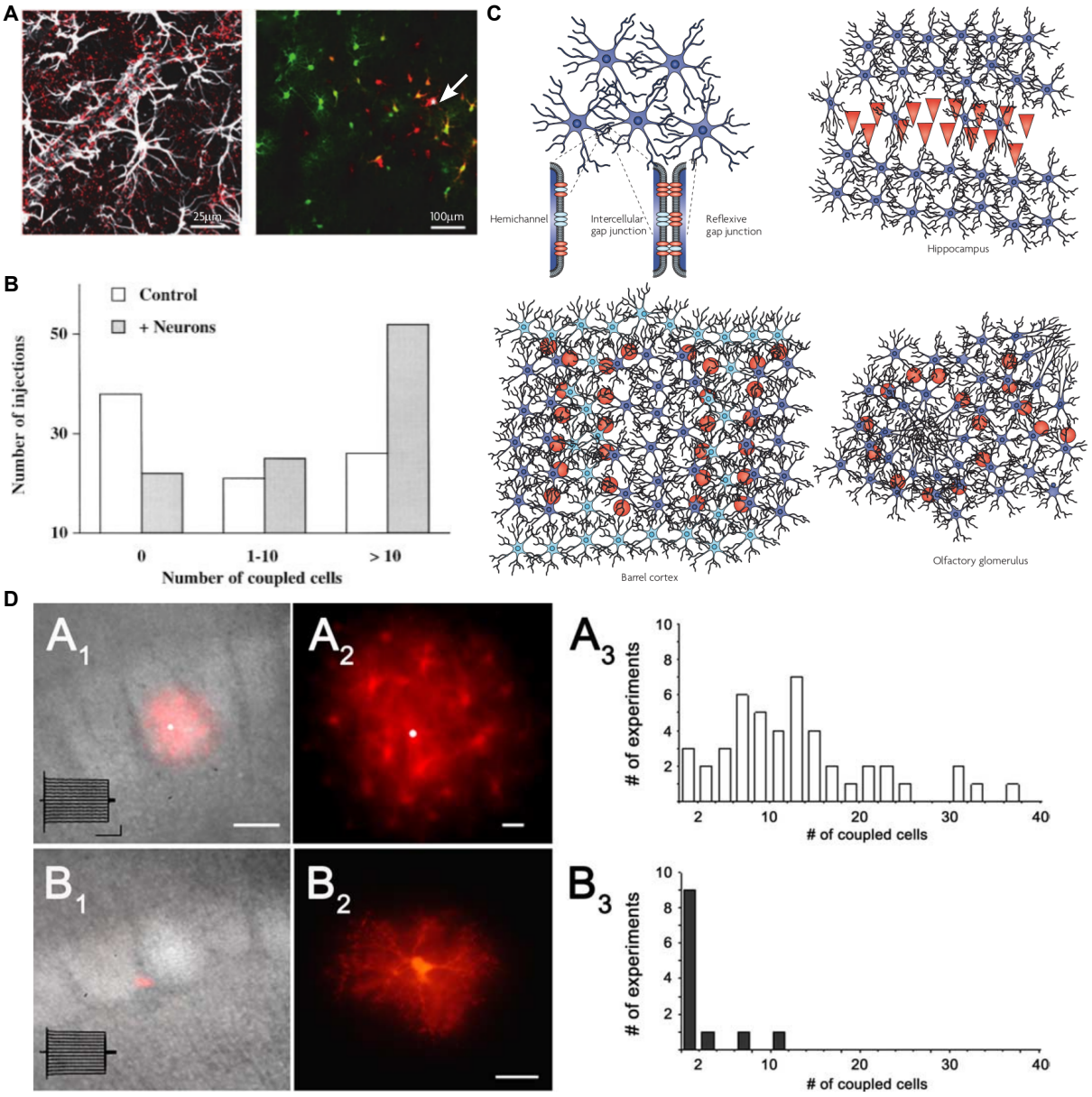

Figure I.7: Astrocyte networks are more complex than syncytia. **A** Left subplot: immunostaining of GFAP (*white*) and Cx30 (*red*). Right subplot: GFP expressing astrocytes (*green*) and biocytin (*red*) that has been injected in the cell pointed by the *white* arrow. The network of astrocytes revealed by the biocytin injection is much more complex than a syncytium, some astrocytes close to the injection site are not part of the network. Taken and modified from Giaume et al. (2010). **B** Sizes of coupling networks (i.e. number of astrocytes to which an intracellular dye diffuses after injection in one astrocyte) in astrocyte cultures with (*grey bars*) and without (*empty bars*) co-cultured neurons. Taken from Rouach et al. (2000). **C** Astrocytes in different brain regions are differently organized. Taken from Giaume et al. (2010). **D** Differential coupling properties of astrocytes in the barrel cortex. Astrocytes in barrels (top row) are coupled to bigger networks than astrocytes between barrels (bottom rows). The size of the networks was asserted by sulforhodamine B injections (*red*). Taken from Houades et al. (2008).

overlapping domains (Bushong et al., 2002), are not connected through their soma but rather through the end of their processes, at the boundaries between their anatomical domains (Giaume et al., 2010). This is illustrated by the left subplot of Figure I.7A in which Cx30, one of the main Cx expressed in astrocytes, is immunostained in *red* (and GFAP in *white*). The right subplot of Figure I.7A illustrates that astrocyte networks are more complex than initially thought: astrocytes express GFP (*green*) and biocytin (*red*) has been injected in the astrocyte marked by the *white* arrow; some astrocytes close to the injection site are not coupled. Figure I.7B shows that even in astrocyte cultures, some astrocytes are completely uncoupled (Rouach et al., 2000); such uncoupled astrocytes were also found in situ (Houades et al., 2006). These network heterogeneities have been reported in different parts of the brain, as represented in Figure I.7C. In the stratum pyramidale of the hippocampus (top right quadrant), the density of neurons affects the way astrocytes are coupled (Rouach et al., 2008). In the barrel cortex of rodents (bottom left quandrant), astrocytes within barrels (top row of Figure I.7D) are much more coupled than between barrels (bottom row of Figure I.7D) (Houades et al., 2008). In the olfactory glomeruli (bottom right quadrant), astrocytes were also more coupled within glomeruli than between (Roux et al., 2011). These local heterogeneities are also reflected in the observation that the total number of coupled astrocytes (obtained via e.g. biocytin-coupling experiments) vary a lot between brain regions: cortical astrocytes can be organized in networks of hundreds of cells (Nimmerjahn et al., 2004) while in the hippocampus, astrocytes in the CA3 region are much less coupled than in CA1 (D'Ambrosio et al., 1998). These variations in coupling can also be at least partially attributed to variations in the expression of connexins (Cx) 43 and 30, which also displays high heterogeneities (Giaume and Theis, 2010); for instance, hypothalamus and hippocampus display higher Cx43 levels than cortex and brain stem astrocytes (Blomstrand et al., 1999a).

Astrocytes networks have recently been proposed as playing roles that could not be mediated by individual astrocytes, Pannasch and Rouach (2013) review all these putative roles. GJC between astrocytes seem to help K^+ spatial buffering by diffusing it through astrocyte networks to distal sites where the extracellular K^+ levels are lower (Wallraff et al., 2006). Intercellular trafficking of energy metabolites (glucose and lactate for example) has been proposed to be mediated by astrocyte networks and to directly contribute to neuronal energy supply (Rouach et al., 2008). Astroglial networks, because of the role they play in transmitter and ion homeostasis have even been shown to tone down hippocampal synaptic transmission in CA1 pyramidal neurons and to indirectly control synaptic strength (Pannasch et al., 2011). ICW in astrocyte networks was suggested to support hippocampal heterosynaptic depression which is involved in learning and memory (Serrano et al., 2006). Astrocyte networks were also proposed, although it remained highly speculative, as involved in the development and plasticity of cortical sensory maps (López-Hidalgo and Schummers, 2014). Finally, animals deficient in Cx30, Cx43 or both display behavioral changes: Cx30-defficient mice displayed increased emotionality and decreased rearing activity (Dere et al., 2003); increased exploratory behavior but decreased motor capacities (Frisch et al., 2003) as well as accelerated hippocampal spreading depression and enhanced locomotory activity (Theis et al., 2003) were observed in mice with astrocyte-directed inactivation of Cx43.

Since astrocyte networks could be regulated by neurons both in terms of Cx expression (Rouach et al., 2000, 2002; Koulakoff et al., 2008) and GJC permeability (Rouach et al., 2002; Orellana et al., 2013), the influence of their structure on their different functions, if any, could be of importance to understand neuron-astrocyte interplay. Detailed experimental data quantifying the strength of diffusive coupling between astrocytes is however lacking; the best quantification available, to our knowledge, reports coupling length constants estimated by fluorescent dye injections in the hippocampal CA1 stratum radiatum in which anisotropic coupling was found (Anders et al., 2014). Modeling astrocyte networks could thus prove useful in determining how different topologies could affect Ca^{2+} signaling.

Chapter II

Modeling astrocyte activity

II.1 Single astrocyte modeling

As we saw in the previous chapter, astrocytes have many functions, some of which are not well understood. These functions usually involve nonlinear mechanisms that are very difficult to approach by intuitive reasoning or thought experiments. The development of computational models can thus bring insights into the functioning of some of these mechanisms. Ca^{2+} signaling, since it can be experimentally investigated at both cellular and subcellular levels with fluorescent Ca^{2+} dyes, has been the subject of modeling in a variety of cells, including astrocytes. Other functions have been less modeled either because of the lack in quantitative experimental data or because the related phenomena have only been recently discovered (Na^+ waves for example). We will thus restrict ourselves to Ca^{2+} signaling; although Ca^{2+} signaling has been treated in many different cell types, we will only present the common mechanisms between these cell types and the specificities of astrocytes.

II.1.1 Ca^{2+} signaling

As we saw in Section I.2, Ca^{2+} signaling in astrocytes can be linked to Ca^{2+} entry from the extracellular space or Ca^{2+} release in the cytoplasm of Ca^{2+} sequestered in intracellular Ca^{2+} stores. We will here focus on models that are store-dependent, other types of models are reviewed in Falcke (2004); Blackwell (2005); Dupont et al. (2007, 2011). Store-dependent Ca^{2+} dynamics ultimately depend on the opening and closing of channels (RyRs or IP_3Rs) on the ER membrane; in astrocytes, the involvement of RyRs is still controversial (Verkhratsky and Butt, 2013) so we will not present models of RyRs (Tang and Othmer, 1994; Keizer and Levine, 1996; Zahradnikova and Zahradnik, 1996) and focus instead on IP_3Rs modeling. Among store-dependent models of Ca^{2+} signaling, the levels of details greatly vary depending on the type of signals that the model

aims at explaining, on the type of cells, and on the spatial scale considered. Opening and closing of IP_3Rs can be modeled at the level of individual channels because their dynamics have been experimentally characterized (Foskett et al., 2007). The opening of single IP_3R channels can lead to Ca^{2+} 'blips' (i.e. local increases in Ca^{2+} concentration) which, if strong enough, can recruit a whole cluster of IP_3R through CICR, provoking a Ca^{2+} 'puff' (Dupont et al., 2011). Since these processes involve a low number of IP_3R channels, they cannot be modeled by deterministic equations and require a stochastic description (Swillens et al., 1999; Williams et al., 2008; Smith and Parker, 2009). Going up in spatial scale, the simultaneous opening of several nearby IP_3R clusters can trigger an intracellular Ca^{2+} wave that engulf the whole cell; in order to model this phenomenon, one has to take space into account by writing partial differential equations (Falcke, 2004). Another approach is to simplify the underlying Ca^{2+} release mechanism and assume that Ca^{2+} release sites are localized in the intracellular space and release a given amount of Ca^{2+} when the local concentration of Ca^{2+} exceeds a threshold; the rest of the intracellular space just diffuses Ca^{2+} and reintegrates it in the ER. These 'threshold' models, or 'fire-diffuse-fire' models, support saltatory intracellular wave propagation (Bugrim et al., 1997; Keizer et al., 1998; Dawson et al., 1999; Coombes and Timofeeva, 2003; Thul et al., 2008). Finally, if one is not interested in the intracellular Ca^{2+} waves but rather in the average Ca^{2+} oscillations in the whole soma of cells, one can adopt a macroscopic description and use deterministic models which can consider detailed chemical reactions assuming that the reactants are numerous and well mixed (Dupont et al., 2007). We will focus here on this type of modeling in which intracellular space is neglected.

Since the models that we will present rely on store-dependent Ca^{2+} release, they share a common description of Ca^{2+} fluxes between the cytoplasm and the ER (Falcke, 2004; Blackwell, 2005). Figure II.1A represents the three Ca^{2+} fluxes that are usually taken into account in store-dependent models:

- J_C, the Ca^{2+} efflux from the ER to the cytosol through IP_3R channels; this flux depends on the opening of IP_3R channels which are gated by IP_3 and cytosolic Ca^{2+};
- J_L, a passive leak from the ER to the cytosol;
- J_P, the reintegration of Ca^{2+} in the ER by SERCA pumps.

The resulting equation for the Ca^{2+} concentration in the cytosol C_{cyt} thus usually reads:

$$\frac{dC_{cyt}}{dt} = J_C + J_L - J_P \tag{II.1}$$

Under the asumption that the total quantity of Ca^{2+} in cytosol and ER is conserved, the Ca^{2+} concentration in the ER follows $\frac{dC_{ER}}{dt} = -\frac{1}{\rho_A}\frac{dC_{cyt}}{dt}$ with $\rho_A = \frac{V_{ER}}{V_{cyt}}$ the ratio between the volumes of the ER and the cytosol. The passive leak term J_L depends on the Ca^{2+} difference between the ER and the cytosol $C_{ER} - C_{cyt}$ and is thus written as:

$$J_L = \Omega'_L(C_{ER} - C_{cyt}) \tag{II.2}$$

with $\Omega'_L = \rho_A\Omega_L$ the rescaled maximal leak rate. Since J_C depends on the number of opened IP_3R channels, it is written as:

$$J_C = \Omega'_C p_{open}(C_{cyt}, I)(C_{ER} - C_{cyt}) \tag{II.3}$$

with $\Omega'_C = \rho_A \Omega_C$ the rescaled maximal release rate (if all IP_3R channels were open) and $p_{open}(C_{cyt}, I)$ the probability that an IP_3R channel is open which depends on the Ca^{2+} and IP_3 concentrations in the cytoplasm C_{cyt} and I. Finally, Ca^{2+} uptake by the SERCA pump J_P is usually modeled using Michaelis-Menten kinetics: SERCA pumps bind two Ca^{2+} ions for each ATP molecule used which results (Blackwell, 2005) in:

$$J_P = O_P \mathcal{H}\left(C_{cyt}^2, K_P\right) \tag{II.4}$$

where the function $\mathcal{H}\left(x^n, K\right)$ denotes the sigmoid (Hill) function $\frac{x^n}{x^n + K^n}$, O_P is the maximal uptake rate and K_P is the SERCA pump Ca^{2+} affinity.

For models that do not take into account Ca^{2+} fluxes between the cytosol and the extracellular space, the total free Ca^{2+} in the astrocyte can be assumed constant and the ODE for C_{ER} is no longer needed, one can instead compute C_{ER} using:

$$C_T = C_{cyt} + \rho_A C_{ER} \tag{II.5}$$

with C_T the free Ca^{2+} concentration that the cytosol would reach if the ER was completely emptied of its free Ca^{2+}. Using this relationship, one can replace $C_{ER} - C_{cyt}$ in the above equations by $\frac{1}{\rho_A}(C_T - (1 + \rho_A)C_{cyt})$ and C_{cyt} by C since the distinction between cytosol and ER is no longer needed. equation (II.1) can thus be rewritten as:

$$\frac{dC}{dt} = (\Omega_C p_{open}(C, I) + \Omega_L)(C_T - (1 + \rho_A)C) - O_P \mathcal{H}\left(C^2, K_P\right) \tag{II.6}$$

Although this Ca^{2+} dynamics equation constitutes a common base for a variety of models (Falcke, 2004), they differ by the way they compute the open probability of IP_3Rs $p_{open}(C, I)$. As presented in Figure I.3B, this probability is a bell-shaped function of C. Foskett et al. (2007) review the experimental evidence for this Ca^{2+} dependence as well as for the IP_3 dependence. Although most models neglect it, IP_3Rs can be expressed as three different subtypes; notably, type 2 IP_3Rs which are the most present in astrocytes (Verkhratsky and Butt, 2013) may display a sigmoid-shaped open probability as a function of Ca^{2+} for low IP_3 values (Ramos-Franco et al., 2000; Sneyd and Dofour, 2002). It is however unlikely that, under physiological circumstances, both low IP_3 and high Ca^{2+} coexist and this particularity is thus usually not taken into account. Different models for IP_3R opening are reviewed in (Falcke, 2004; Sneyd and Falcke, 2005), we will present here the well-known De Young-Keizer model (De Young and Keizer, 1992) and its simplified Li-Rinzel (Li and Rinzel, 1994) version.

II.1.1.1 The De Young-Keizer model

IP_3R channels are composed of four subunits (Foskett et al., 2007) each of which can be activated and mediate a 20pS increase in the channel conductance (Watras et al., 1991). When three subunits are activated, the channel opens during longer periods and more frequently than at other conductance states. Consequently, De Young and Keizer assumed that channels were opened when three of their subunits were activated (Figure II.1B,

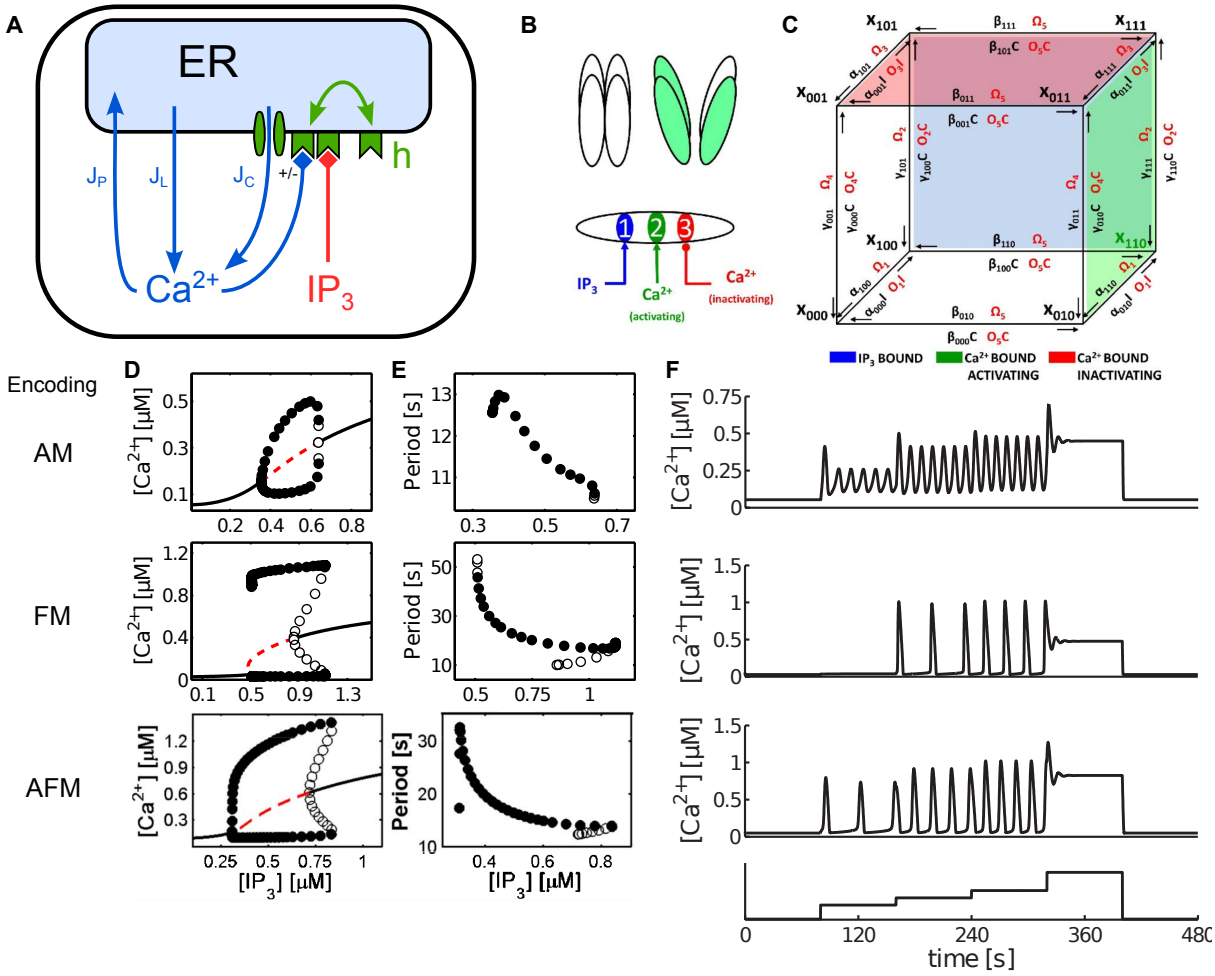

Figure II.1: De Young-Keizer and Li-Rinzel models for IP_3R and Ca^{2+} dynamics. **A** Schematic representation of the Ca^{2+} fluxes in the Li-Rinzel model. **B** Schematic representation of a closed (top left) and open (top right) IP_3 receptor with activated subunits (*light green*) in the De Young-Keizer model. One subunit has 3 binding sites, one for IP_3 (*blue*) and two for Ca^{2+} which are activating (*green*) and inactivating (*red*). Taken from De Pittà (2013). **C** Representation of the eight possible states of each IP_3R subunit in the De Young-Keizer model as a cube whose edges represent the different transitions between states with their associated rates. Taken from De Pittà (2013). **D** Bifurcation diagrams showing different Ca^{2+} encoding of the IP_3 levels. Circles represent stable (full) and unstable (empty) limit cycles while lines represent stable (continuous *black*) and unstable (dashed *red*) fixed points. **E** Periods of oscillations change with the concentration of IP_3 for FM and AFM encoding but is almost constant (≈ 12s) for AM encoding. Same graphical conventions as in D. **F** Ca^{2+} traces for different encoding regimes as the IP_3 concentration is increased by steps (bottom plot). **D, E, F** Taken from De Pittà et al. (2008).

activated subunits are in *green*). In addition to this simplification, each subunit was considered independent and had three binding sites (Figure II.1B, bottom part): one for IP_3, one activating site for Ca^{2+} and one inactivating site for Ca^{2+}. Each of these sites can either be bound (1) or unbound (0); each subunit can thus be in $2^3 = 8$ states. Depending on binding rates of IP_3 and Ca^{2+}, subunits can switch from one state to another according to the transitions represented in Figure II.1C; by denoting by x_{ijk} the fraction of receptors in the state ijk (with $i = 1$ if IP_3 is bound and 0 otherwise, $j = 1$ if the activating Ca^{2+} is bound, $k = 1$ if the inactivating Ca^{2+} is bound), they consider the following transitions:

$$\begin{aligned}
&\text{Binding of } IP_3: && 0jk \underset{\alpha_{0jk}}{\overset{\alpha_{1jk}I}{\rightleftharpoons}} 1jk \\
&\text{Binding of activating } Ca^{2+}: && i0k \underset{\beta_{i0k}}{\overset{\beta_{i1k}C}{\rightleftharpoons}} i1k \\
&\text{Binding of inactivating } Ca^{2+}: && ij0 \underset{\beta_{ij0}}{\overset{\beta_{ij1}C}{\rightleftharpoons}} ij1
\end{aligned}$$

From these transitions, one can write the ODEs for the fraction of subunits that are in each state $\frac{dx_{ijk}}{dt} = \ldots$. The opening probability of an IP_3R channel corresponds to the probability that 3 subunits are activated (i.e. they have bound IP_3 and activating Ca^{2+} but not inactivating Ca^{2+}) and is thus $p_{open} = x_{110}^3$ (De Young and Keizer, 1992). The authors then simplify the model by assuming that IP_3 binding is fast compared to the other bindings; they assume that IP_3 binding is always at equilibrium, which allow the removal of four equations. The resulting system is composed of 4 equations, one for Ca^{2+} and 3 for IP_3R dynamics (one is removed because $\sum_{ijk} x_{ijk} = 1$).

II.1.1.2 The Li-Rinzel model

The model developed by De Young and Keizer can be reduced even further by taking into account the fact that inactivating Ca^{2+} binding is slower than activating Ca^{2+} binding (Tang et al., 1996). After derivation, (Li and Rinzel, 1994), the model can be reduced to two equations, one for the Ca^{2+} concentration, and one for the probability h that a subunit is not inactivated by Ca^{2+} with:

$$p_{open}(C, I) = (m_\infty h)^3 \tag{II.7}$$

In the De Young-Keizer model, the open probability was computed as $p_{open} = x_{110}^3$ (i.e. the probability that 3 subunits are in the 110 activated state). In the Li-Rinzel model m_∞ is the steady state probability that a subunit has bound both IP_3 and activating Ca^{2+}, and h is the probability that it has not bound the inactivating Ca^{2+}; $m_\infty h$ is thus the equivalent to x_{110} in the De Young-Keizer model. m_∞ is computed with:

$$m_\infty = \mathcal{H}(I, d_1)\, \mathcal{H}(C, d_5) \tag{II.8}$$

and the equation for h presented following the Hodgkin-Huxley (HH) formalism:

$$\frac{dh}{dt} = \frac{h_\infty - h}{\tau_h} \tag{II.9}$$

Equation II.6, together with equation (II.7) and II.9, are indeed reminiscent of the HH model of membrane excitability (Hodgkin and Huxley, 1952): C is analogous to the membrane potential V in the HH model in the sense that the Ca^{2+} concentration gradient between cytosol and ER (the difference between membrane potential and Nernst reversial potential in the HH model) is the driving force of excitability. Additionally, in both Li-Rinzel and HH models, channel activation and inactivation are presented as separate factors m and h whose dynamics follow equations similar to equation (II.9). with: h_∞ follows:

$$h_\infty = d_2 \frac{I + d_1}{d_2(I + d_1) + (I + d_3)C} \tag{II.10}$$

and

$$\tau_h = \frac{I + d_3}{\Omega_2(I + d_1) + O_2(I + d_3)C} = \frac{1}{\Omega_h} \tag{II.11}$$

Despite a strong dimensionality reduction, the resulting model closely mimics the behavior of the original De Young-Keizer model (Li and Rinzel, 1994). Notably, the steady state open probability $p_{open_\infty} = (m_\infty h_\infty)^3$ is bell-shaped as a function of Ca^{2+} and sigmoid as a function of IP_3, in agreement with experimental observations (Foskett et al., 2007). This model has thus been adopted in numerous computational studies of astrocyte Ca^{2+} dynamics (Nadkarni and Jung, 2004; Politi et al., 2006; Nadkarni and Jung, 2007; Volman et al., 2007; Nadkarni et al., 2008).

Despite its simple formulation, the Li-Rinzel model still gives rise to interesting Ca^{2+} dynamics. Since the variations in intracellular concentration of IP_3 I are not taken into account, one can treat I as a parameter: for low IP_3 concentrations, no Ca^{2+} oscillations occur, but when IP_3 is increased (e.g. when a GPCR agonist is applied) Ca^{2+} oscillations arise. This can be visualized in Figure II.1D on the top subplot: the bifurcation diagram indicates that above $I \approx 0.3\mu$M, C starts to oscillate and the amplitude of these oscillations increases with I; above $I \approx 0.65\mu$M, Ca^{2+} oscillations stop and the Ca^{2+} concentration in the cell stays elevated (a situation that resembles experimentally observed Ca^{2+} plateaus in some astrocytes, c.f. Figure I.5B for example). Ca^{2+} oscillations for the same set of parameters can be seen in Figure II.1F (top plot); during this simulation, I is increased by steps (bottom plot) and the amplitude of Ca^{2+} oscillations is modified accordingly. For this set of parameters, that correspond to the original Li-Rinzel parameters, changes in IP_3 concentration are encoded in changes in amplitude of Ca^{2+} oscillations. Figure II.1E (top plot) indeed shows that the oscillation frequency stays roughly constant ($\approx 1/12 = 0.083$Hz) as I increases. This set of parameters is thus associated to amplitude modulation (AM) encoding of the IP_3 levels in Ca^{2+} oscillations.

Experimentally, astrocytes have been reported to react to increased stimulus intensity by increases in their Ca^{2+} oscillation frequencies (Parpura, 2004) (which would correspond to frequency modulation, or FM, encoding). At the same time, astrocytes have also been reported to react with increased amplitude of Ca^{2+} spikes or oscillations (Cornell-Bell et al., 1990; Finkbeiner, 1993; Torres et al., 2012); amplitude modulation of Ca^{2+} oscillations by IP_3 could thus account in the model for these behaviors. Interestingly, the Li-Rinzel model can also display FM and mixed amplitude and frequency modulation (AFM) for specific sets of parameters (De Pittà et al., 2008); corresponding bifurcation

diagrams, evolution in oscillation period and Ca^{2+} traces can be seen in Figure II.1D, E and F. Several parameters can be modified in order to switch from one encoding mode to another. Notably, the activating Ca^{2+} binding affinity d_5 (a parameter that regulates how fast IP_3R channels open and CICR occurs) can control the switch between AM and FM modes. But d_5 is not the only parameter that can control this switch, other parameters that are not related to IP_3R opening, like the Ca^{2+} affinity of SERCA pump K_P, their rate of Ca^{2+} uptake, or the leakage rate Ω_L from the ER, are all examples of such parameters (De Pittà et al., 2008; De Pittà, 2013).

Since IP_3 is a parameter in the Li-Rinzel model, it is not possible to simulate agonist-induced Ca^{2+} oscillations: as we saw in Section I.2, agonist-induced GPCR-mediated Ca^{2+} oscillations go through PLCβ activation that increases IP_3 concentration. To account for this activation pathway, one has to model the different processes that lead to the creation and degradation of IP_3. Among the relatively high numbers of such models (Cuthbertson and Chay, 1991; Dupont and Erneux, 1997; Meyer and Stryer, 1988; Kummer et al., 2000; Höfer et al., 2002), we chose to focus on the ChI model (Pittà et al., 2009; Goldberg et al., 2010) since we will use it in the next chapters.

II.1.1.3 The ChI model of calcium dynamics

The ChI model is declined in two main versions, the first one takes into account modulations of IP_3 by Ca^{2+}-dependent enzymes but does not consider GPCR signaling (Goldberg et al., 2010); it can thus be used to investigate astrocytic responses under a generic stimulation (a constant IP_3 influx for example) without considering models of agonist release and diffusion/degradation in the extracellular space. In particular, this model is useful to study ICW in astrocytes networks independently of agonist-dependent stimulation protocols. The second version (which we will call G-ChI) will be presented in Section II.1.2 and takes into account PLCβ-mediated IP_3 creation in response to agonists such as glutamate or ATP; it is thus well suited to investigate neuron-astrocyte interactions.

Figure II.2A shows a schematic representation of the dynamics taken into account by the ChI model (compare to Figure II.1A). The Ca^{2+} signaling model is still based on the Li-Rinzel model (Ca^{2+}, in *blue* and the fraction of IP_3R that have not been inactivated by Ca^{2+} h, in *green*) but the concentration of IP_3 (*red*) is now a dynamical variable that depends on Ca^{2+} dynamics. As evoked in Section I.4.1.1, increases in cytosolic Ca^{2+} concentration have been linked to IP_3 creation by PLCδ and this mechanism is required to support GJC-dependent ICW that propagates to more than a few astrocytes (Venance et al., 1997). The production of IP_3 by PLCδ in the ChI model is thus associated with the flux J_δ in Figure II.2A and corresponds to the more detailed signaling pathway represented in Figure II.2D: Ca^{2+} binds to PLCδ and activates it; PLCδ transforms membrane-bound phosphatidylinositol 4,5-bisphosphate (PIP_2) to freely diffusing IP_3 and diacylglycerol (DAG) by hydrolysis; in return, high concentrations of IP_3 inhibit this process.

In addition to IP_3 creation, the ChI model takes into account two different pathways

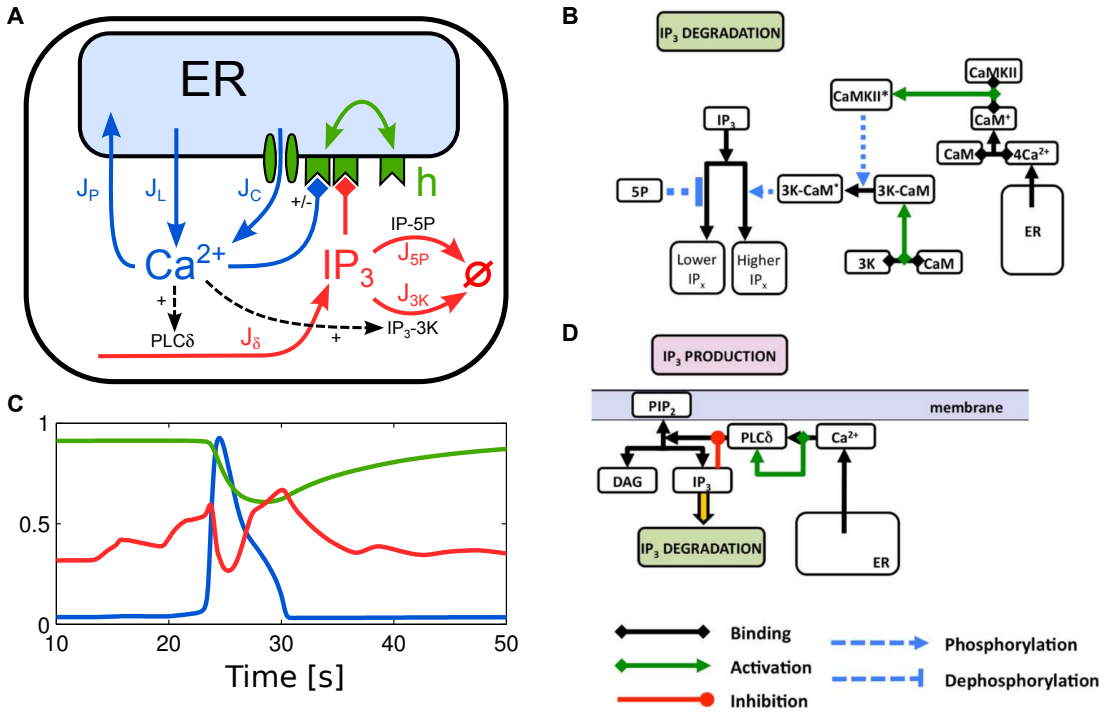

Figure II.2: The ChI model of Ca^{2+} dynamics. **A** Schematic description of the ChI model, in addition to the Ca^{2+} dynamics of the Li-Rinzel model (c.f. Figure II.1A), IP_3 is variable and is produced by $PLC\delta$ and degraded by IP_3-3K and IP-5P. **B** Detailed signaling pathways involved in IP_3 degradation. Taken from Goldberg et al. (2010). **C** Time course of a typical astrocyte activation showing the intracellular Ca^{2+} concentration C (*blue* curve), the fraction of IP_3Rs that are not unactivated by Ca^{2+} h (*green* curve) and the intracellular IP_3 concentration I (*red* curve). **D** Detailed signaling pathways involved in IP_3 production. Taken from Goldberg et al. (2010).

for IP_3 degradation: one that is mediated by Ca^{2+}-independent inositol polyphosphate 5-phosphatase (IP-5P) and corresponds to the J_{5P} IP_3 flux in Figure II.2A; the other that is mediated by Ca^{2+}-dependent IP_3 3-kinase (IP_3-3K) and corresponds to the J_{3K} IP_3 flux in Figure II.2A. Figure II.2B represents the more detailed signaling pathways that mediate IP_3 degradation. While the rate of IP-5P-mediated degradation (dephosphorylation to IP_2) is constant, the rate of IP_3-3K-mediated degradation is controlled by Ca^{2+}: IP_3-3K actually degrades IP_3 (by phosphorylation to IP_4) only when it gets phosphorylated by Ca^{2+}/calmodulin-dependent protein kinase II.

Taking into account the three IP_3 fluxes represented in Figure II.2A, the resulting model reads (Goldberg et al., 2010; De Pittà, 2013):

$$\frac{\mathrm{d}}{\mathrm{d}t}C = J_C(C,h,I) + J_L(C) - J_P(C) \tag{II.12}$$

$$\frac{\mathrm{d}}{\mathrm{d}t}h = \Omega_h(C,I)\cdot(h_\infty(C,I) - h) \tag{II.13}$$

$$\frac{\mathrm{d}}{\mathrm{d}t}I = J_\delta(C,I) - J_{3K}(C,I) - J_{5P}(I) \tag{II.14}$$

with:

$$J_C(C,h,I) = \Omega_C \cdot m_\infty^3 h^3 \cdot (C_T - (1+\rho_A)C) \qquad m_\infty(C,I) = \mathcal{H}(C,d_5)\,\mathcal{H}(I,d_1)$$
$$J_L(C) = \Omega_L \cdot (C_T - (1+\rho_A)C) \qquad J_P(C) = O_P \mathcal{H}\left(C^2, K_P\right)$$
$$h_\infty(C,I) = d_2 \frac{I+d_1}{d_2(I+d_1)+(I+d_3)C} \qquad \Omega_h(C,I) = \frac{\Omega_2(I+d_1)+O_2(I+d_3)C}{I+d_3}$$
$$J_\delta(C,I) = O_\delta \cdot \frac{\kappa_\delta}{\kappa_\delta + I}\mathcal{H}\left(C^2, K_\delta\right) \qquad J_{3K}(C) = O_{3K} \cdot \mathcal{H}\left(C^4, K_D\right)\mathcal{H}(I,K_3)$$
$$J_{5P}(I) = \Omega_{5P} \cdot I$$

The equations for C and h are identical to the Li-Rinzel model. Figure II.2C shows representative traces of C (*blue* curve), h (*green* curve), and I (*red* curve) during the propagation of an ICW. IP_3 concentration first increases without really affecting the cytosolic Ca^{2+}, when IP_3 reaches a certain value (around 22s), the CICR mechanism produces a rapid opening of IP_3R channels associated with the Ca^{2+} spike. This increase in Ca^{2+} decreases h (increases the probability for an IP_3R to be inactivated by Ca^{2+}) and thus terminates the CICR as Ca^{2+} gets reintegrated in the ER by SERCA pumps. When C is high, both PLCδ and IP_3-3K are activated; IP_3-3K however degrades IP_3 faster than PLCδ creates it and the top part of the Ca^{2+} spike is thus associated to fast IP_3 degradation that participates in the stopping of CICR. When C gets back to intermediate concentrations (end of the Ca^{2+} spike), IP_3-3K is no longer activated while PLCδ is still activated; the astrocyte thus creates additional IP_3 that can diffuse to GJC-coupled astrocytes in the case of ICW propagation.

II.1.2 Astrocytic responses to neuronal activity, the G-ChI model

Modeling the GPCR-dependent IP_3 production pathway, since several different receptors (mGluRs and P2YRs for example) activate the same PLCβ-mediated pathway, can be used for simulating both neuron-astrocyte communication (by glutamate (Wang et al., 2006) or ATP (Di-Castro et al., 2011)) and inter-astrocyte paracrine communication through ATP (Leybaert and Sanderson, 2012) (some of these latter models will be reviewed in Section II.2). Neuron-astrocyte signaling however also requires modeling of at least (1) synaptic release, if one just wants to address the encoding of trains of action potentials in astrocytic Ca^{2+} response, and (2) neuronal network dynamics, if one wants to investigate neuron-astrocyte interactions at a network level. We will not address the second point which is still very strongly limited by the scarcity of biological data concerning the way neuron networks could be coupled to astrocytes (Verkhratsky and Butt, 2013).

II.1.2.1 Synaptic transmission

Models of synaptic dynamics can be broadly categorized between stochastic and deterministic; stochastic models are closer to experiments when describing single synapses: the

synaptic release of neurotransmitter is indeed intrinsically stochastic and some action potentials (AP) might not trigger transmitter release. Deterministic models are more suited instead when considering a high number of synapses or when investigating processes in which the exact timing of neurotransmitter release is less important than the average quantity of neurotransmitter released in a given period (with a given frequency of AP). In the case of astrocytes, the time scale of Ca^{2+} dynamics in astrocytes is of the order of seconds (Verkhratsky and Butt, 2013) while the timescale of neurotransmitter release is of the order of milliseconds. The deterministic approach is thus well suited to address synaptic release in the context of neuron-astrocyte communication.

Many synaptic release models have been elaborated in order to account (among other mechanisms) for short-term plasticity mechanisms whereby the quantity of neurotransmitter released by the presynaptic terminal can either be increased or decreased depending on the recent synaptic activity (Zucker and Regehr, 2002; Abbott and Regehr, 2004). As an example, if a synapse has recently been highly active, the quantity of neurotransmitter vesicles that are available for release is usually lower than when the synapse has been silent, thus provoking short-term depression of the synapse (i.e. decreased quantity of released neurotransmitters). We will present here the Tsodyks and Markram (TM) model for short-term synaptic plasticity (Tsodyks and Markram, 1997; Markram et al., 1998) which will be used in Chapter IV.

Figure II.3A schematically represents the TM model; when an AP reaches the presynaptic terminal, it provokes the opening of voltage sensitive channels that allow Ca^{2+} to flow into the presynaptic terminal. Ca^{2+} then provokes, through complex mechanisms (Kandel et al., 2000b), the release of neurotransmitters by exocytosis (i.e. fusion of neurotransmitters-containing vesicles to the presynaptic cell membrane). The TM model is a phenomenological model based on two variables which correspond to the fraction of available resources (called x and represented as *purple* synaptic vesicles in the presynaptic terminal) and the fraction of available resources that are ready for release (called u and represented as the vesicles inside the area delimited by the *dashed green* line). This latter fraction can also be seen as the release probability of available resources. Schematically speaking, when an AP arrives, Ca^{2+} entry transforms (circled number 1) a fraction U_0 of available resources that are not ready for release (vesicles in the *dashed red* rectangle) into vesicles available for release (vesicles in the area delimited by the *dashed green* line); in other words, it increases release probability. The AP also releases the ux available resources ready for release (circled number 2). As Ca^{2+} concentration gets lower after the AP (Ca^{2+} is pumped out by plasma membrane Ca^{2+} ATPase), the release probability decreases with a rate Ω_f (circled number 3). At all time, the released resources are reintegrated at rate Ω_d (circled number 4). The corresponding equations read:

$$\frac{\mathrm{d}}{\mathrm{d}t}u = -\Omega_f u + U_0 \sum_j (1-u)\delta(t-t_j) \tag{II.15}$$

$$\frac{\mathrm{d}}{\mathrm{d}t}x = \Omega_d(1-x) - \sum_j ux\delta(t-t_j) \tag{II.16}$$

the Dirac delta function $\delta(t-t_j)$ models the arrival of an AP at time t_j.

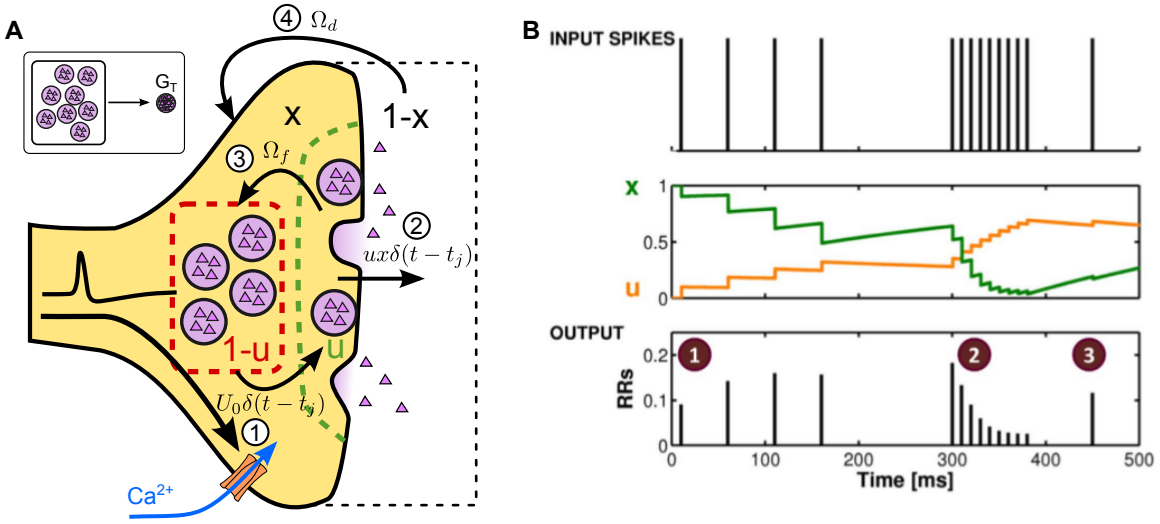

Figure II.3: The Tsodyks-Markram model of synaptic short-term plasticity. **A** Schematic representation of the TM model. The arrival of an AP (circled number 1) activates a fraction U_0 of unactivated available resources (*dashed red* rectangle) and releases (circled number 2) the fraction ux of activated available resources (area delimited by the *dashed green* line) in the synaptic cleft. At all times, activated available resources get unactivated with rate Ω_f (circled number 3) and unavailable resources (in the area delimited by the *dashed black* line) are reintegrated with rate Ω_d (circled number 4). The inset represents the equivalent glutamate vesicle with concentration G_T (c.f. main text). **B** Evolution of x and u (middle row) in response to an input spike train (top row) and the corresponding fraction of released resources (bottom row). $\Omega_d = 1.67\text{s}^{-1}$, $\Omega_f = 1.\text{s}^{-1}$ and $U_0 = 0.1$. Taken from Pittà et al. (2009).

Figure II.3B presents the behavior of the TM model in response to a train of APs (top row). When the spiking frequency is relatively low, successive spikes release increasingly more neurotransmitters (circled number 1 on the bottom row); the synapse is thus said to be facilitating. This is due to the fact that u starts at 0 and increases with each spike while x does not decrease too fast. When the spiking frequency increases however (circled number 2), successive spikes release less and less neurotransmitters; the synapse is said to be depressing. Although the release probability u quickly increases during high frequency spiking, the fraction of available resources x is quickly depleted. Finally, after waiting for some time, the synapse has recovered its released resources and thus respond to the last spike (circled number 3) by a larger release than at the end of the high frequency spikes.

When considering glutamatergic synapses, the glutamate concentration G in the synaptic cleft can be modeled following De Pittà et al. (2011).

$$\frac{\mathrm{d}}{\mathrm{d}t}G = -\Omega_G G + \rho_C G_T \sum_j u(t_j^+)x(t_j^-)\delta(t - t_j) \tag{II.17}$$

where t_j^+ and t_j^- respectively denote the time just after and just before the presynaptic spike occurring at time t_j. G_T denotes the concentration of glutamate if the average number of glutamate vesicles in the presynaptic terminal were all merged into a equivalent vesicle (c.f. inset in Figure II.3A). Since the glutamate is released in a volume that is

different from the volume of the synaptic vesicles, the concentration is rescaled by ρ_C, the ratio between the average volumes of vesicles and synaptic cleft. Finally, in first approximation, the diffusion away from the synaptic cleft and the uptake by astrocyte transporters can be modeled as a simple exponential decay with rate Ω_G. These models are not restricted to glutamatergic synapses and can also be used to model synaptic ATP release.

Because of the relative simplicity of the TM model, one can use mean field analysis (Tsodyks et al., 1998) to compute useful characteristics. Notably, given an input frequency of APs f, one can derive the steady state released resources RR_f as (De Pittà et al., 2011):

$$\langle RR_f \rangle = \rho_C G_T \frac{U_0 \Omega_d (\Omega_f + f)}{\Omega_d \Omega_f + U_0(\Omega_d + \Omega_f) f + U_0 f^2} \tag{II.18}$$

II.1.2.2 GPCR signaling

As mentioned previously, the most documented ways of eliciting Ca^{2+} oscillations in astrocytes are the G_q protein coupled receptors which induce IP_3 creation by PLCβ upon binding of agonists. Although several models of GPCR-mediated IP_3 production exist (Cuthbertson and Chay, 1991; Meyer and Stryer, 1988; Kummer et al., 2000; Höfer et al., 2002), we will present the signaling pathways involved but only one specific model: the G-ChI model (Pittà et al., 2009) that will later be used in Chapter IV.

Figure II.4A schematically represents these signaling pathways: G_q protein coupled receptors are, as their name suggests, associated to a G_q protein that consists in an heterotrimer composed of α, β and γ subunits; upon binding of agonist to the receptor (mGluR or P2YRs for example), the *alpha* subunit dissociates from the receptor and binds to colocalized PLCβ enzymes. This binding increases PLCβ activity which, like PLCδ, provokes the hydrolysis of PIP2 into IP_3 and DAG. This IP_3 production can be stopped or decreased by agonist unbinding from the receptor or by phosphorylation of either PLCβ, G_q protein or the receptor by protein kinase C (PKC) which is activated by DAG and Ca^{2+}. In most models, modeling this signaling pathways adds at least an equation for the fraction of activated receptors (Kummer et al., 2000; Höfer et al., 2002). In the G-ChI model, this is avoided by considering that agonist binding to the receptor and receptor activation is faster than the effective PLCβ-mediated production of IP_3 and can thus be considered at steady state. In consequence, no additional equations are needed but equation (II.14) is modified to account for the PLCβ-created IP_3:

$$\frac{\mathrm{d}}{\mathrm{d}t} I = J_\delta(C, I) + J_\beta(C, G) - J_{3K}(C, I) - J_{5P}(I) \tag{II.19}$$

with G the agonist concentration in the synaptic cleft (c.f. equation (II.17)) and J_β being computed as:

$$J_\beta(C, I) = O_\beta \cdot \mathcal{H}\left((\rho_{so} G)^n, K_G + K_L \cdot \mathcal{H}\left(C, K_{KC}\right)\right) \tag{II.20}$$

The concentration of agonist that effectively reaches the astrocyte in taken as a fraction ρ_{so} (for SpillOver) of the concentration of agonist in the synaptic cleft. O_β is the maximal

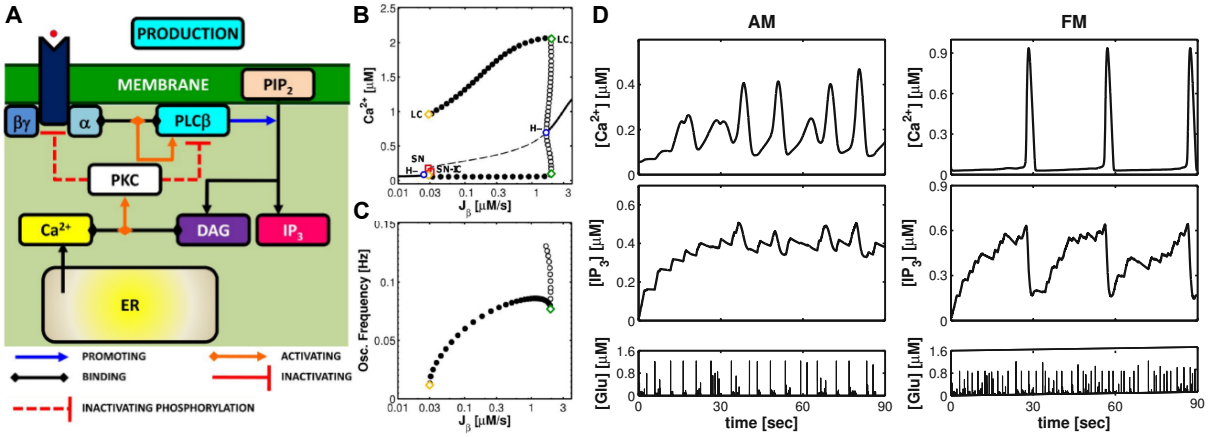

Figure II.4: The G-ChI model for agonist-induced GPCR-dependent Ca^{2+} signaling. **A** Schematic representation of the signaling pathways involved inagonist-dependent GPCR-mediated IP_3 production by PLCβ. Taken from De Pittà (2013). **B** Bifurcation diagram of an AFM parameter set for the G-ChI model. The bifurcation parameter is directly the IP_3 flux associated with PLCβ. Taken from De Pittà (2013). **C** Ca^{2+} oscillation frequency associated with the same value of J_β as in B. Taken from De Pittà (2013). **D** Ca^{2+} and IP_3 traces for AM (left) and FM (right) parameter sets in response to physiologically realistic glutamate stimulation in the G-ChI model. Taken from Pittà et al. (2009).

IP_3 production rate by PLCβ, K_G the agonist affinity of the receptor, K_L a Ca^{2+}/PKC-dependent inhibition factor and K_{KC} the Ca^{2+} affinity of PKC. Finally n denotes the cooperativity of the binding reaction to the receptor. It has been reported that $n = 0.18 - 0.88$ for the binding of glutamate to mGluRs type 1 (Suzuki et al., 2004) and $n = 0.9 - 1$ for binding of ATP to P2Y1Rs (Fam et al., 2000).

Given that the GChI model only differs from the ChI model regarding IP_3 production, both AM and FM encoding modes that we described previously still exist. Figure II.4B shows a bifurcation diagram in which J_β is the bifurcation parameter (and the dynamics of agonist binding are thus not taken into account) and for which the intracellular parameters lead to AFM encoding. The amplitude modulation can readily be seen and the fixed points for low and high values of J_β are present just like in the Li-Rinzel model for low and hight IP_3 concentrations (c.f. Figure II.1D). Figure II.4C shows the increase in Ca^{2+} oscillation frequency as J_β increases. Finally, Figure II.4D display Ca^{2+}, IP_3 and glutamate traces simulated with the GChI model for physiologically realistic neuronal spike trains (Pittà et al., 2009) for different sets of intracellular parameters leading to AM (left column) and FM (right column) encoding properties. Interestingly, going from the glutamate traces to IP_3 and from IP_3 to Ca^{2+} increases the signal smoothness. For FM encoding, IP_3 integrates glutamatergic activity, eventually triggering a Ca^{2+} spike that 'resets' IP_3 levels for a new cycle of integration (De Pittà, 2013).

II.2 Modeling astrocyte networks

In the previous sections, we presented the existence of ICW in astrocyte networks in cell culture and the available intracellular Ca^{2+} models. These models were shown to reproduce the main properties of Ca^{2+} oscillations in single astrocytes. Therefore, we now address the next spatial scale, ICW modeling. To do so, a lot of choices have to be made for which the experimental data is not always available. Notably, since astrocytes actually have very complex morphologies (see Section I.1.2), network models of astrocytes can range from single point astrocytes were every component is well-mixed to detailed morphological reconstructions taking into account intracellular as well as intercellular calcium waves. In addition to that, network modeling is considerably complicated by the presence of two main pathways for ICW propagation, ATP and GJC (see Section I.4.1.1), which might be more or less involved depending on the brain area or the experimental conditions. For each of these pathways, several questions arise; for the ATP pathway the following problems have to be addressed:

- as we saw previously, the mode of release of ATP could either be regenerative or originating from a single point;
- the diffusion of ATP in the extracellular space may be considerably modified by the fact that astrocyte morphology is complex;
- several different types of purinergic receptors have been reported to mediate ATP-dependent ICW.

For the GJC-mediated pathway:

- the intercellular diffusion of IP_3 might also be considerably modified by the complex astrocyte morphologies;
- except for very specific cases (see Section I.4.2), the topologies of astrocyte networks are unknown and even basic measures, like the distribution of the number of coupled neighbors, are not available;
- the dynamic variability of GJC coupling (by PKC phosphorylation for example (Lazrak et al., 1994; Bao et al., 2004; Sirnes et al., 2009; Huang et al., 2013)) might be at play during ICW propagation (at the scale of tens of seconds).

In this section we will present some of the modeling work that has been conducted in the last 20 years regarding ICW propagation in modeled networks by either ATP, GJC or both pathways. We will then present the network version of the ChI (or G-ChI) model that will be used in the following chapters.

II.2.1 Modeling approaches

Regardless of the signaling pathways involved, most network models need to choose the level of details both in terms of signaling pathways (presented in the previous section) and in terms of morphology. Of course these choices depend on the biological questions that the models want to address: as an example, detailed modeling of ATP-mediated pathways is needed when trying to evaluate how the different P2YR subtypes influence wave propagation (Iacobas et al., 2006); astrocytes can instead be modeled with ChI-type mod-

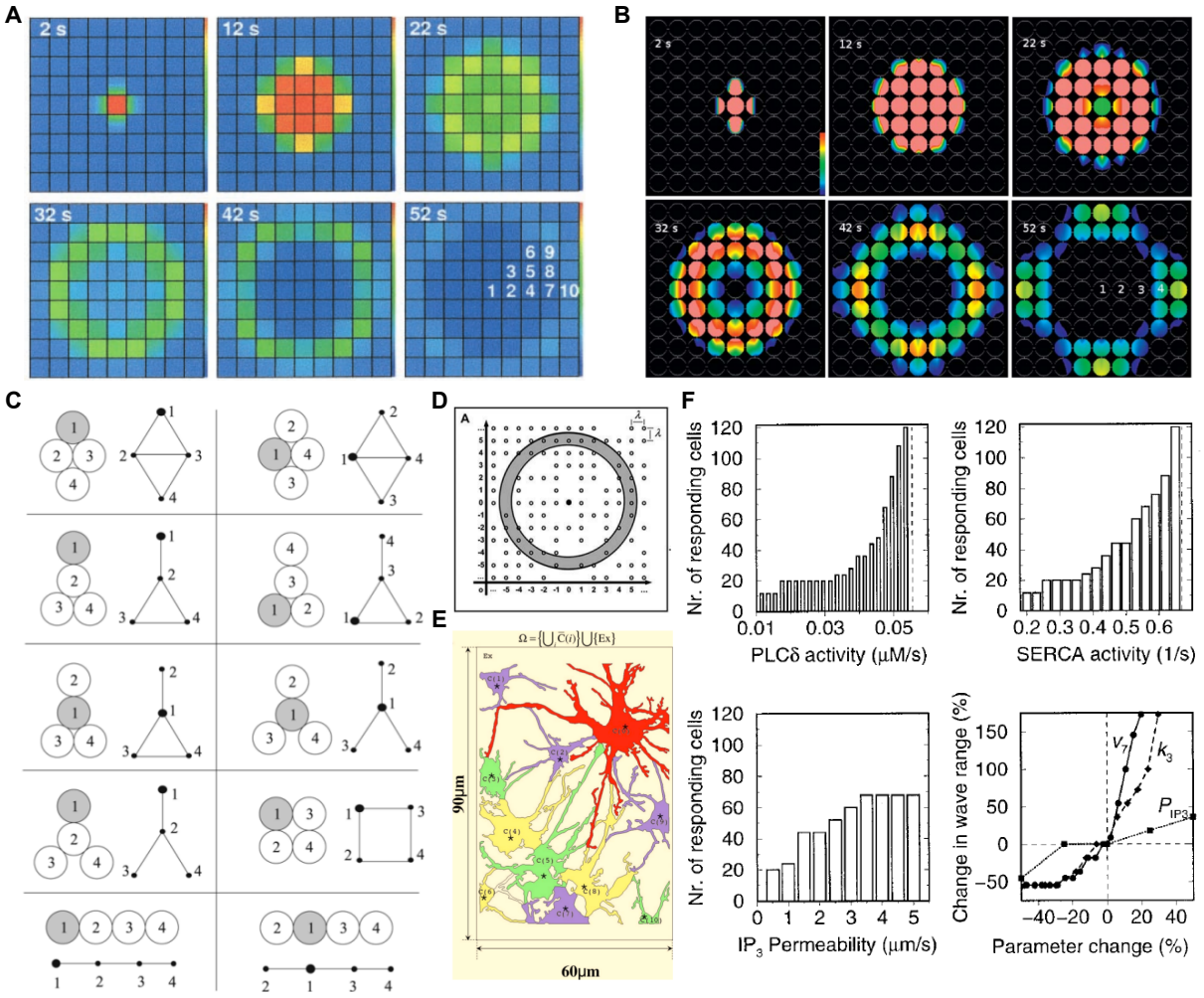

Figure II.5: Different astrocyte network models have been devised in recent years. **A** Example of simulated agonist-evoked ICW propagating through GJC. Colors code different Ca^{2+} concentration (from blue to red). Taken from Höfer et al. (2002). **B** Example of simulated ICW propagation taking into account both GJC and paracrine pathways. Colors code different Ca^{2+} concentration (from black to red). Taken from Edwards and Gibson (2010). **C** Different motifs of small astrocyte networks were tested to determine their effect in an ICW model using GJC. Taken from Dokukina et al. (2008). **D** As in B, this model takes into account both GJC and paracrine pathways but the organization of the astrocyte network is slightly more complicated as some astrocytes are absent from the grid. Taken from Iacobas et al. (2006). **E** Intra- and inter-cellular calcium wave propagation in a small network of modeled astrocytes whose morphology was reconstructed from actual experimental data. Both GJC and paracrine pathways are taken into account. Taken from Kang and Othmer (2009). **F** Influence of several intracellular parameters on ICW propagation in modeled GJC-coupled astrocyte networks. Taken from Höfer et al. (2002).

els when the focus is on agonist-independent intercellular waves (Goldberg et al., 2010). Regarding morphology, one has first to choose between considering detailed intracellular Ca^{2+} waves in each astrocyte (Höfer et al., 2001; Edwards and Gibson, 2010) or describing astrocytes as point cells representing the soma or the entire astrocyte (Iacobas et al., 2006; Dokukina et al., 2008; Goldberg et al., 2010). Modeling intracellular Ca^{2+} waves then necessitates a description of astrocyte morphology. Most models choose to approximate astrocyte as circles (Edwards and Gibson, 2010), squares (Höfer et al., 2002) or even cubes (Bennett et al., 2005) (when 3D astrocyte networks are considered) but very few models actually consider detailed morphological descriptions. The only example we know of the latter approach is from Kang and Othmer (2009) in which the authors use the morphological description displayed in Figure II.5E to model ICW propagation; the description is however limited to a small part of a two dimensional network. Regarding the biophysical models, most of them are related to the Li-Rinzel model that we presented earlier with some differences: notably, store-mediated Ca^{2+} activity and PLCδ activity that allow Ca^{2+}-dependent IP_3 production and is thus important in GJC-mediated ICW is taken into account in GJC-coupled astrocyte networks (Höfer et al., 2002) but not in models that aim at investigating paracrine signaling (Iacobas et al., 2006) that can instead take extracellular Ca^{2+} entry into account. Finally, simplified fire-diffuse-fire types of models (that we mentioned earlier for modeling intracellular Ca^{2+} waves) can also be used as a way to model ICW propagation (Harris and Timofeeva, 2010). We will however focus here on relatively detailed biophysical models that can readily be used to make experimentally testable predictions.

GJC-only models of ICW propagation Models of ICW propagation in astrocyte networks that focus on the GJC-mediated pathway can be categorized according to their coupling topology. Some studies indeed use the simplest possible description: a one-dimensional chain of astrocytes, each one being coupled to the astrocyte preceding and following it; this approach is adopted in Höfer et al. (2001); Ullah et al. (2006); Goldberg et al. (2010); Matrosov and Kazantsev (2011) and has been mostly used to investigate how intracellular parameters affect ICW propagation. Notably, parameters controlling the rate of CICR (Höfer et al., 2001), PLCδ activity (Ullah et al., 2006), or the type of encoding (FM/AFM) (Goldberg et al., 2010). Moving closer to Ca^{2+} waves in culture, some models use two-dimensional networks of astrocytes; in Höfer et al. (2002) for example, the authors model astrocytes as squares on a grid (c.f. Figure II.5A) and each astrocyte is thus coupled to its 4 nearest neighbors. Dokukina et al. (2008) focus instead on the different motifs that can be formed by networks of 4 astrocytes (c.f. Figure II.5C), introducing some variability in the number of neighbors that each astrocyte has. For both 1D and 2D astrocyte networks, the coupling strengths (either in the form of a rate, a permeability or a diffusion coefficient) are usually modified in order to assess their effect on ICW propagation. In Höfer et al. (2001) for example, increases in GJC coupling in 1D chains lead to an increased number of activated cells. In Höfer et al. (2002) the same effect happens in 2D networks but the increase in propagation extent is much lower than what is obtained when increasing PLCδ activity (c.f. Figure II.5F); the authors also investigate the effect of GJC variability on ICW propagation and show that this variability could underlie experimentally observed propagation anisotropy. Dokukina et al. (2008) instead

model a Ca^{2+}-dependent regulation of GJC coupling strength based on the experimental observation that Ca^{2+} activity can trigger, through PKC activation and phosphorylation of Cx43, a decrease in GJC coupling (Bao et al., 2004; Sirnes et al., 2009; Huang et al., 2013). Among these models that only take GJC into account as a communication pathway, very few have focused on the effects of network topology on ICW propagation. Dokukina et al. (2008) for example focus specifically on this but only consider very small networks of 3 or 4 astrocytes for which they test all possible motifs (c.f. Figure II.5C); they show that some motifs can increase the mean oscillation frequency and that variability in GJC strength can prevent ICW propagation.

Models of GJC and paracrine pathways Although some models take into account ATP diffusion without modeling GJC coupling (Bennett et al., 2005; MacDonald et al., 2008), most of the models that take into account ATP signaling also consider GJC coupling. With the exception of Bennett et al. (2005) (that studied ATP signaling in 3D space) most of the studies model 2D networks. Figure II.5B shows ICW propagation in a model (Edwards and Gibson, 2010) with both GJC coupling and ATP diffusion, as in Höfer et al. (2002), the authors consider astrocytes positioned on a 2D grid and model intracellular Ca^{2+} waves; they report that the introduction of ATP signaling increases the extent and duration of the wave but does not change the propagation speed. Interestingly, Iacobas et al. (2006) consider astrocyte networks that are slightly more complicated: as can be seen in Figure II.5D, astrocytes are also positioned on a 2D grid but some of them are randomly removed, leading to variability in GJC coupling. Kang and Othmer (2009), as mentioned previously, simulate intra and intercellular Ca^{2+} waves in a very detailed morphological description of astrocyte morphology (see Figure II.5E); since they only use this specific small network, it is hard to determine to what extent the detailed morphological description played a role in ICW propagation. As mentioned in Section I.4.1.3, the regenerative nature of ATP release is still controversial and the models of ATP signaling usually test both regenerative and non regenerative possibilities. Interestingly, in Kang and Othmer (2009), the authors conclude that ICW propagation needs both GJC and ATP signaling with non-regenerative or partially regenerative ATP release. In contrast, in MacDonald et al. (2008), the authors argue that ATP release must be regenerative to account for experimental ICW propagation extents; in this model however, GJC coupling is not taken into account and the only way to attain long propagation distances is to include regenerative ATP release. Finally, detailed modeling of GJC, ionotropic and metabotropic P2 receptors allowed Iacobas et al. (2006) to show that different P2YR subtypes were associated with different ICW extent and that long-range ICW propagation needed both GJC and non-regenerative ATP release.

For a lot of these models, the influence of intracellular parameters on ICW extent is usually investigated (see Figure II.5F for example). Two classes of parameters can then be distinguished: (1) the parameters that are directly coupled to IP_3 creation by PLCδ or PLCβ always have a strong influence on ICW propagation extent (Höfer et al., 2002; Edwards and Gibson, 2010; Goldberg et al., 2010); (2) parameters that control Ca^{2+} oscillations (basically Li-Rinzel parameters) as the activity of SERCA pumps (Höfer et al., 2002) or the maximal Ca^{2+} release rate from the ER (Höfer et al., 2001). In contrast, the

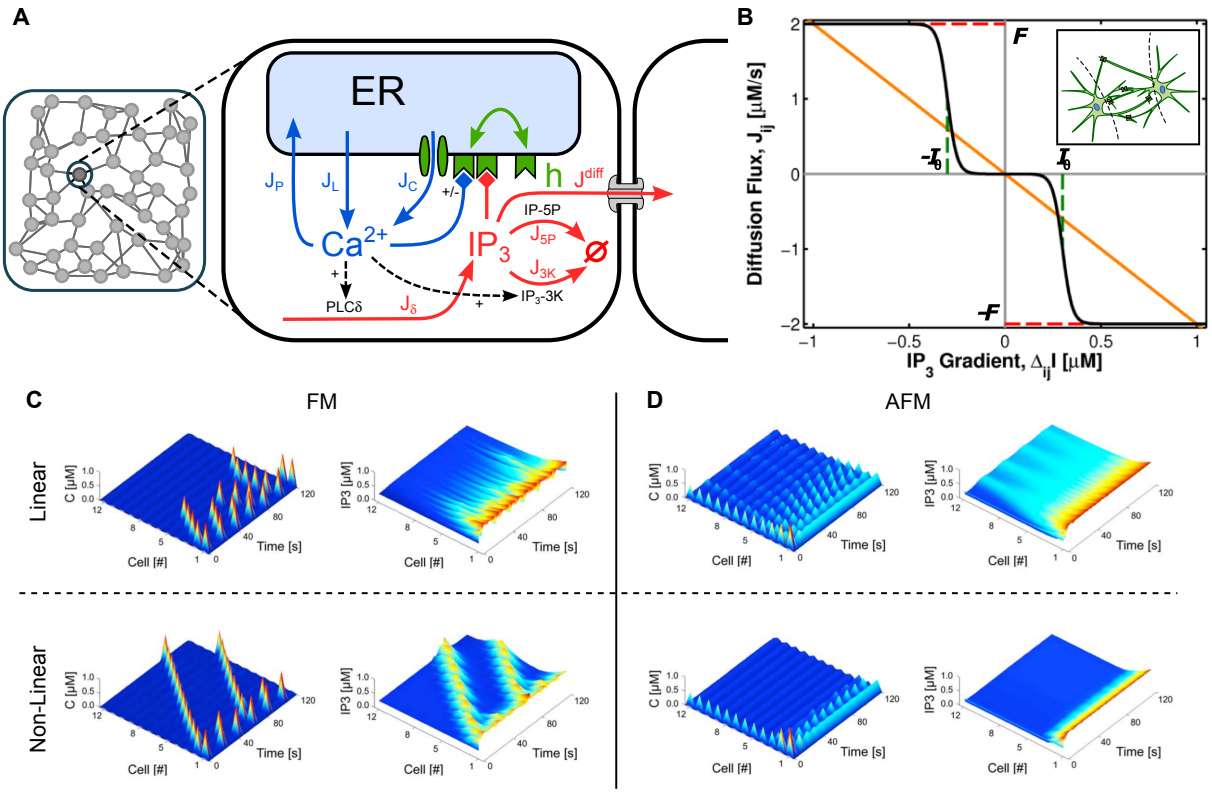

Figure II.6: The network ChI model. **A** Schematic representation of the network ChI model. The main modification consists in an additional flux J^{diff} which models intercellular diffusion of IP_3 across GJC. Although the J_β flux is not represented, the same description applies for the network G-ChI model. **B** Different ways of modeling intercullar diffusion of IP_3 between astrocyte somas. The flux between two astrocyte somas can be modeled as a linear function of the IP_3 difference (*orange* line) or as a nonlinear function (*black* curve) which only allows effective diffusion when the IP_3 difference is above a threhold value I_θ. Inset shows a schematic representation of actual GJC coupling in astrocyte networks: most GJC are located in the distal processes and the diffusion of IP_3 from one soma to another has to go through a complex networks of processes that might lead to nonlinear diffusion. **C** Simulations of ICW propagation in 1D chains of FM encoding astrocytes with one astrocyte (astrocyte number 1) stimulated. Non-linear GJC coupling supports regenerative propagation while Linear coupling leads to spatially-restricted ICW. **D** Same as in C but for AFM encoding astrocytes. These astrocytes prevent ICW propagation altogether. **C** and **D** are taken from Goldberg et al. (2010).

effect of network topology on ICW propagation has not, to our knowledge, been treated in large networks; in addition, few studies have investigated ICW propagation in 3D astrocyte networks although it would be closer to the in vivo situation.

II.2.2 The network ChI model

To address whether network topology can affect ICW propagation, we decided to focus on GJC-mediated ICW propagation by using the network ChI model. Figure II.6A shows

a schematic representation of the network ChI model: astrocytes are represented as *gray* nodes and the links between them represent GJC couplings. In each astrocyte, the variables follow the same dynamics as in the ChI model except that IP_3 can now diffuse through GJC to other astrocytes. The network ChI model, introduced in Goldberg et al. (2010) to model astrocyte chains, can extend both the ChI and the G-ChI models by adding an additional diffusion term in the IP_3 equation:

$$\frac{\mathrm{d}}{\mathrm{d}t}I_i = J_\delta(C_i, I_i) + J_\beta(C_i, G_i) - J_{3K}(C_i, I_i) - J_{5P}(I_i) + J_i^{diff} \tag{II.21}$$

The additional term J_i^{diff} sums IP_3 flows (J_{ij}) from/to any cell j that is directly connected (GJC-coupled) to cell i, i.e. $J_i^{diff} = \sum_{j\in\mathcal{N}_i} J_{ij}$ with $\mathcal{N}_i$ the set of astrocytes that are GJC-coupled to i. The network is defined by a symmetric (because GJC are bidirectional) adjacency matrix $A = (a_{ij})$ with $a_{ij} = 1$ if astrocyte i is GJC coupled to astrocyte j and 0 otherwise.

IP_3 diffusion from one astrocyte i to a neighboring one j can be thought as some function ϕ of the IP_3 concentration gradient between cells i and j, i.e. $\Delta_{ij}I = I_i - I_j$, so that (Crank, 1980):

$$J_{ij} = \phi(\Delta_{ij}I)\ . \tag{II.22}$$

In the simplest scenario, ϕ may be assumed linear (Sneyd et al., 1994; Falcke, 2004), and J_{ij} be described accordingly by Fick's first diffusion law, so that

$$J_{ij} = -F_{ij}\cdot\Delta_{ij}I \tag{II.23}$$

where F_{ij} is the diffusion rate which characterizes the strength of GJC coupling. When considering intercellular propagation of global/whole–cell Ca^{2+} signals, IP_3 diffusion from one cell soma to another has to be considered and equation (II.23) might not be valid for this case. As illustrated on the inset of Figure II.6B in fact, connections between astrocytes through GJCs are mostly at the cell distal processes (Giaume et al., 2010) whose complex morphology and narrow intracellular space (Witcher et al., 2007; Pivneva et al., 2008) could considerably hinder IP_3 diffusion from/to somata. Moreover, GJCs cluster at discrete sites of these processes (Nagy and Rash, 2000), thereby constraining the diffusion pathway of IP_3 from one cell to another. Finally, IP_3 production and degradation in the processes could either promote IP_3 transfer between cells or hamper it. In this fashion, the ensemble of astrocytic processes and GJCs interposed between cell somata (i.e. the region between the *dashed lines* in the inset of Figure II.6B) could be equivalently regarded as a diffusion barrier for IP_3 exchange between cells, and accordingly, IP_3 diffusion between cells could be inherently nonlinear. This scenario is further substantiated by growing experimental evidence suggesting that GJC permeability could be actively modulated by various factors, including different second messengers (Harris, 2001) and Ca^{2+} activity (Bao et al., 2004; Sirnes et al., 2009; Huang et al., 2013) because of PKC phosphorylation of Cx43. Because PKC also takes part in IP_3 degradation as well as in Ca^{2+} signaling, this possibility ultimately hints that GJC permeability could also depend on IP_3 signaling in a nonlinear way (Pittà et al., 2009; De Pittà et al., 2012).
Thus, together with linear diffusion (equation (II.23)), we can consider an alternative expression for J_{ij} to account for nonlinear IP_3 diffusion too. In particular we will assume

below that IP_3 diffusion between two contiguous astrocytes, i and j, can be a threshold function of the IP_3 gradient ideally measured across processes and GJCs in the cell somata (i.e. above and below the *dashed lines* in the inset of Figure II.6B), and is limited by the maximal GJC permeability. Accordingly, a possible expression for J_{ij} reads (Goldberg et al., 2010):

$$J_{ij} = -\frac{F}{2}\left(1 + \tanh\left(\frac{|\Delta_{ij}I| - I_\theta}{\omega_I}\right)\right)\frac{\Delta_{ij}I}{|\Delta_{ij}I|}\,. \tag{II.24}$$

Figure II.6B shows J_{ij} as a function of $\Delta_{ij}I$ in the linear vs. nonlinear approximation of IP_3 diffusion (*orange* vs. *black curves* respectively) where I_θ in equation (II.24) is the threshold gradient for which effective IP_3 diffusion occurs, that is $J_{ij} > 0$ only if $|\Delta_{ij}I| > I_\theta$; whereas ω_I scales how fast J_{ij} increases (decreases) with $\Delta_{ij}I$ beyond this threshold. The parameter F sets the slope of J_{ij} in the linear approximation (equation (II.23)), while in the nonlinear case, it corresponds to the maximal incoming (minimal outgoing) diffusion fluxes.

Goldberg et al. (2010) investigated the behavior of the network ChI model on chains of astrocytes by stimulating one astrocyte and quantifying the resulting propagation extent under different parameter sets and coupling type. Figure II.6C shows representation of ICW for FM encoding astrocytes with both linear (top row) and non-liner (bottom row) GJC coupling while Figure II.6D shows representation of ICW for AFM encoding astrocytes for the same coupling types. Interestingly, AFM astrocytes and linear coupling completely prevented long-range ICW propagation while only FM astrocytes with non-linear coupling could propagate long-range ICWs. As observed by Höfer et al. (2002), increasing PLCδ activity can rescue ICW propagation for linear coupling, but this difference between linear and non-linear coupling illustrates that GJC properties could strongly impact the way ICW are propagated.

The behavior of the network ChI model has been investigated in Goldberg et al. (2010) on an elementary topology; astrocytes were connected as a 1D line with each astrocyte being coupled to its 2 nearest neighbors. In the following chapters, we will investigate Ca^{2+} signaling in more realistic and more complex networks topologies. In the next chapter, we will thus present the main definitions, quantifiers, and topological models that will be useful for the remaining chapters.

Chapter III

Network topologies and dynamics

III.1 Network modeling

The study of networks has historically been led in the framework of graph theory which started as a branch of discrete mathematics. Graph theoreticians originally focused their studies on regular and symmetric structures (e.g. grids) leading to a great number of theoretical results on such graphs. However, real networks are often far from being regular structures and, up to the 1990's, more complex structures were studied within the framework of random graphs (which we will develop later in this section). Subsequent developments led at the end of the 1990's to the emergence of more complex models of networks, resulting from the application of few organizing principles accounting for the observed structures of real networks (like social networks or the internet).

The field of complex networks studies brought new tools to investigate these topologies, allowing to quantify differences between classes of networks and thereby increase our comprehension of their structures. This chapter will first present these quantifiers and introduce well-known complex network models. We will then discuss spatial networks and their topologies. Indeed, real networks are often embedded in space which influences their topology: distant places are for example less likely to be linked by a direct road than close places are. Finally, we will present generic dynamical processes than can take place on networks and the relations between these dynamics and network topologies.

We would like to stress that this chapter is far from reviewing either network models, quantifiers and dynamical processes on networks. The network models and quantifiers that will be presented here have been chosen because we will use them later in the manuscript; the models of network dynamics have been chosen to introduce interactions between topology and dynamics. Readers that are interested in this subject might want to report themselves to review articles Albert and Barabási (2002); Boccaletti et al. (2006); Lesne (2006); Dorogovtsev et al. (2008); Bullmore and Sporns (2009); Barthélemy (2010); Stam (2014).

III.1.1 Definitions

In general, networks can be directed or undirected. As their name suggests it, links between two nodes in directed networks are oriented, they go *from* one node *to* another. In contrast, undirected networks do not make this distinction and are thus used to model bidirectional relations. In particular, since astrocyte networks are coupled with bidirectional GJC, we will only consider here undirected networks.

An undirected graph G is defined as $G = (\mathcal{V}, \mathcal{E})$, with $\mathcal{V}$ a set of nodes and $\mathcal{E}$ a set of e undirected links between these nodes. A graph G is associated to a N by N adjacency matrix A with $N = |\mathcal{V}|$ and $A = (a_{ij})$ where $a_{ij} = 1$ if there is a link between nodes i and j and 0 otherwise.

III.1.2 Quantifiers

This section presents some of the most basic measures used to quantify topological characteristics. We will not present in details the signification of each measure, we will give the definition and a quick insight about what it quantifies. For more information, the interested reader will refer to Boccaletti et al. (2006); Costa et al. (2007); Newman (2003) and to Albert and Barabási (2002); Barthélemy (2010) for additional quantifiers and for detailed explanations regarding the relations between quantifiers and network models.

Degree distribution Each node i is associated to a degree which is defined as the number of nodes to which it is connected.

$$k_i = \sum_{j=1}^{N} a_{ij} \tag{III.1}$$

The degree distribution $P(k)$ of a network corresponds to the probability that a randomly chosen node in the network has degree k; it is one of the most widely used quantifiers. In particular, as we will see later, the shape of this distribution can characterize some network models.

Clustering coefficient The clustering coefficient quantifies how much neighbors of a given node are interconnected, it is defined locally for each node according to :

$$C_i = \frac{2|e_{\mathcal{N}(i)}|}{k_i(k_i - 1)} \tag{III.2}$$

with $|e_{\mathcal{N}(i)}| = \sum_{\substack{j,k \in \mathcal{N}(i) \\ j \neq k}} a_{jk}$ the number of links between the neighbors of node i. And $\mathcal{N}(i)$ the neighborhood operator that returns the topological neighbors of node i.

The clustering coefficient $\langle C \rangle$ of a network is defined as the mean of the local clustering coefficients C_i across all the nodes.

Mean-shortest path The mean-shortest path is the mean length of the shortest path separating two randomly chosen nodes. It is obtained by computing the topological distance d_{ij} separating each pair of nodes in the network.

$$L = \frac{1}{N(N-1)} \sum_{\substack{i,j \in \mathcal{V} \\ i \neq j}} d_{ij} \tag{III.3}$$

Hierarchical clustering coefficient This quantifier has been introduced in Costa and da Rocha (2006) as an extension of the standard clustering coefficient C_i. Indeed, the standard version of the local clustering coefficient (and hence of its mean) only considers the first degree neighbors of a node and is thus very limited in its expression of clustering of the graph. For example, the clustering coefficient of a 2D grid (or lattice) in which each node is linked to its closest 4 neighbors is naught although it is obvious that nodes are somewhat clustered when considering neighbors at a sufficient distance.

Before defining the quantifier, we need to introduce some notations :
- ζ is a set of nodes.
- $\delta_r(\zeta)$ is the set of nodes such that $\forall v \in \delta_r(\zeta)\ \exists w \in \zeta$ s.t. $d_{vw} \leq r$; it can be understood as the set of nodes resulting from the repeated application (r times) of a dilatation operator on ζ.
- $N_r(\zeta)$, $E_r(\zeta)$ are respectively the number of nodes and the number of edges in the subnetwork defined by $\delta_r(\zeta)$.

The hierarchical clustering coefficient can then be defined, for sets ζ composed of a single node u as :

$$cc_r(u) = \frac{2E_r(u)}{N_r(u)(N_r(u)-1)} \tag{III.4}$$

This formula is reminiscent of the standard clustering coefficient ($C_u = cc_1(u)$) but it is now taking into account neighbors up to a distance r. Similarly, the mean of these local hierarchical clustering coefficient, noted $\langle cc_r \rangle$, can be considered to quantify the hierarchical clustering of the whole network.

Other standard metrics can be extended in this framework; the interested reader will refer to Costa and da Rocha (2006) and Costa et al. (2007) for a more detailed presentation.

III.1.3 Network models

Some network models are very well-known and are often considered as "reference" networks when studying unknown networks. These models were developed as an attempt to

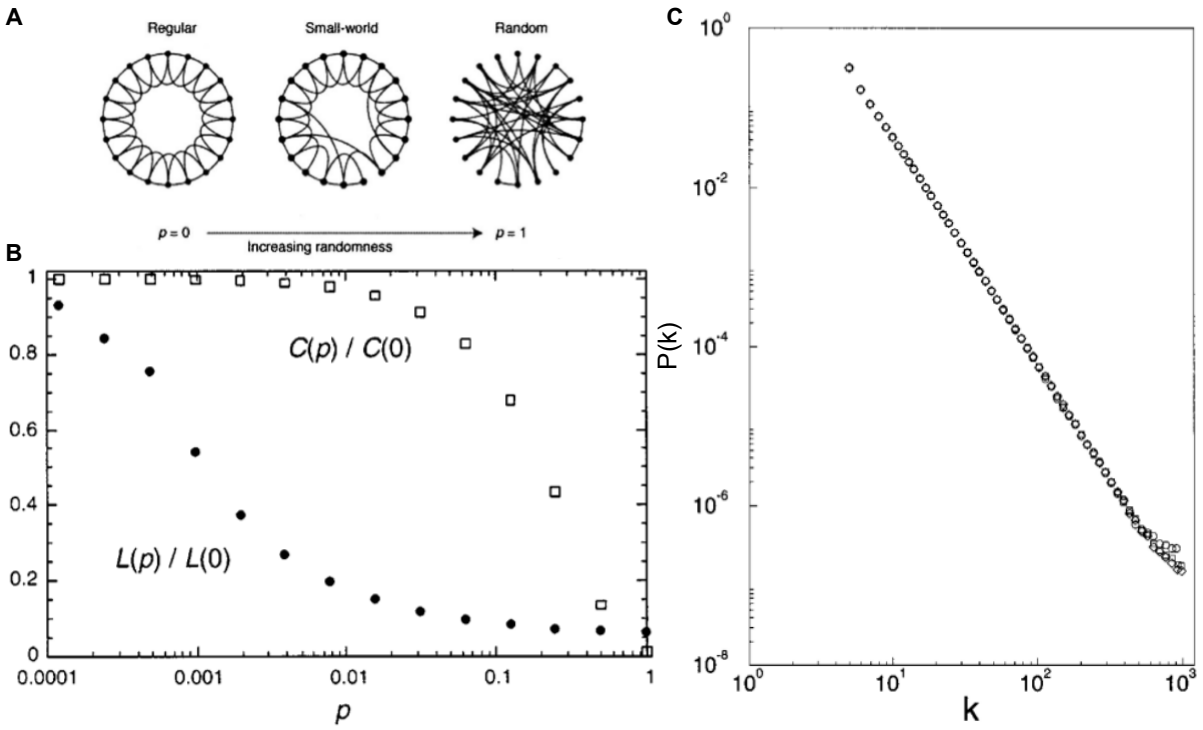

Figure III.1: Small world and scale free networks models. **A** Schematic representation of the rewiring process for small world networks. Taken from Albert and Barabási (2002). **B** Changes in clustering coefficient (*empty squares*) and mean-shortest path (*full circles*) as the rewiring probability increases in small world networks. $C(p)$ and $L(p)$ respectively denote the clustering coefficient and mean-shortest path for ring lattices whose links were rewired with probability p. Taken from Albert and Barabási (2002). **C** Power law degree distribution of a scale free network. Taken and modified from Albert and Barabási (2002).

account for characteristics in real networks that could not be explained in the framework of regular graphs in discrete mathematics.

Random Graphs They are historically the first kind of non regular networks and, although there are several models of random graphs, we will only present the most well-known : the Erdős-Rényi model. According to this model, random networks are created by taking N nodes and adding links with probability p between each possible pair of nodes, leading to e links among the $N(N-1)/2$ possible ones. The expected total number of links is given by $\mathbb{E}(e) = p\frac{N(N-1)}{2}$ and the degree distribution is given by :

$$P(k_i = k) = C_{N-1}^{k} p^k (1-p)^{N-1-k} \tag{III.5}$$

Leading to an average degree $\langle k \rangle = p(N-1) \simeq pN$.

Small-world Networks This network model has been elaborated to account for two characteristics found in real networks : a small average path length and a rather high clustering coefficient. Random networks already account for short average path length but

their clustering coefficient is often very low. Small-world networks interpolates between a regular ring lattice and a random network, conserving these two properties. The construction process, represented in Figure III.1A, usually starts from a regular ring lattice (on the left) and rewires each edge with probability p, thereby creating "shortcuts" in the graph. A variant of the model, introduced by Newman and Watts, only adds shortcuts to the ring lattice without rewiring existing edges. As represented in Figure III.1B, for a restricted range of rewiring probability p, networks have both low average path length and hight clustering coefficient. Indeed, the clustering coefficient is rather high for p close to 0 as it is close to the clustering coefficient of a regular ring lattice ($C = \frac{3(K-2)}{4(K-1)}$ when $N \gg K$ (Albert and Barabási, 2002)). As p increases, the average path length quickly decreases due to the addition of few shortcuts while the clustering coefficient decreases more slowly.

Scale-free Networks Some real networks, like citation networks between scientific authors, have degree distributions that follow a power law : $P(k_i = k) \propto k^{-\gamma}$ (represented in Figure III.1C). When $\gamma < 2$, the network does not have a mean degree (it diverges when the size of the networks tends to infinity); for $\gamma < 3$ the standard deviation of the degree distribution diverges Most scale free networks satisfy $2 < \gamma < 3$ and they thus lack a characteristic degree, or scale (hence their name). Accordingly, they display nodes which are strongly connected called hubs with significant probability.

This property cannot be accounted for by neither random graph models nor small world models. The most known model of scale-free networks, the Barabási-Albert model, accounts for this property by its construction process. Barabási-Albert networks are constructed by starting with a small number of nodes and by incrementally adding nodes. Each added node is connected to m nodes already in the network; the probability $\Pi(k_i)$ of connecting a newly added node to an already present node i is computed so as to introduce a bias to preferentially connect to already highly connected nodes according to:

$$\Pi(k_i) = \frac{k_i}{\sum_j k_j} \tag{III.6}$$

This process, called preferential attachment, is now recognized, in conjunction with growth, as the mechanism responsible for the power-law behavior of degree distributions in this model (Albert and Barabási, 2002). Some scale-free network models can however be constructed statically. We will not present these models here, for more informations on static and evolving scale-free network models, see Boccaletti et al. (2006).

Evolving networks As we pointed out, the dynamic growth process is an important aspect of scale-free network models; this notion of taking into account not only the resulting topology but also the dynamic process from which it resulted has been applied in a variety of studies. Both simple evolution laws (Albert and Barabási, 2002; Boccaletti et al., 2006) (as preferential attachment) and optimization processes (Mathias and Gopal,

2001; Ferrer i Cancho and Solé, 2003) have been shown to yield complex networks with specific characteristics.

Each one of these models and some others (hierarchical networks, modular networks, and a lot of variations of the standard models) are presented in more details in various reviews on complex networks (Albert and Barabási, 2002; Newman, 2003; Boccaletti et al., 2006; Barthélemy, 2010).

III.1.3.1 Spatial Networks

Up until now, the networks we mentioned where fully defined by giving a set of nodes and a set of links between those nodes. However, real networks are often embedded in space and each node is thus associated with a position in this space. Examples of these networks are legions: infrastructure networks as road or plane networks, neural networks, but also networks embedded in a non-physical space (e.g. network of internet pages, as distances can be defined between two pages), etc. We will briefly review some aspects of how space affects network topology.

Generalities The effect of space on network topology is mostly related to the effect of spatial distances on the creation of links between them. Generally, distant nodes will be less likely connected than closer ones.

As these spatial constraints affect link presence and hence topology, a lot of quantifiers are also affected. For example, as the influence of space on the presence of links between two nodes increases, in most spatial networks, the degree of nodes becomes limited as every node can only be linked to its spatial neighborhood. The width of the degree distribution then reflects the variations in density of nodes in space. Among those basic quantifiers affected by space, we can also point out the clustering coefficient and the mean-shortest path; both of these metrics increase with space influence. C increases because spatially close nodes tend to be more connected and the topological neighbors of a node tend to also be spatially close to this node. As space is preventing the existence of long range links (or shortcuts), L is "mechanically" increased as space influence increases. The effect of space influence can however greatly vary from one case to another and the resulting influence on topology is more complex than simple definitive relations of the kind : "increases / decreases". For example, even though space influence generally increases the mean-shortest path, this increase can be counteracted by the formation of regional hubs.

Spatial Network Models Spatial network models can be separated into several classes (Barthélemy, 2010). Two of them will not be detailed here: *geometric graphs* and *optimal networks*. Geometric graphs are elaborated with nodes embedded in a plane in which links are added according to some geometric constraint. Optimal networks aims at minimizing a cost function over the network (e.g.: the minimum spanning tree, a network minimizing

the length of links while connecting all the nodes).

Other spatial network model classes are spatial counterparts to the standard network models we presented previously. Spatial generalizations of the Erdős-Rényi model can be obtained by several ways (Barthélemy, 2010); we will only present the Waxman model here in which nodes are uniformly distributed in space and edges are added between nodes i and j with a probability $\Pi(i,j)$ that is not constant like in the Erdős-Rényi model but depends on the spatial distance $d_E(i,j)$ between nodes i and j:

$$\Pi(i,j) = \beta e^{-d_E(i,j)/d_0} \tag{III.7}$$

Space influence is accounted for by the decreasing exponential term, d_0 being a characteristic length : the lower it is, the stronger the influence of space in the network and vice-versa. Link density is controlled by β, it has a role similar to p in the non-spatial model.

Small world network models can also be generalized to spatial networks and to higher lattice dimensions (the Newman and Watts model was defined on a ring lattice). The same elaboration process is applied with the lattice embedded in space but shortcuts are added taking into account spatial distances between nodes. For each node i, a shortcut is added with probability p and the other end point of the added link is randomly chosen among all other nodes j with probability $q(d_E(i,j))$, taking into account the spatial distance $d_E(i,j)$ between the nodes:

$$q(d_E(i,j)) \sim d_E(i,j)^{-\alpha} \tag{III.8}$$

The resulting networks have small-world properties for α small enough and p high enough.

Finally, scale-free networks can also be spatial networks; although there exists a considerable number of models taking spatial distance into account (Barthélemy, 2010), we will only present one. This model, as the one we presented for standard scale-free networks, builds networks incrementally by starting with a small network and adding node by node. Each added node n is connected to m already existing nodes i by preferential attachment, with probability $\Pi_{n\to i}$ taking spatial distances into account :

$$\Pi_{n\to i} = \frac{k_i e^{-d_E(n,i)/r_c}}{\sum_j k_j e^{-d_E(n,j)/r_c}} \tag{III.9}$$

This construction process thus creates highly connected nodes while restricting links to spatially close nodes when r_c is small enough, similarly to the Waxman model.

Each of these models have parameters controlling the influence of space, allowing wide ranges of behavior from the more restrictive (maximum influence of space) to the least (no influence at all). Biological physical networks of cells are usually subject to space influences as long range links between cells come with a certain "cost". These influences can however vary between networks; for example, long range links may be much more common in neuronal networks than in astrocyte networks.

III.2 Network dynamics

Network dynamics constitute a vast field of study; in this section we briefly review some aspect of it by presenting basic activity propagation models and discussing the influence of network topology on these models. The interested reader may report himself to Boccaletti et al. (2006); Dorogovtsev et al. (2008); Barthélemy (2010).

Activity propagation models can cover processes as different as epidemic spreading, rumor propagation, or the propagation of electrical impulses in neural networks. Simplified versions of these models often involves the definition of a small number of states in which each node can be and of transition rules (possibly stochastic) that link the current state of a node or its neighborhood to its future state.

Processes like epidemic spreading, for example, are often modeled by compartments models: each node of the network can be in different "states", or compartments, and probabilistic rules taking into account the direct neighborhood of nodes account for the transitions between states at each time step (time is discretized) Boccaletti et al. (2006). A lot of these models can be found in the literature, the states and the transition rules depend on the nature of the modeled phenomenon; for example, epidemic spreading will greatly differ whether affected people can recover or not. If nodes can recover and be infected again after a first infection, the corresponding states would thus be Susceptible and Infected and the associated model is generally called after the initials of the usual state transitions; in this case, the transitions would be Susceptible $\rightarrow$ Infected $\rightarrow$ Susceptible and the corresponding model is thus called SIS. If nodes cannot be infected again once they have been infected, there are now three different states: Susceptible,Infected and Removed and the model is called SIR. The behavior of these models with respect to various parameters (rate of spontaneous infection, transmission rates, etc.) can be studied both theoretically (Boccaletti et al., 2006; Hütt and Lesne, 2009) (with mean field approximations) and experimentally (through computer simulations) (Colizza et al., 2007; Müller-Linow et al., 2008; Hütt and Lesne, 2009).

However, the transition rules that govern these models (SIR and SIS) only consider interactions between pairs of nodes (e.g. $S(i) + I(j) \xrightarrow{\lambda} I(i) + I(j)$: a susceptible node i becomes infected with probability λ if an infected node j is adjacent to it). Consequently, those models (also called *independent interaction* models) can't correctly account for processes in which spreading takes place only if a sufficient amount of "infected nodes" are connected to a susceptible one (Dodds and Watts, 2004). These kind of processes, often referred to as *complex propagation*, are accounted for by threshold models (Watts, 2002; Dodds and Watts, 2004; Centola et al., 2007). A simple example of such a model is given in Centola et al. (2007) : a node is activated if a critical fraction Φ or more of its neighbors are activated, otherwise it is unactivated.

Simple models of excitable neurons keep the same basic idea that a node becomes activated consequently to a simultaneous or nearly simultaneous activation of its neighbors. The state of each node is however generally modeled as at least one real variable that can

be viewed as the neuron membrane potential. In integrate and fire models for example (Roxin et al., 2004), the connections are directed and a node is activated when its potential crosses a threshold. Node potentials increase when "parent" nodes become activated (or "fire") and, in certain versions of the model, decrease slowly over time (leaky integrate and fire models).

All these models involve a notion of excitation, be it infection for SIS and SIR models, activation for threshold models or firing for neuronal network models. However, some dynamics do not involve this notion; we will not elaborate on those, but the interested reader can refer to Boccaletti et al. (2006); Arenas et al. (2008) for coupled oscillators networks, to Barthélemy (2010) for considerations on the Ising model and on random walks in spatial networks, and to Weber et al. (2008) for simple reaction-diffusion processes.

III.2.1 Relations between topology and dynamics

As stated before, the network topology can have considerable influence on the dynamics taking place on these networks. We will, in this subsection, present succinctly the results obtained on this question over the past few years for both generic dynamics and neuronal network models. Despite these results, the conditions and the nature of interactions between topology and dynamics on networks strongly depends on the model considered.

Generic dynamics In order to quantify the influence of topology on dynamics, one has to be able to quantify changes in dynamics. This is achieved by the use of different methods and quantifiers which we will not present here in details; among these methods and quantifiers, one can find : co-activation matrices (Müller-Linow et al., 2008), functionnal network extraction (Zhou et al., 2006), mutual information (Hütt and Lesne, 2009), self-sustained activity (Roxin et al., 2004), coherence of spiking (Volman and Perc, 2010) and synchronization measures (Boccaletti et al., 2006).

A clear illustration of topological influence on dynamics is given by the behavior of SIS-type models on hierarchical and scale-free networks (i.e. networks in which nodes are hierarchically clustered): depending on the rate f of spontaneous excitation of nodes, these networks can exhibit two kinds of dynamics. For low values of f the network is centrally excited (propagation is achieved through nodes with high betweenness centrality) whereas, for high values of f, locally clustered excitations or *bursts* are witnessed, matching the hierarchical clusters (Müller-Linow et al., 2008). This dynamic switching seems to be the result of a competition between the spontaneous activation rate f and the network connectivity p, regulating the sizes of effective networks (parts of the global networks on which excitation propagates) (Hütt and Lesne, 2009). The same phenomenons have been shown to happen in the case of coupled phase oscillators (Zhou et al., 2006; Arenas et al., 2006) : progressive synchronization of oscillators reveals underlying topological features of the network (in these cases, its hierarchical modularity). Hence, it is known that specific features of topology, like the presence of hubs or modules, can systematically shape

the dynamical behavior of networks (Müller-Linow et al., 2008). Although modularity supports this switching of dynamical behavior, it has also been shown to slow down diffusion in networks and decrease transport efficiency (Gallos et al., 2007).

Topology can also affect the ability of a network to self-sustain activity; using integrate and fire excitable neurons, it has been shown that self-sustained activity is possible in small world networks for small values of p (shortcut creation probability) but vanishes for large values (Roxin et al., 2004). Increased connectivity forces the dynamics to quickly "saturate" the network, propagation of excitation can then no longer be ensured due to the refractory periods of excitable neurons.

In some cases, when propagation of dynamics is not dependent on locally clustered active nodes, dissasortative degree distribution and the presence of hubs in a network can considerably increase the speed of reaction-diffusion dynamics (Weber et al., 2008) and of propagation dynamics (Centola et al., 2007). Similarly, the addition of random links in small world networks can increase activation propagation speed (Strogatz, 2001). On the contrary, when the propagation of dynamics depends on the simultaneous activation of locally clustered nodes, like in threshold models of dynamics, it has been shown that random links and hub presence impairs propagation (Watts, 2002; Centola et al., 2007).

Artificial neural networks dynamics The importance of topology on artificial neural networks performances, while still an open question, has been recently investigated. We briefly present here some of the results obtained as it underlines the importance of certain topological characteristics on these kinds of dynamics.

Small world topologies are found to be efficient in Bohland and Minai (2001) and Lu et al. (2009); the performances are evaluated respectively on associative memories and on decision-making behavior. According to Lu et al. (2009), small world topologies increase accuracy, decrease reaction time and are also the most resilient to noise and to damages applied to the networks. In accordance with these results (as small world topologies have small average path lengths), it is shown in Adams et al. (2009) that average path length minimization by a genetic algorithm yield good results in associative memories. However, small world topologies are not always optimal; in the case of Hopfield networks, low clustering coefficients were shown to yield better results than higher ones Kim (2004).

Some other studies investigated realistic neural network topologies; for example, laminar structures inspired by cortical microcircuits were shown to perform better than other topologies on generic information-processing tasks using a relatively realistic neuronal model (Haeusler and Maass, 2007). The degree distribution of these laminar structures were found to be the critical parameter influencing performances. More recent investigations of real neuronal network topologies on neocortical neurons highlighted the clustering of neurons in small-world networks (Perin et al., 2011). Relationships between functional network structure of human brains (obtained by fMRI) and neurological disorders are reviewed in Stam (2014).

Part B

Investigating astrocyte network dynamics

Chapter IV

Neuron-astrocyte signaling

This chapter reports experimental results in cell cultures and thus serves two objectives: (1) it allows us to calibrate and experimentally validate the behavior of the network ChI model presented in Section II.2.2; (2) it investigates how neurons communicate with astrocytes.

IV.1 Experiments and model

The work presented in this chapter has been done in collaboration with Yael Hanein's group in Tel Aviv university. They did all the wet lab experiments reported in this chapter and I worked on the modeling part. I would thus like to thank Gillad Wallach, Nitzan Herzog, and Yael Hanein for their involvement in this collaboration.

IV.1.1 Experiments

Sensing by astrocytes of the glutamate released by presynaptic neurons is now a largely accepted fact and one of the major neuron-astrocyte communication pathways (Dani et al., 1992; Venance et al., 1997; Sul et al., 2004; Wang et al., 2006). The detailed signal processing that occurs during this communication is however not really understood. While an increase in neuronal activity has been shown to increase astrocyte activity (Wang et al., 2006; Schummers et al., 2008; Petzold et al., 2008; Nimmerjahn et al., 2009), the protocols used are often ambiguous and do not allow to make the distinction between the effect of increases in overall glutamate quantity imparted by stimulation and more interesting measures like neuronal firing frequency. To investigate this question, we used neuron-astrocytes mixed cell cultures from rat cortices plated on Multi Electrode Arrays (MEA). Figure IV.1 illustrates the experimental setup. Each electrode (*red* circle) activated a restricted set of neurons (*yellow* cells) by injecting current in the culture at a

specific stimulation frequency f, eliciting only one action potential for each stimulation. This particular setup allowed us to precisely set the neuronal firing frequency and observe astrocytic response (*green* cells). To do so, we imaged calcium activity in both neurons and astrocytes with the calcium-sensitive dye Oregon-Green Bapta-I; neurons and astrocytes were distinguished on the basis of their calcium signal shape (neurons responded with a very fast onset while astrocytes were much slower, c.f. Supplementary Figure B.1). In neuron-astrocyte cultures, with maturation of the network, self-generated activity often arises in the form of Spontaneous Bursting Events (SBE) during which neurons fire together at a high frequency (Maeda et al., 1995). These SBEs are separated by periods of low activity and cannot really be avoided without pharmacological treatment. Since this intrinsic activity would have masked the more subtle cross-talk between neurons and astrocytes, and more importantly, since we were not interested in effects brought about by the recurrent activity of neuronal networks, we silenced these SBEs by application of post-synaptic blockers APV (NMDAR antagonist) and CNQX (AMPA/kainate receptors antagonist), effectively blocking neuron-neuron communication (see (5) in Figure IV.1). On a side note, these experiments allowed to show that the activation of neurons did not really depend on the distance between neuron soma and stimulating electrode but that neurons were rather activated through their processes. As an example, the activated neuron in Figure IV.1 gets stimulated by its axon. Knowing in details which neurons were activated is however not relevant in this study and the main interest of this setup is that we can set independently the neuronal firing frequency and the total number of spikes (i.e. the glutamate quantity received by astrocytes). Detailed explanations regarding the experimental setup can be found in Appendix B.1.

Typical protocols involved in these experiments consisted in neuronal stimulation by a subset of electrodes during defined time-windows. Each experiment consisted in the sequential application of stimulations at different frequencies with constant-length pauses in between stimulation windows. We investigated two types of responses from astrocytes to each neuronal stimulation: (1) their *responsiveness*, or the mean amplitude of their calcium signal during stimulation; and (2) their oscillating frequency.

Responsiveness was evaluated at both individual and population levels. Single-cell responsiveness r_i to a specific stimulation frequency f was computed as the area under the $\frac{\Delta F}{F_0}$ curve during the stimulation window minus its value in between the stimulations:

$$r_i(f) = \frac{1}{t_2 - t_1} \int_{t_1}^{t_2} \frac{\Delta F_i}{F_0}(t)dt - r_i^{spont} \tag{IV.1}$$

with $\frac{\Delta F_i}{F_0}(t)$ the normalized fluorescence of astrocyte i at time t, t_1 and t_2 the times at which the stimulation starts and ends, $r_i^{spont} = \frac{1}{T}\int_{spont} \frac{\Delta F_i(t)}{F_0}$ the spontaneous responsiveness, computed in the absence of stimulation (with T the total duration of spontaneous activity). Only a subset of imaged astrocytes responded strongly and very quickly to neuronal stimulation. We classified these cells as *stimulated astrocytes* and we defined the population responsiveness $\langle r(f) \rangle$ for a given experiment and a given stimulation frequency as the average of the single-cell responsiveness of stimulated astrocytes in this experiment. To define an onset frequency above which astrocytes start to respond to neuronal stimulation, we fitted a sigmoid function $S(f)$ to the relationship between neuronal stimulation

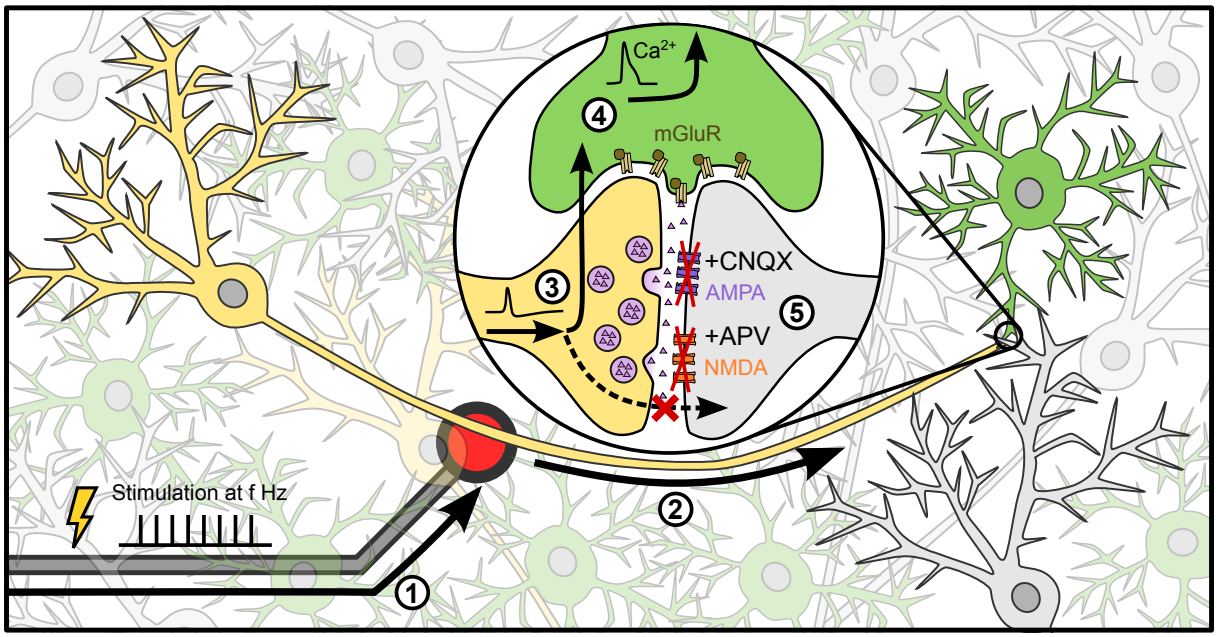

Figure IV.1: Schematic representation of the experimental setup. (1) Electrical stimulation is applied extracellularly by micro electrodes (*red* circle) at a specific stimulation frequency f. (2) Neurons whose soma of processes are close to the electrode are stimulated (*yellow* cells) and elicit an action potential in response to one electrical stimulation; other neurons are silent (*gray* cells). (3) Arrival of the action potentials to pre-synaptic terminals elicit glutamate (*pink* triangles) release. (4) Glutamate binds to mGluRs (*brown* GPCRs), possibly eliciting Ca^{2+} activity in astrocytes (*green* cells) that are contacted by stimulated neurons. (5) Recurrent neuronal activity is prevented by blocking synaptic transmission using CNQX, an AMPA receptor (*purple* channels) antagonist, and APV, a NMDA receptor (*orange* channels) antagonist. Neuronal activity is thus fully controlled by electrical stimulation.

frequency f and responsiveness r_i or $\langle r \rangle$ respectively for single-cell and population onset frequency (see Figure IV.4C):

$$S(f) = A + \frac{B - A}{1 + e^{(C-f)\tau}} \tag{IV.2}$$

with A and B the minimum and maximum responsivenesses, C the midpoint (the frequency corresponding to 50% responsiveness), and τ a parameter controlling the slope of the sigmoid. Once all parameters were estimated, the onset frequency f^* (f_i^* for single-cell) was computed as the frequency corresponding to 10% responsiveness (i.e. $f^* = S^{-1}(0.1)$). This definition of onset frequency was convenient for both experimental and simulated data: since our simulations used the same stimulation protocol as the experiments, the number of data points for the relationship between stimulation frequency and responsiveness was small and the fitted sigmoid allowed to interpolate between those points. For specific simulations independent from the experimental data, we were no longer limited by the restricted number of data points and we could thus compute the *exact onset frequency* as the stimulation frequency corresponding to the inflection point of the responsiveness curve.

Oscillating frequencies were evaluated at single cell level for each experiment using time frequency analysis. We decided to apply wavelet analysis as it provided a good trade off between time and frequency resolution while also avoiding to have to set any time window length (as would be required by short-time fourier transform). Additionally, wavelet analysis was more suited to the Ca^{2+} signals since we used the Morlet wavelet which has a shape similar to astrocyte oscillations. Combining the scales of the wavelet analysis and the dominant frequency of the Morlet function, we were able to compute pseudo-frequencies of astrocyte oscillations during neuronal stimulation. Each astrocyte i was thus associated with wavelet transform coefficients $C_i(t, \omega)$ for each time t and pseudo-frequency ω. Since the stimulation protocol consisted in periods of stimulations alternated by $30s$ pauses, this pattern was spuriously detected by wavelet transform as a pertinent frequency (around $1/30 \approx 0.033$Hz), we thus set a cut off frequency of 0.07Hz under which we discarded all transform coefficients. For each time point t, we only considered the frequency $\hat{\omega}(t)$ that was associated with the maximum transform coefficient:

$$\hat{\omega}(t) = \arg\max_{\omega} C_i(t, \omega) \tag{IV.3}$$

Then, in order to only consider relevant oscillations, we restricted the time frequency-plane to time windows of electrical stimulation (with stimulation frequency f) and only kept the time points whose maximum coefficient was above 70% of the global maximum transform coefficient; each stimulation frequency f was then associated to a set $\Omega_i(f)$ of representative astrocyte frequencies:

$$\Omega_i(f) = \left\{ \hat{\omega}(t) \mid (t \in [t_1, t_2]) \wedge \left(\hat{\omega}(t) \geq 0.7 \times \max_{t'} \hat{\omega}(t') \right) \right\} \tag{IV.4}$$

In the following sections, we will use two measures for each astrocyte i:
- $\langle \Omega_i(f) \rangle$, the average single-cell astrocyte oscillation frequency in response to an electrical stimulation with frequency f;
- Ω_i^{max} the maximal oscillating frequency of astrocyte i, defined as the 95^{th} percentile of all $\Omega_i(f)$ (we did not use the actual maximum to avoid possible artifacts from the wavelet transform).

IV.1.2 Neuron-Astrocyte network modeling

Since early experiments helped us determine that the response of astrocytes was dependent on metabotropic glutamate receptors (c.f. next section), we decided to use the G-ChI model of astrocyte dynamics presented in Section II.1.2 together with GJC couplings organizing astrocytes into networks. Each experiment consisted in a different cell culture, we thus used, for each simulation, a different astrocyte network and different stimulated astrocytes, defining a one to one correspondence between actual experiments and *in silico* experiments. Although we did not ambition to compare results at the single experiment level, and even less at the single cell level, we needed to introduce variability in our simulations to account for the huge inter-experimental variability (presented in the next section). Since we could not estimate intracellular parameters from experimental data, we chose instead to bring variability in the network topology (by estimating it for each

experiment) and in the number and positions of stimulated astrocytes. Although not perfect (it was not sufficient to account for the experimentally observed variability in astrocyte responsiveness), this approach was enough to account for the variability in astrocyte oscillation frequency.

For each experiment, we thus built the corresponding simulated network topology and estimated which astrocytes were stimulated by neurons by analyzing the Ca^{2+} traces and physical positions of cells in the actual experiment. To construct the astrocyte network, we exploited the fact that astrocytes are expected to tile the space they are in, occupying non overlapping anatomical domains (Bushong et al., 2002): astrocytes that are close to each other can be GJC coupled while astrocytes separated by other cells (e.g. neurons) are prevented from coupling because of the 2D nature of cell cultures. In each experiments, cells are identified, as exemplified in Figure IV.2A, on the basis of their Ca^{2+} activity (c.f. Appendix B.1) as being astrocytes (in *green*), neurons (in *red*), or unclassified cells (in *blue*). We decided to apply a simple method for reconstructing astrocyte networks: we first computed cell centers as the center of mass of cell bodies and then constructed the Voronoi diagram of all these points (each cell center i is associated with a region, or anatomical domain, in which all the points are closer to i than to any other cell center). As an example, Figure IV.2B displays a Voronoi diagram in which *green* circles represent astrocytes (other cell centers are not represented). When looking at an immunostaining image of our cell cultures (Figure IV.2C) and superimposing the associated Voronoi diagram, one can see that astrocytes can mainly form GJCs with astrocytes with which they share an anatomical domain boundary (*thick blue* lines). In this example, astrocyte A shares boundaries with 7 other astrocytes (B1 to B7); granted that all of these neighbors are identified as astrocytes from their Ca^{2+} traces, we will create GJCs in the model between A and its 7 neighbors. We thus considered, for all cultures, that all astrocytes that shared a border in the Voronoi diagram were GJC coupled with nonlinear GJC (*thick dark* lines in Figure IV.2B) in the simulations, as described in Section II.2.2.

Once we defined the network topology, we still need to define which astrocytes are directly stimulated by neurons. In the experiments, some astrocytes do not respond to neuronal activity, while some others respond but with varying delay. The astrocytes that are directly stimulated should thus respond earlier than astrocytes that get indirectly activated by another astrocyte through GJC couplings. In order to distinguish between these two cases, we looked, for each astrocyte i and each stimulation frequency f, the time delay Δt_i^f between the start of stimulation and the point at which $\Delta F/F_0$ reaches 60% of its maximal value throughout the experiment. Each astrocyte was defined as stimulated if $\min_f \Delta t_i^f \leq 1.5$s. This 1.5s second threshold was used because it took around 2s for model astrocytes to propagate an activation through GJCs, we thus considered that astrocytes that responded in less than 1.5s were directly stimulated. Examples of stimulated astrocytes are shown in Figure IV.2B in *dark green* and topped by *yellow* lightning symbols. Since we cannot know the exact number of synapses enwrapped by each astrocyte, we simulated an equivalent synapse, representing the average number of synapses enwrapped by an astrocyte, with the Tsodyks-Markram model of dynamical synapse (Tsodyks and Markram, 1997) presented in Section II.1.2.1. This thus added 3 equations on top of the already $4N$ equations from the G-ChI model (with N the number of astrocytes): 2 equa-

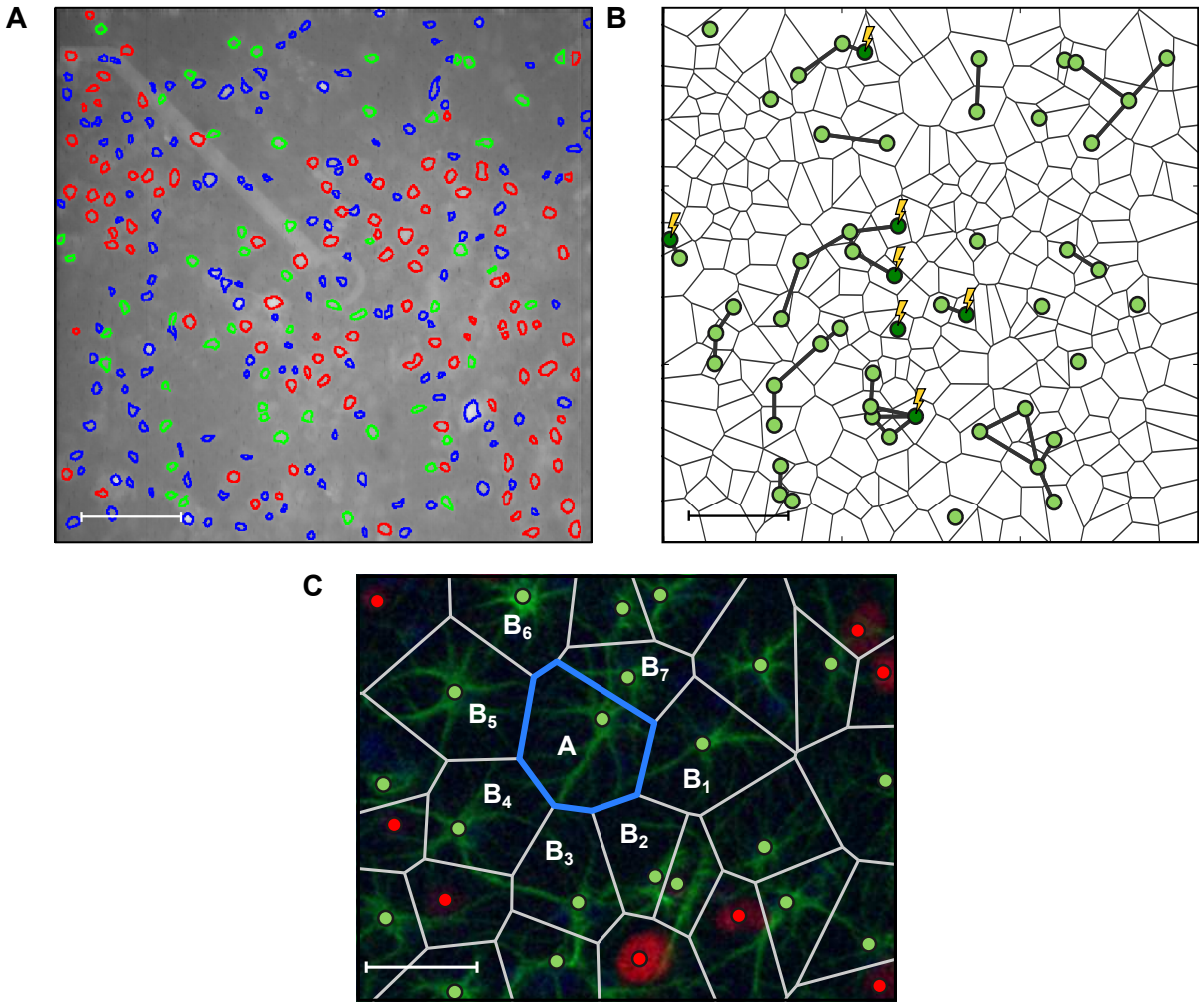

Figure IV.2: Inference of model networks from experimental data. **A**, The experimental culture of Figure IV.3, with neurons segmented in *red*, astrocytes in *green* and unresponsive cells in *blue*. Scale bar is 75 μm. **B**, Model networks constructed using the experimental data of A. Fine *grey* lines delineate the Voronoi diagram computed from the experimental cell positions; *green* circles denote model astrocytes and *dark green* cells with a lightning symbol denote stimulated model astrocytes. Wide *dark grey* lines show the GJC connections between astrocytes. **C** Example of Voronoi diagram (*light gray* lines) superimposed on an immunostaining image (in *red* the neuronal marker NeuN and in *green* the astrocytic marker GFAP). Astrocyte A shares its anatomical region borders (*thick blue* lines) with 7 other astrocytes (B1 through B7). Scale bar is 75 μm. Model networks were inferred according to this process for each experiment.

tions for the dynamical synapse and 1 equation for the glutamate concentration in the extracellular space G. Since we control the firing rate of neurons in the experiments, we just use the electrical stimulation train as the train of presynaptic spikes for the synapse model. To take into account the fact that only some astrocytes are stimulated, we slightly modified equation (II.19) with:

$$\frac{\mathrm{d}}{\mathrm{d}t}I = aJ_\beta(G,C) + J_\delta(C,I) - J_{3K}(C,I) - J_{5P}(I) \tag{IV.5}$$

with $a = 1$ if the astrocyte is stimulated by neurons and 0 otherwise. Given that we defined a one-to-one correspondence between actual experiments and simulations, we measured the exact same quantities in the experiments and in the simulations: responsiveness and both single cell and population level, astrocyte onset frequency and oscillation frequencies.

Parameters for the G-ChI model, presented in Table IV.1, have been set so as to match signal size and typical oscillation frequencies witnessed in the experiments. We first chose to use parameters leading to FM encoding properties (c.f. Section II.1.1.2), as the Ca^{2+} signal shape resembled those observed in the experiments. We then scaled all the time-dependent parameters so that the maximum oscillation frequency in the model corresponded to the maximum oscillation frequency observed in the experiments (≈ 0.2Hz). Finally, we chose ρ_{so}, the fraction of glutamate that spills over to the astrocyte, so that the simulated population onset frequency was close to the experimental one. Since we did not ambition direct cell-to-cell comparisons between simulated and experimental data we did not need to apply automated firring procedures to estimate the model parameters. These three simple choices were instead sufficient to qualitatively reproduce the Ca^{2+} signal shapes, maximum frequency distribution, and population onset frequency.

Table IV.1: Biochemical parameters of the GChI model.

Symbol	Description	Value	Units
	IP_3R kinetics		
d_1	IP_3 binding affinity	0.13	μM
O_2	Inactivating Ca^{2+} binding rate	0.62	$\mu M^{-1} s^{-1}$
d_2	Inactivating Ca^{2+} binding affinity	1.049	μM
d_3	IP_3 binding affinity (with Ca^{2+} inactivation)	0.9434	μM
d_5	Activating Ca^{2+} binding affinity	0.08234	μM
	Calcium fluxes		
C_T	Total ER Ca^{2+} content	2	μM
ρ_A	ER-to-cytoplasm volume ratio	0.185	–
Ω_C	Maximal Ca^{2+} release rate by IP_3Rs	18.56	s^{-1}
Ω_L	Maximal Ca^{2+} leak rate	0.3416	s^{-1}
O_P	Maximal Ca^{2+} uptake rate	2.7846	$\mu M\, s^{-1}$
K_P	Ca^{2+} affinity of SERCA pumps	0.05	μM
	IP_3 production		
O_δ	Maximal rate of IP_3 production by PLCδ	0.4641	$\mu M\, s^{-1}$
K_δ	Ca^{2+} affinity of PLCδ	0.1	μM
κ_δ	Inhibiting IP_3 affinity of PLCδ	1.5	μM
O_β	Maximal rate of IP_3 production by PLCβ	1.105	$\mu M\, s^{-1}$
K_G	Glutamate affinity of the receptor	1.3	μM
K_L	Ca^{2+}/PKC-dependent inhibition factor	10	μM
K_{KC}	Ca^{2+} affinity of PKC	0.6	μM
	IP_3 degradation		
Ω_{5P}	Maximal rate of IP_3 degradation by IP-5P	0.793	s^{-1}
O_{3K}	Maximal rate of IP_3 degradation by IP_3-3K	13.923	$\mu M\, s^{-1}$
K_D	Ca^{2+} affinity of IP_3-3K	1	μM
K_{3K}	IP_3 affinity of IP_3-3K	0.7	μM
	IP_3 diffusion		
F	GJC IP_3 permeability	3.64	s^{-1}
I_θ	Threshold IP_3 gradient for diffusion	0.15	μM
ω_I	Scaling factor of diffusion	0.05	μM
	Synapse dynamics		
Ω_f	Rate of synaptic facilitation	2	s^{-1}
Ω_d	Rate of recovery of released synaptic vesicles	1	s^{-1}
Ω_G	Glutamate clearance rate	60	s^{-1}
U_0	Basal probability of synaptic glutamate release	0.25	–
ρ_C	Volume ratio of synaptic vesicles and mixing volume	6.5×10^{-4}	–
G_T	Total glutamate content of readily releasable vesicles	200	mM
ρ_{so}	Fraction of glutamate that spills over to the astrocyte	0.075	–

IV.2 Astrocyte respond in a frequency-dependent manner to neuronal activity

IV.2.1 Astrocyte response is glutamate-mediated

We first investigated astrocyte responses to electrical stimulation by using a rather simple stimulation protocol: we used 9 electrodes (to activate a substantial number of neurons) with 30s pulse trains at frequencies ranging from 0.2Hz to 70Hz with 30s pauses in between stimulation periods. Examples of neuron responses to this stimulation protocol are shown in Figure IV.3A: when low frequency stimulation was applied, individual neuronal spikes were identifiable from the Ca^{2+} signal (top *red* traces); for higher stimulation frequencies, these responses saturated to plateaus because of the slow Ca^{2+} dynamics of neurons. Some astrocytes (*green* traces) also displayed Ca^{2+} activity during electrical stimulation but its characteristics were different: low stimulation frequencies did not seem to elicit any response while higher stimulation frequencies elicited Ca^{2+} oscillations whose frequency ω seemed to increase with f while being always much lower than those of neurons. We tested whether astrocyte response was directly linked to electrical stimulation by applying TTX, effectively silencing all neuron activity. In these experiments (results on Supplementary Figure B.3), astrocytes did not display the increased activity during electrical stimulation that was observed before. We thus concluded that astrocyte activity depended on neuron activity. To further characterize the communication pathway between neurons and astrocytes, we applied mGluR group I (mGluR1 and mGluR5) antagonists. Ca^{2+} traces from this experiments are shown in Figure IV.3B; neurons (*red* traces) are hardly affected by metabotropic glutamate receptor antagonists, suggesting mGluR group I (which are also expressed by neurons) do not play a role in neurons response to electrical stimulation by the electrodes. On the other hand, astrocytes responses (*green* traces) to electrical stimulation are very strongly diminished. We thus concluded that neuron-to-astrocyte communication in our preparations were mostly glutamate-dependent and mediated by group I metabotropic glutamate receptors. As mentioned in the previous section, this glutamate dependence made us choose the G-ChI model of astrocyte Ca^{2+} dynamics as a model for our cultured astrocytes.

IV.2.2 Frequency dependence of astrocytic response

It seems, when looking at Figure IV.3A, that astrocytes respond more to high frequency stimulation trains than to lower ones. With this stimulation protocol however, since the stimulation duration in constant, the total number of stimulations is increased along with the frequency f; to determine whether astrocytes actually responded to increases in frequency or in total number of stimulations, we devised a new stimulation protocol. We chose to keep the number of stimulation in each train n^{stim} constant and thus decrease the stimulation duration as $T^{stim}(f) = \frac{n^{stim}}{f}$. As for the previous stimulation protocol, we separate stimulation trains by 30s pauses. Additionally, to avoid memory effects due

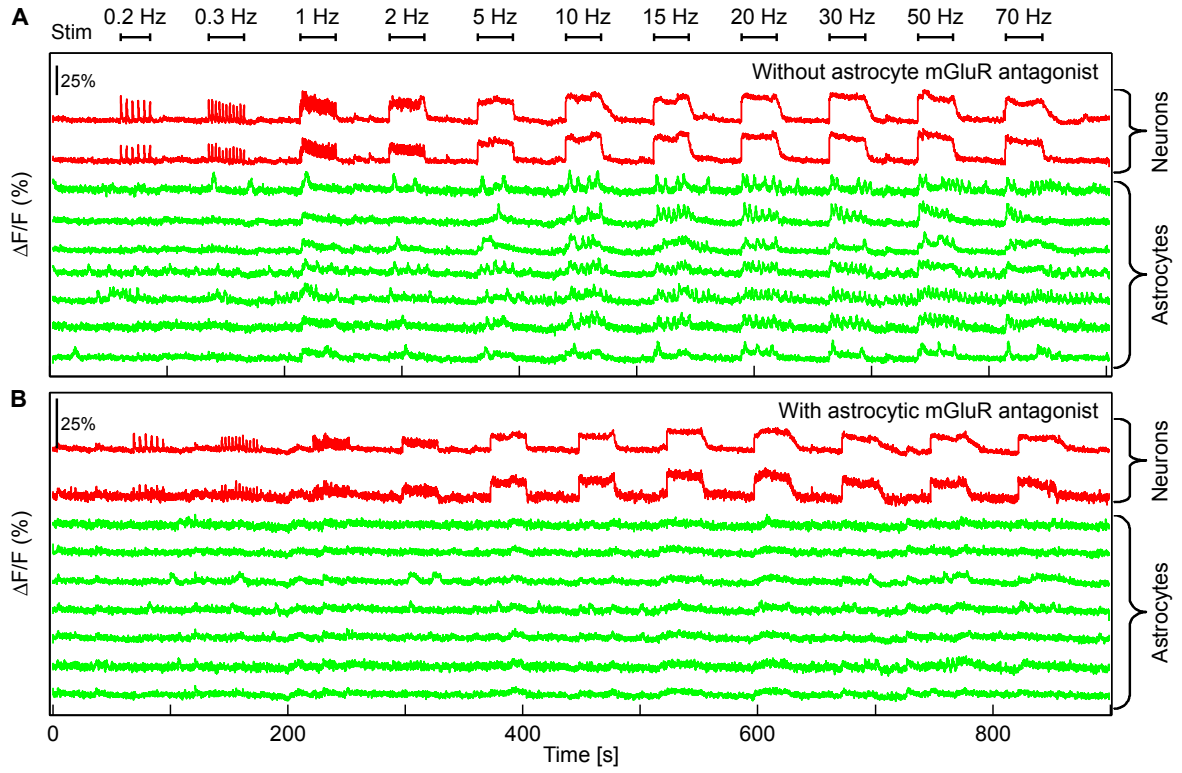

Figure IV.3: Astrocytic response to neuronal activity in the presence of neuronal AMPAR and NMDAR/kainate antagonists, and astrocytic mGluR1 and mGluR5 antagonists. **A**, Ca^{2+} traces of two selected neurons (in *red*), showing stimulated activity according to a multi-frequency protocol, and seven selected astrocytes (in *green*) in presence of neuronal AMPAR and NMDAR/kainate antagonists. **B**, Representative traces of same cells and stimulation protocol as in A, showing no $[Ca^{2+}]_i$ elevations in the presence of neuronal AMPAR and NMDAR/kainate antagonists, and astrocytic mGluR1 and mGluR5 antagonists.

to the order in which the stimulation trains are presented, we randomized their order. A schematic representation of this new stimulation protocol is presented in Figure IV.4A along with selected traces of neurons (*red* traces) and responsive astrocytes (*green* traces). Similarly to previous experiments, neurons respond immediately to electrical stimulation and astrocytes display Ca^{2+} oscillations for high stimulation frequencies while they remain silent at lower frequencies. Since the number of stimulations per stimulation train is constant with this protocol, we concluded that astrocytic response was frequency dependent. This frequency dependence can be better visualized in Figure IV.4B, in which distributions of single-cell responsiveness $r_i(f)$ of all astrocytes in the same experiment were plotted for each stimulation frequency f. As f increases, the average responsiveness increases, showing that this frequency-dependent increase in responsiveness is not restricted to some subset of responsive astrocytes. Interestingly, the cell-to-cell variability also increases with the stimulation frequency: for low stimulation frequencies, all astrocytes are more or less silent, leading to a peaked distribution of single-cell responsiveness (e.g. $f = 2$Hz, *dark blue* curve); for high stimulation frequencies however, all astrocytes display higher $r_i(f)$ but some astrocytes are much more responsive than others

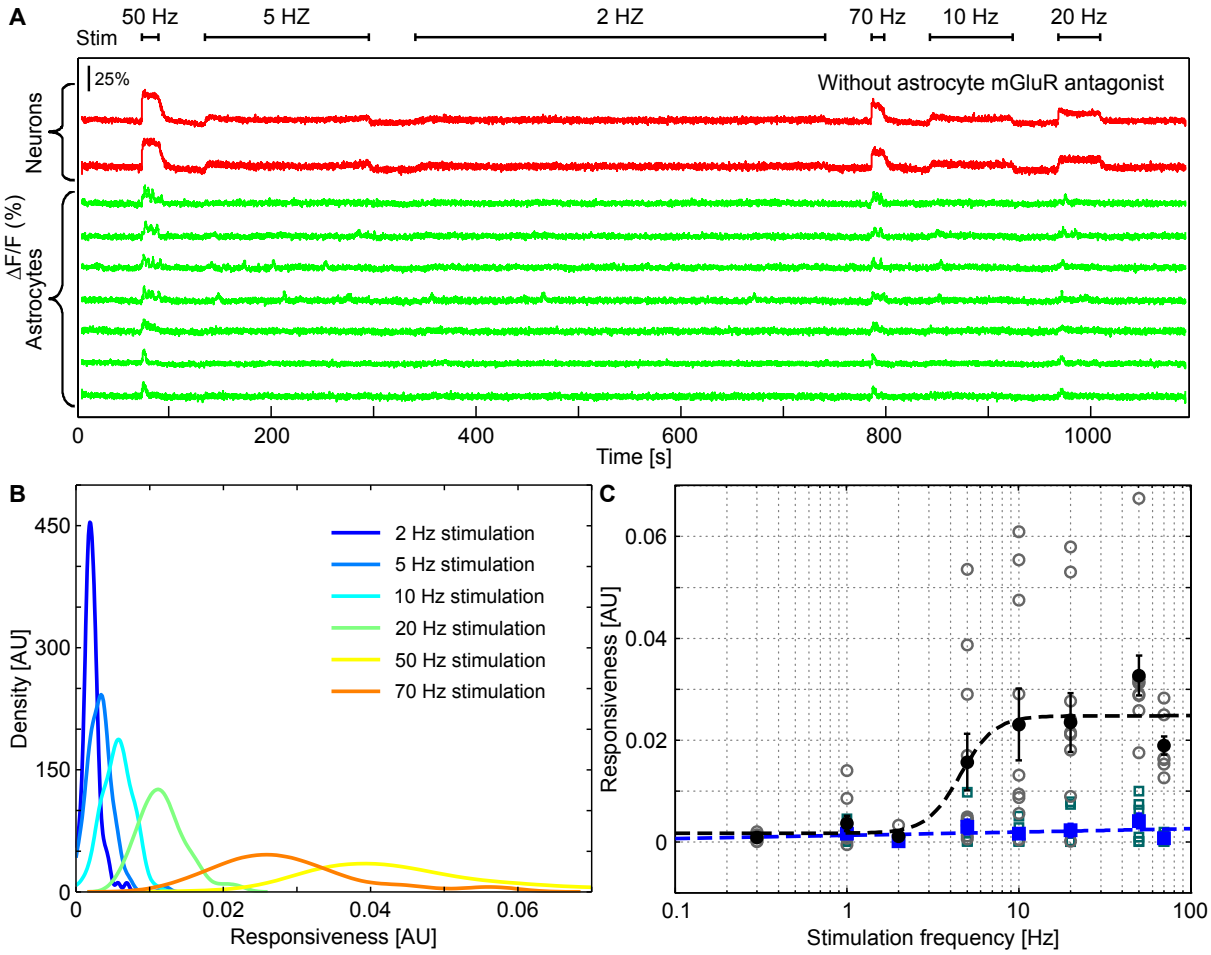

Figure IV.4: Frequency dependent astrocytic response to neuronal activity. **A**, Ca^{2+} traces of two selected neurons (in *red*), showing stimulated activity according to a random multi-frequency protocol, and seven selected astrocytes (in *green*) showing frequency dependent $[\mathrm{Ca}^{2+}]_i$ elevations in response to neuronal activity. Experiments were performed in the presence of neuronal AMPAR and NMDAR/kainate antagonists. For each electrical stimulation frequency, single-cell astrocytes responsivenesses were very variable. Their distribution for the experiment displayed in A is shown in **B**, Increasing the stimulation frequency leads to increases in average astrocyte responsivenesses but it also increased responsiveness variability. **C**, Astrocytic population responsiveness versus stimulation frequency. *Grey* empty circles are population responsivenesses for experiments performed with NMDAR & AMPAR but without (astrocytic) mGluR antagonists ($n = 284$). Corresponding mean result, standard errors (*black* circles and bars), and sigmoid fit (*black dashed* line) are also illustrated. *Turquoise* empty squares are population responsivenesses obtained in the presence of both NMDAR & AMPAR and mGluR antagonists ($n = 239$). Corresponding mean results and standard errors and linear fit are shown as *blue* squares (with bars and *dashed blue* line, respectively).

(e.g. $f = 50$Hz, *yellow* curve). Using our computational model, we will try to determine possible causes for this heterogeneity in single-cell responsiveness. On a side note, for $f = 70$Hz (the highest stimulation frequency) the average responsiveness decreases when compared to $f = 50$Hz and it seems to be due to the short time duration of this stimulation train, not leaving enough time for the astrocytes to react. Responsivenesses of astrocytes at such high stimulation frequencies should thus be interpreted with care. Additionally to cell-to-cell variability, astrocyte responses to stimulation also displayed inter-experiment variability: some preparations responded more strongly than others but the average onset frequency (i.e. the frequency f^* above which astrocyte start to respond, c.f. Section IV.1) was conserved. Figure IV.4C displays the average responsiveness $\langle r_i \rangle$ of all experiments (*empty grey* circles) together with the average responsiveness across experiments (*full black* circles) and its fitted sigmoid function (*black dashed* curve, fitted using equation (IV.2)). As a comparison, we also plotted average astrocyte responsiveness $\langle r_i \rangle$ when mGluR blockers were added (*empty teal* squares) along with the mean across experiments (*full blue* circles) and a linear fit of these points (*dashed blue* line). In these conditions, astrocytes remained silent during stimulation and did not display any onset frequency. Without mGluR blockers however, we used the fitted sigmoid to determine that the average population onset frequency was around $f^* = 2.8 \pm 1.02$ Hz (95% confidence level). As could be expected from the cell-to-cell variability in responsiveness, onset frequencies also displayed a high cell-to-cell variability; some astrocytes started responding to stimulation frequencies as low as 1 Hz and some others needed at least 12 Hz stimulation to respond.

IV.2.3 Astrocyte oscillation frequency displays cell-to-cell variability

As mentioned previously, we investigated calcium oscillation frequencies using wavelet analysis, a type of time-frequency analysis. From the full wavelet transforms, we identified two typical astrocyte response types. *Type I* responses displayed astrocytic activation at a given stimulation frequency f_i^* and their oscillation frequency remained mostly constant when the stimulation frequency f increased. An example of such astrocytic response is displayed in Figure IV.5A. *Type II* responses (Figure IV.5B) were characterized by a marked increase in their oscillation frequency as f increases and by a higher maximum oscillation frequency than type I responses. Rather than corresponding to two distinct types of astrocytes, these two response types should be considered as the two extreme ends of a spectrum of astrocytic responses. Additionally, the experimental noise prevented us from deciding whether type I responses showed small or no increase in their oscillation frequency as the stimulation frequency increased. The distinction between these two response types was thus better established by their different maximum oscillation frequencies. To check that this typology was reflected in the full data, we looked at the distribution of the maximal oscillation frequency Ω_i^{max} (c.f. Section IV.1.1) of all the responding astrocytes (Figure IV.5C). This distribution indeed seemed bimodal: most of the astrocytes exhibited type I responses (*blue* part of the histogram) and oscillated at ≈ 0.1Hz even for high stimulation frequencies; a smaller number of astrocytes exhibited

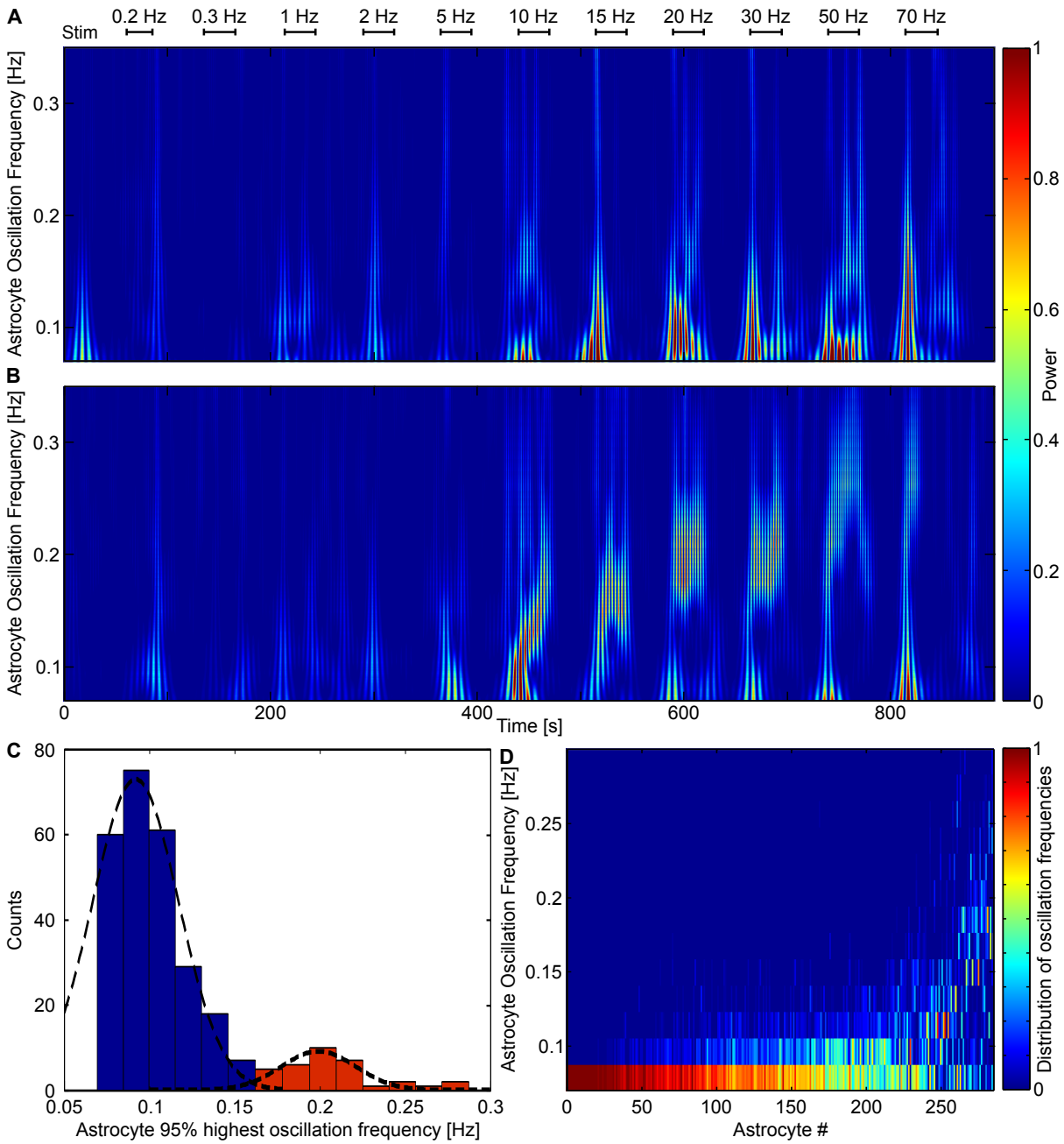

Figure IV.5: Spectral analysis of astrocytic $[Ca^{2+}]_i$ oscillation with wavelet analysis. **A**, Time frequency analysis of a representative astrocyte showing typical low frequency oscillation (Type I). **B**, Time frequency analysis of a representative astrocyte showing higher frequency response that increases with stimulation frequency (Type II). **C**, Histogram of the astrocyte maximal frequency (see Methods). Typical patterns are colored and fit by a Gaussian distribution (Type I cells in *blue*, and Type II cells in *red*). **D**, Distribution of astrocyte oscillation frequencies. Each column corresponds to one astrocyte and shows its oscillation frequency spectrum (binned at 0.02 Hz). Astrocytes were ranked according to their mean oscillating frequency; most of them oscillate at low frequencies but around one third (right part of the panel) responded to stimulations with oscillations as high as 0.2 Hz. ($n = 284$ cells).

type II responses (*red* part of the histogram) and could oscillate up to $\approx$ 0.2Hz. Of course, some astrocytes were in between type I and type II, displaying small increases in oscillation frequency when f increased. To better visualize how astrocytes are distributed among the two types, we considered, for each astrocyte, the distribution of oscillation frequencies ($\langle \Omega_i(f) \rangle$ for all f values) and concatenated all these distributions by ranking them by their mean values. The resulting plot is displayed in Figure IV.5D, with each vertical line corresponding to a given astrocyte from a given experiment; type I responses would be on the left part (around 3/4 of all astrocytes), where all the oscillating frequencies for all stimulation frequencies are around 0.1Hz. Type II responses, constituting the remaining fourth of astrocytes, are visible on the right part, with distributions whose peak slowly increases up to 0.2Hz.

We thus showed that astrocytes in these experiments displayed :

1. frequency dependent responses to neuronal stimulation through metabotropic group I glutamate receptors;
2. cell-specific onset-frequency f_i^* whose cell-to-cell variability was high;
3. cell-specific patterns of variations in oscillation frequency in response to stimulation frequency increases.

In the next section, we use computational modeling to provide plausible explanations to the mechanisms underlying the frequency-dependent response and investigate possible causes for the heterogeneities in onset frequency and oscillation frequency.

IV.3 Modeling astrocyte response to neuronal activity

To investigate the mechanisms responsible for the frequency-dependent astrocyte responses and the heterogeneity in both oscillation frequency and onset frequency, we used the biophysically realistic G-ChI model with the simulation setup presented in Section IV.1.2. Biophysical parameters were set according to Table IV.1 and experiment-specific parameters, like network topology or stimulated astrocytes, were estimated from the experiments. Each experiment thus has a simulated counter-part, allowing inter-simulation and inter-astrocyte variability.

IV.3.1 Reconstructed networks of astrocytes

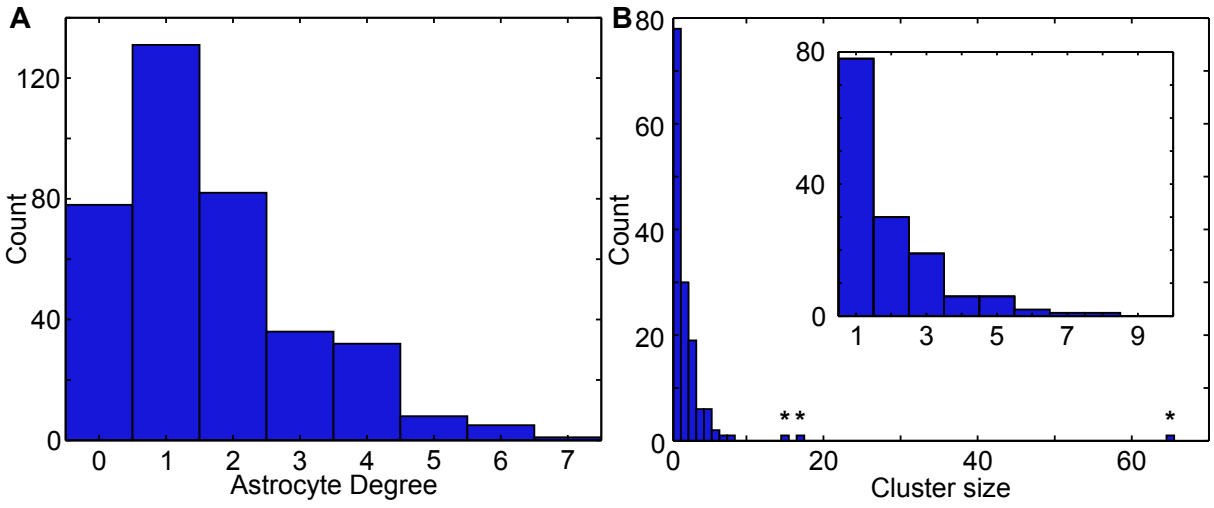

Figure IV.6: Basic properties of inferred networks. **A**, Distribution of astrocyte coupling degree. Most model astrocytes are connected to very few neighbors ($n = 373$). **B**, The distribution of the size of connected astrocyte clusters ($n = 146$). It can be seen that most astrocytes are isolated (inset is a focus on the smallest sizes) but some experiments contain very large clusters of up to 60 astrocytes (indicated by stars).

As previously presented, networks were reconstructed by first computing the Voronoi diagram of cell centers including all cells (neurons, astrocytes and unidentified cells) and then keeping only astrocytes. Thus, astrocytes are only connected if they share a border in the Voronoi diagram. Since cell-cultures are 2D mediums, this prevents the coupling of astrocytes that are physically separated by other non-astrocyte cells. The networks reconstructed using this method are sparsely connected: the degree distribution in Figure IV.6A indicated that most astrocytes (around 1/3) are connected to only 1 neighbor and nearly all astrocytes are connected to less than 4 neighbors. This confirms that astrocytes, as visible in Figure IV.2A are usually separated from each other by other cells. Degree distributions do not however describe how the networks are wired so, to better characterize our reconstructed networks, we looked at the distribution of maximal clusters

of astrocytes. A cluster of astrocytes is defined as a set of astrocytes in which all pairs of astrocytes have a finite topological distance (i.e. there exists a path between them). A cluster is maximal if all the astrocytes connected to its members are also part of the cluster. In a sense, maximal clusters are like 'islands' of astrocytes and their size indicates whether the astrocytes form one big network or are all isolated from each other. The distribution of maximal cluster sizes shown in Figure IV.6B clearly indicated (on the inset) that most clusters are constituted by very few astrocytes (between 1 and 3). Because of the inter-experimental variability, some experiments however displayed large clusters of astrocytes (marked by asterisks) of up to 60 astrocytes. Additionally, the number of isolated astrocytes (≈ 80) was comparable to the number of astrocytes involved in a cluster of more than 10 astroctes (≈ 110). These statistics however differ substantially from the reported size of astrocyte networks in intact tissue (up to hundreds of astrocytes in the neocortex (Nimmerjahn et al., 2004)). This discrepancy could be accounted for by two main phenomenon:

1. Astrocytes that did not exhibit Ca^{2+} activity were discarded from our reconstructed networks (where cell identification is based on Ca^{2+} activity), potentially preventing highly connected clusters by creating "holes".
2. The culture medium imposed a 2D embedding of astrocytes, thus further reducing the number of neighbors that they could contact.

However, in accordance to the fact that most estimated astrocyte networks were disconnected, we did not observe Intercellular Calcium Waves (ICW) within our experimental setup even though astrocytes are known to display high levels of Cx expression in the types of cultures that we used (Koulakoff et al., 2008). Because of this lack of propagating ICWs, we could not apply the topological inference techniques developed in Appendix A.2 to these experiments.

IV.3.2 Frequency-dependent response in modeled astrocytes

Stimulation trains in the simulations were taken from the actual electrical stimulation trains used in the experiments. As an example, we show in Figure IV.7A some selected traces of the simulation corresponding to the experiment displayed in Figure IV.3A. Neuron traces (in our case, stimulation trains) are displayed on top in *red* while astrocyte traces are in *green*. In agreement with the experiments, astrocytes do not respond to stimulation when its intensity is too low and start responding at stimulation frequencies that are cell-specific. The shape of calcium signals is similar to what was seen in the experiments: isolated Ca^{2+} surges for low stimulation intensity and quick oscillations for high stimulation frequency. Interestingly, despite the fact that all astrocytes had the same biophysical parameters, some simulated astrocytes (bottom trace in Figure IV.7A) responded in a very non-stereotypical manner with both low and high amplitude oscillations. Overall, simulated astrocytes displayed variability in both oscillation frequency (compare the top 2 astrocytes to the bottom 2) and onset frequency: the first astrocyte start oscillating at 2Hz stimulation while the bottom one only starts around 20Hz.

To check whether the model also displayed frequency-dependent responses of astrocytes

(and not only intensity-dependent response, as shown in Figure IV.7A), we also simulated experiments in which the number of stimulations in each stimulation period was kept constant (as in Figure IV.4A). By computing the average population responsiveness $\langle r_i(f) \rangle$ shown in Figure IV.7B as a function of stimulation frequency f, we obtained similar results to the experiments (compare to Figure IV.4C). When the stimulation frequency increases, the population responsiveness increases as soon as a frequency onset is crossed and later plateaus for high stimulation frequencies. The population onset frequency $f^* = 1.3 \pm 0.3$Hz (estimated from the *black dashed* sigmoid fit, 95% confidence level, $n = 130$) was in reasonable agreement with the experiments (2.8Hz). In the simulations, the inter-experiment variability (*grey circles* correspond to different experiments) was however lower than in the experiments since we did not have stochasticity in estimating Ca^{2+} concentration in our simulated astrocytes. In contrast, we only considered $\Delta F/F_0$ in the experiments and, depending on dye absorption by astrocytes, dynamical properties of the dye, or Ca^{2+} concentration in astrocytes in resting state, the absolute values of this signals could vary a lot between experiments, impacting the responsiveness values.

IV.3.3 Onset of activity is due to supra-linear IP_3 dynamics

While it is apparent from both the experiments and the simulations that astrocytes only respond to stimulation frequencies above a threshold (defined here as the onset f^* frequency), the biophysical causes of this phenomenon could not be determined with our experimental setup. The Previous simulations allowed us to validate our model against the experimental data by showing that it qualitatively reproduces the main features of astrocyte responsiveness to neuronal stimulation. We were then able to use the model to suggest biophysical causes for the frequency-dependent astrocyte response. To that end, we ran specific experiment-independent simulations in which we tested a large number of small stimulation frequencies to try and determine what happens when the astrocytes start responding to stimulation. Since the only source of variability in the previous simulations was the topology of astrocyte networks, we simulated these different stimulation frequencies for astrocytes with different number of unstimulated neighbors. Figure IV.8A displays single cell responsivenesses $r_i(f)$ for astrocytes with 0 (*blue* curve), 1 (*green* curve), and 2 unstimulated neighbors (*red* curve). We also plotted in Figure IV.8B the corresponding normalized numerical derivatives ($\frac{dr_i}{df} / \max_f \frac{dr_i}{df}$) of the curves in Figure IV.8A so that inflection points (i.e. peaks of $\frac{dr_i}{df} / \max_f \frac{dr_i}{df}$, marked by asterisks) are clearly visible. As evoked in Section IV.1.1, we computed the exact onset frequency as the stimulation frequency corresponding to these inflection points because they correspond to the moment at which astrocytes switch from a non-oscillating regime to an oscillating one. For lower stimulation frequencies, Ca^{2+} levels increase but the astrocyte does not display oscillation, this small increase in Ca^{2+} might thus not be detectable in experiments. For the uncoupled astrocyte, we can clearly see the exact onset frequency around 2Hz as the responsiveness strongly increases. When the number of unstimulated neighbors increase, the onset frequency is increased: with one neighbor, it is shifted to $f_i^* \approx 4.75$Hz and with two neighbors, it gets higher than 10Hz (not shown on the figures). These simulations thus confirm the existence of a frequency threshold that corresponds to an inflexion

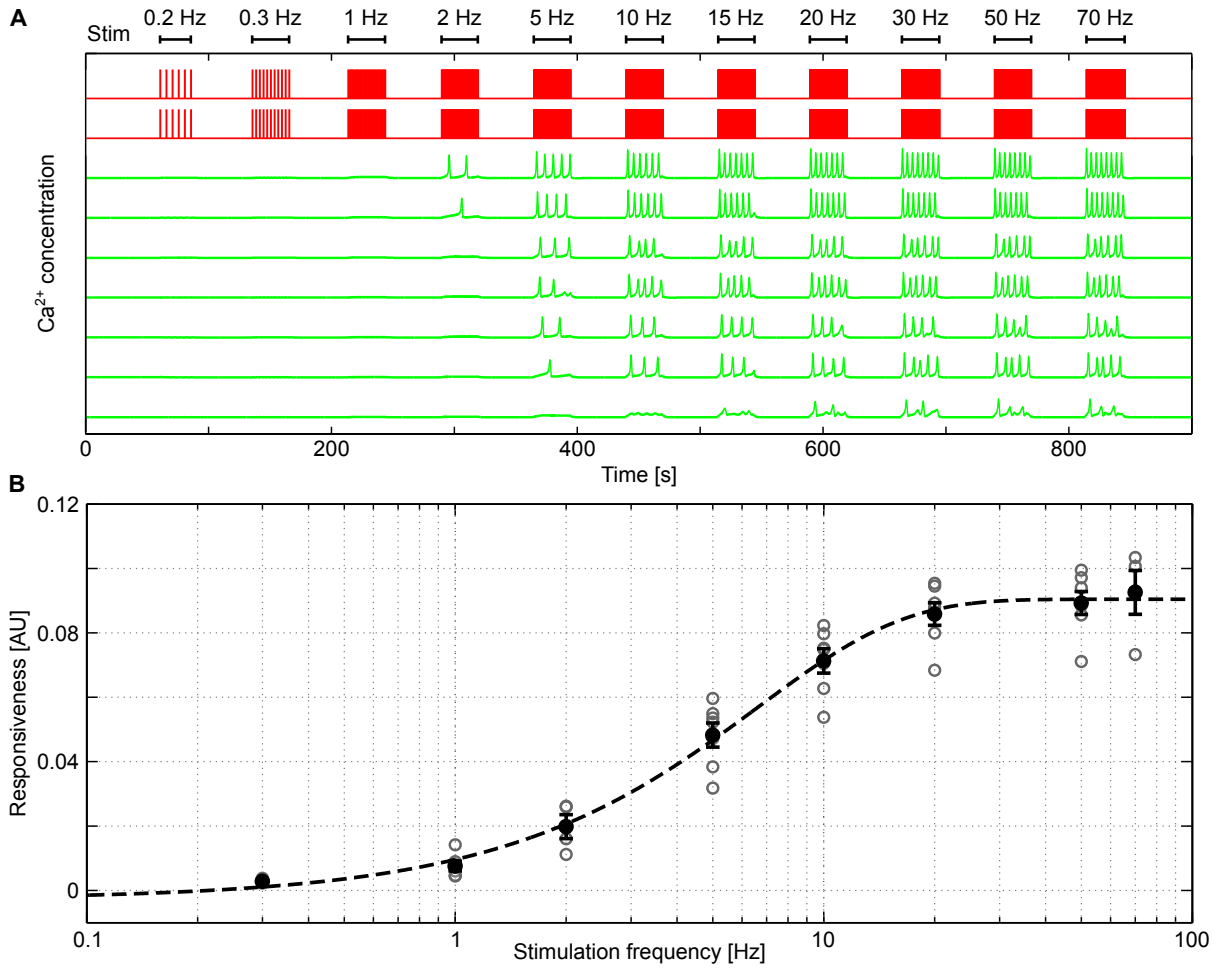

Figure IV.7: Model astrocytes also respond in a frequency-dependent manner to neuronal stimulation. **A**, Astrocyte calcium signals (*green* traces) show a variety of responses, as in the experiments. Some of them start responding at frequencies as low as 2Hz (top trace) while others need up to 20 Hz to elicit a significant response (bottom trace). Astrocytes were stimulated using the *red* neuronal spike train, stimulation frequencies are indicated on top of the figure. **B**, Using the same method as in the experiments (Figure IV.4C), population responsiveness was computed in the simulations and plotted as a function of stimulation frequency for all modeled cultures. *Grey* circles denote population responsivenesses and *black* dots their average value. Error bars indicate standard error and the *black* dashed line shows the sigmoid fit characterizing the frequency-dependent astrocyte response ($n = 130$ cells).

point in the responsiveness curve in linear-linear scale and suggests that the number of unstimulated neighbors of an astrocyte can control its onset frequency.

To understand the existence of the inflexion point in the responsiveness curve, we looked at Ca^{2+} (Figure IV.8C) and IP_3 (Figure IV.8D) concentrations in cells submitted to different stimulation frequencies. In all these simulations, IP_3 quickly increases as glutamate increases in the synapse and then gets degraded by IP-5P until the next synaptic release of glutamate. When the stimulation frequency $f = 0.5$Hz is low, the amount of IP_3 (*light red* curves) produced by a single release of glutamate is approximately equal to the amount degraded in between two synaptic releases, the average IP_3 concentration in the astrocyte thus stays close to resting state concentration; accordingly, Ca^{2+} concentration also stay close to equilibrium as there is not enough IP_3 to open enough IP_3R channels on the ER membrane. When the stimulation frequency increases to $f = 1.5$Hz, IP_3 gets higher but still plateaus slightly above 0.2μM (*bright* red curve), when glutamate-dependent IP_3 creation by PLCβ is counterbalanced by degradation by IP-5P (PLCδ and IP_3-3K are not very active because of the low Ca^{2+} concentration). Since this 'equilibrium' reaches relatively high values of IP_3, the Ca^{2+} concentration (*bright blue* curve) gets slightly higher than resting state but still does not trigger CICR. At last, when the stimulation frequency $f = 2.1$Hz exceeds the onset frequency $f_i^* = 2$Hz, the IP_3 concentration gets high enough (*dark red* curve) to initiate CICR, quickly increasing the cytoplasmic Ca^{2+} concentration (*dark blue* curve) and strongly increasing the responsiveness of the astrocyte.

To investigate in more details the dynamics at play during supra-threshold astrocyte response, we looked simultaneously at the activities of IP_3 producing PLCβ and PLCδ (Figure IV.9A and B), IP_3 degrading IP-5P and IP3-3K (Figure IV.9D), and at the dynamics of Ca^{2+} channels probability of opening or closing (Figure IV.9C) in isolated astrocytes ($k = 0$). From the start of the stimulation ($t = 0$s) to approximately $t = 10$s, IP_3 levels gradually increase after each glutamate release because of PLCβ activity (c.f. *orange* decreasing exponentials in Figure IV.9B); IP-5P activity parallels this increase (*blue* curve in Figure IV.9D) but the creation of IP_3 by PLCβ outweighs its degradation by IP-5P. At the same time, cytosolic IP_3 binds to IP_3 receptors on the ER membrane, gradually increasing the probability of opening (*green* curve in Figure IV.9C) and leading to increased Ca^{2+} release in the cytoplasm. In turn, this increased Ca^{2+} activates PLCδ and further increases IP_3 production (*brown* curve in Figure IV.9A). When the stimulation frequency is sub-threshold (under f_i^*), IP_3 productions by PLCβ and PLCδ equilibrate with IP_3 degradation by IP-5P (IP3-3K only get activated with high Ca^{2+} levels); when the stimulation frequency is supra-threshold however (as is depicted in Figure IV.9), IP_3 eventually reaches a value for which the Ca^{2+} concentration in the cytoplasm triggers CICR as is clearly visible by the strong increase in opening probability of IP_3R channels around $t = 12$s. During the Ca^{2+} surge, high values of Ca^{2+} eventually inactivate IP_3R channels (*red* curve in Figure IV.9C), ending the Ca^{2+} rise (which gets reintegrated into the ER by SERCA pumps), and activating IP_3-3K which contributes to the IP_3 degradation, preventing its accumulation in the cytoplasm. As Ca^{2+} gets reintegrated into the ER, PLCδ activity goes back to resting state levels (*brown* curve at $t = 14$s in Figure IV.9B), allowing IP_3 concentration to decrease (*dark red* trace in Figure IV.8D). If the stimulation is still on, IP_3 again gets gradually increased by PLCβ activity and the whole process

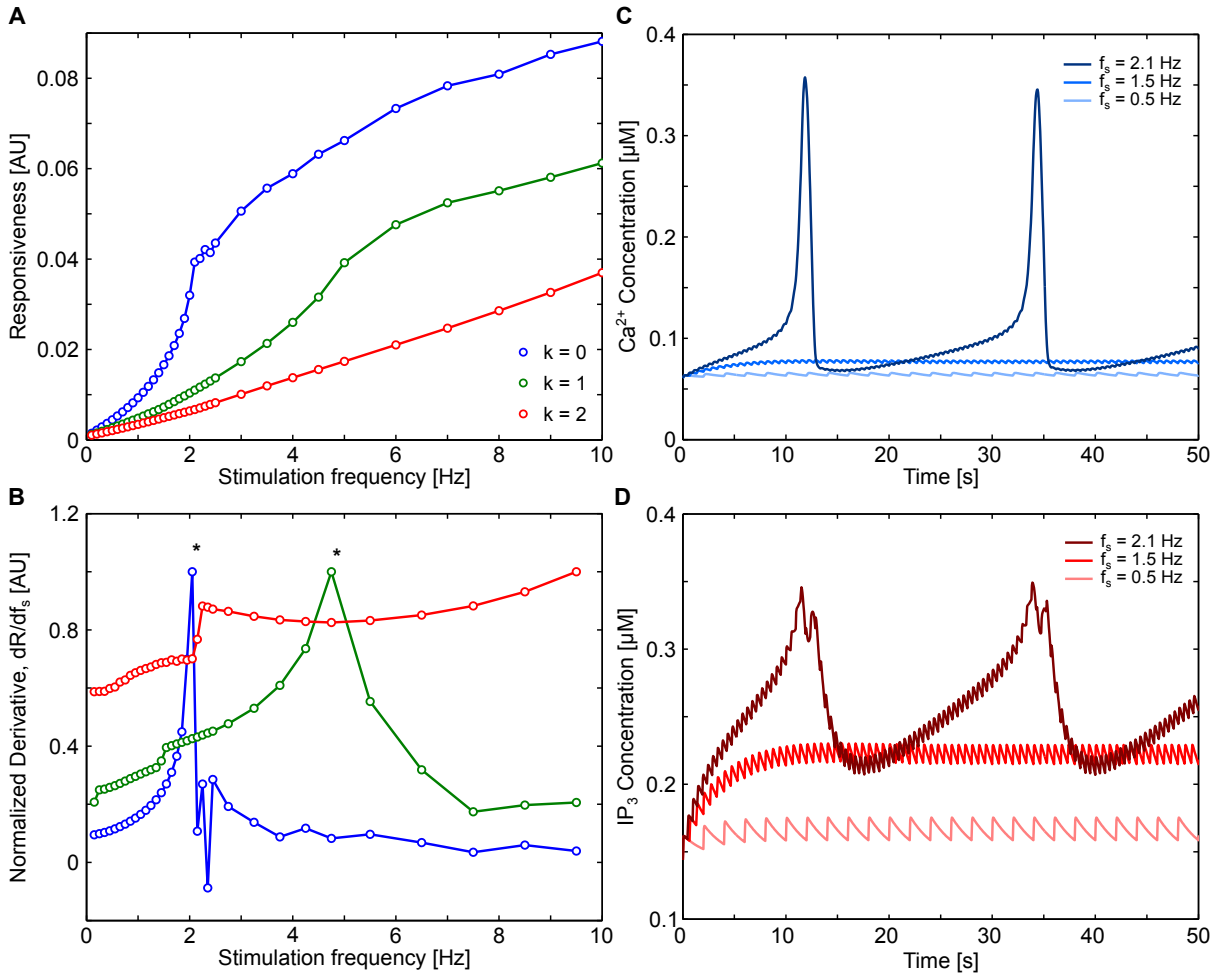

Figure IV.8: Degree-dependent onset and supra-linear IP_3 dynamics. **A**, Single-cell astrocyte responsiveness as a function of stimulation frequency and for different coupling degrees (i.e. number of unstimulated astrocytes to which the stimulated one is coupled). **B**, Normalized derivatives ($(dR/dfs)/\max(dR/dfs)$) of the curves in A; peak values are denoted by stars. Isolated astrocytes ($k = 0$, *blue* line) display a fast increase in responsiveness just before 2 Hz while astrocytes which are linked to one astrocyte ($k = 1$, *green* line) have a much later onset, around 5 Hz. For $k = 2$, *red* line the onset frequency is above 10 Hz. **C**, Ca^{2+} and **D**, IP_3 traces of isolated astrocytes in response to different stimulation frequencies. Above 2 Hz, as shown on A and B, astrocytes start responding with Ca^{2+} oscillations. Below 2 Hz, IP_3 and Ca^{2+} levels reach a frequency-dependent steady-state; when these steady-state concentrations are high enough to trigger CICR (i.e. for high enough stimulation frequency), astrocytes respond with large Ca^{2+} oscillations.

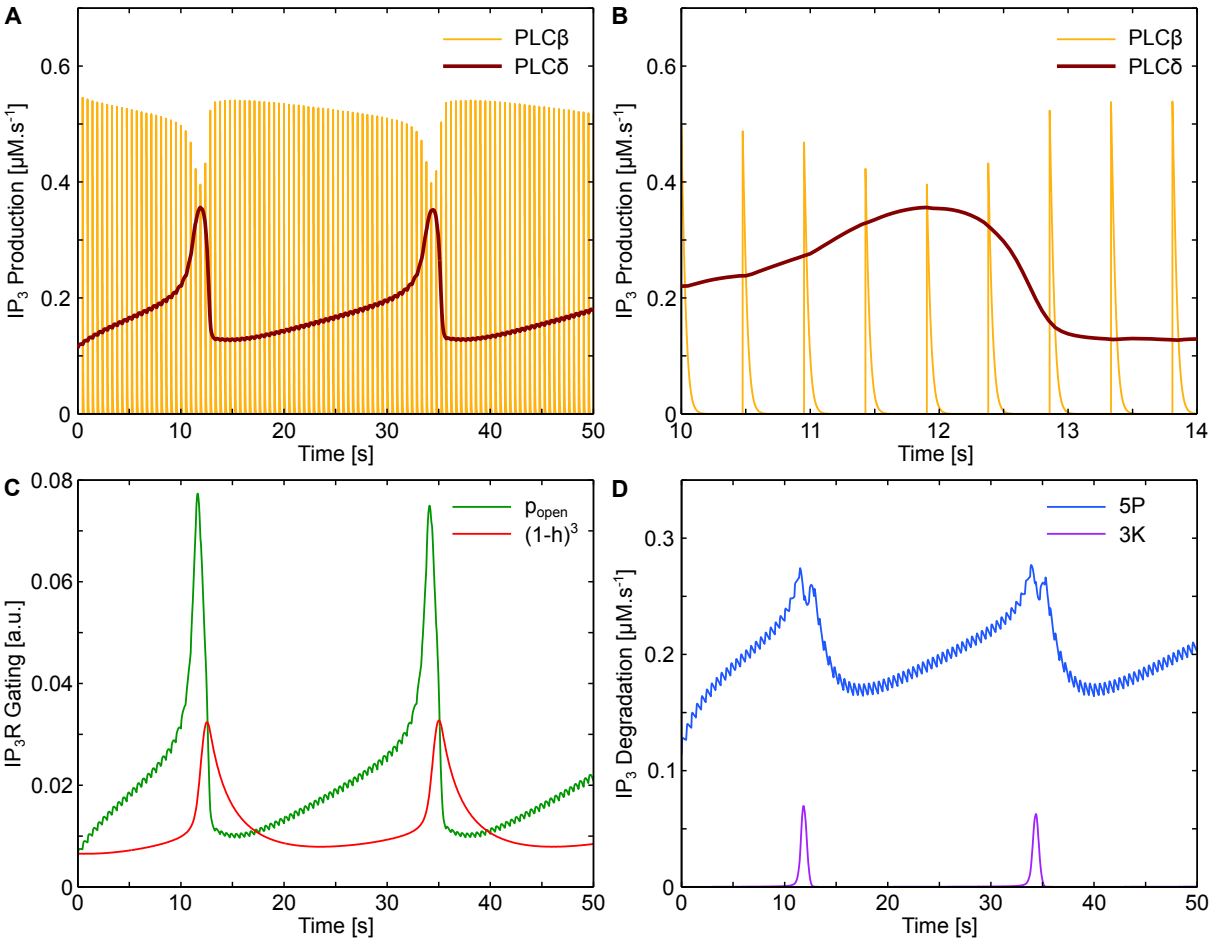

Figure IV.9: Detailed astrocytic response to a 2.1 Hz neuronal stimulation. The spiking behavior displayed by isolated astrocytes for stimulation frequency above 2 Hz can be understood by examining the dynamics of the underlying signaling pathway. *A*, Above 2 Hz, the IP_3 produced by $PLC\beta$ (in *orange*) leads to small opening of IP_3 R channels, increasing the Ca^{2+} concentration in the cytosol. This increased Ca^{2+} level activates $PLC\delta$ IP_3 production (in *brown*). **B**, Detailed view of $PLC\beta$ and $PLC\delta$ IP_3 production during a Ca^{2+} rise. **C**, This positive feedback loop triggers the CICR by increasing the opening probability of IP_3 R channels (in *green*). Further increases in Ca^{2+} inactivates IP_3 R channels (in *red*) thus ending the Ca^{2+} rise as it gets reintegrated into the ER. **D**, During this process, IP_3 is degraded by Ca^{2+}-dependent IP_3-3K enzymes during the Ca^{2+} rise (in *purple*), and by Ca^{2+}-independent IP-5P enzymes (in *blue*).

that we just described takes place again. Interestingly, the time between two Ca^{2+} rises is determined, in this context, by the IP_3 production rate which is directly linked to the glutamate concentration in the extracellular space and thus to the stimulation frequency f.

IV.3.4 Astrocyte oscillation frequencies are GJC-dependent

In the experiments, we observed variability in both oscillation frequencies $\Omega_i(f)$ and onset frequencies f_i^*. Specifically, we found that astrocytic responses could be classified in two main classes according to their oscillatory behavior: type I responses corresponded to astrocytes that were oscillating at frequencies around 0.1Hz and their oscillation frequency did not increase when the stimulation frequency increased (Figure IV.5A); type II responses displayed an increase in their oscillation frequencies from 0.1Hz to 0.2Hz when the stimulation frequency increased (Figure IV.5B). Additionally, astrocytes also displayed inter-experiments and inter-cell variability of onset frequencies f_i^* (see Ca^{2+} traces in Figure IV.3A for example). From the Ca^{2+} traces in Figure IV.7A, we could already see that some astrocytes (like the top two ones) oscillate faster than others (like the last two). To check whether we obtained similar results in all the simulations, we applied the wavelet analysis to each one of the simulated astrocytes. Figure IV.10A displays the wavelet-computed spectrogram of a simulated astrocyte displaying type I response (compare this figure with Figure IV.5A): its response starts at 0.1Hz and stays there when the stimulation frequency increases. Other astrocytes, like the one displayed in Figure IV.10B, seem closer to type II responses (compare the figure with Figure IV.5B): they start responding earlier (i.e. to lower stimulation frequencies) than type I astrocytes with low frequency oscillations (around 0.1Hz) and then increase their oscillation frequency up to 0.2Hz when the stimulation frequency increases. To quantify the repartition of simulated astrocytes in these two experimentally observed classes, we computed the distribution of maximal oscillating frequencies Ω_i^{max}. In the experiments, this distribution was bimodal (Figure IV.5C) with a large peak centered on 0.1 and a smaller one centered around 0.2Hz. In the simulations, the bimodality was not as clear: while the large peak close to 0.1Hz was still there, higher oscillation frequencies were not smoothly distributed on one peak. One could even argue that three peaks are actually formed (around 0.1, 0.15, and 0.2Hz). To get a clearer view, we plotted in Figure IV.10D the distributions of astrocyte frequencies $\Omega_i(f)$ (for all stimulation frequencies); each column represents an astrocyte and the normalized density of the distribution of its oscillating frequencies is color-coded according to the adjacent colorbar. The astrocytes have been sorted by their mean oscillating frequency $\langle\Omega_i\rangle$. We can thus compare this figure with its counterpart built from experimental data (Figure IV.5D): in both experiments and model, most of the astrocytes oscillate mainly at around 0.1Hz (left part of the plots) and some small part of them oscillate at frequencies around 0.2Hz. In between these two extremes (that would correspond respectively to type I and type II astrocytic responses), modeled astrocytes display marginally more variety with roughly one fourth of the astrocytes that cannot fall in either classes. Despite these small differences, the model qualitatively matches the experimental observations even though the different responses types have not been taken into account during parameter calibration. Interestingly, as in the experiments, there are very few astrocytes which display two marked peaks in their distribution of oscillating frequencies, indicating that astrocytes do not switch between type I and type II responses in the course of a simulation.

In the model, these differences in oscillating frequencies are strongly correlated with the

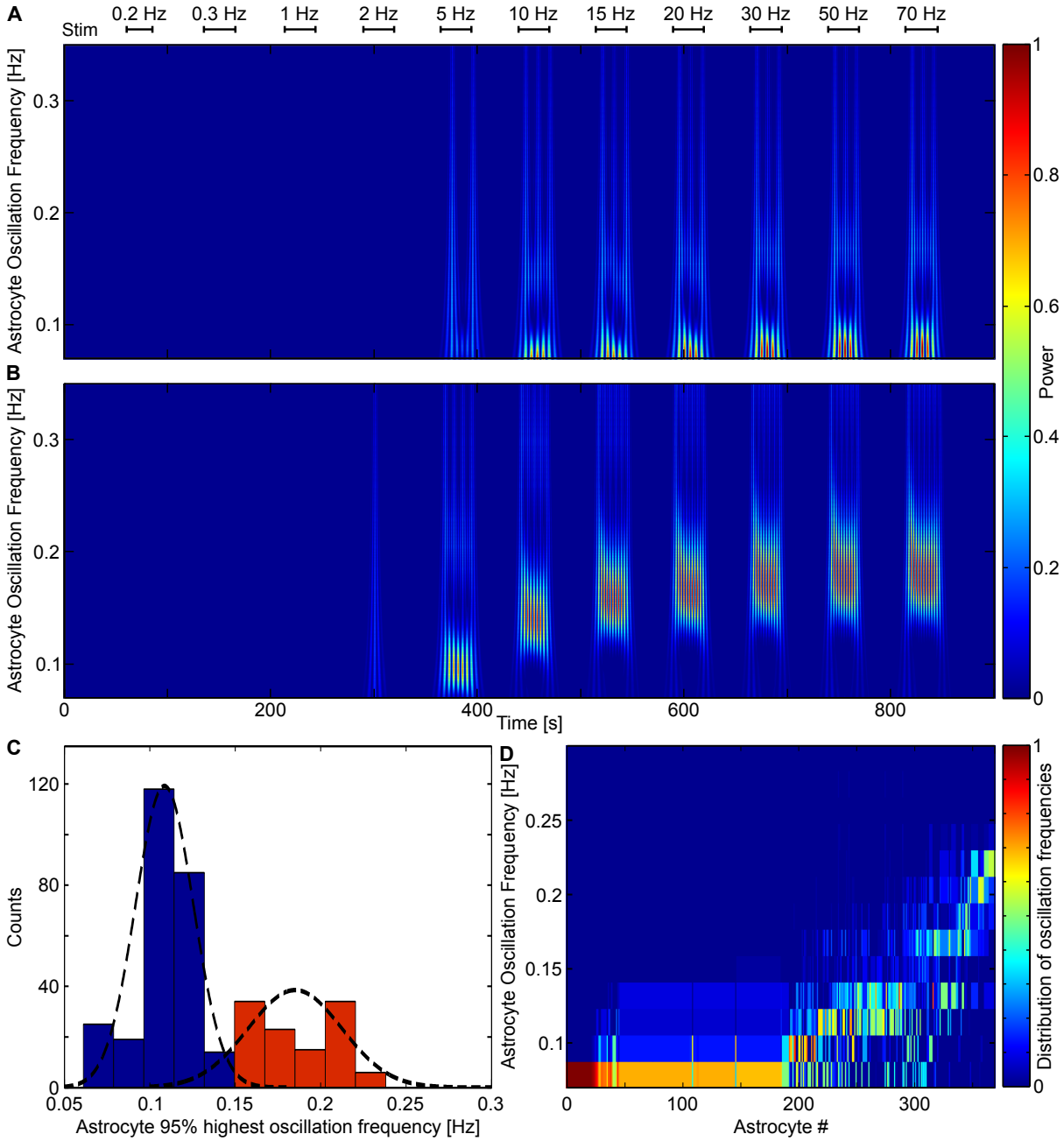

Figure IV.10: Spectral analysis of model astrocytic $[\mathrm{Ca}^{2+}]_i$ oscillations by wavelet analysis. **A**, Time-frequency analysis of a representative astrocyte showing typical low frequency oscillation (Type I response). **B**, Time-frequency analysis of a representative astrocyte showing typical high increasing frequency oscillation (Type II response). **C**, Histogram of the maximal oscillation of astrocytic populations. Typical patterns are colored and fitted by a Gaussian distribution (Type I responses in *blue*, and Type II responses in *red*, total $n = 373$ cells). **D**, the distribution of astrocyte oscillation frequencies. Each column corresponds to one astrocyte and contains its oscillation spectrum (binned at 0.02 Hz). Astrocytes are ranked according to their mean oscillating frequency; most oscillate at low frequencies but around one third (right part of the panel) respond to stimulations with frequencies as high as 0.2 Hz, thus matching the experiments (cf. Figure IV.5D).

number of unstimulated neighbors that an astrocyte has. Figure IV.11A shows the oscillation frequency for astrocytes across all simulations as a function of stimulation frequency and grouped by their number of unstimulated neighbors. Isolated astrocytes ($k = 0$, *dark blue* curve) have the highest oscillation frequency for all stimulation frequencies. They respond to low stimulation frequencies $f = 2$Hz (first data point on the left) by 0.1Hz oscillations; when the stimulation frequency increases, their oscillation frequency increases as well and plateaus around 0.2Hz, just like the type II responses in the experiments. When astrocytes are instead linked to several unstimulated neighbors ($k = 4$, *red* curve), they only respond to high stimulation frequencies with nearly constant oscillating frequencies ≈ 0.1Hz, similarly to type I responses in the experiments. In contrast with the simulations, we did not observe the small increase in oscillation frequency of type I responses in the experimental data. As this increase was relatively low, experimental noise might have prevented us to observe this slight increase. Between these two extremes, astrocytes that are linked with one unstimulated neighbor (*light blue* curve) display an intermediate behavior between type I and type II astrocytes as their oscillating frequencies increase when f increases but do not get higher than 0.15Hz. This figure clearly shows that, in the model, the determining factor for obtaining a type I or a type II response from an astrocyte is actually its number of unstimulated neighbors. As mentioned earlier, increasing the stimulation frequency f leads to higher IP_3 production and thus to higher oscillating frequencies; when a stimulated astrocyte i is coupled to unstimulated ones, the IP_3 created in i by PLCβ gets diffused to its neighbors whose IP_3 levels are low. These neighbors act as IP_3 sinks and effectively lower the average amount of IP_3 in the stimulated astrocyte, lowering its oscillation frequency. In our simulations, we used constant GJC strength F between all connected astrocytes, the different maximal oscillation frequencies thus tend to take discrete values: 0.2Hz for isolated astrocytes, 0.15Hz for astrocytes that are connected to only one unstimulated neighbors and ≈ 0.1Hz for all other cases ($k > 1$, *green*, *orange*, and *red* curves). This helps understand the distribution of maximal oscillation frequencies displayed in Figure IV.10C which seemingly displays 3 distinct peaks centered on these values. In experiments however, GJC-induced permeability between astrocytes might display high variability (Bukauskas et al., 2000; Roux et al., 2011) and there would thus be a continuum of cases between completely isolated astrocytes (which would correspond to the 0.2Hz peak in Figure IV.5C) and strongly GJC-coupled astrocytes (which would correspond to the 0.1Hz peak). Both of the peaks can be understood from the model as discrete cases in the following way: the 0.2Hz peak could be constituted by completely isolated astrocytes which are known to be quite frequent in neuron-astrocyte cocultures (Rouach et al. (2000) report 21% of disconnected astrocytes); and the 0.1Hz peak could be constituted by astrocytes that are GJC coupled to the equivalent of more than $k = 2$ unstimulated neighbors in Figure IV.11A. Above this coupling strength, the oscillating frequency of astrocytes stays constant with increases in coupling to unstimulated neighbors until the ocillations stop because of too important IP_3 losses. In this framework, unresponding astrocytes in the experiments (c.f. *blue* cells in Figure IV.2A) could either be unresponding because they do not enwrap stimulated synapses or because they are strongly coupled (in simulations, astrocytes with $k > 4$ did not display oscillations in response to stimulation). This conclusion sheds a new light on the mean degree ($\langle k \rangle \approx 2$) of our reconstructed astrocytes networks which is small compared to *in situ* reported values ($\langle k \rangle \approx 11$ in Xu et al. (2010)): it could very well be

that all astrocytes that were GJC coupled to a high number of neighbors could not be activated by neuronal stimulation, leading to their categorization as *unclassified cells*.

IV.3.5 Onset and oscillation frequency are negatively correlated

The onset frequency f_i^* of astrocytes, that is an estimation of the minimum stimulation frequency needed to elicit a response (computed as described in Section IV.1.1), was also heterogeneous in model simulations. We can see from Figure IV.11A that the stimulation frequency at which astrocytes start to respond is dependent on their number of unstimulated neighbors, isolated astrocytes start responding at around $f = 2$Hz (leftmost point of the *dark blue* curve) while astrocytes connected to one unstimulated astrocyte do not respond before $f = 5$Hz. It thus seemed that the number of unstimulated neighbors of an astrocyte controls both its oscillating frequency and its onset frequency in the model. Onset frequency and oscillation frequency should thus be negatively correlated: the sooner an astrocyte responds, the higher its oscillating frequency will be. To test this hypothesis, we looked at the mean oscillating frequency $\langle \Omega_i(f) \rangle$ of astrocytes stimulated with $f = 10$Hz (we chose 10Hz to be higher than most onset frequencies but low enough to minimize inter-cell variability in astrocyte responsiveness that increased with f, see Figure IV.4C). Figure IV.11A displays the relationship between onset frequency f_i^* and oscillation frequency $\langle \Omega_i(10) \rangle$ for all astrocytes (*grey* circles) responding to a $f = 10$Hz stimulation in the simulations; as expected, onset frequency and oscillation frequency were strongly negatively correlated (Spearman's $\rho = -0.8$ with a very low p-value $p = 5.1 \times 10^{-28}$). On Figure IV.11C, we tested this hypothesis in the same conditions on the experimental data and also found a strongly significant negative correlation (Spearman's $\rho = -0.6$ with $p = 2.4 \times 10^{-5}$). Of course the exact shape of the relationship differs between the model and the experiments: while the onset frequencies range between 4 and 8Hz in the model, they are much more spread out in the experiments (between 1 and 14Hz). Since we could not estimate the number of unstimulated neighbors of a given astrocyte in the experiments, testing this relationship constituted an indirect way to look for potential GJC effects on both onset frequency and oscillating frequency.

IV.3.6 Theoretical insights on the influence of GJC coupling and biophysical parameters

This section focuses on more theoretical aspects, the biologically inclined reader might want to skip directly to the conclusions, on page 130.

To investigate which model parameters were involved in the relationship between stimulation frequency, extracellular glutamate, and intracellular IP_3, we computed theoretical estimates of astrocyte response to stimulation. We consider, as represented in Figure IV.12A, an astrocyte which is continuously stimulated at frequency f and has already reached equilibrium; that is, during the time $\Delta t = 1/f$ between two synaptic releases,

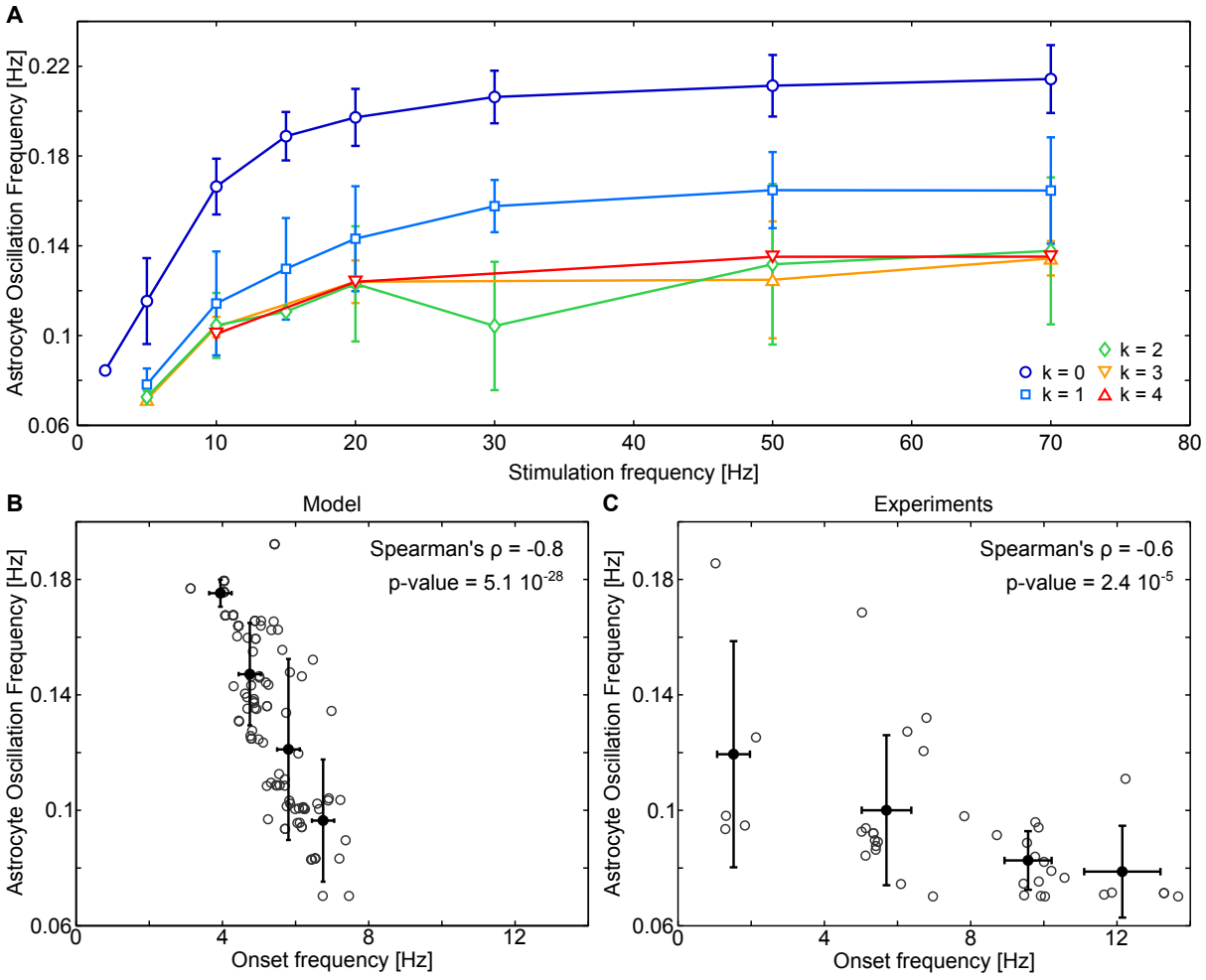

Figure IV.11: Astrocyte oscillation frequencies and relation to onset frequency. **A**, Increasing the stimulation frequency increases the astrocyte oscillation frequencies. Whatever the coupling degree k, the oscillation frequency reaches a plateau for high stimulation frequencies. The height of this plateau however strongly depends on the astrocyte degree. Isolated astrocytes oscillate much faster than connected ones. Errorbars denote standard deviation ($n = 130$ astrocytes). **B**, In the model, astrocytes that display high frequency oscillations also respond earlier (for smaller onset frequencies) than slowly oscillating astrocytes. The analysis was restricted to stimulated astrocytes ($n = 130$). **C**, The same effect is visible in experimental data; while the range of onset frequencies wider, the negative correlation between oscillation frequency and onset frequency is very significant. The analysis was restricted to strongly stimulated astrocytes which responded to at least one stimulation in less than 1.5 s ($n = 40$). For A and B, *grey* circles denote single-cell astrocyte responses from all simulations or cultures, while *black* dots denote averages of the data after splitting in 4 classes. Error bars show corresponding standard deviation. Astrocytes were submitted to 10 Hz stimulations and onset values were computed as explained in the methods section.

its concentration of extracellular glutamate and of intracellular IP_3 gets exactly to equilibrium values G^* (*red* lines) and I^* respectively: in Δt seconds, the diffusion in the extracellular space (exponential decreases of *blue* curves) counteracts exactly the quantity of glutamate released by the synapse and IP-5P degrades the quantity of IP_3 generated by PLCβ. To estimate the concentration of glutamate in the extracellular space, we first use an approximation of the steady-state response of the dynamical synapse (see Section II.1.2.1) given by:

$$\langle RR_f \rangle = \rho_C G_T \frac{U_0 \Omega_d (\Omega_f + f)}{\Omega_d \Omega_f + U_0(\Omega_d + \Omega_f) f + U_0 f^2} \tag{IV.6}$$

with $\langle RR_f \rangle$ the average quantity of glutamate released by a presynaptic spike when the stimulation frequency is f. Figure IV.12B shows normalized values of $\langle RR_f \rangle$ (*purple* curve) and $f \times \langle RR_f \rangle$ (*orange* curve). As expected, $\langle RR_f \rangle$ decreases as the stimulation frequency f increases because of presynaptic glutamate depletion (we used a depressing synapse); the average quantity of glutamate released per second $f \times \langle RR_f \rangle$ increases with stimulation frequency but is bounded because its reintegration in the presynaptic terminal is the limiting step. This can be derived from equation (IV.6) as $\lim_{f \to \infty} f \times \langle RR_f \rangle = \Omega_d \rho_C G_T$. Since, between two spikes, the only term in the equation governing glutamate concentration is a constant negative rate $-\Omega_G$ (representing diffusion away from the extracellular space and glutamate take-up by astrocytic glutamate transporters), we can compute the concentration of glutamate t seconds after a spike that occurred at $t = 0$s with $G(t) = G(0)e^{-\Omega_G t}$. We can see from Figure IV.12A that the equilibrium glutamate concentration G^* must thus be a solution to:

$$G^* = (G^* + \langle RR_f \rangle) e^{-\Omega_G / f} \tag{IV.7}$$

From which we can obtain G^*:

$$G^* = \langle RR_f \rangle \frac{e^{-\Omega_G / f}}{1 - e^{-\Omega_G / f}} \tag{IV.8}$$

We can thus estimate the quantity of IP_3 created by PLCβ by considering its activity J_β (defined in equation (II.20)) when Ca^{2+} concentrations are low:

$$J_\beta \approx O_\beta \mathcal{H}\left((\rho_{so} G)^{0.7}, K_G\right) \tag{IV.9}$$

By integrating J_β between 0 (time of presynaptic release) and $\Delta t = 1/f$ (time of the next presynaptic release), we get the quantity of IP_3 generated by one presynaptic glutamate release Q_β:

$$Q_\beta = O_\beta \int_0^{1/f} \mathcal{H}\left((\rho_{so}(G^* + \langle RR_f \rangle) e^{-\Omega_G t})^{0.7}, K_G\right) dt \tag{IV.10}$$

$$= \frac{O_\beta}{0.7 \Omega_G} \log\left(\frac{(\rho_{so}(G^* + \langle RR_f \rangle))^{0.7} + K_G^{0.7}}{(\rho_{so}(G^* + \langle RR_f \rangle) e^{-\Omega_G / f})^{0.7} + K_G^{0.7}} \right) \tag{IV.11}$$

When the stimulation frequency is low enough so that most of the IP_3 production by PLCβ is done during a short time compared to the time Δt between two spikes (Figure IV.9B shows that the time needed for the IP_3 production rate (*orange* curve) to get

back to values close to 0 is small compared to the time between two presynaptic releases), we can estimate the PLCβ equilibrium IP_3 concentration I^*_β, that verifies:

$$I^*_\beta = (I^*_1 + Q_\beta)e^{-\Omega_{5P}/f} \tag{IV.12}$$

The actual equilibrium IP_3 concentration must however take into account both equilibrium IP_3 concentration I^*_β that results from IP_3 synthesis from PLCβ, and resting-state IP_3 concentration I^*_δ that results from basal activation of PLCδ. We thus computed the total equilibrium IP_3 concentration I^* with:

$$I^* = Q_\beta \frac{e^{-\Omega_{5P}/f}}{1 - e^{-\Omega_{5P}/f}} + I^*_\delta \tag{IV.13}$$

with $I^*_\delta = 0.14\mu$M, the resting-state IP_3 concentration in astrocytes with parameters from Table IV.1. Since estimating the calcium response to increases in IP_3 concentrations would be too complicated, we only looked at how the opening probability of Ca^{2+} channels on the ER increased with IP_3 concentration. We can see from equation (II.7) and equation (II.8) that, for constant and low Ca^{2+}, the opening probability is proportional to an IP_3-dependent value $p1$ with:

$$p_1 = \left(\frac{I^*}{I^* + d_1}\right)^3 \tag{IV.14}$$

While I^* is already nonlinearly depending on the stimulation frequency f, the Ca^{2+} response of the astrocyte (here proxied by the opening probability p_1) is itself a nonlinear function of I^*. equation (IV.14) thus constitutes an additional layer of nonlinearity, contributing to the nonlinearity in the frequency response curve (Figure IV.8A).

Using these estimations, we can investigate the role of coupling degree. Since unstimulated neighbors provide a way to degrade IP_3, we assumed that an increase in coupling degree was comparable to an increase in degradation rate Ω_{5P}. We thus used $\Omega_{5P} = (k+1)\Omega^{default}_{5P}$ for computing p_1 values for different coupling degrees k. Figure IV.12C shows values of p_1 as a function of the stimulation frequency f and colored according to coupling degree k. For isolated astrocytes ($k = 0$, *blue* curve), the opening probability is a nonlinear function of stimulation frequency that reflects the behavior observed in population responsiveness. When increasing to $k = 1$ (*green* curve), the maximum p_1 values (for high f) are already much lower than those of isolated astrocytes. Interestingly, as in the full model, small increases in coupling degree (going from 0 to 1) strongly decreases astrocyte response (proxied here by open probability) while subsequent increases in coupling degree ($k \geq 2$, *red*, *orange*, *brown*, *black* curves) only marginally reduce astrocyte response. Additionally, the specific stimulation frequency f_θ at which p_1 reaches an arbitrary threshold p_θ (which would be the equivalent of the onset frequency in the previous experiments) gets higher as k increases. This can be better visualized in Figure IV.12D in which a heat map displays p_1 (z-axis, color-coded according to the colorbar) as a function of both stimulation frequency f (x-axis) and coupling degree k (y-axis); *colored horizontal dashed* lines represent the lines along which the curves in Figure IV.12C have been computed and *thick black* lines are isolines taken at different p_θ values which help visualize how the 'onset frequency' f_θ relates to the coupling degree k. For small p_θ values (leftmost isolines) f_θ increases

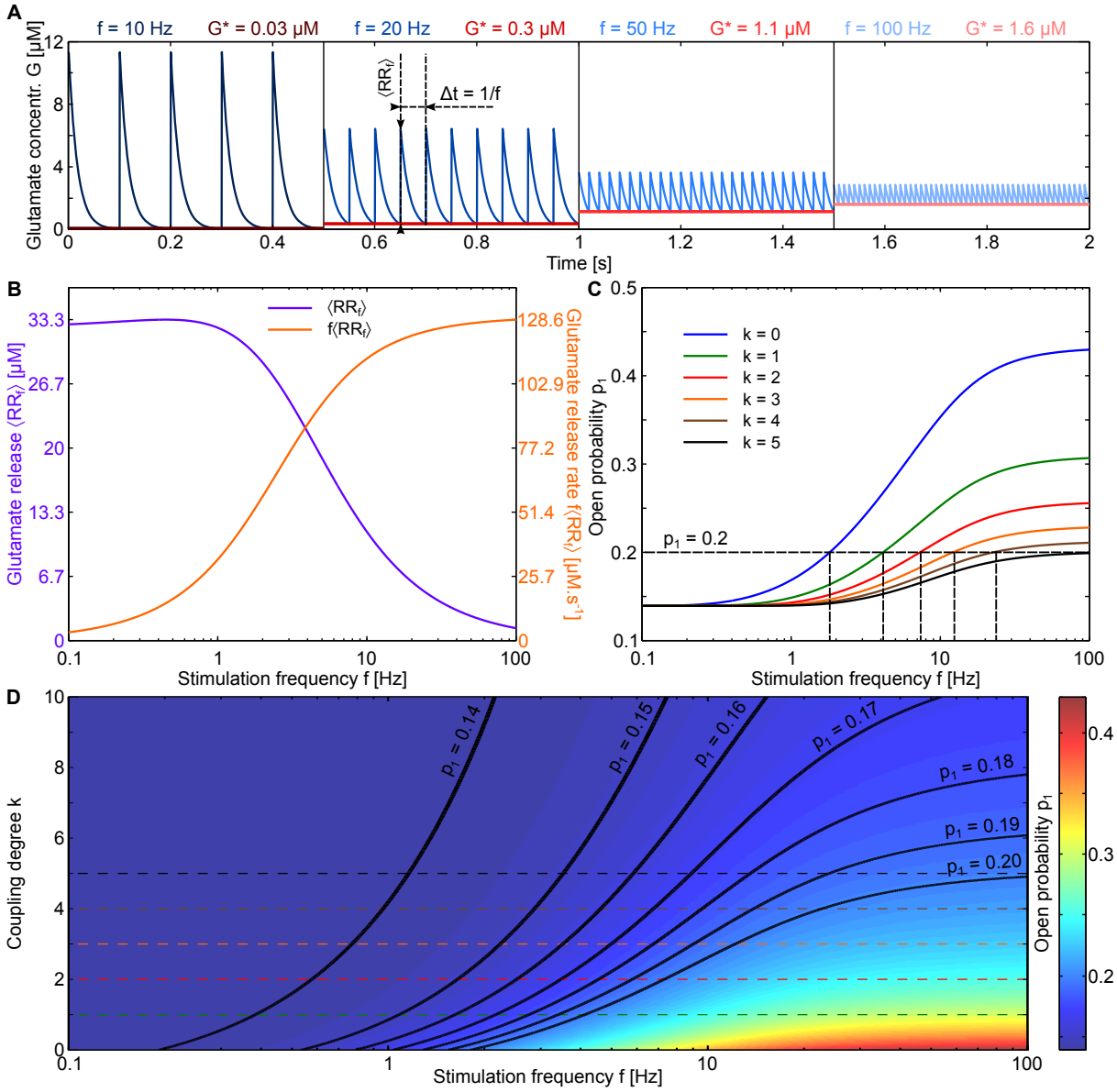

Figure IV.12: Estimations of Ca^{2+} channels opening probability. **A** Evolution of extracellular glutamate concentration G at equilibrium under different stimulation frequencies f (*blue* curves). As f increases, the equilibrium glutamate concentration G^* (*red* lines) goes up while the quantity of glutamate released by each spike $\langle RR_f \rangle$ diminishes. **B** While the average quantity of glutamate $\langle RR_f \rangle$ (*purple* curve) released by depressing Tsodyks-Markram synapses decreases when the stimulation frequency f increases, the average quantity of glutamate released per second $f\langle RR_f \rangle$ (*orange* curve) increases with f and reaches a plateau for high stimulation frequencies. Scales for the two curves are different and are color-coded. **C** We can estimate the opening probability of Ca^{2+} channels on the ER as a function of stimulation frequency f. This opening probability is proportional to p_1 (defined in equation (IV.14)) whose values are plotted for different cell degrees k according to the legend. Isolated astrocytes (*blue* curve) display early and strong response to stimulation while coupled astrocytes are less and less responsive as their coupling degree k increases. Coupling degree were emulated by using $\Omega_{5P} = (k+1)\Omega_{5P}^{default}$ as described in the text. The *black dashed* line corresponds to the continuous black line with $p_1 = 0.20$ on D. **D** Opening probability p_1 as a function coupling degree k and stimulation frequency f; p_1 values are color-coded according to the colormap. *Thick black* lines represent isolines along which $p_1 = p_\theta$ and help visualize the relationship between coupling degree and 'onset frequency' f_θ (see text). As in the full model, increasing the coupling degree increases the onset frequency and decreases the astrocyte response (characterized here by p_1). *colored dashed* lines represent the lines along which the curves from B were computed.

almost linearly with k (it appears exponential because of the logarithmic scale of the x-axis of Figure IV.12D), in contrast to the opening probability which quickly drops when k increases (see Figure IV.12C and D). For high p_θ values however (rightmost isolines), high coupling degree prevents astrocyte activation altogether as p_θ cannot be reached even for very high stimulation frequencies. In the full model simulations, astrocytes whose coupling degree was above 5 did not respond whatever the stimulation frequency, a situation that would correspond to the isoline $p_\theta = 0.19$: onset frequency varies from $f_\theta \approx 2$Hz to ≈ 20Hz for coupling degrees below 5 but the p_θ threshold cannot be reached for astrocytes with higher coupling degrees ($k > 5$) even for very high stimulation frequencies.

In this simple approximation, variability in onset frequency and oscillation frequency are indistinctively brought about by variability in coupling degree or by variability in the expression of IP-5P across astrocytes. Until now, we considered only variation in coupling degree and kept Ω_{5P} constant in the full simulations. An alternative hypothesis to explain the variability in onset frequency and oscillation frequency would thus be that variability in IP-5P quantity across astrocytes could be sufficient to account for the bimodality in oscillation frequency (c.f. Figure IV.5C and Figure IV.10C). We tested this hypothesis by comparing the distributions of estimated open probabilities p_1 for two populations of astrocytes simulated with equation (IV.14). The two populations only differed by their distributions of Ω_{5P} values: the first population had Ω_{5P} values drawn from a truncated normal distribution (to remove negative values) with mean μ_N and variance σ_N^2 chosen such that they match the mean and variance of the second population; the second population had Ω_{5P} values distributed according to the coupling degree distribution of the networks that we reconstructed previously (c.f. Figure IV.6A). The probability density function $f_{\Omega_{5P}}$ of the second population (corresponding to the random variable F) was computed according to:

$$f_{\Omega_{5P}}(x) = \sum_{k'=0}^{\infty} P(k = k') \times \frac{1}{\sigma\sqrt{2\pi}} \exp\left(-\frac{\left(x - (k'+1)\Omega_{5P}^{default}\right)^2}{2\sigma^2} \right) \tag{IV.15}$$

with $P(k = k')$ the probability that an astrocyte has degree k' in the reconstructed networks (c.f. Figure IV.6A) and $\sigma = 0.2\text{s}^{-1}$ the standard deviation of a normally distributed noise. We added a small normally distributed noise to take into account the fact that two astrocytes which are coupled to the same number of other astrocytes can be more or less coupled according to the strength of the GJC (i.e. the quantity of channel-forming Cx proteins). The probability density function $g_{\Omega_{5P}}$ of the first population (corresponding to the random variable G) was computed according to:

$$g_{\Omega_{5P}}(x) = \frac{\frac{1}{\sigma_N\sqrt{2\pi}} \exp\left(-\frac{(x-\mu_N)^2}{2\sigma_N^2} \right)}{A} \tag{IV.16}$$

for $x \geq 0$ and with $\mu_N = \mathbb{E}(F)$, $\sigma_N^2 = \text{Var}(F)$ and $A = 1 - \int_{-\infty}^{0} \frac{\exp\left(-\frac{(x'-\mu_N)^2}{2\sigma_N^2} \right)}{\sigma_N\sqrt{2\pi}} dx'$ the normalization factor. Distributions of Ω_{5P} values for both populations can be visualized in Figure IV.13 (*blue* histograms and densities, A for the first population and C for

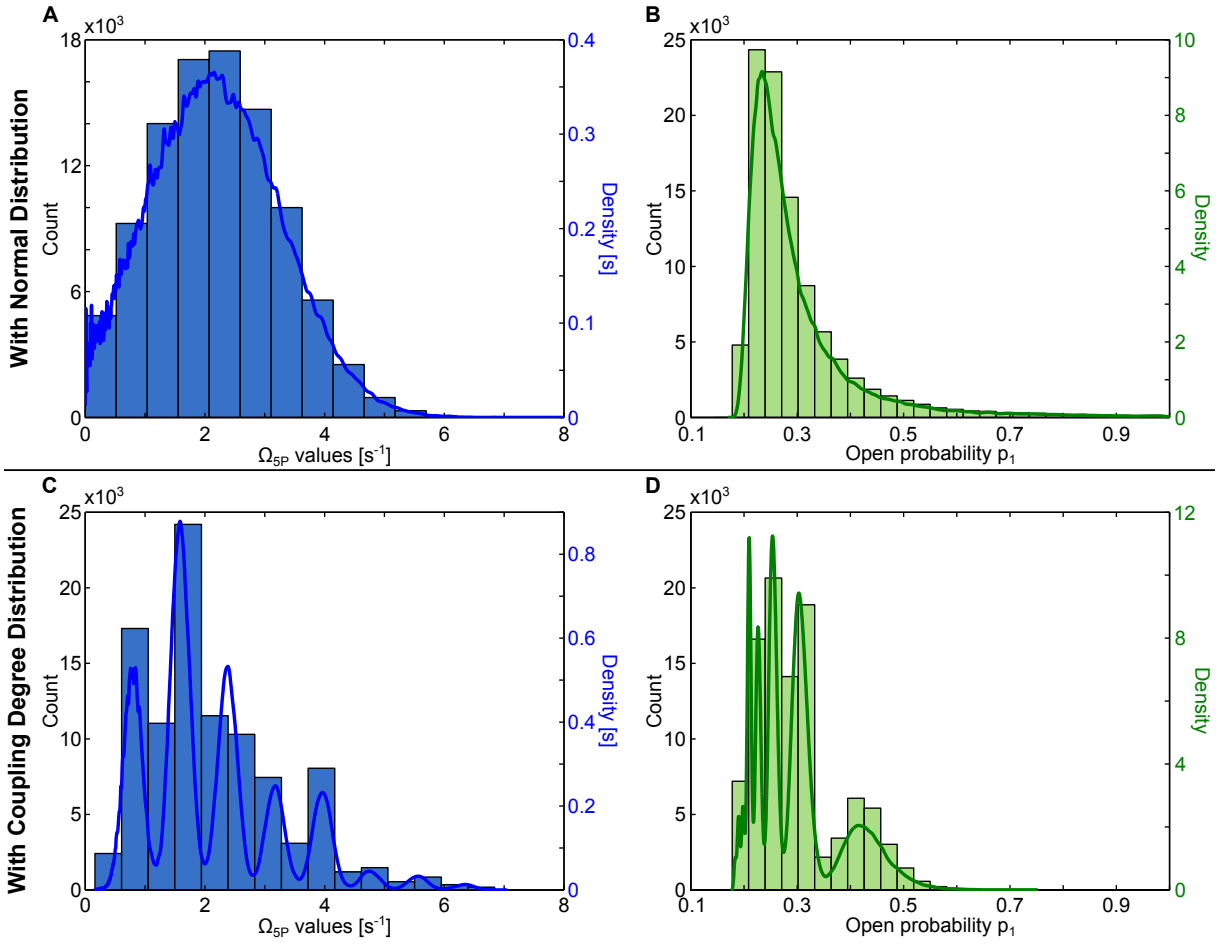

Figure IV.13: Normally distributed Ω_{5P} values cannot yield a bimodal p_1 distribution. We simulated, using equation (IV.14), two populations of 10^5 astrocytes whose values of Ω_{5P} were taken according to probability density functions $g_{\Omega_{5P}}$ and $f_{\Omega_{5P}}$. The first population, corresponding to the **top row** had Ω_{5P} values taken from a truncated normal distribution (with probability density function $g_{\Omega_{5P}}$ defined in equation (IV.16)); **A** displays an histogram of these values (left y-axis) alongside with an estimated density (*dark blue* line with right y-axis scale) and **B** displays the unimodal histogram and density (*green* line) of the resulting estimated open probabilities p_1. The second population, corresponding to the **bottom row** had Ω_{5P} values taken from a multimodal distribution constructed from the coupling degree distribution of reconstructed networks (see Figure IV.6A) whose probability density function $f_{\Omega_{5P}}$ was defined in equation (IV.15); **C** displays an histogram and the density (*dark blue* line) of these values, each mode corresponding to a specific coupling degree (the leftmost mode corresponds to $k = 0$, the next to $k = 1$, etc.), and **D** displays an histogram and the density (*green* line) of the resulting estimated open probabilities p_1 which is also bimodal with the rightmost mode, corresponding to high p_1 values being separated from the rest. With experimental noise, and as suggested by the histogram, this distribution can appear bimodal, as the ones in Figure IV.5C and Figure IV.10C. All p_1 values were computed with a stimulation frequency $f = 70$Hz (the maximum frequency used in the experiments) and other parameters were taken as in Table IV.1. The densities were estimated in MATLAB with the ksdensity function.

the second) alongside with their associated distribution of estimated open probability p_1 (*green* histograms and densities, B for the first population and D for the second).

When Ω_{5P} values are distributed normally, the open probability p_1 has a unimodal distribution (Figure IV.13B); the normal distribution is transformed into a distribution with a peak of 'low' p_1 values centered on 0.25 and a continuously decreasing tail of higher values. Schematically, the peak is due to the right part of the histogram in Figure IV.13A ($\Omega_{5P} \geq 1\text{s}^{-1}$) while the tail is due to the low Ω_{5P} values. In the second population however, when Ω_{5P} values are distributed according to the coupling degree distribution of reconstructed networks, the distribution of p_1 values is multimodal: for each peak in Figure IV.13C (corresponding to the different coupling degree as distributed in Figure IV.6A), there is a corresponding peak in Figure IV.13D. Because of experimental noise, the different peaks on the left will however not be distinguishable and, as shown by the histogram, the distribution will appear to be bimodal with most values in the left peak corresponding to low open probabilities and few high open probabilities in the right peak. These high open probabilities correspond to the isolated astrocytes (leftmost mode in Figure IV.13C) while the low open probabilities correspond to all the other modes ($\Omega_{5P} \geq 1\text{s}^{-1}$) which yield comparable open probabilities (as already seen in Figure IV.12C). The bimodality in astrocyte oscillation frequency (here proxied by estimated open probability p_1) can thus only be accounted for if the distribution of Ω_{5P} is multimodal (at least bimodal with a mode at low Ω_{5P} values). This is readily done when the astrocytes display different coupling degrees which seems to be a simple explanation for Ω_{5P} multimodality but we cannot rule out the possibility that, in uniformly coupled astrocytes networks (with the same coupling degree for all astrocytes), the quantity of IP-5P could be low in a minority of astrocytes and high enough to have $\Omega_{5P} \geq 1\text{s}^{-1}$ in others. This possibility even seems reasonable since astrocytes are known to display heterogeneous properties in other regards (like membrane potential (McKhann et al., 1997) or morphology (Verkhratsky and Butt, 2013)). Additionally, one could also obtain a bimodality in oscillation frequency distribution if the oscillation frequency saturates for high opening probability values, that is if all tail values of Figure IV.13B would lead to similar high oscillating frequencies. We will discuss this possibility in the next section.

Altogether, this estimation of Ca^{2+} channel opening probability indicates that the nonlinearity of the astrocyte response when the stimulation frequency increases is already present even when considering only glutamate and IP_3 dynamics. Of course, an additional layer of nonlinearity is due to the CICR mechanism that further increases Ca^{2+} channel opening probability when the Ca^{2+} concentration increases. The dependence of both onset-frequency and oscillation frequency to GJC coupling degree of astrocytes can be accounted for by the competition between IP_3 synthesis by PLCβ and IP_3 degradation by IP-5P (either directly in the astrocyte or in its GJC coupled neighbors) taken into account in the computation of the estimated steady-state IP_3 concentration I^* (equation (IV.13)). To account for the bimodality of astrocyte oscillation frequencies, the model would suggest that IP_3 degradation/loss (either by direct degradation by IP-5P or by diffusion to neighboring unstimulated astrocytes) in astrocytes should be multimodal with some astrocytes (those displaying the high frequency oscillations) having significantly lower degradation/loss than others; in contrast, normally distributed IP-5P degradation rates

cannot yield a bimodal oscillation frequency distribution unless some specific conditions are met.

IV.4 Discussion

The links between neuronal activity and astrocytic Ca^{2+} responses are numerous and well documented (Volterra and Meldolesi, 2005). As summarized in a recent review article (Rusakov et al., 2014), Ca^{2+} increases in astrocytic soma and processes can be attributed to a wide variety of recently established mechanisms. Examples include: the reversal of the Na^+/Ca^{2+} exchanger caused by glutamate uptake by astrocytes (Kirischuk et al., 2012; Reyes et al., 2012); activity-dependent changes in extracellular Ca^{2+} (Rusakov and Fine, 2003; Torres et al., 2012); Ca^{2+} entry through purinergic receptors P2X1/5 (Palygin et al., 2010); Ca^{2+} entry through AMPA receptors in Bergmann glia (Saab et al., 2012); and finally, Ca^{2+} entry through TRPA1 and TRPV4 channels (Shigetomi et al., 2012; Dunn et al., 2013). The most documented pathway allowing Ca^{2+} increases in astrocytes in response to neuronal activity however involves G protein-coupled receptor cascades, and specifically the creation of IP_3 resulting from the activation of group I metabotropic glutamate receptors (Porter and McCarthy, 1996; Pasti et al., 1997). Although this mGluR pathway was well documented, the exact mechanisms linking the dynamics of neurons to specific Ca^{2+} signals in astrocytes are still unknown. In particular, the properties that a neuronal stimulation must have in order to elicit Ca^{2+} responses in astrocytes are hitherto unresolved.

In this chapter, we investigated neuron to astrocyte communication using combined experimental and modeling approaches. We established in Section IV.2 that astrocytes respond in a nonlinear frequency-dependent manner to neuronal activity through activation of group I mGluRs. Along with inter-experimental variability, we evidenced a cell-to-cell variability in both astrocytic oscillation frequency and onset frequency. In particular, we proposed the existence of two typical types of responses to neuronal stimulation: type I responses showed late reaction (i.e. high onset frequency) together with low (0.1Hz) and constant oscillation frequency as stimulation frequency increased; type II responses instead displayed early activity (i.e. low onset frequency) at low oscillation frequencies but quickly increased to high oscillation frequencies (0.2 Hz) as stimulation frequency increased. We then turned to modeling, in Section IV.3, to investigate plausible mechanisms accounting for these effects and variabilities. We thus proposed that the observed variability in both oscillating frequency and onset frequency might be brought forth by heterogeneity in GJC coupling between astrocytes. We showed, in the simulations, that lowly coupled or isolated cells started responding at low frequency stimulations and displayed high frequency Ca^{2+} oscillations, compatible with the type II experimentally observed responses; highly coupled astrocytes instead displayed high onset frequencies and low oscillating frequencies, compatible with the type I experimentally observed responses.

Many of the works investigating astrocytic responses to neuronal activity actually investigate intensity-dependent responses (i.e. higher astrocytic responses when the cumulated neuronal activity increased). Several *in vivo* experiments report intensity-dependent responses:

– visualization of astrocytes in the visual cortex of ferrets together with image stimulations showed that astrocytic responses were stronger when local neuronal activity was

higher (Schummers et al., 2008);
- whisker stimulation was found to elicit astrocytic activity which was inhibited by mGluR blockers in the barrel cortex of adult mice (Wang et al., 2006);
- odor stimulation was reported to provoke mGluR5-dependent astrocytic activity in the olfactory glomeruli of mice (Petzold et al., 2008);
- motor behavior in mice was shown to elicit astrocytic responses in Bergmann glia that were dependent on glutamatergic transmission (Nimmerjahn et al., 2009);
- finally, sensory stimulations of rats were shown to elicit activity-dependent astrocytic responses in the somatosensory cortex (Ghosh et al., 2013).

Experiments on slices further demonstrated that low frequency neuronal activity (0.1-10 Hz) usually does not trigger astrocyte responses (Porter and McCarthy, 1996; Pasti et al., 1997) while high frequency stimulations (20-50 Hz) of neuronal afferents readily provoked astrocytic responses (Fellin et al., 2004; Perea and Araque, 2005a). These experiments however varied together the frequency of stimulation and the total number of stimulations and could not determine whether astrocytic response was frequency-dependent or just intensity-dependent. In this chapter, we showed, by using the same number of stimulations and changing only the stimulation frequency, that astrocyte responses are frequency-dependent and both onset frequency and oscillation frequency are cell-specific characteristics.

In the Section IV.3, we provided plausible explanations for this observed frequency-dependent response of astrocyte. Unfortunately, our experimental setup only allowed us investigate Ca^{2+} dynamics in the cell soma. We could not account for the full multiscale characteristics of Ca^{2+} signaling in astrocytes (c.f. Section I.2.2) since main and thiner processes were not visible through calcium imaging. These finer (at both temporal and spatial scales) dynamics can only be investigated by higher resolution techniques (Di-Castro et al., 2011; Panatier et al., 2011; Kanemaru et al., 2014) and even in these cases, simultaneous imaging of both soma and processes can be challenging because of the strong difference in fluorescence intensity (Di-Castro et al., 2011). Interestingly, recent investigations of Ca^{2+} dynamics in processes have revealed that low frequency stimulation elicit responses in astrocyte processes that usually do not propagate to the soma (Panatier et al., 2011; Di-Castro et al., 2011; Shigetomi et al., 2013). In physiological conditions, the frequency of local Ca^{2+} events in processes is thus much higher than the frequency of somatic events (Di-Castro et al., 2011; Kanemaru et al., 2014). While this difference in activity frequency between soma and processes could point towards separated activity of these two compartments, some Ca^{2+} events elicited in processes were shown to propagate to the soma (Volterra et al., 2014). A very recent *in vivo* study even showed that sensory stimulation elicited Ca^{2+} activity in the processes that then propagated to the cell soma in the somatosensory cortex of mice (Kanemaru et al., 2014). The detailed mechanisms allowing this activity integration in processes to the soma are however unknown (Volterra et al., 2014). Interestingly, the additional layer of complexity brought forth by the structure of processes might play a role in the frequency-dependent response of astrocytes that we observed. Larger processes could even themselves have frequency-dependent response to neuronal stimulations. Future experimental work on this subject will most likely shed light on how astrocytic integration of neuronal activity happens in details.

The main model prediction was that the variability in astrocytic oscillation frequency and onset frequency reflected heterogeneities in cell-to-cell GJC coupling. In simulations, highly coupled astrocytes displayed high onset frequency and low oscillation frequency while isolated astrocytes responded early with high frequency oscillations. The presence of GJC coupling in neuron-astrocyte cell cultures is a well established fact. Cx 30 and 43 which form the majority of GJC in astrocytes (Giaume et al., 1991; Rouach et al., 2002; Koulakoff et al., 2008) are expressed in astrocytes during both embryonic (Cina et al., 2007) and postnatal (Aberg et al., 1999; Koulakoff et al., 2008) cortical development. Their expression is even increased in mixed neuron-astrocyte cultures such as the ones we used (Koulakoff et al., 2008). We provided indirect evidence for this possible GJC influence in astrocytic responses by showing that, as in the model, oscillation frequency and onset frequency were negatively correlated in the experimental data. This negative correlation could however also stem from variability in cell-specific biophysical parameters. In particular, variability in IP-5P concentration among astrocytes would lead to similar effects: astrocytes with low IP-5P would display low onset frequency and high oscillation frequency because of the impaired IP_3 degradation and astrocytes with increased IP_3 degradation (higher IP-5P concentrations) would respond later with low frequency oscillations. We investigated this possibility and proposed that IP-5P concentrations would need to be multimodaly distributed among astrocytes in order to reproduce the bimodal distribution of oscillation frequency observed in the experiments. Additionally, variability in CICR parameters could also be involved in the observed response variability.

Whether GJC couplings or cell-specific biophysical parameters are at play have thus not been unequivocally asserted yet. Several lines of evidence in the literature however point towards a role of GJC couplings. First, the model predicts the presence of isolated astrocytes which respond to stimulation with high frequency oscillations. Such isolated astrocytes have been documented in the mouse barrel cortex (Houades et al., 2008), in the hippocampus and cerebral cortex of the developing mouse (Houades et al., 2006), among olfactory ensheating cells (non-myelinating glial cells that are comparable to astrocytes) (Rela et al., 2010), and in cell cultures at different levels depending on whether neurons were included in the culture (21% of isolated astrocytes when cocultured with neurons and 44% with astrocytes only) (Rouach et al., 2000). Whether these isolated astrocytes also display high frequency oscillations in response to neuronal activity is however unknown yet. Some papers showed that GJC reduction in astrocytes can lead to higher frequency oscillations: application of endothelin ET-1, a compound known to reduce GJC coupling (Blomstrand et al., 2004; Orellana et al., 2013), on mixed neuron-astrocyte cultures promoted Ca^{2+} oscillations (Blomstrand et al., 1999b); Niemann-Pick type C mice that exhibit reduced GJC coupling have been shown to display increased Ca^{2+} activity (Sáez et al., 2013). Although it is possible that these studies displayed increased Ca^{2+} oscillations through other pathways (ET-1 is known to directly elicit Ca^{2+} oscillations for example (Blomstrand et al., 1999b)), the GJC coupling hypothesis might be at play. A more convincing case is provided by Pasti et al. (1995, 1997); the authors show that nitric oxide gradually increases astrocyte oscillation frequency over periods ranging from 2 to 60 minutes while they specifically state that nitric oxide does not have direct oscillation-inducing effects on astrocytes. Interestingly, although they did not mention it in the articles, nitric oxide is known to reduce GJC coupling between astrocytes (Bolaños and

Medina, 1996; Ball et al., 2011). It could thus very well be that the increase in astrocyte oscillation frequency that they witness is directly linked to the reduction of GJC coupling induced by nitric oxide. Unfortunately, Pasti et al. did not test this hypothesis and future experiments will thus be needed to determine whether GJC could be responsible for the observed variability in astrocytic responses.

As pointed out in Section IV.3.1, our reconstructed astrocyte networks, having a mean degree of 1.63, are much less connected than actual networks *in situ* which display mean degrees around 11 (Xu et al., 2010). We quickly evoked in Section IV.3.1 that the 2D embedding imposed by the cell culture and the misclassification of silent astrocytes might have decreased the mean degree. First, the reduction of mean degree imposed by the 2D embedding can be approximated by computing the mean degree of a Voronoi diagram with a number of nodes comparable to our reconstructed networks ($\approx$ 70 astrocytes). Such a theoretical network displays a mean degree of only ≈ 5.3 neighbors per astrocyte; while this represents a strong decrease compared to 3D networks (a Voronoi diagram in 3D leads to a mean degree of ≈ 15), it is still much higher than our reconstructed networks. During the reconstruction process, the presence of neurons or unclassified cells prevents astrocytes from connecting with each other. This process can thus be approximated by randomly removing nodes from a given Voronoi diagram; this operation will gradually decrease the network mean degree until it eventually becomes disconnected. Overall, identified astrocytes constituted $\approx 24\%$ of all the cells, including the unclassified ones. We checked that a 2D Voronoi diagram in which 24% of the domains (randomly chose) are set to astrocytes has a mean degree of 1.42, in close agreement with the mean degree of our reconstructed networks. This indicates that astrocytes are approximately evenly positioned among other cells and the actual networks can be estimated by Voronoi diagrams with randomly positioned neurons and astrocytes. Since unclassified cells constituted $\approx 50\%$ of all the cells, we investigated whether silent astrocytes could be part of these cells. To this end, we estimated the astrocyte to neuron ratio from immunostaining pictures of our cultures and found it to be close to 1 (≈ 0.87). Among classified cells, we found the same astrocyte to neuron ratio (≈ 0.93), indicating that the identification from Ca^{2+} signals did not seem to be biased towards neurons or astrocytes. This also implies that approximately half of the unclassified cells were probably silent astrocytes (according to the Ca^{2+} traces) which, according to the model, could be either highly coupled to unstimulated neighbors, preventing them from activating, or could not enwrap synapses from active neurons. If all the cells were correctly identified and neurons prevented astrocyte connections (as we assumed for our reconstructed networks), we would expect an astrocytic network mean degree of ≈ 2.58; out reconstructed networks are thus slightly less connected than they should be because of the absence of silent astrocytes. Remarkably however, 20.91% of the astrocytes in our reconstructed networks were isolated, in very strong agreement with Rouach et al. (2000) who reported, using dye injections, 21% isolated astrocytes in neuron-astrocyte cocultures.

Regarding the size of astrocyte clusters, 35% of astrocytes in the reconstructed networks were part of a cluster of more than 10 astrocytes. In neuron-astrocytes coculture, patch clamp dye injections reported that 53% of the astrocytes were part of a cluster of more than 10 astrocytes (Rouach et al., 2000); this study however used a much higher astrocyte to

neuron ratio (≈ 1.9) than what we estimated in our cultures (≈ 0.32), possibly increasing the astrocyte-astrocyte contacts. Altogether, although some astrocytes are lacking, the statistics of our reconstructed networks do not seem aberrant in regard to previously published data that investigated actual astrocyte networks by dye injections.

Cell cultures are often criticized for being too remote from actual physiological processes and for displaying artifactual or pathological behaviors. Although we agree with these critiques, the MEA setup allowed us to precisely control neuronal stimulation frequency while simultaneously imaging the activity of a high number of neurons and astrocytes, which would have been much more difficult in more physiologically relevant preparations. Since this degree of control on neuronal activity was necessary to test the frequency-dependent responses of astrocytes, we saw MEA as a good trade-off between degree of control and biological relevance. A specific concern that can however be raised regarding cell cultures is the possibility that the physiological state of astrocytes in cell culture would be close to what happens in reactive astrogliosis, a graded process that occur in response to pathological states (see Section I.1.4). The effects of astrogliosis on astrocytes can range from small changes in gene expression to dramatic changes in cellular morphology and even to the formation of glial scars (Sofroniew, 2009; Verkhratsky and Butt, 2013). Astrocytic hypertrophy or increased expression of GFAP protein are classical signs of reactive astrogliosis (Zamanian et al., 2012; Verkhratsky and Butt, 2013; Pekny et al., 2014). After visual inspection of immunostaining pictures of our cultures (as displayed on Supplementary Figure B.1B), it did not seem that astrocytes displayed hypertrophy but we could not definitively rule out the possibility of mild reactive astrogliosis. Cultured astrocytes are notoriously different from adult astrocytes in vivo in both their morphology and their gene expression profiles. In particular, cultured neonatal astrocytes obtained with the McCarthy-DeVellis method (McCarthy and De Vellis, 1980) are known to display markers specific to reactive astrogliosis (Zamanian et al., 2012). It is however not clear whether this effect is also displayed when using different culture methods. McCarthy-DeVellis astrocytes are purified astrocyte-only cultures whereas our cultures include neurons (which are known to regulate gene expression in astrocytes (Koulakoff et al., 2008)) and other glial cells, possibly changing the way astrocytes react to cell culture. Altogether, since we could not conclusively assess whether astrocytes in our cultures were reactive or not, our results should be interpreted with care and might reflect unphysiological behavior. In particular, reactive astrocytes are known to display altered Ca^{2+} signaling during pathological states such as ischemia (Ding et al., 2009), Alzheimer's disease (Kuchibhotla et al., 2009) and brain trauma (Sieger et al., 2012). Of particular relevance to our study, reactive astrogliosis has also been shown to mediate both G-protein coupled receptor signaling and increases in Cx43 expression (De Bock et al., 2014).

Finally, and most importantly, we showed in this chapter that local topological characteristics, as the number of unstimulated neighbors, could affect the Ca^{2+} response of astrocytes, setting for example the onset frequency above which an astrocyte responds to neuronal activity and its oscillation frequency. Both characteristics can be expected to be of considerable importance in the way astrocytes interact with neurons. Highly coupled astrocyte subnetworks could serve as specific detectors of high neuronal activity while less coupled networks could be more sensitive to low frequency activity. Additionally, since

Ca^{2+} activity could be linked to gliotransmitter release from astrocyte (Navarrete et al., 2013), quickly oscillating astrocytes could interact with neurons with different properties than slowly oscillating ones. Since the degree of GJC coupling varies throughout the brain and the developmental stage (Aberg et al., 1999; Montoro and Yuste, 2004; Giaume, 2010) and GJC permeability and Cx expression can be regulated by various signals (Rouach et al., 2002; Orellana et al., 2013), GJC should be considered, not only for their capacity to increase diffusion across an astrocytic syncytium, but also for the way that they could alter Ca^{2+} signaling at the individual cell level. Since astrocytes also display prominent collective behavior during Ca^{2+} waves, we decided to investigate how topological characteristics could influence these behaviors in the next chapter.

Chapter V

Static topological influences

Intercellular calcium wave (ICW) propagation in actual astrocyte networks have been consistently observed across different preparation types. Since the first reports of evoked Ca^{2+} waves in cell cultures (Cornell-Bell et al., 1990; Blomstrand et al., 1999a; Scemes et al., 2000), concerns however grew regarding their physiological relevance. Subsequent investigations focused on slices, which conserved the morphological and architectural structure of brain tissue, showing both evoked (Sul et al., 2004) and spontaneous (Schipke et al., 2002; Weissman et al., 2004) Ca^{2+} waves. Even more recently, ICW were shown to occur spontaneously *in vivo* under physiological (Kurth-Nelson et al., 2009; Kuga et al., 2011) and pathological (Kuchibhotla et al., 2009) conditions. Across these different setups, the characteristics of ICWs however vary substantially; as an example, the wave extent can range from very restricted (less than 10 astrocytes) (Sul et al., 2004; Sasaki et al., 2011) to local propagation (around 30 astrocytes) (Tian et al., 2006) to even regenerative propagation (more than 100 astrocytes) (Kuga et al., 2011). In these experiments, the wave speed usually ranges from 10 to 20 $\mu m.s^{-1}$(Scemes and Giaume, 2006) with exceptionally high values going up to 60 $\mu m.s^{-1}$(Kuga et al., 2011). Several candidate differences between these experiments have been put forward to account for the different ICW characteristics they display: (1) the brain regions in which astrocytes were observed (Blomstrand et al., 1999a; Peters et al., 2005b); (2) the stimulation protocol (if any) used to trigger an ICW (Scemes and Giaume, 2006); and (3) the intracellular biophysical "parameters" of the astrocytes (one readout of which is the shape of individual calcium traces, c.f. Section I.2.2.2). Some authors however pointed out that the discrepancies of ICW extent could not be factored out by taking into account these differences (Scemes and Giaume, 2006). One thus needs to consider other potential sources of variability to account for these differences.

Until recently, astrocytes were thought of as cells that organize into an indistinctively coupled syncytium. This view was however challenged by several articles reporting regional organization in astrocytic GJC coupling (Houades et al., 2008; Roux et al., 2011) which would be more accurately described as networks (Giaume et al., 2010). While astrocytes have been suggested to form non-overlapping domains that 'tile' the brain

space (Bushong et al., 2002), their detailed spatial arrangement and coupling patterns *in vivo* remain largely unclear. Our understanding of these networks have however improved over the last few years. The expression of Cx30 and Cx43, the proteins responsible for the formation of GJC (Giaume et al., 1991; Rouach et al., 2002; Koulakoff et al., 2008), has been shown to change across brain regions (Blomstrand et al., 1999a) and through development (Aberg et al., 1999; Montoro and Yuste, 2004). Even inside a given brain region, such as the olfactory glomeruli (Roux et al., 2011) or the somatosensory cortex (Houades et al., 2008), specific structures display local increases in GJC couplings while neighboring astrocytes outside these structure are less coupled. More generally, dye-coupling experiments in astrocyte networks have shown that a significant number of astrocytes are not GJC coupled to any of their neighbors (Houades et al., 2006, 2008; Rela et al., 2010). The rules at play for deciding whether two astrocytes are GJC coupled are far from trivial and astrocytes have thus been proposed to form intricate networks defining precise anatomical and functional domains (Pannasch and Rouach, 2013). The variation of network properties across brain regions could thus be a candidate source of ICW extent variability.

The recognition of the complexity and variability of astrocyte networks is however recent, so that the effect of those networks on calcium signaling and ICW propagation have not, to our knowledge, been investigated. The first and most obvious reason for this lies in the experimental challenge that mapping a full astrocyte network represents (Giaume, 2010). Classical experimental tools such as dye-coupling or scrape loading experiments are not suited to such a task and electrical measurement of GJC conductance by patch-clamp experiments are far too impractical since a very high number of pairs of astrocytes should be tested. Computational tools, with mathematical modeling and simulations, thus appear more suited to investigate this question. The effects and behaviors seen in models can then be used to propose experimentally testable predictions and coherent explanations of apparently discordant data.

In Chapter IV, we validated our ChI model against experimental data, showing that it can quantitatively reproduce important features of astrocyte Ca^{2+} signaling under neuronal stimulation. Unfortunately, probably because our cultured networks seemed to often be disconnected, we did not witness propagating Ca^{2+} waves within our experimental setup. To investigate ICW propagation in astrocyte networks, we thus decided to use the same ChI model with simulated network topologies and chose to address this question by monitoring ICW propagation on different coupling organizations while keeping all intracellular parameters constant.

V.1 Investigating ICW propagation in model astrocyte networks

In this chapter, we will investigate how different topologies could influence ICW propagation in astrocyte networks. To do so, we will use our previously presented models of

astrocyte calcium dynamics with several types of network topology. Before presenting the simulations, we will describe, in this section the parameters, algorithms and procedures that we will use throughout this chapter.

V.1.1 Astrocyte model

Since we are only interested in the propagation of ICW, independently of the stimulation method, we chose to use the basic ChI model (and not the G-ChI model). Consequently, we did not simulate in this chapter any neuronal or synaptic activity and only triggered ICW with a simple stimulation protocol described below. Being interested in the way network topology affects ICW propagation, we kept intracellular parameters and stimulation protocol constant as in Table V.1 (unless specified otherwise) and changed only the network topology. These parameters allow the same FM encoding properties (i.e.'spike-like' activations of astrocytes, see Section II.1.1.2) as the parameters we used in the Chapter IV; the main difference is the maximum Ca^{2+} oscillation frequency: while, in the previous chapter, we were modeling fast Ca^{2+} oscillations in individual astrocytes without ICW propagation, we are here modeling astrocyte activations at a lower frequency, as experimentally observed in spontaneous or triggered Ca^{2+} waves among astrocytes (Scemes et al., 2000; Sasaki et al., 2011; Kuga et al., 2011) and in accordance with experimentally measured propagation speeds. The main difference thus consists in a scaling down of the time-dependent parameters. Since we did not experimentally observe ICW in the previous chapter, the threshold gradient for IP_3 diffusion I_θ was set to a low value as well as the regeneration of IP_3 by PLCδ; now that we want to model ICW propagation, we increase both (the reasons guiding these increases will be explained in Section V.3). The parameters whose value changed are reported in bold in Table V.1. As represented in Figure V.1A, we used different network topologies grouped in 5 classes that presented different properties. Since, with the ChI model, each astrocyte corresponds to 3 equations (equation (II.12), II.13, and II.14), each simulation of a given network consisted in the numerical integration from $t = 0$ to $t = T$, by a 4^{th} order Runge-Kutta scheme with time step $\delta t = 0.01$s, of a $3N$ dimensional ODE with N the number of astrocytes in the network. Once the ICW was initiated, we measured its extent N_{act} as the number of astrocytes that were activated at least once during the whole simulation. As represented in Figure V.1B, we considered an astrocyte as being activated whenever its Ca^{2+} concentration was over $C_\theta = 0.7\mu$M.

V.1.2 Network construction

Since, in actual astrocyte networks, spatial positioning of individual astrocytes and network topology seem to be strongly related (Bushong et al., 2002), we decided to spatially embed all our networks in a 3D space by using biologically realistic spatial distributions. With the notable exception of purely random networks (Erdős-Rényi networks, leftmost network in Figure V.1A) that were used as a control topology, all the network classes

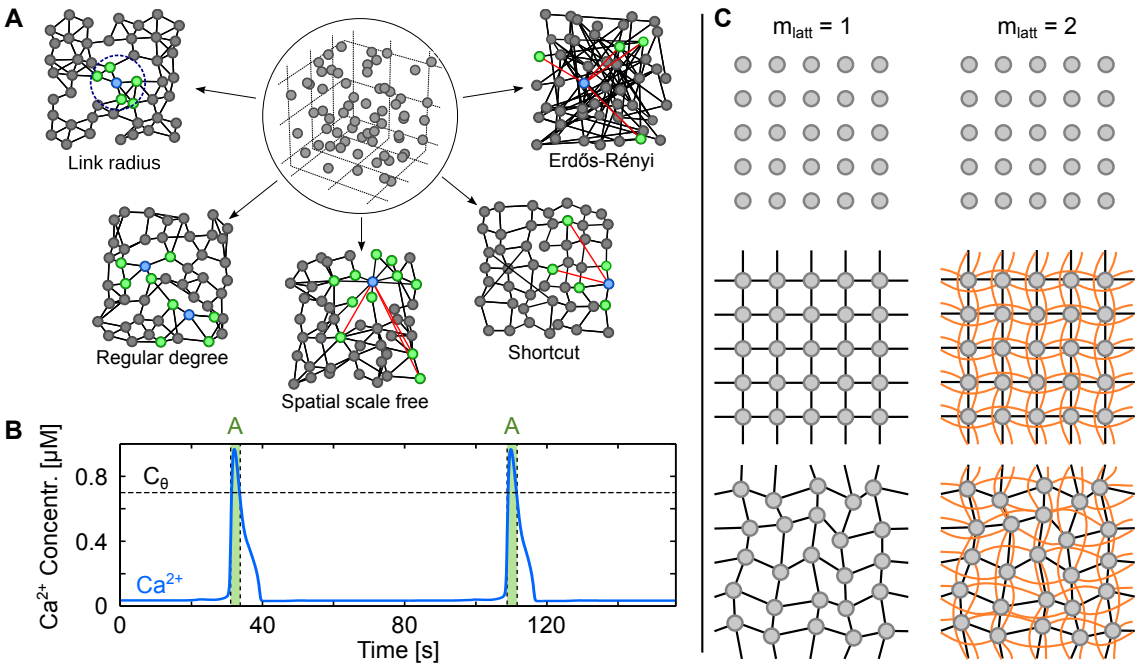

Figure V.1: Modelling three-dimensional astrocyte networks. A The astrocytes (*circles*) are first positioned on a cubic lattice. The positions are then jittered by random values so as to reproduce experimentally-derived cell distance statistics (*circled panel*). The astrocytes are then GJC-coupled (*black lines*) according to different coupling rules, yielding distinct types of coupling organizations (*other panels*). For clarity, the networks illustrated here are two-dimensional, but the networks used in the study are systematically three-dimensional. *Red links* denote shortcuts, *green* cells locate the cells that are GJC-coupled to the *blue* one. **B** Typical trace from simulation of the *ChI* model that gives the intracellular Ca^{2+} dynamics in each cell of the network. Astrocytes are considered activated (A, *green-shaded regions*) when their cytosolic Ca^{2+} concentration (*blue traces*) exceeds the threshold $C_\theta = 0.7$ μM (*black dashed lines*). Astrocyte parameters as in Table V.1. **C** Schematic representation of the wiring of lattices. Astrocytes are first positioned on a regular grid (top row). They are then wired to their nearest neighbors. When $m_{latt} = 1$ (left column), astrocytes are only wired to their 4 nearest neighbors (*black* links, 6 in 3D); when $m_{latt} = 2$, astrocytes are additionally wired to their two-hop neighbors (*orange* links). Astrocyte positions are then randomly jittered.

Table V.1: Biochemical parameters of the astrocyte network model.

Symbol	Description	Value	Units
	IP_3R kinetics		
d_1	IP_3 binding affinity	0.13	μM
O_2	Inactivating Ca^{2+} binding rate	**0.2**	$\mu M^{-1}s^{-1}$
d_2	Inactivating Ca^{2+} binding affinity	1.049	μM
d_3	IP_3 binding affinity (with Ca^{2+} inactivation)	0.9434	μM
d_5	Activating Ca^{2+} binding affinity	0.08234	μM
	Calcium fluxes		
C_T	Total ER Ca^{2+} content	2	μM
ρ_A	ER-to-cytoplasm volume ratio	0.185	–
Ω_C	Maximal Ca^{2+} release rate by IP_3Rs	**6**	s^{-1}
Ω_L	Maximal Ca^{2+} leak rate	**0.11**	s^{-1}
O_P	Maximal Ca^{2+} uptake rate	**0.9**	$\mu M\,s^{-1}$
K_P	Ca^{2+} affinity of SERCA pumps	0.05	μM
	IP_3 production		
O_δ	Maximal rate of IP_3 production by PLCδ	**0.7**	$\mu M\,s^{-1}$
K_δ	Ca^{2+} affinity of PLCδ	0.1	μM
κ_δ	Inhibiting IP_3 affinity of PLCδ	1.5	μM
	IP_3 degradation		
Ω_{5P}	Maximal rate of IP_3 degradation by IP-5P	**0.21**	s^{-1}
O_{3K}	Maximal rate of IP_3 degradation by IP_3-3K	**4.5**	$\mu M\,s^{-1}$
K_D	Ca^{2+} affinity of IP_3-3K	1	μM
K_{3K}	IP_3 affinity of IP_3-3K	0.7	μM
	IP_3 diffusion		
F	GJC IP_3 permeability (linear)	2	s^{-1}
	GJC IP_3 permeability (nonlinear)	**2**	$\mu M\,s^{-1}$
I_θ	Threshold IP_3 gradient for diffusion	**0.3**	μM
ω_I	Scaling factor of diffusion	0.05	μM
I_{bias}	IP_3 bias	2	μM
	Simulation		
T	Simulation time	200	s
t_s	Stimulation time	200	s

that we used were subject to spatial constraints on link formation. We constructed all networks with a two-step procedure: (1) we defined a spatial organization, by positioning each astrocyte in a 3D space (unless specified otherwise); (2) we defined a topological structure, by linking astrocytes according to specific rules for each network class and parameter combinations.

V.1.2.1 Spatial structure

While detailed topological informations on astrocyte networks are still lacking in the literature, it is much easier to find statistics of the way astrocytes are positioned. For example, Sasaki et al. (2011) obtained, in the rat hippocampus, the distribution of distances between nearest neighbors and measured that these distances were on average of 50μm with minimal values at 20μm and a coefficient of variation of ~ 0.25. To reproduce a similar distribution, we first positioned $N = 11^3$ simulated astrocytes on a 3D regular grid with inter-node distance a and then jittered each node by applying a gaussian noise with mean 0 and variance σ^2. We estimated a and σ^2 by minimization of squared error to match the mean, minimum value, and coefficient of variation to the experimental one. The resulting parameter values are reported in Table V.2. Simulated astrocytes thus occupied a cubic volume with a side length of approximately $(11 \times a) \approx 0.8$mm (i.e. ≈ 0.5mm^3).

V.1.2.2 Topological structure

We used 5 different network classes; each one is represented in 2D form in Figure V.1A. We wanted our networks to span a large range of network properties in order to find which properties affected ICW propagation. Accordingly, we considered networks in which spatial constraint on the formation of links ranged from strong (Link radius networks on the left side) to nonexistent (purely random Erdős-Rényi networks, on the right side). In between these two extremes, we explored different degree distributions (networks with hubs as spatial scale free networks, in the center) as well as networks whose basic topology is strongly spatially constrained but to which we added a small proportion of long distance links (in *red* on the figure). The networks displayed in Figure V.1A are in 2D for readability but all the networks we simulated were in 3D unless specified otherwise; *blue* nodes are selected nodes of interest, *green* nodes are neighbors of the blue ones and *red* links are long-distance links. Network classes were constructed in the following way:

Link radius networks were constructed by linking each astrocyte i to astrocytes j whose spatial distance to i $d_{i,j} \leq d$. In other words, every astrocyte i was linked to all astrocytes that were in a sphere of radius d centered on i. This radius is represented in Figure V.1A by a *blue dashed* circle. The degree distribution of these networks displayed a small amount of variability around the mean degree $\langle k \rangle$, since astrocytes positions have been previously jittered, without allowing the presence of highly coupled astrocytes.

Regular degree networks were constructed by linking each astrocyte to its k nearest neighbors ($k = 4$ on the figure) and preventing long distance links by forbidding links longer than 150μm. In order not to introduce directional biases on the links, they are added in k_{reg} iterations; at each iteration m, each node is selected exactly once (the order is randomly defined for each iteration) and linked to their nearest node i having a degree $k_i < m$ and satisfying the maximum link distance constraint. The degree distribution of

these networks was thus peaked around k with very few astrocytes having a lower degree because of boundary effects (nodes near the edges cannot always satisfy the maximum link distance constraint).

Spatial scale free networks were incrementally constructed using a preferential attachment process with spatial constraints (Barthélemy, 2010). Astrocytes were gradually added to the network and each new astrocyte was connected with m_{sf} astrocytes in the network according to degree-dependent and distance-dependent probabilities. The probability for a new astrocyte i to be connected to astrocyte j was computed with $p_{i\to j} \propto k_j \exp(-d_{ij}/r_c)$; with k_j the degree of astrocyte j, d_{ij} the euclidean distance between astrocytes i and j, and r_c the parameter controlling the influence of space on the formation of links. When r_c is small, links are restricted to close neighbors while high r_c values allow the formation long distance links. The probability is rescaled so that all the probabilities (associated to each astrocyte j in the network) sum to 1. Since $p_{i\to j}$ is proportional to the degree k_j of astrocyte j, newly added astrocytes tend to connect to already highly connected astrocytes. This 'rich get richer' rule gives rise to hubs, i.e. highly connected astrocytes. These spatial scale free networks thus allow us to study both the effect of space on the formation of links and of high degree astrocytes on ICW propagation. Specifically, the presence of highly connected astrocytes (over 20 neighbors, twice as much as the estimated mean degree of 3D astrocyte networks in situ (Xu et al., 2010)) in networks that still display nearest-neighbor like coupling is of particular interest since high heterogeneity in coupling have been observed in some restricted areas (Houades et al., 2008; Roux et al., 2011).

Shortcut networks were constructed in a similar way as small-world networks (Watts, 1999): contrary to the other networks, we started by positioning astrocytes on a cubic lattice (i.e. a 3D grid with equally spaced points) with internode distance a and we linked each astrocyte to its nearest neighbors at distances that are multiples of a and lower or equal to $a \times m_{latt}$ (with m_{latt} as in Table V.2). This process is described in Figure V.1C. Since we are in a $D = 3$ dimensional space, each node can only have $2m_{latt}D$ neighbors. Detailed description of these lattices can be found in Watts (1999). We then rewired each link with probability p_s so that one of its endpoint was randomly chosen. Finally, we jittered the nodes positions as explained before. Depending on the value of p_s, these networks can bear so-called 'small-world' features (Albert and Barabási, 2002).

Erdős-Rényi networks were constructed by linking each pair of nodes with probability p independently of their distance or existing degree. Since the formation of links in these networks is completely independent from the spatial organization of astrocytes, these networks are biologically unrealistic. We can however use them as a control to better understand which properties help or hinder ICW propagation.

Since all network classes are associated with parameters, each network class can be used to generate several topologies with different properties. Additionally, with the exception

of shortcut networks with $p_s = 0$, all the procedures to generate the networks comport random aspects. For each network class and parameter combination, we thus simulated 20 realizations of networks on which we measured some specific characteristic (like the mean-shortest path L or the number of activated astrocytes N_{act}), and we usually plotted the mean and standard deviation of these characteristics (except if indicated otherwise in the figure caption). The parameter ranges that we used are reported in Table V.2. Since the wiring of some networks is random, it is possible that some subparts of these networks are disconnected from the rest. To minimize this, we ensured that, for all the parameters that we used, the ratio of mutually unreachable node pairs was less than 2% (i.e. among all node pairs i, j, there were at most 2% of node pairs k, m for which no path existed from between k and m).

Table V.2: Spatial and topological parameters of the astrocyte network model.

Symbol	Description	Values			Units
		min	step	max	
	Spatial organization				
a	Internode distance		70		μm
σ^2	Variance of the gaussian noise		55		μm
	Network topology				
k	Degree of regular networks	3	1	15	-
d	Linking distance for link radius networks	80	5	120	μm
r_c	Spatial parameter for spatial scale free networks	2	1	4	μm
-	-	5	20	105	μm
m_{sf}	New links for spatial scale free networks	2	1	5	-
m_{latt}	Linking distance for shortcut networks	1	1	3	-
p_s	Edge rewiring probability for shortcut networks	0	0.02	0.1	-
-	-	0.2	0.1	0.4	-
p	Linking probability for Erdős-Rényi networks	$\frac{5}{N-1}$	$\frac{1}{N-1}$	$\frac{15}{N-1}$	-

V.1.2.3 IP_3 diffusion function

Quantitative measures of diffusion through GJC generally focus on their conductance when current is passed; the diffusion of electrically neutral second-messenger like IP_3 has not however, to our knowledge, been quantitatively investigated. The choice of a function linking the IP_3 difference between two cells and the resulting IP_3 flux is thus not straightforward. As presented in Section II.2.2, GJC could be modeled by linear or nonlinear functions; while the default choice would be a linear function, in Goldberg et al. (2010), the authors argue that contrary to linear GJC, nonlinear GJC can allow long distance ICW propagation. While biological evidence to such nonlinear GJC is still lacking, we showed in Section II.2.2 that under some conditions, the complex morphology of astrocytes could lead to nonlinear soma-to-soma diffusion even when the diffusion in underlying subcompartments was linear. Since nonlinear GJC allowed larger ICW extent than linear, we decided to use nonlinear GJC as a default choice so that effects of topology would

be more apparent. We however checked that we observed qualitatively similar effects of topology on ICW with both linear and nonlinear GJC (cf. Figure V.5A and V.13A) and that the local mechanisms of ICW propagation were also the same (cf. Section V.3). Additionally, we investigated the effects of both GJC strength F and nonlinear IP_3 threshold for diffusion I_θ on ICW propagation and showed that nonlinear diffusion with small I_θ was similar to linear diffusion (cf. Section V.3).

V.1.3 Stimulation protocol

The exact way of initiating an ICW is not of particular relevance since we are mainly interested in the effect of network topology on wave propagation, we just need to stimulate one astrocyte and look at how the ICW propagates from there. We were faced with different choices to initiate an ICW: (1) use the G-ChI model (as in Section IV.1) and stimulate an astrocyte by a simulated neuronal spike train; (2) add a constant flux term to equation (II.14) for the stimulated astrocyte; and (3) couple the stimulated astrocyte to a reservoir astrocyte whose IP_3 concentration is set constant. The first solution adds 1 equation to the system and is essentially equivalent to the second: when the synapse releases glutamate at a given frequency, PLCβ will produce IP_3 and, since astrocyte dynamics are slow compared to synaptic ones, the averaged production will be essentially the same as a constant flux term. The third possibility allows one to control the concentration of IP_3 in the stimulated cell to a much better extent than with a constant flux term. Additionally, the third possibility can be thought of as patching the reservoir cell with a pipette whose IP_3 concentration is controlled. Since this solution did not add additional equations to the system and could be viewed as an actual experimental procedure, we chose the third solution: we GJC-coupled the stimulated cell of each network with a reservoir cell whose IP_3 concentration was kept constant at $I_{bias}\mu$M. We chose the central cell in the 3D domain as the stimulated cell in all of the simulations in order to minimize boundary effect as much as possible. In order to determine the strength I_{bias} and the duration t_s of the stimulation, we simulated all classes of networks with different values of both of these parameters and monitored the ICW extent N_{act}. Figure V.2 presents the results of some of these simulations: In all network classes, propagation reaches a maximum when $I_{bias} \geq 1.75\mu$M and $t_s \geq 50$s. To ensure that ICW unfolded to their full extent without exposing astrocytes to unrealistically high IP_3 concentrations, we stimulated the cell during the whole simulation ($t_s = T$) with $I_{bias} = 2\mu$M.

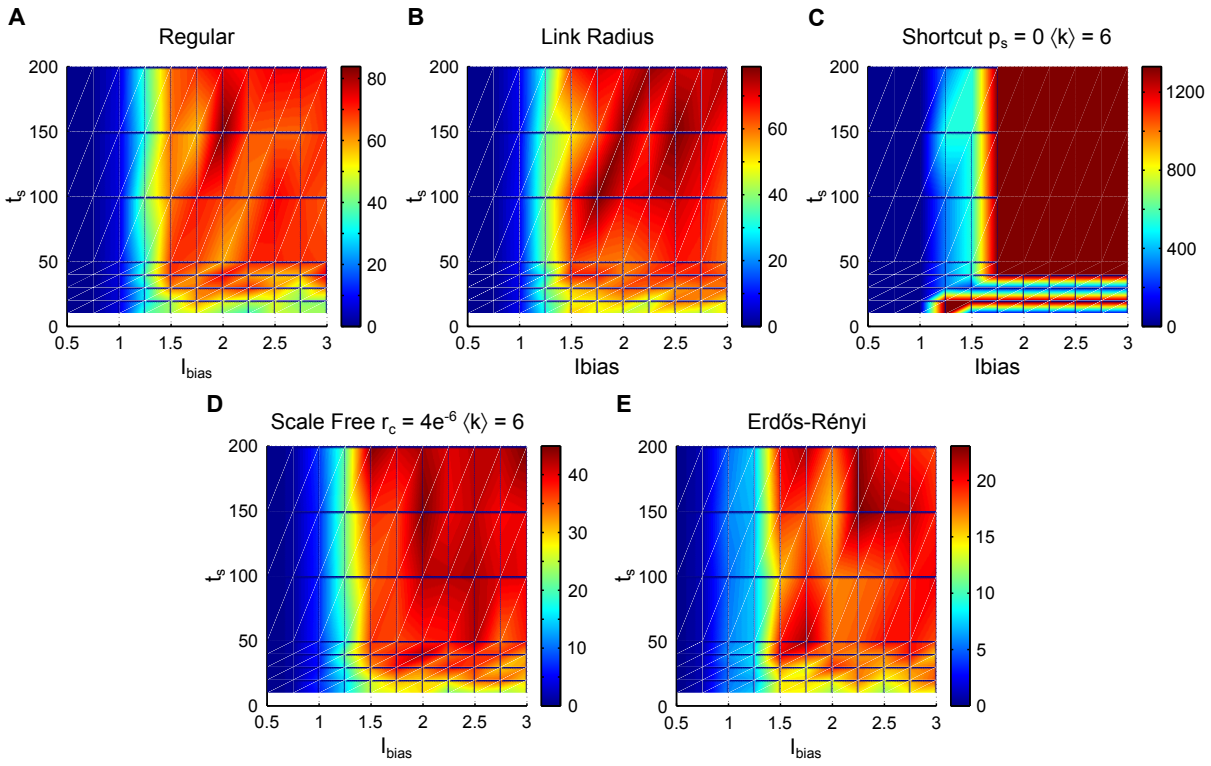

Figure V.2: Protocol of astrocyte stimulation used in the simulations. In all astrocyte networks considered in this study, ICW propagation was triggered by a step IP_3 concentration gradient (I_{bias}) applied to the astrocyte at the center of the network. The duration (t_s) of the step was fixed at 200 s to ensure that ICW could unolfd to their full extent. This extent was determined by looking at the number of astrocytes activated by an ICW (N_{act}, *colorbars*) as a function of stimulation time and IP_3 bias. All networks shown in the figure were characterized by $\langle k \rangle = 6$. (**A**) Regular networks with $k = 6$; (**B**) Link Radius networks with $d = 85$ μm ; (**C**) Shortcut networks with $m = 1$ and $p_s = 0$; (**D**) Spatial Scale Free networks with $m_{sf} = 3$ and $r = 4$ μm; and (**E**) Erdős-Rényi with $p = 6/(N-1)$. I_{bias} was varied from 0.5 μM and 3 μM by steps of 0.5 μM; t_s was varied from 10 to 50s by steps of 10s and from 50 to 200s by steps of 50s. The data show the means value of N_{act} for 20 realizations of the same network topology. Note that colorbars vary between subfigures.

V.2 ICW propagation in specific network topologies

V.2.1 ICW propagation in simulated networks

In all simulations, although propagation extent strongly depended on network topology (as we will address in Section V.2.2), ICW propagations followed the general behavior represented in Figure V.3A: A first wave was elicited from the stimulated cell (*red* circle), propagated regeneratively to its maximum extent (bottom right subfigure), and eventually stopped either when reaching the borders of the network or before because of propagation failure. During this process, since the central node was stimulated during the whole simulation, other waves were elicited (see the *green* circle on the bottom row of subfigures) and propagated to roughly the same distance as the previous one. ICWs thus propagated in a pulsatile manner, with successive waves that seemed to be mostly independent from each other.As can be seen in Figure V.3A, ICWs did not always propagate with a circular shape (see $t = 28$ and 36.1s where the wave stopped propagating in the bottom left part of the network whereas it continued elsewhere); because of network heterogeneities, the contours of ICWs were often irregular. This characteristic is particular to GJC-dependent ICWs and as been observed in ICWs elicited in cell culture in which GJC were known to be involved in wave propagation (Peters et al., 2005b).

Wave speed varied during wave propagation; as illustrated in Figure V.3B, the first stimulation-induced steps of propagation (top row of Figure V.3A and peak of Figure V.3B) were very quick, reaching propagation speeds of up to $\approx 60\mu\text{m.s}^{-1}$, but the subsequent regenerative propagation displayed lower speeds (bottom row of Figure V.3A and middle part of Figure V.3B), between 10 and $20\mu\text{m.s}^{-1}$ in agreement with experimentally reported speeds (Scemes and Giaume, 2006). We measured on average propagating speed for each wave by measuring, at each time step, the distance between the stimulated node and the farthest astrocyte that activated in a 10s time window. This distance is represented in Figure V.3C; the first wave (in *red*) propagates up to $\approx 500\mu\text{m}$ until it stops and the propagation distance gets back to lower values, corresponding to another propagating wave (in *yellow*). We segmented individual waves (associated with strictly increasing parts of Figure V.3C) and computed an average wave speed as the ratio between overall spanned distance and the time needed to span this distance (represented by the slope of *black dashed* lines in Figure V.3C).

We only computed spatial wave speeds on spatially constrained networks because long distance links rendered spatial speed values meaningless. We also computed propagation distances in number of hops (i.e. topological distance) but these values were not very informative since, as we will see in Section V.2.2, spatially unconstrained networks did not propagate ICW on large extents. Overall, the different spatially constrained topologies did not display substantial differences in spatial wave speeds and large waves propagated at roughly the same speed $\approx 17\mu\text{m.s}^{-1}$ regardless of the network. We excluded small waves since the wave initiation is much faster than the actual propagation. Figure V.3D shows that wave speed was however affected by the diffusion threshold values I_θ that controls the

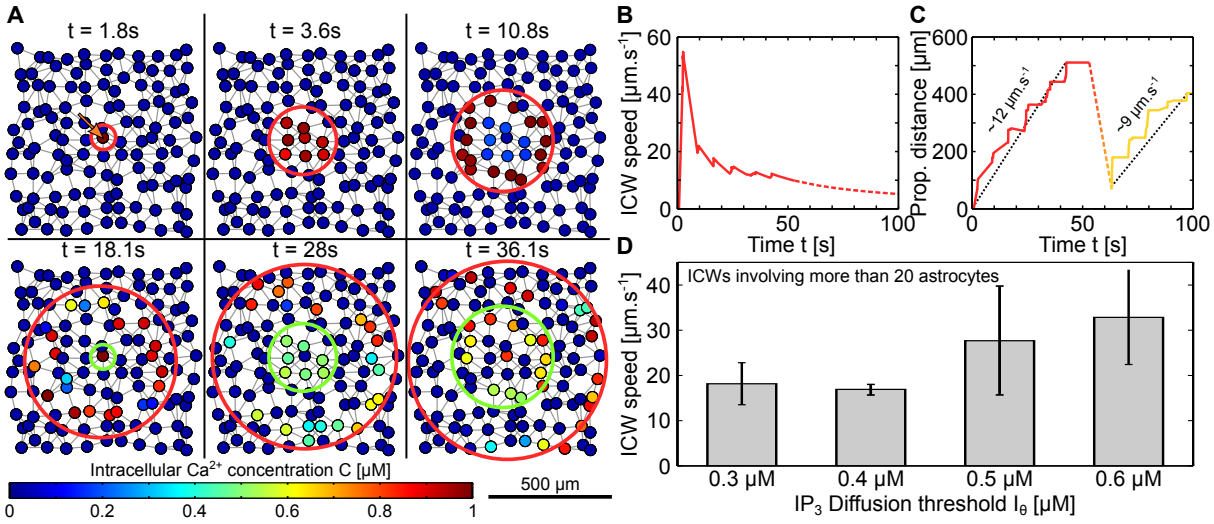

Figure V.3: ICW propagation under continuous stimulation is pulsatile with decreasing speed. **A** Illustration of ICW propagation in 2D Link radius networks with $N = 121$ and $d = 110\mu$m. The first wave (*red* circle) propagates quickly from the stimulated node (*orange* arrow in the top left subfigure) at the beginning and slows down after $t \approx 15$s; while the first wave is still propagating, a second wave (*green* circle) starts propagating from the stimulated node. During a simulation, several waves propagate in a pulsatile manner. Node color indicate Ca^{2+} concentration according to the colorbar. GJC coupling are represented as *gray* links. **B** Propagation speed of the first wave, the first nodes are quickly activated but the speed soon stabilizes at around $\approx 15\mu$m.s^{-1} until the wave eventually stops (the *dashed* part of the curve decreases in $1/t$). **C** We can estimate the propagation speed from the instantaneous propagation distance. Since ICW propagate in a pulsative manner, we compute the wave speed as the ratio between propagation distance until it reaches its highest value and the time it took to reach this distance. **D** Resulting wave speed were computed in spatially restricted networks only (because long distance link make this value meaningless) and were found to be mostly independent from network parameters for ICW that encompassed more than 20 astrocytes. The IP_3 diffusion threshold I_θ, when doubled from 0.3μM to 0.6μM, increased propagation speed from $\approx 18\mu$m.s^{-1} to $\approx 33\mu$m.s^{-1}. Bars±Error-bars plot mean±standard deviation across 20 realizations of all spatially constrained network topologies (Shortcuts with $p_s = 0$, Regular degree, and Link radius) that displayed ICW with more than 20 activated astrocytes.

needed IP_3 gradient between two astrocytes to achieve effective IP_3 diffusion. Increasing I_θ from 0.3μM to 0.6μM increased the wave speed from $\approx 18\mu$m.s^{-1} to $\approx 33\mu$m.s^{-1}. We will address this effect of I_θ on propagation speed together with its effect on propagation extent, in Section V.3.

Since the successive ICWs usually spanned the same distance (as already seen from Figure V.2, in which additional stimulation over $t = 50$s did not activate any more nodes), we only considered wave extent in terms of number of activated cells N_{act}during the course of the whole simulation. Using this measure, Figure V.4 shows 3D representations of typical simulations (in which all astrocytes activated during the course of the simulation are represented as *green* circles) and shows that mere variations in network topology can reproduce the experimentally observed differences in wave extent, controlling the switch from small extents (tens of activated *green* cells, Figure V.4A) to local propagation (≈ 50

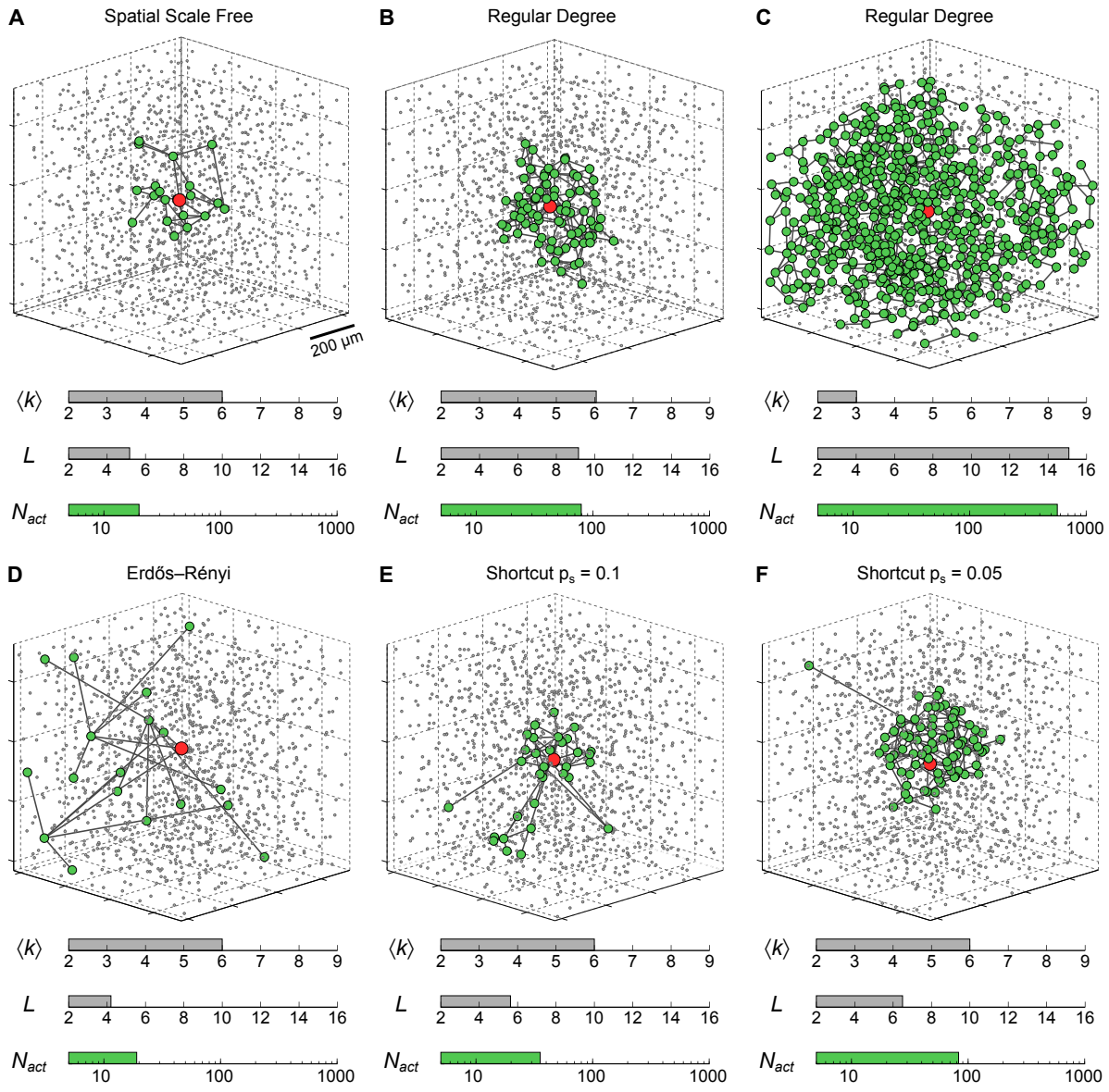

Figure V.4: Intercellular Ca^{2+} waves in 3D astrocyte networks of different coupling organizations. Changing the organization of the couplings between astrocytes dramatically affects the extent of propagation of ICWs, as quantified by the number of activated astrocytes (N_{act}). The six networks in this figure feature the same number of cells (*gray dots*). *Green circles* denote astrocytes that were activated by the ICW triggered via stimulation of the *red* astrocyte in the center of the network. **A** $r_c = 25\,\mu$m, $m_{sf} = 3$; **B** $\langle k \rangle = 6$; **C** $\langle k \rangle = 3$; **D** $p = \frac{5}{N-1}$; **E** $p_s = 0.1$, $m_{latt} = 1$; **F** $p_s = 0.05$, $m_{latt} = 1$. Astrocyte parameters as in Table V.1.

activated cells, Figure V.4B) to even regenerative propagation (hundreds of activated cells, Figure V.4C). In the next subsection, we will try to understand how these simple changes in network topology control ICW extent.

V.2.2 Sparse connectivity and short distance links favor ICW propagation

To quantify the differences between topologies, we introduce two classical quantifiers of complex networks (see Section III.1.2):
- the mean degree $\langle k \rangle$, that quantifies the average number of neighbors of astrocytes;
- the mean-shortest path L (Albert and Barabási, 2002; Barthélemy, 2010) which represents the mean distance (in terms of number of links) between any two astrocytes.

It is worth noting that these two quantities can be linked. Indiscriminate augmentation of the mean degree $\langle k \rangle$ for example, generally decreases the mean-shortest path L by adding new paths and thus reducing the distance between any two astrocytes. The mean-shortest path L can however easily be changed independently of $\langle k \rangle$ by simply rewiring existing nodes.

On Figure V.4, $\langle k \rangle$ and L are reported under each simulation alongside with the total number N_{act} of astrocytes that got activated (in *green*) during the ICW. These two characteristics seem to play a role in ICW propagation; indeed, networks with low mean-shortest path (e.g. Figure V.4A) seem to prevent ICW propagation. When increasing the mean-shortest path (i.e. decreasing the quantity of long-distance links) while keeping $\langle k \rangle$ constant, propagation extent is increased four-fold, from 20 cells in spatial scale free networks (Figure V.4A) to 80 cells in regular degree networks (Figure V.4B). The presence of long-distance links, associated to small L values, thus seems to impair ICW propagation and restricting links to spatially close astrocytes, as in regular degree networks, seems to favor ICW propagation. When keeping the same spatially constrained coupling organization (i.e. regular degree networks), reducing $\langle k \rangle$ facilitates ICW propagation: regular degree networks can indeed switch from supporting local propagation (Figure V.4B) when $\langle k \rangle = 6$ to supporting regenerative ICW that spans roughly all the network when $\langle k \rangle = 3$ (Figure V.4C). The role of mean-shortest path in ICW propagation is further illustrated by the effect of long-distance links (or shortcuts). While keeping $\langle k \rangle = 6$ constant, if one starts with a purely random coupling strategy (i.e. Erdős-Rényi networks, Figure V.4D) and gradually reduces the amount of shortcuts (by controlling the rewiring probability p_s in shortcut networks), the ICW supported by these networks gradually increase their extents from very restricted ones in the case of completely random networks (less than 20 cells in Figure V.4D) to increasingly higher extents: $\approx$ 35 cells with $p_s = 0.1$ in Figure V.4E and up to ≈ 80 cells with $p_s = 0.05$ in Figure V.4F.

These impressions are confirmed when looking at the relationship between $\langle k \rangle$, L and the ICW extent N_{act}. Figure V.5A shows, for all network architectures, how the ICW extent N_{act} changes as the mean degree $\langle k \rangle$ is increased. For each network architecture (represented in different colors), parameters controlling the topology were varied as described in Section V.1. Each point of Figure V.5 corresponds to the mean ICW extent across 20 realizations of the same network parameters and error bars plot standard deviation. It is clear from Figure V.5A that all network architectures follow the same qualitative trend: the higher the mean degree, the lower the ICW extent. In other words, and in contrast to what is usually considered to be true in network propagation models (Zanette,

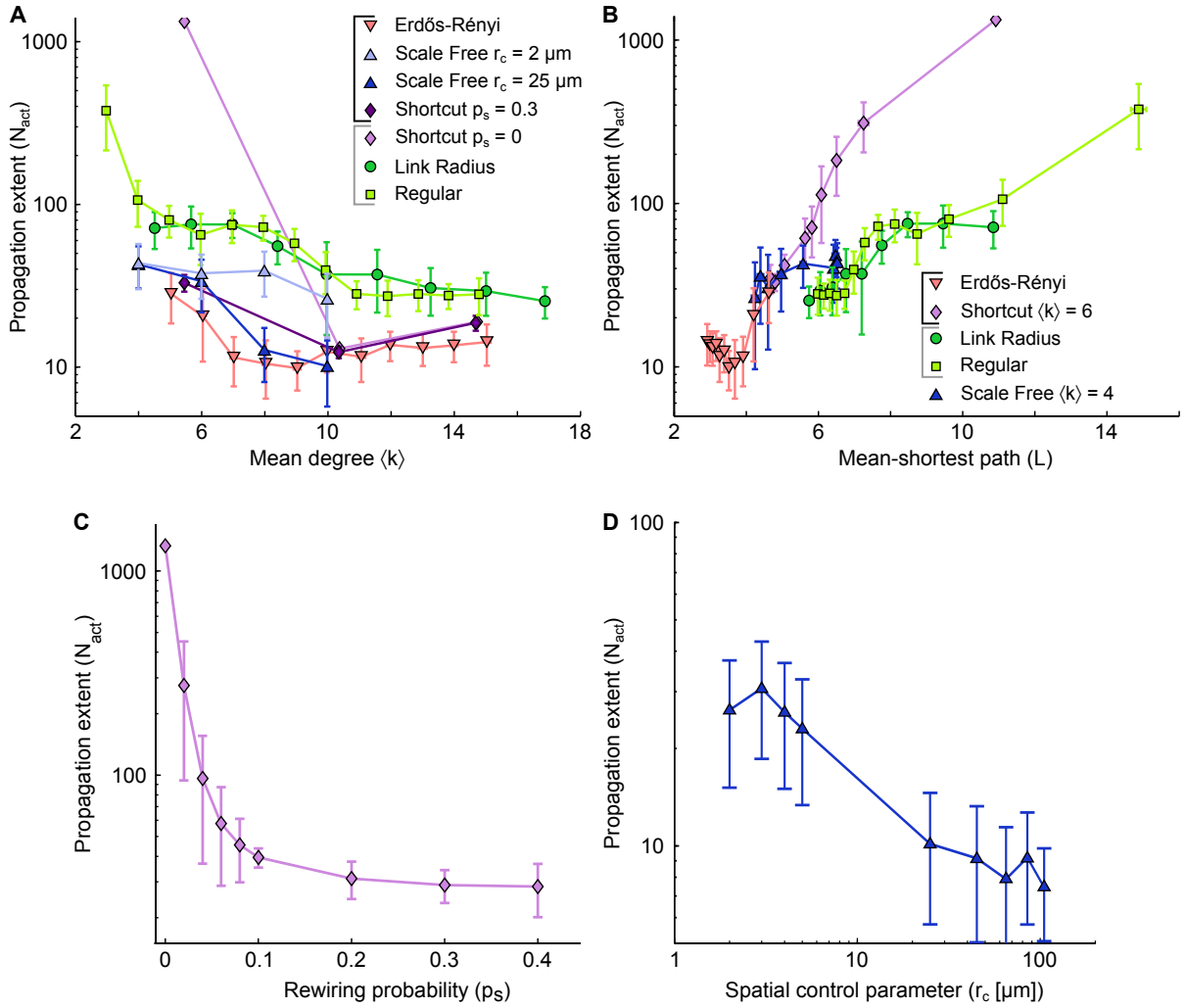

Figure V.5: Dependence of the extent of ICW propagation on the main quantifiers of the coupling organization. **A** Extent of ICW propagation (quantified by the number of activated cells, N_{act}) as a function of the mean degree $\langle k \rangle$ and **B** of the mean-shortest path L. The number of activated cells segregates spatially–constrained (link radius, regular degree and shortcut with $p_s = 0$) from spatially–unconstrained coupling organizations (shortcut with $p_s > 0$, and Erdős-Rényi). **C** Extent of propagation in shortcut networks as a function of the rewiring probability p_s. **D** Extent of propagation in spatial scale free networks as a function of the parameter r_c that controls the trade-off between scale–free structure and the restriction of the couplings to short distances. **C** and **D** suggest that ICW propagation is favored by short-distance GJC couplings between astrocytes while long–distance couplings hinder propagation. Simulations as described in Figure V.4. Data points±errorbars correspond to mean values±standard deviation over 20 sampled networks with the same statistical parameters (see Methods). The shortcut networks in **C** were all built with $\langle k \rangle = 6$ (i.e. $m_{latt} = 1$). The spatial scale free networks in **D** were built with $\langle k \rangle = 10$ (i.e. $m_{sf} = 5$). Astrocyte parameters as in Table V.1.

2002; Dyhrfjeld-Johnsen et al., 2007), increasing the connectivity of the network actually impairs signal propagation in our model astrocyte networks. In this figure, the network architectures seem to fall into two different propagation classes: (1) spatially unconstrained networks, in which long distance links are allowed (e.g. Erdős-Rényi in *light red triangles* and shortcut networks with $p_s = 0.3$ in *dark purple diamonds*); and (2) spatially constrained networks whose links are restricted to spatially close astrocytes (Link radius networks in *dark green circles* and regular degree networks in *light green squares*). For a given $\langle k \rangle$, spatially constrained networks always support larger ICW extents than spatially unconstrained networks. Spatial scale free coupling organizations have a parameter r_c that allows to continually change from spatially constrained to spatially unconstrained networks as can be seen in Figure V.5A: when r_c is small, ensuring that links are only established between nearby astrocytes, ICW extent behaves as spatially constrained networks do (*light blue triangles*); when r_c is high, allowing long distance links, the ICW extent behaves as spatially unconstrained networks (*dark blue triangles*). This behavior together with the fact that, for a given $\langle k \rangle$ value, the difference between spatially constrained and unconstrained networks can be up to 10 folds, indicate that the mean degree is not the only determinant of ICW propagation. As we saw in Figure V.4, the presence or absence of long distance links seems to be the other important factor.

The mean-shortest path L of a network is a way to quantify how much the links are spatially constrained: for networks of the same size, L decreases when short distance links are rewired to long distances. Figure V.5B shows the relationship between L and ICW extent N_{act}; all coupling organizations again follow the same qualitative behavior: the higher the mean-shortest path (i.e. the more spatially constrained the network is), the better the propagation. As with the mean degree, the same two classes appear: spatially constrained networks are clustered together (link radius in *dark green circles* and regular degree networks in *light green squares*) and separated from spatially unconstrained networks (Erdős-Rényi random networks in *light red triangles* and shortcuts networks in *light purple diamonds*). Spatial scale free networks again constitute a continuous transition from spatially constrained to spatially-unconstrained networks as their r_c parameters increases (*dark blue triangles*). This transition from spatially constrained network to spatially unconstrained can be seen for shortcut networks in Figure V.5C and for spatial scale free networks in Figure V.5D. As soon as some long distance links are introduced in shortcut networks, ICW extent drops very quickly and the same phenomenon happens in spatial scale free networks as long distance links are increasingly allowed by increasing r_c. Interestingly, the fact that, in our model of astrocyte networks, long-distance links actually impair signal propagation is at odds with the conclusions drawn by many studies on signal propagation wherein low mean-shortest path and shortcuts are associated with better propagation (Roxin et al., 2004). Such conclusions have even been drawn in the case of model neural networks (Dyhrfjeld-Johnsen et al., 2007), hinting that the principles at play in astrocyte network propagation might be different from those at play in neuronal networks.

We tried to determine whether wave extent could be better explained by other classical network characteristics (that are also linked to the spatial influence on links) such as the mean clustering coefficient $\langle C \rangle$ (Figure V.6A and C), the mean hierarchical clustering

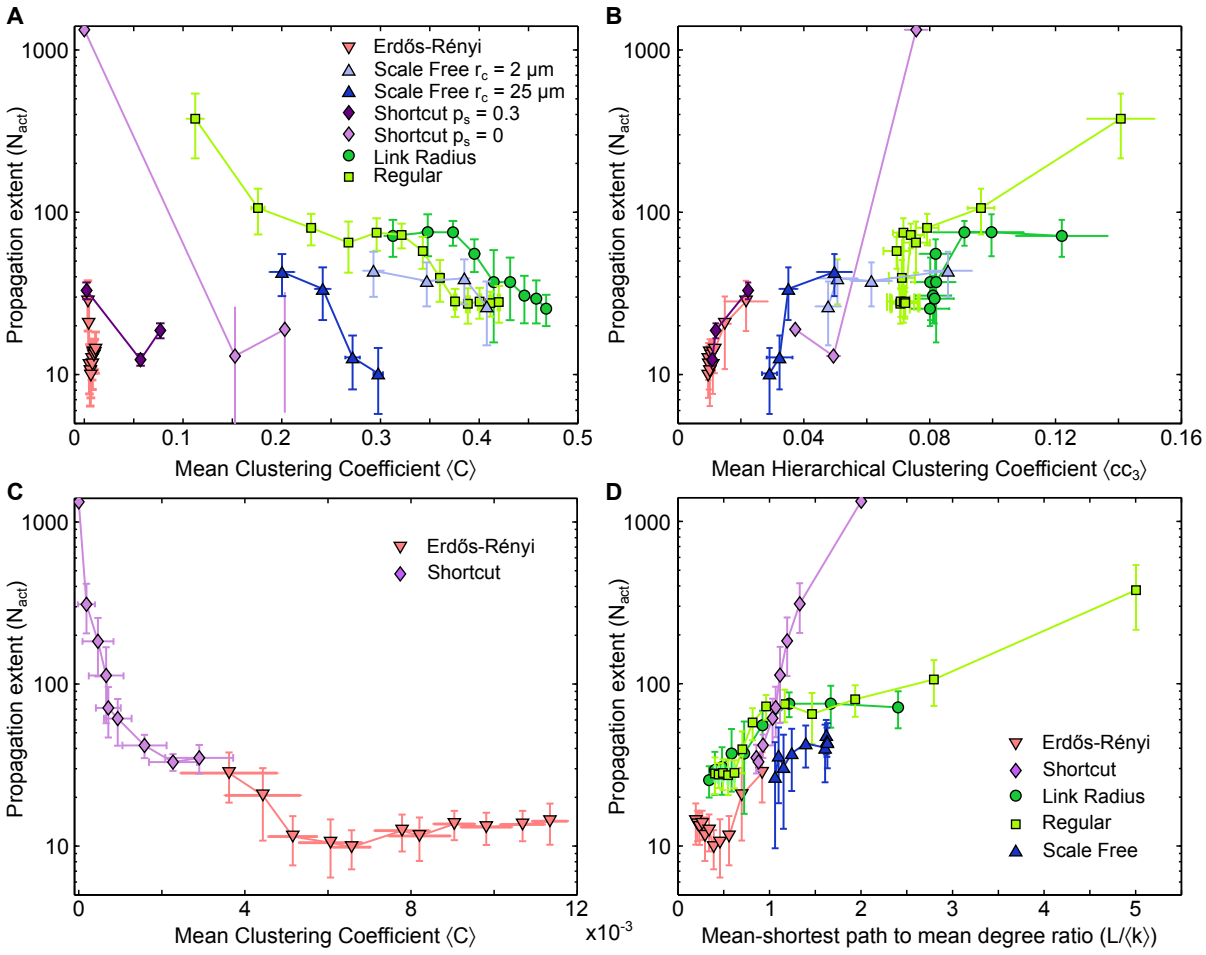

Figure V.6: Effect of clustering on ICW propagation. Extent of ICW propagation quantified by the number of activated cells (N_{act}) as a function of **A** the mean clustering coefficient $\langle C \rangle$ and **B** the mean hierarchical clustering coefficient $\langle cc_d \rangle$ with $d = 3$. **C** Zoom on the low $\langle C \rangle$ values (appearing to form a vertical line in **A**). Differently from other network parameters, such as mean degree and mean-shortest path, the effect of cell clustering on ICW propagation is complex and does not reveal any specific trend. **D** The mean-shortest path to mean degree ratio $L/\langle k \rangle$ does not explain the propagation extent better than $\langle k \rangle$ and L taken separately. Data are plotted as mean±std for 20 different network realizations with the same topology. Clustering coefficients were computed according to Refs Costa and da Rocha (2006); Boccaletti et al. (2006); Feldt et al. (2010).

coefficient $\langle cc_3 \rangle$ (Figure V.6B) or even composite measures like the ratio between mean-shortest path and the mean degree $L/\langle k \rangle$ (Figure V.6D). None of these characteristics were able to account for ICW extent better than $\langle k \rangle$and L taken separately. In particular, the ratio $L/\langle k \rangle$ cannot account correctly for this phenomenon because, for a given network with N nodes on which $N_{act} \ll N$, increasing the number of nodes to $N' > N$ while keeping the density of links constant will not change N_{act} but will change L.

It thus seems that the number of neighbors of each node is a strong determinant of ICW extent. When talking about real GJC, one should however not only be concerned with the number of neighbors that an astrocyte might have but should also be concerned about the

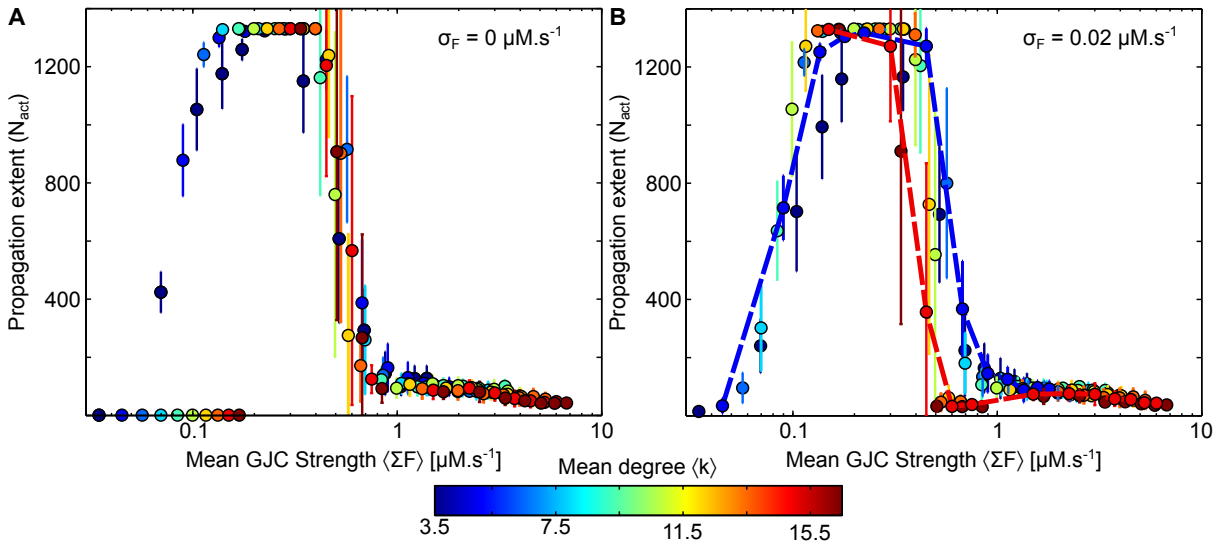

Figure V.7: Changes of GJC strength and mean degree in Link Radius networks. **A** In a first approach the strength F of the GJC couplings between two coupled cells are identical for every coupled cell pairs. Whatever the mean degree of the network, the ICW extent is dictated by the mean GJC strength per node $\langle \Sigma F \rangle = \langle k \rangle F$. **B** When the GJC strengths are randomly chosen from a normal distribution, the dependence on $\langle \Sigma F \rangle$ is essentially preserved, except that the optimal range of $\langle \Sigma F \rangle$ values diminishes when the network mean degree is large (*dashed red lines*). All points represent 20 realizations of a given parameter combination. Curves and points are color-coded according to the mean degree $\langle k \rangle$. Astrocyte parameters as in Table V.1 except for F that was varied between 0 and 0.05 by steps of 0.01 and between 0.1 and 0.4 by steps of 0.05. Link Radius parameters as in Table V.2.

strength of each cell-to-cell junction which can be linked to the expression of Cx proteins and to their phosphorylation state. In the following subsection, we investigate how ICW extent changes when GJC strength F changes and when variability of cell-to-cell junction strengths is introduced.

V.2.3 GJC strength and variability

In this subsection, we restricted our analysis to link radius networks since the properties of this coupling organization (spatially constrained and distributed degrees) are arguably closest to actual astrocyte networks. Morphological and dye coupling experiments have indeed shown that connected astrocytes are spatially close (Bushong et al., 2002; Houades et al., 2008) and the number of astrocytes connected to a given astrocyte can vary from cell to cell (Rouach et al., 2000). In order to investigate how GJC strength impacts ICW propagation, we varied both the network mean degree $\langle k \rangle$ and the individual GJC coupling strength F; to compare the effect of F on networks with different mean degrees, we considered the mean GJC strength per cell $\langle \Sigma F \rangle = \frac{\sum_{i=1}^{N} \sum_{j \in \mathcal{N}_i} F_{ij}}{N}$. From Figure V.7A, we can see that $\langle \Sigma F \rangle$ is a very good predictor of ICW extent N_{act}, as the curves associated

to different network degrees all collapse on the same curve. Furthermore, the dependency of N_{act}on GJC strength is not monotonous: Highest ICW extent are actually attained for intermediate values of $\langle \Sigma F \rangle$. When $\langle \Sigma F \rangle > 1\mu\text{M.s}^{-1}$, ICW extent decreases with increasing GJC strength, in accordance to what we observed in Section V.2.2 when we increased $\langle k \rangle$. In this regime, increasing $\langle k \rangle$ or F has the same effect. When $\langle \Sigma F \rangle < 0.1\mu\text{M.s}^{-1}$, IP_3 diffusion between cells gets slower than its degradation by IP_3-3K and 5P and wave propagation is prevented. For intermediate $\langle \Sigma F \rangle$ values, ICW extents get very strong and all networks are spanned by the ICWs. This regime of propagation is however different from the one we observed in our previous simulations: while, in a standard ICW, Ca^{2+} and IP_3 levels in a given astrocyte come back to their equilibrium value after the passage of an ICW front (Figure V.8A, top figure and Figure V.8C), in this intermediate regime of $\langle \Sigma F \rangle$, Ca^{2+} and IP_3 levels stay elevated after the passage of an ICW (Figure V.8A, bottom figure and Figure V.8D). This difference in propagation regimes actually stems from the fact that, as depicted in Figure V.8D, during the moment after astrocyte activation (marked by *black dashed* lines in Figure V.8A), because the of the weak GJC coupling, the outflux of IP_3 to unactivated neighbors is small. IP_3 cannot be evacuated from the astrocyte and its concentration increases, in turn leading to increased Ca^{2+} outflux from the ER that activates PLCδ until eventually all IP_3 fluxes (J_δ, $-J_{5P}$ and $-J_{net}$) equilibrate at high IP_3 concentration. This state corresponds to the rightmost stable equilibrium on ChI model bifurcation diagrams (see Section II.1.1.2). In contrast, during 'normal' propagation, as depicted in Figure V.8C, the after-activation excess IP_3 is readily diffused to unactivated neighbors, allowing the astrocyte to come back to its original resting state. When considering only the 'standard' regime of ICW propagation (i.e. the right-hand side part of Figure V.7A), these results confirm what we obtained when varying $\langle k \rangle$ only: an increase in GJC coupling, mediated either by an increase in the actual GJC strength F or by an increase in the mean degree $\langle k \rangle$, actually decreases ICW extent.

Cell-to-cell junctions in actual astrocyte networks however display variability when measured by electrical (Xu et al., 2010) or dye (Roux et al., 2011) coupling experiments. We thus investigated whether this variability in GJC coupling could play a role in ICW propagation in model astrocyte networks. To do so, we ran simulations where each cell-to-cell junction had its strength drawn from a Normal distribution with mean F and variance σ_F^2. Values were restricted between 0 and $2F$ to avoid negative GJC strength while keeping F as the mean GJC strength. As shown in Figure V.7B, the relationship between $\langle \Sigma F \rangle$ and N_{act} did not fundamentally change when we introduced variability. The only notable difference is the early failure in propagation for networks with high $\langle k \rangle$ values (*red dashed* line) compared to low $\langle k \rangle$ networks (*dark blue dashed* line). Accordingly, with constant mean GJC strength $F = 0.1\mu\text{M.s}^{-1}$, increasing the variability in strongly connected networks decreases by two-folds ICW extent N_{act} (Figure V.8B, *dark red* line). In contrast, for networks with a low mean degree, variability in GJC strength did not have any significant effect on ICW extent (Figure V.8B, *dark blue* line). Networks with small mean degree are thus beneficial for ICW propagation in two ways: (1) with constant GJC strength, they support high ICW extents; (2) they are robust to variability in cell-to-cell junction strengths.

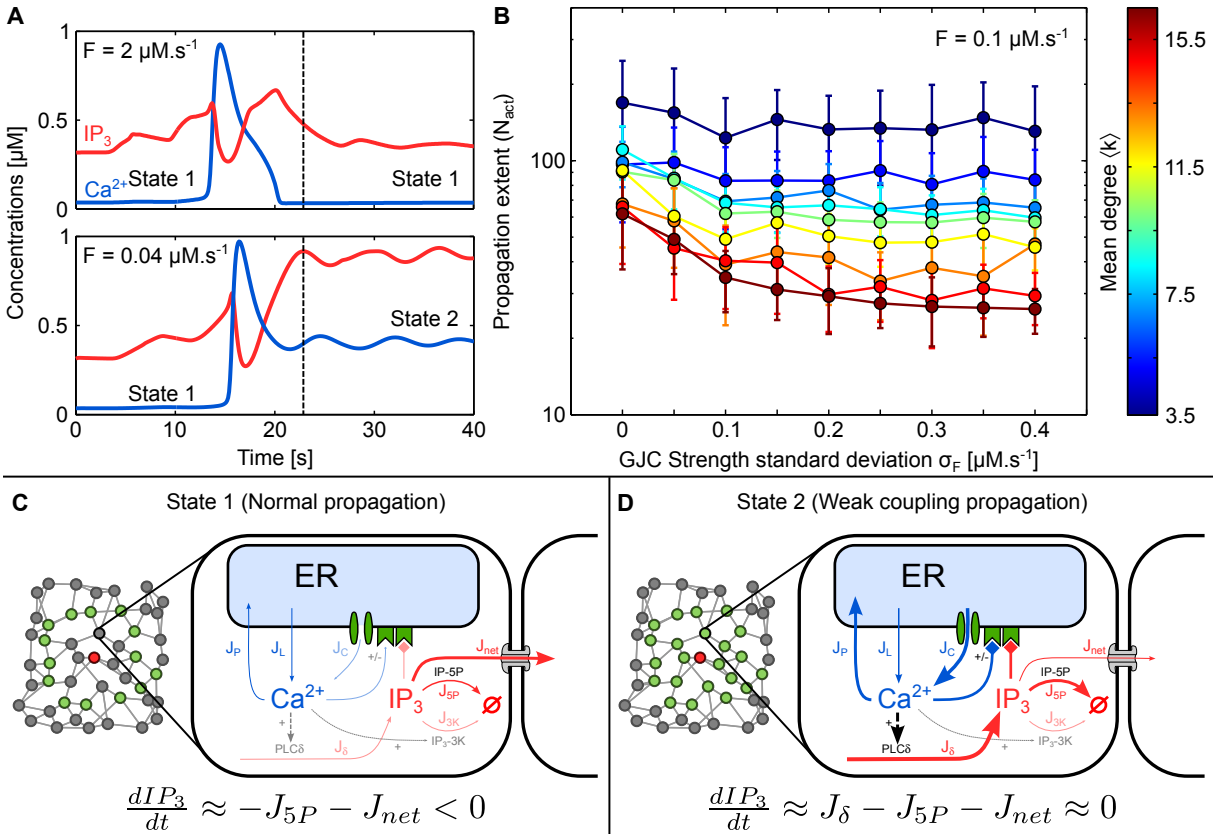

Figure V.8: Variations of GJC strength. **A** For low values of GJC strength F, the equilibrium state of astrocytes in networks is switched by the arrival of the ICW from steady-state 1 (low Ca^{2+} values) to steady-state 2 (larger Ca^{2+} values) where the resting concentrations of IP_3 (in *red*) and Ca^{2+} (in *blue*) are much higher. **B** Increasing GJC variability (σ_F) hardly has an effect on low degree networks (*blue* curves) while it decreases ICW extent by up to 50% for high degree networks (*red* curves). All points represent 20 realizations of a given parameter combination. Data points in are color-coded according to the mean degree $\langle k \rangle$ of the networks. Astrocyte and network parameters as in Figure V.7. **C** Illustration of normal propagation in a simulated astrocyte network: after the ICW (*green* nodes) elicited by stimulation of the *red* node, astrocytes go back in state 1 because of a high IP_3 outflux to their inactivated neighbors. **D** Illustration of weak coupling propagation, in which astrocytes stay activated (i.e. in state 2) after the ICW passage (*green* nodes) because the IP_3 outflux is too small to prevent IP_3 accumulation which lead to an equilibrium state with high Ca^{2+} concentration.

V.2.3.1 GJC coupling normalization

Since we showed that the mean degree $\langle k \rangle$ of simulated astrocyte networks is controlling ICW propagation, one could wonder whether this effect is brought about by the presence of degree heterogeneity and specifically by high degree astrocytes that could prevent ICW propagation. In our simulated network, when an astrocyte i increases its degree k_i, it simultaneously increases its cumulated GJC coupling strength $\sum_{j \in \mathcal{N}_i} F_{ij} = k_i F$. Its it thus impossible to distinguish the effect of the increase in degree itself from the total increase in GJC coupling. The same issue arises when simulating neuronal networks, when new excitatory chemical synapses are added on a neuron's dendritic tree, its overall excitability is necessarily increased. To keep excitability constant, synaptic weights are usually scaled down by some function of the neuron degree when new synapses are added (Van Vreeswijk and Sompolinsky, 1996, 1998; Lerchner et al., 2006). This process, called *synaptic scaling*, allows to distinguish between effects attributable to cell degree and effects related to overall increase in coupling and has mainly been observed experimentally for post-synaptic terminals (Turrigiano, 2008). Unfortunately, we cannot apply the same type of scaling in astrocyte networks because of the bidirectionality of GJC coupling. When rescaling synapses, one only needs to consider the degree of the neuron at hand; in astrocytes however, the same coupling strength F_{ij} describes the coupling from i to j and vice versa. If astrocytes i and j have different degrees $k_i \neq k_j$ should we then rescale the GJC strength by k_i or k_j ? Ideally, we would like to scale all GJC to new values F'_{ij} so that each pair of astrocytes i and j have identical cumulated GJC coupling strength $\sum_{k \in \mathcal{N}_i} F'_{ik} = \sum_{k \in \mathcal{N}_j} F'_{jk}$, and the average cumulated GJC coupling strength $\langle \Sigma F \rangle$ remains identical before and after scaling. Although this is not achievable because of the bidirectionality of GJC, we devised a scaling function that reduces the strength of GJC coupling between high degree nodes:

$$F'_{ij} = F_0 \left(1 + \frac{2\rho - (k_i + k_j)}{2(\max(k) - \rho)} \right) \text{ with } \rho = \frac{\mu^{(2)}(k)}{\mu^{(1)}(k)} \tag{V.1}$$

with $\mu^{(1)}(k)$ and $\mu^{(2)}(k)$, the first and second moments of the degree distribution, and $\max(k)$ the highest degree in the network. We demonstrate in Section C.1.1 that this function does not change $\langle \Sigma F \rangle$. Figure V.9 shows examples of cumulated GJC coupling distribution before (*blue histograms*) and after (*red histograms*) scaling. Because of the scaling down of GJCs between high degree nodes, the number of high ΣF values is diminished. Since the goal of this rescaling is to scale down the links of high degree nodes, we only applied it to networks which displayed heterogeneities in their degree distributions: Link Radius, Erdős-Rényi, and Spatial scale free (shortcut networks have essentially the degree distribution of lattices when p_s is small and of Erdős-Rényi networks when p_s gets higher). The effect of scaling is shown on several network topologies in Figure V.9A to H. These figures show the distributions of ΣF values before (*blue* histograms) and after (*red* histograms) rescaling across all the astrocytes from 20 realizations of the same network topology (parameters are described in the caption). On all network types, the rescaling diminished the number of highly coupled astrocytes (high ΣF values) and increased the number of intermediate coupling strengths. In particular, in Spatial Scale Free networks (Figure V.9A to D), the strongly coupled astrocytes (i.e. the hubs of the spatial scale

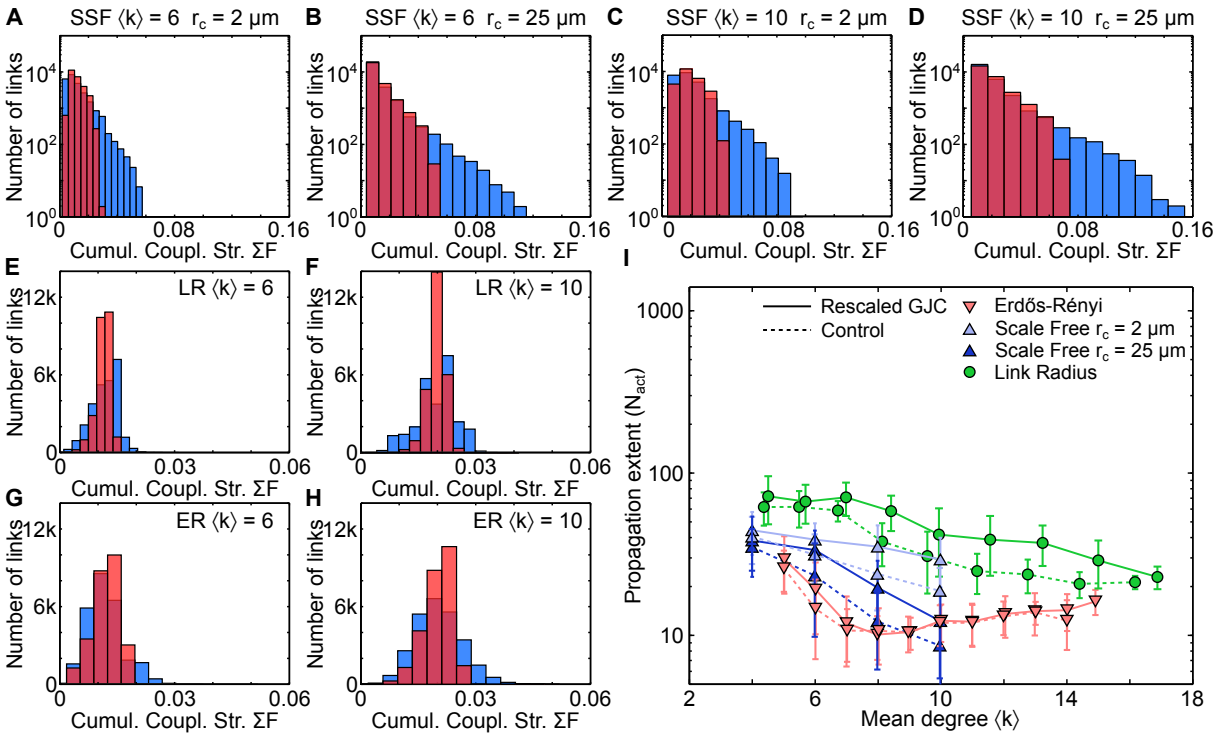

Figure V.9: GJC normalization has only minor effect on ICW propagation. **A** to **H** Distributions of cumulated coupling strengths ΣF before (*blue* histograms) and after (*red* histograms) rescaling of the GJC couplings with equation (V.1). Each histogram comprises the $20 \times N$ astrocytes from 20 realizations of the same network parameters: Spatial Scale Free networks with **A** $m_{sf} = 3$ (i.e. $\langle k \rangle = 6$) and $r_c = 2\mu$m, **B** $m_{sf} = 3$ and $r_c = 25\mu$m, **C** $m_{sf} = 5$ (i.e. $\langle k \rangle = 10$) and $r_c = 2\mu$m, **D** $m_{sf} = 5$ and $r_c = 25\mu$m; Link Radius networks with **E** $d = 85\mu$m(i.e. $\langle k \rangle \approx 6$) and **F** $d = 100\mu$m(i.e. $\langle k \rangle \approx 10$); Erdős-Rényi networks with **G** $\langle k \rangle = 6$ and **H** $\langle k \rangle = 10$. The effect of rescaling on ICW propagation is shown on **I**: rescaled networks (*solid* lines) support marginally higher propagation extents than original networks (*dashed* lines). Data points±errorbars correspond to mean values±standard deviation over 20 sampled networks with the same statistical parameters (see Methods). Astrocyte parameters as in Table V.1 except for F that has been rescaled according to equation (V.1) for (*solid* curves).

free networks, see Section III.1.3) had their links strongly scaled down. This scaling did not however significantly change ICW propagation in our simulated networks (see Figure V.9I), ICW propagation on rescaled Erdős-Rényi networks (*solid red* curve with *red* triangles) was nearly identical to its unscaled counterpart (*dashed red* curve with *red* triangles) and not really enhanced; the enhancement was marginally better for Link Radius (*solid green* curve with *green* circles) and Spatial Scale Free (*solid light blue* and *solid dark blue* with matching triangles) networks with a maximum increase of ≈ 20 activated astrocytes for Link Radius networks. Additionally, the decrease in $N_{act}$when $\langle k \rangle$ increases was still observed in rescaled networks, indicating that high degree nodes might not be responsible for this phenomenon.

While we showed in this section that the main determinants of ICW propagation in model astrocyte networks are the mean degree $\langle k \rangle$ and mean-shortest path L of networks, we

still lack a mechanistic explanation linking local propagation mechanisms and these two network-level average characteristics. In the following section, we investigate the local propagation mechanisms at play in the model and how these mechanisms link $\langle k \rangle$ and L to ICW extent.

V.3 Local propagation mechanisms

This section focuses on more theoretical aspects, the biologically inclined reader might want to skip directly to the conclusions, on page 171.

In order to understand how network-level characteristics such as mean degree $\langle k \rangle$ and mean-shortest path L can control ICW extent, as we showed in Section V.2.2, we investigate here the local propagation mechanisms that are at play in our model astrocyte networks. To this end, we first simulated propagation in simplified tree-like networks. We then inferred, from these simulations, two simple propagation rules and verified that these rules were indeed at play in full network propagation. Finally, we explain how these rules can link $\langle k \rangle$ and L to ICW extent.

V.3.1 Local connectivity model

We first remind the reader that ICW propagation follows a stereotypical sequence of steps: (1) one cell gets activated when its IP_3 level goes high enough so as to trigger CICR; (2) just after CICR, IP_3 is created by PLCδ while Ca^{2+} levels are still high; (3) this additional IP_3 will diffuse to unactivated neighbors and, if it crosses the CICR threshold in one of these cells, the ICW is transmitted to this cell, going back to step (1). Figure V.10A represents a schematic view of a propagating ICW front; astrocytes **A** and **B**, like all cells of the wave front (*light green* squares), just got activated and are susceptible to transmit the ICW to cells **C** and **D** (*grey* circles). The first thing that one might notice is that cells that have a high number of unactivated neighbors (like cell **B**) will share their PLCδ-produced IP_3 among a lot of cells and each of these will thus receive less IP_3 (as represented by thin *red arrows*). On the contrary, activated cells that have few unactivated neighbors (like cell **A**) will share their IP_3 among fewer cells and each of these cells will thus receive more IP_3 (as represented by thicker *red* arrows). From this rationale, we hypothesize that activated cells can be differentially 'activating': their propensity to transmit activation to neighboring unactivated cells will depend on their number of unactivated neighbors. Let us now focus on the cells receiving IP_3 from the ICW front (cells **C** and **D**). The local accumulation of IP_3 necessary to trigger CICR in these cells will be counteracted by diffusion to their unactivated neighbors (*blue* arrows to the rightmost cells). For example, cell **C**, which has twice as much unactivated neighbors as cell **D** will be harder to activate. From this rationale, we hypothesize that unactivated cells are differentially 'activable': their propensity to get activated will depend on the number of their unactivated neighbors.

These rationales however only hold if the quantity of IP_3 Q_0 produced during a typical cell activation is constant and does not depend on the cell degree. In this case, each unactivated neighbor receives $\frac{Q_0}{k_i^*}$ (where k_i^* is the number of unactivated neighbors of i) each time i is activated. We checked that this assertion is verified in the full network propagation experiments that we presented in Section V.2.2. For each astrocyte activation

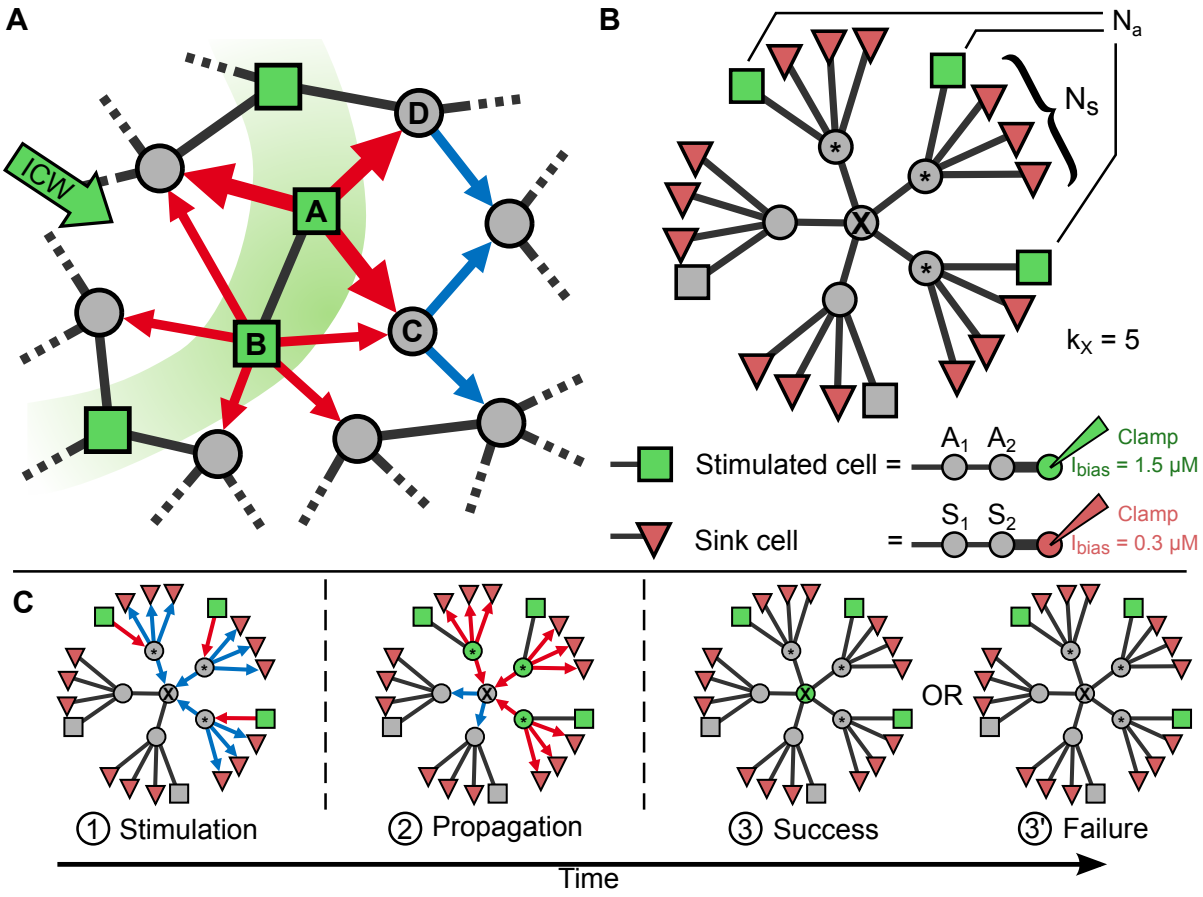

Figure V.10: Local propagation in astrocyte networks. **A** Ca^{2+} propagation to one astrocyte depends on the number of its activated connected neighbors. Unactivated cells (*gray* nodes) act in fact as IP_3 sinks, thus hindering IP_3 accumulation and CICR regeneration. In this fashion, an activated cell (*green* squares) like B that is connected to more unactivated cells than A, is less likely to allow propagation to its neighbors than the latter. For the same reason, an unactivated cell like D, which is connected to a smaller number of unactivated cells than C, is more likely to get activated. **B** Locally, ICW propagation through astrocyte networks may be approximated considering Ca^{2+} propagation from the periphery to the central cell X in a two–hop k_X-ary tree. Accordingly, activation of cell X can be studied varying (1) the number N_a of stimulated cells (*green* squares) out of the k_X stimulable cells (*gray* squares, a maximum of one per branch) and (2) the number N_s of sink cells (*red triangles*) in each branch. Astrocyte parameters as in Table 1; each sink cell is coupled to one cell that is in turn coupled to an IP_3 clamped cell (*red* circle being clamped) with $I = I_{bias} = 0.3046$ μM (equilibrium value). Small network parameters varied as in Table V.3. **C** Illustration of the course of a small network simulation: (1) stimulated cells get activated and diffuse their IP_3 (*red* arrows) to intermediate cells (marked by stars); (2) intermediate cells get activated and share their IP_3 between sink cells and the central cell (marked by an X); (3) depending on whether the central cell received enough IP_3, it either gets activated (step 3) or stays unactivated (step $3'$).

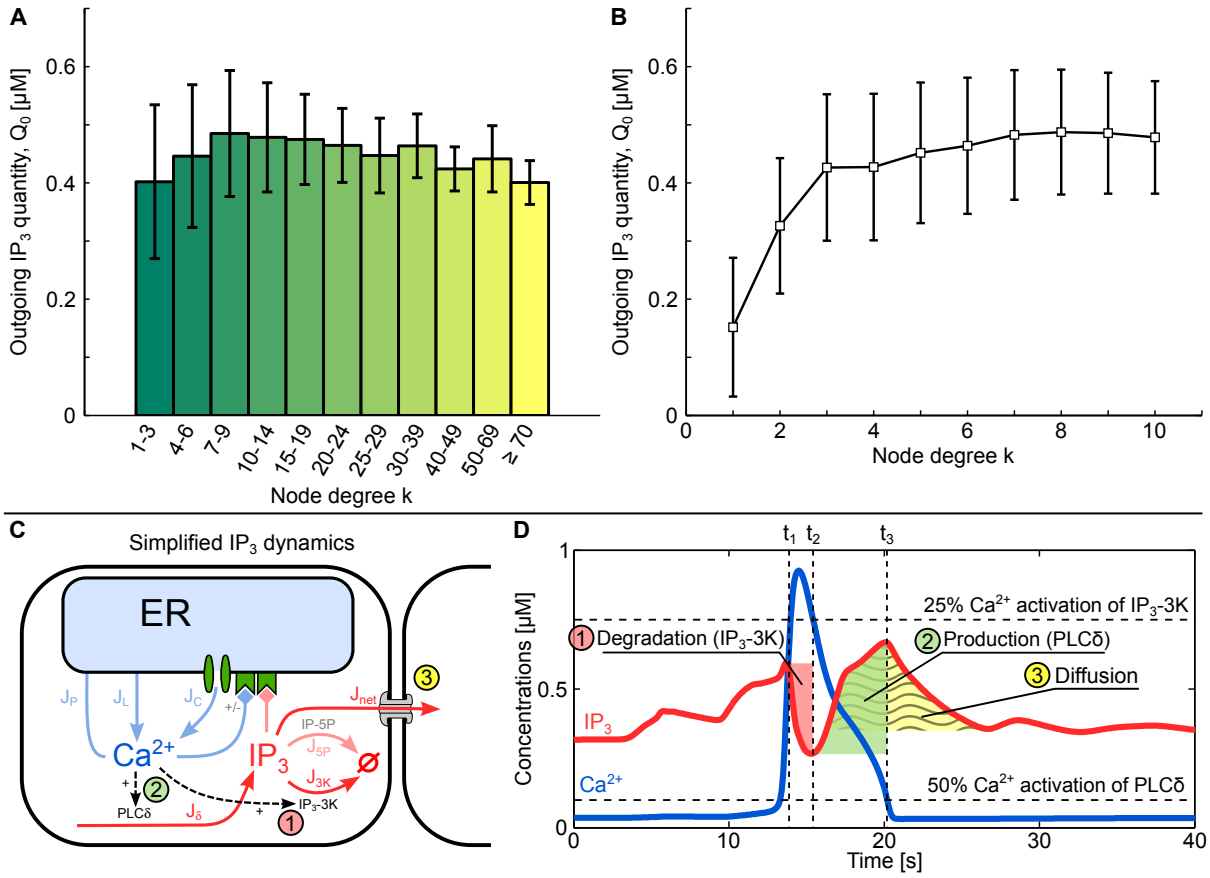

Figure V.11: Outgoing IP_3 quantity Q_0 does not depend on node connectivity. Outgoing IP_3 quantities Q_0 were obtained by integrating outgoing IP3 fluxes J_{ij} across all neighbors of each activated cell during 7s (propagation time as determined in Figure 5). **A** Q_0 is almost constant for all node degrees k. **B** Detailed values for each degree k; for $k \leq 2$, Q_0 is however lower as IP_3 can only leak to 1 or 2 cells. Stimulated nodes or neighbors of stimulated nodes were not taken into account as their outflux is biased by stimulation. Data±errorbars: mean±std on all activated nodes of degree k for 20 realizations of networks of same topology and networks parameters as in Table 2. Model parameters as in Table 1. **C** Simplified representation of what happens during a stereotypical Ca^{2+} rise. **D** Typical Ca^{2+} and IP_3 traces during the activation of an astrocyte.

in the simulations, we integrated IP_3 outfluxes to all neighbors during a time window of duration $\Delta t_{flux} = 7$s (which corresponds to the typical transmission time with the parameters that we used). Figure V.11A displays the mean IP_3 quantity Q_0 transfered by one cell (i.e. its cumulated outfluxes) binned by cell degree k; For all degree bins, Q_0 only displays small variations around 0.4μM. Detailed values for small cell degrees are displayed in Figure V.11B; for $k \geq 3$, Q_0 stays relatively constant. As represented in Figure V.11C and D, this can be understood by looking at the PLCδ production term in equation (II.14); the production of IP_3 mainly depends on the cytoplasmic Ca^{2+} since IP_3-dependent inhibition of PLCδ activity is negligible for IP_3 concentrations lower than $\kappa_\delta = 1.5\mu$M. During the Ca^{2+} peak, the following events take place:

1. When Ca^{2+} quickly increases during CICR, at time $t = t_1$ (in Figure V.11D), it activates both PLCδ (which creates IP_3) and IP_3-3K (which degrades IP_3); the overall result is however dominated by IP_3-3K activity and IP_3 thus decreases (*red* part of the IP_3 curve in Figure V.11D).

2. when Ca^{2+} starts getting reintegrated into the ER, at time $t = t_2$, IP_3-3K is no longer strongly activated while PLCδ remains activated, the overall activity now results in IP_3 creation (*green* part of the IP_3 curve on **D**) which readily diffuses to unactivated neighbors (*yellow wavy* part of the IP_3 curve in Figure V.11D).

3. When Ca^{2+} returns to equilibrium, at time $t = t_3$, PLCδ is no longer substantially activated and the excess IP_3 continues diffusing to unactivated neighbors (*yellow wavy* part of the IP_3 curve in Figure V.11D).

The *green* shaded area in Figure V.11D is thus responsible for the bulk of the IP_3 production in the astrocyte. Since this production only depends on Ca^{2+} concentration (see Figure V.11C *green* circle labeled 2) and since the Ca^{2+} peak has a stereotypical shape, IP_3 production is thus nearly identical for every astrocyte activation, regardless of the number of unactivated neighbors it might have. In particular, lowered IP_3 concentration due to diffusion to unactivated neighbors does not affect IP_3 production. The specific case $k = 1$ is not of interest to our study because the astrocyte has been activated by its only neighbor and will thus not propagate the ICW further. For $k = 2$, random networks are below the percolation threshold (Albert and Barabási, 2002) (i.e. they consist of small disconnected sub-components) and are thus unable to propagate ICW regardless. For chain networks however, ICW transmission is possible and we must keep in mind that the 'constant Q_0' approximation that we use in this section no longer holds for chain networks or networks which have a significant amount of cells with degree 2. For such low degrees, unactivated neighbors are unable to drain IP_3 quickly enough from activated astrocytes; it thus accumulates and gets degraded by IP-5P instead of being used to elicit CICR in a neighboring astrocyte. For astrocytes with either low degree or low GJC strength F, if IP_3 accumulates above a certain threshold, it can cause the cell to switch from cell state (1) to cell state (2) (Figure V.8), in which IP_3 and Ca^{2+} levels always stay elevated. The cumulated IP_3 outflux in a given time window is smaller for these astrocytes but, because their Ca^{2+} concentration is high enough to activate PLCδ but too low to activate IP_3-3K, they produce IP_3 for an indefinitely long time. Q_0 values for these astrocytes is thus virtually infinite, explaining why very low degree or low GJC strength F both lead to very high propagation extents.

Table V.3: Local connectivity model parameters.

Symbol	Description	Values			Units
		min	step	max	
k_X	Degree of cell X (center cell)	3	1	15	-
N_a	Number of stimulated branches	1	1	k_X	-
N_s	Number of sink neighbors in each branch	0	1	5	-

To quantitatively investigate how the local network structure influences ICW transmission, we simulated a simplified tree-like model of an astrocyte neighborhood (Figure V.10B). We considered a central astrocyte together with its two-hop tree-like neighborhood: the central astrocyte X was linked with k_X astrocytes and each of these astrocytes was linked to N_s 'sink' astrocytes (*red* triangles) and one 'stimulable' astrocyte (squares). Sink astrocytes (*red* triangles in Figure V.10B and S_1 cell in the legend) were linked to one astrocyte (S_2 cell in the legend) that was prevented from activating by being coupled to an IP_3-clamped astrocyte at equilibrium (*red* circle being clamped in the legend). We chose not to directly couple the sink cells to IP_3-clamped cells in order to allow their activation, as it might happen in full network propagation. During a simulation of this simplified tree-like model, we stimulate N_a stimulable astrocytes (*green* squares) among the k_X branches and monitor whether the central node X gets activated when the wave propagates from the periphery to the center. As for the sink cells, the stimulated astrocytes (*green* squares in Figure V.10B and A_1 cell in the legend) are not directly stimulated to avoid boundary effect but are instead coupled to an astrocyte (A_2 cell in the legend) which is stimulated by being coupled to an IP_3-clamped astrocyte until it activates. After its activation, we remove the clamped cell in order not to add any additional IP_3. Once the stimulated cells become activated, the events represented in Figure V.10C unfold:

1. IP_3 diffuses (*red* arrows) from stimulated cells to the intermediate cells (cells marked by stars) and leaks from the intermediate cells to sink cells and to the central cell (*blue* arrows), if intermediate cells get activated, we proceed to step 2.
2. The constant quantity of IP_3 Q_0 produced by intermediate cells is shared among sink cells and the central cell [1] which also leaks IP_3 to the 2 unactivated intermediate cells.
3. The central cell gets activated if it received enough IP_3 and if it did not leak too much IP_3 to unactivated intermediate cells (step 3). Otherwise, it stays unactivated (step 3′).

With this setup, k_X can be thought of as the network mean degree $\langle k \rangle$: when it increases, the central astrocyte gets harder to activate because it leaks IP_3 to a higher number of cells; we will refer to this process as a decrease of the central cell's 'activability'. When making the parallel between this simplified tree-like network and an actual astrocyte network, we can see the stimulated cells as the ICW front and the sink cells as unactivated parts of the network, that will take IP_3 from the wave front. When the number of sink cells increases, activated intermediate need to share their IP_3 among a higher number of unactivated neighbors (*red* arrows in Figure V.10C, step 2) and will thus give less IP_3

1. the stimulated cells still have high IP_3 concentration at this point so they do not act as sinks

to the central cell; we will refer to this process as a decrease in the 'activatingness' of activated intermediate cells. The two control parameters k_X and N_s thus allow us to separately change the intermediate cells 'activatingness' and the central cell 'activability'.

For each combination of k_X and N_s, we vary the number of stimulated cells N_a from 1 to k_X (c.f. Table V.3). We denote the minimum number of stimulated branches that are needed to activate the central astrocyte X by $N_\theta(k_X, N_s)$. This value changes when k_X and N_s are varied but, as shown in Figure V.12A, $N_\theta(k_X, N_s)$ increases almost linearly with N_s and the slope of this increase depends on k_X: the higher k_X, the higher the slope. This first relationship can easily be understood by looking at Figure V.10C during the propagation step 2: the $N_\theta(k_X, N_s)$ intermediate nodes that are linked to X in the stimulated branches (*grey* cells marked by a star) activate and produce a quantity Q_0 of IP_3 through PLCδ; this IP_3 is then mainly shared among the N_s sink astrocytes and the central cell (since the stimulated branch has already high IP_3 levels); since the network is symmetric, the central cell receives the same amount of IP_3 Q_i from each neighbor i in a stimulated branch. The quantity of IP_3 Q_X received by the central cell thus reads:

$$Q_X(k_X, N_s) = \sum_{i=1}^{k_X} Q_i = \sum_{i=1}^{N_\theta(k_X,N_s)} \frac{Q_0}{N_s+1} = \frac{N_\theta(k_X, N_s)Q_0}{N_s+1} \tag{V.2}$$

We thus define the minimum normalized IP_3 quantity $\psi_\theta(k_X, N_s)$ required to activate the central cell as:

$$\psi_\theta(k_X, N_s) = \frac{Q_X(k_X, N_s)}{Q_0} = \frac{N_\theta(k_X, N_s)}{N_s+1} \tag{V.3}$$

Since $N_\theta(k_X, N_s)$ and N_s+1 are roughly proportional (see Figure V.12A), for a given k_X, we define the mean normalized IP_3 quantity $\Psi_\theta(k_X) = \frac{1}{N_s^{max}+1}\sum_{N_s=0}^{N_s^{max}} \psi_\theta(k_X, N_s)$ needed to activate a node of degree k_X as the average $\psi_\theta(k_X, N_s)$ values across the different N_s values (with N_s^{max} the highest N_s value). For simplicity, we denote $\Psi_\theta(k_X)$ as Ψ_θ.

We expressed Ψ_θ values as a function of central cell degree k_X for nonlinear (Figure V.12B) and linear (Figure V.12C) GJC. For both GJC types, increasing the central cell degree k_X increases the normalized IP_3 quantity Ψ_θ needed to activate the cell. This means that the central cell must receive more IP_3 in order to get activated when its degree increases. We can interpret this as a consequence of the second rule of propagation that we stated earlier: cells are less 'activable' when they have high numbers of unactivated neighbors. Increasing cell degree effectively increases the quantity of IP_3 that will leak out of it before it gets activated (*blue* arrows in Figure V.10A), thus increasing the quantity of IP_3 needed to activate it. In most cases, increased degree thus impairs local IP_3 accumulation; this is no longer true however when the threshold gradient for diffusion with nonlinear GJC I_θ is high enough. For $I_\theta = 0.4\mu$M (Figure V.12B, *blue* triangles) and $I_\theta = 0.5\mu$M (Figure V.12B, *purple* triangles), IP_3 can never leak out of a cell before it gets activated and Ψ_θ thus becomes essentially independent from k_X. This effect cannot be observed with linear GJC since IP_3 diffuses even for low gradients, systematically hindering IP_3 accumulation in astrocytes. Accordingly, Ψ_θ always increases with k_X for linear GJC regardless of the GJC strength F (Figure V.12C). To quantify the effect of cell degree on ICW propagation, we considered the slope $\gamma = d\Psi_\theta/dk_X$ of the relationship

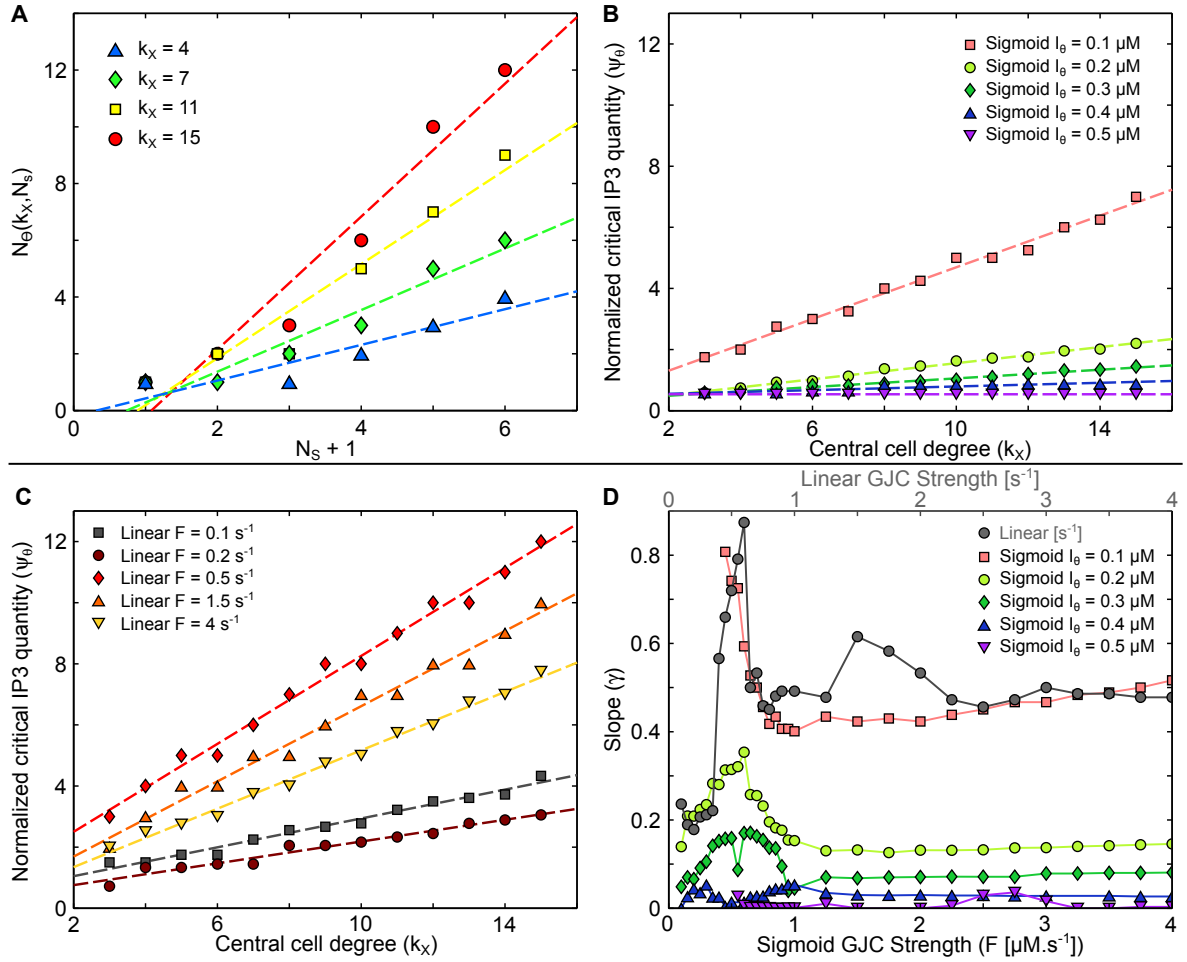

Figure V.12: Threshold stimuli for propagation depend on local connectivity. **A** The minimum number of branches (N_θ) in the k_X-ary tree (Figure V.10B) that have to be activated to allow ICW propagation to cell X, increases with the number of sink cells (N_s) in an essentially linear fashion (*dashed lines*). The mean normalized IP_3 quantity Ψ_θ needed to activate cell X generally increases in a linear fashion (*dashed lines*) with the degree k_X of the central cell. This holds true for both **B** nonlinear and **C** linear intercellular IP_3 diffusion, although the linear dependence on k_X is different in the two cases. **D** Except for very low threshold values for IP_3 intercellular diffusion, the slope γ ($d\Psi_\theta/dk_X$) of the linear fit of Ψ_θ vs. k_X is generally steeper for linear than nonlinear IP_3 diffusion. That is, for the same central cell degree k_X, the number of peripheral cells that need to be activated to ensure ICW propagation through cell X is larger with linear IP_3 diffusion than with nonlinear one. Note that F is not expressed in the same units for linear (s^{-1}) and nonlinear ($\mu M.s^{-1}$) IP_3 diffusion. **B**, **C**: Data points correspond to mean values of $\Psi_\theta(k_X, N_s)$ computed for $N_s = \{0, \ldots, 5\}$. Stimulus protocol and model parameters as in Figure V.10.

between Ψ_θ and k_X. Figure V.12D shows γ values for nonlinear and linear GJC as a function of GJC strength F; for nonlinear GJC with IP_3 diffusion threshold $I_\theta \geq 0.2$ (*light green* circles, *dark green* diamonds, *purple* and *blue* triangles), γ increases with F for low GJC strengths but as soon as F becomes greater than $0.5\mu M.s^{-1}$, it continuously decrease until it stabilizes at a non-zero value. Consistent with Figure V.12B, increasing the value of the IP_3 diffusion threshold I_θ lowers γ regardless of GJC strength. Nonlinear GJC with $I_\theta = 0.1\mu M$ (*light pink* squares), since their threshold for IP_3 diffusion is smaller, display γ values that follow closely that of linear GJC (*gray* circles) for $F \geq 0.5\mu M.s^{-1}$. For linear GJC however, γ displays a slightly different type of behavior as F increases: (1) Low F values around $0.25s^{-1}$ facilitate propagation (Figure V.12C, *grey* squares and *brown* circles); (2) further increases in GJC strength allows faster IP_3 leak from the central cell, thus preventing propagation and increasing γ; (3) beyond $F = 0.6s^{-1}$, γ decreases back, reaching values close to those reached by nonlinear GJC with low I_θ, but never goes back to its minimal value at small GJC strength F.

The main prediction of these figures are that:

1. Linear GJC (as it leads to higher γ slopes than nonlinear GJC) should impair ICW propagation in full network propagation. Additionally, the best propagation extent for linear GJC should be obtained with low GJC coupling strength F.
2. Nonlinear GJC with high I_θ values (as they allow the accumulation of more IP_3 in astrocytes) should increase ICW extent in full network simulations.

In the next subsection, we go back to full network propagation and ensure that the local propagation mechanisms that our analysis suggested are indeed at play in the full network model.

V.3.2 Local effects control full network propagation

If the above local propagation analysis extends to full network propagation, we should witness two phenomena: (1) with linear GJC, ICW extent should be always smaller than with nonlinear GJC and maximum for $F = 0.25s^{-1}$; (2) for nonlinear GJC, ICW extent should increase with higher I_θ values. Moreover, we checked in Appendix C.1.2 that normalized IP_3 quantities received by astrocytes were above Ψ_θ for activated astrocytes and below Ψ_θ for unactivated ones.

Linear GJC When simulating full network propagation with the same settings as in Section V.2.2 but with linear GJC with $F = 0.25s^{-1}$, ICW extent was greatly reduced compared to nonlinear GJC (cf Figure V.13A) and higher GJC strength F could only decrease N_{act} (inset for networks with $\langle k \rangle \approx 6$, corresponding to the *black dashed* line on the main figure). Similarly to the simulations in Section V.2.2, the network mean degree $\langle k \rangle$ still had a deleterious effect on wave propagation, in accordance with the local propagation analysis since Ψ_θ always increased with cell degree for linear GJC (Figure V.12C). Interestingly, further reduction of GJC coupling (lower than $0.2s^{-1}$) lead to full network

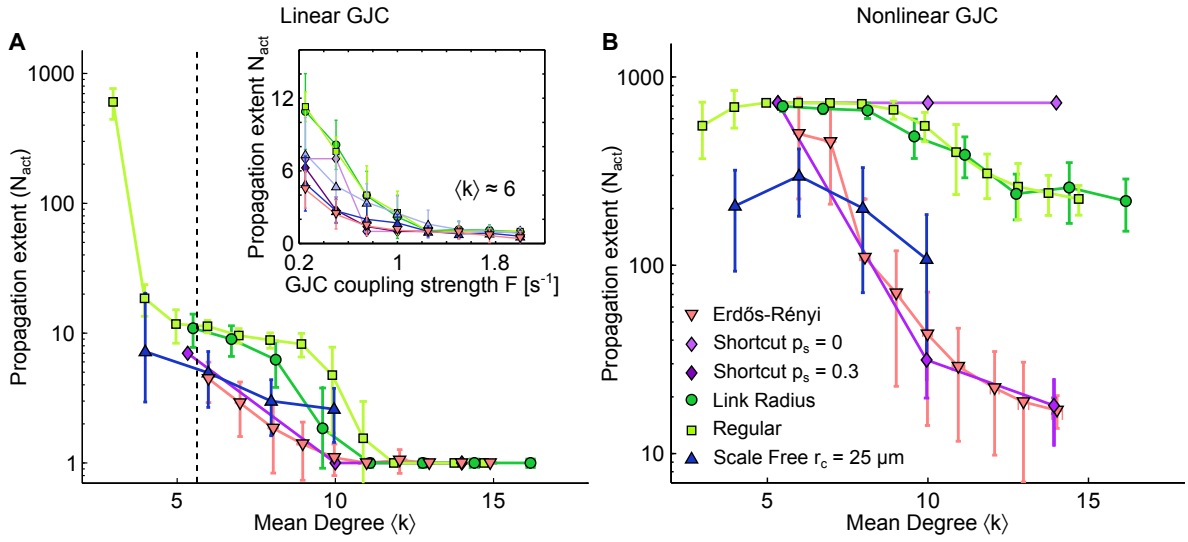

Figure V.13: Dependence of ICW propagation on IP3 diffusion. **A** Extent of ICW propagation (N_{act}) in astrocyte networks generally decreases with the cell mean degree ($\langle k \rangle$) but it is generally limited to few cells (<10) in the assumption of linear intercellular IP3 diffusion, independently of network topology. The only possible exception is for spatially–constrained networks such as regular networks with $\langle k \rangle \leq 3$. **Inset** shows the decrease of ICW extent N_{act} when the GJC coupling strength F is increased in networks with $\langle k \rangle \approx 6$ (*dashed black* line in the main figure). In contrast to the main figure, the y-scale is linear. **B** In contrast, the propagation extent is much larger in presence of a threshold (I_θ) for intercellular IP3 diffusion (I_θ). Comparison with Figure 3A in particular, suggests that in the same network, the larger this threshold, the larger N_{act}. Data±errorbars: mean±std on 20 realizations of networks of same topology. **A**: $F = 0.25$ s^{-1}; **B**: $I_\theta = 0.5$, $F = 2$ μM s^{-1}. Other parameters as in Figure 3A.

propagations of state 2 astrocyte equilibrium (not shown on figures), as we witnessed in nonlinearly coupled astrocyte networks in Section V.2.3.

Nonlinear GJC With nonlinear GJC, using $I_\theta = 0.5\mu$M, ICW extents were greatly improved for all networks as displayed in Figure V.13B. Increasing mean degree $\langle k \rangle$ however also decreases N_{act}, hinting that the degree of cells could act not only on ICW propagation by increasing IP_3 leak from unactivated cells but could also decrease the 'activatingness' of astrocytes. In accordance with Figure V.12B, lowering I_θ from 0.5μM to 0.1μM continuously decreased ICW extent for all network classes.

To check that the normalized quantity of IP_3 Ψ_θ needed to activate the central cell in our simplified network was also at play in full network propagation, we estimated normalized IP_3 quantities received by activated astrocytes in full network propagation by relying on the same assumption than in Section V.3.1: namely that the IP_3 from an activated astrocyte is divided evenly among its unactivated neighbors. These estimations confirmed in full network propagation, the behavior observed in our simplified tree-like network: activated astrocytes received estimated normalized IP_3 quantities that were above the Ψ_θ

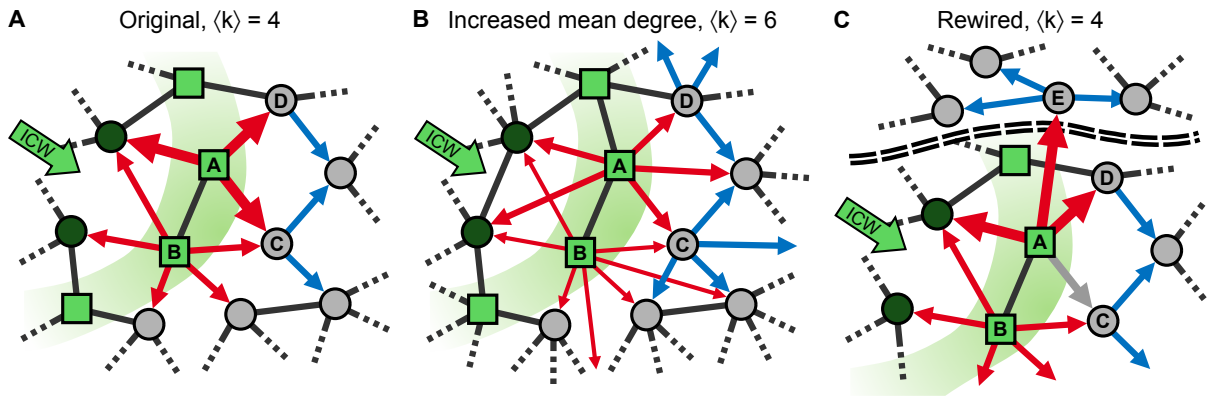

Figure V.14: Effect of shortcuts on ICW propagation. Connections (in *grey*) of astrocyte A in the local network of Figure V.10A were rewired from cells marked by '*' to a cell E located in a far unactivated area of the same network (separated by *dashed lines*). **A** The additional connection between cells A and E reduces the IP_3 supply from cell A to cells C and D hindering ICW propagation to them. **B** Similarly, cell C is supplied by less IP_3 if it were not connected with A but only with B due to the existence of the long distance connection between A and E. Long distance connections thus generally hamper ICW propagation, as they reduce IP_3 supply to individual cells, counteracting its accumulation up to the CICR threshold.

threshold while unactivated astrocytes received sub-threshold normalized IP_3 quantities. We then measured actual IP_3 quantities received by astrocytes in full network propagation by integrating the J^{diff} term in equation (II.21). These measured values were also above threshold for activated astrocytes and below threshold for unactivated ones. Detailed simulations and analysis are reported in Section C.1.2.

This local propagation analysis has thus shed light on how mean degree $\langle k \rangle$ and mean-shortest path L can have such a strong influence on ICW propagation. The two propagation rules that we inferred from local propagation analysis both play a role in these effects. To illustrate this, let us consider an original network with low mean degree and no long-distance links (Figure V.14A) and imagine what happens when the mean degree is increased (Figure V.14B) or when long distance links are added (Figure V.14C). Increasing the mean degree (Figure V.14B) has two different effects; first, since astrocytes can be differentially 'activating' depending on their number of unactivated neighbors, their 'activatingness' is decreased as they split the constant quantity of IP_3 that they produce (Q_0) among a larger number of astrocytes (smaller *red* arrows). Since the quantity of IP_3 received by unactivated astrocytes is thus decreased, it is harder for them to cross their activation threshold ψ_θ. The activated astrocytes are not the only ones affected since increasing the mean degree also impacts the second propagation rule: unactivated astrocytes leak IP_3 (*blue* arrows) to their unactivated neighbors quicker (with k_u unactivated neighbors, the outflux with nonlinear GJC can be up to $k_u F$). This second effect corresponds to the increase of ψ_θ with the cell degree visible in Figure V.12B. Reductions in mean-shortest path can be achieved through two main ways: (1) increasing the mean degree, whose effect have already been discussed, and (2) adding long-distance links, or shortcuts in the network without changing $\langle k \rangle$. Figure V.14C represents a network in which a long distance link have been added by rewiring an edge between cells **A** and **C**

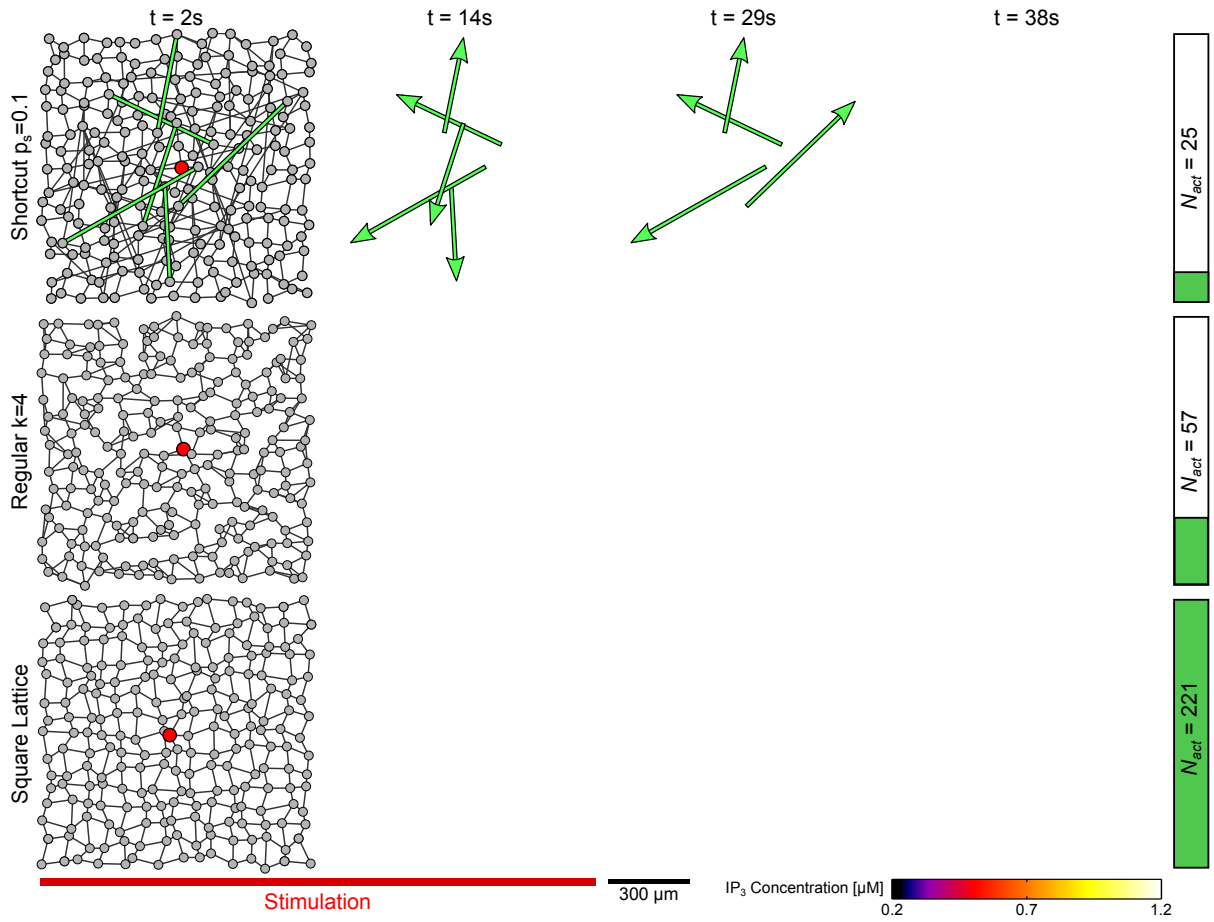

Figure V.15: Effect of long-distance GJC-coupling on ICW propagation. Snapshots of IP_3 concentration (see Supplementary Material S1.4) at different time instants in three 2D networks (shown in the *leftmost panels*): a shortcut network with $p_s = 0.1$ (*top row*); a regular network with $\langle k \rangle = 4$ (*middle row*); and a square lattice also with $\langle k \rangle = 4$ (*bottom row*). The presence of long-distance connections (*green edges*) in the shortcut network causes IP_3 transport away from the wave front, hampering ICW propagation. This is reflected by a considerably lower value of the number of cells activated by the ICW (N_{act}, *right vertical bars*) in the shortcut network compared to the other two networks. The ICW was triggered by stimulating the astrocyte marked in *red* (*leftmost panels*) from 0 s to 25 s (*red bar*). Astrocyte parameters as in Table V.1. Snapshots computed as explained in Appendix A.1.

(*gray* arrow) to a distant unactivated cell **E**, remote from the ICW front (the remote part of the network is separated by a *black dashed* double line). Having done so, cell **A** still has the same 'activatingness' but the quantity of IP_3 that used to be received by cell **C** is now 'lost' in a remote part of the network. If a link is instead rewired from cell **B** (on the ICW front) to cell **E**, cell **A** decreases its activatingness by increasing its number of unactivated neighbors. Both of these scenarios hamper wave propagation.

To illustrate the impact of long distance links on ICW propagation, we monitored IP_3 concentrations during ICW propagation on 2D astrocyte networks with different topologies. Figure V.15 illustrates how an ICW propagates on networks ranging from very

organized and spatially constrained topologies (square lattice, *bottom row*), to spatially constrained topologies (regular degree network, *middle row*), to spatially unconstrained topologies with long distance links (shortcut network with $p_s = 0.1$, *top row*). In all these networks, the mean degree $\langle k \rangle = 4$ is constant and the differences in ICW extent (*green* bar on the right) can only be attributed to either the presence of long distance links or to the detailed network topology. As expected from the local analysis, ICW propagation in spatially unconstrained networks is highly impaired due to the leak of IP_3 to regions of the network remote from the propagation front (*green* arrows on *top row*). As the ICW unfolds (snapshots from left to right), the number of long distance links in the region spanned by the ICW grows until the loss of IP_3 to distant parts of the network eventually terminate the ICW at $t = 29$s (last columns). In contrast, for spatially constrained networks, IP_3 from activated astrocytes is not 'lost' in distant part of the networks and the ICW thus propagates after $t = 29s$ (last column) and activate at least twice as many astrocytes. Finally, as previously observed in full 3D network stimulations (Figure V.5A), lattice topologies support much better propagation than regular degree networks despite their remarkable resemblances (they exhibit the exact same degree distribution and are both spatially constrained). This particular behavior will be investigated in Section V.5.

We have therefore unveiled above the local propagation rules that account for the effect of $\langle k \rangle$ and L on ICW extent. In the next section, we simulate a reduced model of ICW propagation based on these two simple propagation rules.

V.4 A simplified model of ICW propagation

V.4.1 ICW propagation in astrocyte networks can essentially be described by a three-state model

Having extracted two simples rules of ICW propagation from our local propagation analysis, we now simulate a very simplified three-state model of ICW propagation to check whether these simple rules can indeed account for the effects of $\langle k \rangle$ and L on ICW extent. In this section, we will thus forget about the full ChI model and work on a very simplified stochastic cell automaton-like model. In this latter, an astrocyte can only be in one of three states: (U)nactivated, which constitutes the resting state; (A)ctivated, which represents the time during which the astrocyte produces IP_3 in the full ChI model; and (R)efractory, which is a state that always follows the activated one and in which an astrocyte no longer gives IP_3 to its neighbors but cannot get activated. In this simplified UAR model (named after the 3 states), time is increased in discrete steps; at each time step, astrocytes can switch from one state to another according to some transition probabilities. We designed these three states and their transitions by examining the actual dynamics of astrocytes in the full ChI model. Figure V.16 shows, on the left, Ca^{2+} and IP_3 traces from two astrocytes (cell 1 and cell 2) which are linked by GJC and support an ICW traveling from cell 1 to cell 2. We illustrate on the full traces the equivalent states in the UAR model: the activated state starts when IP_3 levels cross the threshold for CICR initiation (*dotted black* horizontal line) and ends when IP_3 levels go under the threshold for nonlinear GJC diffusion (*dashed black* horizontal line). During this time, which lasts approximately $\tau_A = 9.5$s, IP_3 diffuses from cell 1 to cell 2 in which IP_3 eventually crosses the threshold for CICR initiation, leading to its activation. The time delay between activation of cell 1 and cell 2, or the transmission time, is approximately $\tau_U = 7$s. After being activated, the cell enters the refractory state which duration was estimated from the maximum period of oscillation $T = 16$s of the ChI model; the time during which the cell stays in the refractory period is thus $\tau_R = T - \tau_A = 6.5$s. Cells are then back in the unactivated state and stay unactivated until the next ICW arrives. In the UAR model, the transition probabilities (top right part of Figure V.16) were devised according to the behavior of the ChI model. In the ChI model, although the time spent in the activated and refractory states is variable, it is mostly independent from the activity of neighboring astrocytes and mainly dependent on the internal biophysical parameters that determine the creation of IP_3 and the oscillation frequency. In consequence, we decided, in the UAR model, to use constant transition rates (or probabilities) $k^{A \to R}$ and $k^{R \to U}$ to model the switching between activated, refractory, and unactivated states; the time spent in these two states thus displays variability while begin independent from other astrocytes. The remaining transition, from unactivated to activated, is however more complex since it depends on the activity of other astrocytes; it will thus be modeled by an activity-dependent transition probability $p^{U \to A}$ which takes into account the activity of neighboring astrocytes. The resulting UAR model display activity traces (right part of Figure V.16) that resemble those of the full ChI model (left part) despite being considerably much simpler.

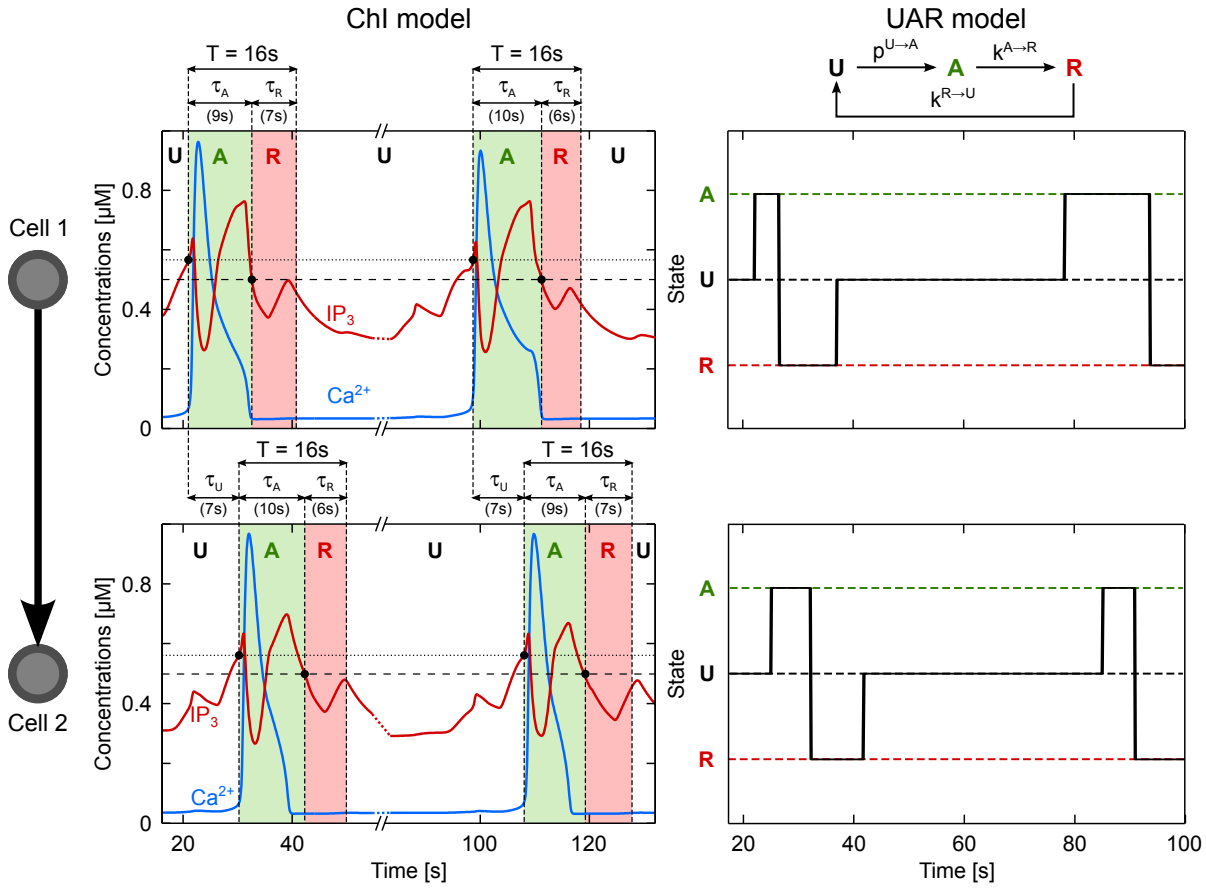

Figure V.16: A simplified description of ICW propagation. The propagation of an ICW through an astrocyte may be regarded as a three-state process, as illustrated here for the case of two connected astrocytes (cell 1, *top panel*; cell 2, *bottom panel*). These astrocytes are in the unactivated state (U) when at rest. Upon arrival of an ICW (when the IP_3 level crosses the threshold for CICR initiation, *dotted line*), the transient increase of intracellular Ca^{2+} (*blue traces*) occurring first in cell 1 then in cell 2, activates these cells (A, *green regions*). Following activation, each cell recovers to rest through a refractory period (R) when their IP_3 value falls below the threshold gradient for intercellular diffusion (*dashed line*). The time constant of each transition may be estimated accordingly. τ_U coincides with the delay between the Ca^{2+} increases in cell 1 and in cell 2. τ_A is estimated by the time interval from the beginning of the Ca^{2+} elevation to the point where IP_3 gets below the diffusion threshold. Finally, τ_R is estimated by $\tau_A + \tau_R = T$ where T ($= 16$ s in this example) represents the minimum period of Ca^{2+} oscillations in a single cell. Astrocyte parameters as in Table V.1.

Our UAR model is reminiscent of SIR models of infection propagation (Newman, 2003) or SERS models of activity (Müller-Linow et al., 2008). In the UAR model, the rates $k^{A\to R} = 1/\tau_A$ and $k^{R\to U} = 1/\tau_R$ (the rates at which cells switch from the activated state to the refractory one and from the refractory to the unactivated, respectively) are constant and are calibrated such that the mean waiting time in each state A and R matches the times in the full ChI model. These rates correspond to the infected to resistant transition in the SIR models and to the excited to refractory and refractory to susceptible in the SERS model. In both of these models however, the transition of a node i from the basal susceptible state to the infected (or excited) state usually depends on the immediate neighborhood of i. For example, in the SERS model presented in Müller-Linow et al. (2008), a node gets excited if there is at least another excited node in its neighborhood. The strongest difference between the UAR model and these other models thus resides in the activation probability $p^{U\to A}$ which takes into account the two rules of local propagation. For a given cell i, we need to known the 'activatingness' of i's neighbors at time t to determine whether it will get activated, we thus first compute a value $\beta_j(t)$ that is comparable, in the ChI model, to the normalized quantity of IP_3 $Q_{j\to i}/Q_0$ that each neighbor j will give to i with:

$$\beta_j(t) = \begin{cases} 1/N_j^{\mathrm{u}}(t) & \text{if } j \text{ is in the activated state at time } t \\ 0 & \text{otherwise} \end{cases} \tag{V.4}$$

with $N_j^{\mathrm{U}}(t)$ the number of unactivated neighbors of cell j at time t. In Section V.3, we showed that an astrocyte could only get activated if the total normalized quantity of IP_3 that it received exceeded a degree-dependent threshold ψ_θ. Accordingly, in the UAR model, the equivalent to the normalized quantity of IP_3 received by i is the sum of the 'activatingnesses' of i's neighbors. The activation probability is thus defined as:

$$p_i^{U\to A} = \begin{cases} k^{U\to A} & \text{if } \sum_{j\in\mathcal{N}_i}\beta_j \geq \vartheta_i \\ 0 & \text{otherwise} \end{cases} \tag{V.5}$$

with $\mathcal{N}_i$ the set of i's neighbors and ϑ_i the threshold below which the cell cannot get activated (similar to Ψ_θ defined in Section V.3, equation (V.3)). Consequently, as in the local propagation analysis, the activation probability of an astrocyte depends on the node's degree through its activation threshold ϑ (c.f. Figure V.12B):

$$\vartheta_i = a \times k_i + b \tag{V.6}$$

With k_i the degree of cell i and a and b corresponding respectively to the slope and intercept of the curves in Figure V.12B. Values of these parameters for all UAR simulations are given in Table V.4. Simulation time was taken to be identical to full ChI model simulations, $T_{sim} = 200$s. To initiate the ICW, we kept the central astrocyte and its neighbors in the activated state during the whole simulation as these cells were consistently activated by IP_3 stimulation (cf Figure C.2 for $r = 1$) for almost all networks (with the exception of some spatial scale free networks).

Table V.4: UAR model parameters.

Symbol	Description	Values	Units
τ_U	Average time needed to activate an astrocyte	7	s
τ_A	Average activation time of an astrocyte	9	s
τ_R	Average refractory time of an astrocyte	6.5	s
a	Slope of the relationship between k_i and ϑ_i	0.02	-
b	Intercept of the relationship between k_i and ϑ_i	0.205	-

V.4.2 The UAR model qualitatively reproduces full ChI model ICW extents

Figure V.17 displays UAR model simulations using the same networks that we used in Figure V.5 for full ChI model simulations. The qualitative behavior observed for all networks is the same in the UAR model as in the full ChI model. Figure V.17A shows the relationship between the mean degree $\langle k \rangle$ and the ICW extent N_{act}; as in Figure V.5A, increasing the mean degree decreased ICW extent for all networks and the same segregation is observed between spatially constrained networks which support large ICWs and spatially-unconstrained networks which do not. The behavior of spatial scale free networks is less clear than with the full ChI model; when long distance links are authorized ($r_c = 25\mu$m, *dark blue* triangles), ICW propagation is impaired compared to spatial scale free networks without long distance links ($r_c = 2\mu$m, *light blue* triangles). Figure V.17B shows ICW extent as a function of mean-shortest path L, the behavior of all networks is again the same one as observed in the full ChI model (cf Figure V.5B): decreasing the mean-shortest path (by adding shortcuts for example) always impairs ICW propagation. As for $\langle k \rangle$, the networks are segregated between spatially constrained and spatially unconstrained networks and spatial scale free networks (*dark blue* triangles) can be in either one of these two groups depending on the value of r_c, a behavior that was also witnessed with the full ChI model. This effect of L is not only due to the fact that increasing $\langle k \rangle$ usually amounts to decreasing L. It can indeed be seen in Figure V.17C that even at constant $\langle k \rangle$, adding long-distance links in shortcut networks by increasing the rewiring probability p_s also decreases ICW extent as it did in the full ChI model (cf Figure V.5C). While the detailed values of N_{act} are not the same between the ChI and the UAR model, their behaviors when $\langle k \rangle$ or L are varied are qualitatively identical in both cases. Interestingly, the UAR model even reproduces the difference in propagation extent between cubic lattices (i.e. shortcut networks with $p_s = 0$ and $m_{latt} = 1$) and regular degree networks with $k = 6$ (Figure V.17D). Both of these networks are spatially constrained and share the same mean degree $\langle k \rangle = 6$. The protocols that we used to create them are very similar and yet cubic lattices propagate ICWs to a much larger extent than regular degree networks.

In the next section, we investigate the cause of these discrepancies by looking at ICW propagation as a shell-by-shell activation process and by taking into account the shell structure of networks.

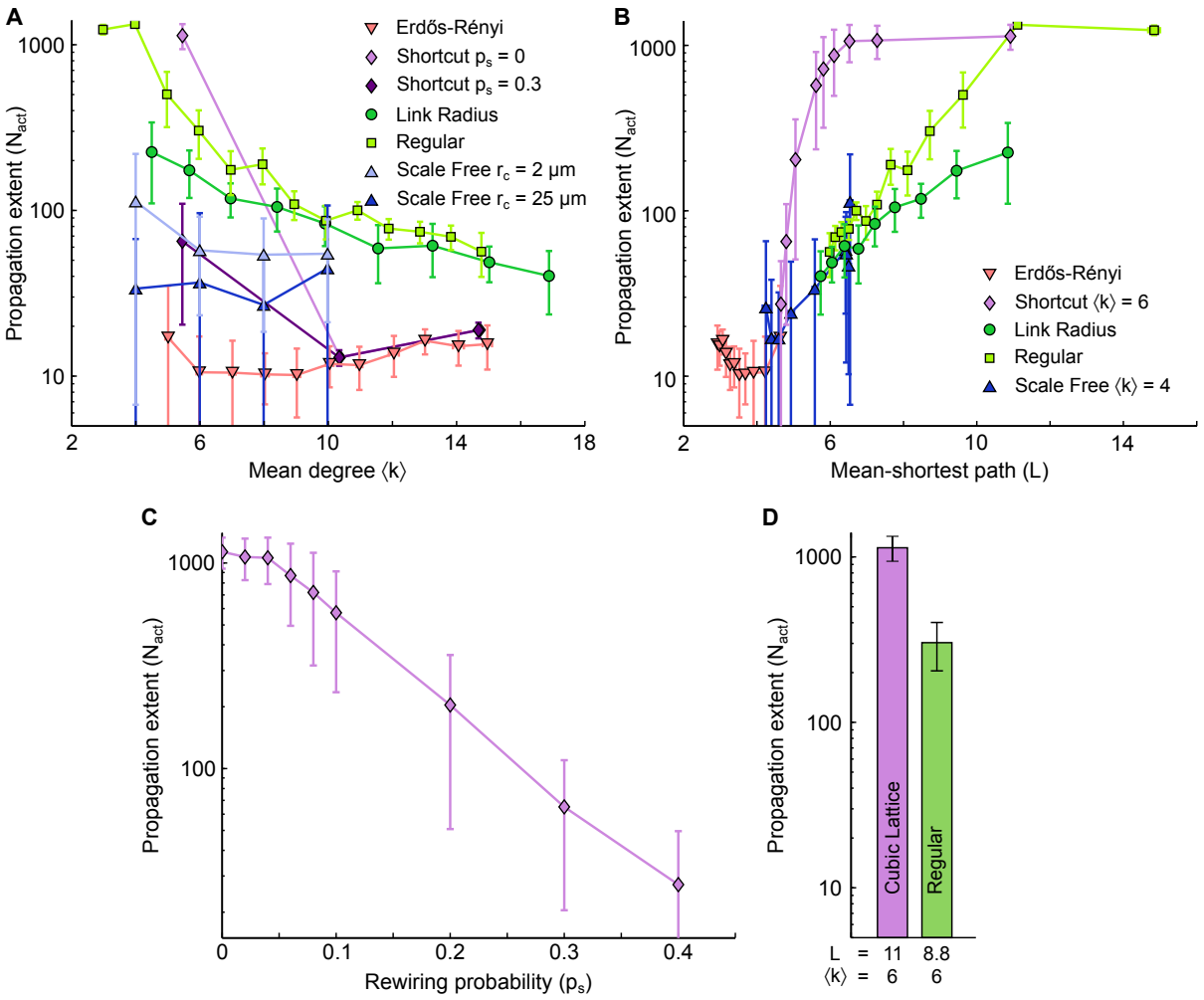

Figure V.17: ICW propagation simulated in the simplified UAR model. **A** The extent of ICW propagation (N_{act}) as a function of $\langle k \rangle$ and **B** L was recomputed for the same coupling networks as in Figure V.5 but with astrocytes that were modelled with the simplified three–state UAR model. The similarity of N_{act} values thus obtained compared to those obtained in Figure V.5 with the *ChI* model provides the simplified model with biophysical consistency. This supports our statement that the activation state of the two–hop neighborhood of individual cells ("the cells that are connected to the cells that are connected to me") is crucial to ICW propagation. **C** In shortcut networks, a large density of long–distance couplings between astrocytes hampers ICW propagation, like with the *ChI* model in Figure V.5. **D** Propagation extent for cubic lattices and regular networks of same mean degree. Data points±errorbars correspond to mean values±standard deviation over 20 networks of similar topology. Parameters of the simplified model (see text) as in Table V.4 (τ values were estimated like in Figure V.16.)

V.5 Shell analysis

As we have seen in Section V.2 and Section V.4, both ChI and UAR models display a peculiar phenomenon: cubic lattices and regular degree networks with $k = 6$ exhibit very similar topologies, but the ICW extents they support that can differ by 10-folds. While these two networks have the same mean degree $\langle k \rangle$, this difference could be accounted for by a difference in mean-shortest path. And indeed, cubic lattices have larger mean-shortest path ($L \approx 11$) than regular degree networks with $k = 6$ ($L \approx 8.8$). As showed in Figure V.19C however, even regular degree networks with smaller $\langle k \rangle = 4$ and same L as cubic lattices (*light green*), while supporting marginally larger ICW than with $k = 6$, still differ from cubic lattices by approximately 10-folds. Both network classes were however constructed in a similar way: while cubic lattices (see the 2D example in Figure V.18A) were built by starting from a regular grid, connecting each node to its 6 nearest neighbors and then only moving nodes to match experimental cell-to-cell distances distribution (see methods), regular degree networks nodes (see the 2D example in Figure V.18B) were first moved and then connected to their 6 nearest neighbors. In order to understand how this seemingly small difference could be sufficient to increase ICW extent by 10 folds, we decided to consider a more detailed view of network structure by looking at ICW propagation as a shell-by-shell activation process.

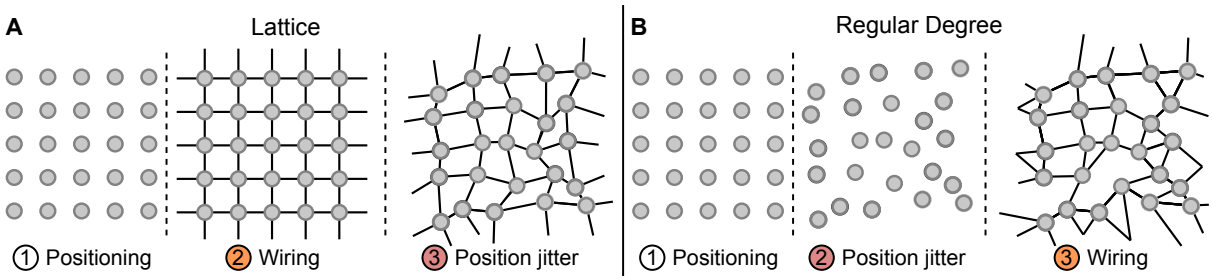

Figure V.18: Construction process of lattices and regular degree networks. **A** Illustration of the construction process for lattices (i.e. shortcut networks with $p_s = 0$). The nodes are first positioned on a grid, each node is then connected to its nearest neighbors (c.f. Section V.1.2.2) and the nodes are finally jittered. **B** In contrast, for Regular Degree networks, the nodes are readily jittered after positioning on a grid and are then wired to their nearest neighbors. These examples are in 2D for clarity but the networks used in the simulations are 3D.

V.5.1 Network shell structure

A shell r is defined by the set of nodes that are at topological distance r from a reference node. Figure V.19A represents the first three shells of a square lattice around a reference node (*big red* node), the first shell (*orange* nodes marked with '1') is composed of the nodes that are one link away from the reference node (i.e. directly linked to it), the second shell (*yellow* nodes) is composed of the nodes that are two links away from the reference node, etc. In ICW propagation experiments, taking the stimulated node as the reference, an ICW can be seen as sequential activations of shells 1, 2, etc. In other words,

it can be considered a shell-by-shell activation process even though all the nodes in a given shell will not necessarily get activated or might not activate at precisely the same moment. In this context, ICW propagation might depend on the exact shell structure (i.e. the number of nodes in each shell, the number of links between shells, etc.). Figure V.19B illustrates how these shell structures differ between lattices and regular degree networks; we remind the reader that while the schematics are in 2D for readability, all networks in simulations are 3D. While, in the regular degree networks (right), nodes of a given shell can share links with nodes of the same shell (*blue* links), in lattices this never happens and all the links going out of a given shell go either to the previous shell or to the next one (*red* arrows). To quantify these differences, we define the following quantities illustrated in Figure V.19D: the number of nodes N^r that are in shell r; the number of intra-shell links W^r in shell r (i.e. links between nodes of the same shell, in *blue*); and the number of links E^r between shell r and shell $r+1$ (*red* arrows).

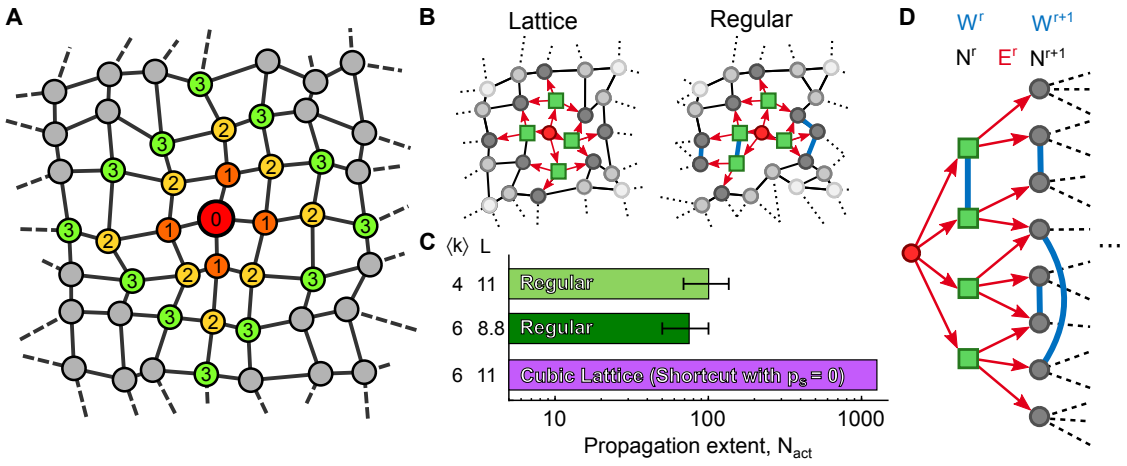

Figure V.19: Shell structure. **A** Illustration of shells 1 to 3 in a generic network; nodes are colored according to their topological distance (*numbers*) from a *red* reference node. A shell is a set of nodes that have the same topological distance r to the reference node (thus the same color in the figure). **B** 2D representation of ICW propagation (*red arrows*) in a cubic lattice and a regular network with identical mean degree. *Bright green squares* represent activated cells while *red circles* denote cells that were stimulated. **C** Despite sharing similar topological features, propagation in the cubic lattice may activate up to 10-fold more cells than in regular networks. **D** Shell analysis reveals that this difference in ICW propagation may be attributable to the connections between cells within the same r-th shell (W^r) in regular networks, which reduce the quantity of IP_3 given to astrocytes in the next shell $r+1$, thus resulting in earlier propagation failures than in cubic lattices. Definitions of N^r, W^r, and E^r are given in the main text. Cubic lattices were built by shortcut networks with $p_s = 0$ and $m_{latt} = 1$ (see "Methods"). Model parameters as in Table V.1.

When a fraction ρ^r of the nodes in shell r get activated, they will produce a quantity of IP_3 proportional to the number of activated astrocytes (because each one produces a fixed amount of IP_3 Q_0, as shown in Section V.3). The total IP_3 produced by shell r will thus be $\rho^r N^r Q_0$; this IP_3 will be shared among: (1) the N^{r-1} astrocytes of the preceding shell; (2) the $\hat{N}^r$ unactivated astrocytes in shell r linked to the activated astrocytes in the same shell; and (3) the N^{r+1} astrocytes of the next shell. The number of unactivated

astrocytes in shell r is $(1-\rho^r)N^r$ so $\hat{N}^r = (1-\rho^r)N^r \times p_W^r$ with p_W^r the probability for an unactivated astrocyte in shell r to be connected to an activated astrocytes in the same shell. Assuming that links inside a shell are uniformly distributed, we can compute the probability p_0^r that an unactivated astrocytes in shell r is linked to none of the activated astrocytes of the same shell:

$$p_0^r = \left(1 - \frac{2W^r}{N^r(N^r-1)}\right)^{\rho^r N^r} \tag{V.7}$$

Since $2W^r/(N^r(N^r-1)) \ll 1$ for all the networks we study, we use Taylor expansion at order one to get a simplified expression for p_W^r:

$$p_W^r = 1 - p_0^r \approx 1 - \left(1 - \rho^r N^r \frac{2W^r}{N^r(N^r-1)}\right) = \frac{2\rho^r W^r}{N^r - 1} \tag{V.8}$$

We can thus derive $\hat{N}^r$:

$$\hat{N}^r = 2\rho^r(1-\rho^r)W^r \frac{N^r}{N^r-1} \approx 2\rho^r(1-\rho^r)W^r \tag{V.9}$$

because $N^r/(N^r-1)$ quickly becomes very close to 1 as r increases; as an example, in the second shell of a cubic lattice, $N^r/(N^r-1) \approx 1.06$ and in the third shell of an Erdős-Rényi network with the same mean degree $\langle k \rangle = 6$, $N^r/(N^r-1) \approx 1.007$. We can thus compute the normalized mean IP_3 quantity $\langle \Psi^r \rangle$ (from its non-normalized version $\langle \hat{\Psi}^r \rangle$) that each astrocyte in the preceding, current and next shell will receive on average:

$$\langle \Psi^r \rangle = \frac{\langle \hat{\Psi}^r \rangle}{Q_0} = \frac{\rho^r N^r}{N^{r-1} + 2\rho^r(1-\rho^r)W^r + N^{r+1}} \tag{V.10}$$

As can be inferred from equation (V.10), lattices will have higher $\langle \Psi^r \rangle$ values (and should thus support large ICW extents) since they do not have intra-shell links (i.e. $W^r = 0$) so all the IP_3 is only shared among shells $r-1$ and $r+1$. This only happens however when $\rho^r < 1$; in these cases, lattices have an advantage over other spatially constrained networks, but if $\rho^r = 1$ this advantage no longer holds and $\langle \Psi^r \rangle$ will only depend on the size of each shell.

V.5.2 Shell-by-shell model of propagation

Although equation (V.10) provides us with a candidate explanation for the difference of ICW extent between Regular Degree networks and cubic latices, it might well be that the decrease in $\langle \Psi^r \rangle$ introduced by intra-shell links in regular degree network might not be sufficient to account for the difference in ICW extent. To test whether the shell structure could really account for this difference in ICW extent while also predicting ICW propagation in the other network topologies, we devised a shell propagation model whose derivation and parameters are detailed in Appendix C.2. The main idea behind the shell analysis is exposed in Figure V.20 and explained in the caption. The shell structure is sufficient to quantitatively account for the ICW extent in all network types (see Figure V.20B and C). Interestingly, the shell analysis suggests that the activation of the first shells control the large-scale propagation of ICW.

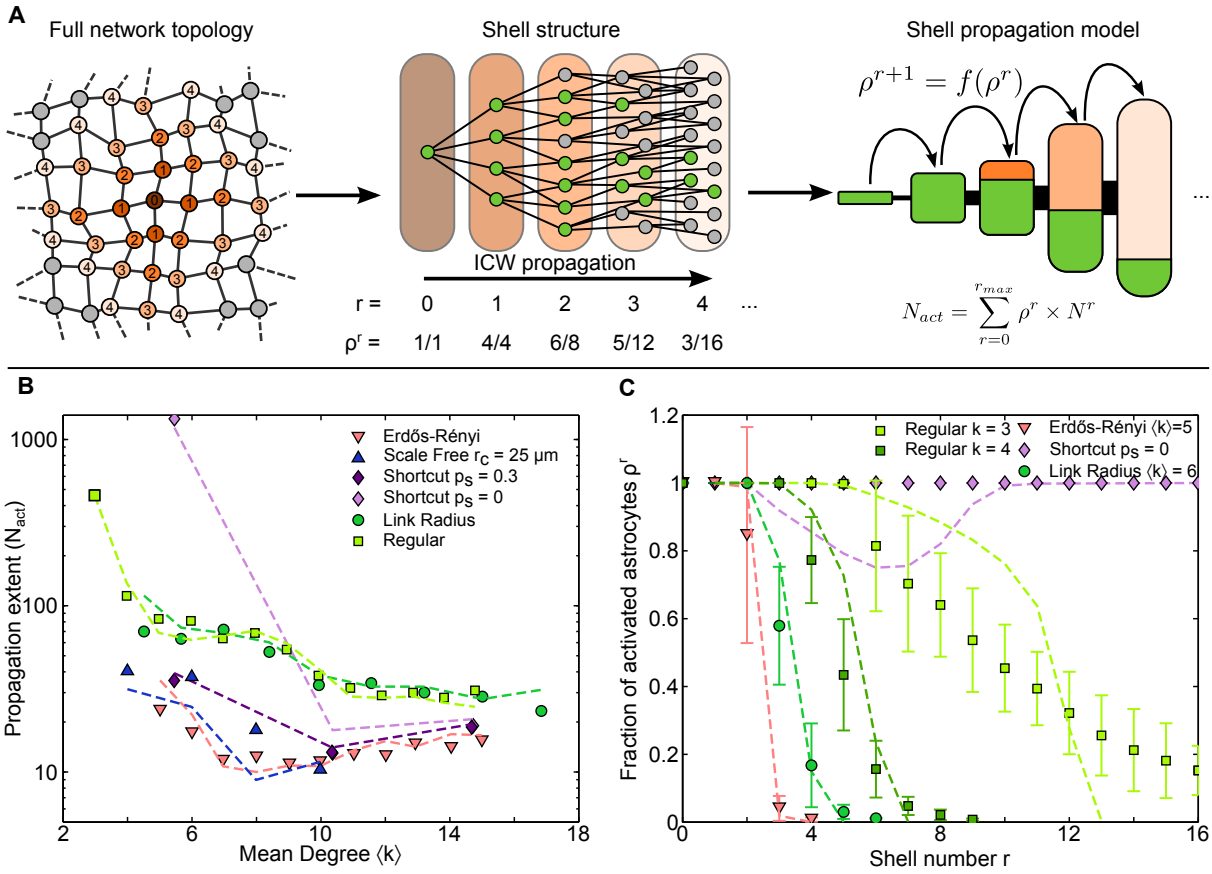

Figure V.20: Shell propagation model. **A** Schematic representation of the simplifications introduced by the shell propagation model. Each network is decomposed in successive shells (*brown* to *light orange* nodes on the left) and nodes are grouped according to their shell number r (middle). When an ICW propagates, it activates (*green* circles) successively astrocytes in shells 0 through 4; at the early stages of propagation, all nodes of a given shell get activated, but as the wave progresses, some astrocytes stay unactivated because of some specific reason (e.g. not enough IP_3 received or too many sink neighbors). In shell 2 for example, only 6 astrocytes out of 8 get activated. This process continues until the number of activated astrocytes in shell 4 is too few to propagate the ICW any further. In this description, we took the full details of network topology into account, we just grouped nodes by their shell number. The principle of the shell propagation model (right) is to greatly simplify the shell structure by taking only into account the size of each shell (represented as different sizes of compartment) and the number of links between shells (represented as the thickness of the links between compartment). Each compartment is then associated to an activation ratio ρ^r (ratio of the compartment surface covered in *green*) that is computed recursively until $\rho^r \approx 0$. We then estimate the number of activated astrocytes by summing over the compartments. **B** The shell propagation model (*dashed* lines) quantitatively reproduces the ICW extent obtained from the full network propagation (symbols). **C** The shell propagation model (*dashed* lines) also matches the ratios of activated astrocytes in each shell in the full network propagations (symbols).

V.6 Discussion

In many instances, the variability observed in the propagation range of intercellular calcium waves (ICW) in astrocyte populations (Charles, 1998; Scemes and Giaume, 2006; Sasaki et al., 2011; Kuga et al., 2011) cannot be accounted for by the type of preparation or by stimulation protocol (Scemes and Giaume, 2006). Our model of ICW in 3D coupling networks suggests that this variability can be due to a mere change in the spatial organization (or topology) of the astrocyte network. In our simulations, the mean degree $\langle k \rangle$ and mean-shortest path L of the coupling networks were found to be the main topological characteristics controlling propagation. Quite surprisingly, increasing the number of cells coupled to each astrocyte or adding long–distance GJC couplings actually reduced the extent of ICW propagation. Moreover, all types of ICW propagations ranges could be reproduced in our model with spatially constrained networks (Link Radius and Regular) just by changing $\langle k \rangle$. Our model therefore predicts that variations in the organization of the GJC couplings control the range of ICW propagation.

A first experimental element in favor of our hypothesis is the observation that regenerative ICW are far more frequent in cell cultures than in slices or *in vivo* experiments (Scemes and Giaume, 2006). Since a 2D embedding imposes a lower mean degree (compared to 3D), this observation supports our hypothesis. As already presented in Section I.4, *in vivo*, the organization of astrocyte coupling networks has recently attracted attention as several articles demonstrated variability between brain regions (Giaume et al., 2010). For instance, heterogeneities in coupling organization were found in mouse olfactory glomeruli (Roux et al., 2011), and somatosensory cortex (Houades et al., 2008). Locally, astrocyte density may control the astrocyte coupling organization, as in the stratum pyramidale of the hippocampus (Rouach et al., 2008). These local heterogeneities are also reflected in the observation that the total number of coupled astrocytes (obtained via e.g. biocytin-coupling experiments) vary a lot between brain regions: cortical astrocytes can be organized in networks of hundreds of cells (Nimmerjahn et al., 2004) while in the hippocampus, astrocytes in the CA3 region are much less coupled than in CA1 (D'Ambrosio et al., 1998). These variations in coupling can also be at least partially attributed to variations in the expression of connexins (Cx) 43 and 30, which also displays high heterogeneities (Giaume and Theis, 2010); for instance, hypothalamus and hippocampus display higher Cx43 levels than cortex and brain stem astrocytes (Blomstrand et al., 1999a). According to our hypothesis, this regional variability of the organization of the astrocyte coupling network could explain the regional variability of the extent of ICW propagations.

While the heterogeneity of the coupling organization is being increasingly recognized (Giaume et al., 2010), only a few studies have addressed the relationship between the coupling properties of the astrocytes (or their Cx expression) and ICW propagation. According to our hypothesis, in regions in which GJC intercellular communication is the main ICW pathway (retina (Newman, 2001), striatum (Venance et al., 1997) and cerebral cortex (Iwabuchi et al., 2002; Haas et al., 2006)), one should observe increased ICW extent when the astrocytes are less coupled, or when Cx expression is lower. Blomstrand et al. (Blomstrand et al., 1999a) quantified both the extent of dye coupling and ICW

propagation as well as Cx43 expression in astrocyte cultures from different brain regions. In accordance with our hypothesis, an inverse relationship between ICW extent and GJC coupling was reported for two brain regions: hypothalamus was found to be highly GJC-coupled and to support small extent ICW whereas the neocortex, that was less GJC-coupled, exhibited larger ICW (Blomstrand et al., 1999a). More generally, GJC coupling in regions where intercellular GJC is the predominant pathway for ICW propagation is often reported to be lower than in other brain regions like in the striatum (Rouach et al., 2002) and cortex (Blomstrand et al., 1999a; Aberg et al., 1999). In the CA3 region of the hippocampus, known to be less coupled than CA1 (D'Ambrosio et al., 1998), neuronal activity is able to trigger long range ICW (Dani et al., 1992). On the contrary, increased coupling induced by forced expression of Cx43 was found to decrease ICW extent in human 1321N1 astrocytoma cells (Suadicani et al., 2004). Taken together, these articles confirm our hypothesis: highly coupled astrocyte networks display small extent ICW while less coupled ones display larger ICW.

As we already discussed in Section IV.4, if astrocytes are indeed organized in independent non overlapping domains (Bushong et al., 2002), the organization of their coupling can be expected to be close to a Voronoi diagram of the cell centers (Aurenhammer, 1991). The mean degree of a Voronoi diagram in three dimensions is ≈ 15, a value that should prevent ICW propagation according to our simulation results (see Figure V.5A for $\langle k \rangle = 15$). Actual astrocyte networks however differ from a pure Voronoi diagram because some of the astrocytes can be disconnected from the GJC network (Theis and Giaume, 2012). For instance, in cocultures of rat striatal neurons and astrocytes, as previously pointed out, 21% of the astrocytes were found to be disconnected from the network (Rouach et al., 2000). This figure even increases to 40% of disconnection in cultures with only astrocytes. Removing 21% or 40% of the nodes from a Voronoi diagram leads to a mean degree $\langle k \rangle \approx 11.7$ or 8.9, respectively. Interestingly, these values of the mean degree are close to values reported in situ: $\langle k \rangle \approx 11$ neighbors in CA1 rat hippocampus (Xu et al., 2010). Our simulations show a strong increase in the ICW propagation range when the mean degree becomes smaller than $\approx 8 - 10$ (Figure V.5A). Interestingly, both Cx30 and Cx43 expression and permeability can be regulated by neurons (Rouach et al., 2000; Koulakoff et al., 2008; Roux et al., 2011), possibly via extracellular K^+ (Pina-Benabou et al., 2001). This K^+-triggered increase in GJC communication was also recently reported to decrease ICW extent in astrocyte networks (see Figure 3 in Scemes and Spray (2012)), in accordance with our hypothesis. Therefore, neurons could modulate mean degree of the astrocyte coupling network and even trigger a switch between $\langle k \rangle \approx 12$ and $\langle k \rangle \approx 8$ thus allowing the propagation of ICW to longer ranges.

The coupling organization in astrocyte networks also changes during development. During the first postnatal weeks, astrocytes show large increases in Cx43 expression that persists until adulthood (Aberg et al., 1999; Montoro and Yuste, 2004). Intercellular calcium waves are frequently observed during development (Parri et al., 2001; Weissman et al., 2004; Fiacco and McCarthy, 2006; Scemes and Giaume, 2006; Kunze et al., 2009) and are thought to be much less frequent in adults under non pathological conditions (Fiacco and McCarthy, 2006; Scemes and Giaume, 2006). In most parts of the brain, Cx43 becomes strongly expressed between postnatal day 10 (Aberg et al., 1999) and the third postnatal

week (Rouach et al., 2002). In agreement with our hypothesis, spontaneous astrocyte calcium activity in the rat ventrobasal thalamus decreases by five fold between postanatal day 10 and 14 (Parri et al., 2001). In mice CA1 stratum radiatum in the hippocampus, realistic stimulation with caged IP_3 failed to elicit ICW in individuals ranging from postnatal day 10 to 14 (Fiacco and McCarthy, 2004). The astrocytes of the neocortex are known to be sparsely coupled during postnatal days 1-3 (Aberg et al., 1999), where ICW were found to be propagating (Iwabuchi et al., 2002). On the opposite, in the CA1 region of the hippocampus, astrocytes are highly coupled during postnatal day 10-14 (Aberg et al., 1999) and they do not support wave propagation with similar stimulation protocols (Fiacco and McCarthy, 2004). Taken together, these observations support our hypothesis, since ICW activity seems to be predominant during early postnatal development when astrocytes are less coupled, and tends to diminish with age as Cx expression gets stronger.

In several regions of the brain, intercellular IP_3 transfer through GJC coupling is however not the major pathway for ICW. Indeed, ICW propagation through the activation of P2Y receptors by diffusing extracellular ATP is the dominant pathway in the corpus callosum (Schipke et al., 2002), CA1 hippocampus (Haas et al., 2006) and the cerebellum (Hoogland et al., 2009). In these regions, ICW can be elicited through ATP application and are strongly diminished by P2Y receptor antagonists (Hoogland et al., 2009; Kuga et al., 2011). ATP activation of P2Y1 receptors leads to IP_3 production via PLCβ activation but ATP also has a P2Y-mediated effect on GJC permeability, that was reported to decrease gap junction coupling (Rouach et al., 2002; Même et al., 2004; Orellana et al., 2013). A network with initially strong GJC-coupling would not support long range ICW propagation via the intercellular GJC pathway according to our model. However, the release of ATP in such a network, by down-regulating GJC permeability, would decrease the coupling and facilitate ICW propagation. In support of this hypothesis, the expression of P2Y1R in Cx43 expressing cells increases ICW extent while the expression of Cx43 in the absence of P2Y1 reduced it (Suadicani et al., 2004). Collectively, these articles also support our hypothesis and offer an attractive perspective: long-range ICW can be elicited in an astrocyte network (i) if its mean degree of GJC coupling is low - for regions in which GJC is the predominant pathway; or (ii) if the mean degree is large, for regions in which ATP is the predominant pathway, but if propagation is rescued by the down-regulation of GJC permeability by ATP.

The topological determinants of signal propagation in astrocyte networks thus seem different from those at play in neuronal networks. Signal is propagated from one astrocyte to the other by diffusion from a single IP_3 pool (the astrocyte) while neurons communicating through chemical synapses use distinct pools of neurotransmitters located in each of their synapses. This difference is actually the strongest one in our view: while increasing the number of neighbors in astrocyte networks dilutes away IP_3 and decreases ICW propagation, increasing the number of neighbors in neuronal networks only implies the addition of new synapses and can thus only increase the network excitability. In agreement with this view, increased connectivity (i.e. mean degree) has been shown to promote synchronization in model networks of excitable neurons (Wang et al., 1995; Golomb and Hansel, 2000) and to control the switch between asynchronized states and partially synchronized (or coherent) states (Olmi et al., 2010; Luccioli et al., 2012; Tattini et al., 2012). In

the present study, the presence of hubs and long range connections between astrocytes impaired ICW extent. In contrast, broad in-degree distributions (allowing the presence of hubs) has been shown to increase the mean activity in model neuronal networks while broad out-degree distributions increased the amplitude of cross-correlation in synaptic currents (Roxin, 2011). Finally, Dyhrfjeld-Johnsen et al. (2007) showed that network hyperexcitability during simulated sclerosis can be directly linked to the presence of long distance links in the network: when these long distance links were removed during maximal sclerosis, network hyperexcitability decreased. Theoretical studies suggested that to keep network activity balanced, synaptic weights of each neuron should be rescaled by some function of the neuron degree (Van Vreeswijk and Sompolinsky, 1996, 1998; Lerchner et al., 2006). This *synaptic scaling* mechanism has mainly been observed experimentally for post-synaptic terminals (Turrigiano, 2008). In astrocyte networks, one could wonder whether such a mechanism would influence ICW propagation. Unfortunately, because of the bidirectionality of these networks, rescaling GJC strength is not as straightforward as for neuronal networks (conductances in both direction should be equal $g_{ij} = g_{ji}$ but k_i can be different from k_j). Neuronal networks can also be bidirectional when neurons are coupled by GJC-mediated electrical synapses. While being restricted to certain adult neuronal subpopulations (Söhl et al., 2005), these GJC are still functionally relevant and have been shown to mediate synchronization between neurons both experimentally (Connors and Long, 2004) and in modeling studies (Chow and Kopell, 2000; Lewis and Rinzel, 2003). The effect of GJC topological properties such as connectivity and rewiring on signal propagation could however be more subtle. Because of the similarity between the term governing the diffusion of IP_3 between astrocytes ($F \times (I_i - I_j)$) and the term governing GJC-coupling at electrical synapses ($g \times (V_i - V_j)$), GJC-coupled neuronal networks are of particular relevance to our study. Accordingly, the effects of network topology on signal propagation in GJC-coupled neuronal networks bear some resemblance with the effects described here for astrocyte networks. In Volman et al. (2011), it is shown that increasing GJC conductance or connectivity could help reduce epileptic seizures by mechanisms similar to what we observed in astrocyte networks (subthreshold activity gets diluted among neighbors). Further increases in connectivity however enhanced seizure activity (and thus signal propagation), in contrast with what we observed in astrocyte networks. Increased rewiring of GJC-coupled model neurons has been shown to impair signal detection but, differently from astrocyte networks, weak connectivity and coupling, while enhancing signal detection, impaired signal propagation (Volman and Perc, 2010). Altogether, those behaviors reported for neuronal networks do not match the observations we reported here for model astrocyte networks. These differences in the dynamics-topology relationships bring new light on the well-known observation that neurons form highly connected networks with long distance links while astrocytes usually restrict their couplings to a handful of nearby neighbors (Bushong et al., 2002). The topology of each of these cellular networks thus appears adapted for optimal signal transmission.

Chapter VI

Stochastic Resonance

We suggested in the previous chapters that astrocytic responses to stimulation could be modulated and possibly controled by the strength of GJC couplings and by the specific topologies that they form. In these chapters, astrocytes only displayed Ca^{2+} activity in response to external stimulation either by neurons in Chapter IV or by other astrocytes in Chapter V. Astrocytes however routinely display, in culture, in slices and in vivo, spontaneous Ca^{2+} oscillations that can be independent from neuronal activity (Nett et al., 2002; Tashiro et al., 2002; Hirase et al., 2004). These oscillations occur at frequencies ranging between 0.003 Hz (Parri et al., 2001; Nett et al., 2002; Hirase et al., 2004) and 0.03 Hz (Tashiro et al., 2002; Nett et al., 2002) and can be mediated by various pathways. One of these pathways involves the random opening of IP_3 receptor clusters on the ER membrane (Bootman et al., 1997; Shuai and Jung, 2002): when IP_3 receptor clusters are far from each other, small Ca^{2+} puffs originating from the random opening of IP_3R channels stay localized and are usually not sufficient to initiate CICR. When IP_3R clusters are close to each other, these small Ca^{2+} puffs are strongly amplified by the opening of neighbouring clusters and a supercritical wave nucleus can arise, generating a Ca^{2+} wave spanning the whole astrocyte. It is however not well established whether this spontaneous Ca^{2+} activity serves any purpose or if it could just be regarded as a kind of detrimental noise. The overall picture gets even more complex when considering the detailed astrocyte morphology and the Ca^{2+} signaling events that they host. As presented in Section I.1.2, astrocytes in the brain have complex morphologies: they extend several main processes from their soma and these processes are further ramified in high numbers of thiner processes that enwrap synapses. Both thin and main processes display a variety of Ca^{2+} signals that can occur either in response to (Di-Castro et al., 2011; Panatier et al., 2011; Kanemaru et al., 2014) or independent from neuronal activity (Shigetomi et al., 2010; Di-Castro et al., 2011).

Astrocytes thus display spontaneous Ca^{2+} activity spanning several spatial and temporal scales: from very frequent (0.03 Hz per subregions) localized TTX-insensitive events (Di-Castro et al., 2011) (Figure VI.1C), to rarer events (0.016 Hz per process) encompassing a whole astrocyte process (Di-Castro et al., 2011; Kanemaru et al., 2014) (Figure VI.1B), to even more infrequent events (0.003 to 0.03 Hz per astrocyte) activating the cell soma

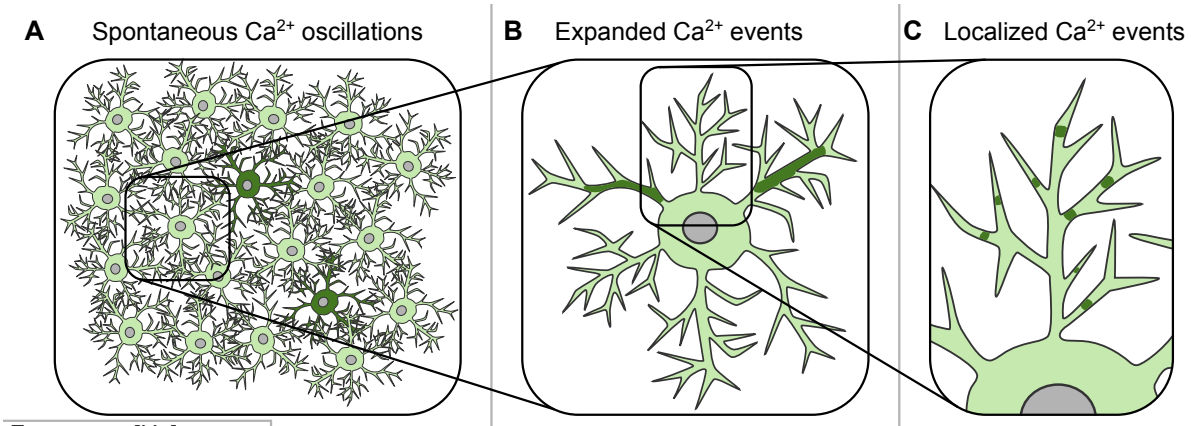

Frequency [Hz]			
per subregion (1 µm)	-	-	~ 0.03 Hz
per process (20 µm)	-	~ 0.016 Hz	~ 1.2 Hz
per astrocyte (50 µm)	~ 0.015 Hz	~ 0.12 Hz	~ 9 Hz

Figure VI.1: Spatial and temporal scales of spontaneous Ca^{2+} activity in astrocytes. **A** Spontaneous activations in astrocyte networks, *dark green* astrocytes represent spontaneously activated astrocytes. **B** Spontaneous activation of main processes in a single astrocyte, activated parts of main processes are represented in *dark green*. **C** Spontaneous activation in small subparts of astrocytic processes, activated subparts are represented in *dark green*.

(Nett et al., 2002; Tashiro et al., 2002) (Figure VI.1A). When looking at the frequencies of these events per astrocyte, one can see in Figure VI.1 that they span 3 orders of magnitude (from 10^{-2} to 10^{1} Hz) while their spatial extents span nearly 2 orders of magnitude (from 1 to 50 μm). Given this multiscale presence of spontaneous activity, it is natural to wonder whether it plays any role in signal integration by astrocytes at any of these scales. In this chapter, we will thus focus on the possibles roles and effects of spontaneous Ca^{2+} activity in network-wide Ca^{2+} wave propagation. We will focus on how spontaneous activation of astrocytes can affect stimulated Ca^{2+} wave propagation on different astrocyte network topologies.

VI.1 Noise and stochastic resonance in astrocyte networks

VI.1.1 Modeling spontaneous activation in astrocyte networks

Astrocytic spontaneous oscillations have been frequently reported under various experimental conditions (Parri et al., 2001; Nett et al., 2002; Poskanzer and Yuste, 2011). While some oscillations are neuronally-evoked and some others are independent from neuronal activity, we will be interested in this section by Ca^{2+} oscillations that do not propagate to neighboring astrocytes, regardless of the underlying activation pathway. Astrocyte networks, as parts of their processes, display spontaneous activity but, in contrast with the

main processes, they display much more complex topologies (Giaume et al., 2010). In this section, we will thus investigate the interplay between network topology and stochastic propagation dynamics. We will particularly focus on stochastic-resonance type of effects on ICW propagation.

To this end, we simulated astrocyte networks with the same basic model as in Chapter V, individual astrocytes parameters were all set identical according to Table V.1 and the same networks were constructed with parameters taken from Table V.2. The main difference resided in the stimulation protocol and the way we implemented the stochastic spontaneous activity. Each point in the following figures consists in the repetition of 20 stochastic resonance protocols, each comprising three 200s simulations:
- Noise only simulations (with activation frequency f_n) were only subjected, for each astrocyte, to a poissonian train of activations (details below);
- Signal only simulations (with activation frequency f_s) were stimulated as in Chapter V by coupling the central cell to a virtual cell with constant IP_3 level IP_3^{bias} ;
- Signal and noise simulations (with activation frequency f_{s+n}) were subjected to both poissonian trains of activations and stimulation of the central cell.

In order to be able to compare these different frequencies, all 3 simulations were run on the exact same network topologies with the same poissonian trains for the noise. Experiments were run with two different signal intensities corresponding to $IP_3^{bias} = 1$ and 1.5μMthat induced respectively low and medium ICW extents (in contrast with Chapter V in which we wanted to investigate fully developed ICW). We measured stochastic resonance (SR) by considering the resonance strength $\chi(\zeta_n) = \frac{f_{s+n} - f_n}{f_s}$, the ratio between the activation frequency attributable to the interaction between ICW and spontaneous activations and the frequency attributable to ICW propagation only. We used activation frequencies and not ICW extents since, for high spontaneous activation frequencies, all nodes were activated at least once in the simulation.

In simulations with noise, each astrocyte was assigned a poissonian train t_i which was incrementally constructed by drawing inter-event delays from an exponential distribution with mean $\tau_n = 1/\zeta_n$ (with ζ_n the noise frequency). To avoid boundary effects [1], we started at $t = -5\tau_n$ and drew new events until $t \geq 0$. Since ODE integration started at $t = 0$s, these initial events were discarded. When the simulation time t matches an event i at time t_i, the leak term in equation (II.12) was multiplied by 2 (or equivalently, Ω_L for astrocyte i was multiplied by 2) until the astrocyte got activated (i.e. until $C \geq 0.7\mu$M). This quickly elicited a Ca^{2+} oscillation in the astrocyte at which point we switched back to normal leak from the ER. When t eventually reached t_{i+1}, the same algorithm was applied. Parameters specific to this stochastic-resonance setup are summarized in Table VI.1.

High intensity stimulations, such as the one we used in Chapter V to study fully developed calcium waves, were not very sensible to noise. Under this stimulation (i.e. with $IP_3^{bias} = 2\mu$M), since most networks supported waves with high numbers of activated cells N_{act} (more than 100), the addition of random astrocyte activation did not significantly improve wave propagation. For those networks that displayed low N_{act} however

1. if we start to draw delays from $t = 0$s, we implicitly assume that all astrocytes got spontaneously activated at $t = 0$s

Table VI.1: Parameters for the investigation of stochastic resonance in astrocyte network.

Symbol	Description	Values			Units
		min	step	max	
τ_n	Mean inter-event time for the noise stimulation	20	20	100	s
-	-	200	100	500	s
-	-	700	300	1300	s
-	-	2400	1000	4400	s
-	-	6500	2000	10500	s
-	-	13000	2000	15000	s
IP_3^{bias}	Stimulation intensity for the signal	1	0.5	1.5	μM

(essentially spatially unconstrained networks such as Erdős-Rényi, spatial scale free, and shortcut networks with $p_s > 0$, see Figure V.5), the addition of spontaneous astrocyte activation helped wave propagation as measured by $\chi(\zeta_n)$. To see whether similar effects could be present for spatially constrained networks, we decided to lower the stimulation intensity so that basal wave propagation would get smaller.

VI.1.2 Astrocyte networks display degree-dependent stochastic resonance

Low intensity stimulations are not qualitatively different from high intensity. Figure VI.2A and B display respectively the wave propagation extent N_{act} as a function of the network mean degree $\langle k \rangle$ for two stimulation intensities $IP_3^{bias} = 1$ and 1.5μM. Both cases display behaviors that are qualitatively identical to what we saw in Chapter V: increases in network mean degree $\langle k \rangle$ lead to decreases in ICW extent N_{act} and spatially constrained networks (regular degree in *light green* squares and link radius in *dark green* circles) supported bigger ICW extent than spatially unconstrained networks (Erdős-Rényi in *light red* triangles, and shortcut networks with $p_s > 0$ in *dark purple* diamonds). As we saw in Figure V.5, spatial scale free networks, whose topology can be adjusted through r_c values from spatially constrained (low r_c, *light blue* triangles) to spatially unconstrained networks (high r_c, *dark blue* triangles), could support both high and low wave propagation according to r_c values. The slight increase in N_{act} as $\langle k \rangle$ increases that is noticeable for spatially constrained networks in Figure VI.2A and for Erdős-Rényi networks in Figure VI.2B was already noticeable in Figure V.5A for Erdős-Rényi networks and corresponds to the activation of the neighbors of the stimulated cell. N_{act} thus follows the $N_{act} = \langle k \rangle$ line (*black dashed* line) for some increases in $\langle k \rangle$ until it eventually drops below it, indicating that even the neighbors of the stimulated cell were not activated.

Astrocyte networks display stochastic resonance. These stimulation intensities thus displayed ICWs whose extents ranged from local activation of neighbors (around the

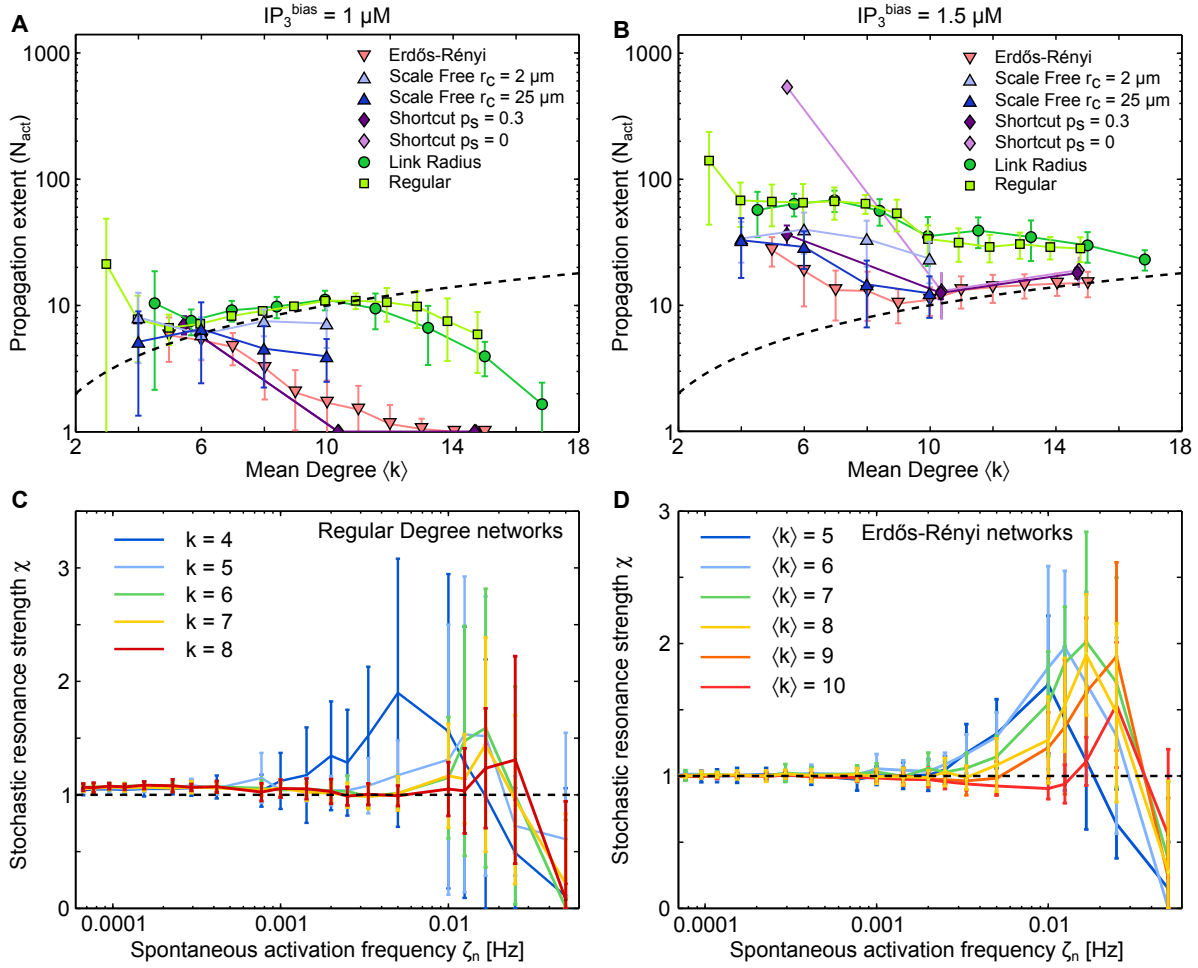

Figure VI.2: Network propagation under weak stimulation. The propagation extent N_{act} of ICWs elicited by **A** weak ($IP_3^{bias} = 1\mu$M) and **B** medium ($IP_3^{bias} = 1.5\mu$M) stimulation intensities displayed the same qualitative behavior as for high intensity stimulation (c.f. Figure V.5A): increases in the network mean degree $\langle k \rangle$ led to impaired ICW propagation for all network types. Slight increases in N_{act} only correspond to the activation of the neighbors of the stimulated node as indicated by the $N_{act} = \langle k \rangle$ *black dashed* line. **C** Regular degree networks displayed SR for various mean degrees (color-coded) as measured by values of $\chi(\zeta_n)$ above 1 (*black dashed* line) for specific spontaneous activation frequencies ζ_n and under low stimulation intensity ($IP_3^{bias} = 1\mu$M). **D** The same type of effect was also displayed by Erdős-Rényi networks for higher stimulation intensity ($IP_3^{bias} = 1.5\mu$M). Data points±errorbars correspond to mean values±standard deviation over 20 sampled networks with the same statistical parameters (see Section VI.1.1).

$N_{act} = \langle k \rangle$ line) to the activation of 100 cells. In the latter case (spatially constrained networks in Figure VI.2B for example), the addition of noise usually did not have any effect on the wave propagation ($\chi(\zeta_n)$ was close or lower than 1). Around the $N_{act} = \langle k \rangle$ line however, the addition of spontaneous astrocyte activation facilitated wave propagation for specific values of the activation frequency ζ_n. As an example, Figure VI.2C displays values of the SR indicator $\chi(\zeta_n)$ for regular degree networks (which are spatially constrained) under low stimulation intensity ($IP_3^{bias} = 1\mu$M) and for different mean degrees $\langle k \rangle$. For $\langle k \rangle = 4$ (*dark blue* curve), no SR effects were present for low frequencies of spontaneous activation ζ_n; for $\zeta_n = 0.005$Hz however, $\chi(\zeta_n)$ went up to 2, indicating that the response to stimulation was doubled by the presence of spontaneous oscillations. When the frequency of spontaneous oscillations ζ_n was further increased, this increase got weaker until it eventually dropped below 1 for $\zeta_n \geq 0.016$Hz, indicating that spontaneous oscillations now impaired wave propagation. It thus seems that even spatially constrained astrocyte networks (which are more realistic than networks with long distance links), can display stochastic resonance-like effects: small frequency spontaneous activations can increase ICW propagation while higher spontaneous oscillation frequencies are detrimental to wave propagation. The same type of effect is visible in Figure VI.2D for Erdős-Rényi networks with a higher stimulation intensity ($IP_3^{bias} = 1.5\mu$M) although the exact spontaneous oscillation frequency ζ_n for which $\chi(\zeta_n)$ differs from spatial regular networks. In general, different networks displayed peaks in stochastic resonance for different ζ_n frequencies. To quantify this, we computed for each network network:
– ζ^*, the resonant frequency for which $\chi(\zeta_n)$ reached its maximal value;
– χ^*, the strength of stochastic resonance (i.e. the maximal $\chi(\zeta_n)$ value).

Stochastic resonant frequency ζ^* is linked to network mean degree. Figure VI.3 displays SR effects for several networks: $\chi(\zeta_n)$ values (z-axis) are color-coded and are plotted as a function of spontaneous activation frequency ζ_n (x-axis) and a specific network characteristic (y-axis). For Figure VI.3A through E, the y-axis increases with the mean degree $\langle k \rangle$ of the networks; for Figure VI.3F, the y-axis corresponds to the rewiring probability of shortcut networks. The color-code is adapted for each subfigures such that $\chi(\zeta_n)$ values that are below 0.9 appear in nuances of *blue*, values above 1.1 appear in nuances of *yellow* and *red*, and values between 0.9 and 1.1 appear in *green*. The absence of effect of spontaneous activations on ICW propagation thus corresponds to *green* zones, SR appears in *yellow* to *red* colors while detrimental effects appear in *blue*. On each subfigure, a *thick black* line indicates the resonant frequency ζ^* when the stochastic resonance strength was high enough ($\chi^* \geq 1.2$). Figure VI.3A and B show the SR obtained in weakly stimulated spatially constrained networks (respectively for Regular Degree and Link Radius networks). Both networks display SR for all mean degrees, and the resonant frequency ζ^* seems to increase with the network mean degree $\langle k \rangle$. Very high mean degrees (*dark shaded* zones) have very strong $\chi_(\zeta_n)$ values but must be interpreted with care: as we saw in Figure VI.2A, both spatially constrained networks display a drop below the $N_{act} = \langle k \rangle$ line for high degrees and are thus very weakly activated by the stimulation. Since $\chi_(\zeta_n) = \frac{f_{s+n} - f_n}{f_s}$, when the frequency f_s of astrocyte activation by the signal only gets close to 0, $\chi(\zeta_n)$ diverges. We thus restricted our following analysis to networks with $N_{act} \geq \frac{1}{2}\langle k \rangle$ in order to avoid artificially high $\chi(\zeta_n)$ values.

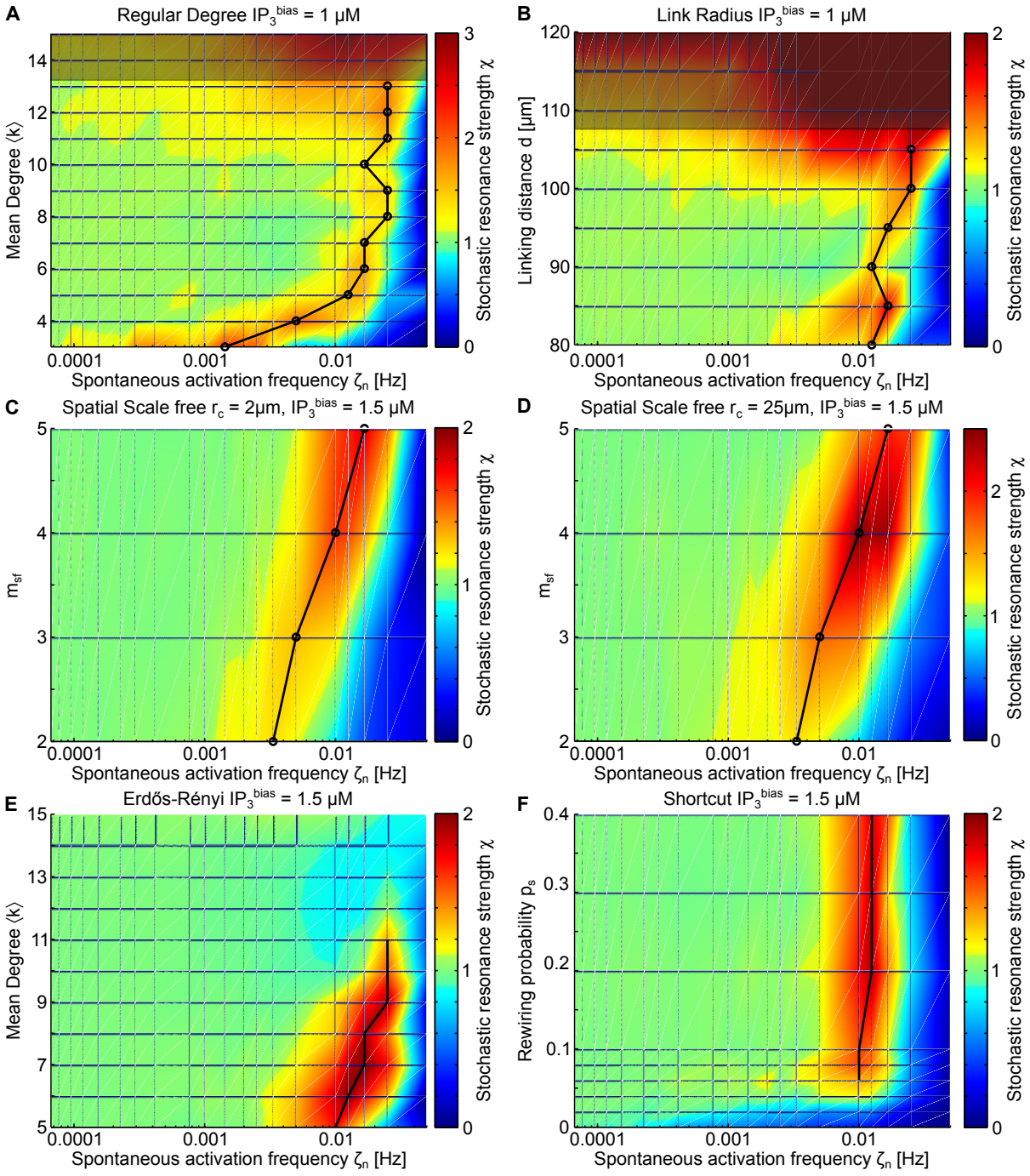

Figure VI.3: Networks react differently to noise but generally display stochastic resonance. Heatmap representations of SR effects. Mean $\chi(\zeta_n)$ values are color coded and plotted for different network types and stimulation conditions. Colorbars are adapted to each subplot so that *blue* regions denote $\chi(\zeta_n) \leq 0.9$ (i.e. the spontaneous activation of astrocytes is detrimental to ICW propagation), *green* regions denote $0.9 \geq \chi(\zeta_n) \leq 1.1$ (i.e. no effect from spontaneous activations), and *yellow* to *red* regions denote $\chi(\zeta_n) \geq 1.1$ (i.e. stochastic resonance). For networks which have $\chi^* \geq 1.2$, the *thick black* line plots the resonant frequency ζ^*. **A** Regular Degree networks, *shaded* area denote networks for which $N_{act}$was too small to assess stochastic resonance. **B** Link Radius networks. **C** Spatial Scale Free networks with $r_c = 2\mu$m. **D** Spatial Scale Free networks with $r_c = 25\mu$m. **E** Erdős-Rényi networks. **F** Shortcut networks with $\langle k \rangle = 6$ (i.e. $m_{latt} = 1$); y-axis values correspond to different rewiring probabilities p_s. **A** and **B** were weakly stimulated ($IP_3^{bias} = 1\mu$M) while **C** to **F** were stimulated with $IP_3^{bias} = 1.5\mu$M. Simulations as in Figure VI.2.

Since the spatially unconstrained networks almost always failed to activate enough astrocytes under weak stimulation (see Figure VI.2C), we looked at their behavior under medium stimulation intensity. Figure VI.3C and D show SR for spatial scale free networks with respectively $r_c = 2\mu$m (closer to spatially constrained networks) and $r_c = 25\mu$m (closer to spatially unconstrained networks). While the stochastic resonance is higher for $r_c = 25\mu$m (colorbars are different), both networks display an increase in resonant frequency as the network mean degree increases. Figure VI.3E also show increases in resonant frequency as the mean degree increases; above $\langle k \rangle = 11$ however, stochastic resonance stops and the spontaneous activation of astrocytes is only detrimental to ICW propagation. Finally, other network parameters, such as the rewiring probability p_s in Shortcut networks or r_c in spatial scale free networks don't seem to influence the resonant frequency ζ^*. As an example, Figure VI.3F shows the different SR effects as the rewiring probability p_s of Shortcut networks with $\langle k \rangle = 6$ (i.e. $m_{latt} = 1$) increases. Interestingly, SR only occurs in shortcut networks for a sufficiently high value of rewiring probability; spontaneous oscillations are always detrimental when $p_s = 0$. These 6 subfigures display a somewhat complex picture of SR in astrocyte networks: while increasing the mean degree $\langle k \rangle$ increases the resonant frequency ζ^*, networks which share the same mean degree do not necessarily display the same stochastic resonance strength χ^* (compare for example Figure VI.3C and D for $\langle k \rangle = 8$).

Quantifying stochastic resonance To assert whether mean degree increases generically increased the resonant frequency in all network types, we computed the resonant frequency ζ^* of all networks which displayed a stochastic resonance strength $\chi^* \geq 1.2$ and on which the propagation of ICW without spontaneous activation activated a number of astrocytes $N_{act} \geq \frac{1}{2}\langle k \rangle$ higher than half of the network mean degree. Figure VI.4A shows these ζ^* values as a function of the network mean degree for the five network types. Solid colored lines are linear regressions of corresponding network types. The resonant frequency was indeed correlated to the mean degree, as assessed by a significantly high value of Spearman's rank correlation coefficient $\rho = 0.64$. While Erdős-Rényi , Shortcut, Link Radius, and Regular networks seemed to follow the same relationship (as indicated by their close regression lines), spatial scale free networks seemed to display slightly lower resonant frequencies for a given mean degree.

This relationship between mean degree $\langle k \rangle$ and resonant frequency ζ^* can be recovered from a very simplistic view of network topology, using the local propagation rules that we determined in Section V.3. Figure VI.4B shows a tree-like network (with astrocytes of degree k) in which an ICW propagated from the activated cell **A** (*green* circle) to the unactivated cell **B** (center *gray* cell). As this ICW propagates, some astrocytes are spontaneously activated (*yellow cells* marked C_2 and C_3). Since **A** is activated, according to the hypothesis stated in Section V.3, it will share its IP_3 (*red* arrows) among its unactivated neighbors **B** and $\mathbf{C}_1$. The fact that $\mathbf{C}_2$ was spontaneously activated will thus increase the quantity of IP_3 received by **B**. Additionally, spontaneously activated neighbors of **B** will also increase the quantity of IP_3 that it will receive as $\mathbf{C}_3$ will share its IP_3 among its unactivated neighbors; thus, if $\mathbf{C}_3$ also has a spontaneously activated neighbor ($\mathbf{C}_5$), it will give even more IP_3 to **B**. Assuming that the IP_3 transfer between

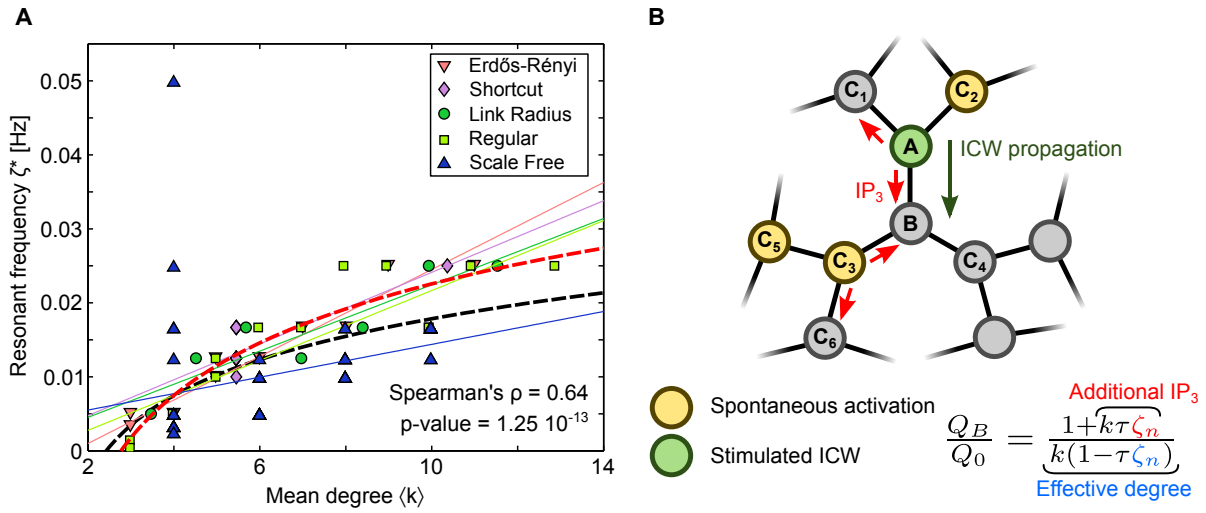

Figure VI.4: Network degree changes the resonant frequency. **A** Relationship between the network mean degree $\langle k \rangle$ and the resonant frequency ζ^* for networks which displayed a stochastic resonance strength of at least $\chi^* \geq 1.2$. As quantified by a high Spearman's rank correlation coefficient $\rho = 0.64$, all networks display the same qualitative behavior, as the mean degree increases, the resonant frequency also increases. *Solid* colored lines are linear regression lines for the different network types (colors are matching the symbols' colors). While most networks seem to share the same behavior, Spatial Scale Free networks (*solid blue* line and *blue* triangles) display marginally lower resonant frequencies for high mean degree values. Simulation parameters as in Figure VI.3. *Thick dashed* lines correspond to theoretical estimations of ζ^* using equation (VI.3) parameters A, B, and τ being fitted with (*black dashed* line, $A = 0.054$, $B = 0.28$, $\tau = 22.16$s) and without (*red dashed* line, $A = 0.08$, $B = 0.14$, $\tau = 19.29$s) taking into account Spatial Scale Free networks. **B** Schematic representation of ICW propagation (*green* cell A) in a tree-like network under spontaneous activation of astrocytes (*yellow* cells). We refer the reader to the text for a detailed description of this figure.

cell **A** and **B** takes τ seconds, the fraction of astrocytes in the network that will get spontaneously activated during this time is $\tau \times \zeta_n$ (we assume here that this fraction is always lower than 1, i.e. during τs, some astrocytes are not spontaneously active). We can thus write the quantity of IP_3 $Q_A = \frac{Q_0}{k(1-\tau\zeta_n)}$ (all astrocytes are considered to have the same degree k) that astrocyte **A** will give to astrocyte **B**, i.e. the total quantity of IP_3 that it will produce divided among the number of its inactive neighbors (for simplicity, we assume that **B** can also get spontaneously activated). Astrocyte **B** will also receive a quantity of IP_3 $Q_S = \frac{k\tau\zeta_n Q_0}{k(1-\tau\zeta_n)}$ from its $k\tau\zeta_n$ spontaneously activated neighbors (as $\mathbf{C}_3$ in Figure VI.4B) that will each split their IP_3 among $k(1-\tau\zeta_n)$ unactivated neighbors (as **B** and $\mathbf{C}_6$), for the sake of simplicity, we neglect the fact that **A** is already activated (this does not qualitatively change the results). Overall, we can thus approximate the quantity of IP_3 Q_B received by **B** as:

$$Q_B = Q_A + Q_S = Q_O \frac{1 + k\tau\zeta_n}{k(1-\tau\zeta_n)} \tag{VI.1}$$

We showed in Section V.3 that an astrocyte gets activated if it receives a normalized quantity of IP_3 higher than $\Psi_\theta = Ak + B$ which is a linear function of k. If the frequency of

spontaneous activation ζ_n becomes too high, astrocyte **B** will receive a normalized quantity of IP_3 $\frac{Q_B}{Q_0} > \Psi_\theta$ will get activated regardless of whether astrocyte **A** is propagating an ICW or not; in this case, the behavior of the network will be dominated by noise. Conversely, if ζ_n is too small, **B** will receive a sub-threshold normalized quantity of IP_3 $\frac{Q_B}{Q_0} < \Psi_\theta$ and will thus be unable to propagate the ICW. When ζ_n is tuned precisely to be close to the activation threshold $\frac{Q_B}{Q_0} \approx \Psi_\theta$, the network will be especially sensitive to activation and **A**'s ICW will be amplified by the spontaneous activations: it will display SR. We thus want to determine the resonant frequencies ζ^* that verifies:

$$\frac{1 + k\tau\zeta^*}{k(1 - \tau\zeta^*)} = Ak + B \tag{VI.2}$$

Which yields:

$$\zeta^* = \frac{kB + k^2A - 1}{\tau k(B + kA + 1)} \tag{VI.3}$$

Figure VI.4A displays this theoretical curve with two sets of parameters A, B and τ fitted with (*thick dashed black* line) or without (*thick dashed red* line) taking into account Spatial Scale Free Networks. Of course, the dispersion of the simulated points is too large to assess whether the specific shape of the relationship is correct, and while the fitted values of A and B are close to the ones we estimated in Section V.3, the relatively high values of τ seem to overestimate the time needed to transmit an ICW (which is closer to 10s). This simple approximation can however help us understand the mechanisms underlying SR. When the spontaneous activation frequency ζ_n increases, the normalized IP_3 quantity that astrocyte **B** (in Figure VI.4B) will receive increases through two mechanisms:

1. As illustrated by the *red* ζ_n term in Figure VI.4B, since spontaneously activated astrocytes also produce IP_3 , they increase the amount of IP_3 that **B** receives.
2. As illustrated by the *blue* ζ_n term in Figure VI.4B, the spontaneous activation of an astrocyte prevents it from becoming a sink to incoming ICW (e.g. astrocyte $\mathbf{C}_2$).

The second point can be seen as a way to dynamically lower the mean degree of a network, the spontaneously active astrocytes do not act as sinks to astrocytes that were activated by an ICW, as if they were removed from the network; the effective mean degree of the network thus becomes $\langle k \rangle (1 - \tau\zeta_n)$. As we saw in Chapter V, networks with lower mean degrees support larger ICW extents. Then, even if the spontaneous activation of some astrocytes did not produce enough IP_3 to significantly help the activation of neighboring astrocytes, it could still play a role in SR by dynamically reducing the mean degree of the network. We tested this hypothesis by running the exact same simulations (on the same networks) except that we replaced spontaneous activations by a 10s spontaneous temporary disconnection from the network. This type of spontaneous events thus did not add any IP_3 to the network, it just dynamically decreased its mean degree $\langle k \rangle$. Dynamically disconnecting astrocytes from the network can thus be seen as a dynamical control of the GJC permeability; the durations we use here are however far from experimental evidence that points towards longer times (minutes or hours) (Pasti et al., 1997; Blomstrand et al., 2004; Roux et al., 2011). This simulation is thus just used to disentangle the effects of network effective degree from the other effects at play during SR. Detailed results are reported in Appendix D.1.

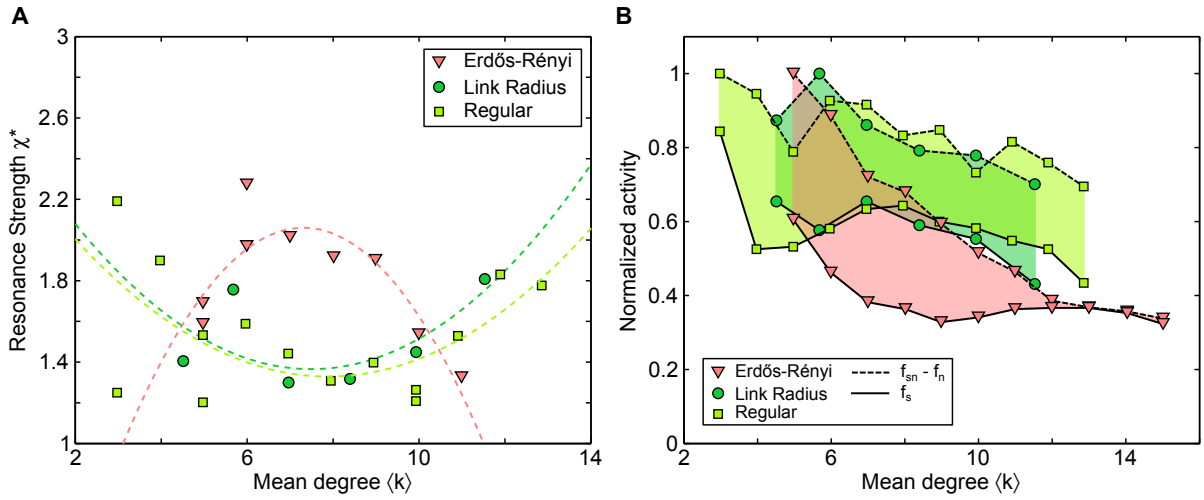

Figure VI.5: Networks respond differently to stochastic resonance protocols. **A** Stochastic resonance strengths χ^* as function of the mean degree $\langle k \rangle$ for several network types. Erdős-Rényi networks tend to support maximum stochastic resonance for intermediate mean degree while Link Radius and Regular Degree networks have the opposite behavior. *Colored dashed* lines are fitted parabolas to help visualization.**B** Stochastic resonance strengths are better understood by looking at the distance (*colored shaded areas*) between the activation frequency of astrocytes without spontaneous activation (*black solid* lines) and the activation frequency helped by the spontaneous activations (i.e. the difference between the activation frequency of astrocytes with stimulation and spontaneous activation f_{s+n} and the activation frequency of astrocytes with only spontaneous activation f_n). While spatially constrained networks are always helped by spontaneous activation, Erdős-Rényi networks do not achieve better ICW propagation with spontaneous activations for $\langle k \rangle > 11$. Activation frequencies were normalized by network types (i.e. divided by the highest activation frequency for this network) for visualization purposes. $IP_3^{bias} = 1.5\mu$M for Erdős-Rényi networks and 1μM for the other two networks.

Overall, we cannot explain the stochastic resonance effects just by considering the dynamic reduction in mean degree that it produces (c.f. Appendix D.1 for details). When considering both this effect and the addition of IP_3 resulting from spontaneous astrocyte activations, we can account for the relationship between the network mean degree $\langle k \rangle$ and the resonant frequency ζ^* but we cannot predict which networks will display SR and at which strength. Since the local analysis do not consider network structure, its predictions fail in many cases. One can see, just by looking at Figure VI.3E that Erdős-Rényi networks with high mean degrees do not display SR despite its prediction by local analysis. Additionally, as displayed in Figure VI.5A, SR strength χ^* display different profiles for Regular Degree and Link Radius networks (*green* squares and circles with associated *dashed* curves) and Erdős-Rényi (*red* triangles and *dashed* curve) networks: while it is stronger in the two spatially constrained networks for low ($\langle k \rangle \leq 5$) and high ($\langle k \rangle \geq 10$) degrees and lower for intermediate degrees, it as actually the reverse for Erdős-Rényi networks. Figure VI.5B shows the actual dynamics at work in these networks: for all network types, *solid black* lines denote the frequency of astrocyte activation without spontaneous activation f_s while the *dotted black* lines denote the difference between activation frequency with stimulation and spontaneous activation f_{sn} and the activation frequency with only spontaneous activation f_n. The space between these two

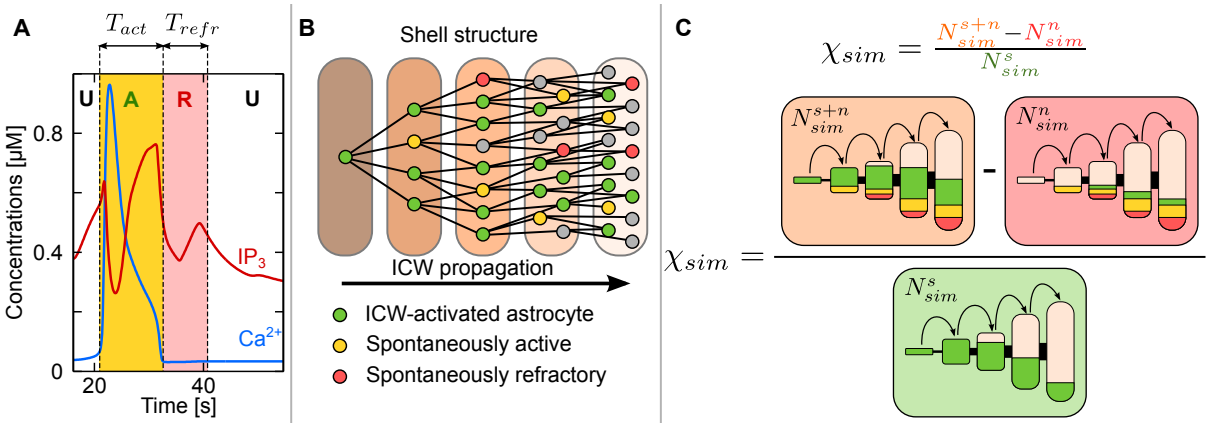

Figure VI.6: Stochastic shell propagation model. **A** Spontaneously activated astrocytes can be seen as having two distinct states during an activation: an 'activated' state (*yellow* shaded region) during which it gives IP_3 to its neighbors, and a refractory state (*red* shaded region) during which it acts as an IP_3 sink. The times T_{act} and T_{refr} during which it stays in each of these states is thus important for the effect that spontaneous activation will have on ICW propagation. **B** The stochastic shell propagation model introduces two additional states that an astrocyte can be in: spontaneously activated in their active state (*yellow* circles) and spontaneously activated in their refractory state (*red* circles). The former helps ICW propagation by increasing the amount of IP_3 produced by each shells while the latter prevents IP_3 propagation by acting as an unactivable IP_3 sink. **C** We quantify the stochastic resonance strength χ_{sim} in the same way as in the full ChI model simulations: we substract the number of astrocyte activated only by spontaneous activation N^n_{sim} (*red* shaded box) from the number of astrocytes activated by the ICW and spontaneous activations N^{s+n}_{sim} (*orange* shaded box). We then divide this quantity by the number of astrocytes activated by the ICW without spontaneous activations (*green* shaded box).

curves (emphasized by *colored shaded* regions) thus denotes the importance of SR. For spatially constrained networks, *dotted* and *solid* curves stay apart even for high mean degrees $\langle k \rangle$, maintaining SR. For Erdős-Rényi networks however, above $\langle k \rangle > 11$, the two curves collapse, indicating that the drop in SR strength is due to the fact that spontaneous activations no longer helps ICW propagation. This specific phenomenon cannot be understood from the simplistic explanation invoked in the local analysis; in order to better our understanding of SR in astrocyte networks, we thus decided to investigate it by taking into account network topologies.

VI.1.3 Network shell structure controls stochastic resonance

VI.1.3.1 The stochastic shell propagation (SSP) model

To improve our understanding of stochastic resonance and its interaction with network topologies, we decided to adapt our shell propagation model by incorporating spontaneous astrocyte activation. The detailed formulation of this new stochastic shell propagation model can be found in Appendix D.2. We present in Figure VI.6 the general ideas that

were used to devise this model. First and foremost, we hitherto considered that spontaneously activated astrocytes were either adding IP_3 to the network or preventing its loss by dynamically reducing the network mean degree. One of the other consequences of spontaneous astrocyte activation is that, as previously pointed out, it can prevent ICW transmission when the ICW encounters astrocytes that are left in their refractory period by the spontaneous activation; during this refractory period, astrocytes not only act as ICW barriers but also as IP_3 sinks that cannot get activated. Figure VI.6A illustrates this effect by showing typical Ca^{2+} and IP_3 traces of an astrocyte that just got activated; during its active period (*yellow shaded* region marked by an A), astrocytes give IP_3 to their neighbors, but during their refractory period (*red shaded* region marked by an R), they can actually receive IP_3 from other activated astrocytes (as it happened on this specific trace where IP_3 goes up before reaching the end of the refractory period) without being able to get activated. An important parameter of the model is thus the fraction of time $\gamma = \frac{T_{act}}{T_{act}+Trefr}$ during which the astrocyte actually gives IP_3 to its neighbors. The higher γ, the more 'source-like' (i.e. the more IP_3 they give) spontaneously activated astrocytes become and the better the supposed effect they will have on ICW propagation. In our stochastic shell propagation model, we took that fact into consideration by considering, as displayed in Figure VI.6B, that astrocytes in each shell can be in 4 different states: either (1) unactivated (*grey* circles); (2) activated by the ICW (*green* circles); (3) spontaneously activated and in the 'active', IP_3-giving, state (*yellow* circles); and (4) spontaneously activated and in the refractory phase. When propagating the ICW from the first shell to the last, only the unactivated nodes can get activated by the ICW. High frequencies of spontaneous activation thus effectively block the ICW propagation by leaving no astrocytes available for ICW activation. Spontaneously activated astrocytes in their active state in shell r were considered as activated astrocytes from the ICW in the sense that they gave their IP_3 to the astrocytes of the preceding shell $r-1$, to the unactivated astrocytes of shell r and to the next shell $r+1$. Additionally, when propagating the ICW, the shell $r+1$ on the wave front not only received IP_3 from the preceding shell r, as we did in the basic shell propagation model (see Appendix C.2), but also received IP_3 from the spontaneously activated nodes in the shell $r+1$ and in the next shell $r+2$. As in the full ChI model simulations, we needed to determine a spontaneous activation frequency that we varied during SR protocols. Figure VI.6C illustrates, for each value of spontaneous activation, the way we computed the stochastic resonance strength χ_{sim}; we first simulated ICW propagation with stimulation and spontaneous activation (*orange shaded* box) and measured the number of astrocytes activated by the ICW N_{sim}^{s+n} (*green* sub-compartments in the shells) without taking into account the astrocytes that were spontaneously activated (*yellow* and *red* sub-compartments). We next computed the number of astrocytes that were activated without stimulation, i.e. just with spontaneous activations (*smaller green* sub-compartments in the *red* shaded box), and subtracted it from N_{sim}^{s+n} to quantify how many of the astrocytes activated in the *orange* box were due to synergistic effects between stimulation and spontaneous activations. We then divide this by the number of astrocytes activated by the ICW without spontaneous activation N_{sim}^{s} (*green* box) to obtain χ_{sim}, our quantifier of stochastic resonance in the stochastic shell propagation model.

As explained in Appendix D.2, we first fit the shell propagation parameters to the ICW propagation extents without spontaneous activation for both stimulation intensi-

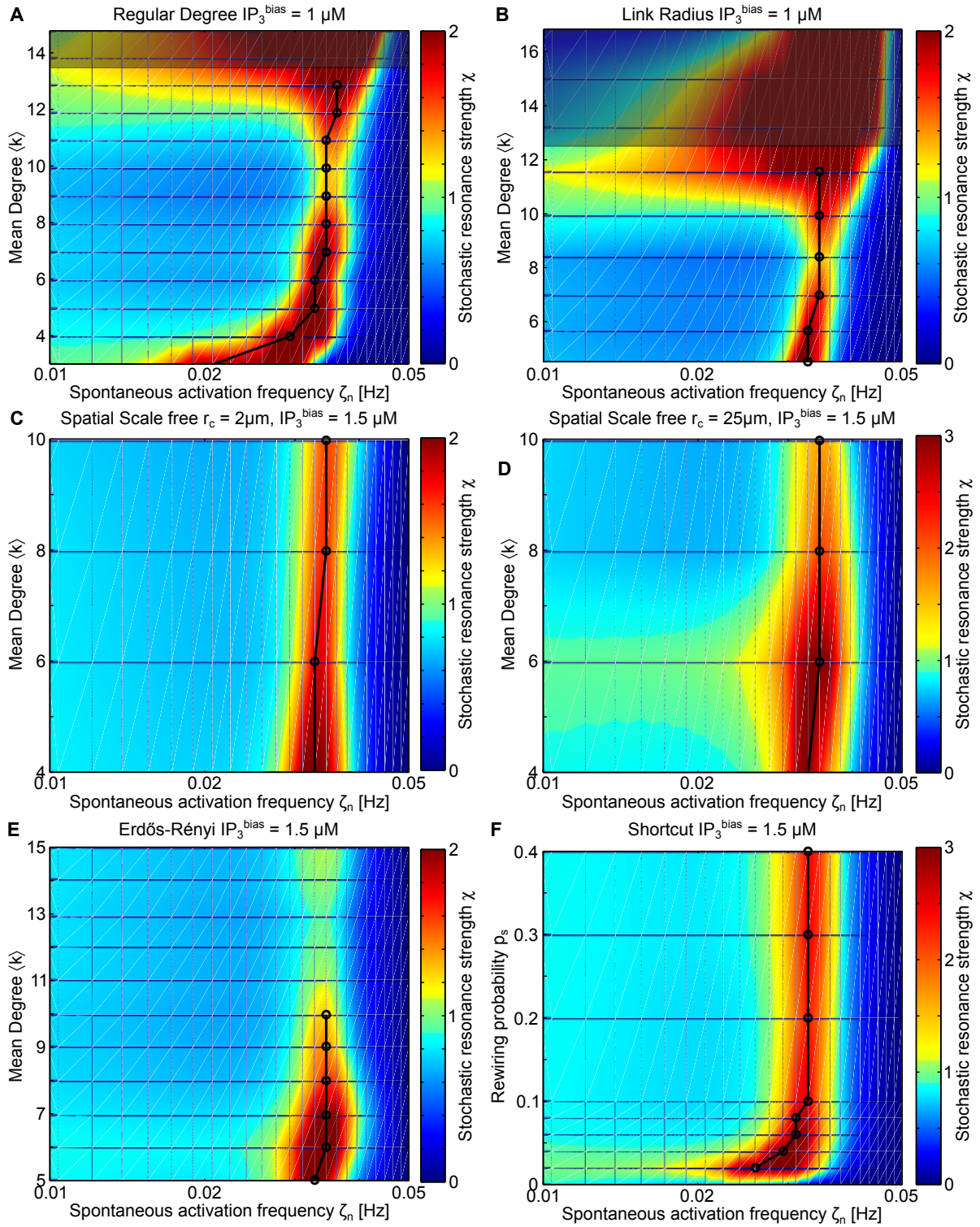

Figure VI.7: The stochastic shell propagation model qualitatively reproduces stochastic resonance. Heatmap representations of stochastic resonance effects. Mean $\chi(\zeta_n)$ values are color coded and plotted for different network types and stimulation conditions. Colorbars are adapted to each subplot as in Figure VI.3. For networks which have $\chi^*_{sim} \geq 1.2$, the *thick black* line plots the resonant frequency ζ^*. **A** Regular Degree networks, *shaded* area denote networks for which N_{act} was too small to assess stochastic resonance. **B** Link Radius networks. **C** Spatial Scale Free networks with $r_c = 2\mu$m. **D** Spatial Scale Free networks with $r_c = 25\mu$m. **E** Erdős-Rényi networks. **F** Shortcut networks with $\langle k \rangle = 6$ (i.e. $m_{latt} = 1$); y-axis values correspond to different rewiring probabilities p_s. **A** and **B** were weakly stimulated ($D \approx 100$) while **C** to **F** were stimulated with $D \approx 300$. Simulations and parameters as detailed in Appendix D.2, with $p_{ii} = 0.32$.

ties $IP_3^{bias} = 1$ and 1.5μM. We then only calibrated γ to reproduce qualitatively the stochastic resonance obtained in the full ChI model. We would thus like to point out that we did not fit the shell propagation parameters to reproduce the SR, we do not then expect to get a quantitative match to the SR that we got in the full ChI model. Simulations of this simplified stochastic shell propagation (SSP) model qualitatively reproduces the SR effects that we observed in the full ChI model. Figure VI.7A and B respectively show the SR induced on the Regular Degree and Link Radius spatially constrained networks with weak stimulation intensity. One can see by comparing with Figure VI.3A and B that the correspondence is quite good despite the fact that the values of ζ are different; this difference stems from the fact that the actual parameter controlling the ratio of spontaneously activated cells $f_n = \tau\zeta$ is proportional to ζ with τ a free parameter that was set close to the value fitted from Figure VI.4A ($\tau = 20$s). Spatially unconstrained networks also display the same type of SR that we witnessed in Figure VI.3: Spatial Scale Free networks (Figure VI.7C and D) display slight increases in their resonant frequency when their mean degree increased; Erdős-Rényi networks only displayed SR for small mean degrees (Figure VI.7E); and Shortcut networks (Figure VI.7F) did not display SR for $p_s = 0$ but, in contrast with Figure VI.3F, they displayed increasing resonant frequencies for low rewiring probabilities.

When γ, the parameter controlling the fraction of time during which spontaneously activated astrocytes are IP_3 sources is low (i.e. below 0.25), no SR occurs and the spontaneous activations are always detrimental to ICW propagation regardless of their frequency. When γ is increased up to 0.32 (as in Figure VI.7), networks display small SR with resonance strength $\chi^*_{sim} \leq 10$. Further increases in γ elicit SR in all the networks with increased resonance strength χ^*_{sim} that was much higher than the values obtained in the full ChI model simulations. Figure VI.8A shows the relationship between the network mean degree $\langle k \rangle$ and the resonant frequency ζ^*_{sim} for two different γ values ($\gamma = 0.5$ for the main figure and $\gamma = 0.32$ for the inset). The stochastic shell propagation model clearly reproduces the relationship observed in the full ChI model simulations (the resonant frequency increases with the network mean degree, see Figure VI.4A) as quantified by comparable Spearman's correlation coefficients. Interestingly, increasing γ overall decreased ζ^*_{sim} and modified the shape of the relationship, with a more graded increase in resonant frequency with the mean degree (compare the inset and the main figure). The shape obtained with $\gamma = 0.5$ is closer to what we reported in Figure VI.4A but SR strength χ^*_{sim} were much higher than χ^* in the ChI model for this γ value. As pointed out previously, the exact values of resonant frequencies ζ^*_{sim} are not expected to quantitatively match those reported in the full ChI model. Figure VI.8B shows the SR strength χ^*_{sim} as a function of the mean degree $\langle k \rangle$ for the same networks that we showed in Figure VI.5A. *Colored dashed* lines are fitted parabolas for visualization; similarly to what we observed in the full ChI model, Link Radius and Regular Degree networks display high resonance strength for low and high mean degrees and lower resonance for medium mean degrees. Erdős-Rényi networks show high resonance strength for low degrees and stop displaying SR for $\langle k \rangle > 10$. In contrast with the full ChI model simulations however, SR in Erdős-Rényi networks was approximately twice as low as in Regular and Link Radius networks (the scale for Erdős-Rényi , in *red*, on the right part of the figure, is different to compare the shapes). As a general rule, SR in the SSP model was higher than in the full ChI model, probably

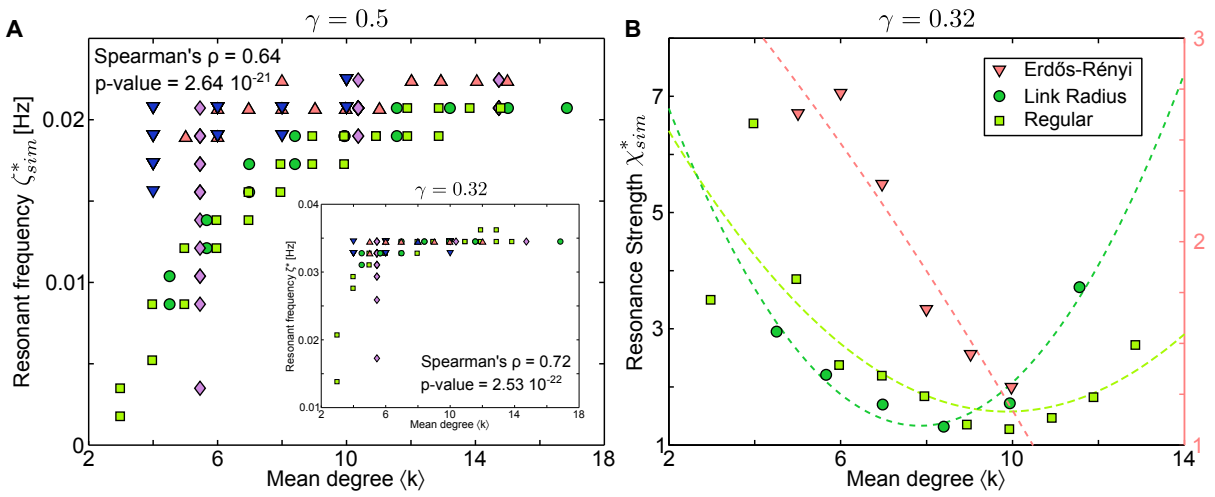

Figure VI.8: The resonant frequency ζ^* is also degree-dependent in the stochastic shell propagation model. **A** Relationship between resonant frequency in the SSP model ζ^*_{sim} and network mean degree $\langle k \rangle$. As in the full ChI model simulations (see Figure VI.4A), the resonant frequency increases with the network mean degree as quantified with the Spearman's correlation coefficients reported on the main figure and on the inset. Going from $\gamma = 0.32$ (inset) to $\gamma = 0.5$ (main figure) changes the shape of the relationship by making the increase in resonant frequency more gradual. Networks are displayed if they show a SR strength $\chi^*_{sim} \geq 1.2$ and if the ICW propagation without spontaneous activation N^s_{sim} was higher than $\frac{\langle k \rangle}{2}$. **B** Relationship between SR strength in the SSP model χ^*_{sim} and network mean degree $\langle k \rangle$. As in the full ChI model (see Figure VI.5A), both Link Radius (*dark green* circles) and Regular Degree (*light green* squares) networks show high SR strengths for low and high mean degrees and lower SR strengths for intermediate mean degrees. Erdős-Rényi networks (*red* triangles) show much lower SR strengths (we used a separate *red* scale on the right too compare the shapes) but, as in the full ChI model simulations, they stop displaying SR for high mean degrees. Simulations as in Figure VI.7. Similarly to Figure VI.5A, Erdős-Rényi networks were stimulated with $D \approx 300$ while Regular Degree and Link Radius networks were weakly stimulated with $D \approx 100$.

because of the simplifications that we imposed; the main point of Figure VI.8B is to show that Erdős-Rényi networks display decreasing SR strength with increasing mean degree and do not support SR for high network mean degrees while Regular Degree and Link Radius networks do. Altogether, these qualitative matches between the SSP model and the full ChI model indicate that we captured the main determinants of SR in astrocyte networks in the SSP model. In order to understand the precise mechanisms at play during SR, we now turn to investigate what determines the presence of SR in the SSP model.

Investigating stochastic resonance in the SSP model The full analysis is described in Appendix D.2.2, we only report here the main conclusions. The network-dependent value Ψ^{min}_{struct}, that quantifies how much IP_3 is received by the most limiting shell (i.e. the shell at which ICW propagation usually fails), was found to control ICW propagation in both SSP model and full network ChI model simulations. In the context of SR, Ψ^{min}_{struct} values seem to capture at least parts of the SR phenomenon in the ChI model:
– It accounts for the variability in resonant frequencies, showing that Ψ^{min}_{struct} values can be

seen as 'ditches' or 'gaps' that need to be filled by increasing the spontaneous activation frequency and thus increasing the overall IP_3 in the network.
- It accounts for the absence of SR in networks with very low Ψ_{struct}^{min}, as the frequency of spontaneous activations that would be needed to 'fill the gap' is too high to allow ICW propagation as almost all the astrocytes get spontaneously activated.
- Finally, it accounts for the high resonance strength displayed mostly by spatially-unconstrained networks at intermediate Ψ_{struct}^{min} values.

VI.2 Discussion

Spontaneous astrocyte activity is observed throughout brain regions, experimental preparations, and spatial scales. Depending on these conditions, its frequency can vary from 0.015 Hz per astrocyte (Nett et al., 2002), when considering full astrocyte activation in astrocyte networks, up to 10 Hz per astrocyte, when considering spontaneous activation of small subparts of processes (Di-Castro et al., 2011). When scaling the frequency of these spontaneous events to their specific spatial scale however, the resulting frequencies are near ≈ 0.02Hz (c.f. the minor diagonal of the table in Figure VI.1). Both the roles and effects of spontaneous activations are currently unknown; some authors think that they might influence neuronal excitability (Parpura et al., 1994; Kang et al., 1998; Pasti et al., 2001) but their influence on Ca^{2+} dynamics themselves has not really been investigated. With our model, we simulated ICW propagation with varying spontaneous activation frequencies and quantified how much spontaneous activations are helping or hindering ICW propagation. We found that some networks, including spatially constrained ones, display stochastic resonance phenomenon: for a specific spontaneous activation frequency, the resonant frequency ζ^*, ICW propagation can be improved by a factor ranging between 1.5 and 3. Interestingly, this resonant frequency was found to depend on the network mean degree: the more coupled the network, the higher the resonant frequency.

In the model, the resonant frequencies ζ^* range from ≈ 0.001 Hz for networks with a very low mean degree (Regular Degree network with $\langle k \rangle = 3$) to ≈ 0.02 Hz for networks whose mean degree is higher than ≈ 6; changes in mean degree can thus increase the resonant frequency by more than 10 folds. Interestingly, spontaneous activation frequencies in experiments also span large frequency ranges: in situ experiments report spontaneous activation frequencies that range from ≈ 0.003 Hz to 0.03 Hz: Nett et al. (2002) report spontaneous oscillations in hippocampus in situ that range from 0.00347 to 0.0333 Hz and are independent of age (animals were between 10 and 17 days); Poskanzer and Yuste (2011) report spontaneous oscillations at ≈ 0.0075 Hz in cortex in situ in 13-15 days animals; Parri et al. (2001) report spontaneous oscillations in the ventrobasal thalamus in situ that range from 0.0062 Hz for young (less than 10 days) animals and is reduced to 0.0018 Hz in older (more than 10 days) animals. These experimental values are in relatively close agreement with the resonant frequencies obtained in the model, indicating that spontaneous activations could mediate ICW propagation by stochastic resonance phenomenon in situ (assuming that the model correctly describes ICW propagation).

In pathological conditions, such as epilepsy or Alzheimer's disease, which might be also linked to increased expression of Cx43 (Rouach et al., 2002), the spontaneous oscillation frequency seems to be increased: Tashiro et al. (2002) report spontaneous oscillations at ≈ 0.03 Hz in the cortex of 14 days old epileptic animals while Poskanzer and Yuste (2011) reported oscillations at 0.0075 Hz in the same region with same age control animals. In the cortex of mice with Alzheimer's disease, Kuchibhotla et al. (2009) showed that spontaneous oscillations frequency was higher than in wild type animals. These increases in spontaneous oscillation frequency (up to 4 fold for Tashiro et al. (2002)) are accompanied with increases in Cx43 expression (Rouach et al., 2002); the model predicts that, in

order to stay in the spontaneous resonance frequency range, increases in coupling should be compensated by increases in spontaneous oscillation frequencies. Of course these observations are just anecdotal evidence and the increase in oscillation frequency could be completely unrelated to the increase in Cx43 expression.

Spontaneous oscillations in vivo have also been shown to be affected by experimental conditions. Anesthetized animals notably display reduced spontaneous oscillation frequencies (Thrane et al., 2012), going from ≈ 0.002 Hz in the neocortex of awake mice down to ≈ 0.000333 Hz in anesthetized animals. If stochastic resonance phenomenon were at play in ICW propagation in vivo, these changes in spontaneous oscillation frequencies could explain the apparent lack of ICW in anesthetized animals. Imaging techniques might also modify spontaneous oscillation frequency: Kuga et al. (2011) recently showed in the hippocampus of mice that increasing the power of the imaging laser could increase the spontaneous oscillation frequency from 0.0016 Hz (for 8 mW) up to 0.0125 Hz (for 30 mW). Interestingly, large-scale ICW were only observed when the spontaneous oscillation frequency was around ≈ 0.002 Hz (i.e. when the power of the laser was small); this behavior would correspond in the model to low mean degree networks ($\langle k \rangle \approx 3.5$) that can propagate large-scale waves at a resonant frequency around 0.002 Hz (c.f. Figure VI.3A) but in which increases in spontaneous oscillation frequency over 0.005 Hz completely prevents the propagation of large-scale ICWs.

In order to address stochastic resonance experimentally, one might need to look at more detailed data than just average spontaneous oscillation frequencies. The previous example might thus be of interest in experimental investigations: using laser power or pharmacological approaches that specifically control spontaneous oscillation frequency might be interesting strategies to assess whether stochastic resonance phenomenon are at play in astrocyte networks. Alternatively, one could also screen old experimental data reporting ICW propagation and compute spontaneous activation frequencies with a sliding window. Stochastic resonance could then be at plays if, before each ICW, the spontaneous activation frequency of astrocytes increased (if the basal frequency is below the resonant frequency) or decreased (if the basal frequency is above the resonant frequency). This latter method would however target a different kind of stochastic resonance: in the previous examples, we considered that the ICWs did not originate from the spontaneous oscillations but were facilitated by them (the network is always in resonant frequency); with the sliding window method, we expect that the basal spontaneous oscillation frequency is not associated with stochastic resonance (and thus prevents ICW propagation) but can be transiently switched to stochastic resonance by increases or decreases in spontaneous oscillation frequency.

Finally, stochastic resonance phenomenon could depend not only on intrinsic spontaneous oscillations due to random opening of intracellular Ca^{2+} stores, but could also depend on neuron-activated astrocytes. Wang et al. (2006); Schummers et al. (2008); Poskanzer and Yuste (2011) show for example that astrocyte activation frequency can be increased following neuronal stimulation. Additionally, the same type of dynamics might be at play for subcellular Ca^{2+} signaling: as presented at the beginning of the chapter, spontaneous oscillations also occur in main processes (Di-Castro et al., 2011), in small parts

of subprocesses (Kanemaru et al., 2014), and even in the smallest sheet-like subprocesses (Shigetomi et al., 2013). The same type of questions thus arise: does this spontaneous activity play a role (in stochastic resonance-like mechanisms for example) or can it be considered as detrimental but unavoidable 'noise' in Ca^{2+} signaling ?

Chapter VII

Conclusion and perspectives

Chapters IV, V and VI had independent discussions, we will thus only briefly summarize their main findings here, present common conclusions and discuss future work.

We first investigated in Chapter IV astrocytic Ca^{2+} activity at the single cell level, considering their individual responses to neuronal stimulations both in experimental conditions and in simulations. This first step allowed us to check that the basic Ca^{2+} signaling properties of the model were conform to what was observed experimentally. Our collaborators showed experimentally with a MEA setup that astrocytes in mixed neuron-glia cultures responded to neuronal stimulation in a frequency-dependent manner and not only in an intensity-dependent manner, as was shown until now in the literature. Additionally, two types of astrocyte responses were observed: some astrocytes responded early to low frequency neuronal stimulation and with high Ca^{2+} oscillation frequencies, while other astrocytes responded only to high frequency neuronal stimulation and with low frequency Ca^{2+} oscillations. Investigation of this neuron-astrocyte communication system with the model showed that both frequency-dependent responses and variability in onset and oscillation frequencies could be emulated in simulations. The frequency-dependent response of astrocytes was due in the model to supralinear IP_3 dynamics; since IP_3 diffused by GJC between astrocytes, simulated astrocytes displayed different responses depending on their coupling degree. Notably, isolated astrocytes were shown to coincide in the model with those astrocytes that responded to low frequency stimulation with high frequency Ca^{2+} oscillations while astrocytes that were GJC-coupled to several neighbors displayed low frequency Ca^{2+} oscillations and only responded to high frequency neuronal stimulation. This result shows that topological properties of astrocyte networks can control individual astrocyte responses to stimulation.

From this conclusion, and from the experimentally observed heterogeneity in both astrocyte network topologies and ICW extents, we decided to investigate in Chapter V whether astrocyte network topology could control ICW extent and thus account for the diversity of ICW extents in different brain regions. We investigated this question by simulating ICW propagation in large 3D astrocyte networks in which the biophysical parameters of each

astrocyte were kept constant and only the network topologies were changed. Changing the topology alone indeed allowed to switch between very small ICW extents (≈ 10 astrocytes) to regenerative ICWs which spanned the whole networks. Quite counter-intuitively, ICW propagation was shown to be maximal when the networks were sparsely coupled (i.e. had a low mean degree $\langle k \rangle$) and when links were restricted to spatially close astrocytes (i.e. when the mean-shortest path L was high). These effects were explained in the model by the specific mechanisms that drive GJC-dependent ICW: in contrast to activity propagation in excitatory neuronal networks with chemical synapses (in which the addition of new synapses does not decrease the strength of other synapses), the addition of new connections or long-distance connections between astrocytes ultimately increases IP_3 leak to unactivated neighbors and thus provokes early ICW failure. These strong differences could explain why astrocytes (at least their protoplasmic subtype) only make contact with spatially close neighbors (Bushong et al., 2002) while neurons can send long distance processes to other neurons without jeopardizing activation propagation. These basic mechanisms of IP_3 leak were shown, in a very simplified SERS-type model, to be able to qualitatively account for the effects of topology on ICW propagation. Additionally, more detailed descriptions of network topologies using shell analysis was shown to quantitatively account for these effects and hinted that the switch between spatially-restricted and regenerative propagations depended on the activation of the first shells. In this light, the relationship between ATP-mediated and GJC-mediated pathways of ICW propagation might be reconsidered: numerous experiments (Scemes et al., 2000; Bowser and Khakh, 2007; Kuga et al., 2011) show ICW extent decreased by both GJC-blockers and P2YRs antagonists, indicating that both pathways are involved; non regenerative ATP could very well mediate the ATP-dependent pathway (Arcuino et al., 2002). Since GJC-dependent long-range ICW propagation can only be achieved if the astrocyte network has a low mean degree or if the first shells are simultaneously activated, the non regenerative ATP release could be an effective mechanism to activate the first shells in highly coupled astrocyte networks without wasting high quantities of ATP by regenerative ATP release. These results are also of interest because astrocyte network topologies could be dynamically modified by signaling molecules (Rouach et al., 2002) and notably by neuronal activity (Rouach et al., 2000).

In Chapter VI, we addressed the effects of spontaneous astrocyte activations on ICW propagation. These spontaneous activations are witnessed in different brain regions, with different preparations (in situ, in vivo), and at different spatial scales (astrocyte, main processes, subprocesses). Their effects are not really understood; they might influence neuronal activity but their effects on inter-astrocyte communications has not been characterized. To address this question, we simulated ICW propagation under random spontaneous activations with different frequencies. We showed that, for specific frequency ranges (and reaching maximal effect at a given resonant frequency), spontaneous activations helped ICW propagation via stochastic resonance. The resonant frequency was specific to each network and mainly depended on the mean degree of the network: the higher the mean degree, the higher the resonant frequency. This effect was shown to be linked to additional IP_3 creation by the spontaneous activations and not by the dynamical reduction in mean degree that they may produce. Additionally, we showed that shell descriptions of astrocyte networks could qualitatively account for the stochastic resonance

phenomenon displayed in the different networks while hinting that spontaneous activations played their most useful role in the first shells. This result can be extended to ICW propagation under several simultaneous stimulations: stimulations that are close to each other are more likely to lead to large-scale ICW than if they are far apart. Since this stochastic resonance phenomenon depends on the activation of astrocytes independently of how they are activated, neurons could also control the switch between normal ICW propagation and stochastic resonance-assisted ICW propagation.

The conclusions from these chapters point towards significant roles for astrocyte network topologies in Ca^{2+} signaling and thus call for further investigation. In particular, the fact that GJC permeability is regulated by a large variety of signaling molecules (Rouach et al., 2002; Orellana et al., 2013) points toward dynamic control of astrocyte network topologies, possibly by neurons (Rouach et al., 2000; Pina-Benabou et al., 2001). We recently chose to start modeling the dynamic regulation of GJC exerted by astrocytic uptake of excess neuronal K^+. The uptake of K^+ by astrocyte was indeed linked to CamKII-mediated phosphorylation of GJC, increasing their permeability (Pina-Benabou et al., 2001); Ca^{2+} dependent phosphorylation of GJC by PKC could constitute the reverse mechanism (Bao et al., 2004; Sirnes et al., 2009; Huang et al., 2013) and the interplay between the two mechanisms could create preferential paths between astrocytes. Inter-astrocyte K^+ diffusion (Wallraff et al., 2006) could increase GJC permeability not only in the astrocyte that took-up the excess K^+ but also in neighboring astrocytes. Appendix E.2 presents the preliminary model that we developed and some proof of concept regarding its effect on ICW propagation.

Regarding the previous speculations on the interplay between ATP-mediated and GJC-mediated pathways of ICW propagation, we would like to test our hypothesis in a model that actually takes into account P2YRs-mediated IP_3 production and ATP release. Notably, since ATP release has been proposed to depend on hemichannels, it would be interesting to see whether increases in Cx43 expression can simultaneously increase GJC coupling and provide the ATP-dependent pathway needed to still be able to propagate ICW in strongly coupled networks.

When first imaging experiments were conducted in astrocyte processes (Panatier et al., 2011; Di-Castro et al., 2011), most Ca^{2+} events seemed to be restricted to subparts of astrocyte processes, leading to the hypothesis that different subparts of processes could be separate units independently regulating individual synapses. Recent progresses made by Ca^{2+} indicators, and notably the development of genetically encoded Ca^{2+} indicators (GECI), allowed simultaneous imaging of astrocyte soma, main processes and very fine subprocesses (Shigetomi et al., 2013; Kanemaru et al., 2014; Haustein et al., 2014). These new imaging experiments revealed very frequent Ca^{2+} activity in the whole astrocyte territory and especially in distant processes. Interestingly, a large part of this activity seems to be independent from neuronal activity (Haustein et al., 2014) and, in contrast to previous studies that presented very rare propagation of activity from processes to soma, these new techniques reveal that this happens more frequently than previously expected (Kanemaru et al., 2014; Haustein et al., 2014). These observations question the integration of activity by the complex astrocyte morphology and thus prompt us to start investigating

intracellular Ca^{2+} signaling in astrocytes. In a first attempt to do so, we calibrated our Ca^{2+} signaling model to fit experimental data taken from Di-Castro et al. (2011) (see Appendix E.1); we next plan to investigate: (1) how spontaneous activity could affect neuron-evoked signaling events in 1D processes; (2) how more complex morphologies like Y branches or several subprocesses connected to a main process could integrate neuronal activity; (3) how the activity in the main processes can get integrated in the astrocyte soma. Interestingly, studying these problems might shed new light on the frequency-dependent responses of astrocytes that we investigated in Chapter IV. Since the shell analysis in Chapter V essentially reduces propagation in a full astrocyte network to a propagation in a 1D chain of compartments with varying volumes and diffusion strength, we are very much interested in the possible similarities between Ca^{2+} signal propagation at the subcellular level (in processes) and at intercellular level.

Altogether, these exciting recent experimental discoveries prompt the development of modeling efforts in collaboration with experimentalists. In the long term, understanding how astrocyte integrate neuronal stimulations in their complex morphology is of particular importance for developing a coherent theory of neuron-astrocyte communication at the single astrocyte level. Modeling the network levels, for both astrocytic and neuronal networks, will then necessitate much more morphological informations (how many astrocytes can one neuron contact, what are the connections between neurons that are contacted by a given astrocyte, etc.) than currently available. In anticipation of the worlds of complexity that may be revealed, I hope that these steps will be taken in the next decades but I'm entirely sure that they can only be taken in close collaboration with experimentalists.

Bibliography

Abbott, L. F. and Regehr, W. G. (2004). Synaptic computation. *Nature*, 431:796–803.

Aberg, N. D., Rönnbäck, L., and Eriksson, P. S. (1999). Connexin43 mRNA and protein expression during postnatal development of defined brain regions. *Dev. Brain Res.*, 115(1):97–101.

Adams, R., Calcraft, L., and Davey, N. (2009). Using a genetic algorithm to investigate efficient connectivity in associative memories. *Neurocomputing*, 72(4-6):732 – 742. Brain Inspired Cognitive Systems (BICS 2006) / Interplay Between Natural and Artificial Computation (IWINAC 2007).

Aguado, F., Espinosa-Parrilla, J. F., Carmona, M. A., and Soriano, E. (2002). Neuronal activity regulates correlated network properties of spontaneous calcium transients in astrocytes in situ. *J. Neurosci.*, 22(21):9430–9444.

Agulhon, C., Fiacco, T. A., and McCarthy, K. D. (2010). Hippocampal short- and long-term plasticity are not modulated by astrocyte Ca^{2+} signaling. *Science*, 327(5970):1250–1254.

Agulhon, C., Sun, M.-Y., Murphy, T., Myers, T., Lauderdale, K., and Fiacco, T. A. (2012). Calcium signaling and gliotransmission in normal vs. reactive astrocytes. *Frontiers in pharmacology*, 3.

Albert, R. and Barabási, A.-L. (2002). Statistical mechanics of complex networks. *Rev. Mod. Phys.*, 74(1):47–97.

Anders, S., Minge, D., Griemsmann, S., Herde, M. K., Steinhäuser, C., and Henneberger, C. (2014). Spatial properties of astrocyte gap junction coupling in the rat hippocampus. *Philosophical Transactions of the Royal Society B: Biological Sciences*, 369(1654):20130600.

Anderson, C. M., Bergher, J. P., and Swanson, R. A. (2004). ATP-induced ATP release from astrocytes. *J. Neurochem.*, 88:246–256.

Araque, A., Martìn, E., Perea, G., Arellano, J., and Buño, W. (2002). Synaptically released acetylcholine evokes Ca^{2+} elevations in astrocytes in hippocampal slices. *J. Neurosci.*, 22(7):2443–2450.

Araque, A., Sanzgiri, R. P., Parpura, V., and Haydon, P. G. (1999). Astrocyte-induced modulation of synaptic transmission. *Can. J. Physiol. Pharm.*, 77:699–706.

Arcuino, G., Lin, J. H.-C., Takano, T., Liu, C., Jiang, L., Gao, Q., Kang, J., and Nedergaard, M. (2002). Intercellular calcium signaling mediated by point-source burst release of ATP. *Proc. Natl. Acad. Sci. USA*, 99(15):9840–9845.

Arenas, A., Díaz-Guilera, A., Kurths, J., Moreno, Y., and Zhou, C. (2008). Synchronization in complex networks. *Physics Reports*, 469(3):93 – 153.

Arenas, A., Díaz-Guilera, A., and Pérez-Vicente, C. J. (2006). Synchronization reveals topological scales in complex networks. *Phys Rev Lett*, 96(11):114102.

Arizono, M., Bannai, H., Nakamura, K., Niwa, F., Enomoto, M., Matsu-ura, T., Miyamoto, A., Sherwood, M. W., Nakamura, T., and Mikoshiba, K. (2012). Receptor-selective diffusion barrier enhances sensitivity of astrocytic processes to metabotropic glutamate receptor stimulation. *Science signaling*, 5(218):ra27.

Aurenhammer, F. (1991). Voronoi diagrams—a survey of a fundamental geometric data structure. *ACM Comput. Surv.*, 23(3):345–405.

Bains, J. S. and Oliet, S. H. R. (2007). Glia: they make your memories stick! *Trends Neurosci.*, 30(8):417–424.

Ball, K. K., Harik, L., Gandhi, G. K., Cruz, N. F., and Dienel, G. A. (2011). Reduced gap junctional communication among astrocytes in experimental diabetes: contributions of altered connexin protein levels and oxidative–nitrosative modifications. *Journal of neuroscience research*, 89(12):2052–2067.

Bao, X., Altenberg, G. A., and Reuss, L. (2004). Mechanism of regulation of the gap junction protein connexin 43 by protein kinase C-mediated phosphorylation. *Am J Physiol Cell Physiol*, 286(3):C647–C654.

Barthélemy, M. (2010). Spatial networks. *Phys. Rep.*, 499:1–101.

Bedner, P. and Steinhäuser, C. (2013). Altered Kir and gap junction channels in temporal lobe epilepsy. *Neurochem Int.*

Bennett, M., Farnell, L., and Gibson, W. (2005). A quantitative model of purinergic junctional transmission of calcium waves in astrocyte networks. *Biophysical journal*, 89(4):2235–2250.

Bergersen, L., Morland, C., Ormel, L., Rinholm, J. E., Larsson, M., Wold, J. F. H., Rø e, r. A. T., Stranna, A., Santello, M., Bouvier, D., Ottersen, O. P., Volterra, A., and Gundersen, V. (2012). Immunogold detection of L-glutamate and D-serine in small synaptic-like microvesicles in adult hippocampal astrocytes. *Cereb. Cortex*, 22(7):1690–1697.

Bernardinelli, Y., Magistretti, P. J., and Chatton, J.-Y. (2004). Astrocytes generate na+-mediated metabolic waves. *Proceedings of the National Academy of Sciences of the United States of America*, 101(41):14937–14942.

Bernardinelli, Y., Salmon, C., Jones, E. V., Farmer, W. T., Stellwagen, D., and Murai, K. K. (2011). Astrocytes display complex and localized calcium responses to single-neuron stimulation in the hippocampus. *J Neurosci*, 31(24):8905–8919.

Berridge, M. J., Bootman, M. D., and Roderick, H. L. (2003). Calcium signalling: dynamics, homeostasis and remodelling. *Nat. Rev. Mol. Cell. Biol.*, 4:517–529.

Bezzi, P., Gundersen, V., Galbete, J. L., Seifert, G., Steinhäuser, C., Pilati, E., and Volterra, A. (2004). Astrocytes contain a vesicular compartment that is competent for regulated exocytosis of glutamate. *Nat. Neurosci.*, 7(6):613–620.

Blackwell, K. T. (2005). Modeling calcium concentration and biochemical reactions. *Brains Minds Media*, 1:27.

Blomstrand, F., Aberg, N. D., Eriksson, P. S., Hansson, E., and Rönnbäck, L. (1999a). Extent of intercellular calcium wave propagation is related to gap junction permeability and level of connexin-43 expression in astrocytes in primary cultures from four brain regions. *Neuroscience*, 92(1):255–265.

Blomstrand, F., Giaume, C., Hansson, E., and Rönnbäck, L. (1999b). Distinct pharmacological properties of ET-1 and ET-3 on astroglial gap junctions and Ca^{2+} signaling. *Am J Physiol*, 277(4 Pt 1):C616–C627.

Blomstrand, F., Venance, L., Sirén, A.-L., Ezan, P., Hanse, E., Glowinski, J., Ehrenreich, H., and Giaume, C. (2004). Endothelins regulate astrocyte gap junctions in rat hippocampal slices. *European Journal of Neuroscience*, 19(4):1005–1015.

Boccaletti, S., Latora, V., Moreno, Y., Chavez, M., and Hwang, D.-U. (2006). Complex networks: structure and dynamics. *Phys. Rep.*, 424(4-5):175 – 308.

Bohland, J. W. and Minai, A. A. (2001). Efficient associative memory using small-world architecture. *Neurocomputing*, 38-40:489 – 496.

Boison, D., Chen, J.-F., and Fredholm, B. B. (2009). Adenosine signaling and function in glial cells. *Cell Death & Differentiation*, 17(7):1071–1082.

Bolaños, J. P. and Medina, J. M. (1996). Induction of nitric oxide synthase inhibits gap junction permeability in cultured rat astrocytes. *Journal of neurochemistry*, 66(5):2091–2099.

Bonder, D. E. and McCarthy, K. D. (2014). Astrocytic gq-gpcr-linked ip3r-dependent ca2+ signaling does not mediate neurovascular coupling in mouse visual cortex in vivo. *The Journal of Neuroscience*, 34(39):13139–13150.

Bootman, M., Niggli, E., Berridge, M., and Lipp, P. (1997). Imaging the hierarchical ca2+ signalling system in hela cells. *The Journal of Physiology*, 499(Pt 2):307–314.

Bowser, D. N. and Khakh, B. S. (2007). Vesicular ATP is the predominant cause of intercellular calcium waves in astrocytes. *J. Gen. Physiol.*, 129(6):485–491.

Breskin, I., Soriano, J., Moses, E., and Tlusty, T. (2006). Percolation in living neural networks. *Physical review letters*, 97(18):188102.

Bugrim, A. E., Zhabotinsky, A. M., and Epstein, I. R. (1997). Calcium waves in a model with a random spatially discrete distribution of ca2+ release sites. *Biophysical Journal*, 73(6):2897–2906.

Bukauskas, F. F., Jordan, K., Bukauskiene, A., Bennett, M. V., Lampe, P. D., Laird, D. W., and Verselis, V. K. (2000). Clustering of connexin 43-enhanced green fluorescent protein gap junction channels and functional coupling in living cells. *Proc Natl Acad Sci U S A*, 97(6):2556–2561.

Bullmore, E. and Sporns, O. (2009). Complex brain networks: graph theoretical analysis of structural and functional systems. *Nature Reviews Neuroscience*, 10(3):186–198.

Burnstock, G., B Fredholm, B., and Verkhratsky, A. (2011). Adenosine and atp receptors in the brain. *Current topics in medicinal chemistry*, 11(8):973–1011.

Bushong, E. A., Martone, M. E., Jones, Y. Z., and Ellisman, M. H. (2002). Protoplasmic astrocytes in CA1 stratum radiatum occupy separate anatomical domains. *J. Neurosci.*, 22(1):183–192.

Carmignoto, G. and Haydon, P. G. (2012). Astrocyte calcium signaling and epilepsy. *Glia*, 60(8):1227–1233.

Centola, D., Eguíluz, V. M., and Macy, M. W. (2007). Cascade dynamics of complex propagation. *Physica A*, 374(1):449 – 456.

Charles, A. (1998). Intercellular calcium waves in glia. *Glia*, 24(1):39–49.

Charles, A. C., Dirksen, E. R., Merrill, J. E., and Sanderson, M. J. (1991). Intercellular signalling in glial cells: calcium waves and oscillations in response to mechanical stimulation and glutamate. *Neuron*, 6:983–992.

Charles, A. C., Naus, C., Zhu, D., Kidder, G. M., Dirksen, E. R., and Sanderson, M. J. (1992). Intercellular calcium signaling via gap junctions in glioma cells. *The Journal of cell biology*, 118(1):195–201.

Chow, C. C. and Kopell, N. (2000). Dynamics of spiking neurons with electrical coupling. *Neural Comput.*, 12(7):1643–1678.

Chow, S.-K., Yu, D., MacDonald, C. L., Buibas, M., and Silva, G. A. (2009). Amyloid β-peptide directly induces spontaneous calcium transients, delayed intercellular calcium waves and gliosis in rat cortical astrocytes. *ASN neuro*, 2(1):AN20090035.

Cina, C., Bechberger, J. F., Ozog, M. A., and Naus, C. C. G. (2007). Expression of connexins in embryonic mouse neocortical development. *J Comp Neurol*, 504(3):298–313.

Clarke, L. E. and Barres, B. A. (2013). Emerging roles of astrocytes in neural circuit development. *Nat Rev Neurosci*.

Coco, S., Calegari, F., Pravettoni, E., Pozzi, D., Taverna, E., Rosa, P., Matteoli, M., and Verderio, C. (2003). Storage and release of ATP from astrocytes in culture. *J. Biol. Chem.*, 278(2):1354–1362.

Colizza, V., Barrat, A., Barthélemy, M., and Vespignani, A. (2007). Predictability and epidemic pathways in global outbreaks of infectious diseases: the sars case study. *BMC Med*, 5:34.

Connors, B. W. and Long, M. A. (2004). Electrical synapses in the mammalian brain. *Annu. Rev. Neurosci.*, 27:393–418.

Coombes, S. and Timofeeva, Y. (2003). Sparks and waves in a stochastic fire-diffuse-fire model of ca 2+ release. *Physical Review E*, 68(2):021915.

Cornell-Bell, A. H., Finkbeiner, S. M., Cooper, M. S., and Smith, S. J. (1990). Glutamate induces calcium waves in cultured astrocytes: long-range glial signaling. *Science*, 247(4941):470–473.

Costa, Rodrigues, F. A., Travieso, G., and Boas, V. P. R. (2007). Characterization of complex networks: A survey of measurements. *Advances in Physics*, 56(1):167–242.

Costa, L. d. F. and da Rocha, L. E. C. (2006). A generalized approach to complex networks. *Eur. Phys. J. B*, 50:237–242.

Cotrina, M. L., Lin, J. H., López-García, J. C., Naus, C. C., and Nedergaard, M. (2000). ATP-mediated glia signaling. *J. Neurosci.*, 20(8):2835–2844.

Cotrina, M. L., Lin, J. H.-C., Alves-Rodrigues, A., Liu, S., Li, J., Azmi-Ghadimi, H., Kang, J., Naus, C. C. G., and Nedergaard, M. (1998). Connexins regulate calcium signaling by controlling ATP release. *Proc. Natl. Acad. Sci. USA*, 95(26):15735–15740.

Crank, J. (1980). *The mathematics of diffusion*. Oxford University Press, USA, 2 edition.

Cuthbertson, K. S. R. and Chay, T. R. (1991). Modelling receptor-controlled intracellular calcium oscillators. *Cell Calcium*, 12:97–108.

D'Ambrosio, R., Wenzel, J., Schwartzkroin, P. A., McKhann, G. M., and Janigro, D. (1998). Functional specialization and topographic segregation of hippocampal astrocytes. *J. Neurosci.*, 18(12):4425–4438.

Dani, J. W., Chernjavsky, A., and Smith, S. J. (1992). Neuronal activity triggers calcium waves in hippocampal astrocyte networks. *Neuron*, 8(3):429–440.

Dawson, S. P., Keizer, J., and Pearson, J. E. (1999). Fire–diffuse–fire model of dynamics of intracellular calcium waves. *Proceedings of the National Academy of Sciences*, 96(11):6060–6063.

De Bock, M., Decrock, E., Wang, N., Bol, M., Vinken, M., Bultynck, G., and Leybaert, L. (2014). The dual face of connexin-based astroglial ca 2+ communication: A key player in brain physiology and a prime target in pathology. *Biochimica et Biophysica Acta (BBA)-Molecular Cell Research*.

de Groot, J. and Sontheimer, H. (2011). Glutamate and the biology of gliomas. *Glia*, 59(8):1181–1189.

De Pittà, M., Volman, V., Berry, H., and Ben-Jacob, E. (2011). A tale of two stories: Astrocyte regulation of synaptic depression and facilitation. *PLoS Comput Biol*, 7(12):e1002293.

De Pittà, M., Volman, V., Berry, H., Parpura, V., Liaudet, N., Volterra, A., and Ben-Jacob, E. (2012). Computational quest for understanding the role of astrocyte signaling in synaptic transmission and plasticity. *Front. Comp. Neurosci.*, 6:98.

De Pittà, M., Volman, V., Levine, H., Pioggia, G., De Rossi, D., and Ben-Jacob, E. (2008). Coexistence of amplitude and frequency modulations in intracellular calcium dynamics. *Phys. Rev. E*, 77(3):030903(R).

De Pittà, M. D. (2013). *Information processing and memory in astrocyte-modulated synapses*. PhD thesis, Tel Aviv University.

De Saint Jan, D. and Westbrook, G. (2005). Detecting activity in olfactory bulb glomeruli with astrocyte recording. *J. Neurosci.*, 25(11):2917–2924.

De Vuyst, E., Wang, N., Decrock, E., De Bock, M., Vinken, M., Van Moorhem, M., Lai, C., Culot, M., Rogiers, V., Cecchelli, R., et al. (2009). Ca< sup> 2+</sup> regulation of connexin 43 hemichannels in c6 glioma and glial cells. *Cell calcium*, 46(3):176–187.

De Young, G. W. and Keizer, J. (1992). A single-pool inositol 1, 4, 5-trisphosphate-receptor-based model for agonist-stimulated oscillations in ca2+ concentration. *Proceedings of the National Academy of Sciences*, 89(20):9895–9899.

Decrock, E., Vinken, M., Bol, M., D'Herde, K., Rogiers, V., Vandenabeele, P., Krysko, D. V., Bultynck, G., and Leybaert, L. (2011). Calcium and connexin-based intercellular communication, a deadly catch? *Cell calcium*, 50(3):310–321.

Deitmer, J. W. and Rose, C. R. (2010). Ion changes and signalling in perisynaptic glia. *Brain research reviews*, 63(1):113–129.

Dere, E., Souza-Silva, M. A. D., Frisch, C., Teubner, B., Söhl, G., Willecke, K., and Huston, J. P. (2003). Connexin30-deficient mice show increased emotionality and decreased rearing activity in the open-field along with neurochemical changes. *Eur J Neurosci*, 18(3):629–638.

Di-Castro, M. A., Chuquet, J., Liaudet, N., Bhaukaurally, K., Santello, M., Bouvier, D., Tiret, P., and Volterra, A. (2011). Local Ca^{2+} detection and modulation of synaptic release by astrocytes. *Nature Neurosci.*, 14(10):1276–1284.

Ding, F., O'Donnell, J., Thrane, A. S., Zeppenfeld, D., Kang, H., Xie, L., Wang, F., and Nedergaard, M. (2013). α_1-adrenergic receptors mediate coordinated ca^{2+} signaling of cortical astrocytes in awake, behaving mice. *Cell calcium*, 54(6):387–394.

Ding, S., Wang, T., Cui, W., and Haydon, P. G. (2009). Photothrombosis ischemia stimulates a sustained astrocytic ca2+ signaling in vivo. *Glia*, 57(7):767–776.

Dodds, P. S. and Watts, D. J. (2004). Universal behavior in a generalized model of contagion. *Phys. Rev. Lett.*, 92(21):218701.

Dokukina, I., Gracheva, M., Grachev, E., and Gunton, J. (2008). Role of network connectivity in intercellular calcium signaling. *Physica D*, 237(6):745 – 754.

Domercq, M., Brambilla, L., Pilati, E., Marchaland, J., Volterra, A., and Bezzi, P. (2006). P2Y1 receptor-evoked glutamate exocytosis from astrocytes: control by tumor necrosis factor-α and prostaglandins. *J. Biol. Chem.*, 281:30684–30696.

Dorogovtsev, S. N., Goltsev, A. V., and Mendes, J. F. F. (2008). Critical phenomena in complex networks. *Rev. Mod. Phys.*, 80(4):1275–1335.

Dunn, K. M., Hill-Eubanks, D. C., Liedtke, W. B., and Nelson, M. T. (2013). Trpv4 channels stimulate ca2+-induced ca2+ release in astrocytic endfeet and amplify neurovascular coupling responses. *Proceedings of the National Academy of Sciences*, 110(15):6157–6162.

Dupont, G., Combettes, L., Bird, G. S., and Putney, J. W. (2011). Calcium oscillations. *Cold Spring Harbor perspectives in biology*, 3(3):a004226.

Dupont, G., Combettes, L., and Leybaert, L. (2007). Calcium dynamics: spatio-temporal organization from the subcellular to the organ level. *International review of cytology*, 261:193–245.

Dupont, G. and Erneux, C. (1997). Simulations of the effects of inositol 1,4,5-trisphosphate 3-kinase and 5-phosphatase activities on Ca^{2+} oscillations. *Cell Calcium*, 22(5):321–331.

Dyhrfjeld-Johnsen, J., Santhakumar, V., Morgan, R. J., Huerta, R., Tsimring, L., and Soltesz, I. (2007). Topological determinants of epileptogenesis in large-scale structural and functional models of the dentate gyrus derived from experimental data. *J. Neurophysiol.*, 97(2):1566–1587.

Edwards, J. R. and Gibson, W. G. (2010). A model for Ca^{2+} waves in networks of glial cells incorporating both intercellular and extracellular communication pathways. *J Theor Biol*, 263(1):45–58.

Eroglu, C. and Barres, B. A. (2010). Regulation of synaptic connectivity by glia. *Nature*, 468(7321):223–231.

Estrada-Sánchez, A. M. and Rebec, G. V. (2012). Corticostriatal dysfunction and glutamate transporter 1 (glt1) in huntington's disease: interactions between neurons and astrocytes. *Basal ganglia*, 2(2):57–66.

Eytan, D. and Marom, S. (2006). Dynamics and effective topology underlying synchronization in networks of cortical neurons. *The Journal of neuroscience*, 26(33):8465–8476.

Falcke, M. (2004). Reading the patterns in living cells: the physics of Ca^{2+} signaling. *Adv. Phys.*, 53(3):255–440.

Fam, S., Gallagher, C., and Salter, M. (2000). $P2Y_1$ purinoceptor-mediated Ca^{2+} signaling and Ca^{2+} wave propagation in dorsal spinal cord astrocytes. *J. Neurosci.*, 20(8):2800–2808.

Farahani, R., Pina-Benabou, M. H., Kyrozis, A., Siddiq, A., Barradas, P. C., Chiu, F.-C., Cavalcante, L. A., Lai, J. C. K., Stanton, P. K., and Rozental, R. (2005). Alterations in metabolism and gap junction expression may determine the role of astrocytes as "good samaritans" or executioners. *Glia*, 50(4):351–361.

Feldt, S., Wang, J. X., Shtrahman, E., Dzakpasu, R., Olariu, E., and Zochowski, M. (2010). Functional clustering in hippocampal cultures: relating network structure and dynamics. *Phys. Biol.*, 7(4):046004.

Fellin, T., Pascual, O., Gobbo, S., Pozzan, T., Haydon, P. G., and Carmignoto, G. (2004). Neuronal synchrony mediated by astrocytic glutamate through activation of extrasynaptic NMDA receptors. *Neuron*, 43(5):729–743.

Ferrer i Cancho, R. and Solé, R. V. (2003). Optimization in complex networks. In Pastor-Satorras, R., Rubi, M., and Diaz-Guilera, A., editors, *Statistical Mechanics of Complex Networks*, volume 625 of *Lecture Notes in Physics*, pages 114–126. Springer Berlin / Heidelberg. 10.1007/978-3-540-44943-0-7.

Fiacco, T. A., Agulhon, C., Taves, S. R., Petravicz, J., Casper, K. B., Dong, X., Chen, J., and McCarthy, K. D. (2007). Selective stimulation of astrocyte calcium in situ does not affect neuronal excitatory synaptic activity. *Neuron*, 54:611–626.

Fiacco, T. A. and McCarthy, K. D. (2004). Intracellular astrocyte calcium waves in situ increase the frequency of spontaneous AMPA receptor currents in CA1 pyramidal neurons. *J. Neurosci.*, 24(3):722–732.

Fiacco, T. A. and McCarthy, K. D. (2006). Astrocyte calcium elevations: properties, propagation, and effects on brain signaling. *Glia*, 54(7):676–690.

Fields, R. D., Araque, A., Johansen-Berg, H., Lim, S.-S., Lynch, G., Nave, K.-A., Nedergaard, M., Perez, R., Sejnowski, T., and Wake, H. (2013). Glial biology in learning and cognition. *The Neuroscientist*, page 1073858413504465.

Figley, C. R. and Stroman, P. W. (2011). The role(s) of astrocytes and astrocyte activity in neurometabolism, neurovascular coupling, and the production of functional neuroimaging signals. *Eur J Neurosci*, 33(4):577–588.

Finkbeiner, S. M. (1993). Glial calcium. *Glia*, 9:83–104.

Foskett, J. K., White, C., Cheung, K.-H., and Mak, D.-O. D. (2007). Inositol trisphosphate receptor ca2+ release channels. *Physiological reviews*, 87(2):593–658.

Fredholm, B. B. (2012). Rethinking the purinergic neuron-glia connection. *Proc. Natl. Acad. Sci. USA*.

Frisch, C., Theis, M., De Souza Silva, M. A., Dere, E., Söhl, G., Teubner, B., Namestkova, K., Willecke, K., and Huston, J. P. (2003). Mice with astrocyte-directed inactivation of connexin43 exhibit increased exploratory behaviour, impaired motor capacities, and changes in brain acetylcholine levels. *European Journal of Neuroscience*, 18(8):2313–2318.

Gallos, L. K., Song, C., Havlin, S., and Makse, H. A. (2007). Scaling theory of transport in complex biological networks. *Proc Natl Acad Sci U S A*, 104(19):7746–7751.

Ghosh, A., Wyss, M. T., and Weber, B. (2013). Somatotopic astrocytic activity in the somatosensory cortex. *Glia*, 61(4):601–610.

Giaume, C. (2010). Astroglial wiring is adding complexity to neuroglial networking. *Front Neuroenergetics*, 2.

Giaume, C., Fromaget, C., el Aoumari, A., Cordier, J., Glowinski, J., and Gros, D. (1991). Gap junctions in cultured astrocytes: single-channel currents and characterization of channel-forming protein. *Neuron*, 6(1):133–143.

Giaume, C., Koulakoff, A., Roux, L., Holcman, D., and Rouach, N. (2010). Astroglial networks: a step further in neuroglial and gliovascular interactions. *Nat. Rev. Neurosci.*, 11(2):87–99.

Giaume, C. and Theis, M. (2010). Pharmacological and genetic approaches to study connexin-mediated channels in glial cells of the central nervous system. *Brain Res. Rev.*, 63(1-2):160–176.

Goldberg, M., Pittà, M. D., Volman, V., Berry, H., and Ben-Jacob, E. (2010). Nonlinear gap junctions enable long-distance propagation of pulsating calcium waves in astrocyte networks. *PLoS Comput Biol*, 6(8).

Golomb, D. and Hansel, D. (2000). The number of synaptic inputs and the synchrony of large, sparse neuronal networks. *Neural comput.*, 12(5):1095–1139.

Golovina, V. A. (2005). Visualization of localized store-operated calcium entry in mouse astrocytes. close proximity to the endoplasmic reticulum. *The Journal of physiology*, 564(3):737–749.

Golovina, V. A. and Blaustein, M. P. (1997). Spatially and functionally distinct ca2+ stores in sarcoplasmic and endoplasmic reticulum. *Science*, 275(5306):1643–1648.

Gordon, G., Baimoukhametova, D., Hewitt, S., Rajapaksha, W., Fisher, T., and Bains, J. (2005). Norepinephrine triggers release of glial ATP to increase postsynaptic efficacy. *Nat. Neurosci.*, 8(8):1078–1086.

Gordon, G. R. J., Choi, H. B., Rungta, R. L., Ellis-Davies, G. C. R., and MacVicar, B. A. (2008). Brain metabolism dictates the polarity of astrocyte control over arterioles. *Nature*, 456(7223):745–749.

Gordon, G. R. J., Iremonger, K. J., Kantevari, S., Ellis-Davies, G. C. R., MacVicar, B. A., and Bains, J. S. (2009). Astrocyte-mediated distributed plasticity at hypothalamic glutamate synapses. *Neuron*, 64:391–403.

Goritz, C., Mauch, D. H., and Pfrieger, F. W. (2005). Multiple mechanisms mediate cholesterol-induced synaptogenesis in a cns neuron. *Molecular and Cellular Neuroscience*, 29(2):190–201.

Gorry, P. A. (1990). General least-squares smoothing and differentiation by the convolution (savitzky-golay) method. *Analytical Chemistry*, 62(6):570–573.

Grosche, A. and Reichenbach, A. (2013). Developmental refining of neuroglial signaling? *Science*, 339(6116):152–153.

Guthrie, P. B., Knappenberger, J., Segal, M., Bennett, M. V. L., C. A. C., and Kater, S. B. (1999). ATP released from astrocytes mediates glial calcium waves. *J. Neurosci.*, 19:520–528.

Haas, B., Schipke, C. G., Peters, O., Söhl, G., Willecke, K., and Kettenmann, H. (2006). Activity-dependent ATP-waves in the mouse neocortex are independent from astrocytic calcium waves. *Cereb. Cortex*, 16(2):237–246.

Haeusler, S. and Maass, W. (2007). A statistical analysis of information-processing properties of lamina-specific cortical microcircuit models. *Cereb Cortex*, 17(1):149–162.

Halassa, M. and Haydon, P. (2010). Integrated brain circuits: astrocytic networks modulate neuronal activity and behavior. *Annu. Rev. Physiol.*, 72:335–355.

Halassa, M. M., Fellin, T., Takano, H., Dong, J.-H., and Haydon, P. G. (2007). Synaptic islands defined by the territory of a single astrocyte. *J Neurosci*, 27(24):6473–6477.

Halassa, M. M., Florian, C., Fellin, T., Munoz, J. R., Lee, S.-Y., Abel, T., Haydon, P. G., and Frank, M. G. (2009). Astrocytic modulation of sleep homeostasis and cognitive consequences of sleep loss. *Neuron*, 61(2):213–219.

Han, J., Kesner, P., Metna-Laurent, M., Duan, T., Xu, L., Georges, F., Koehl, M., Abrous, D. N., Mendizabal-Zubiaga, J., Grandes, P., et al. (2012). Acute cannabinoids impair working memory through astroglial cb< sub> 1</sub> receptor modulation of hippocampal ltd. *Cell*, 148(5):1039–1050.

Han, X., Chen, M., Wang, F., Windrem, M., Wang, S., Shanz, S., Xu, Q., Oberheim, N. A., Bekar, L., Betstadt, S., et al. (2013). Forebrain engraftment by human glial progenitor cells enhances synaptic plasticity and learning in adult mice. *Cell Stem Cell*, 12(3):342–353.

Hansen, N. (2006). The cma evolution strategy: A comparing review. In Lozano, J., Larrañaga, P., Inza, I., and Bengoetxea, E., editors, *Towards a New Evolutionary Computation*, volume 192 of *Studies in Fuzziness and Soft Computing*, pages 75–102. Springer Berlin Heidelberg.

Harris, A. L. (2001). Emerging issues in connexin channels: biophysics fills the gap. *Quarterly Rev. Biophys.*, 34:325–472.

Harris, J. and Timofeeva, Y. (2010). Intercellular calcium waves in the fire-diffuse-fire framework: Green's function for gap-junctional coupling. *Physical Review E*, 82(5):051910.

Hassinger, T. D., Guthrie, P. B., Atkinson, P. B., Bennett, M. V. L., and Kater, S. B. (1996). An extracellular singaling component in propagation of astrocytic calcium waves. *Proc. Natl. Acad. Sci. USA*, 93(23):13268–13273.

Haustein, M. D., Kracun, S., Lu, X.-H., Shih, T., Jackson-Weaver, O., Tong, X., Xu, J., Yang, X. W., O'Dell, T. J., Marvin, J. S., et al. (2014). Conditions and constraints for astrocyte calcium signaling in the hippocampal mossy fiber pathway. *Neuron*, 82(2):413–429.

Haydon, P. G. and Carmignoto, G. (2006). Astrocyte control of synaptic transmission and neurovascular coupling. *Physiol. Rev.*, 86:1009–1031.

Hazell, A. S., Sheedy, D., Oanea, R., Aghourian, M., Sun, S., Jung, J. Y., Wang, D., and Wang, C. (2010). Loss of astrocytic glutamate transporters in wernicke encephalopathy. *Glia*, 58(2):148–156.

Henneberger, C., Papouin, T., Oliet, S. H. R., and Rusakov, D. A. (2010). Long-term potentiation depends on release of D-serine from astrocytes. *Nature*, 463(7278):232–236.

Hirase, H., Qian, L., Barthó, P., and Buzsáki, G. (2004). Calcium dynamics of cortical astrocytic networks in vivo. *PLoS Biol.*, 2(4):E96.

Hodgkin, A. L. and Huxley, A. F. (1952). A quantitative description of membrane current and its application to conduction and excitation in nerve. *J. Physiol.*, 117:500–544.

Höfer, T., Politi, A., and Heinrich, R. (2001). Intercellular Ca^{2+} wave propagation through gap-junctional Ca^{2+} diffusion: a theoretical study. *Biophys J*, 80(1):75–87.

Höfer, T., Venance, L., and Giaume, C. (2002). Control and plasticity of intercellular calcium waves in astrocytes: a modeling approach. *J Neurosci*, 22(12):4850–4859.

Holtzclaw, L. A., Pandhit, S., Bare, D. J., Mignery, G. A., and Russell, J. T. (2002). Astrocytes in adult rat brain express type 2 inositol 1, 4, 5-trisphosphate receptors. *Glia*, 39(1):69–84.

Hoogland, T. M., Kuhn, B., Göbel, W., Huang, W., Nakai, J., Helmchen, F., Flint, J., and Wang, S. S.-H. (2009). Radially expanding transglial calcium waves in the intact cerebellum. *Proc. Natl. Acad. Sci. USA*, 106(9):3496–3501.

Houades, V., Koulakoff, A., Ezan, P., Seif, I., and Giaume, C. (2008). Gap junction-mediated astrocytic networks in the mouse barrel cortex. *J. Neurosci.*, 28(20):5207–5217.

Houades, V., Rouach, N., Ezan, P., Kirchhoff, F., Koulakoff, A., and Giaume, C. (2006). Shapes of astrocyte networks in the juvenile brain. *Neuron glia biology*, 2(01):3–14.

Huang, Y.-F., Liao, C.-K., Lin, J.-C., Jow, G.-M., Wang, H.-S., and Wu, J.-C. (2013). Antofine-induced connexin43 gap junction disassembly in rat astrocytes involves protein kinase Cβ. *Neurotoxicology*, 35:169–179.

Hütt, M.-T. and Lesne, A. (2009). Interplay between topology and dynamics in excitation patterns on hierarchical graphs. *Front Neuroinformatics*, 3:28.

Iacobas, D. A., Suadicani, S. O., Spray, D. C., and Scemes, E. (2006). A stochastic two-dimensional model of intercellular Ca^{2+} wave spread in glia. *Biophysical Journal*, 90(1):24 – 41.

Iadecola, C. and Nedergaard, M. (2007). Glial regulation of the cerebral microvasculature. *Nat Neurosci*, 10(11):1369–1376.

Ikegaya, Y., Le Bon-Jego, M., and Yuste, R. (2005). Large-scale imaging of cortical network activity with calcium indicators. *Neuroscience research*, 52(2):132–138.

Iwabuchi, S., Kawahara, K., Makisaka, K., and Sato, H. (2002). Photolytic flash-induced intercellular calcium waves using caged calcium ionophore in cultured astrocytes from newborn rats. *Exp. Brain. Res.*, 146(1):103–116.

Jaiswal, J., Fix, M., Takano, T., Nedergaard, M., and Simon, S. (2007). Resolving vesicle fusion from lysis to monitor calcium-triggered lysosomal exocytosis in astrocytes. *Proc. Natl. Acad. Sci. USA*, 104(35):14151–14156.

Jourdain, P., Bergersen, L. H., Bhaukaurally, K., Bezzi, P., Santello, M., Domercq, M., Matute, C., Tonello, F., Gundersen, V., and Volterra, A. (2007). Glutamate exocytosis from astrocytes controls synaptic strength. *Nat Neurosci*, 10(3):331–339.

Kandel, E. R., Schwartz, J. H., and Jessell, T. M. (2000a). *Principles of Neural Science*, chapter I.2, pages 20–21. McGraw-Hill Medical, 4th edition.

Kandel, E. R., Schwartz, J. H., and Jessell, T. M. (2000b). *Principles of Neural Science*, chapter III.14, pages 264–277. McGraw-Hill Medical, 4th edition.

Kanemaru, K., Sekiya, H., Xu, M., Satoh, K., Kitajima, N., Yoshida, K., Okubo, Y., Sasaki, T., Moritoh, S., Hasuwa, H., et al. (2014). In vivo visualization of subtle, transient, and local activity of astrocytes using an ultrasensitive ca< sup> 2+</sup> indicator. *Cell reports*.

Kang, J., Jiang, L., Goldman, S. A., and Nedergaard, M. (1998). Astrocyte-mediated potentiation of inhibitory synaptic transmission. *Nat. Neurosci.*, 1(8):683–692.

Kang, M. and Othmer, H. G. (2009). Spatiotemporal characteristics of calcium dynamics in astrocytes. *Chaos*, 19(3):037116.

Keizer, J. and Levine, L. (1996). Ryanodine receptor adaptation and Ca^{2+}-induced Ca^{2+} release-dependent Ca^{2+} oscillations. *Biophys. J.*, 71:3477–3487.

Keizer, J., Smith, G. D., Ponce-Dawson, S., and Pearson, J. E. (1998). Saltatory propagation of ca< sup> 2+</sup> waves by ca< sup> 2+</sup> sparks. *Biophysical journal*, 75(2):595–600.

Kettenmann, H. and Ransom, B. R. (2004). *Neuroglia, The concept of neuroglia: A historical perspective*. Oxford University Press, New York, 1st edition.

Kettenmann, H. and Schachner, M. (1985). Pharmacological properties of gamma-aminobutyric acid-, glutamate-, and aspartate-induced depolarizations in cultured astrocytes. *The Journal of neuroscience*, 5(12):3295–3301.

Kim, B. J. (2004). Performance of networks of artificial neurons: the role of clustering. *Phys Rev E Stat Nonlin Soft Matter Phys*, 69(4 Pt 2):045101.

Kimelberg, H. K. (2009). Astrocyte heterogeneity or homogeneity? In *Astrocytes in (patho) physiology of the nervous system*, pages 1–25. Springer.

Kirischuk, S., Parpura, V., and Verkhratsky, A. (2012). Sodium dynamics: another key to astroglial excitability? *Trends in neurosciences*, 35(8):497–506.

Koulakoff, A., Ezan, P., and Giaume, C. (2008). Neurons control the expression of connexin 30 and connexin 43 in mouse cortical astrocytes. *Glia*, 56(12):1299–1311.

Kuchibhotla, K. V., Lattarulo, C. R., Hyman, B. T., and Bacskai, B. J. (2009). Synchronous hyperactivity and intercellular calcium waves in astrocytes in alzheimer mice. *Science*, 323(5918):1211–1215.

Kuga, N., Sasaki, T., Takahara, Y., Matsuki, N., and Ikegaya, Y. (2011). Large-scale calcium waves traveling through astrocytic networks in vivo. *J. Neurosci.*, 31(7):2607–2614.

Kummer, U., Olsen, L. F., Green, A. K., Bomberg-Bauer, E., and Baier, G. (2000). Switching from simple to complex oscillations in calcium signaling. *Biophys. J.*, 79:1188–1199.

Kunze, A., Congreso, M. R., Hartmann, C., Wallraff-Beck, A., Hüttmann, K., Bedner, P., Requardt, R., Seifert, G., Redecker, C., Willecke, K., Hofmann, A., Pfeifer, A., Theis, M., and Steinhäuser, C. (2009). Connexin expression by radial glia-like cells is required for neurogenesis in the adult dentate gyrus. *Proc. Natl. Acad. Sci. USA*, 106(27):11336–11341.

Kurth-Nelson, Z. L., Mishra, A., and Newman, E. A. (2009). Spontaneous glial calcium waves in the retina develop over early adulthood. *J Neurosci*, 29(36):11339–11346.

Lacar, B., Young, S. Z., Platel, J.-C., and Bordey, A. (2011). Gap junction-mediated calcium waves define communication networks among murine postnatal neural progenitor cells. *European Journal of Neuroscience*, 34(12):1895–1905.

Larsson, M., Sawada, K., Morland, C., Hiasa, M., Ormel, L., Moriyama, Y., and Gundersen, V. (2011). Functional and anatomical identification of a vesicular transporter mediating neuronal ATP release. *Cereb. Cortex*, 22(5):1203 –1214.

Latour, I., Hamid, J., Beedle, A. M., Zamponi, G. W., and Macvicar, B. A. (2003). Expression of voltage-gated ca2+ channel subtypes in cultured astrocytes. *Glia*, 41(4):347–353.

Lazrak, A., Peres, A., Giovannardi, S., and Peracchia, C. (1994). Ca-mediated and independent effects of arachidonic acid on gap junctions and ca-independent effects of oleic acid and halothane. *Biophysical journal*, 67(3):1052–1059.

Lee, H. S., Ghetti, A., Pinto-Duarte, A., Wang, X., Dziewczapolski, G., Galimi, F., Huitron-Resendiz, S., Piña-Crespo, J. C., Roberts, A. J., Verma, I. M., et al. (2014). Astrocytes contribute to gamma oscillations and recognition memory. *Proceedings of the National Academy of Sciences*, 111(32):E3343–E3352.

Lee, S., Yoon, B., Berglund, K., Oh, S., Park, H., Shin, H., Augustine, G., and Lee, C. (2010). Channel-mediated tonic GABA release from glia. *Sci. STKE*, 330(6005):790–796.

Lerchner, A., Ursta, C., Hertz, J., Ahmadi, M., Ruffiot, P., and Enemark, S. (2006). Response variability in balanced cortical networks. *Neural comput.*, 18(3):634–659.

Lesne, A. (2006). Complex networks: from graph theory to biology. *Letters in Mathematical Physics*, 78(3):235–262.

Lewis, T. J. and Rinzel, J. (2003). Dynamics of spiking neurons connected by both inhibitory and electrical coupling. *J. Comput. Neurosci.*, 14(3):283–309.

Leybaert, L., Paemeleire, K., Strahonja, A., and Sanderson, M. J. (1998). Inositol-trisphosphate-dependent intercellular calcium signaling in and between astrocytes and endothelial cells. *Glia*, 24(4):398–407.

Leybaert, L. and Sanderson, M. J. (2012). Intercellular ca2+ waves: mechanisms and function. *Physiological reviews*, 92(3):1359–1392.

Li, D., Ropert, N., Koulakoff, A., Giaume, C., and Oheim, M. (2008). Lysosomes are the major vesicular compartment undergoing Ca^{2+}-regulated exocytosis from cortical astrocytes. *J. Neurosci.*, 28(30):7648–7658.

Li, Y. and Rinzel, J. (1994). Equations for InsP(3) receptor-mediated $[Ca^{2+}]$i oscillations derived from a detailed kinetic model: a hodgkin-huxley like formalism. *Journal of Theoretical Biology*, 166(4):461–473.

Liu, Q., Xu, Q., Arcuino, G., Kang, J., and Nedergaard, M. (2004a). Astrocyte-mediated activation of neuronal kainate receptors. *Proc. Natl. Acad. Sci. USA*, 101(9):3172–3177.

Liu, Q.-S., Xu, Q., Kang, J., and Nedergaard, M. (2004b). Astrocyte activation of presynaptic metabotropic glutamate receptors modulates hippocampal inhibitory synaptic transmission. *Neuron Glia Biol.*, 1:307–316.

López-Hidalgo, M. and Schummers, J. (2014). Cortical maps: a role for astrocytes? *Current opinion in neurobiology*, 24:176–189.

Lovatt, D., Xu, Q., Liu, W., Takano, T., Smith, N., Schnermann, J., Tieu, K., and Nedergaard, M. (2012). Neuronal adenosine release, and not astrocytic atp release, mediates feedback inhibition of excitatory activity. *Proc. Natl. Acad. Sci. USA*, 109(16):6265–6270.

Lu, S., Fang, J., Guo, A., and Peng, Y. (2009). Impact of network topology on decision-making. *Neural Netw*, 22(1):30–40.

Luccioli, S., Olmi, S., Politi, A., and Torcini, A. (2012). Collective dynamics in sparse networks. *Phys. Rev. Lett.*, 109(13):138103.

Lungarella, M., Ishiguro, K., Kuniyoshi, Y., and Otsu, N. (2007). Methods for quantifying the causal structure of bivariate time series. *Int. J. Bifurcation Chaos*, 17(03):903–921.

Ma, W., Compan, V., Zheng, W., Martin, E., North, R. A., Verkhratsky, A., and Surprenant, A. (2012). Pannexin 1 forms an anion-selective channel. *Pflügers Archiv-European Journal of Physiology*, 463(4):585–592.

MacDonald, C. L., Yu, D., Buibas, M., and Silva, G. A. (2008). Diffusion modeling of atp signaling suggests a partially regenerative mechanism underlies astrocyte intercellular calcium waves. *Frontiers in neuroengineering*, 1.

Maeda, E., Robinson, H., and Kawana, A. (1995). The mechanisms of generation and propagation of synchronized bursting in developing networks of cortical neurons. *The Journal of neuroscience*, 15(10):6834–6845.

Malarkey, E. B. and Parpura, V. (2008). Mechanisms of glutamate release from astrocytes. *Neurochemistry international*, 52(1):142–154.

Marchaland, J., Calì, C., Voglmaier, S. M., Li, H., Regazzi, R., Edwards, R. H., and Bezzi, P. (2008). Fast subplasma membrane Ca^{2+} transients control exo-endocytosis of synaptic-like microvesicles in astrocytes. *J. Neurosci.*, 28(37):9122–9132.

Markram, H., Pikus, D., Gupta, A., and Tsodyks, M. (1998). Potential for multiple mechanisms, phenomena and algorithms for synaptic plasticity at single synapses. *Neuropharmacology*, 37:489–500.

Mathias, N. and Gopal, V. (2001). Small worlds: how and why. *Phys Rev E Stat Nonlin Soft Matter Phys*, 63(2 Pt 1):021117.

Matrosov, V. V. and Kazantsev, V. B. (2011). Bifurcation mechanisms of regular and chaotic network signaling in brain astrocytes. *Chaos*, 21(2):023103.

McCarthy, K. D. and De Vellis, J. (1980). Preparation of separate astroglial and oligodendroglial cell cultures from rat cerebral tissue. *The Journal of cell biology*, 85(3):890–902.

McKhann, G. M., D'Ambrosio, R., and Janigro, D. (1997). Heterogeneity of astrocyte resting membrane potentials and intercellular coupling revealed by whole-cell and gramicidin-perforated patch recordings from cultured neocortical and hippocampal slice astrocytes. *The Journal of neuroscience*, 17(18):6850–6863.

Même, W., Ezan, P., Venance, L., Glowinski, J., and Giaume, C. (2004). ATP-induced inhibition of gap junctional communication is enhanced by interleukin-1 β treatment in cultured astrocytes. *Neuroscience*, 126(1):95–104.

Metea, M. R. and Newman, E. A. (2006). Glial cells dilate and constrict blood vessels: a mechanism of neurovascular coupling. *J Neurosci*, 26(11):2862–2870.

Meyer, T. and Stryer, L. (1988). Molecular model for receptor-stimulated caclium spiking. *Proc. Natl. Acad. Sci. USA*, 85:5051–5055.

Min, R. and Nevian, T. (2012). Astrocyte signaling controls spike timing-dependent depression at neocortical synapses. *Nat. Neurosci.*, 15(5):746–753.

Montana, V., Malarkey, E. B., Verderio, C., Matteoli, M., and Parpura, V. (2006). Vesicular transmitter release from astrocytes. *Glia*, 54:700–715.

Montoro, R. J. and Yuste, R. (2004). Gap junctions in developing neocortex: a review. *Brain Res. Rev.*, 47(1-3):216–226.

Mothet, J.-P., Pollegioni, L., Ouanounou, G., Martineau, M., Fossier, P., and Baux, G. (2005). Glutamate receptor activation triggers a calcium-dependent and SNARE protein-dependent release of the gliotransmitter D-serine. *Proc. Natl. Acad. Sci. USA*, 102(15):5606–5611.

Müller-Linow, M., Hilgetag, C. C., and Hütt, M.-T. (2008). Organization of excitable dynamics in hierarchical biological networks. *PLoS Comput. Biol.*, 4(9):e1000190.

Mulligan, S. J. and MacVicar, B. A. (2004). Calcium transients in astrocyte endfeet cause cerebrovascular constrictions. *Nature*, 431(7005):195–199.

Nadkarni, S. and Jung, P. (2004). Dressed neurons: modeling neural-glial interactions. *Phys. Biol.*, 1:35–41.

Nadkarni, S. and Jung, P. (2007). Modeling synaptic transmission of the tripartite synapse. *Phys. Biol.*, 4:1–9.

Nadkarni, S., Jung, P., and Levine, H. (2008). Astrocytes optimize the synaptic transmission of information. *PLoS Comput. Biol.*, 4(5):e1000088.

Nagy, J. I. and Rash, J. E. (2000). Connexins and gap junctions of astrocytes and oligodendrocytes in the CNS. *Brain Res. Rev.*, 32(1):29–44.

Navarrete, M., Perea, G., de Sevilla, D., Gómez-Gonzalo, M., Núñez, A., Martín, E., and Araque, A. (2012). Astrocytes mediate in vivo cholinergic-induced synaptic plasticity. *PLoS Biol.*, 10(2):e1001259.

Navarrete, M., Perea, G., Maglio, L., Pastor, J., de Sola, R. G., and Araque, A. (2013). Astrocyte calcium signal and gliotransmission in human brain tissue. *Cereb Cortex*, 23(5):1240–1246.

Nedergaard, M. (1994). Direct signaling from astrocytes to neurons in cultures of mammalian brain cells. *Science*, 263(5154):1768–1771.

Nedergaard, M., Ransom, B., and Goldman, S. A. (2003). New roles for astrocytes: Redefining the functional architecture of the brain. *Trends in neurosciences*, 26(10):523–530.

Nedergaard, M., Rodríguez, J. J., and Verkhratsky, A. (2010). Glial calcium and diseases of the nervous system. *Cell calcium*, 47(2):140–149.

Nedergaard, M. and Verkhratsky, A. (2012). Artifact versus reality—how astrocytes contribute to synaptic events. *Glia*, 60(7):1013–1023.

Nett, W. J., Oloff, S. H., and McCarthy, K. D. (2002). Hippocampal astrocytes in situ exhibit calcium oscillations that occur independent of neuronal activity. *J Neurophysiol*, 87(1):528–537.

Newman, E. A. (2001). Propagation of intercellular calcium waves in retinal astrocytes and müller cells. *J. Neurosci.*, 21(7):2215–2223.

Newman, E. A. and Zahs, K. R. (1997). Calcium waves in retinal glial cells. *Science*, 275:844–847.

Newman, E. A. and Zahs, K. R. (1998). Modulation of neuronal activity by glial cells in the retina. *J Neurosci*, 18(11):4022–4028.

Newman, M. E. J. (2003). The structure and function of complex networks. *SIAM Review*, 45(2):167–256.

Nimmerjahn, A., Kirchhoff, F., Kerr, J. N. D., and Helmchen, F. (2004). Sulforhodamine 101 as a specific marker of astroglia in the neocortex in vivo. *Nat. Methods*, 1(1):31–37.

Nimmerjahn, A., Mukamel, E. A., and Schnitzer, M. J. (2009). Motor behavior activates bergmann glial networks. *Neuron*, 62(3):400–412.

Nizar, K., Uhlirova, H., Tian, P., Saisan, P. A., Cheng, Q., Reznichenko, L., Weldy, K. L., Steed, T. C., Sridhar, V. B., Macdonald, C. L., Cui, J., Gratiy, S. L., Sakadzic, S., Boas, D. A., Beka, T. I., Einevoll, G. T., Chen, J., Masliah, E., Dale, A. M., Silva, G. A., and Devor, A. (2013). In vivo stimulus-induced vasodilation occurs without ip3 receptor activation and may precede astrocytic calcium increase. *J Neurosci*, 33(19):8411–8422.

Oberheim, N. A., Takano, T., Han, X., He, W., Lin, J. H. C., Wang, F., Xu, Q., Wyatt, J. D., Pilcher, W., Ojemann, J. G., Ransom, B. R., Goldman, S. A., and Nedergaard, M. (2009). Uniquely hominid features of adult human astrocytes. *J Neurosci*, 29(10):3276–3287.

Oberheim, N. A., Tian, G.-F., Han, X., Peng, W., Takano, T., Ransom, B., and Nedergaard, M. (2008). Loss of astrocytic domain organization in the epileptic brain. *The Journal of Neuroscience*, 28(13):3264–3276.

Olmi, S., Livi, R., Politi, A., and Torcini, A. (2010). Collective oscillations in disordered neural networks. *Phys. Rev. E*, 81(4):046119.

Orellana, J. A., Martinez, A. D., and Retamal, M. A. (2013). Gap junction channels and hemichannels in the CNS: Regulation by signaling molecules. *Neuropharmacology*.

Palygin, O., Lalo, U., Verkhratsky, A., and Pankratov, Y. (2010). Ionotropic nmda and p2x< sub> 1/5</sub> receptors mediate synaptically induced ca< sup> 2+</sup> signalling in cortical astrocytes. *Cell calcium*, 48(4):225–231.

Panatier, A. and Oliet, S. H. (2006). Neuron–glia interactions in the hypothalamus. *Neuron glia biology*, 2(01):51–58.

Panatier, A., Vallée, J., Haber, M., Murai, K., Lacaille, J., and Robitaille, R. (2011). Astrocytes are endogenous regulators of basal transmission at central synapses. *Cell*, 146:785–798.

Pannasch, U., Freche, D., Dallérac, G., Ghézali, G., Escartin, C., Ezan, P., Cohen-Salmon, M., Benchenane, K., Abudara, V., Dufour, A., et al. (2014). Connexin 30 sets synaptic strength by controlling astroglial synapse invasion. *Nature neuroscience*.

Pannasch, U. and Rouach, N. (2013). Emerging role for astroglial networks in information processing: from synapse to behavior. *Trends. Neurosci.*

Pannasch, U., Vargová, L., Reingruber, J., Ezan, P., Holcman, D., Giaume, C., Syková, E., and Rouach, N. (2011). Astroglial networks scale synaptic activity and plasticity. *Proc Natl Acad Sci U S A*, 108(20):8467–8472.

Papouin, T., Ladépêche, L., Ruel, J., Sacchi, S., Labasque, M., Hanini, M., Groc, L., Pollegioni, L., Mothet, J., and Oliet, S. (2012). Synaptic and extrasynaptic NMDA receptors are gated by different endogenous coagonists. *Cell*, 150(3):633–646.

Parnis, J., Montana, V., Delgado-Martinez, I., Matyash, V., Parpura, V., Kettenmann, H., Sekler, I., and Nolte, C. (2013). Mitochondrial exchanger nclx plays a major role in the intracellular ca2+ signaling, gliotransmission, and proliferation of astrocytes. *The Journal of Neuroscience*, 33(17):7206–7219.

Parpura, V. (2004). Glutamate-mediated bi-directional signaling between neurons and astrocytes. In Hatton, G. I. and Parpura, V., editors, *Glial-neuronal signaling*, pages 365–396. Kluwer Academic Publisher, Boston, MA.

Parpura, V., Basarsky, T. A., Liu, F., Jeftinija, K., Jeftinija, S., and Haydon, P. G. (1994). Glutamate-mediated astrocyte–neuron signalling.

Parpura, V. and Zorec, R. (2010). Gliotransmission: exocytotic release from astrocytes. *Brain Res. Rev.*, 63:83–92.

Parri, H. R., Gould, T. M., and Crunelli, V. (2001). Spontaneous astrocytic Ca^{2+} oscillations in situ drive NMDAR-mediated neuronal excitation. *Nat. Neurosci.*, 4(8):803–812.

Pascual, O., Ben Achour, S., Rostaing, P., Triller, A., and Bessis, A. (2011). Microglia activation triggers astrocyte-mediated modulation of excitatory neurotransmission. *Proc. Nat. Acad. Sci. USA*, pages 1–9.

Pascual, O., Casper, K. B., Kubera, C., Zhang, J., Revilla-Sanchez, R., Sul, J. Y., Takano, H., Moss, S. J., McCarthy, K., and Haydon, P. G. (2005). Astrocytic purinergic signaling coordinates synaptic networks. *Science*, 310:113–116.

Pasti, L., Pozzan, T., and Carmignoto, G. (1995). Long-lasting changes of calcium oscillations in astrocytes a new form of glutamate-mediated plasticity. *Journal of Biological Chemistry*, 270(25):15203–15210.

Pasti, L., Volterra, A., Pozzan, T., and Carmignoto, G. (1997). Intracellular calcium oscillations in astrocytes: a highly plastic, bidirectional form of communication between neurons and astrocytes *in situ*. *J. Neurosci.*, 17(20):7817–7830.

Pasti, L., Zonta, M., Pozzan, T., Vicini, S., and Carmignoto, G. (2001). Cytosolic calcium oscillations in astrocytes may regulate exocytotic release of glutamate. *J. Neurosci.*, 21(2):477–484.

Patrushev, I., Gavrilov, N., Turlapov, V., and Semyanov, A. (2013). Subcellular location of astrocytic calcium stores favors extrasynaptic neuron–astrocyte communication. *Cell calcium*, 54(5):343–349.

Paukert, M., Agarwal, A., Cha, J., Doze, V. A., Kang, J. U., and Bergles, D. E. (2014). Norepinephrine controls astroglial responsiveness to local circuit activity. *Neuron*, 82(6):1263–1270.

Pekny, M., Wilhelmsson, U., and Pekna, M. (2014). The dual role of astrocyte activation and reactive gliosis. *Neuroscience letters*, 565:30–38.

Pellerin, L. and Magistretti, P. J. (2011). Sweet sixteen for anls. *Journal of Cerebral Blood Flow & Metabolism*, 32(7):1152–1166.

Perea, G. and Araque, A. (2005a). Glial calcium signaling and neuron-glia communication. *Cell Calcium*, 38(3-4):375–382.

Perea, G. and Araque, A. (2005b). Properties of synaptically evoked astrocyte calcium signal reveal synaptic information processing by astrocyte. *J. Neurosci.*, 25(9):2192–2203.

Perea, G. and Araque, A. (2007). Astrocytes potentiate transmitter release at single hippocampal synapses. *Science*, 317:1083–1086.

Perea, G., Navarrete, M., and Araque, A. (2009). Tripartite synapses: astrocytes process and control synaptic information. *Trends Neurosci*, 32(8):421–431.

Perin, R., Berger, T. K., and Markram, H. (2011). A synaptic organizing principle for cortical neuronal groups. *Proc Natl Acad Sci U S A*, 108(13):5419–5424.

Peters, J. L., Cassone, V. M., and Zoran, M. J. (2005a). Melatonin modulates intercellular communication among cultured chick astrocytes. *Brain research*, 1031(1):10–19.

Peters, J. L., Earnest, B. J., Tjalkens, R. B., Cassone, V. M., and Zoran, M. J. (2005b). Modulation of intercellular calcium signaling by melatonin in avian and mammalian astrocytes is brain region-specific. *J. Comp. Neurol.*, 493(3):370–380.

Petravicz, J., Fiacco, T., and McCarthy, K. (2008). Loss of IP_3 receptor-dependent Ca^{2+} increases in hippocampal astrocytes does not affect baseline CA1 pyramidal neuron synaptic activity. *J. Neurosci.*, 28(19):4967–4973.

Petzold, G. C., Albeanu, D. F., Sato, T. F., and Murthy, V. N. (2008). Coupling of neural activity to blood flow in olfactory glomeruli is mediated by astrocytic pathways. *Neuron*, 58(6):897–910.

Pfrieger, F. W. and Barres, B. A. (1997). Synaptic efficacy enhanced by glial cells in vitro. *Science*, 277(5332):1684–1687.

Pina-Benabou, M. H. D., Srinivas, M., Spray, D. C., and Scemes, E. (2001). Calmodulin kinase pathway mediates the K^+-induced increase in gap junctional communication between mouse spinal cord astrocytes. *J. Neurosci.*, 21(17):6635–6643.

Pittà, M. D., Goldberg, M., Volman, V., Berry, H., and Ben-Jacob, E. (2009). Glutamate regulation of calcium and IP3 oscillating and pulsating dynamics in astrocytes. *J. Biol. Phys.*, 35(4):383–411.

Pivneva, T., Haas, B., Reyes-Haro, D., Laube, G., Veh, R., Nolte, C., Skibo, G., and Kettenmann, H. (2008). Store-operated Ca^{2+} entry in astrocytes: different spatial arrangement of endoplasmic reticulum explains functional diversity in vitro and in situ. *Cell Calcium*, 43(6):591–601.

Politi, A., Gaspers, L. D., Thomas, A. P., and Höfer, T. (2006). Models of IP_3 and Ca^{2+} oscillations: frequency encoding and identification of underlying feedbacks. *Biophys. J.*, 90:3120–3133.

Porter, J. T. and McCarthy, K. D. (1996). Hippocampal astrocytes in situ respond to glutamate released from synaptic terminals. *J Neurosci*, 16(16):5073–5081.

Poskanzer, K. E. and Yuste, R. (2011). Astrocytic regulation of cortical UP states. *Proc Natl Acad Sci U S A*.

Ramos-Franco, J., Bare, D., Caenepeel, S., Nani, A., Fill, M., and Mignery, G. (2000). Single-channel function of recombinant type 2 inositol 1,4,5-trisphosphate receptor. *Biophys. J.*, 79(3):1388–1399.

Rattay, F. (1999). The basic mechanism for the electrical stimulation of the nervous system. *Neuroscience*, 89(2):335–346.

Rela, L., Bordey, A., and Greer, C. A. (2010). Olfactory ensheathing cell membrane properties are shaped by connectivity. *Glia*, 58(6):665–678.

Reyes, R. C. and Parpura, V. (2008). Mitochondria modulate ca2+-dependent glutamate release from rat cortical astrocytes. *The Journal of Neuroscience*, 28(39):9682–9691.

Reyes, R. C., Verkhratsky, A., and Parpura, V. (2012). Plasmalemmal na+/ca2+ exchanger modulates ca2+-dependent exocytotic release of glutamate from rat cortical astrocytes. *ASN neuro*, 4(1):AN20110059.

Rodríguez, J. J. and Verkhratsky, A. (2011). Neuroglial roots of neurodegenerative diseases? *Molecular neurobiology*, 43(2):87–96.

Rossi, D. and Volterra, A. (2009). Astrocytic dysfunction: insights on the role in neurodegeneration. *Brain research bulletin*, 80(4):224–232.

Roßner, S., Lange-Dohna, C., Zeitschel, U., and Perez-Polo, J. R. (2005). Alzheimer's disease β-secretase bace1 is not a neuron-specific enzyme. *Journal of neurochemistry*, 92(2):226–234.

Rouach, N., Avignone, E., Même, W., Koulakoff, A., Venance, L., Blomstrand, F., and Giaume, C. (2002). Gap junctions and connexin expression in the normal and pathological central nervous system. *Biol. Cell.*, 94(7-8):457–475.

Rouach, N., Glowinski, J., and Giaume, C. (2000). Activity-dependent neuronal control of gap-junctional communication in astrocytes. *J. Cell. Biol.*, 149(7):1513–1526.

Rouach, N., Koulakoff, A., Abudara, V., Willecke, K., and Giaume, C. (2008). Astroglial metabolic networks sustain hippocampal synaptic transmission. *Science*, 322(5907):1551–1555.

Roux, L., Benchenane, K., Rothstein, J. D., Bonvento, G., and Giaume, C. (2011). Plasticity of astroglial networks in olfactory glomeruli. *Proc. Natl. Acad. Sci. USA*.

Roxin, A. (2011). The role of degree distribution in shaping the dynamics in networks of sparsely connected spiking neurons. *Front. Comput. Neurosci.*, 5.

Roxin, A., Riecke, H., and Solla, S. A. (2004). Self-sustained activity in a small-world network of excitable neurons. *Phys. Rev. Lett.*, 92(19):198101.

Rusakov, D. and Fine, A. (2003). Extracellular ca< sup> 2+</sup> depletion contributes to fast activity-dependent modulation of synaptic transmission in the brain. *Neuron*, 37(2):287–297.

Rusakov, D. A., Bard, L., Stewart, M. G., and Henneberger, C. (2014). Diversity of astroglial functions alludes to subcellular specialisation. *Trends in neurosciences*, 37(4):228–242.

Saab, A. S., Neumeyer, A., Jahn, H. M., Cupido, A., Šimek, A. A., Boele, H.-J., Scheller, A., Le Meur, K., Götz, M., Monyer, H., et al. (2012). Bergmann glial ampa receptors are required for fine motor coordination. *Science*, 337(6095):749–753.

Sabirov, R. Z. and Okada, Y. (2009). The maxi-anion channel: a classical channel playing novel roles through an unidentified molecular entity. *The Journal of Physiological Sciences*, 59(1):3–21.

Sáez, P. J., Orellana, J. A., Vega-Riveros, N., Figueroa, V. A., Hernández, D. E., Castro, J. F., Klein, A. D., Jiang, J. X., Zanlungo, S., and Sáez, J. C. (2013). Disruption in connexin-based communication is associated with intracellular ca2+ signal alterations in astrocytes from niemann-pick type c mice. *PloS one*, 8(8):e71361.

Santello, M., Bezzi, P., and Volterra, A. (2011). TNFα controls glutamatergic gliotransmission in the hippocampal dentate gyrus. *Neuron*, 69:988–1001.

Santello, M. and Volterra, A. (2009). Synaptic modulation by astrocytes via Ca^{2+}-dependent glutamate release. *Neuroscience*, 158(1):253–259.

Santello, M. and Volterra, A. (2012). TNF*alpha* in synaptic function: switching gears. *Trends in Neurosci.*, 35(10):638–647.

Sasaki, T., Kuga, N., Namiki, S., Matsuki, N., and Ikegaya, Y. (2011). Locally synchronized astrocytes. *Cereb. Cortex*.

Savitzky, A. and Golay, M. J. (1964). Smoothing and differentiation of data by simplified least squares procedures. *Analytical chemistry*, 36(8):1627–1639.

Scemes, E. and Giaume, C. (2006). Astrocyte calcium waves: What they are and what they do. *Glia*, 54(7):716–725.

Scemes, E. and Spray, D. C. (2012). Extracellular K^+ and astrocyte signaling via connexin and pannexin channels. *Neurochem. Res.*, 37(11):2310–2316.

Scemes, E., Suadicani, S. O., and Spray, D. C. (2000). Intercellular communication in spinal cord astrocytes: fine tuning between gap junctions and P2 nucleotide receptors in calcium wave propagation. *J. Neurosci.*, 20(4):1435–1445.

Schipke, C., Haas, B., and Kettenmann, H. (2008). Astrocytes discriminate and selectively respond to the activity of a subpopulation of neurons within the barrel cortex. *Cereb. Cortex*, 18(10):2450–2459.

Schipke, C. G., Boucsein, C., Ohlemeyer, C., Kirchhoff, F., and Kettenmann, H. (2002). Astrocyte Ca^{2+} waves trigger responses in microglial cells in brain slices. *FASEB J.*, 16(2):255–257.

Schummers, J., Yu, H., and Sur, M. (2008). Tuned responses of astrocytes and their influence on hemodynamic signals in the visual cortex. *Science*, 320(5883):1638–1643.

Serrano, A., Haddjeri, N., Lacaille, J., and Robitaille, R. (2006). GABAergic network activation of glial cells underlies heterosynaptic depression. *J. Neurosci.*, 26(20):5370–5382.

Shears, S. (1992). Metabolism of inositol phosphates. *Advances in second messenger and phosphoprotein research*, 26:63.

Shein, M., Volman, V., Raichman, N., Hanein, Y., and Ben-Jacob, E. (2008). Management of synchronized network activity by highly active neurons. *Physical biology*, 5(3):036008.

Shigetomi, E., Bushong, E. A., Haustein, M. D., Tong, X., Jackson-Weaver, O., Kracun, S., Xu, J., Sofroniew, M. V., Ellisman, M. H., and Khakh, B. S. (2013). Imaging calcium microdomains within entire astrocyte territories and endfeet with gcamps expressed using adeno-associated viruses. *The Journal of general physiology*, 141(5):633–647.

Shigetomi, E., Kracun, S., Sofroniew, M. V., and Khakh, B. S. (2010). A genetically targeted optical sensor to monitor calcium signals in astrocyte processes. *Nature neuroscience*, 13(6):759–766.

Shigetomi, E., Tong, X., Kwan, K. Y., Corey, D. P., and Khakh, B. S. (2012). Trpa1 channels regulate astrocyte resting calcium and inhibitory synapse efficacy through gat-3. *Nature neuroscience*, 15(1):70–80.

Shuai, J.-W. and Jung, P. (2002). Stochastic properties of ca< sup> 2+</sup> release of inositol 1, 4, 5-trisphosphate receptor clusters. *Biophysical journal*, 83(1):87–97.

Sieger, D., Moritz, C., Ziegenhals, T., Prykhozhij, S., and Peri, F. (2012). Long-range ca< sup> 2+</sup> waves transmit brain-damage signals to microglia. *Developmental cell*, 22(6):1138–1148.

Sirnes, S., Kjenseth, A., Leithe, E., and Rivedal, E. (2009). Interplay between PKC and the MAP kinase pathway in connexin43 phosphorylation and inhibition of gap junction intercellular communication. *Biochem Biophys Res Commun*, 382(1):41–45.

Skupin, A. and Falcke, M. (2010). Statistical analysis of calcium oscillations. *Eur. Phys. J.-Spec. Top.*, 187:231–240.

Skupin, A., Kettenmann, H., Winkler, U., Wartenberg, M., Sauer, H., Tovey, S. C., Taylor, C. W., and Falcke, M. (2008). How does intracellular Ca^{2+} oscillate: by chance or by clock? *Biophys. J.*, 94:2404–2411.

Smith, I. and Parker, I. (2009). Imaging the quantal substructure of single IP_3R channel activity during Ca^{2+} puffs in intact mammalian cells. *Proc. Natl. Acad. Sci. USA*, 106(15):6404.

Sneyd, J., Charles, A. C., and Sanderson, M. J. (1994). A model for the propagation of intracellular calcium waves. *Am. J. Physiol.*, 266(35):C293–C302.

Sneyd, J. and Dofour, J.-F. (2002). A dynamic model of the type-2 inositol trisphosphate receptor. *Proc. Natl. Acad. Sci. USA*, 99(4):2398–2403.

Sneyd, J. and Falcke, M. (2005). Models of the inositol trisphosphate receptor. *Progress in biophysics and molecular biology*, 89(3):207–245.

Sofroniew, M. V. (2009). Molecular dissection of reactive astrogliosis and glial scar formation. *Trends in neurosciences*, 32(12):638–647.

Söhl, G., Maxeiner, S., and Willecke, K. (2005). Expression and functions of neuronal gap junctions. *Nat. Rev. Neurosci.*, 6(3):191–200.

Spray, D. C., Ye, Z.-C., and Ransom, B. R. (2006). Functional connexin "hemichannels": a critical appraisal. *Glia*, 54(7):758–773.

Stam, C. J. (2014). Modern network science of neurological disorders. *Nature Reviews Neuroscience*, 15(10):683–695.

Steinhäuser, C., Seifert, G., and Bedner, P. (2012). Astrocyte dysfunction in temporal lobe epilepsy: K^+ channels and gap junction coupling. *Glia*, 60(8):1192–1202.

Stetter, O., Battaglia, D., Soriano, J., and Geisel, T. (2012). Model-free reconstruction of excitatory neuronal connectivity from calcium imaging signals. *PLoS Comput Biol*, 8(8):e1002653.

Stobart, J. L. and Anderson, C. M. (2013). Multifunctional role of astrocytes as gatekeepers of neuronal energy supply. *Front Cell Neurosci*, 7:38.

Strogatz, S. H. (2001). Exploring complex networks. *Nature*, 410(6825):268–276.

Suadicani, S. O., Flores, C. E., Urban-Maldonado, M., Beelitz, M., and Scemes, E. (2004). Gap junction channels coordinate the propagation of intercellular Ca^{2+} signals generated by P2Y receptor activation. *Glia*, 48(3):217–229.

Suadicani, S. O., Pina-Benabou, M. H. D., Urban-Maldonado, M., Spray, D. C., and Scemes, E. (2003). Acute downregulation of Cx43 alters P2Y receptor expression levels in mouse spinal cord astrocytes. *Glia*, 42(2):160–171.

Sul, J.-Y., Orosz, G., Givens, R. S., and Haydon, P. G. (2004). Astrocytic connectivity in the hippocampus. *Neuron Glia Biol.*, 1(1):3–11.

Sun, W., McConnell, E., Pare, J.-F., Xu, Q., Chen, M., Peng, W., Lovatt, D., Han, X., Smith, Y., and Nedergaard, M. (2013). Glutamate-dependent neuroglial calcium signaling differs between young and adult brain. *Science*, 339(6116):197–200.

Suzuki, A., Stern, S. A., Bozdagi, O., Huntley, G. W., Walker, R. H., Magistretti, P. J., and Alberini, C. M. (2011). Astrocyte-neuron lactate transport is required for long-term memory formation. *Cell*, 144(5):810–823.

Suzuki, Y., Moriyoshi, E., Tsuchiya, D., and Jingami, H. (2004). Negative cooperativity of glutamate binding in the dimeric metabotropic glutamate receptor subtype I. *J. Biol. Chem.*, 279(34):35526–35534.

Swillens, S., Dupont, G., Combettes, L., and Champeil, P. (1999). From calcium blips to calcium puffs: theoretical analysis of the requirements of interchannel communication. *Proc. Natl. Acad. Sci. USA*, 96(24):13750–13755.

Tang, Y. and Othmer, H. (1994). A model of calcium dynamics in cardiac myocytes based on the kinetics of ryanodine-sensitive calcium channels. *Biophys. J.*, 67:2223–2235.

Tang, Y., Stephenson, J. L., and Othmer, H. G. (1996). Simplification and analysis of models of calcium dynamics based on IP_3-sensitive calcium channel kinetics. *Biophys. J.*, 70:246–263.

Tashiro, A., Goldberg, J., and Yuste, R. (2002). Calcium oscillations in neocortical astrocytes under epileptiform conditions. *J Neurobiol*, 50(1):45–55.

Tattini, L., Olmi, S., and Torcini, A. (2012). Coherent periodic activity in excitatory erdös-renyi neural networks: The role of network connectivity. *Chaos*, 22(2):023133.

Theis, M. and Giaume, C. (2012). Connexin-based intercellular communication and astrocyte heterogeneity. *Brain Res.*, 1487:88–98.

Theis, M., Jauch, R., Zhuo, L., Speidel, D., Wallraff, A., Döring, B., Frisch, C., Söhl, G., Teubner, B., Euwens, C., Huston, J., Steinhäuser, C., Messing, A., Heinemann, U., and Willecke, K. (2003). Accelerated hippocampal spreading depression and enhanced locomotory activity in mice with astrocyte-directed inactivation of connexin43. *J Neurosci*, 23(3):766–776.

Thrane, A. S., Thrane, V. R., Zeppenfeld, D., Lou, N., Xu, Q., Nagelhus, E. A., and Nedergaard, M. (2012). General anesthesia selectively disrupts astrocyte calcium signaling in the awake mouse cortex. *Proc Natl Acad Sci U S A*, 109(46):18974–18979.

Thul, R., Smith, G., and Coombes, S. (2008). A bidomain threshold model of propagating calcium waves. *Journal of mathematical biology*, 56(4):435–463.

Tian, G.-F., Azmi, H., Takano, T., Xu, Q., Peng, W., Lin, J., Oberheim, N., Lou, N., Wang, X., Zielke, H. R., et al. (2005). An astrocytic basis of epilepsy. *Nature medicine*, 11(9):973–981.

Tian, G. F., Takano, T., Lin, J. H.-C., Wang, X., Bekar, L., and Nedergaard, M. (2006). Imaging of cortical astrocytes using 2-photon laser scanning microscopy in the intact mouse brain. *Adv. Drug Deliver. Rev.*, 58(7):773–787.

Tolias, A. S., Sultan, F., Augath, M., Oeltermann, A., Tehovnik, E. J., Schiller, P. H., and Logothetis, N. K. (2005). Mapping cortical activity elicited with electrical microstimulation using fmri in the macaque. *Neuron*, 48(6):901–911.

Torres, A., Wang, F., Xu, Q., Fujita, T., Dobrowolski, R., Willecke, K., Takano, T., and Nedergaard, M. (2012). Extracellular ca2+ acts as a mediator of communication from neurons to glia. *Science signaling*, 5(208):ra8.

Tsai, H.-H., Li, H., Fuentealba, L. C., Molofsky, A. V., Taveira-Marques, R., Zhuang, H., Tenney, A., Murnen, A. T., Fancy, S. P. J., Merkle, F., Kessaris, N., Alvarez-Buylla, A., Richardson, W. D., and Rowitch, D. H. (2012). Regional astrocyte allocation regulates cns synaptogenesis and repair. *Science*, 337(6092):358–362.

Tsodyks, M., Pawelzik, K., and Markram, H. (1998). Neural networks with dynamic synapses. *Neural Comput.*, 10:821–835.

Tsodyks, M. V. and Markram, H. (1997). The neural code between neocortical pyramidal neurons depends on neurotransmitter release probability. *Proc Natl Acad Sci U S A*, 94(2):719–723.

Turrigiano, G. G. (2008). The self-tuning neuron: synaptic scaling of excitatory synapses. *Cell*, 135(3):422–435.

Ullah, G., Jung, P., and Cornell-Bell, A. H. (2006). Anti-phase calcium oscillations in astrocytes via inositol (1, 4, 5)-trisphosphate regeneration. *Cell calcium*, 39(3):197–208.

Van Vreeswijk, C. and Sompolinsky, H. (1996). Chaos in neuronal networks with balanced excitatory and inhibitory activity. *Science*, 274(5293):1724–1726.

Van Vreeswijk, C. and Sompolinsky, H. (1998). Chaotic balanced state in a model of cortical circuits. *Neural comput.*, 10(6):1321–1371.

Veléz-Fort, M, A. E. and Angulo, M. C. (2012). Central role of GABA in neuron-glia interactions. *Neuroscientist*, 18:237–250.

Venance, L., Stella, N., Glowinski, J., and Giaume, C. (1997). Mechanism involved in initiation and propagation of receptor-induced intercellular calcium signaling in cultured rat astrocytes. *J. Neurosci.*, 17(6):1981–1992.

Verkhratsky, A. and Butt, A. M. (2013). *Glial physiology and pathophysiology*. John Wiley & Sons.

Verkhratsky, A., Krishtal, O., and Burnstock, G. (2009). Purinoceptors on neuroglia. *Mol. Neurobiol.*, 39(3):190–208.

Verkhratsky, A., Rodríguez, J. J., and Parpura, V. (2012a). Calcium signalling in astroglia. *Mol Cell Endocrinol*, 353(1-2):45–56.

Verkhratsky, A., Sofroniew, M. V., Messing, A., Rempe, D., Rodríguez, J. J., Nedergaard, M., et al. (2012b). Neurological diseases as primary gliopathies: a reassessment of neurocentrism. *Asn neuro*, 4(3):AN20120010.

Volman, V., Ben-Jacob, E., and Levine, H. (2007). The astrocyte as a gatekeeper of synaptic information transfer. *Neural Comput.*, 19:303–326.

Volman, V. and Perc, M. (2010). Fast random rewiring and strong connectivity impair subthreshold signal detection in excitable networks. *New Journal of Physics*, 12(4):043013.

Volman, V., Perc, M., and Bazhenov, M. (2011). Gap junctions and epileptic seizures - two sides of the same coin? *PLoS One*, 6(5):e20572.

Volterra, A., Liaudet, N., and Savtchouk, I. (2014). Astrocyte ca2+ signalling: an unexpected complexity. *Nature Reviews Neuroscience*, 15(5):327–335.

Volterra, A. and Meldolesi, J. (2005). Astrocytes, from brain glue to communication elements: the revolution continues. *Nat Rev Neurosci*, 6(8):626–640.

Wallraff, A., Köhling, R., Heinemann, U., Theis, M., Willecke, K., and Steinhäuser, C. (2006). The impact of astrocytic gap junctional coupling on potassium buffering in the hippocampus. *J Neurosci*, 26(20):5438–5447.

Walz, W. (2000). Role of astrocytes in the clearance of excess extracellular potassium. *Neurochemistry international*, 36(4):291–300.

Wang, F., Smith, N. A., Xu, Q., Fujita, T., Baba, A., Matsuda, T., Takano, T., Bekar, L., and Nedergaard, M. (2012). Astrocytes modulate neural network activity by ca2+-dependent uptake of extracellular k+. *Science signaling*, 5(218):ra26.

Wang, X., Golomb, D., and Rinzel, J. (1995). Emergent spindle oscillations and intermittent burst firing in a thalamic model: specific neuronal mechanisms. *Proc. Natl. Acad. Sci. USA*, 92(12):5577–5581.

Wang, X., Lou, N., Xu, Q., Tian, G.-F., Peng, W. G., Han, X., Kang, J., Takano, T., and Nedergaard, M. (2006). Astrocytic Ca^{2+} signaling evoked by sensory stimulation in vivo. *Nat Neurosci*, 9(6):816–823.

Watras, J., Bezprozvanny, I., and Ehrlich, B. E. (1991). Inositol 1,4,5-trisphosphate-gated channels in cerebellum: presence of multiple conductance states. *J. Neurosci.*, 11(10):3239–3245.

Watts, D. J. (1999). *Small worlds: the dynamics of networks between order and randomness*, chapter 2, pages 33–36. Princeton university press.

Watts, D. J. (2002). A simple model of global cascades on random networks. *Proc Natl Acad Sci U S A*, 99(9):5766–5771.

Weber, S., Hütt, M.-T., and Porto, M. (2008). Pattern formation and efficiency of reaction-diffusion processes on complex networks. *EPL (Europhysics Letters)*, 82(2):28003.

Weissman, T. A., Riquelme, P. A., Ivic, L., Flint, A. C., and Kriegstein, A. R. (2004). Calcium waves propagate through radial glial cells and modulate proliferation in the developing neocortex. *Neuron*, 43(5):647–661.

Williams, G. S., Molinelli, E. J., and Smith, G. D. (2008). Modeling local and global intracellular calcium responses mediated by diffusely distributed inositol 1, 4, 5-trisphosphate receptors. *Journal of theoretical biology*, 253(1):170–188.

Winship, I., Plaa, N., and Murphy, T. (2007). Rapid astrocyte calcium signals correlate with neuronal activity and onset of the hemodynamic response *in vivo*. *J. Neurosci.*, 27(23):6268–6272.

Witcher, M., Kirov, S., and Harris, K. (2007). Plasticity of perisynaptic astroglia during synaptogenesis in the mature rat hippocampus. *Glia*, 55(1):13–23.

Wu, Y.-W., Tang, X., Arizono, M., Bannai, H., Shih, P.-Y., Dembitskaya, Y., Kazantsev, V., Tanaka, M., Itohara, S., Mikoshiba, K., et al. (2014). Spatiotemporal calcium dynamics in single astrocytes and its modulation by neuronal activity. *Cell calcium*, 55(2):119–129.

Xu, G., Wang, W., Kimelberg, H. K., and Zhou, M. (2010). Electrical coupling of astrocytes in rat hippocampal slices under physiological and simulated ischemic conditions. *Glia*, 58(4):481–493.

Yang, J., Ruchti, E., Petit, J.-M., Jourdain, P., Grenningloh, G., Allaman, I., and Magistretti, P. J. (2014). Lactate promotes plasticity gene expression by potentiating nmda signaling in neurons. *Proceedings of the National Academy of Sciences*, 111(33):12228–12233.

Zahradnikova, A. and Zahradnik, I. (1996). A minimal gating model for the cardiac calcium release channel. *Biophysical journal*, 71(6):2996–3012.

Zamanian, J. L., Xu, L., Foo, L. C., Nouri, N., Zhou, L., Giffard, R. G., and Barres, B. A. (2012). Genomic analysis of reactive astrogliosis. *The Journal of Neuroscience*, 32(18):6391–6410.

Zanette, D. H. (2002). Dynamics of rumor propagation on small-world networks. *Phys. Rev. E*, 65(4):041908.

Zhang, J.-M., Wang, H.-K., Ye, C.-Q., Ge, W., Chen, Y., Jiang, Z.-L., Wu, C.-P., Poo, M.-M., and Duan, S. (2003). ATP released by astrocytes mediates glutamatergic activity-dependent heterosynaptic suppression. *Neuron*, 40:971–982.

Zhang, Y. and Barres, B. A. (2010). Astrocyte heterogeneity: an underappreciated topic in neurobiology. *Curr Opin Neurobiol*, 20(5):588–594.

Zhang, Z., Chen, G., Zhou, W., Song, A., Xu, T., Luo, Q., Wang, W., Gu, X., and Duan, S. (2007). Regulated ATP release from astrocytes through lysosome exocytosis. *Nat. Cell Biol.*, 9(8):945–953.

Zhou, C., Zemanová, L., Zamora, G., Hilgetag, C. C., and Kurths, J. (2006). Hierarchical organization unveiled by functional connectivity in complex brain networks. *Phys Rev Lett*, 97(23):238103.

Zorec, R., Araque, A., Carmignoto, G., Haydon, P., Verkhratsky, A., and Parpura, V. (2012). Astroglial excitability and gliotransmission: An appraisal of Ca^{2+} as a signaling route. *ASN Neuro*, 4(2):e00080.

Zucker, R. S. and Regehr, W. G. (2002). Short-term synaptic plasticity. *Annual review of physiology*, 64(1):355–405.

Appendix A

Methods and algorithms

A.1 ChI model methods and algorithms

Snapshots of ICW propagation in Figure V.15 were obtained from simulations of 2D networks with the *ChI* model. Image resolution was first fixed (75×75 pixels there) and each pixel scaled from 0 to 1. At each time t, each pixel $P_{xy}(t)$ in column x and row y was then computed using:

$$P_{xy}(t) = \frac{(\kappa_{xy}(t) - \chi_{xy}) - \min_{i,t} I_i(t)}{\max_{i,t} I_i(t) - \min_{i,t} I_i(t)} \tag{A.1}$$

where $I_i(t)$ is the IP_3 concentration of astrocyte i at time t. The term $\kappa_{xy}(t)$ is the contribution of signals to the pixel (x, y) while χ_{xy} is a term added to improve contrast with extra-cellular spaces:

$$\kappa_{xy}(t) = \frac{\sum_{i=0}^{N} I_i(t) e^{-\alpha || \overrightarrow{c_i} - \overrightarrow{c_{xy}^{img}} ||}}{\sum_{i=0}^{N} e^{-\alpha || \overrightarrow{c_i} - \overrightarrow{c_{xy}^{img}} ||}} \tag{A.2}$$

$$\chi_{xy} = \frac{\gamma}{2} \left(\tanh \left(\frac{\min_i || \overrightarrow{c_i} - \overrightarrow{c_{xy}^{img}} || - \beta}{\beta} \right) + 1 \right) \tag{A.3}$$

where N is the number of astrocytes; $\overrightarrow{c_i}$ is the position of cell i; $\overrightarrow{c_{xy}^{img}}$ is the rescaled position of the pixel in μm; α is a rescaling factor; β is the default length of intercellular space; and γ determines the intensity of the darkening of extracellular space. In this study: $\alpha = 10\ \mu\text{m}^{-1}$; $\beta = 35\ \mu$m and $\gamma = 4$. Finally, during the rendering process if P_{xy} was found below 0 or above 1, it was set to 0 or 1 respectively.

Table A.1: ICW visualization parameters.

Symbol	Description	Values min	step	max	Units
α	Distance rescaling factor		10		μm$^-$1
β	Default length of intercellular space		35		μm
γ	Intensity of darkening of extracellular space		4		-

A.2 Functional topology of astrocyte networks

Functional topology from calcium signals in astrocyte networks of unknown connectivity was reconstructed by the "functional" adjacency matrix **A** defined as:

$$A_{ij} = \mathrm{H}\left(\Phi_{ij} - \theta\right) \tag{A.4}$$

where $\mathrm{H}(\cdot)$ is the Heaviside function, θ is a threshold, and Φ_{ij} is a measure of the coupling strength between cells i and j estimated on the basis of the calcium traces in each cells. In particular, two different estimators for Φ_{ij} were considered in this study: (1) the maximum cross-correlation (MCC) Stetter et al. (2012):

$$MCC_{ij} = \max_{|\Delta t|} \frac{\sum_{t=\Delta t}^{T} C_i(t) C_j(t-\Delta t)}{\sum_{t=\Delta t}^{T} C_i(t) \sum_{t=\Delta t}^{T} C_j(t)} \quad \text{for } \Delta t_{min} \leq |\Delta t| \leq \Delta t_{max} \tag{A.5}$$

where T represents the width of the time window of observation of calcium signals (note that correlations for times smaller than Δt were not considered; and (2) the transfer entropy (TE) defined as Lungarella et al. (2007):

$$TE_{ij} = \sum_{C_i(t+1), \mathbf{C_i^m}, \mathbf{C_j^m}} p(C_i(t+1), \mathbf{C_i^m}, \mathbf{C_j^m}) \log \frac{p(C_i(t+1)|\mathbf{C_i^m}, \mathbf{C_j^m})}{p(C_i(t+1)|C_i^m))} \tag{A.6}$$

where $\mathbf{C_i^m} = \big(C_i(t), C_i(t-1), \ldots, C_i(t-m+1)\big)$ is the m-dimensional embedding vector and m is the embedding dimension. The embedding dimension $m = 8$ was chosen so as to cover a period of 8 s which was above the average time measured in simulations, for an ICW to propagate from one cell to another.

To combine spatial information given by a Voronoi diagram constructed from the astrocytes positions and information obtained from functional topology extraction, we devised simple methods that we called spatial MCC (SMCC) and spatial TE (STE): we start from the adjacency matrix of the Voronoi diagram and we remove links between nodes i and j for which MCC_{ij} or TE_{ij} is less than the α^{th} percentile of the full MCCnz or TE distribution. The best results were obtained with $\alpha = 94$, this is akin to setting a maximum mean degree $k_{max} \approx 7.5$ that the inferred network can have (its minimum mean degree is 0).

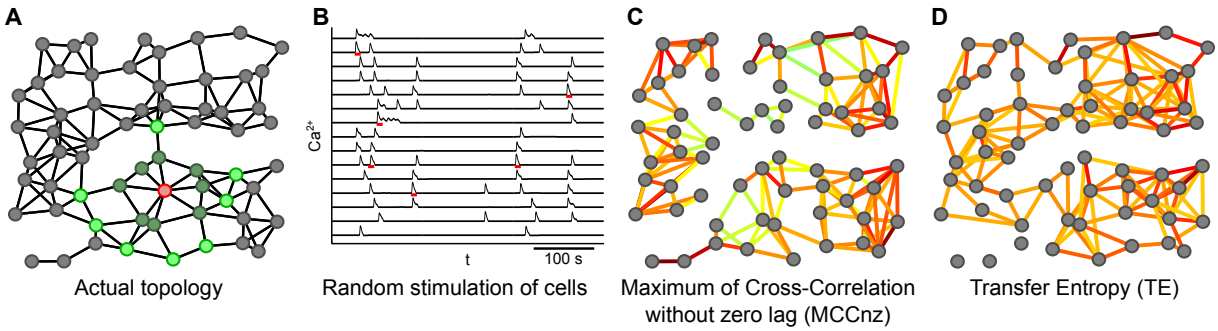

Figure A.1: Schematic view of functional topology inference. Functional topology aims at reconstructing real network (**A**) by connections inferred from (**B**) intracellular Ca2+ traces from all cells of the network. To simulate experimental nucleation rates, astrocytes were properly simulated (*red marks*) as described in Methods. (**C,D**) Examples of network connections reconstructed respectively by MCC and TE (*solid colored links*).

In order to simulate Poissonian nucleation rates of calcium signals in astrocytes reported in cell cultures or brain slices Skupin et al. (2008); Skupin and Falcke (2010), astrocytes in a modelled network were independently stimulated three times on average for 10 s for a total simulated time $T = 10^4$ s with a probability $p_{stim} = 1/310^{-3}$. In this fashion, the time interval between two consecutive astrocyte activations was exponentially distributed and equal on average to 3000 s.

A.2.1 Functional topology estimations

Although ICWs with similar propagation ranges have been observed in different brain regions, the topology of the underlying astrocyte networks remains unresolved. However, in light of the above analysis that elucidated a clear link between network topology and the extent of ICW propagation, it seems reasonable to use the information contained in Ca^{2+} traces of cells activated by an ICW to infer possible salient features of the underlying network connectivity. With this aim, both maximum cross correlation (MCC) and transfer entropy (TE) were computed to infer functional connections between astrocytes by knowledge of their intracellular Ca^{2+} dynamics.

Figure A.1 illustrates the rationale beyond the inference methods in the reconstruction of functional topologies of astrocyte networks. In close analogy with experiments, Ca^{2+} dynamics of all cells (Figure A.1B) of a simulated astrocyte network (Figure A.1A) were used to compute either the MCC or the TE between any cell pair of the network. In this fashion, each pair of cells was associated with a value of MCC or TE that quantified how much one cell influenced the activation of the other, and could be regarded as a measure of the likelihood that those two cells were connected (*color–coded links* in Figures A.1C,D). Only those cells pairs whose MCC or TE values were above a certain threshold (θ) however, were ultimately considered to be effectively connected, while other possible links below such threshold were discarded.

The choice of the threshold θ may clearly affect the goodness of the reconstructed topology with respect to the real network connectivity. In particular, because θ sets the number of connections in the reconstructed network, it controls both mean degree ($\langle k_{func} \rangle$) and mean shortest path (L_{func}) of this latter. With this regard, to test the validity of the adopted inference methods, θ was preliminary tuned to obtain reconstructed networks with the same mean degree of the real network (i.e. $\langle k_{func} \rangle = \langle k_{topo} \rangle$), and the ensuing mean shortest path of the reconstructed networks (L_{func}) was plotted as a function of the real L_{topo} both for TE–based (Figure A.2A) and MCC–based reconstructions (Figure A.3A). It may be seen that both MCC and TE generally allow good estimations of the real mean shortest path of the network, regardless of the underlying topology, since the majority of data cluster along the diagonal $\langle \hat{L} \rangle = L$ (*dashed line*). On the other hand, the deviation of L_{func} from the diagonal line increases for large values of L_{topo} for MCC–based reconstructions, suggesting that this method could be less reliable than TE to detect long–distance links in the network. Accordingly, for the purpose of generality, in the reminder of this section we will focus on TE–based reconstructions.

In practice, the mean degree of the astrocytes networks considered in experiments is not known, so that the reliability of the above inference methods in realistically reconstructing network topology depends on a preliminary good estimation of $\langle k_{topo} \rangle$. With this regard, tiling of brain space by astrocytes suggests that the arrangement of these cells in networks could follow a simple proximity rule whereby each astrocyte would be connected mainly (if not only) with those cells found at the boundaries of its anatomical domain Bushong et al. (2002); Halassa et al. (2007). In agreement with this possibility therefore, the mean degree ($\langle k_{voronoi} \rangle$) of the network resulting from the Voronoi diagram constructed around astrocyte positions in space was considered as the basis to estimate $\langle k_{topo} \rangle$ in realistic astrocyte networks. The results of the reconstructions performed assuming $\langle k_{func} \rangle = \langle k_{voronoi} \rangle$ are summarized for different network topologies in Figure A.2B in terms of ROC curves. These curves were obtained by plotting the fraction of real connections effectively reconstructed (true positives) as a function of the fraction of spurious ones that were erroneously added in the reconstruction (false positives). The more the ROC curve above the *dashed* diagonal line, the more realistic the reconstruction.

It may be seen from Figure A.2C that the mere Voronoi diagram could be used to infer at least 70% of the connections either in regular degree or link radius networks. This is likely because the limited length of connections in these networks resembles the proximity rule emerging from the connections of the Voronoi diagram Barthélemy (2010). For the same reason, shortcut, scale free or Erdős-Rény networks could not be reliably reconstructed by the Voronoi diagram instead due to the presence of long–distance links between their cells. Figure A.2B shows that functional topology TE–based inference generally allow to reconstruct non-spatially constrained networks with a good level of reliability (higher than $\sim$60%) but is less efficient than a simple Voronoi diagram for spatially constrained networks.

Indeed, the caveat of TE–based reconstruction is however that cells that are linked by a short path, such as for example cells in a two–hop neighborhood of an astrocyte, may be erroneously linked. This is reflected in Figure A.2B by almost coincident ROC curves for regular degree and link radius networks, and may be attributed to the fact that TE reconstruction is based on sole functional connectivity which does not include any information on the effective spatial arrangement of astrocytes in the network. To include

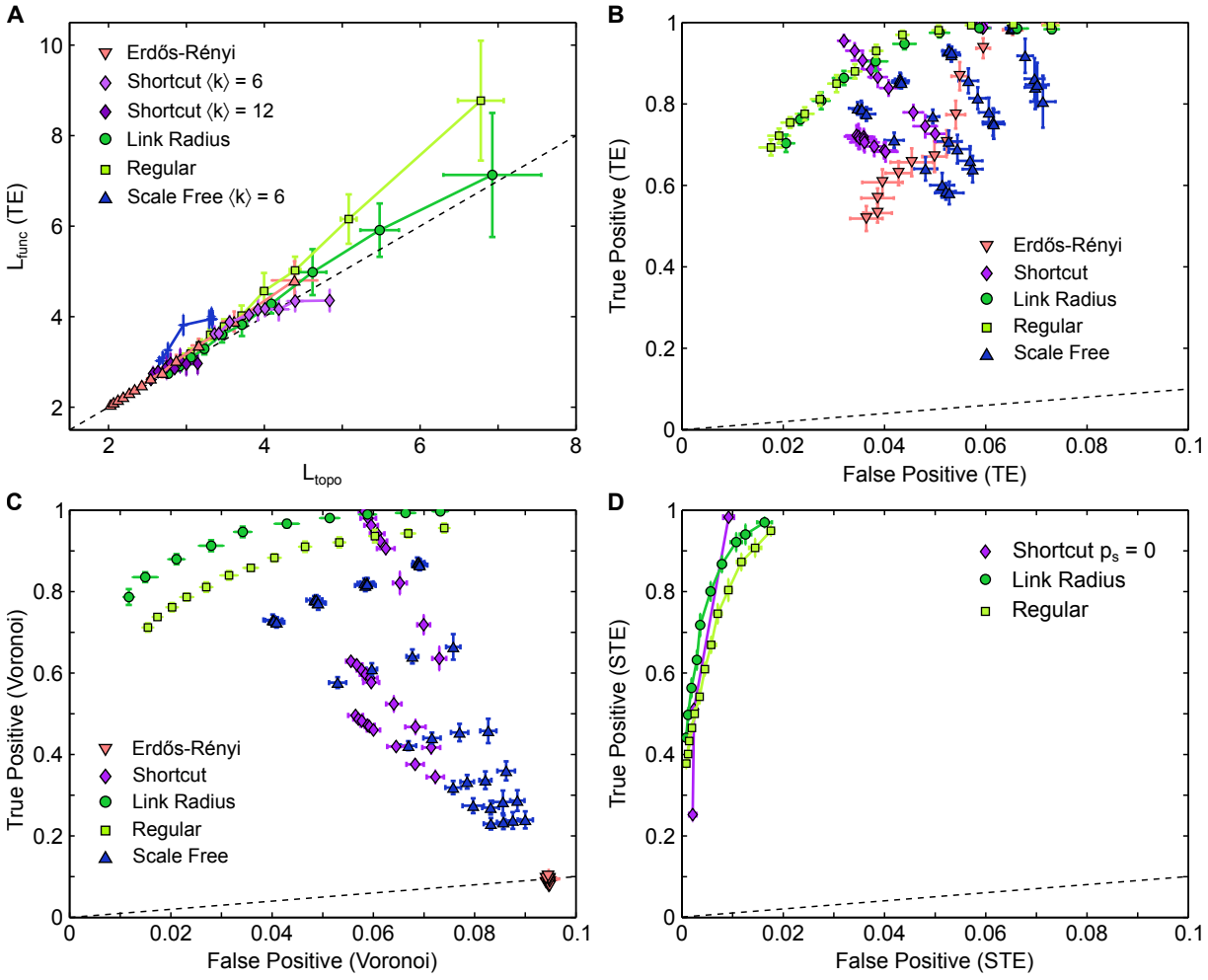

Figure A.2: Functional topology can provide hints regarding local connectivity. **(A)** Mean-shortest path L_{func} of the inferred topology obtained by TE setting $\langle k_{func} \rangle = \langle k_{topo} \rangle$, as a function of actual mean-shortest path L_{topo}. The black dashed line is the first diagonal $L_{func} = L_{topo}$. **(B,C and D)** Receiver Operating Characteristic (ROC) curve presenting the fraction of links in the actual topology that are detected in the inferred one (true positives) as a function of the fraction of non-existing links in the actual topology present in the inferred one (false positives). **(B)** The TE technique was used to extract the inferred topologies, setting $\langle k_{func} \rangle = \langle k_{voronoi} \rangle$ as a threshold. **(C)** The inferred topology was built from a Voronoi diagram. **(D)** The STE technique was used to extract the inferred topologies. Each point corresponds to an average across 20 realizations of 3D network topology. Error bars plot standard deviation and the data is grouped by network types.

such information, the TE may be computed not on all cell pairs but rather only on those connected by the Voronoi diagram (i.e. the STE method presented previously). As shown in Figure A.2D this procedure resulted in a strong decrease in false positives accompanied by a decrease in true positives for high degree networks: not all links are detected but the ones that are detected have a high probability to correspond to actual links.

Interestingly, as presented in Figure A.4, although the SMMCnz technique is less efficient than the STE technique to reconstruct networks, it can be used to estimate the

actual network mean degree $\langle k_{topo} \rangle$: there is a correlation between the actual mean degree and the reconstructed one that could be used to estimate mean degrees in experimental preparation supporting ICW propagation.

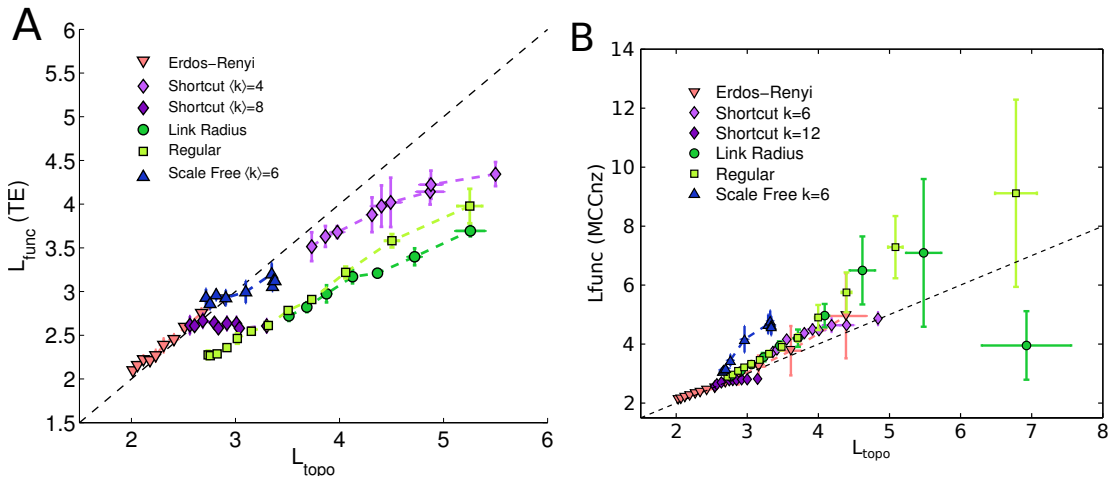

Figure A.3: Mean-shortest path L_{func} of functional topology extracted by TE using $\langle k_{func} \rangle = \langle k_{topo} \rangle$, as a function of actual mean-shortest path L_{topo}. Each point corresponds to the mean L_{func} value across 20 realisations of topology. Error bars plot standard deviation and the data is grouped by network types. The black dashed is the $L_{func} = L_{topo}$ line. **(A)** L_{topo} estimations using TE on 2D networks. **(B)** L_{topo} estimations using MCCnz on 3D networks.

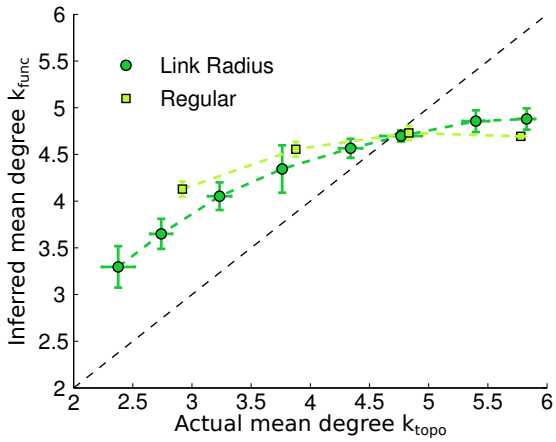

Figure A.4: Mean degree k_{func} of functional topology extracted by SMCCnz, as a function of actual mean degree k_{topo}. Each point corresponds to the mean L_{func} value across 20 realisations of topology. Error bars plot standard deviation and the data is grouped by network types. The black dashed is the $k_{func} = k_{topo}$ line. As the SMCCnz technique only allows the estimation of functional topologies with $k_{func} \leq k_{voronoi}$, the networks for which $k_{topo} > k_{voronoi}$ are not displayed on this graph.

Appendix B

Experimental material and methods

B.1 Experimental setup for MEA cell cultures

This section is directly taken from the article that was accepted in PLoS Computational Biology (but not yet published) and this part has been written by our collaborators in Tel-Aviv university: Gilad Wallach, Nitzan Herzog and Yael Hanein.

B.1.1 Preparation and growth of cultured networks

Dissociated cortical cultures were prepared from surgically removed cortices of E18 Sprague Dawley rat embryos. The cortical tissue was digested by 0.065% trypsin (Biological Industries, Beit Haemek, 03-046-1) in phosphate-buffered saline (Beit Haemek, 02-023-1) for 15 min, followed by mechanical dissociation by trituration. Cells were re-suspended in a modified essential medium (MEM) without phenol red nor glutamine (Gibco, 21200-046), complemented with 5% horse serum (Beith Haemek 04-004-1), 5 $mg.ml^{-1}$ gentamycin (Beith Haemek 03-035-1), 50 μM glutamine (Beith Haemek 03-020-1) and 0.02 mM glucose (BDH101174Y). Cells were then plated on multielectrode arrays (MEAs) (500/30iR-Ti or HD 30/10iR-ITO, by Multi Channel Systems) coated by poly-D-lysine (PDL, Sigma, catalog no. p-7889), at density of 3500–4500 mm^{-2} (that is $\sim 2.10^6$ cells per culture). Cultures were maintained at 37°C with 5% CO2 at 95% of humidity. The growth medium was partially replaced every 3–4 days (approximately 30%).

B.1.2 Pharmacology

Suppression of synapse efficacy was obtained by adding ~ 1 μM b-cyano-7-nitroquinoxaline-2,3-dione (CNQX) which is a α-amino-3-hydroxy-5-methyl-4-isoxazelepropionic acid re-

ceptor (AMPAR) antagonist, and $\sim$ 3 μM (2R)-amino-5-phosphonovaleric acid (APV) which is a N-methyl-D-aspartate receptor (NMDAR) antagonist to the recording medium. This approach was shown to reduce functional connectivity in neuronal cultures (Breskin et al., 2006). Neuronal action potentials were blocked by 1.5 μM of the sodium channel blocker tetrodotoxin (TTX). Inhibition of astrocytic metabotropic glutamate receptors mGluR5 and mGluR1 was achieved by adding to the bath 25μM 6-Methyl-2-(phenylethynyl)pyridine hydrochloride (MPEP) and 50μM (S)-(+)-a-amino-4-carboxy-2-methylbenzeneacetic acid (LY367385) respectively (Bernardinelli et al., 2011). All chemicals were purchased from Sigma-Aldrich.

B.1.3 Immunocytochemistry

Cultures were washed twice in phosphate buffered solution (PBS), then fixed by 4% paraformaldehyde (Merck) solution for 10 min, and left in PBS before staining. To perform immunocytochemical staining, fixed cultures were washed three times with PBS (10 min/wash) and permeabilized by 0.5% triton X-100 (Sigma-Aldrich) in PBS for 10 min. Cultures were then blocked with 2% BSA, 10% normal donkey serum and 0.5% triton X-100 solution in PBS for 1 hr at room temperature and incubated overnight at 4°C with primary antibodies GFAP (1:400 Sigma-Aldrich) and NeuN (1:200, Millipore). Cultures were further washed by PBS (3 times, 10 min/wash) and incubated for 1hr at room temperature with the appropriate secondary antibodies: Alexa fluor 488 goat anti rabbit IgG (1:400, Jackson) for the detection of GFAP, and Cy-3 donkey anti-mouse IgG (1:700, Jackson) for NeuN. Finally, after another wash by PBS (3 times, 10 min/wash), cultures were mounted with aqueous DAPI-containing medium (VECTASHIELD Mounting Medium with DAPI, Vector Laboratories, H-1200).

B.1.4 Electrophysiology and Ca2+ imaging

Rectangular and biphasic 400μs-long current pulses of 25-35 μA were applied to cell cultures by an extracellular multi-electrode array (MEA) using a dedicated 4-channel stimulus generator (STG 2004, Multi Channel Systems). Ca^{2+} imaging was performed in open air environment, and accordingly culture medium was replaced by buffered-ACSF medium (10 mM HEPES, 4 mM KCl, 2 mM $CaCl^2$, 1 mM $MgCl^2$, 139 mM NaCl, 10 mM D-glucose, adjusted with sucrose to an osmolarity of 325 mOsm, and with NaOH to a pH of 7.4). Cultures were washed three times to remove traces of incubation medium and incubated in ACSF with 3μM Oregon-Green BAPTA-I (Invitrogen 06807, one vial with 6.7 μl Anhydrous-DMSO for stock of 6 mM) and same volume of Pluronic acid F-127 (Biotium 59000, stock 10% w/v after mixing 1 g vial in 10 ml DDW) for 30 min. Following incubation, cultures were washed again and kept in ACSF. During recordings, cultures were kept at 37°C. Time lapse data were taken with an Olympus upright microscope (BX51WI) fitted with an EMCCD camera (Andor Ixon-885) and a $\times$20 water immersion objective (Olympus, UMPLFLN 20XW NA 0.5). This setup allowed the visualization of

cells residing on top of non-transparent electrodes. Fluorescent excitation was delivered by a 120 W mercury lamp (EXFO x-cite 120PC) coupled with a dichroic mirror with a filter to match the dye spectrum (Chroma T495LP). Camera control utilized Andor propriety SOLIS software. Time-lapse recordings were performed at 2×2 binning mode for resolution of 500×502 and 51.948 fps. Time lapse sequences were collected via a dedicated 12 bit Andor data acquisition card installed on a personal computer, spooled to a high capacity hard drive and stored as uncompressed multi-page TIFF file libraries. The effect of bleaching was very moderate and addressed by using normalization of fluorescence values ($\Delta F/F_0$). In cell cultures at the culture stage observed in this paper (DIV 14-27), neural activity typically organizes as periodic synchronized bursting events in which most neurons fire once or several times within a short time interval (population bursts) (Maeda et al., 1995; Eytan and Marom, 2006; Shein et al., 2008). The amplitude and extension of these bursts of neural activity are so large that they eclipse the subtler crosstalk between neurons and glial cells. To overcome this issue and focus on the neuron-glia interactions, we used synaptic blockers APV and CNQX (see "Pharmacology") which suppress the spontaneous bursting events. Each Ca^{2+} imaging session typically consisted in the observation of 3-4 different fields of view per each neuron-astrocyte culture dish.

B.1.5 Analysis of Ca^{2+} data

Ca^{2+} imaging data was stored as uncompressed TIFF library, where pixel values represented fluorescence intensity. Boundaries of cell somata were semi-automatically segmented from the time-averaged Ca^{2+} image using a custom code implemented in MATLAB (The MathWorks Inc., Natick, Massachussetts, USA), followed by manual adjustments. Ca^{2+} variations in the astrocyte cell bodies were estimated as normalized changes of fluorescence signal from baseline($\Delta F/F_0$). Local baseline fluorescence (F_0) was evaluated from the histograms of the signal within a running time window. Time windows without cellular activity were best fit by a single Gaussian (due to white noise), whereas those with cellular activity were best fit by two Gaussians (due to white noise and activity). For display purposes, the signal was smoothed by convolution with a 50-data point-large Savitsky-Golay filter of polynomial degree 7 (Savitzky and Golay, 1964; Gorry, 1990). Neuronal signals were distinguished from astrocytic signals based on typical dynamic time scales, and physiological properties of their calcium signals (Ikegaya et al., 2005). Neurons were characterized by fast variations in Ca^{2+} activity during spike onset, whereas astrocytes exhibited slowly varying signals (Figure B.1).

B.1.6 Mapping stimulation efficacy

To validate our electrical stimulation conditions we first mapped the efficacy of MEA stimulations relative to the triggering of Ca^{2+} transients. To define a proper stimulation charge density range, we performed an activation safety mapping.Based on these experiments, we defined a maximal stimulation range of 1.4-1.7$\frac{\mathrm{mC}}{\mathrm{cm}^2}$. The stimulation efficacy

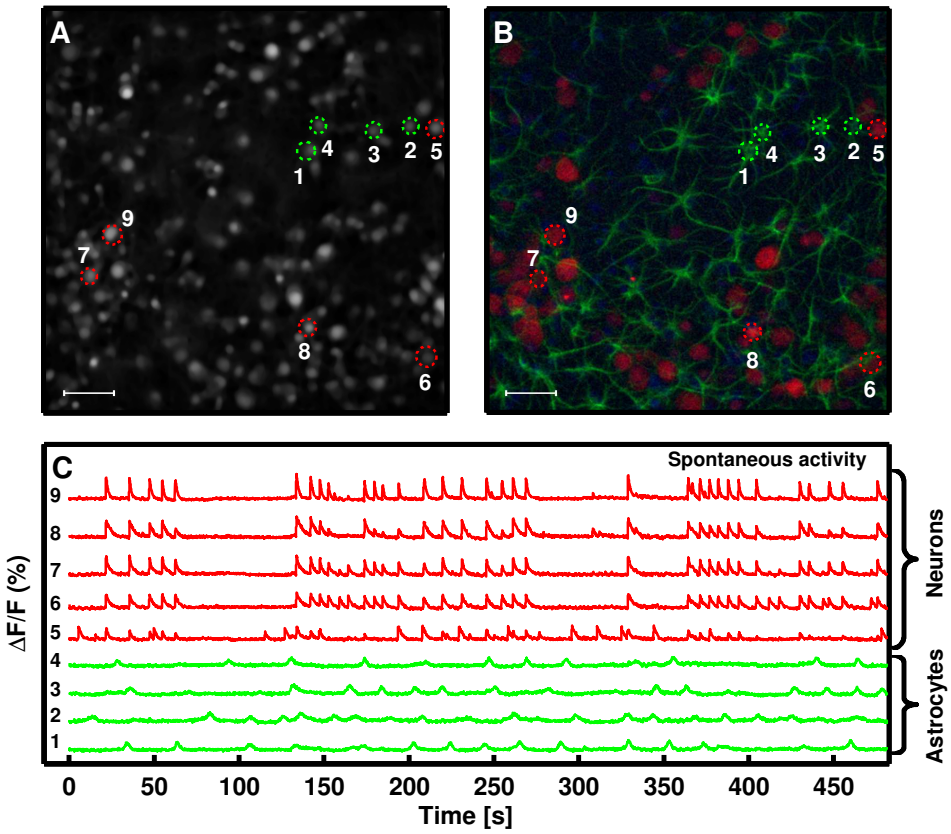

Figure B.1: Immunostaining to distinguish neurons from astrocytes. **A**, Image of recorded culture with marked cells. **B**, Combined pseudo-color immunostaining image of same field of view and marked cells as shown in A. *Red* - neuronal marker NeuN. *Green* – astrocytic marker GFAP. *Blue* – nuclei visualization agent DAPI. **C**, Spontaneous Ca^{2+} traces of same neurons and astrocytes (in *red* and *green* respectively) as marked in A, B. Scale bars are 75μm. Culture was 14 DIV.

was explored by mapping the location of activated neurons relative to the stimulating electrode. Figure B.2A shows neuronal activation maps at three different stimulation amplitudes (response probability is color coded). This figure shows that the distance between a neuron soma and the stimulation electrode is not highly correlated to the amplitude of the stimulation needed to activate it. Indeed, some of the neurons located far from the electrode are activated by lower stimulation amplitudes than neurons located close to the electrode. This suggests that activation is transmitted over long distances by the neuronal processes. This effect is further illustrated in Figure B.2B which shows the increase in the number of activated cells with increased charge density averaged over three cultures and eight electrodes. Activation ratio reaches a saturation level, suggesting that electrical stimulation activates processes at the electrode vicinity. Figure B.2C shows activation maps depicting the response to stimulations applied at two different electrodes (highlighted). Each electrode activated a unique set of neurons and the neuron population that responded to both electrodes was very small. This confirms that the distance between neuron and electrode is not a dominant factor determining response probability. Altogether these results indicate that in our MEA setup, electrical neuronal activation is dominated by the activation of neuronal processes rather than by that of the soma and

is highly non-localized (Rattay, 1999; Tolias et al., 2005).

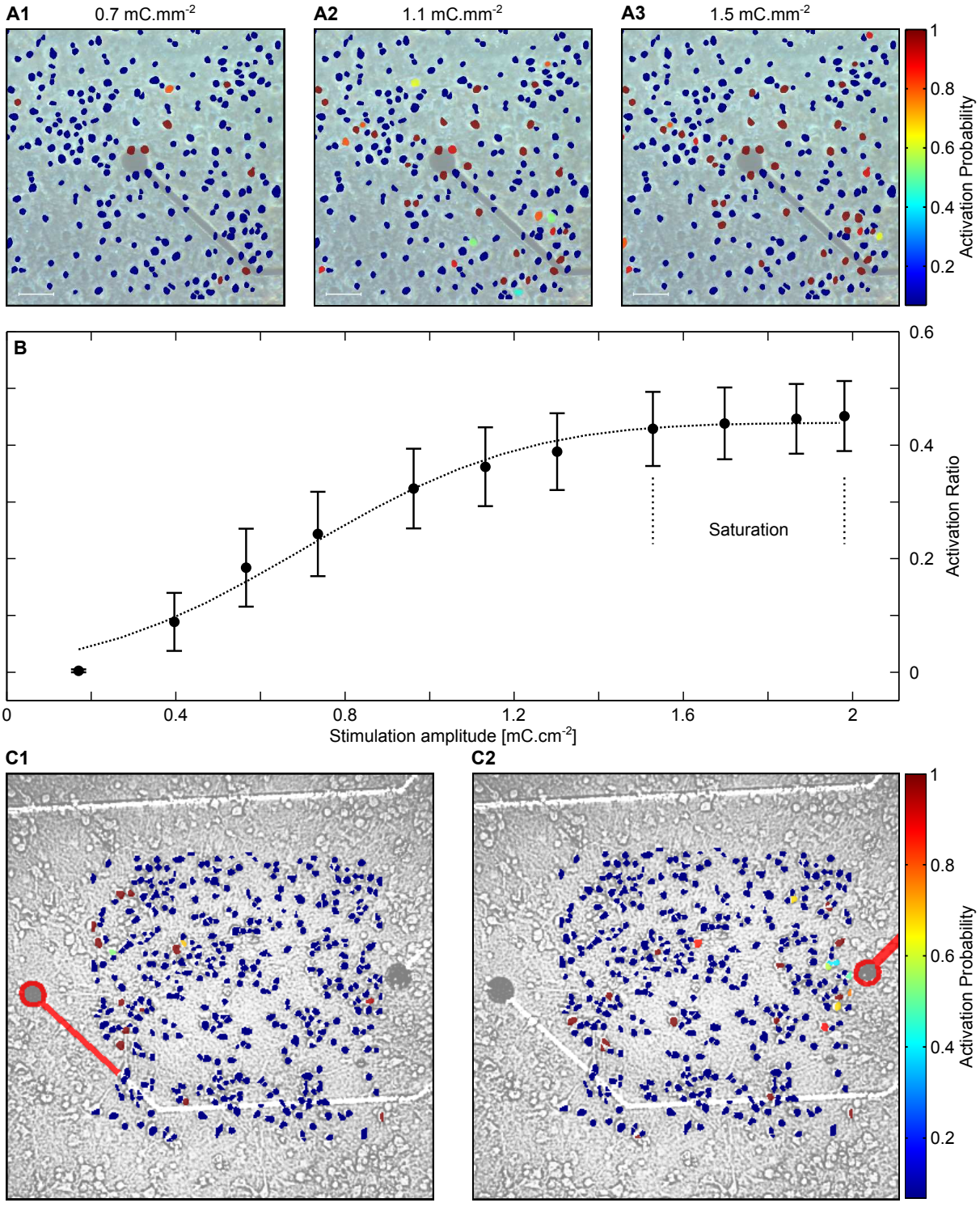

Figure B.2: Geometric mapping of electrical activation. **A**, Response probability color coded activation maps for different stimulation amplitudes showing a clear correlation between stimulation amplitude and number of activated neurons (scale bar 50 μm). **B**, Proportion of activated neurons as a function of stimulation amplitude, indicating a saturation zone. **C**, Recordings incorporating stimulations from different electrodes provide insight regarding mechanism of electrical stimulation. Each electrode activates a unique set of neurons with a very small neuronal population that responds to both.

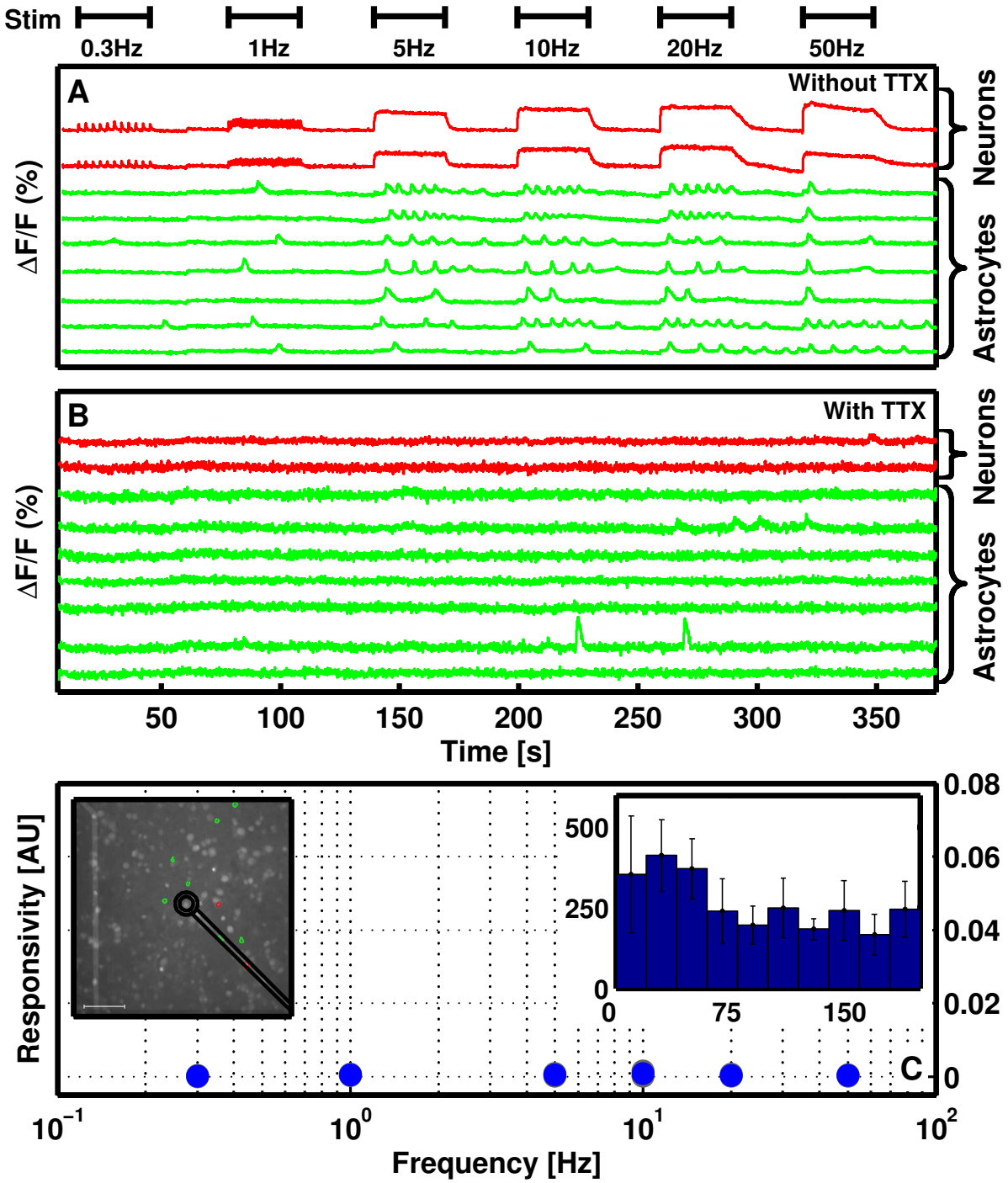

Figure B.3: Astrocytic response is not a direct effect of electrical stimulation. **A**, Traces of two selected neurons (in *red*), showing stimulated activity according to protocol, and seven selected astrocytes (in *green*) in presence of neuronal AMPAR and NMDAR/kainate antagonists. **B**, Traces of same cells and stimulation protocol as in A, showing no neuronal and astrocytic Ca^{2+} elevations in the presence of neuronal AMPAR and NMDAR/kainate antagonists, and TTX. **C**, Astrocytic responsivity as a function of stimulation frequency in presence of TTX show no astrocytic frequency dependence (N=20). Left inset shows image of recorded culture with specified cells from A, B. Electrode is marked in *black*, and scale bar indicates 75 μm. Right inset is a histogram of responsive astrocytes per area as a function of radius from electrode in μm ($N = 277$).

Appendix C

ICW propagation in model astrocyte networks

C.1 ICW Propagation in astrocyte networks: verifications and further details

C.1.1 GJC rescaling

We demonstrate here that $\sum_{i>j} F_{ij} aij = \sum_{i>j} F'_{ij} a_{ij}$ with a_{ij} an element of the astrocyte network adjacency matrix. We remind the reader that $\rho = \frac{\mu^{(2)}(k)}{\mu^{(1)}(k)}$, with $\mu^{(1)}(k)$ and $\mu^{(2)}(k)$ the 1st and 2nd moments of the degree distribution. We note E the number of edges in the graph. In networks that were not rescaled we have $\forall(i,j) F_{ij} = F_0$. We only consider here networks for which $\max(k) \neq \rho$.

$$F'_{ij} = F_0\left(1 + \frac{2\rho - (k_i + k_j)}{2(\max(k) - \rho)}\right) \tag{C.1}$$

$$\sum_{i>j} F'_{ij} a_{ij} = \sum_{i>j} a_{ij} F_0\left(1 + \frac{2\rho - (k_i + k_j)}{2(\max(k) - \rho)}\right) \tag{C.2}$$

$$= F_0 E + F_0 \frac{2\sum_{i>j} a_{ij}\rho - \sum_{i>j} a_{ij}(k_i + k_j)}{2(\max(k) - \rho)} \tag{C.3}$$

$$= F_0 E + F_0 \frac{2E\frac{\sum_m k_m^2}{\sum_m k_m} - \sum_{i>j} a_{ij}(k_i + k_j)}{2(\max(k) - \rho)} \tag{C.4}$$

We know that

$$\sum_m k_m = 2E$$

Let's look at $\sum_{i>j} a_{ij}(k_i + k_j)$, it can be rewritten with a sum over the edges between i and j with the operators $start(e)$ and $end(e)$ returning the two nodes linked by the edge (order has no importance) :

$$\sum_{i>j} a_{ij}(k_i + k_j) = \sum_{e\in\mathcal{E}} k_{start(e)} + k_{end(e)}$$

As the sum is over all the edges, for each node i, the term k_i will be present exactly k_i times in the sum because k_i links are attached to node i and i will intervene either in the form of $start(e)$ or $end(e)$. This implies that :

$$\sum_{e\in\mathcal{E}} k_{start(e)} + k_{end(e)} = \sum_i k_i^2$$

If we now inject these in equation (C.4) :

$$\begin{aligned}
\sum_{i>j} F'_{ij} a_{ij} &= F_0 E + F_0 \frac{\sum_m k_m^2 - \sum_m k_m^2}{2(\max(k) - \rho)} && \text{(C.5)}\\
&= F_0 E && \text{(C.6)}\\
&= \sum_{i>j} F_{ij} aij && \text{(C.7)}
\end{aligned}$$

C.1.2 Measurements and estimations of normalized IP_3 quantities received by astrocytes in full network simulations

Estimations for activated astrocytes on the ICW frontier To further check that our local propagation analysis holds in full network propagation, we estimated the normalized IP_3 quantities received by cells i that got activated on the furthest wave front (Ψ_i) and by cells that were connected to the wave front but that were not activated ($\overline{\Psi_i}$). Similarly to what we did in Section V.3, we assume here that activated astrocytes split their IP_3 evenly among their unactivated neighbors. The normalized quantity of IP_3 Ψ_i received by an astrocyte i is then the sum of normalized quantities of IP_3 β_j given by its activated neighbors j. We thus computed Ψ_i for each cell on the ICW frontier as:

$$\Psi_i = \max_{t_i^{act}} \Psi_i(t_i^{act}) = \max_{t_i^{act}} \sum_{j\in\mathcal{N}_i} \beta_j(t_i^{act}) = \max_{t_i^{act}} \sum_{j\in\mathcal{N}_i} \frac{A_j(t_i^{act} - \Delta t, t_i^{act})}{\sum_{k\in\mathcal{N}_j} (1 - A_k(t_j^{act}, t_i^{act}))} \qquad \text{(C.8)}$$

with t_i^{act} the times at which cell i was activated; $\beta_j(t_i^{act})$ an estimation of the normalized quantity of IP_3 going out of cell j to each of its neighbors before the activation of i at t_i^{act}; $A_j(t_1, t_2) = 1$ if cell j was activated between time t_1 and t_2 and 0 otherwise; Δt a

time window whose length is of the order of the transmission time between cells during an ICW (in this case, $\Delta t = 7$s). Cell i was considered as being part of the furthest wave front (or the ICW frontier) if it was activated at least once and if, for each of its neighbors j that got activated at least once, j was always closer (in terms of topological distance) to the stimulation point than i.

Estimations for unactivated astrocytes connected to the ICW frontier Then, we estimated the normalized quantity of IP_3 $\overline{\Psi_i}$ received by a cell i connected to cells on the ICW frontier but that *never* got activated, as:

$$\overline{\Psi_i} = \sum_{j \in \mathcal{N}_i} \beta_j(t_j^{act}) = \sum_{j \in \mathcal{N}_i} \frac{A_j(0,\infty)}{\min\limits_{t_j^{act}} \sum\limits_{k \in \mathcal{N}_j} (1 - A_k(t_j^{act}, t_j^{act} + \Delta t))} \tag{C.9}$$

Note that this estimation is an upper bound; since the considered astrocyte never got activated, we cannot compute the IP_3 it received before its activation so we instead estimate the maximum quantity of IP_3 that it received during the whole simulation.

Figure C.1A displays the mean normalized IP_3 quantity $\langle \Psi \rangle = \frac{1}{\text{card}(\mathcal{F})} \sum_{i \in \mathcal{F}} \Psi_i$ received by astrocytes on the ICW frontier during full network propagation as a function of network mean degree (with $\mathcal{F}$ the set of astrocytes on the ICW frontier). As expected from local propagation analysis, nearly all networks displayed $\langle \Psi \rangle$ values above the Ψ_θ threshold for activation defined earlier (*black dashed* line). Interestingly, spatially-constrained networks (*light green* squares, *dark green* circles, and *light purple* diamond) are segregated from spatially unconstrained ones (*blue* triangles, *light red* triangles, and *purple* diamonds), displaying much higher $\langle \Psi \rangle$ than these latter. The same segregation was observed when we looked at ICW extent in Figure V.5, hinting that spatially-constrained networks support larger ICW because they favor higher quantities of IP_3 $\langle \Psi \rangle$. The causes of these differences will be investigated in Section V.5. Figure C.1B confirms that the quantity of IP_3 received by astrocytes is the determinant factor of wave propagation: the upper bound on normalized IP_3 quantity $\langle \overline{\Psi} \rangle$ received by unactivated astrocytes near the ICW frontier is close or below the threshold for activation Ψ_θ. Similarly to $\langle \Psi \rangle$, $\langle \overline{\Psi} \rangle$ difference between spatially constrained and spatially unconstrained networks increased with $\langle k \rangle$, with spatially constrained networks being much closer to the activation threshold than spatially unconstrained ones. These two figures show that the simple propagation mechanisms used in the local propagation analysis, considering only the two-hop neighborhood of each astrocytes, seems to also apply in the case of full network propagation.

Measurements of received IP_3 quantities To further check that the $\langle \Psi \rangle$ values that we measured are indeed related to actual IP_3 quantities received by astrocytes, we integrated the IP_3 influx in each astrocyte during a sliding window of length $\Delta t = 10$s. We chose to describe each astrocyte i by two values: (1) the highest IP_3 quantity Q_i that it received during Δt in the whole simulation; (2) its distance r to the stimulated node. We next considered ρ^r, the fraction of astrocytes at a distance r from the stimulated node

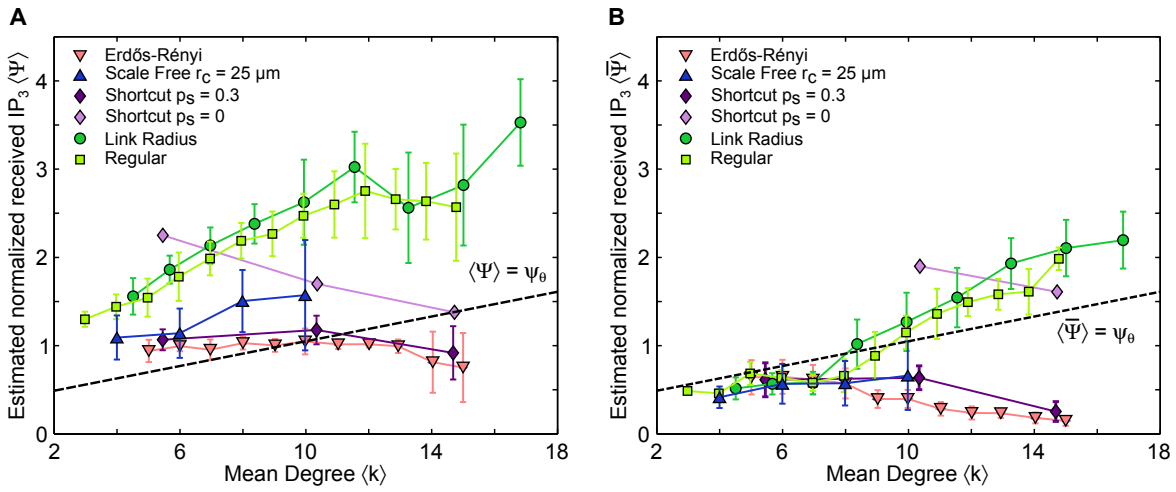

Figure C.1: Application of local analysis to whole network propagation. Estimations of normalized IP_3 quantities received by **A** activated astrocytes on on the ICW front and **B** unactivated astrocytes connected to the ICW front, were plotted against the mean degree $\langle k \rangle$ for all the networks used in Chapter V. **A** Nearly all networks are above the threshold quantity Ψ_θ needed to propagate ICW (reported as the *dashed black line*). Only spatially unconstrained networks with high degree were below threshold. Since these points correspond to networks in which only the first neighbors of the stimulated nodes were activated, our estimations do not take the bias IP_3 flux generated by stimulation into account. Without this bias, these cells would not have got activated. **B** Cells that were not activated despite being connected to cells on the ICW front usually received sub-threshold IP_3 quantities $\langle \overline{\Psi} \rangle$. Spatially constrained networks with high $\langle k \rangle$are above threshold but under the quantities of IP_3 received by activated cells. Data points are shown as mean±std for 20 different network realizations of each topology. Parameters as in Table V.1. Network parameters as in Table V.2.

that got activated at least once during the whole simulation, and $\langle Q_i \rangle^r$, the mean quantity of IP_3 received by nodes at a distance r from the stimulated node. This two measures allowed us to investigate how the quantity of IP_3 received by astrocytes changes as their distance from the stimulated node increases and the fraction of activated node decreases. Examples of $\langle Q_i \rangle^r$ and ρ^r are displayed in Figure C.2. In order to compare the different networks, we computed the normalized $\langle Q_i \rangle^r$ (divided by $Q_0 = 0.4\mu$M) and computed its distance to the normalized IP_3 threshold Ψ_θ (that depends on network mean degree). Accordingly, Figure C.2A displays this value as the distance from the stimulated node r increases for several network classes. Regenerative ICW propagation on 3D lattices (i.e. shortcut networks with $p_s = 0$ and $m_{latt} = 1$, *purple* diamonds) is associated with an above-threshold IP_3 quantity received by astrocytes for all r values while the large, but not regenerative, ICWs that propagate on regular degree networks with $k_{reg} = 3$ (*light green* squares) fall below the threshold for high r values. Non regenerative ICW with low extent on either spatially constrained (regular degree with $k_{reg} = 5$, *dark green* squares) or unconstrained (Erdős-Rényi with $\langle k \rangle = 5$, *red* triangles) networks quickly fall below threshold as r increases, stopping ICW propagation much earlier than in the two other networks. Figure C.2B displays activation densities for each as the distance from the stimulated node r increases; interestingly, from the examples presented, it seems that

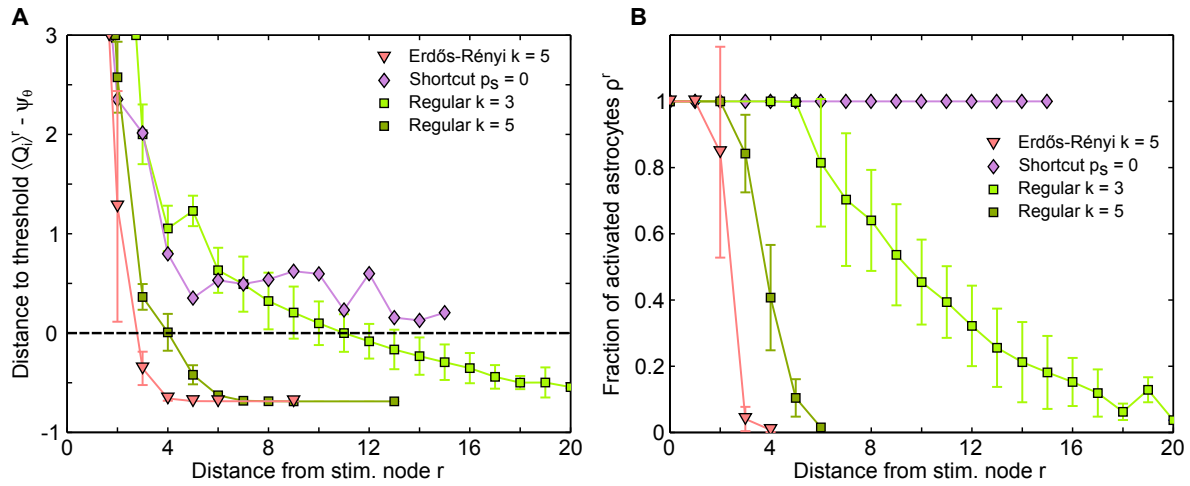

Figure C.2: ICW propagation and IP_3 quantites received by astrocytes. As the distance from the stimulated node r increases we monitored **A** the difference between the mean normalized IP_3 quantities received by astrocytes $\langle Q_i \rangle^r$ and the IP_3 threshold for activation Ψ_θ, and **B** the fraction of activated astrocytes ρ^r. Networks supporting regenerative propagation like cubic lattices (shortcut networks with $p_s = 0$ and $m_{latt} = 1$, *purple* diamonds) maintain ρ^r near 1 thanks to supra-threshold IP_3 quantities received by astrocytes and this, for all r. In contrast, the IP_3 received by astrocytes in networks that do not support regenerative waves (Regular with $k = 5$, *dark green* squares, and Erdős-Rényi networks with $\langle k \rangle = 5$, *red* triangles) soon falls, for small r values, below the IP_3 threshold and consequently, very few astrocytes get activated. Data points are shown as mean±std for 20 different network realizations of each topology. Parameters as in Table V.1. Network parameters as in Table V.2. Due to the stimulation method, IP_3 quantities received for $r \leq 2$ are quite high and are thus not displayed on **A** for readability.

the fraction of activated astrocytes at distance r falls below 0.5 as soon as the mean IP_3 quantity received by nodes at the same distance falls below the IP_3 threshold Psi_θ. A synthetic visualization of this effect is displayed in Figure C.3. We plotted the mean IP_3 quantity received by nodes at a distance r^* from the stimulated node in Figure C.3A; we defined r^* as the r value for which $\rho^r = 0.5$, since most of the time none of the discrete values of r matched ρ^r, we made linear interpolations between discrete r values. Schematically speaking, this figure is the equivalent of Figure C.1A with actual integrated IP_3 quantities: nodes at distance r^* are on the wave frontier and this figure shows that nearly all network classes display received IP_3 quantites above the threshold Ψ_θ (*black dashed* line). We next binned all ρ^r values for all r in all network classes and looked at the mean received IP_3 quantities $\langle Q_i \rangle^r$. Figure C.3B shows that distances at which few nodes are activated ($\rho^r < 0.5$, *red shaded* rectangles) are associated with below-threshold IP_3 quantities while distances at which a high fraction of astrocytes are activated ($\rho^r > 0.5$, *green shaded* regions) are associated with supra-threshold IP_3 quantities. All together, these additional measures of received IP_3 quantites confirm that our local propagation analysis still holds for full network propagation and for different network classes. In order to get activated, an astrocyte i must receive a normalized IP_3 quantity Q_i over the IP_3 threshold $\Psi_\theta = A\langle k \rangle + B$ defined in the local propagation analysis.

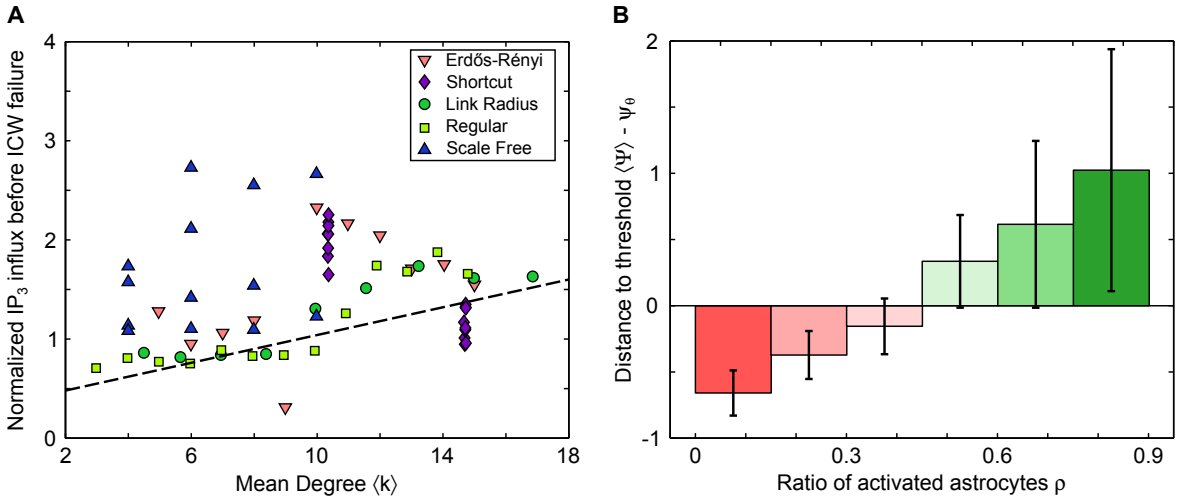

Figure C.3: Actual IP_3 quantities received by astrocytes. A The mean normalized IP_3 quantity received by astrocytes when the ICW is ending (i.e. for cells at a distance r^* from the stimulated node, with $\rho^{r^*} = 0.5$) is just over the IP_3 threshold for activation Ψ_θ for nearly all networks. When $\langle k \rangle$ increases, the quantity of IP_3 received by astrocytes also increasers in order to maintain an activation ratio of $\rho^{r^*} = 0.5$. **B** Taking into consideration all networks and all distances from stimulated node r, we binned $\langle Q_i \rangle^r - \Psi_\theta$ values by ρ^r values into 6 bins from 0 to 0.9 (we discarded values to close to 1 one for readability reasons, as in Figure C.2A). When the quantity of IP_3 received is below threshold (*red* bars), few astrocytes get activated (i.e. $\rho^r < 0.5$), and when it gets above threshold (*green* bars), most astrocytes get activated ($\rho^r > 0.5$). Error bars plot mean±standard deviation for each bin. Parameters as in Figure C.2.

C.2 ICW propagation as a shell-by-shell activation process

In this section, we will present the detailed development of the shell-by-shell propagation model which is evoked in Section V.5.

C.2.1 Inter-shell links control IP_3 repartition

The crude estimation $\langle \Psi^r \rangle$ (obtained in Section V.5) of the mean quantity of IP_3 given by shell r to its neighbors can give an idea of how well a network might be able to propagate ICW but is not the most pertinent quantity at play during ICW. Indeed, wave propagation only depends on whether astrocytes in shell $r+1$ will activate; we should thus consider the mean quantity of IP_3 given by shell r to astrocytes in shell $r+1$ since it can in principle differ from the IP_3 quantity received by astrocytes of shell $r-1$: for shells of same sizes, IP_3 will diffuse more rapidly to the shell to which it has the more links. Additionally, the quantity of IP_3 received by each astrocyte of a given shell will also depend on the number of nodes in this shell. With our definitions, there are E^{r-1} links between shell $r-1$ and r, and E^r links between r and $r+1$. If $N^{r-1} = N^{r+1}$, the astrocytes in shel $r+1$ will get more IP_3 if $E^r > E^{r-1}$. However, when $N^{r+1} > N^{r-1}$, if an equal amount of IP_3 is going to the two shells, each astrocyte in shell $r+1$ will receive less IP_3 than those in shell $r-1$. Computing the fraction of IP_3 that goes from shell r to each astrocytes of shell $r+1$ can thus be seen as solving an ODE system with one equation per shell (assuming that everything is 'well-mixed' inside each shell and approximating it as a single compartment), taking into account its size (or volume) and diffusive coupling terms whose strength depends on E^r and E^{r-1}. If we just simulate such a system, without any IP_3 degradation, the concentrations of IP_3 will eventually equilibrate and each astrocyte will have received the same amount of IP_3 regardless of its shell. When IP_3 gets degraded however, the diffusion speed becomes important. Since IP_3 in astrocytes is continuously degraded by IP-5P, we added a degradation rate ω' to equilibrium I^*, yielding the following system;

$$\begin{cases} N^{r-1} \dfrac{dI^{r-1}}{dt} &= FE^{r-1}(I^r - I^{r-1}) - \omega' N^{r-1}(I^{r-1} - I^*) \\ N^{r} \dfrac{dI^{r}}{dt} &= -F\left(E^{r-1}(I^r - I^{r-1}) + E^r(I^r - I^{r+1})\right) - \omega' N^r(I^r - I^*) \\ N^{r+1} \dfrac{dI^{r+1}}{dt} &= FE^r(I^r - I^{r+1}) - \omega' N^{r+1}(I^{r+1} - I^*) \end{cases} \quad \text{(C.10)}$$

As can be seen from the above equations, we implemented diffusive coupling as linear diffusion with F being the strength of each link. To simulate the activation of shell r, we started the simulation at $t = 0$ with $I^r = I^{high}$ and $I^{r-1} = I^{r+1} = I^*$ (nodes in shell r are activated while nodes in shell $r-1$ and $r+1$ are at equilibrium). The ODE system was then integrated until $t = 100$s while recording the total quantity of IP_3 Q^{r-1} and Q^{r+1} received respectively by shells $r-1$ and $r+1$. Since we already have an expression for

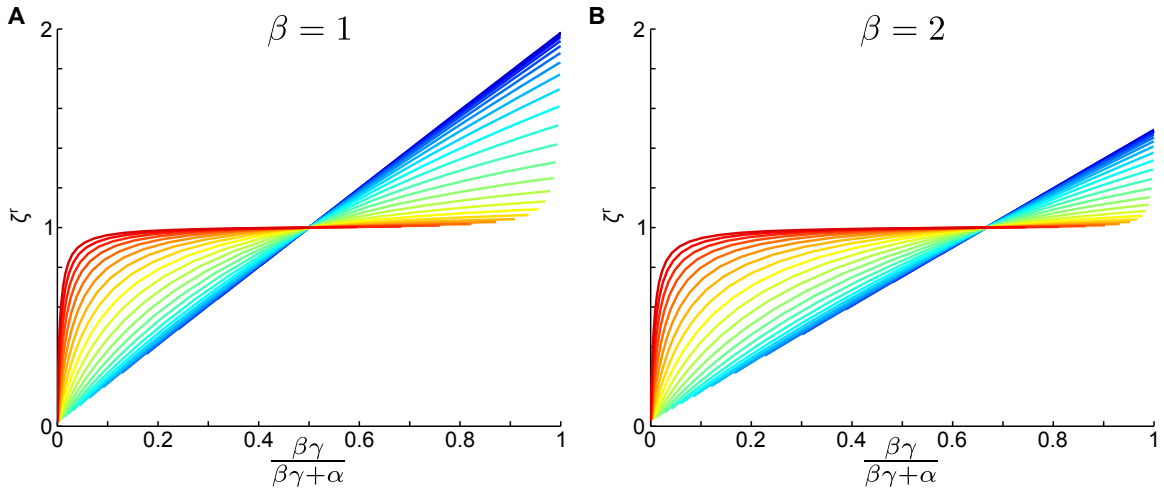

Figure C.4: IP_3 repartition primarily depends on the number of links going to $r+1$. Both figures display ζ^r values as the ratio of outgoing links to the total number of links $\frac{E^r}{E^r+E^{r-1}} = \frac{\beta\gamma}{\beta\gamma+\alpha}$ increases. Each curve is associated with a different α value, color-coded according to α values (logarithmic scale and going from 10^{-2}-blue to 10^{2}-red). The point at which $\zeta^r = 1$ changes depending on the chosen β value. With **A** $\beta = 1$, all curves display $\zeta^r = 1$ at $\frac{\beta\gamma}{\beta\gamma+\alpha} = 1/2$; for **B** $\beta = 2$, this increases to $2/3$. Around the point at which $\zeta^r = 1$, ζ^r can be approximated by a linear function. We kept $\omega = 1$ constant for both **A** and **B**. Simulations as described in the text.

$\langle \Psi^r \rangle = \frac{Q^{r-1}+Q^{r+1}}{N^{r-1}+N^{r+1}}$ and are interested in Q^{r+1}/N^{r+1}, we would like to determine:

$$\zeta^r = \frac{\frac{Q^{r+1}}{N^{r+1}}}{\frac{Q^{r-1}+Q^{r+1}}{N^{r-1}+N^{r+1}}} \tag{C.11}$$

i.e. the ratio between the average quantity of IP_3 received by astrocytes in $r+1$ and the average quantity of IP_3 received by astrocytes in $r-1$ and $r+1$. This ratio was found to be independent from the specific values assigned to N^r and N^{r-1}, but depended instead on the value of N^{r+1}/N^{r-1}; we thus kept $N^{r-1} = N^r = 1$ in all our simulations and investigated how ratios between shell size and coupling strengths controlled the repartition of IP_3 between shells $r-1$ and $r+1$. To this end, we defined three ratios $\alpha = \frac{E^{r-1}}{N^{r-1}}$, $\beta = \frac{N^{r+1}}{N^{r-1}}$, and $\gamma = \frac{E^r}{N^{r+1}}$ that actually control the behavior of the system. Additionally, we rescaled the whole system by $1/F$, introducing $\omega = \omega'/F$, the effective degradation rate. We can thus rewrite the system as:

$$\begin{cases} \frac{dI^{r-1}}{dt} &= \alpha(I^r - I^{r-1}) - \omega(I^{r-1} - I^*) \\ \frac{dI^r}{dt} &= -\alpha(I^r - I^{r-1}) - \beta\gamma(I^r - I^{r+1}) - \omega(I^r - I^*) \\ \frac{dI^{r+1}}{dt} &= \gamma(I^r - I^{r+1}) - \omega(I^{r+1} - I^*) \end{cases} \tag{C.12}$$

Since this system cannot be easily solved to obtain a simple analytical expression of ζ^r, we numerically integrated it with MATLAB ODE solver with adaptive time-stepping.

We first kept ω, β and α constant while varying γ. Figure C.4A and B display ζ^r values as a function of the ratio between outgoing links and the total number of links $\frac{E^r}{E^r+E^{r-1}} = \frac{\beta\gamma}{\beta\gamma+\alpha}$. For all values of ω, β, and α that we used, ζ^r as a function of $\frac{E^r}{E^r+E^{r-1}}$ always had the same shape: monotonically increasing and almost linear near $\zeta^r = 1$. This can easily be understood since increasing the number of links to $r+1$ will of course increase the quantity of IP_3 that it will receive. When $\zeta^r = 1$, astrocytes in shells $r-1$ and $r+1$ receive exactly the same quantity of IP_3; when $\beta = 1$, this happens at $\frac{E^r}{E^r+E^{r-1}} = 0.5$ (Figure C.4A) and when $\beta = 2$, this happens at $\frac{E^r}{E^r+E^{r-1}} = \frac{2}{3}$ (Figure C.4B). These values only depended on β and were found to follow $\frac{\beta}{\beta+1}$. In other words, in order for astrocytes of shell $r+1$ to receive more IP_3 than those of shell $r-1$, we need $\frac{E^r}{E^r+E^{r-1}} > \frac{N^{r+1}}{N^{r+1}+N^{r-1}}$: the larger N^{r+1}, the larger E^r must be. Since, with the networks that we used, $\frac{E^r}{E^r+E^{r-1}}$ is generally close to $\frac{N^{r+1}}{N^{r+1}+N^{r-1}}$, we approximated the relationship between ζ^r and $\frac{E^r}{E^r+E^{r-1}}$ with a linear function whose slope only depended on α (different colors in Figure C.4):

$$\zeta^r \approx S(\alpha)\left(\frac{\beta\gamma}{\beta\gamma+\alpha} - \frac{\beta}{1+\beta}\right) + 1 \tag{C.13}$$

with $S(\alpha)$ being the α-dependent slope near $\zeta^r = 1$.

We next explored how $S(\alpha)$ depended on α for different values of β and ω. As can be seen in Figure C.5A, B, and C, $S(\alpha)$ behaved as a broken power-law: for small α values, $S(\alpha)$ was constant but for high α values, $S(\alpha)$ behaved as a power-law with negative exponent -1. The point around which $S(\alpha)$ transitions from constant to power law depends on ω. When omega is small (Figure C.5A, $\omega = 0.1$), $S(\alpha)$ transitions into the negative exponent power law for very low α; when ω increases, the transition point shifts to higher α values (around 1 for Figure C.5B and around 20 for Figure C.5C). $S(\alpha)$ can thus be approximated by:

$$S(\alpha) \approx C(\beta)\frac{\alpha_t(\omega)}{\alpha_t(\omega)+\alpha} \tag{C.14}$$

with $C(\beta)$ a prefactor that we determine from the value of $S(\alpha)$ when α is small, and $\alpha_t(\omega)$ the transition point between the two regimes that depends only on ω. Several fits of this function to simulations are displayed as *black dashed* lines in Figure C.5A, B, and C.

Since ω is a free parameter in our simulations (it does not depend on the network structure), we couldn't evaluate the $\alpha_t(\omega)$ value that we should use to match the full ChI simulations; we thus considered $\alpha_t(\omega)$ as a free parameter. The only remaining unknown is $C(\beta)$ whose values as a function of β and ω are displayed in Figure C.5D. Changing ω only had little impact on $C(\beta)$ so we approximated it as a single broken power law:

$$C(\beta) \approx \frac{1+\beta}{\beta} \tag{C.15}$$

this approximation is plotted in Figure C.5D as a *black dashed* line and matches the simulations quite well. We can now express the full ζ^r approximation:

$$\zeta^r = \frac{\alpha_t(\omega)}{\alpha_t(\omega)+\alpha}\left(\frac{\beta\gamma}{\beta\gamma+\alpha}\frac{1+\beta}{\beta} - 1\right) + 1 \tag{C.16}$$

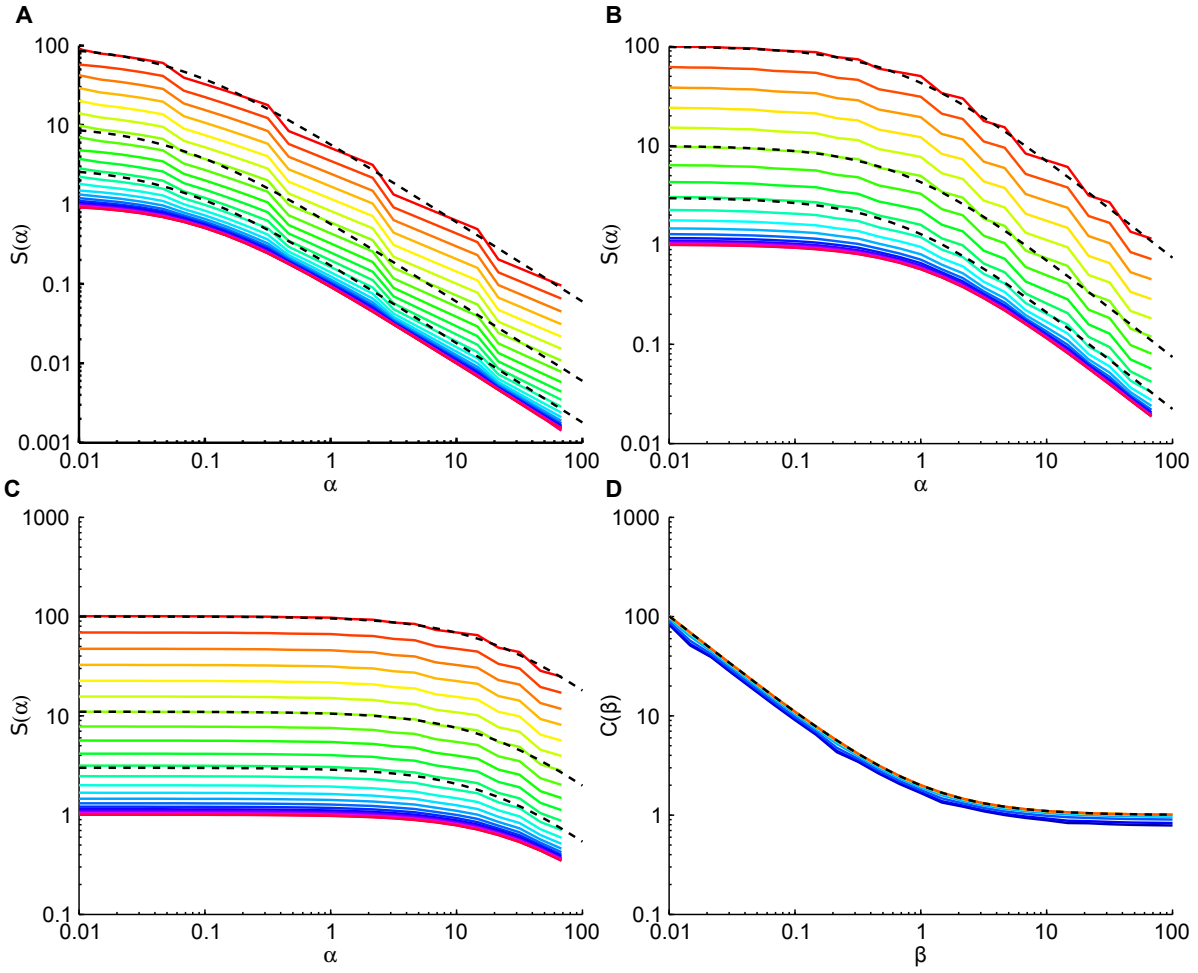

Figure C.5: $S(\alpha)$ can be approximated by broken power laws. The relationship between $S(\alpha)$ and α can be approximated, for all values of ω and β, by a broken power law of α whose transition point depends on ω. $S(\alpha)$ is constant for low α and behaves as a power law with negative exponent -1 for high α values. $\alpha_t(\omega)$, the α value around which $S(\alpha)$ transitions between these two regimes depends only on ω. For **A** $\omega = 0.1$, $S(\alpha)$ transitions nearly immediately in the decreasing power law, i.e. $\alpha_t(\omega) \approx 0.06$ is small; for **B** $\omega \approx 1.3$, $\alpha_t(\omega) \approx 0.75$; and for **C** $\omega \approx 36$, $\alpha_t(\omega) \approx 22$. Each curve corresponds to a different β value, color-coded according β values (from 10^{-2} (pink) to 10^2 (red), logarithmic scale). Approximations of $S(\alpha)$ are plotted as *black dashed* lines using equation (C.14). **D** The prefactor $C(\beta)$ only depends on β values as the different curves, corresponding to different ω values, roughly collapse on a single curve which can be approximated by equation (C.15) (*black dashed* line). Simulations as described in the text.

Or, with actual network structure values:

$$\zeta^r = \frac{\alpha_t(\omega)}{\alpha_t(\omega) + \frac{E^{r-1}}{N^{r-1}}} \left(\frac{E^r}{E^r + E^{r-1}} \frac{N^{r-1} + N^{r+1}}{N^{r+1}} - 1 \right) + 1 \tag{C.17}$$

Combining $\langle \Psi^r \rangle$ and ζ^r, we can approximate the quantity of IP_3 received by astrocytes in shell $r+1$. $\zeta^r = \frac{\langle Q_i^{r+1} \rangle}{\langle Q_i^{r-1} \rangle + \langle Q_i^{r+1} \rangle}$ is the ratio between the quantity of IP_3 received on average by nodes of shell $r+1$ and the quantity of IP_3 received on average by nodes of both shells $r-1$ and $r+1$. Since we are interested in the quantity of IP_3 going to astrocytes of shell $r+1$, we will consider the $2\rho^r(1-\rho^r)W^r$ unactivated astrocytes in shell r and the N^{r-1} unactivated astrocytes in shell $r-1$ to be part of a single 'sink' shell. We thus replaced, in equation (C.17), N^{r-1} by $N^{r-1} + \hat{N}^r$ and E^{r-1} by $E^{r-1} + \hat{W}^r$ to obtain $\hat{\zeta}^r$. The average quantity of IP_3 $\langle \Psi^r_{out} \rangle$ that astrocytes of shell r will give to astrocytes of shell $r+1$ will thus be:

$$\begin{aligned} \langle \Psi^r_{out} \rangle &= \hat{\zeta}^r \times \langle \Psi^r \rangle \\ &= \left(\frac{\alpha_t(\omega)}{\alpha_t(\omega) + \frac{E^{r-1} + \hat{W}^r}{N^{r-1} + \hat{N}^r}} \left(\frac{E^r}{E^r + E^{r-1} + \hat{W}^r} \frac{N^{r-1} + \hat{N}^r + N^{r+1}}{N^{r+1}} - 1 \right) + 1 \right) \\ &\quad \times \frac{\rho^r N^r}{N^{r-1} + \hat{N}^r + N^{r+1}} \end{aligned} \tag{C.18}$$

with $\hat{N}^r$ the estimated number of unactivated astrocytes in shell r connected to activated astrocytes in the same shell (defined in equation (V.9)), and $\hat{W}^r$ the number of links between activated and unactivated astrocytes of shell r. We computed $\hat{W}^r$ with very simple approximations: each astrocytes of shell r is linked on average to $2\frac{W^r}{N^r}$ astrocytes in the same shell; the number of intra-shell links connected to activated astrocytes in shell r is thus $\rho^r N^r \frac{W^r}{N^r} = 2\rho^r W^r$; taking into account the probability $(1-\rho^r)\frac{N^r}{N^r - 1} \approx 1 - \rho^r$ that the other endpoints of these links are attached to unactivated astrocytes in shell r, we get $\hat{W}^{=} 2\rho^r(1-\rho^r)W^r$.

C.2.2 Shell structure model of ICW propagation

Before devising our full shell structure model of ICW propagation, we still need to investigate two issues: (1) *how will we stimulate our model in an equivalent way to the IP_3 stimulation used in the full ChI model ?* (2) *how can we link the average IP_3 quantity $\langle \Psi^r_{out} \rangle$ received by astrocytes in shell $r+1$ to the activation ratio ρ^{r+1} in this shell ?* We tackled these two questions by looking at normalized IP_3 quantities received by astrocytes in full ChI network simulations. As in Section V.3, we integrated IP_3 influxes in each astrocyte during a sliding time-window of $\Delta t = 10$s (the average activation time of astrocytes) and considered, for each astrocyte, the highest quantity of IP_3 received during Δt in the whole simulation.

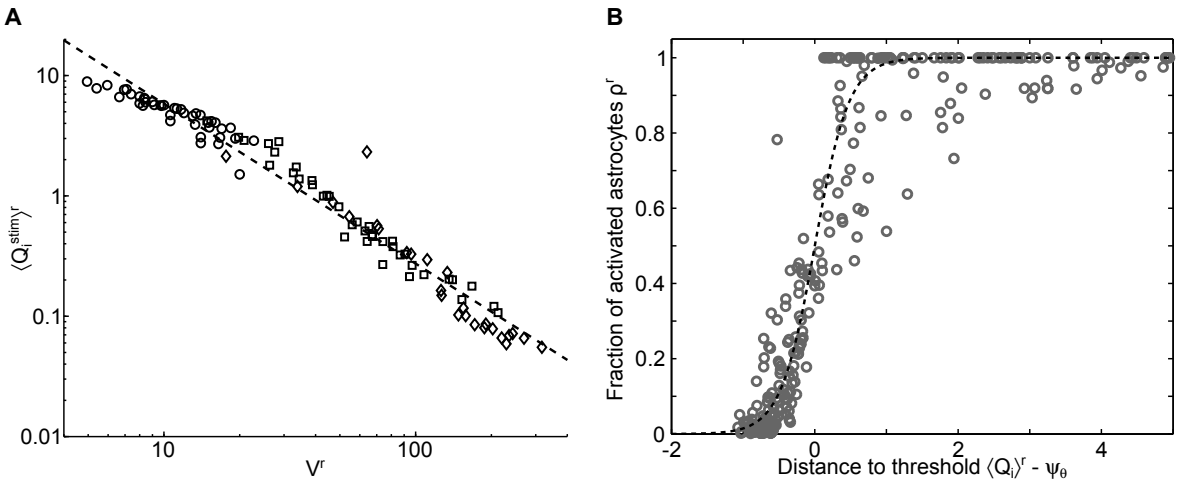

Figure C.6: Stimulation and activation ratios In addition to the IP_3 generated from shell $r-1$, astrocytes of shell r also receive IP_3 from the stimulation protocol that we use. This additional IP_3 decreases as r increases and is basically non-existent for shells $r > 3$ (not shown here). We can see from **A** that the quantity of stimulation-induced IP_3 $\langle Q_i^{stim} \rangle^r$ received by astrocytes of shell r decreases as a power law of the number of astrocytes V^r between shells 0 and r. Points are color-coded according to their corresponding network classes; regardless of the network class, $\langle Q_i^{stim} \rangle^r$ can be well approximated by a power law (equation (C.19), *blask dashed* line). **B** The ratio of activated astrocytes ρ^r in shell r depends on the supra-threshold quantity of IP_3 $\langle Q_i \rangle^r - \psi_\theta(\langle k \rangle)$ received on average by astrocytes of shell r. This relationship was approximated by a sigmoid function centered on $\langle Q_i \rangle^r - \psi_\theta(\langle k \rangle) = 0$ (equation (C.21), *black dashed* curve) fitted by minimizing the square error. Each point corresponds to mean values across 20 realizations for a given shell on a given network class with a given parameter set. All networks and all shells are displayed on this figure. $\psi_\theta(\langle k \rangle) = A\langle k \rangle + B$ was computed according to the parameters estimated from Figure V.12B: $A = 0.07$ and $B = 0.35$. ChI model and network parameters as in Figure V.5.

C.2.2.1 Stimulation and activation function

We remind the reader that, in the full ChI model simulations, astrocytes were stimulated by coupling the central cell to a virtual cell whose IP_3 concentration was kept constant at $I_{bias} = 2\mu$M. This procedure, comparable to clamping an astrocyte with a patch pipette, creates large IP_3 influxes to astrocytes near the stimulated cell. Consequently, astrocytes in the first shells (1, 2 and 3 to a lesser extent) receive IP_3 from two distinct sources: (1) from the stimulated cell; (2) from the activation of astrocytes in previous shells. We can already estimate the quantity of IP_3 generated by previous shells by $\langle \Psi_r \rangle$ (we use $\hat{\zeta}^r = 1$ for now because we have yet no way of estimating $\alpha_t(\omega)$); we can thus estimate the quantity of IP_3 received from the stimulated cell by substracting $\langle \Psi_r \rangle$ from $\langle Q_i \rangle^r$ (the normalized mean quantity of IP_3 received by astrocytes in shell r in full ChI model simulations). Given that each astrocyte degrades IP_3, we expect that the stimulation-induced additional IP_3 in shell r should decrease as the number of astrocytes between shell 0 and r increases. Figure C.6A displays $\langle Q_i^{stim} \rangle^r = \langle Q_i \rangle - \langle \Psi^{r-1} \rangle$, the estimated quantity of IP_3 received by astrocytes in shell r that can be attributed to stimulation, as

a function of $V^r = \sum_{r'=0}^{r} N^{r'}$, the number of cells in shells 0 to r. Despite the fact that the relationship only spans one and a half decade, the data collapse is quite good and $\langle Q_i^{stim} \rangle^r$ can be modeled as a power law of V^r:

$$\langle \Psi_{stim}^r \rangle = D(V^r)^\eta \tag{C.19}$$

with D and η free parameters that should be close to their fitted values (*black dashed* line) displayed in Figure C.6A: $D \approx 124$ and $\eta \approx -1.3$.

The total quantity of IP_3 $\langle \Psi_{tot}^{r+1} \rangle$ given on average by astrocytes of shell r and by stimulation to astrocytes of shell $r+1$ thus reads:

$$\langle \Psi_{tot}^{r+1} \rangle = \langle \Psi_{out}^r \rangle + \langle \Psi_{stim}^{r+1} \rangle \tag{C.20}$$

Given a $\langle \Psi_{tot}^r \rangle$ quantity of IP_3 received by astrocytes of shell r, we would now like to know the fraction of astrocytes in r that will get activated. From Section V.3, we already determined that astrocytes activate if the normalized quantity of IP_3 that they receive exceeds a degree-dependent threshold $\psi_\theta(k)$. We thus plotted in Figure C.6B the fraction ρ^r of activated astrocytes in r as a function of the supra-threshold quantity of IP_3 $\langle Q_i \rangle^r - \psi_\theta(\langle k \rangle)$ received by astrocytes of shell r. As previously seen from Figure C.3, when the quantity of IP_3 received on average by astrocytes of shell r is exactly equal to the activation threshold, approximately half of the shell gets activated. Sub-threshold quantities activate less than half the shell and supra-threshold quantities activate more than half. We decided to model this behavior by a sigmoid function centered on $\langle Q_i \rangle^r - \psi_\theta(\langle k \rangle) = 0$ whose slope was fitted by minimization of square error (*black dashed* line) from the data displayed in Figure C.6B. The ratio of activated astrocytes in shell $r+1$ can thus be computed with:

$$\rho^{r+1} = \frac{1}{2}\left(\tanh\left(\frac{\langle \Psi_{tot}^{r+1} \rangle - \psi_\theta(\langle k \rangle)}{\delta}\right) + 1\right) \tag{C.21}$$

with δ a free parameter that should be close to the value fitted in Figure C.6B ($\delta \approx 0.48$) and according to Section V.3, $\psi_\theta(\langle k \rangle)$ was computed by:

$$\psi_\theta(\langle k \rangle) = A\langle k \rangle + B \tag{C.22}$$

with A and B free parameters that should be close to $A \approx 0.07$ and $B \approx 0.35$ (estimated from Figure V.12B).

C.2.2.2 Shell propagation model quantitatively fits ChI model propagation

Starting from shell 0, i.e. the stimulated astrocyte, we can now compute ρ^r iteratively with equation (C.21) using only the mean degree $\langle k \rangle$ and the shell structure of a network. To validate this shell propagation model, we computed for each network class and each parameter combinations, the mean shell structure of the corresponding networks across 20 realizations. In each realization i, we computed N_i^r, E_i^r, and W_i^r by starting from the stimulated node ($r = 0$) and increasing r until all nodes were spanned (i.e. $N^r =$

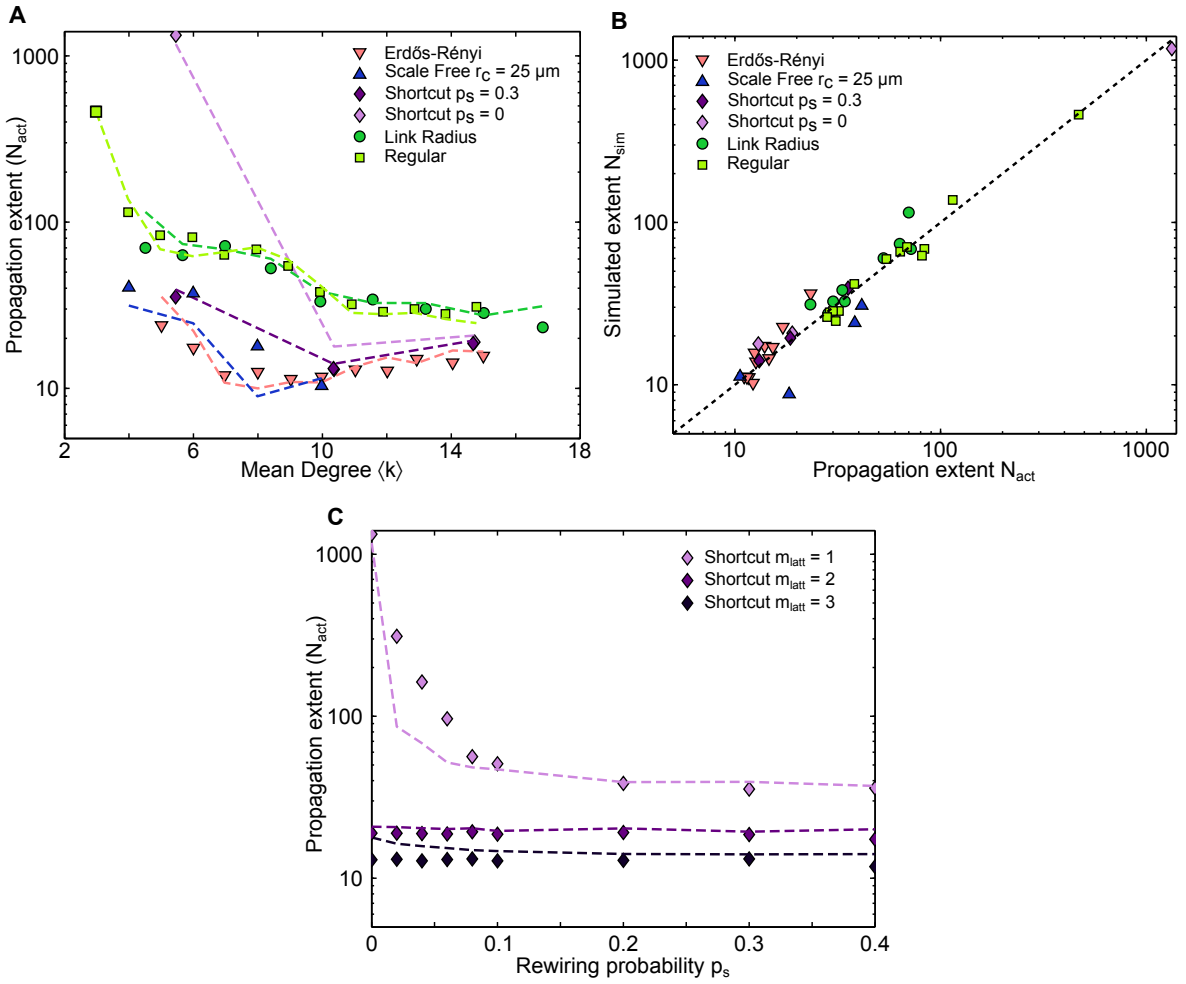

Figure C.7: Shell structure is enough to quantitatively fit full ChI model ICW propagation **A** Shell model parameters were estimated with the CMA-ES procedure in order to fit a subpart of all the network parameter combinations. Symbols represent full ChI model propagation extents (N_{act}) while dashed lines represent shell model propagation extents (N_{sim}). **B** displays N_{sim} as a function of N_{act}, all network classes are on the diagonal, i.e. the shell propagation model fits the full ChI model very well. In log-log scale $r^2 = 0.9511$ and in linear-linear scale, $r^2 = 0.9847$. **C** Shell model also emulates ChI model for networks on which it was not fitted. Increasing the rewiring probability p_s in shortcut networks dramatically decreases ICW extent in both shell (dashed lines) and ChI (symbols) models. Network parameters as in Figure V.5A, ChI model parameters as in Table V.1, shell model parameters as in Table C.1.

0 and $V^r = N$ with N the total number of astrocytes in the network). The values that we next use to simulate ICW propagation in the shell-to-shell model are averages across all realizations: $N^r = \langle N_i^r \rangle$, $E^r = \langle E_i^r \rangle$, and $W^r = \langle W_i^r \rangle$. In order to compare shell propagations to full ChI model propagations, we compared the number of activated astrocytes N_{sim} in the shell propagation model N_{sim} to the number of activated astrocytes N_{act} in the full ChI model. We computed N_{sim} by:

$$N_{sim} = \sum_{r=0}^{R} \rho^r \times N^r \tag{C.23}$$

with R being the shell at which $\rho^R N^R < 1$ (i.e. either less than one astrocyte would get activated or $N^R = 0$). In order to calibrate the model, we attempted to find a combination of all free parameters (α_t from equation (C.18), D and η from equation (C.19), δ from equation (C.21), and A and B from equation (C.22)) that would allow one to predict N_{act} with N_{sim} for all networks displayed in Figure V.5A. We fitted these parameters using the CMA-ES fitting procedure (Hansen, 2006) with a fitness function that computed the square error in log-log scale (so that the points are not all overwhelmed by high N_{act} values):

$$F = \sum_{\text{networks}} \left(\log(N_{act}) - \log(N_{sim})\right)^2 \tag{C.24}$$

Fitted values are reported in Table C.1. While B and α_t have values comparable to what could be expected from previous analysis, the other parameters (low values for A and δ) seem to indicate that IP_3 quantities considered in the shell model are lower than those at play in the full ChI model. The shell propagation model however fits very well the full ChI model simulations as can be seen from Figure C.7A: all network classes are well fitted and, contrary to the UAR model, the shell-to-shell propagation model quantitatively reproduces the behavior of the full ChI model despite only taking the shell-structure into account. Figure C.7B illustrates the goodness of the fit as nearly all networks fall on the diagonal $N_{sim} = N_{act}$ (*black dashed* line) and $r^2 = 0.9847$ in linear-linear scale. Additionally, on shortcut networks, the shell model behaves as the ChI model when the probability of rewiring p_s is increased (see Figure C.7C). Since the parameters in Table C.1 were not estimated from the curves in Figure C.7C, we can consider that the shell propagation model really captures the essential features of ICW propagation in our modeled astrocyte networks. We can thus use this model to investigate how the exact topological structure of a network controls ICW propagation.

C.2.2.3 Early shell activation determines ICW extent

Given that the main condition for ICW propagation in the shell model is to have receive a supra-threshold IP_3 quantity in each of the shells, we first looked at how the shell structure influences this IP_3 quantity. As examples, we show in Figure C.8A the supra-threshold normalized IP_3 quantity $\langle \Psi_{out}^r \rangle - \psi_\theta(\langle k \rangle)$ that astrocytes of shell r will receive on average when the preceding shell is fully activated (i.e. $\rho^{r-1} = 1$). These values do not take into account the IP_3 quantity attributable to the stimulation protocol and only

Table C.1: Shell analysis propagation model parameters.

Symbol	Equ.	Description	Values
α_t	C.18	Transition point between the regimes in Figure C.5B	3.5639
D	C.19	Quantity of IP_3 received by the stimulated cell	3227.4
η	C.19	Exponent of the decrease of $\langle \Psi^r_{stim} \rangle$ by V^r	2.6849
δ	C.21	Steepness of the activation function	0.0694
A	C.22	Slope of the relationship between $\langle k \rangle$ and ψ_θ	0.00053112
B	C.22	Intercept of the relationship between $\langle k \rangle$ and ψ_θ	0.3271

reflects structural properties of the networks. From these examples, it appears that most of the networks are barely above threshold (*black dashed* line) for $r \leq 2$, meaning that the ICW propagation would fail right at the beginning, before reaching shells in which $\langle \Psi^r_{out} \rangle - \psi_\theta(\langle k \rangle)$ would be higher. Of course, in the full ChI model simulations, this effect is prevented by our stimulation protocol that increases the IP_3 quantities received by early shells. When taking into account both structural and stimulation-generated supra-threshold IP_3 quantities ($\langle \Psi^r_{tot} \rangle - \psi_\theta(\langle k \rangle)$), as shown in Figure C.8B, it appears that stimulation forces the activation of shell $r = 1$ in all networks, and of shell $r = 2$ in most networks (with the exception of spatially unconstrained networks such as Erdős-Rényi networks, *red triangles*). Interestingly, with the stimulation-caused increase in IP_3 quantities for small r, all networks display a minimal value of $\langle \Psi^r_{tot} \rangle - \psi_\theta(\langle k \rangle)$ for some $r > 1$. This implies that the ICW propagation will be the most likely to stop at this shell if the IP_3 quantity received by astrocytes of this shell is to small compared to the threshold $\psi_\theta(\langle k \rangle)$. The shell r^* at which a network will have its minimal received IP_3 quantities is degree-dependent: small degree networks (like the regular degree networks with $k = 3$) have $r^* \approx 6$ while higher degree networks (like regular degree with $k = 6$ or Erdős-Rényi with $\langle k \rangle = 5$) have $r^* = 2$; network with even higher mean degrees all have $r^* = 1$ (data not shown).

In contrast to what Figure C.8A and B display, actual IP_3 quantities received by shell r depend on the activation fraction of shell $r - 1$: as soon as ρ^{r-1} falls below 1, the IP_3 quantities received by shell r gets lower than those presented in Figure C.8A and B. On Figure C.8C, we thus show the supra-threshold IP_3 quantities received by shell r when ρ^r is determined by equation (C.21). As long as $\rho^{r-1} = 1$, these values match those reported in Figure C.8B; when the IP_3 quantity received by shell r becomes small (Regular degree networks with $k = 6$ and Erdős-Rényi networks with $\langle k \rangle = 5$ at $r = 2$ in Figure C.8B), ρ^r gets lower than 1 and the IP_3 quantity received by shell $r + 1$ is thus decreased. In those same networks, the IP_3 quantity received by shell $r+1$ thus fall under the activation threshold, leading to propagation failure. For networks that maintain a sufficient activation fraction ρ^r in each shell r, like regular degree networks with $k = 3$ and cubic lattice networks, the IP_3 quantity received by shell $r+1$ stays above threshold, ensuring a much larger ICW. Since structural IP_3 quantities $\langle \Psi^r_{out}$ increase with r, if a network can maintain its activation ratio ρ^r high enough during the first shells, it will then propagate regenerative ICW. In other words, regenerative ICWs can be obtained in

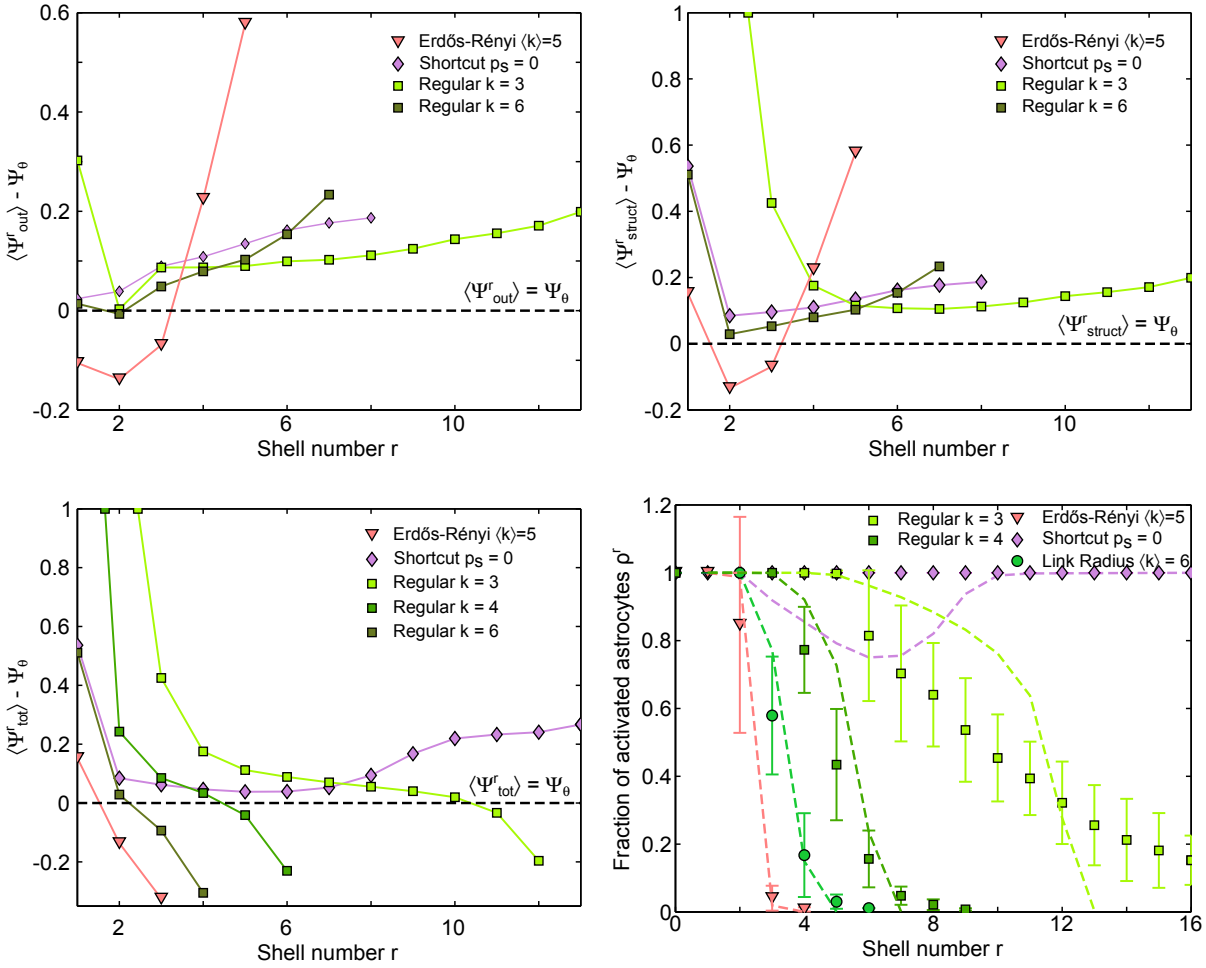

Figure C.8: Early shell activation determines ICW propagation. **A** Considering only the structure-generated IP_3 quantities $\langle \Psi^r_{out} \rangle$ received by shell r when shell $r-1$ is fully activated reveals that most networks are under the threshold for activation $\psi_\theta(\langle k \rangle)$ (*black dashed line*) in the first two or three shells. This means that a minimal stimulation that would only activate one astrocyte (shell 0) or part of the first shell would not be able to trigger an ICW. **B** With our stimulation protocol however, the first shells receive additional IP_3 quantities that we modeled by $\langle \Psi^r_{stim} \rangle$ (equation (C.19)). This ensures that at least shell 1 is fully activated (all networks are above-threshold for $r = 1$) and marginally increases the quantity of IP_3 received by shell 2. Interestingly, $\langle \Psi^r_{tot} \rangle$ is lower for small r values, meaning that early shells are the 'weak link' in the propagation chain, they are the most likely to stop ICW propagation by not getting activated enough. **C** $\langle \Psi^r_{tot} \rangle$ as a function of r in actual shell model simulations shows that ICW stops quickly in networks that have low values of $\langle \Psi^r_{tot} \rangle$ in early shells (Erdős-Rényi networks in *red triangles* and regular degree network with $k = 6$ in dark yellow). **D** Comparison between activation ratios ρ^r in shell model (*dashed lines*) and in full ChI model (*solid line and symbols*). Activation ratios are fairly identical in both models, showing that the shell model of propagation is a good approximation of the full network propagation. Network parameters as in Figure V.5A, ChI model parameters as in Table V.1, shell model parameters as in Table C.1.

all networks if the initial number of activated astrocytes is high enough. This number of astrocytes that must be activated in order to propagate regenerative ICW of course depends on the network. Schematically, the higher the value of $\langle \Psi_{tot}^{r^*} \rangle - \psi_\theta(\langle k \rangle)$, the smaller this number. Regenerative waves can thus be easily triggered in cubic lattice networks because $\langle \Psi_{tot}^{r^*} \rangle$ is well above threshold and the structure-caused IP_3 quantity $\langle \Psi_{out}^{r}$ grows quite fast as r increases.

Figure C.8D displays activation fractions in both shell (*dotted lines*) and ChI (*full lines*) models, showing that the agreement between both models is not only on the totla number of activated astrocytes N_{act} and N_{sim} but also on the detailed activation fractions as the ICWs unfold in the different networks. The stronger differences between both models are visible for networks which support very high (regular degree with $k = 3$) and regenerative (cubic lattices) propagations: while qualitative behaviors are the same (high values for ρ^r across all r for cubic lattices and decreasing ρ^r values for regular degree networks with $k = 3$), the detailed values are somewhat different. For networks on which ICW propagation stops more rapidly however, the quantitative agreement is actually quite good and propagation in the shell model follows closely that of the full ChI model. In both models, propagation failure is due to lower IP_3 quantities received by shells with low r values and the agreement between both indicate that we can investigate potential consequences of this fact with the shell model. We will do so in Section VI.1, as it seems to play a role in how noise can influence ICW propagation.

Overall, the shell propagation model matches the full ChI model very closely for most networks (spatially constrained but also spatially unconstrained). Since this model relies on average values N^r, E^r, and W^r for describing the shell structure, it does not work very well for networks which display high variability of these indicators. Among all the networks that we tested, only the spatial scale free networks were subject to such high variability because of the presence of hubs: shell structure can be quite different depending on whether the reference node is a hub or not. Despite this lack of quantitative agreement between shell model and full ChI model on spatial scale free networks, the qualitative behavior is the same: increasing $\langle k \rangle$ decreases propagation extent in both models. Knowing that the shell structure will determine ICW extent, it would be interesting to describe the shell structure with a reduced set of parameters. For example, in spatially constrained networks N^r can be described by a power law when r is high enough:

$$N^r \approx F d r^{d-1} \tag{C.25}$$

with F the prefactor and d the dimension of the embedding space. Similarly, in spatially-unconstrained networks such as infinite Erdős-Rényi networks, N^r can be described by:

$$N^r \approx \langle k \rangle (\langle k \rangle - 1)^{r-1} \tag{C.26}$$

with mean degree $\langle k \rangle$. In both of these examples, we can generate shell structures from very restricted sets of parameters. Schematically, the stronger the rise in N^r, the lower ICW extent will be; if we compute $\langle \Psi^r \rangle$ with $\rho^r = 1$ for both of these examples (equation (V.10)) we get:

$$\langle \Psi^r \rangle = \frac{r^{d-1}}{(r-1)^{d-1} + (r+1)^{d-1}} \underset{r \to \infty}{=} \frac{1}{2} \tag{C.27}$$

for spatially constrained networks and:

$$\langle \Psi^r \rangle = \frac{\langle k \rangle - 1}{1 + (\langle k \rangle - 1)^2} \leq \frac{1}{2} \quad \text{for} \quad \langle k \rangle \geq 2 \tag{C.28}$$

for spatially unconstrained networks. Since we need $\langle k \rangle > 2$ to be above the percolation threshold in Erdős-Rényi networks, $\langle \Psi^r \rangle$ is always higher in spatially constrained networks than in spatially unconstrained.

Appendix D

Stochastic resonance analysis

D.1 Stochastic resonance with random node removal

Dynamic regulation of network mean degree cannot entirely account for stochastic resonance Figure D.1A to F display the stochastic resonance strengths χ^* that we obtain when simulating spontaneous temporary removal of astrocytes from the network instead of spontaneous activations of astrocytes. This figure can be compared with Figure VI.3 to assess whether this modified SR protocol can display the same effects as the original one. From a basic inspection, one can see that stochastic resonance is much less strong in Figure D.1 than in Figure VI.3 on all the networks displayed. Shortcut networks for example (Figure D.1F) did not show any SR even when the rewiring probability p_s was increased. Spatial Scale Free networks as well as Erdős-Rényi networks (Figure D.1C,D, and E) displayed mild SR with patterns similar to the original SR protocol: Spatial Scale Free networks displayed early detrimental effects of noise for low mean degrees (bottom parts of Figure D.1C and D) while Erdős-Rényi networks essentially did not show SR for high degrees (with the notable exception for $\langle k \rangle = 15$). Spatially constrained networks (Figure D.1A and B) displayed much weaker SR for medium strength stimulation ($IP_3^{bias} = 1.5\mu$M) and did not display any for weak stimulations, in contrast to what we observed in the basic SR protocol. Overall, while it is striking that dynamic removal of astrocytes from the network can elicit stochastic resonance-like effects, the strength of these effects do not compare with those we obtained by spontaneous activation of astrocytes.

To further investigate the dissimilarities between our two stochastic resonance protocols, we looked at the relationship between the network mean degree $\langle k \rangle$and the resonant frequency ζ^* in modified stochastic resonance protocol. According to our local analysis, if we only remove astrocytes, the resonant frequency ζ^* should verify:

$$\frac{1}{k(1-\tau\zeta^*)} = Ak(1-\tau\zeta^*) + B \tag{D.1}$$

compared with equation (VI.2), we only removed the IP_3 creation term ($k\tau\zeta^*$) from

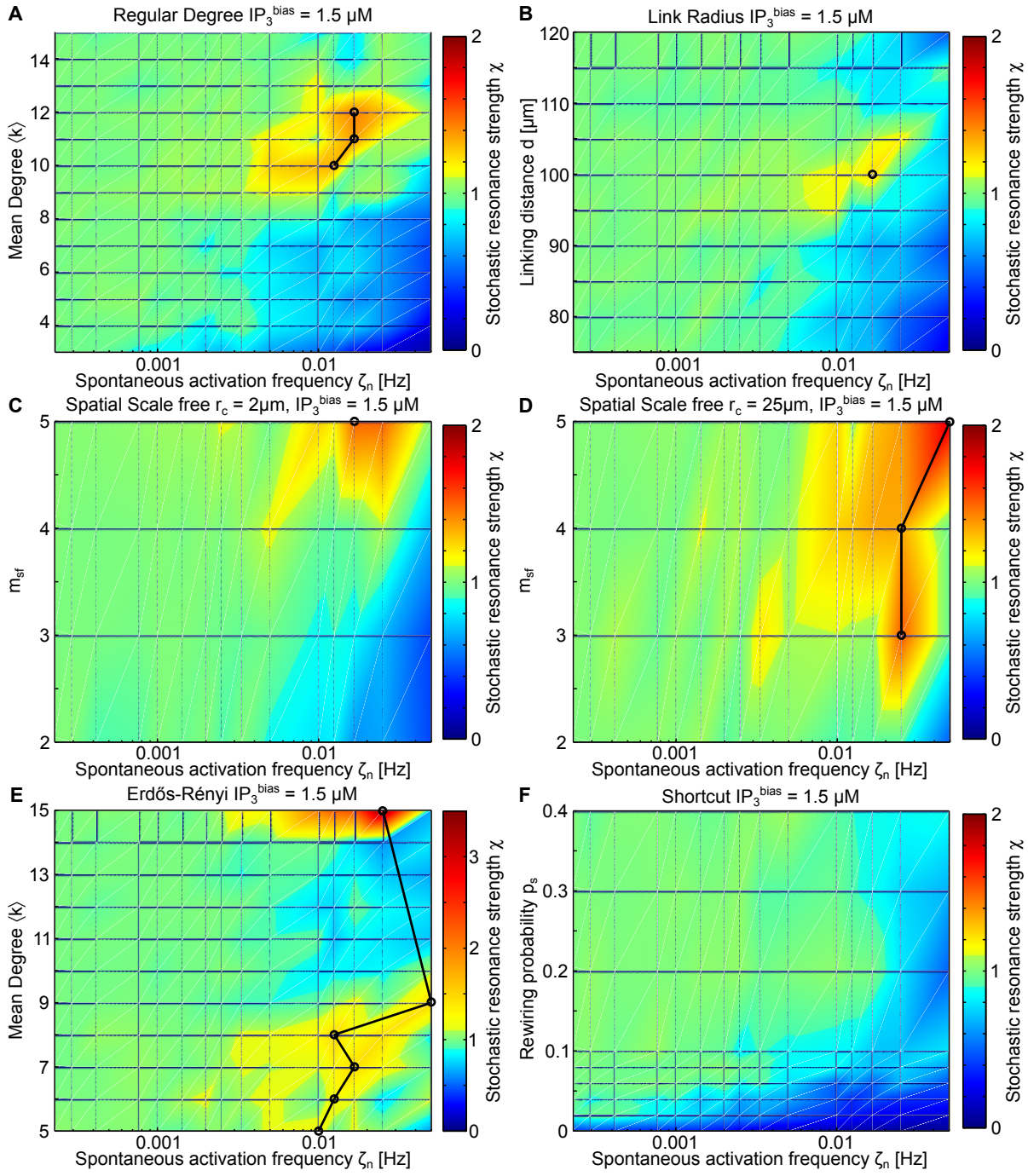

Figure D.1: Dynamic regulation of the mean degree can have stochastic resonance-like effects. **A** Heatmap representations of stochastic resonance effects. Mean $\chi(\zeta_n)$ values are color coded and plotted for different network types and stimulation conditions. Colorbar are adapted to each subplot as in Figure VI.3. For networks which have $\chi^* \geq 1.2$, the *thick black* line plots the resonant frequency ζ^*. Overall, dynamic regulation of the network mean degree $\langle k \rangle$ by spontaneous temporary removing of astrocytes from the network cannot reproduce the same effect than our basic SR protocol (compare with Figure VI.3). **A** Regular Degree networks. **B** Link Radius networks. **C** Spatial Scale Free networks with $r_c = 2\mu$m. **D** Spatial Scale Free networks with $r_c = 25\mu$m. **E** Erdős-Rényi networks. **F** Shortcut networks with $\langle k \rangle = 6$ (i.e. $m_{latt} = 1$); y-axis values correspond to different rewiring probabilities p_s. **A** to **F** were stimulated with $IP_3^{bias} = 1.5\mu$M. Note that subplots **A** and **B** were not weakly stimulated as in Figure VI.3, since weak stimulations did not elicit SR in these networks. Simulations as described in the text.

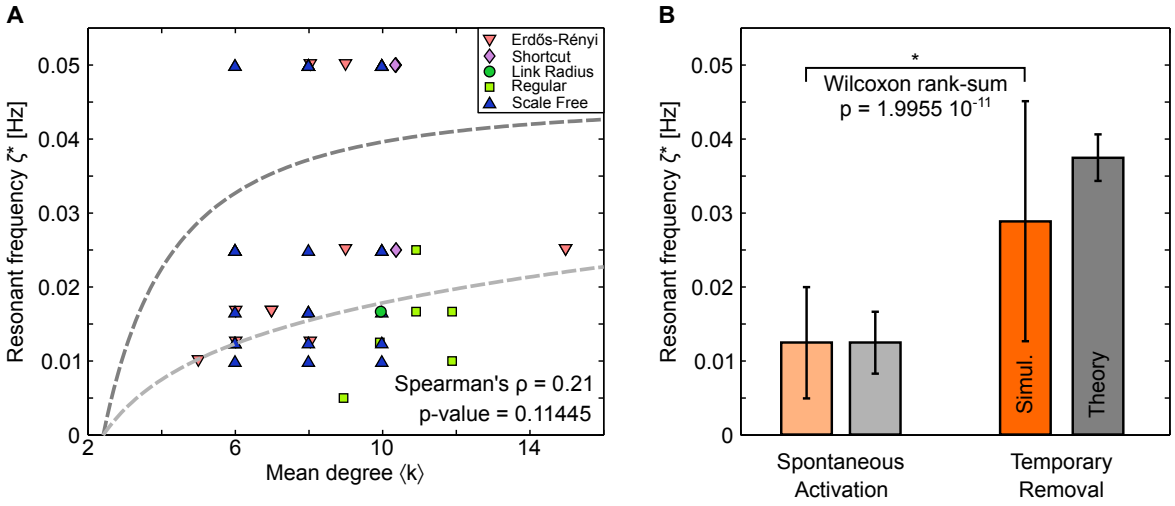

Figure D.2: Dynamic regulation of the mean degree cannot account for the relationship between $\langle k \rangle$ and ζ^*. **A** Relationship between the network mean degree $\langle k \rangle$ and the resonant frequency ζ^* obtained during our modified stochastic resonance protocol. Only networks which displayed a stochastic resonance strength of at least $\chi^* \geq 1.2$ are displayed. In contrast with Figure VI.4, the network mean degree $\langle k \rangle$and the resonant frequency ζ^* do not seem to be significantly correlated, as assessed by a low Spearman's rank correlation coefficient $\rho = 0.21$ ($p-$value ≈ 0.11). Simulation as in Figure D.1. *Thick dashed* lines correspond to theoretical estimations of ζ^* using equation (VI.3) (*light gray*, corresponding to the fit of basic stochastic resonance) and equation (D.2) (*dark gray*, corresponding to the node removal protocol). Parameters A, B, and τ were taken as in Figure VI.4. **B** Despite loosing the relationship with the mean degree, the resonant frequencies displayed in the node removal protocol (*dark orange* bar) are significantly higher than those displayed in normal stochastic resonance (*light orange* bar). For each point point in Figure VI.4A, we computed the predicted resonant frequency using equation (VI.3) and we did the same with points in **A** using equation (D.2). The resulting mean and standard deviations are reported beside the simulated ones (*light gray* bar for basic stochastic resonance and *dark gray* bar for node removal protocol. As expected, the resonant frequency is also predicted to be higher by the local analysis.

spontaneously activated astrocytes. This leads to[1]:

$$\zeta^* = \frac{-\sqrt{B^2 + 4A} + B + 2kA}{2\tau kA} \tag{D.2}$$

We show in Figure D.2A the resonant frequencies ζ^* displayed by networks during the node removal protocol together with the local analysis prediction (*dashed dark gray* line). In contrast to Figure VI.4A, the relationship between the mean degree of networks $\langle k \rangle$and the resonant frequency is lost (the correlation is not significant) and the dispersion is very high. While the local analysis fails to capture the loss of the relationship, it stills show an increase in average resonant frequency that is also present in the simulations. Figure D.2B indeed shows the mean and standard deviation of resonant frequencies for normal SR (*light orange* bar) and node removal simulations (*dark orange* bar). The latter are significantly higher than the former as assessed by a Wilcoxon rank-sum test ($p \approx 2.10^{-11}$). Of course, the same increase in captured by the local analysis (*gray* bars): since we decreased the

1. The other solution necessitate negative parameter values to fit the simulated points

quantity of IP_3 that spontaneously activated nodes provided, it is expected that the decrease in mean degree has to be that more pronounced to get the same effect.

D.2 Stochastic resonance and shell structure

Since the shell propagation model quantitatively account for ICW propagation in modeled astrocyte networks by only considering the shell structure of the networks, we wondered whether it could also shed light on the stochastic resonance effects witnessed in Section VI.1. To investigate this, we modified the shell propagation model in order take into account spontaneous activation of astrocytes.

D.2.1 Spontaneous activation in shells

As we described in Section VI.1, spontaneous astrocyte activation has two main effects: (1) it adds IP_3 to the networks; (2) it prevents leaking of IP_3 from activated astrocytes. As described in Section V.4, we can distinguish 3 states in which an astrocyte can be: (U)nactivated, (A)ctivated and (R)efractory (see Figure D.3A). These three states likely play specific roles during stochastic resonance: the U and A states are of course needed for ICW propagation, but the R state was not taken into account in the shell propagation model as we only focused on the ICW front. Once the ICW activated a given shell, we did not further simulate what happened in this shell. In the case of stochastic resonance however, the whole network is subject to activity before and after the ICW passage. We thus need to consider that some of the astrocytes that are part of a shell might be in the refractory state because of previous spontaneous activation. As an example, if an astrocytes gets spontaneously activated just before an incoming ICW, it will be in refractory period when the ICW will reach it and will thus fail to transmit the ICW. This refractory state thus add a detrimental effect to spontaneous activations that we did not consider before. In the shell propagation model, we have 2 main types of astrocytes:

1. activated astrocytes, that act as sources of IP_3;
2. unactivated astrocytes, that act as IP_3 sinks;

To account for spontaneous activations, we need two additional types of spontaneously active astrocytes: the ones that act as IP_3 sources and the ones that are in their refractory period and act as IP_3 sinks. Table D.1 presents the resulting 4 different states that astrocytes can be in, whether they can get activated by an ICW, and their corresponding frequency. Figure D.3B shows a schematic view of ICW propagation (*green* cells) under stochastic resonance protocols. An ICW is elicited at the center of the network (*red* arrow) and propagates to the first shell ($t = 1$, top left quadrant) while spontaneous activation occur all over the network with a constant rate. Some spontaneously activated astrocytes are IP_3 sources (*yellow* cells, they are in their activated state) while others act as unactivable IP_3 sinks (*red* cells, they are in their refractory state).

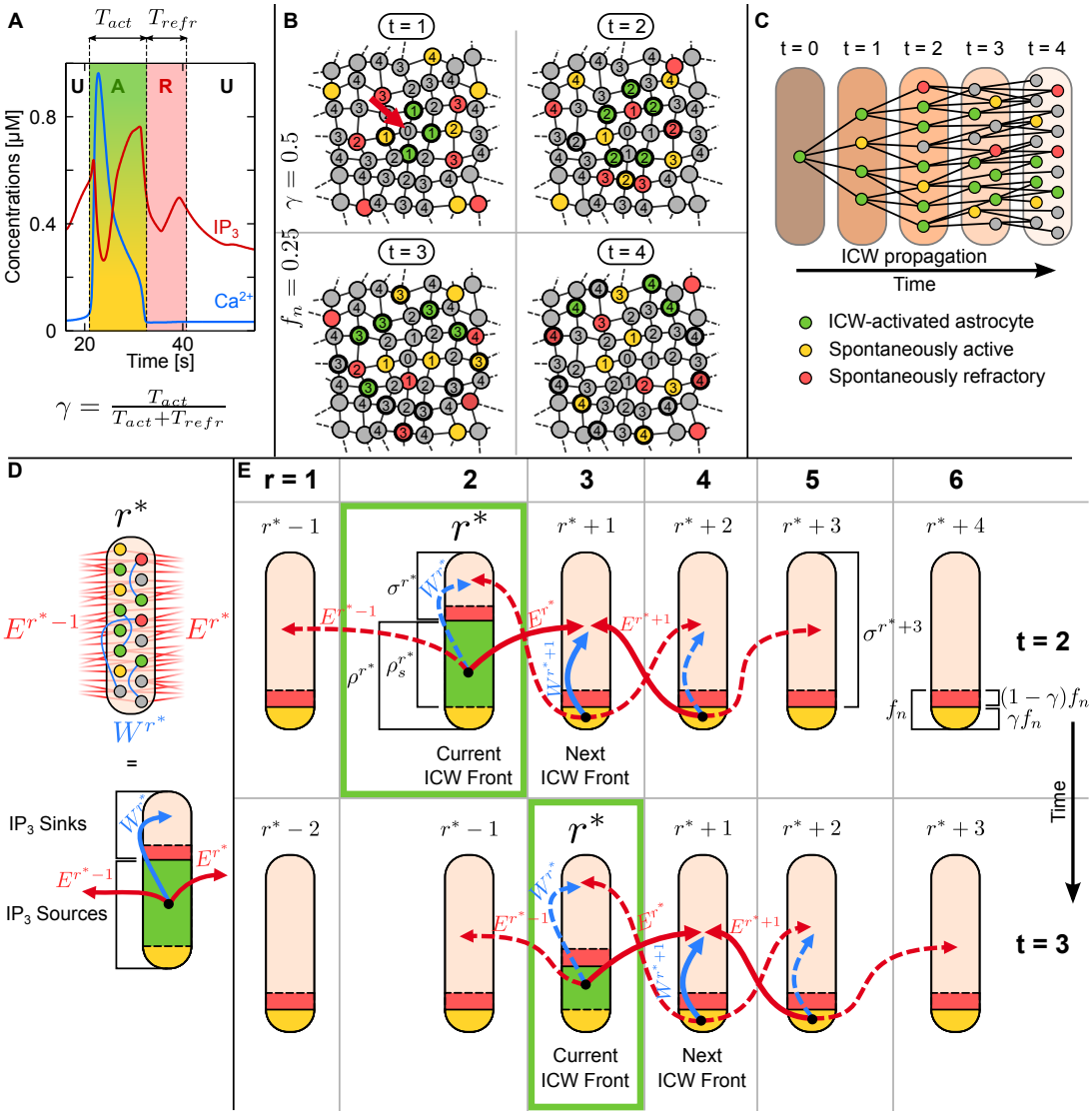

Figure D.3: Schematic representation of the stochastic shell propagation model. **A** While, in the basic shell propagation model, we do not take the refractory state (*red* shaded zone) into account, we need to integrate it in the stochastic shell propagation model as the spontaneously active astrocytes of shell r can be in their refractory state when the ICW reaches r. We compute $\gamma = \frac{T_{act}}{T_{act}+T_{refr}}$ to determine the relative number of active and refractory astrocytes in shells; the higher γ, the better the effect of spontaneously active astrocytes. **B** Schematic representation of the propagation of an ICW elicited at the cell center (*red* arrow) which is propagating under spontaneous activation of astrocytes with $f_n = 0.25$. Cells can be ICW activated (*green* cells), unactivated (*gray* cells), spontaneously active (*yellow* cells), and refractory (*red* cells). **C** The same ICW can be visualized as the activation of successive shells 0 to 4 at times $t = 0$ to $t = 4$ (arbitrary time units). **D** We simplify the detailed shell topology (top part) by considering that it can be approximated by a single compartment with 4 sub-compartments (each one corresponding to one of the four states that we described before). The sizes of these sub-compartment are given in Table D.1 (column 'Probability'). **E** Schematic representation of the IP_3 fluxes at play during the transmission of an ICW under spontaneous activations of astrocytes. In the basic shell propagation model, we only needed to consider the quantity of IP_3 (*solid red* arrow) given by the ICW front r^* to the next shell; to do this, we also needed to consider shell $r^* - 1$ and the unactivated astrocytes of shell r^* that were both acting as IP_3 sinks (*dashed red* arrow and *dashed blue* arrow). Under spontaneous astrocyte activation, shell $r^* + 1$ also receives IP_3 from the spontaneously activated astrocytes in itself (*solid blue* arrow) and in shell $r^* + 2$ (*solid red* line).

Table D.1: Possible states of astrocytes in the stochastic shell propagation model.

State	Role	Activable ?	Probability
Activable and Activated	IP_3 source	yes	$(1-f_n)\rho_s^r$
Activable and Unactivated	IP_3 sink	yes	$(1-f_n)(1-\rho_s^r)$
Spontaneously activated	IP_3 source	no	γf_n
Spontaneously refractory	IP_3 sink	no	$(1-\gamma)f_n$

Astrocyte states and their frequencies in shells Considering the spontaneous activation frequency ζ_n, we first define the ratio of spontaneously activated astrocytes $f_n = \tau\zeta_n$ (in either activated or refractory state) in any shell during a time τ that is the typical time for ICW transmission between 2 shells. Among these astrocytes, some are in their active (IP_3 giving) state while other are in their refractory state. To account for this difference, we introduce γ, the ratio of time that spontaneously activated astrocytes will stay in their active state:

$$\gamma = \frac{T_{act}}{T_{act} + T_{refr}} \tag{D.3}$$

with T_{act} and T_{refr} respectively the time that astrocytes spend in their active and refractory state. During τ seconds, in a shell with N^r astrocytes, there will thus be $\gamma f_n N_r$ spontaneously activated astrocytes in their **active state**, and $(1-\gamma)f_n N_r$ spontaneously activated astrocytes in their **refractory state**. We then make the distinction between **activable** astrocyte and **unactivable** astrocytes (c.f. column 'Activable ?' in Table D.1): all astrocytes that are spontaneously activated (in either their active or refractory state) cannot get activated by an ICW and are thus unactivable astrocytes while the other astrocytes are activable; the probability for an astrocyte to be activable is thus $1-f_n$. Among these activable astrocytes, we need to make the distinction between those that will get activated by the ICW and those that will stay unactivated. To achieve this distinction, we introduce ρ_s^r (s for signal), the ratio of astrocytes activated by the ICW among all activable astrocytes of shell r.

IP_3 sinks and sources In this revised shell-propagation model, we consider that only one shell r^* can be activated at a given time. We will thus compute ρ^{r^*} incrementally, as in the basic shell propagation model, and consider that, if we are currently considering the ICW activated shell r^*, $\rho_s^r = 0$ for all $r \neq r^*$. In any shell r, the probability ρ^r for an astrocyte in this shell to be an IP_3 source is simply:

$$\rho^r = \gamma f_n + (1-f_n)\rho_s^r \tag{D.4}$$

The probability σ^r for an astrocyte in r to be an IP_3 sink is:

$$\sigma^r = (1-\gamma)f_n + (1-f_n)(1-\rho_s^r) = 1-\rho^r \tag{D.5}$$

These different quantities are represented in Figure D.3D and E as ratios of a shell represented as a single compartment with 4 sub-compartments corresponding to the 4 states of Table D.1.

IP_3 exchange between shells We now focus on the conditions, represented in Figure D.3E, for propagating the ICW front from shell r^* to r^*+1. In the basic shell propagation model, we only considered shell r^*-1, r^* and r^*+1 to compute the ratio of activations in r^*+1. The shells r^*-1 and the unactivated astrocytes of shell r^* were IP_3 sinks that diminished the quantity of IP_3 that r^*+1 received from r^* (*solid red* arrow). In the stochastic shell propagation model, we need to consider additional shells since, in every shell, there is a fraction γf_n of spontaneous IP_3 sources (*yellow* sub-compartment). The next ICW front r^*+1 thus also receives IP_3 from its own spontaneously activated astrocytes (*solid blue* arrow) and the spontaneously activated astrocytes of shell r^*+2 (*solid red* arrow). To compute the former, we also need to take into account the shell r^*+3 that will act as an IP_3 sink and diminish the quantity of IP_3 received from shell r^*+2.

Shell compartments can be of two types: sink compartments and source compartments. The following computations will involve a lot of IP_3 quantity exchanges between shell compartments and we thus need to introduce some convenient notation. Let us assume that a source compartment **A** is sharing its IP_3 among a target compartment of interest **T** and a sink compartment **S**. As we saw in Section C.2, the quantity of IP_3 that will be received by **T** depends on the number of nodes N_A, N_T, and N_S of compartments **A**, **T**, and **S**, and also on the number of links $L_{A\to T}$, and $L_{A\to S}$ between compartment **A** and **T** and **S** respectively. We thus define, according to equation (C.18), the normalized quantity of IP_3 received by T from A as:

$$\Psi(N_A,N_T,N_S,L_{A\to T},L_{A\to S})=\left(\frac{\alpha_t}{\alpha_t+\frac{L_{A\to S}}{N_S}}\left(\frac{L_{A\to T}}{L_{A\to T}+L_{A\to S}}\frac{N_T+N_S}{N_T}-1\right)+1\right)\times\frac{N_A}{N_T+N_S} \tag{D.6}$$

Let us now remind the different types of compartments:
- The number of astrocytes in the whole sink compartment of shell r is denoted as $\sigma^r N^r$ and consists in the two sub-compartments represented in Figure D.3E as *light brown* and *red* areas separated by a *dashed* line.
- The number of astrocytes in the sink compartment of shell r that are linked to astrocytes in the source compartment of the same shell is denoted as $\hat{N}^r$.
- The number of astrocytes in the source compartment of shell r is denoted as $\rho^r N^r$ and consists in the two sub-compartments represented in Figure D.3E as *green* and *yellow* areas separated by a *dashed* line.

Let us also remind the different types of links:
- The number of links between shell r and $r+1$ is denoted as E^{r+1}.
- The number of links in shell r between the activated astrocytes and the unactivated ones is denoted as $\hat{W}^r$

As it can be seen in Figure D.3E, each source compartments of shells r^*, r^*+1, and r^*+2 send a part of their IP_3 to the sink compartment of the target shell r^*+1. Let us thus compute the normalized quantities of IP_3 that each of these shells contribute to r^*+1. First, the shell r^* gives a normalized quantity of IP_3 $\langle\Psi^{r^*\to r^*+1}\rangle$ to r^*+1 that is computed using equation (D.6) as:

$$\Psi^{r^*\to r^*+1}=\Psi(\rho^{r^*}N^{r^*},\sigma^{r^*+1}N^{r^*+1},\sigma^{r^*-1}N^{r^*-1}+\hat{N}^{r^*},E^{r^*},E^{r^*-1}+\hat{W}^{r^*}) \tag{D.7}$$

The shell r^*+1 then gives IP_3 to itself through its spontaneously active compartment (*solid blue* arrow) :

$$\Psi^{r^*+1\to r^*+1} = \frac{\hat{N}^{r^*+1}}{\sigma^{r^*+1}N^{r^*+1}} \times \Psi(\rho^{r^*+1}N^{r^*+1}, \hat{N}^{r^*+1}, \sigma^{r^*}N^{r^*} + \sigma^{r^*+2}N^{r^*+2}, \hat{W}^{r^*+1}, E^{r^*} + E^{r^*+1}) \tag{D.8}$$

with $\frac{\hat{N}^{r^*}}{\sigma^{r^*+1}N^{r^*+1}}$ a factor that rescales the averaged IP_3 quantity received by unactivated astrocytes of shell r^*+1 linked to activated astrocytes of the same shell to the average IP_3 received by all unactivated astrocytes of shell r^*+1. The shell r^*+2 finally gives:

$$\Psi^{r^*+2\to r^*+1} = \Psi(\rho^{r^*+2}N^{r^*+2}, \sigma^{r^*+1}N^{r^*+1}, \sigma^{r^*+3}N^{r^*+3} + \hat{N}^{r^*+2}, E^{r^*+1}, E^{r^*+2} + \hat{W}^{r^*+2}) \tag{D.9}$$

We thus compute the normalized IP_3 quantity $\Psi_{tot}^{r^*+1}$ received on average by astrocytes of shell r^*+1 (i.e. the next ICW front) by:

$$\Psi_{tot}^{r^*+1} = \Psi^{r^*\to r^*+1} + \Psi^{r^*+1\to r^*+1} + \Psi^{r^*+2\to r^*+1} + \Psi_{stim}^{r^*+1} \tag{D.10}$$

with $\Psi_{stim}^{r^*+1}$ computed as in equation (C.19). To incrementally compute ρ^{r^*} we then follow these steps, starting from $r^* = -1$:

1. Compute the normalized IP_3 quantity $\langle \Psi_{tot}^{r^*+1} \rangle$ received on average by astrocytes of shell r^*+1;
2. Determine $\rho_s^{r^*+1}$ with equation (C.21);
3. Put $\rho_s^{r^*}$ to 0.
4. If $\lfloor \rho^{r^*+1}N^{r^*+1} \rfloor > 0$, add 1 to r^* and go back to step 1; otherwise stop the propagation.

For each value of r^*, from the start of propagation to the end, we compute the number of astrocytes that were activated in each shell as $N_{sim}^{s+n} = \sum_{r^*=0}^{\infty} \rho_s^{r^*} N^{r^*}$. Note that we use $\rho_s^{r^*}$ and not ρ^{r^*} in order to discard the spontaneous activations. We can also compute the number of activated astrocytes without stimulation N_{sim}^{n} by putting $\Psi_{stim}^{r+1} = 0$ in equation (D.10), and the number of activated astrocytes without any spontaneous activation N_{sim}^{s}. In consequence, we can then compute the same indicator of stochastic resonance that we use in Section VI.1:

$$\chi_{sim} = \frac{N_{sim}^{s+n} - N_{sim}^{n}}{N_{sim}^{s}} \tag{D.11}$$

D.2.2 Investigating stochastic resonance in the stochastic shell propagation model

IP_3 quantities received by shells We show, in Figure D.4A (top figure), the values Ψ_{struct}^{r} taken by Ψ_{tot}^{r} assuming that all the activable astrocytes are activated in all shells ($\rho_s^r = 1$). These values thus only depends on the network structure and change when

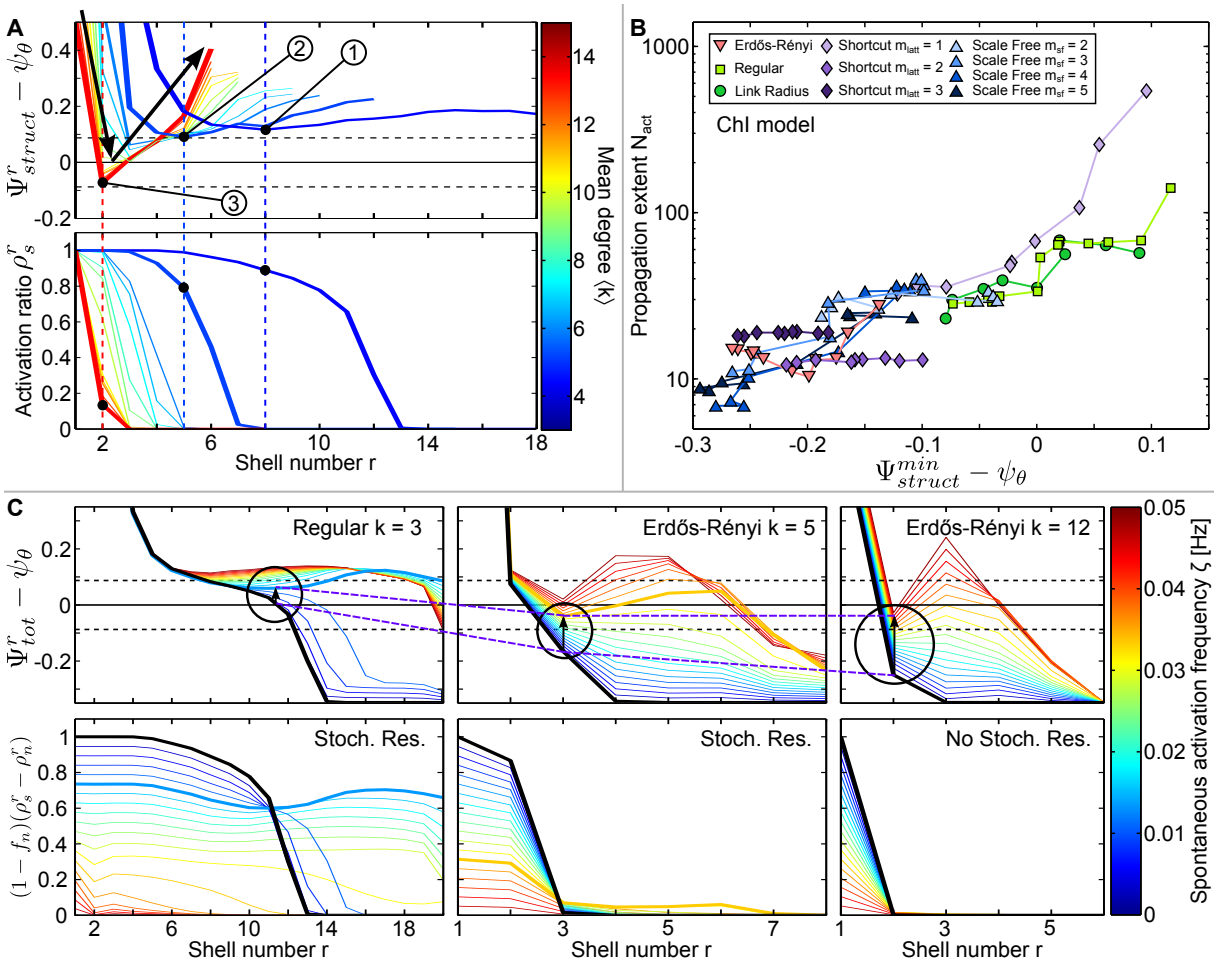

Figure D.4: Early shells control stochastic resonance. **A** As illustrated on the top plot, normalized structural IP_3 quantities received by shell r Ψ_{struct}^r all have a stereotypical shape: a decrease phase (downward *black* arrow) until it reaches its minimum value Ψ_{struct}^{min} and goes up again (upward *black* arrow). If the minimum value is below the IP_3 threshold (*black* dot pointed by the circled number 3, the threshold is represented as a *solid horizontal black* line), the propagation stops right away, as illustrated on the bottom plot with a sudden drop (*thick red* curve) in the activation ratio ρ_s^r of activable astrocytes. For supra threshold values of Ψ_{struct}^{min} (*black* dots pointed by circled numbers 1 and 2), the activation ratio ρ_s^r decreases but more slowly. All curves correspond to Regular Degree networks and the curve color corresponds to the network mean degree $\langle k \rangle$. Top and bottom horizontal *black dashed* lines mark respectively the normalized IP_3 quantity needed to activate 90 and 10% of the activable astrocytes in the shell. **B** ICW propagation extent N_{act} in the full ChI model simulations, as described in Chapter V, as a function of the difference between the minimum value of normalized quantity of IP_3 Ψ_{struct}^{min} and the treshold IP_3 quantity needed to activate an astrocyte ψ_θ. Ψ_{struct}^{min} is strongly linked to the ICW extent. **C** The top row shows, for different network, the actual IP_3 quantity received by each shell as the ICW unfolds in the SSP model. Different colors correspond to different spontaneous activation frequencies and the *thick colored* curves correspond to the resonant frequency. Bottom row shows, for each shell, the ratio of astrocytes that are activated by synergistic effects between the ICW and spontaneous activation (i.e. a visual way to represent SR). From left to right, the depth of the Ψ_{struct}^{min} 'ditch' (indicated by the vertical *black* arows linked by *purple dashed* lines) increases and the spontaneous activation frequency needed to sustain the ICW gets higher. For the left and middle columns, there exist frequencies low enough for the ICW to be facilitated without spontaneous activations preventing its propagation. For the rightmost column however, the spontaneous activation frequency that would be needed to 'fill the ditch' is so high that it also prevents ICW propagation; in consequences, these networks do not display SR. Simulations with $D = 299$ and as in Figure VI.7.

Table D.2: Stochastic shell propagation model parameters.

Symbol	Equ.	Description	Values
α_t	C.18	Transition point between the regimes in Figure C.5B	0.35
D	C.19	Quantity of IP_3 received by the stimulated cell (medium stim.)	299.9049
-	-	- (weak stim.)	99.9683
η	C.19	Exponent of the decrease of $\langle \Psi^r_{stim} \rangle$ by V^r	2.0988
δ	C.21	Steepness of the activation function	0.0795
A	C.22	Slope of the relationship between $\langle k \rangle$ and ψ_θ	0
B	C.22	Intercept of the relationship between $\langle k \rangle$ and ψ_θ	0.348
γ	D.3	Time fraction of the active state during spontaneous activation	0.32 - 0.5

progressing through the shells of a network. On the figure, the different curves correspond to Regular Degree networks with different color-coded mean degrees $\langle k \rangle$. Regardless of the mean degree, the shape of these curves is always the same: Ψ^r_{struct} starts at high values for the first shells, then quickly drops to a minimum value and increases back (indicated by *thick black* arrows). The *horizontal solid black* line denote the threshold IP_3 quantity needed to activate half of the activable astrocytes while the *top and bottom horizontal dashed black* lines denote the values for which respectively 90% and 10% of the activable astrocytes will get activated. As an example, let us focus on what happens in Regular Degree networks with $k = 3$ (rightmost *thick dark blue* curve); as long as Ψ^r_{struct} is well above threshold, the activation ratio ρ^r_s of the corresponding shell (Figure D.4A, bottom figure) stays close to 1, i.e. all activable astrocytes are activated by the ICW. At the minimum Ψ^r_{struct} value for shell $r = 8$ (*black dot indicated by the circled number* 1), despite being above threshold, the ratio of activated astrocyte (bottom figure, rightmost *thick dark blue* curve) slowly decreases until the ICW stops at $r = 13$. Of course, during this decrease, Ψ^r_{struct} increases again, but as the fraction of activated astrocytes ρ^r_s started going below 1, the actual normalized IP_3 quantity Ψ^r_{tot} that shells above $r = 8$ receive is lower than Ψ^r_{struct}. The minimum value that Ψ^r_{struct} reaches is thus critical to determine how the ICW will propagate further:

- if it is well above threshold (as for Regular Degree networks with $k = 3$), the ICW will continue its propagation for a high number of shells;
- if it gets lower (as for Regular Degree networks with $k = 4$, *thick blue* curve with the black dot indicated by the circled number 2), the ICW will propagate to less shells;
- finally, if it is below threshold (as for Regular Degree networks with $k = 15$, *thick red* curve with the black dot indicated by the circled number 3), the ICW will quickly stop.

The minimum Ψ^r_{struct} value determines the ICW extent For each network type and each parameter combinations, we computed the minimum value Ψ^{min}_{struct} taken by Ψ^r_{struct}, we then subtracted the threshold IP_3 quantity ψ_θ and plotted in Figure D.4B the resulting values against the total number of astrocytes activated N_{act} in standard ChI model simulations (such as described in Chapter V). For all network types and all parameters combinations, reducing Ψ^{min}_{struct} consistently led do decreases in the ICW extent

N_{act}. Additionally, all networks collapse on the same curve, strongly indicating that Ψ^{min}_{struct} is the determining quantity controlling ICW extent. Interestingly, the existence of this 'ditch' in all networks thus predicts that if one stimulates the shell corresponding to this ditch, one might be able to restore ICW propagation in networks that could not support it with single node stimulations. In the context of stochastic resonance, spontaneous activations could thus, by increasing the quantity of IP_3 above Ψ^{min}_{struct}, help the network to 'escape' from the 'ditch' and restore ICW propagation.

Spontaneous activations as 'ditch-fillers' To comment on the effects of spontaneous activation on this Ψ^{min}_{struct}-controlled ICW propagation, we first need to remind the reader that not only do spontaneously activated astrocytes add IP_3 to the network, they also prevent ICW propagation to nodes that are currently spontaneously active. To investigate ICW propagation under spontaneous activations, we should not look at the fraction ρ^r_s of activable astrocytes that are activated, but we should rather look at the total fraction of astrocytes that are ICW-activated $(1-f_n)\rho^r_s$ with $f_n = \tau\zeta_{sim}$ the fraction of astrocytes that are spontaneously activated during a period τ. Additionally, to quantify the astrocytes that were activated because of synergistic effects between ICW and spontaneous activation, we need to subtract the ratio of astrocytes $(1-fn)\rho^r_n$ [1] that get activated when only spontaneous activations occur (and no stimulation). We thus plotted, in Figure D.4C (bottom row), the fractions of astrocytes activated by SR effects $(1-fn)(\rho^r_s - \rho^r_n)$ for three different networks (three columns) without spontaneous activation (*thick black* line) and for different frequencies of spontaneous activations (*color-coded* curves, with the *thick colored* curve representing the maximum SR frequency). Alongside with these, we plotted the normalized quantities of IP_3 Ψ^r_{tot} received by shell r (Figure D.4C top row) for the same networks and with the same graphical conventions. We saw in Figure D.4A that Regular Degree networks with $k = 3$ propagated an ICW quite far in the network but this ICW eventually stopped because of a too low Ψ^{min}_{struct} value. The addition of small frequency spontaneous activation (*thin dark blue curves*, top row, left column), while reducing the number of activated astrocytes in early shells, marginally increase ICW extent; but as soon as the spontaneous activation frequency manages to 'fill the ditch' (represented by the small circled *black* arrow), the ICW is regenerated and propagated to the end of the network (*thick blue curve*, bottom row, left column). Further increases in spontaneous activation frequency only lowers the number of astrocytes to which the ICW propagates (*green* to *red* thin curves). For Erdős-Rényi networks with $k = 5$ (middle column), the situation is the same but frequency of spontaneous activations needed to 'fill the ditch' and extend the ICW to further shells in the network is higher (≈ 0.035 Hz compared with ≈ 0.015Hz for Regular degree networks with $k = 3$). We represented this difference by a longer *black* arrow going from the IP_3 quantity received without spontaneous activation to the IP_3 quantity received with spontaneous activation at maximum SR. Although small, the activation fraction that arises from synergistic effects between ICW and spontaneous activation (*thick orange curve*, bottom row, middle column) propagates much further than the original ICW (*thick black* curve). Finally, when the depth of the 'ditch' is too high,

1. we use ρ^r_n as a shorthand for ρ^r_s when only spontaneous activation occur, i.e. with $D = 0$, see Appendix D.2

as for Erdős-Rényi networks with $k = 12$ (right column), the spontaneous activation frequency that would be needed to attain the same Ψ^r_{tot} levels as in lower degree networks (represented by the top *dashed purple* line linking arrowheads) is too high (≈ 0.045Hz) to allow ICW propagation. All spontaneous activation frequencies thus fail to increase ICW extent either because the increase in Ψ^r_{tot} that they provoke is too small to fill the 'ditch' or because very few nodes are left unactivated by spontaneous activations and the ones that are unactivated support ICW as well with or without stimulation (and thus $(1 - fn)(\rho^r_s - \rho^r_n) \approx 0$). This mechanism thus explains why Erdős-Rényi networks do not support SR for high mean degrees as seen in Figure VI.8B and Figure VI.7E.

Ψ^{min}_{struct} also determines SR in the full ChI model simulations Given the preceding conclusions, we decided to check whether Ψ^{min}_{struct} values controlled SR in both the SSP model and the ChI model. Figure D.5A shows the resonant frequencies ζ^*_{sim} for all networks as a function of $\Psi^{min}_{struct} - \psi_\theta$, as expected from the previous considerations, both values are strongly correlated as assessed by high values of Spearman's correlation coefficient ($\rho = -0.8$ for $\gamma = 0.5$ and $\rho = -0.55$ for $\gamma = 0.32$). The inset shows the same relationship but for a lower γ value; similarly to what we saw in Figure VI.8A, higher γ values make the relationship more gradual and reduces the resonant frequency. Interestingly, the correlation between ζ^*_{sim} and $\Psi^{min}_{struct} - \psi_\theta$ is stronger than with the mean degree $\langle k \rangle$ for $\gamma = 0.5$ ($\rho = -0.85$ versus $\rho = 0.64$). Figure D.5B shows the relationship between the resonant frequency ζ^* in the actual ChI simulations and the difference between Ψ^{min}_{struct} and ψ^{ChI}_θ (the IP_3 threshold in the ChI model, derived from the local analysis [1]); although the correlation is much lower than in the SSP model, it is still strongly significant (Spearman's $\rho = -0.49$ with $p = 2.24\ 10^{-7}$). Spatial Scale Free networks are however mainly responsible for the loss of correlation, when estimating Spearman's correlation coefficient on all networks except spatial scale free, we obtained $\rho = -0.72$ ($p = 1.42.10^{-8}$, linear regression in *green dashed* line). It thus seems that, as we already saw in Figure VI.4A, Spatial Scale Free networks display peculiar behaviors that we cannot fully account for, neither by looking at the mean degree nor by looking at Ψ^{min}_{struct}. Although the dependence of the resonant frequency on Ψ^{min}_{struct} in the full ChI model is a confirmation of its importance, we first devised the SSP model to understand the presence or absence of SR and the different SR strength that we observed in the ChI model simulations. In the SSP model, the SR strength χ^*_{sim} is dependent on Ψ^{min}_{struct} in an interesting manner. Figure D.5C shows the relationship between these two values for $\gamma = 0.5$ and for all networks and stimulation strengths [2]. The resonance strength is lower for very low and very high Ψ^{min}_{struct} values and higher for intermediate Ψ^{min}_{struct} values, forming a bell shape with very high resonance strength at the middle. As we already saw from Figure D.4, very low Ψ^{min}_{struct} values prevent high SR because it demands high spontaneous activation frequencies (as visible in Figure D.5A) to escape the 'ditch' while these high frequencies prevent ICW propagation. Networks that have high Ψ^{min}_{struct} values already propagate ICW to a high number of astrocytes without spontaneous activation (as shown in Figure D.4B) and thus have a smaller margin for improvement with SR. In contrast, networks with

1. $\psi^{ChI}_\theta = A\langle k \rangle + B$ with $A = 0.07$ and $B = 0.2$, c.f. Section V.3
2. The same plot for $\gamma = 0.32$ displayed lower χ^*_{sim} values but was much less clear than for $\gamma = 0.5$

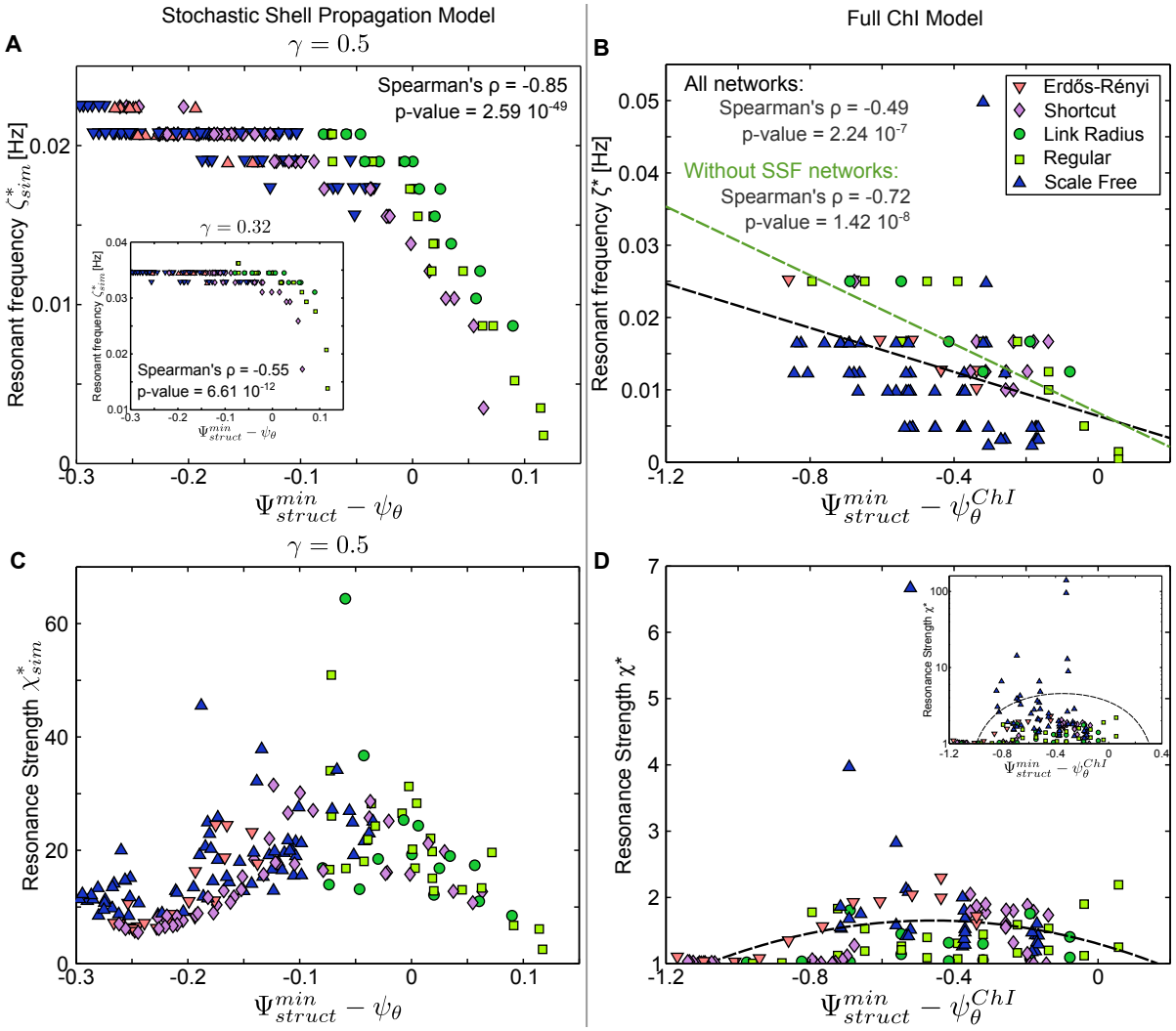

Figure D.5: Ψ^{min}_{struct} values also control stochastic resonance in the ChI model. **A** Resonant frequency ζ^*_{sim} in the SSP model as a function of the difference between Ψ^{min}_{struct} and the IP_3 threshold ψ_θ. ζ^*_{sim} is better explained by Ψ^{min}_{struct} than by the network mean degree (compare with Figure VI.8). **B** Same relationship as on A but for the full ChI model. Although the resonant frequency ζ^* is not well correlated to Ψ^{min}_{struct} for Spatial Scale Free networks, all the other network types are strongly correlated (*green dashed* linear regression and reported Spearman's correlation coefficient). *Black dashed* line corresponds to linear regression for all network types. **C** Ψ^{min}_{struct} can also account for the SR strength χ^*_{sim} in the SSP model: low and high values lead to relatively low SR strength while intermediate values allow very strong SR (see main text for an explanation). **D** SR strength χ^* in the full ChI model arguably follows the same behavior than in the SSP model. The main figure does not take into account Spatial Scale Free networks with $r_c > 10\mu$m while the inset takes all networks into account. *Black dashed* curves represent parabolas fitted to all data points. **A, B, C and D**: all symbols follow the legend in B; only the networks which supported ICW extent above $3/4$ of their mean degree were considered. **A and B**: only networks that displayed a SR strength χ^* or χ^*_{sim} greater than 1.2 were considered. **A and C**: simulations as in Figure VI.8, data corresponds to both $D \approx 300$ and $D \approx 100$. **B and D**: simulations as in Figure VI.4, data points correspond to both $IP_3^{bias} = 1.5\mu$Mand $IP_3^{bias} = 1\mu$M.

intermediate values of Ψ_{struct}^{min} support small ICWs without spontaneous activation and have thus a large margin for improvement and they can achieve SR for intermediate frequencies of spontaneous activation that do not prevent ICW propagation. In the full ChI model, the relationship between the resonance strength χ^* and $\Psi_{struct}^{min} - \psi_\theta^{ChI}$, shown in Figure D.5D (and inset) is less clear than in the SSP model. Networks with very low Ψ_{struct}^{min} do not display SR, but the bell-shaped behavior obtained in the SSP model seem to mainly apply to Erdős-Rényi and Shortcut networks in the full ChI model. Spatially constrained networks (Regular Degree and Link Radius) show a much less clear behavior with relatively high resonance strength for high Ψ_{struct}^{min} values. Finally, Spatial Scale Free networks are the ones that display the highest resonance strengths; the main figure only display SSF networks with $rc < 10\mu$Mwhile the inset displays all networks (with a logarithmic y-scale). In both main figure and inset, SSF networks show high resonance strength for intermediate values of Ψ_{struct}^{min}, as in the SSP model.

Altogether, Ψ_{struct}^{min} values seem to capture at least parts of the SR phenomenon in the ChI model:

- It accounts for the variability in resonant frequencies, showing that Ψ_{struct}^{min} values can be seen as 'ditches' or 'gaps' that need to be filled by increasing the spontaneous activation frequency and thus increasing the overall IP_3 in the network.
- It accounts for the absence of SR in networks with very low Ψ_{struct}^{min}, as the frequency of spontaneous activations that would be needed to 'fill the gap' is too high to allow ICW propagation as almost all the astrocytes get spontaneously activated.
- Finally, it accounts for the high resonance strength displayed mostly by spatially-unconstrained networks at intermediate Ψ_{struct}^{min} values, as we just explained in the previous paragraph.

Appendix E

Preliminary work

E.1 ICW propagation in astrocyte main processes

Up until now, we adressed two different spatial scales of astrocytes: we first investigated cell specific Ca^{2+} responses in Chapter IV and we then turned to the higher spatial scale at which astrocyte networks operate in Chapter V. In this chapter, we will go down one spatial scale by modeling Ca^{2+} dynamics in astrocyte processes. As we talked about in Section II.1, Ca^{2+} and IP_3 dynamics in astrocytes are often modeled using one of two different approaches: one can either use (1) Partial Differential Equations (PDEs) with which you can explicitly model the diffusion of both Ca^{2+} and IP_3 in space, or (2) compartmental modeling, where we cut down the space in small compartments, we assume that Ca^{2+} and IP_3 are well-mixed in each compartment and we compute diffusion by coupling terms between compartments. When modeling astrocyte networks, this compartmental approach, in which one compartment is a whole astrocyte, seems quite natural as the intracellular diffusion is faster than the intercellular one and we can assume that the intra-cellular dynamics are faster than the intercellular ICW transmission. In contrast, astrocyte processes constitute intracellular space and we can no longer rely on the difference of diffusion between and within compartments to justify compartmental modeling. Several lines of evidence however indicate that astrocyte processes might display some kind of compartmentalization. From a functional point of view, the smallest Ca^{2+} events are often restricted to portions of astrocytic processes of $\approx 1\mu$m(Panatier et al., 2011; Di-Castro et al., 2011), constituting the basic unit of Ca^{2+} activity in processes. That functional compartmentalization of astrocyte processes might be caused by several anatomical compartmentalization of ER stores (Golovina and Blaustein, 1997), metabotropic receptors targeted by synapses (Di-Castro et al., 2011; Panatier et al., 2011; Arizono et al., 2012), or IP_3 receptors (Holtzclaw et al., 2002). Given this experimental evidence supporting compartmentalization of astrocyte processes, we decided to use compartmental modeling with each compartment having its own Ca^{2+} dynamics modeled by the G-ChI model (see Section II.1.2). Additionally, in accordance with the functional compartmentalization of Ca^{2+} activity (Panatier et al., 2011) and the relatively small effective diffusion coefficient

of Ca^{2+} ($D_{Ca^{2+}} \approx 20\mu m.s^{-2}$ (Höfer et al., 2002), around 10 time smaller than that of IP_3 (Ullah et al., 2006)), we neglected Ca^{2+} diffusion between compartment and only considered IP_3 diffusion. Since Ca^{2+} dynamics in processes are different, in terms of signal shape and duration, from Ca^{2+} dynamics in the soma, we needed to calibrate our model parameters with experimentally observed Ca^{2+} signals in astrocyte processes. We first calibrated most of the parameters, as described in details in De Pittà (2013), so that Ca^{2+} signal shape matched the signals observed in experiments (Di-Castro et al., 2011; Panatier et al., 2011). Some of the parameters could however not be determined this way. In particular, the ER-to cytoplasm volume ratio ρ_A, the maximal rate of IP_3 production by PLCβ O_β, and the inter-compartment coupling strength F were still unknown as they were primarily related to the amplitude of Ca^{2+} in response to synaptic stimulation (ρ_A and O_β) and to the way Ca^{2+} signals propagate along the process (F). To estimate these parameters, we decided to use published data from Di-Castro et al. (2011) reporting relative Ca^{2+} amplitudes and delays of propagation along astrocyte processes.

Figure E.1A is taken from Di-Castro et al. (2011) and illustrates an expanded Ca^{2+} event that they recorded along a main astrocyte process. The process was segmented in several ROI (*colored* lines) and Ca^{2+} activity was measured with two-photon line-scan imaging. In the supplementary materials of Di-Castro et al. (2011), the authors provide the characterization of three different expanded events in terms of delays of propagation and fraction of the highest Ca^{2+} signal for each ROI. To determine parameters that we could not estimate in processes otherwise, we fitted values of ρ_A, O_β, and F in each individual subcompartment using the CMAES fitting procedure (Hansen, 2006). The resulting delays and amplitudes for each of the three expanded events are displayed in Figure E.1D alongside with schematic representation of the stimulated subcompartments in Figure E.1B and simulated Ca^{2+} traces corresponding to the fitted parameters in Figure E.1C. The fit is really good for all three expanded events and provided us with estimates for subcellular ChI parameters (c.f. Table E.1).

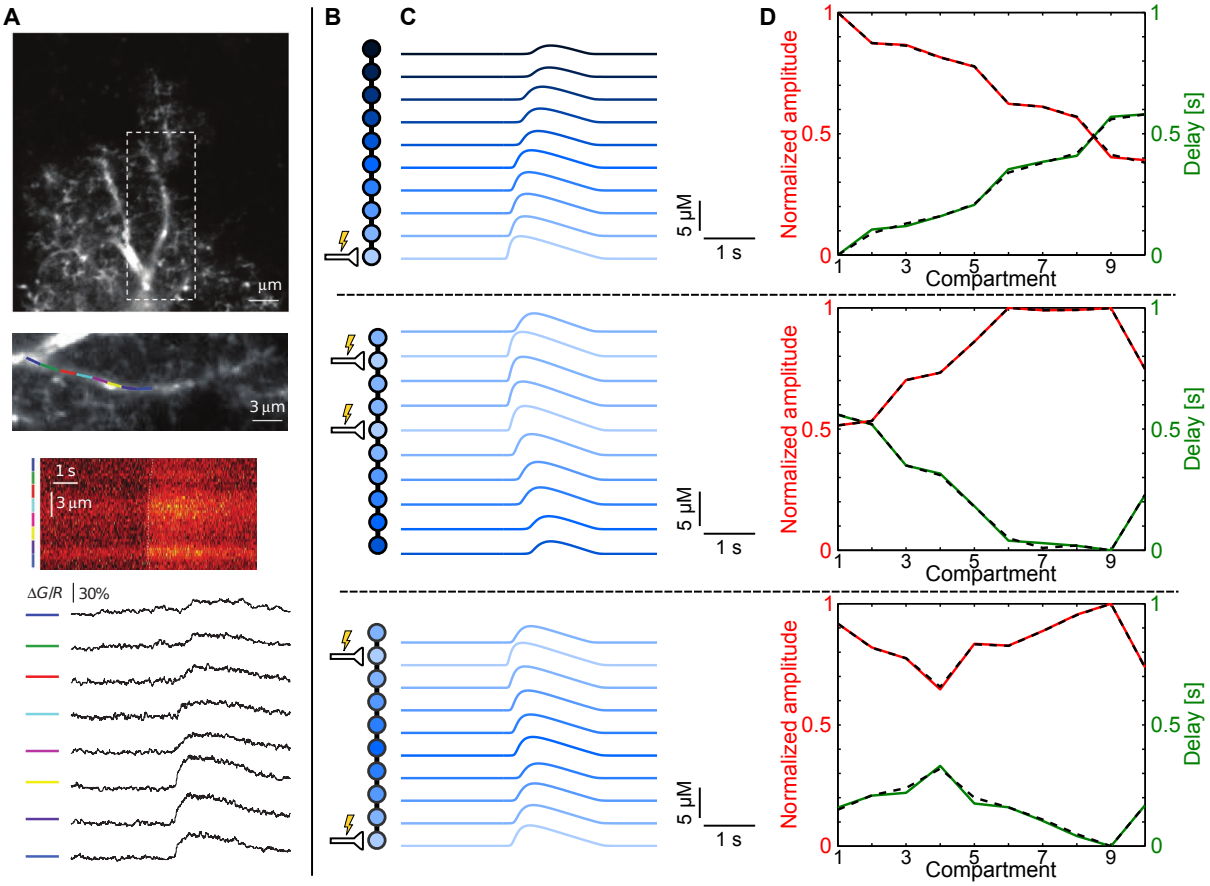

Figure E.1: Free parameters were fitted using published experimental data. **A** Representation of the experimental setup from Di-Castro et al. (2011) with which they measured propagation characteristics of three expanded events. Taken from Di-Castro et al. (2011). **B** Schematic representation of the position of the stimulated subcompartments (presynaptic terminals with lightning symbols). **C** Ca^{2+} signals resulting from the best fits. Color code according to the distance from the stimulated subcompartment (light blue for the stimulated subcompartments and increasingly darker blue for the other subcompartments). **D** Delays of propagation in *green* and relative Ca^{2+} amplitude in *red*, *dashed lines* represent values from GChI model simulations with fitted parameters while *solid lines* represent data from Di-Castro et al. (2011).

Table E.1: Parameters of the GChI model for processes.

Symbol	Description	Value	Units
	IP_3R kinetics		
d_1	IP_3 binding affinity	0.1	μM
O_2	Inactivating Ca^{2+} binding rate	0.68	$\mu M^{-1}s^{-1}$
d_2	Inactivating Ca^{2+} binding affinity	0.3085	μM
d_3	IP_3 binding affinity (with Ca^{2+} inactivation)	0.1	μM
d_5	Activating Ca^{2+} binding affinity	0.08	μM
	Calcium fluxes		
C_T	Total ER Ca^{2+} content	10	μM
ρ_A	ER-to-cytoplasm volume ratio	**1.0849**	–
Ω_C	Maximal Ca^{2+} release rate by IP_3Rs	18	s^{-1}
Ω_L	Maximal Ca^{2+} leak rate	0.05	s^{-1}
O_P	Maximal Ca^{2+} uptake rate	3	$\mu M\,s^{-1}$
K_P	Ca^{2+} affinity of SERCA pumps	0.1	μM
	IP_3 production		
O_δ	Maximal rate of IP_3 production by PLCδ	0.1	$\mu M\,s^{-1}$
K_δ	Ca^{2+} affinity of PLCδ	0.5	μM
κ_δ	Inhibiting IP_3 affinity of PLCδ	1	μM
O_β	Maximal rate of IP_3 production by PLCβ	**13.6561**	$\mu M\,s^{-1}$
K_G	Glutamate affinity of the receptor	20	μM
K_L	Ca^{2+}/PKC-dependent inhibition factor	80	μM
K_{KC}	Ca^{2+} affinity of PKC	0.5	μM
	IP_3 degradation		
Ω_{5P}	Maximal rate of IP_3 degradation by IP-5P	0.2	s^{-1}
O_{3K}	Maximal rate of IP_3 degradation by IP_3-3K	4	$\mu M\,s^{-1}$
K_D	Ca^{2+} affinity of IP_3-3K	0.5	μM
K_{3K}	IP_3 affinity of IP_3-3K	1	μM
	IP_3 diffusion		
F	GJC IP_3 permeability	**39.4839**	s^{-1}

E.2 GJC regulation by neuronal activity

This work is very preliminary, we just show a schematic description of the model and the current state of equations.

E.2.1 Potassium buffering

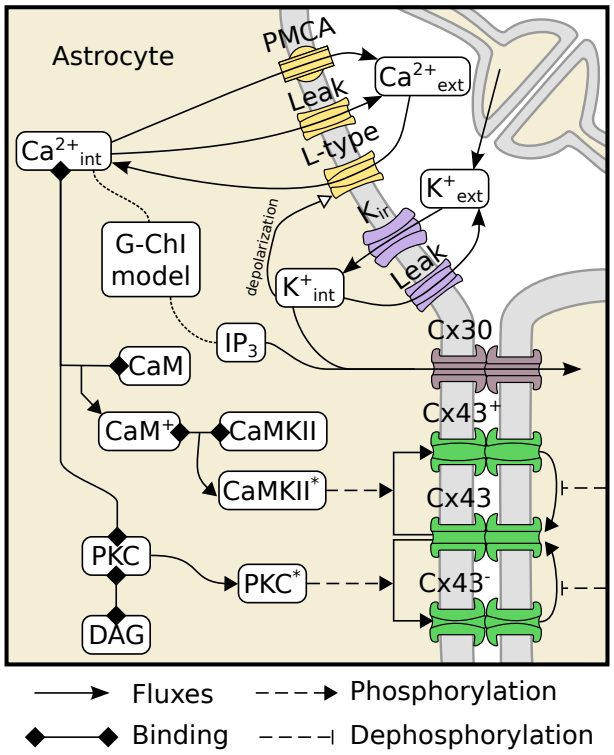

Figure E.2: Schematic representation of the K-ChI model. Increases in extracellular K^+ depolarizes astrocytes and lead to the opening of L-type channels. The large Ca^{2+} entry induces CamKII-mediated phosphorylation of Cx43 in $Cx43^+$ which have a higher permeability. When store-mediated oscillations occur, PKC is activated and phosphorylates Cx43 in $Cx43^-$ which impairs GJC permeability. K^+ diffuses through GJC and can thus provoke the same effects in neighboring astrocytes. These mechanisms are expected to mediate the creation of preferential pathways of Ca^{2+} signaling built between astrocytes that are exposed to high extracellular K^+ concentrations.

E.2.1.1 Potassium concentrations and membrane potential

Extracellular potassium concentration

$$\frac{d[K_o^+]_j}{dt} = \frac{I_{K,j}}{V_{ext}F} - \Omega_K([K_o^+]_j - [K_o^+]_{bl}) + \frac{Q_K}{V_{ext}} \sum_{t_i} \delta(t - t_i) \tag{E.1}$$

With $I_{K,j}$ the potassium current going through the membrane of cell j, defined in equation (E.15)

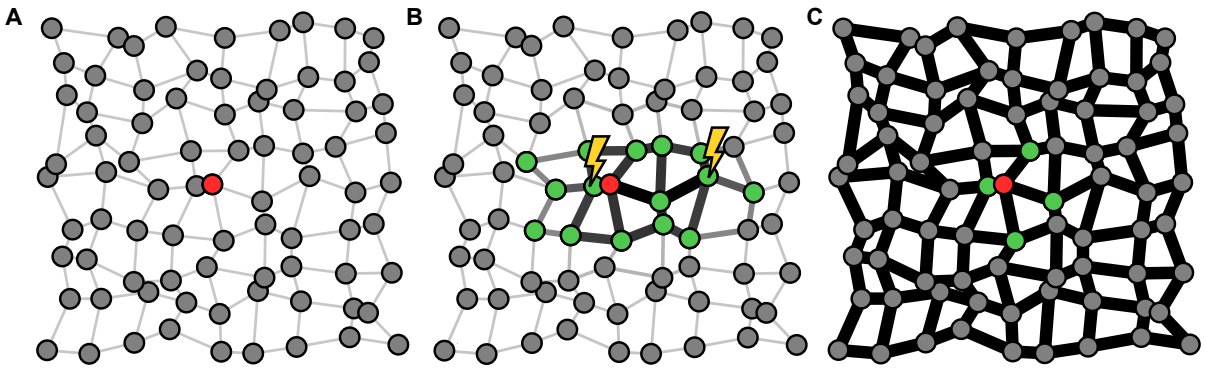

Figure E.3: Proof of concept for the KChI model. **A** Astrocyte network in resting state, a short stimulation of the *red* node does not produces any ICW. **B** After increases in extracellular K^+ concentration at astrocytes marked by lightning symbols, the strength of GJC in their neighborhood has changed (width and darkness of lines represent GJC permeability). Because of this local increases, when the *red* node is stimulated in the same way as in A, an ICW propagates (*green* nodes) in the zone influenced by the K^+-mediated GJC increase. **C** The increase in ICW extent is not linked to an augmentation in GJC conductance since increasing all GJC conductances (represented by thick black lines everywhere) also prevented ICW propagation.

Intracellular potassium concentration

$$V_a \frac{d[K_i^+]_j}{dt} = \frac{-I_{K,j}}{F} - \sum_k J_K^{j \to k} \tag{E.2}$$

With $J_K^{j \to k}$ the potassium flux between astrocytes j and k, defined in equation (E.27).

Membrane potential

$$C_a \frac{d\Phi_j}{dt} = -(I_{K,j} + I_{Ca,j} + I_{Cl,j} + I_{Na,j}) - F \sum_k J_K^{j \to k} \tag{E.3}$$

With $I_{Ca,j}$ the Ca^{2+} current generated by L-type channels and leak, defined in equation (E.16); $I_{Cl,j}$ and $I_{Na,j}$ the Cl^- and Na^+ currents generated by leak conductance, defined in equation (E.25) and equation (E.26).

Gating variables for L-type Ca^{2+} channels

Activating variable

$$\frac{dm'_j}{dt} = \frac{m'_{\infty,j} - m'_j}{\tau_{m',j}} \tag{E.4}$$

With $m'_{\infty,j}$ the steady-state value defined in equation (E.20), and $\tau_{m',j}$ the time constant, defined in equation (E.21).

Inactivating variable

$$\frac{dh'_j}{dt} = \frac{h'_{\infty,j} - h'_j}{\tau_{h'}} \tag{E.5}$$

With $h'_{\infty,j}$ the steady-state value defined in equation (E.24).

E.2.1.2 G-ChI model

Calcium content

Cytosolic calcium

$$V_{cyt}\frac{dC_{cyt,j}}{dt} = J_{C,j} + J_{L,j} - J_{P,j} - \frac{I_{Ca,j}}{2F} \tag{E.6}$$

With $J_{C,j}$ the IP3R-mediated Ca^{2+} efflux from the ER (defined in equation (E.31)); $J_{L,j}$ the Ca^{2+} leak from the ER (defined in equation (E.32)); and $J_{P,j}$ the SERCA pump-mediated Ca^{2+} influx to the ER (defined in equation (E.33)).

Endoplasmic reticulum calcium

$$V_{ER}\frac{dC_{ER,j}}{dt} = -J_{C,j} - J_{L,j} + J_{P,j} \tag{E.7}$$

IP3

$$\frac{dI_j}{dt} = J_{\delta,j} + s_j J_{\beta,j} - J_{3K,j} - J_{5P,j} - \sum_k J_{IP_3}^{j\to k} \tag{E.8}$$

with $J_{IP_3}^{j\to k}$ the GJC-mediated diffusion to astrocyte k, defined in equation (E.34).

IP3R gating variable

$$\frac{dh_j}{dt} = \Omega_{h,j} \cdot (h_{\infty,j} - h_j) \tag{E.9}$$

E.2.1.3 GJC phosphorylation

One of these two scheme must be selected.

First scheme

$$\frac{d\gamma_j^+}{dt} = k_{act}(1-\gamma^+)[\text{CaMKII}^*]_j - k_{inh}\gamma^+[\text{PKC}^*]_j \tag{E.10}$$

With $[\text{CaMKII}^*]$ and $[\text{PKC}^*]$ defined in equation (E.35) and equation (E.37).

Second scheme

$$\frac{d\gamma_j^+}{dt} = k_{act}(1-\gamma^+-\gamma^-)[\text{CaMKII}^*]_j - k_{ph}\gamma^+[\text{Phos}] \tag{E.11}$$

$$\frac{d\gamma_j^-}{dt} = k_{act}(1-\gamma^+-\gamma^-)[\text{PKC}^*]_j - k_{ph}\gamma^-[\text{Phos}] \tag{E.12}$$

E.2.1.4 Detailed expressions

Kir channels conductance

$$G_{Kir,j} = \frac{G_{Kir}^{max}}{\sqrt{[K_o^+]_j(1+\exp(\frac{\Phi_j - V_h - E_{K,j}}{V_s}))}} \tag{E.13}$$

Nernst potential of charge carrier X for the membrane of astrocyte j

$$E_{X,j} = \frac{RT}{z_X F}\ln\left(\frac{[X_o^+]_j}{[X_i^+]_j}\right) \tag{E.14}$$

With z_X the valence of charge carrier X.

Potassium current through the membrane of astrocyte j

$$I_{K,j} = S_a(G_{leak} + G_{Kir,j})(\Phi_j - E_{K,j}) \tag{E.15}$$

With $G_{Kir,j}$ the conductance of Kir channels, defined in equation (E.13); and $E_{K,j}$ the Nernst potential for potassium defined in equation (E.14).

Calcium current through the membrane of astrocyte j

$$I_{Ca,j} = S_a(I_{Ca,j}^{leak} + I_{Ca,j}^{L-type} + I_{Ca,j}^{PMCA}) \tag{E.16}$$

With:

Leak calcium current

$$I_{Ca,j}^{leak} = G_{leak}(\Phi_j - E_{Ca,j}) \tag{E.17}$$

With $E_{Ca,j}$ the Nernst potential for calcium defined in equation (E.14)

L-type calcium channels current

$$I_{Ca,j}^{L-type} = m'_j h'_j P_{CaL} 2vF \frac{C_{cyt,j} - [Ca_o^{2+}]_j \exp(-v)}{1-\exp(-v)} \tag{E.18}$$

With $v = 2\frac{\Phi_j F}{RT}$.

PMCA pump calcium current

$$I_{Ca,j}^{PMCA} = 2FO_{MP}\mathcal{H}\left(C_{cyt,j}^2, K_{MP}\right) \tag{E.19}$$

Gating sub variables for L-type calcium channels

Steady-state activation

$$m'_{\infty,j} = \frac{O_m}{1 + \exp\left(\frac{\Phi_j - V_{m,1/2)}}{V_{m,slope}}\right)} \tag{E.20}$$

Activation time constant

$$\tau_{m',j} = \frac{1}{\alpha_{m,j} + \beta_{m,j}} \tag{E.21}$$

With:

$$\alpha_{m,j} = \frac{O_{\alpha,m}(\Phi_j + V_{\alpha,m,1/2})}{\exp\left(\frac{\Phi_j - V_{\alpha,m,1/2}}{V_{\alpha,m,slope}}\right) - 1} \tag{E.22}$$

$$\beta_{m,j} = O_{\beta,m}\exp\left(\frac{\Phi_j}{V_{\beta,m,slope}}\right) \tag{E.23}$$

Steady-state inactivation

$$h'_{\infty,j} = \frac{O_h}{1 + \exp\left(\frac{\Phi_j - V_{h,1/2}}{V_{h,slope}}\right)} \tag{E.24}$$

Chlore current through the membrane of astrocyte j

$$I_{Cl,j} = S_a G_{leak}(\Phi_j - E_{Cl,j}) \tag{E.25}$$

With $E_{Cl,j}$ the Nernst potential for chlore defined in equation (E.14).

Sodium current through the membrane of astrocyte j

$$I_{Na,j} = S_a G_{leak}(\Phi_j - E_{Na,j}) \tag{E.26}$$

With $E_{Na,j}$ the Nernst potential for sodium defined in equation (E.14).

Potassium Flux between astrocytes

$$J_K^{i\to j} = S_{ij} P_K^{ij} v \frac{[K_i^+]_j - [K_i^+]_i \exp(v)}{1 - \exp(v)} \tag{E.27}$$

with $v = \frac{F(\Phi_i - \Phi_j)}{RT}$

Mean permeability of a GJC in astrocytes j for a given molecule

First scheme

$$P_{mol}^j = P_{mol}^{basal}(\gamma_j^+(\alpha^+ - \alpha^-) + \alpha^-) \tag{E.28}$$

Second scheme

$$P_{mol}^j = P_{mol}^{basal}(\gamma_j^+(\alpha^+ - 1) + \gamma_j^-(\alpha^- - 1) + 1) \tag{E.29}$$

Mean permeability of GJC between astrocytes i and j for a given molecule

$$P_{mol}^{ij} = a_{ij} \min(P_{mol}^i, P_{mol}^j) \tag{E.30}$$

With $A = (a_{jk})$ the adjacency matrix of astrocyte network.

Intracellular calcium terms

IP_3R-mediated Ca^{2+} efflux from the ER

$$J_{C,j} = \Omega_C' \cdot m_{\infty,j}^3 h_j^3 \cdot (C_{ER,j} - C_{Cyt,j}) \tag{E.31}$$

With $\Omega_C' = V_{ER}\Omega_C$ and $m_{\infty,j}$ as in the ChI model.

Ca^{2+} leak from the ER

$$J_{L,j} = \Omega_L' \cdot (C_{ER,j} - C_{Cyt,j}) \tag{E.32}$$

With $\Omega_L' = V_{ER}\Omega_L$ from ChI model.

SERCA pump-mediated Ca^{2+} influx to the ER

$$J_{P,j} = O_P' \cdot \mathcal{H}\left(C_{cyt,j}^2, K_P\right) \tag{E.33}$$

With $O_P' = V_{cyt}O_P$ from ChI model.

IP_3 terms Other terms didn't change.

GJC-mediated IP_3 diffusion

$$J_{IP_3}^{j\to k} = \frac{S_{jk}}{V_{cyt}} P_{IP_3}^{jk} \cdot f(I_j - I_k) \tag{E.34}$$

With $\frac{S_{jk}}{V_{cyt}} P_{IP_3}^{basal} = F$ in ChI model and f is the transfer function.

IP_3R gating terms These terms didn't change.

Activated CaMKII

$$[\text{CaMKII}^*]_j = O'_{CK} \mathcal{H}\left(C_{cyt,j}^4, K_d\right) \tag{E.35}$$

According to reactions :

$$\text{CaMKII}^* + 3\text{K} \underset{\text{k}_2}{\overset{\text{k}_1}{\rightleftharpoons}} \text{CaMKII}^*3\text{K} \xrightarrow{\text{k}^*} \text{CaMKII}^* + 3\text{K}^* \xrightarrow{\Omega_1} 3\text{K}$$

and

$$3\text{K}^* + \text{IP}_3 \underset{\text{k}_4}{\overset{\text{k}_3}{\rightleftharpoons}} 3\text{K}^*\text{IP}_3 \xrightarrow{\text{k}_5} 3\text{K}^* + \text{IP}_4$$

The additional parameter O'_{CK} for $[\text{CaMKII}^*]_j$ sets O_{3K} values according to:

$$O_{3K} = \frac{k_5 k^*}{\Omega_1} \mathcal{H}\left([3K], \frac{k_2 + k^*}{k_1}\right) \cdot O'_{CK} = \zeta_{3K} \cdot O'_{CK} \tag{E.36}$$

Activated PKC

$$[\text{PKC}^*]_j = [\text{PKC}]_T \cdot \mathcal{H}\left(C_{cyt,j}, K_{KC}\right) \tag{E.37}$$

The additional parameter $[\text{PKC}]_T$ sets ζ values according to:

$$\zeta = \frac{O_{KC}}{\Omega_N} \cdot [\text{PKC}]_T = \xi_{KC} \cdot [\text{PKC}]_T \tag{E.38}$$

FOLIO ADMINISTRATIF

THESE SOUTENUE DEVANT L'INSTITUT NATIONAL DES SCIENCES APPLIQUEES DE LYON

NOM : **LALLOUETTE** DATE de SOUTENANCE : 04/12/2014

Prénoms : Jules Marcel André

TITRE :

Modélisation des réponses calciques de réseaux d'astrocytes : Relations entre topologie et dynamiques

(Modeling calcium responses in astrocyte networks : Relationships between topology and dynamics)

NATURE : Doctorat Numéro d'ordre : 2014ISAL2015

Ecole doctorale : École Doctorale Informatique et Mathématiques (ED512)

Spécialité : Informatique

RESUME :
Pendant les 20 dernières années, les astrocytes, un type de cellules cérébrales ayant été jusque là relativement ignoré des neuroscientifiques, ont peu à peu gagné en notoriété grâce à de multiples découvertes. Contrairement aux neurones, ces cellules ne transmettent pas de signaux électriques mais communiquent par des changements intracellulaire de leurs concentrations en calcium. Des découvertes récentes semblent indiquer que, loins d'agir en autarcie, les astrocytes répondent à l'activité neuronale et sembleraient, bien que cela soit plus débattu, moduler la transmission synaptique par le relargage de molécules spécifiques appellées `gliotransmetteurs' (en référence aux neurotransmetteurs). Comme les neurones, les astrocytes forment des réseaux et communiquent leur activité calcique par diffusion d'un astrocyte à l'autre, formant ainsi de véritables vagues de calcium intercellulaires. Deux réseaux, de neuronnes et d'astrocytes, cohabitent ainsi dans le cerveau ; mais, alors que les réseaux de neuronnes ont fait l'objet de recherches expérimentales et théoriques, les réseaux d'astrocytes restent encore mal connus. Ainsi, il n'a été découvert que très récement que la topologie de ces réseaux pourrait s'averer plus complexe que la vision qui dominait jusqu'alors : celle d'un syncitium astrocytaire dépourvu de spécificités topologiques. Les travaux présentés dans cette thèse portent principalement sur l'effet que ces différentes topologies pourraient avoir sur la signalisation calcique astrocytaire. En effet, autant au niveau subcellulaire qu'inter-cellulaire, les mécanismes gouvernant l'activité calcique des astrocytes restent mals connus. Même dans le cas le plus documenté de la réponse somatique des astrocytes à une stimulation neuronale, les caractéristiques précises que la stimulation doit avoir pour évoquer une réponse des astrocytes sont inconnues. Il en est de même pour la transmission de vagues de calcium dans des réseaux d'astrocytes: on ignore encore les possibles effets de la complexité récemment documentée des réseaux d'astrocytes sur la propagation de ces vagues. Enfin, au niveau subcelulaire, les astrocytes possèdent une morphologie ramifiée extrèmement complexe qui possède elle-même une activité calcique. Les travaux présentés dans cette thèse utilisent des outils de modélisation et de simulation afin de déterminer les répercussions que l'organisation en réseaux des astrocytes pourrait avoir sur leurs dynamiques calciques. En résumé, nous proposons que la topologie des réseaux d'astrocytes a (1) des répercussion au niveau cellulaire, modulant la réponse des astrocytes à des stimulations neuronales; (2) contrôle la propagation de vagues de calcium inter-astrocytaire en la favorisant lorsque les réseau sont peu couplés; (3) joue un rôle important dans l'apparation de phénomènes de résonance stochastique; (4) peut être dynamiquement modulée par l'activité neuronale.

MOTS-CLES :
Astrocyte, signalisation calcique, réseaux complexes, topologie de réseau, neurosciences computationnelles.

Laboratoire (s) de recherche :

Laboratoire d'Informatique en Image et Systèmes d'information

LIRIS CNRS UMR5205

Directeur de thèse:

Hugues Berry, INRIA

Président de jury :

Composition du jury :

Bruno Cessac (Directeur de Recherche INRIA, rapporteur)
Marja-Leena Linne (Research Team Leader , rapportrice)
Laurent Venance (Directeur de Recherche INSERM)
Aude Panatier (Chargée de Recherche CNRS)
Alain Destexhe (Directeur de Recherche CNRS)
Hédi Soula (Maître de conférence INSA)
Hugues Berry (Directeur de recherche INRIA).